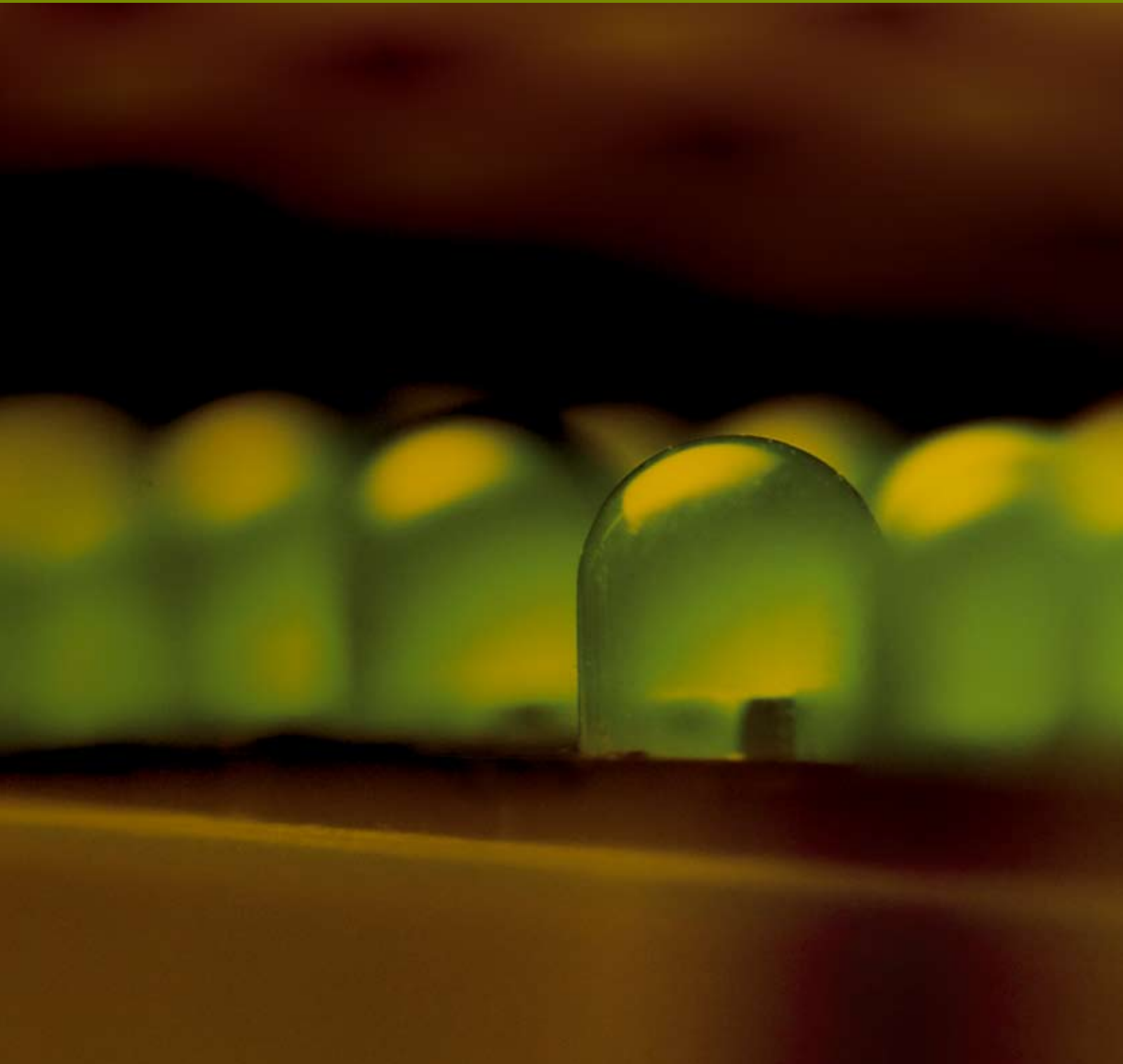


*Advances in OptoElectronics*

# **Recent Advances in Solar Cells**

**Guest Editor: Armin Aberle**





---

# **Recent Advances in Solar Cells**

Advances in OptoElectronics

---

## **Recent Advances in Solar Cells**

Guest Editor: Armin Aberle



---

Copyright © 2007 Hindawi Publishing Corporation. All rights reserved.

This is a special issue published in volume 2007 of "Advances in OptoElectronics." All articles are open access articles distributed under the Creative Commons Attribution License, which permits unrestricted use, distribution, and reproduction in any medium, provided the original work is properly cited.

## Editor-in-Chief

Frank Shi, University of California, USA

## Associate Editors

Armin G. Aberle, Australia  
Xian An Cao, USA  
Alison Chaiken, USA  
W.-C. Chen, Taiwan  
Philippe Goldner, France  
Volker Haerle, Germany  
Jung Y. Huang, Taiwan  
Alex K-Y. Jen, USA  
Dragana M. Jovic, Serbia  
A. J. Kenyon, UK

H. S. Kwok, China  
J. L. Lakshmana Rao, India  
Yalin Lu, USA  
Jong ha Moon, South Korea  
Bert Jan Offrein, Switzerland  
John Pern, USA  
Adrian Podoleanu, UK  
R. Reisfeld, Israel  
Lucimara Stolz Roman, Brazil  
Jayanta Kumar Sahu, UK

Somenath N. Sarkar, India  
Christian Seassal, France  
Devanand K. Shenoy, USA  
Vasily Spirin, Mexico  
Chang Q. Sun, Singapore  
Pieter L. Swart, South Africa  
Andreas Tuennermann, Germany  
C. P. Wong, USA  
Jianping Zhang, USA  
Nikolay Zheludev, UK

## Advisory Editors

Larry Crane, USA  
Hideya Kumomi, Japan

Alfred Margaryan, USA

P. M. Rentzepis, USA

# Contents

**Recent Advances in Solar Cells**, Armin Aberle

Volume 2007, Article ID 60319, 2 pages

**Industrial Silicon Wafer Solar Cells**, Dirk-Holger Neuhaus and Adolf Münzer

Volume 2007, Article ID 24521, 15 pages

**High-Efficiency Crystalline Silicon Solar Cells**, S. W. Glunz

Volume 2007, Article ID 97370, 15 pages

**Sliver Solar Cells: High-Efficiency, Low-Cost PV Technology**, Evan Franklin, Vernie Everett, Andrew Blakers, and Klaus Weber

Volume 2007, Article ID 35383, 9 pages

**Wafer Surface Charge Reversal as a Method of Simplifying Nanosphere Lithography for Reactive Ion Etch Texturing of Solar Cells**, Daniel Inns, Patrick Campbell, and Kylie Catchpole

Volume 2007, Article ID 32707, 4 pages

**Application of CBD-Zinc Sulfide Film as an Antireflection Coating on Very Large Area**

**Multicrystalline Silicon Solar Cell**, U. Gangopadhyay, K. Kim, S. K. Dhungel, H. Saha, and J. Yi

Volume 2007, Article ID 18619, 5 pages

**Advances in Contactless Silicon Defect and Impurity Diagnostics Based on Lifetime Spectroscopy and Infrared Imaging**, Jan Schmidt, Peter Pohl, Karsten Bothe, and Rolf Brendel

Volume 2007, Article ID 92842, 9 pages

**Silicon Thin-Film Solar Cells**, Guy Beaucarne

Volume 2007, Article ID 36970, 12 pages

**Annealing Kinetic Model Using Fast and Slow Metastable Defects for Hydrogenated-Amorphous-Silicon-Based Solar Cells**, Seung Yeop Myong

Volume 2007, Article ID 30569, 8 pages

**Polycrystalline Silicon Thin-Film Solar Cells on AIT-Textured Glass Superstrates**,

Per I. Widenborg and Armin G. Aberle

Volume 2007, Article ID 24584, 7 pages

**Rapid Thermal Annealing and Hydrogen Passivation of Polycrystalline Silicon Thin-Film Solar Cells on Low-Temperature Glass**, Mason L. Terry, Daniel Inns, and Armin G. Aberle

Volume 2007, Article ID 83657, 11 pages

**Thin-Film Solar Cells Based on the Polycrystalline Compound Semiconductors CIS and CdTe**,

Michael Powalla and Dieter Bonnet

Volume 2007, Article ID 97545, 6 pages

**Advances in High-Efficiency III-V Multijunction Solar Cells**, Richard R. King, Daniel C. Law, Kenneth M. Edmondson, Christopher M. Fetzer, Geoffrey S. Kinsey, Hojun Yoon, Dimitri D. Krut, James H. Ermer, Raed A. Sherif, and Nasser H. Karam

Volume 2007, Article ID 29523, 8 pages



---

**Recent Advances in Dye-Sensitized Solar Cells**, F. O. Lenzmann and J. M. Kroon  
Volume 2007, Article ID 65073, 10 pages

**Review of Recent Progress in Dye-Sensitized Solar Cells**, Fan-Tai Kong, Song-Yuan Dai,  
and Kong-Jia Wang  
Volume 2007, Article ID 75384, 13 pages

**Recent Advances in Organic Solar Cells**, Thomas Kietzke  
Volume 2007, Article ID 40285, 15 pages

**Silicon Quantum Dots in a Dielectric Matrix for All-Silicon Tandem Solar Cells**, Eun-Chel Cho,  
Martin A. Green, Gavin Conibeer, Dengyuan Song, Young-Hyun Cho, Giuseppe Scardera,  
Shujuan Huang, Sangwook Park, X. J. Hao, Yidan Huang, and Lap Van Dao  
Volume 2007, Article ID 69578, 11 pages

## Editorial

# Recent Advances in Solar Cells

**Armin Aberle**

*ARC Photovoltaics Centre of Excellence, School of Photovoltaic and Renewable Energy Engineering,  
The University of New South Wales, Sydney, NSW 2052, Australia*

Received 23 December 2007; Accepted 23 December 2007

Copyright © 2007 Armin Aberle. This is an open access article distributed under the Creative Commons Attribution License, which permits unrestricted use, distribution, and reproduction in any medium, provided the original work is properly cited.

The photovoltaics (PV) industry is booming, with annual growth rates well in excess of 30% per year over the last decade. This explosive growth has been driven by rapidly increasing fossil fuel prices, an almost universal acceptance of the link between global warming and human activity, the growing realisation of a gap between the increasing global demand for energy and the ability to supply, the implementation of market development programs to accelerate the deployment of sustainable energy options (particularly in Germany and Japan, but more recently also in Spain, France, Italy, South Korea, and several US states), and the escalating interest of the financial investment community in the business opportunities created by this rapid expansion. Sector revenue was over €15 billion in 2007 and is expected to exceed €100 billion/year within less than 10 years. Many studies have identified PV as the most promising of presently known energy generation options for a globally sustainable energy future, and many experts are convinced that PV—due to its unique advantages—will conquer a significant share of the global power market in the coming decades.

While current PV module production is around 3 GW<sub>p</sub> (gigawatt peak) per year, production levels of hundreds of gigawatts per year are required to contribute measurably to global electricity generation. The main challenge along this path is ongoing incremental reductions of the cost of PV-generated electricity (€/kWh). This requires continuous reductions of the manufacturing cost per unit area of the PV modules (€/m<sup>2</sup>), continuous improvements of the energy conversion efficiency of the modules (i.e., an improved W<sub>p</sub>/m<sup>2</sup> figure), or a combination of both, giving lower €/W<sub>p</sub> costs for the modules.

Today's mainstream PV technology (market share of about 90%) is based on crystalline silicon wafers. As outlined in this special issue, despite their maturity, silicon wafer-based PV technologies still have enormous potential with respect to lowering the €/W<sub>p</sub> costs of PV modules.

While today's silicon wafer-based modules cost €2-3 per W<sub>p</sub> to fabricate, it is realistic to assume that in 10 years, they will be fabricated at costs of €1.2-1.5 per W<sub>p</sub>. Thus, given the high conversion efficiency of silicon wafer-based modules, their proven long-term stability in the field (>20 years), and the robustness of the solar cell fabrication process, this PV technology is likely to dominate the PV market for at least another decade.

Due to greatly reduced semiconductor material consumption and the ability to (i) fabricate the solar cells on inexpensive large-area foreign substrates and (ii) to monolithically series-connect the fabricated solar cells, thin-film photovoltaics has the potential of achieving module fabrication costs of well below €1 per W<sub>p</sub>. As described in this special issue, thin-film PV technologies are developing rapidly, both in the laboratory and in industry. While amorphous silicon-based PV modules have been around for more than 20 years, recent industrial developments include the first polycrystalline silicon thin-film solar cells on glass and the first tandem solar cells based on stacks of amorphous and microcrystalline silicon films (micromorph cells). Globally, more than a dozen thin-film silicon PV lines are presently being commissioned or planned for amorphous and/or micromorph solar cells. The coming years will show whether these new thin-film silicon PV factories can compete with the established silicon wafer-based PV technologies. Significant thin-film PV production levels are presently also being set up for CIS (copper indium diselenide) and CdTe (cadmium telluride). The latter technology is expanding particularly rapidly, primarily due to First Solar. This company alone now has a global production capacity of about 200 MW<sub>p</sub>/year for thin-film PV modules.

Another area that is developing very well is the highest-performance concentrator solar cells based on epitaxial gallium arsenide films and their relatives. The article by Richard King's team at Spectrolab reports on the world's first 40%

efficient solar cells. This landmark result was achieved for a commercially relevant light concentration level ( $\sim 200$  suns) and a small number of solar cells in the stack (three). These very high cell efficiencies give hope that concentrator PV systems will soon be commercially competitive in many cloud-free regions of the world.

As can be concluded from the articles on dye-sensitised solar cells, this technology is also promising and has the potential to be commercially relevant for standard 1-sun applications within a decade. Furthermore, this special issue contains an article on “futuristic” solar cells based on silicon quantum dots. Artificial semiconductor materials featuring nanostructures might be necessary to realise the ultimate dream of ultra-high PV efficiency at low cost.

*Armin Aberle*

## Review Article

# Industrial Silicon Wafer Solar Cells

Dirk-Holger Neuhaus<sup>1</sup> and Adolf Münzer<sup>2</sup>

<sup>1</sup>Deutsche Cell GmbH, Berthelsdorfer Straße 111 A, 09599 Freiberg/Saxony, Germany

<sup>2</sup>SolarWorld Industries Deutschland GmbH, Otto-Hahn-Ring 6, 81739 München, Germany

Received 19 May 2007; Accepted 14 September 2007

Recommended by Armin Aberle

In 2006, around 86% of all wafer-based silicon solar cells were produced using screen printing to form the silver front and aluminium rear contacts and chemical vapour deposition to grow silicon nitride as the antireflection coating onto the front surface. This paper reviews this dominant solar cell technology looking into state-of-the-art equipment and corresponding processes for each process step. The main efficiency losses of this type of solar cell are analyzed to demonstrate the future efficiency potential of this technology. In research and development, more various advanced solar cell concepts have demonstrated higher efficiencies. The question which arises is “why are new solar cell concepts not transferred into industrial production more frequently?”. We look into the requirements a new solar cell technology has to fulfill to have an advantage over the current approach. Finally, we give an overview of high-efficiency concepts which have already been transferred into industrial production.

Copyright © 2007 D.-H. Neuhaus and A. Münzer. This is an open access article distributed under the Creative Commons Attribution License, which permits unrestricted use, distribution, and reproduction in any medium, provided the original work is properly cited.

## 1. INTRODUCTION

The photovoltaic industry has produced 2.54 GW of solar cells in 2006 [1]. 89.9% of these cells were made from mono- and multicrystalline silicon wafers, 7.4% from thin films (a-Si, CdTe, CIS), and 2.6% from silicon ribbons (EFG, string ribbons). In 1975, screen printing was first applied to solar cells for the formation of the front and rear contacts replacing expensive vacuum metallization [2]. In 2006, around 86% of all produced wafer-based silicon solar cells are still featuring screen-printed front and back contacts. Since 1975, process and equipment for the screen-printed solar cell has been further optimized and new technologies have been introduced to improve this technology. (i) Silicon nitride as an antireflection coating with excellent surface and bulk passivation properties [3]. (ii) Texture of the front surface to reduce reflection of mono- and multicrystalline silicon [4, 5]. (iii) Laser edge isolation and single-side etching for the electrical separation of the front and rear contacts [6, 7]. Today the standard screen-printed solar cell reaches average efficiencies of around 15% for multicrystalline and of around 16.5% for Czochralski silicon in the industry. Various research groups all over the world have been working on more advanced solar cell concepts and they successfully reached efficiencies well above 20% [8–10]. However, only a few of these more advanced technologies were introduced

into industrial production [11–15] having a market share of 14% of all wafer-based silicon solar cells in 2006.

In this article, we will look into processes and equipment currently used to produce standard screen-printed solar cells. We will then analyze the main optical and electrical losses occurring in this type of solar cell before we give an overview on more advanced solar cells with a higher efficiency potential produced by a few companies. Furthermore, we will look into the requirements a new solar cell technology has to fulfill to be used by the photovoltaic industry.

## 2. SCREEN-PRINTED SILICON SOLAR CELLS

Most screen-printed solar cells fabricated in the industry today are using the process sequence summarized in Table 1. This sequence consists of a relatively small number of process steps. Process equipment for this type of solar cell is commercially available, with a variety of different equipment and consumable manufacturers. A schematic drawing of this type of solar cell is shown in Figure 1. Today, the standard screen-printed solar cell reaches average efficiencies of around 15% for multicrystalline and around 16.5% for Czochralski silicon in industrial production. In the following sections, the process and most commonly used equipment for each process step is summarized.

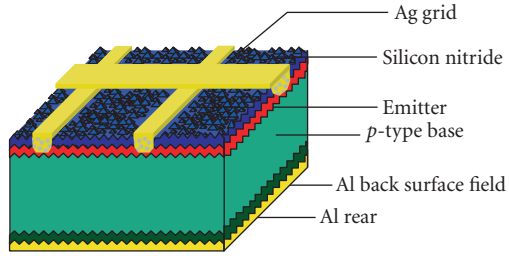


FIGURE 1: Schematic drawing of a solar cell with a silicon nitride antireflection coating and a screen-printed silver front and aluminum rear contacts.

TABLE 1: Process sequence for screen-printed solar cells.

- (1) Saw damage removal, texture, and cleaning of *p*-type silicon wafer
- (2) Phosphorus diffusion
- (3) Plasma edge isolation (alternatively, this process is often replaced by a single-side etching step integrated into the wet bench for phosphorus glass removal or by laser edge isolation placed after the firing step)
- (4) Phosphorus glass removal (and single-side etching for edge isolation)
- (5) Silicon nitride deposition
- (6) Ag screen printing of the front contact and drying
- (7) Al/Ag screen printing of the rear busbars and drying
- (8) Al screen printing of the rear and drying
- (9) Cofiring of the front and rear contacts
- (10) IV measurement and sorting

### 2.1. Saw damage removal, texture, and cleaning

Wire sawing is used to cut silicon ingots into wafers. This process induces small cracks penetrating around  $10\ \mu\text{m}$  deep into the wafer surface as shown in the left cross-section image of Figure 2. Saw damage has to be removed from the wafer surface, because it reduces the mechanical strength of the wafer and increases recombination in the surface region. Alkaline [4, 16, 17] or acidic [5, 18, 19] solutions as well as plasma etching can be used for saw damage removal. In addition, this process step is normally used to form a surface texture that reduces the total reflection of the wafer. After etching, the wafer is cleaned to remove metal and organic contaminants that would cause an increase of surface and bulk recombination during the following high-temperature process steps.

A solution of sodium hydroxide NaOH or potassium hydroxide KOH and water is normally used for alkaline saw damage removal on multi- or monocrystalline silicon wafers. The etching reaction can be summarized as  $\text{Si} + 2\text{H}_2\text{O} + \text{HO}^- \rightarrow \text{HSiO}_3^- + \text{H}_2$  and takes place in three reaction steps: (i) oxidation of silicon; (ii) formation of a solvable salt; and (iii) dissolving of the salt in water.

Alkaline etching has different etch rates for different crystallographic orientations. This anisotropy results in small pyramids with a square base randomly distributed over the wafer surface for monocrystalline silicon wafers with a (100) surface orientation. To improve the lateral uniformity

and the anisotropy of the etching process, isopropyl alcohol (IPA) is added to the etching solution. Applying this texture the total reflection of a polish-etched planar, silicon wafer can be reduced from 35 to 12% [4].

After texturing, the wafers are rinsed in deionized (DI) water, cleaned in hydrochloric acid (HCl), rinsed in DI water, cleaned in hydrofluoric acid (HF), rinsed in DI water, and finally dried in hot air. HCl removes metal impurities from the wafer surface. HF etches the native silicon dioxide off, removes metals with this surface, and forms a hydrophobic surface.

Alkaline saw damage removal, texture, and cleaning are performed in batch processes. Wafers are held in cassettes that allow chemicals to wet the entire surface. These cassettes are moved automatically from one to the other tank filled with chemicals and water for etching, cleaning, rinsing, and drying. For process control, the loaded cassettes are weighed before and after etching to determine the etching depth from the difference in weight.

Acidic texturing is an isotropic process. It is not dependent on the crystallographic orientation and it is therefore suited for saw damage removal and texturing of multicrystalline silicon. A solution of HF, nitric acid ( $\text{HNO}_3$ ), and water was introduced for saw damage removal and texture of multicrystalline silicon wafers [4]. The reaction takes place in two reaction steps: (i) oxidation given as  $3\text{Si} + 4\text{HNO}_3 \rightarrow 3\text{SiO}_2 + 2\text{H}_2\text{O} + 4\text{NO}$  and (ii) etching of silicon oxide given as  $3\text{SiO}_2 + 18\text{HF} \rightarrow 3\text{H}_2\text{SiF}_6 + 6\text{H}_2\text{O}$

Batch and inline equipment is commercially available for the acidic texture. For the inline process, the wafers are moved horizontally on rolls through tanks. For cleaning, DI water is sprayed onto the wafers. A typical process sequence is as follows: (i) saw damage removal and texture in  $\text{H}_2\text{O}$ ,  $\text{HNO}_3$ , and HF, (ii) spray rinse, (iii) KOH to etch porous silicon off that was formed during acidic texture, (iii) spray rinse, (iv) HCl clean, (v) spray rinse, and (vi) air drying. The etching time of commercial equipment is around 2 minutes per wafer adding up to around 2000 wafer/h for  $156 \times 156\ \text{mm}^2$  wafers.

The solar cell efficiency depends strongly on the etching depth of the acidic texture. If the etching depth is too shallow, crystal defects remain and the open-circuit voltage as well as the short-circuit current is reduced. If the etching depth is too deep, the surface roughness increases decreasing the open-circuit voltage and short-circuit current (increased surface recombination). The best solar cell efficiency has been found for an etching depth between 4 to  $5\ \mu\text{m}$  [18]. A solar cell efficiency improvement of 7% relative has been demonstrated if acidic-etched wafers were used instead of NaOH-etched wafers [19, 20]. Figure 2(c) shows a SEM microscopic surface image of an acidic-textured multicrystalline silicon wafer.

### 2.2. Diffusion

Most commonly used in the photovoltaic industry is a tube diffusion process. The wafers are vertically placed into a quartz boat. The boat moves into a quartz tube and is heated up to around 800 to  $900^\circ\text{C}$ . Nitrogen flows as a carrier gas

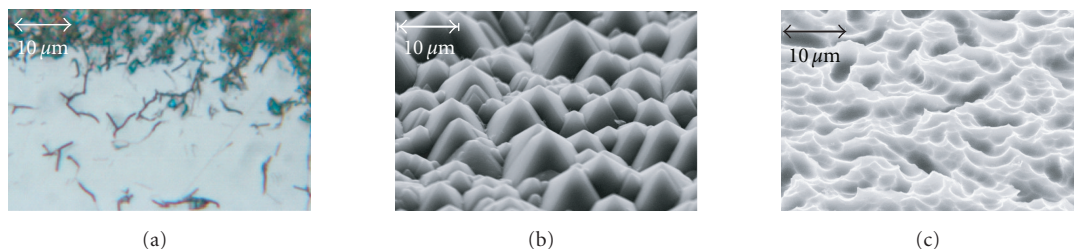


FIGURE 2: (a) Cross-section image of a wafer after wire sawing. (b) Top view of a wafer after alkaline texture in KOH, IPA, and water forming random pyramids. (c) SEM microscopic image of the surfaces of an acidic-textured multicrystalline silicon wafer [19].

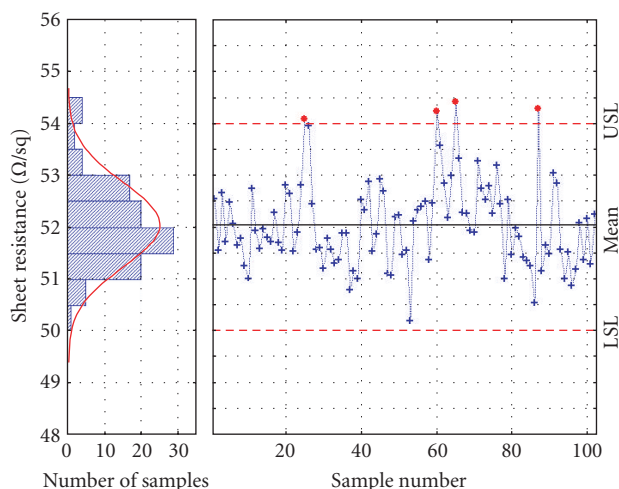


FIGURE 3: Control chart of the emitter sheet resistance measured with a contact-less inline method with the upper (USL) and lower specification limit (LSL) for the sheet resistance.

through a bubbler filled with liquid phosphorus oxychloride  $\text{POCl}_3$ . The formed gaseous  $\text{POCl}_3$  is mixed with  $\text{O}_2$  and conducted directly into the heated quartz tube. Phosphorus oxide  $\text{P}_2\text{O}_5$  deposits onto the wafer surfaces. The released  $\text{Cl}_2$  removes metal impurities. At the involved temperatures, phosphorus diffuses into the silicon forming a  $pn$  junction with the  $p$ -type base.

An alternative method is the deposition of diluted phosphoric acid  $\text{H}_3\text{PO}_4$  onto the wafer surface. The wafer moves horizontally on a conveyor belt through mist consisting of  $\text{H}_3\text{PO}_4$  and water. The drive-in of the phosphorus is performed on a conveyor belt firing furnace [21].

For the standard screen-printed solar cell, an emitter sheet resistance of 40 to 60  $\Omega/\text{sq}$  is normally in use. Figure 3 illustrates a control chart for the emitter sheet resistance measured with a contact-less inline method.

Phosphorus diffusion reduces the concentration of impurities by gettering. Impurity gettering is improved by increasing the diffusion time and reducing the peak temperature if the sheet resistance has to stay the same [22]. Additionally, it was shown that a double-sided diffusion gives better efficiencies than a single-sided diffusion [23].

### 2.3. Phosphorus glass removal and edge isolation

Phosphorus glass on the wafer surface is etched off using HF. It is very common to use a batch wet bench for this process. Most recently, inline equipment became commercially available to remove the phosphor glass. In addition, this equipment can perform single-side etching on the wafer to remove the emitter from one side [24]. The solar cell is transported on the surface of an etching bath in such a way that only the back side of the wafer is wetted. Using a solution of  $\text{H}_2\text{O}$ , HF,  $\text{HNO}_3$ , and  $\text{H}_2\text{SO}_4$ , the emitter is completely removed from the back side of the wafer. Consequently, the front and the rear sides of the solar cell are electrically isolated. The single-side etch is therefore an alternative process to plasma etching or laser edge isolation [7, 25, 26].

### 2.4. Silicon nitride deposition

A layer of silicon nitride  $\text{SiN}_x\text{:H}$  with up to 40 at% of hydrogen [3] is deposited onto the front side of the solar cell as an antireflection coating. After screen printing, the Ag contacts are fired through the  $\text{SiN}_x\text{:H}$  layer. To minimize optical losses, the  $\text{SiN}_x\text{:H}$  film has a thickness of around 75 nm and a refractive index of around 2.05. In addition,  $\text{SiN}_x\text{:H}$  serves as a good surface passivation to reduce recombination losses of the emitter [27–29]. Furthermore, hydrogen is released from the hydrogen-rich  $\text{SiN}_x\text{:H}$  film during a postdeposition anneal reducing bulk recombination in multicrystalline silicon [29, 30]. For the first screen-printed silicon solar cells, titanium dioxide  $\text{TiO}_2$  or thermally grown silicon dioxide  $\text{SiO}_2$  was used as an antireflection coating. However,  $\text{TiO}_2$  has no surface or bulk passivation properties; and the refractive index of  $\text{SiO}_2$  is too low for optimal optical performance [3]. The surface passivation properties of  $\text{SiO}_2$  are excellent, but it does not passivate bulk defects in multicrystalline silicon. Furthermore, oxidation requires high temperatures creating additional defects within multicrystalline silicon and reducing equipment throughput.

Today, plasma-enhanced chemical vapor deposition (PECVD) is most widely used in the photovoltaic industry to deposit  $\text{SiN}_x\text{:H}$  as an anti reflection coating. The PECVD method was invented in the field of microelectronics by Sterling and Swann in 1965 [31]. In 1981, the PECVD

method was first applied to solar cells by Hezel and Schörner [32]. Kyocera in Japan was the first company that used the PECVD method commercially for screen-printed multicrystalline silicon solar cells achieving good optical properties as well as good surface and bulk passivation [33]. A good overview of various  $\text{SiN}_x\text{:H}$  deposition techniques, its surface, and bulk passivation properties and its application to solar cells is given by Aberle [34] and Duerickx and Szlufcik [3]. Generally, there are four basic methods to form  $\text{SiN}_x\text{:H}$  films: (i) plasma-enhanced chemical vapour deposition (PECVD); (ii) atmospheric pressure chemical vapor deposition (APCVD); (iii) low-pressure chemical vapor deposition (LPCVD); and (iv) sputtering.

In the PECVD process, the deposited  $\text{SiN}_x\text{:H}$  film is formed in a reaction of silane  $\text{SiH}_4$  and ammonia  $\text{NH}_3$  at a temperature between 200 and 450°C and a pressure between 0.1 and 1 mbar. In *direct* PECVD, the process gasses are excited by an alternating electromagnetic field where the wafers form the electrodes. In batch systems, the wafers are loaded into graphite boats acting as electrodes. The wafers are processed in a quartz tube. An alternative approach is the *remote* PECVD process. For this method, the plasma excitation is spatially separated from the wafer. A linear plasma source is used, in which microwaves from an external source are coupled into the process chamber. The wafers are loaded onto CFC carriers and are moved horizontally through the plasma chamber. Direct and remote PECVD systems have the highest market share in the photovoltaic industry, because of their high throughput and low process temperatures.

In the LPCVD process, dichlorosilane  $\text{SiH}_2\text{Cl}_2$  and ammonia  $\text{NH}_3$  are used to form the  $\text{SiN}_x\text{:H}$  film on the wafer surface at a pressure between 0.01 and 1 mbar and temperatures around 750°C.  $\text{SiN}_x\text{:H}$  films deposited by means of the LPCVD method have a much lower hydrogen content than films deposited with the PECVD method. Consequently, the PECVD process is better suited for the bulk passivation of multicrystalline silicon. LPCVD batch systems are commercially available with a lower throughput than PECVD systems, because of the required cooling time for the process temperature of 750°C.

In the APCVD process, the chemical reaction takes place between silane  $\text{SiH}_4$  and ammonia  $\text{NH}_3$  at temperatures between 700 and 1000°C and atmospheric pressure (1000 mbar) to deposit  $\text{SiN}_x\text{:H}$  films. The APCVD method is mostly used in microelectronics.

Recently, it has been demonstrated that sputtered  $\text{SiN}_x\text{:H}$  films achieve similar surface and bulk passivation properties as  $\text{SiN}_x\text{:H}$  films deposited by PECVD [35, 36]. For this process, wafers are moved horizontally on a CFC carrier through the inline system. Two boron-doped silicon targets are alternately sputtered in argon and nitrogen using a mid-frequency power supply to deposit  $\text{SiN}_x$  onto the silicon wafer. By adding reactive gases like  $\text{H}_2$  or  $\text{NH}_3$ , the refractive index and the hydrogen content of the  $\text{SiN}_x\text{:H}$  layer can vary independently. For the sputter deposition of  $\text{SiN}_x\text{:H}$ , a temperature between 350 and 400°C and a base pressure of 0.001 to 0.03 mbar are used.

## 2.5. Screen printing of the front contact

Screen printing has its origins in stencil printing, a method which has already been used 1000 years ago. Stencil printing did not allow printing closed inside patterns such as the character “O.” The idea of screen printing developed when loose parts of the stencil were connected with fine wires. Later, the fine wires were replaced by a screen with area-blocked and area-open spaces where the ink can go through. Screen printing is extensively used for textile printing. During the 2nd World War, electronic circuit boards were manufactured using this technology. In 1975, screen printing was first applied to solar cells for the formation of front and rear contact printing Ag and Al pastes, respectively [2]. Today, screen-printing equipment for the formation of the front and rear contacts of solar cells is commercially available, with various manufactures for equipment, screens, and pastes. Screen-printing equipment is robust, simple, and can easily be automated. Most commercial screen printing lines have a net throughput of around 1000 and 2000 wafers/h for single and double lines, respectively. Solar cells up to  $210 \times 210 \text{ mm}^2$  in size can be processed on these lines.

The silicon wafer is moved on a conveyor belt or walking beam onto a printing table. The screen mounted into an aluminium frame has areas that are blocked off with a stencil (positive of the front grid to be printed) and areas that are open where the paste will go through later on. The screen is positioned and placed on top of the front side of the wafer with a defined distance between wafer and screen (snap-off distance). In the next step, a squeegee is moved without pressure over the screen to fill the screen openings uniformly with Ag paste (flooding of the screen). The squeegee is then moved with a defined pressure over the screen pressing the screen locally against the wafer surface and pushing the Ag paste from the filled areas of the screen onto the wafer surface. Due to the screen tension, the screen snaps off from the wafer in all areas where the squeegee is not pressing the screen against the wafer. After printing, the wafer is transported on a conveyor belt or walking beam through a drying furnace before being placed onto the next printing table for printing the rear side. At the end of the printing process, the front and the rear contacts are fired simultaneously in a firing furnace. A discussion of the impact of the different printing parameters on the quality of the print is given by Holmes and Loabsy [37].

The screen-printed front contact has to have the following features: (i) low contact resistance; (ii) no junction shunting; (iii) low specific resistance; (iv) high aspect ratio; (v) good adhesion to silicon; (vi) firing through  $\text{SiN}_x$ ; and (vii) good solderability for series interconnection with tabbing ribbons within the module.

The Ag paste for the formation of front contacts consists of (i) Ag powder (70 to 80 wt%), (ii) lead borosilicate glass  $\text{PbO-B}_2\text{O}_3\text{-SiO}_2$  (1 to 10 wt%), and organic components (15 to 30 wt%). The Ag powder sinters during firing and causes good lateral conductivity of the fingers. The  $\text{PbO-B}_2\text{O}_3\text{-SiO}_2$  frits are essential for the contact formation during

firing. PbO-B<sub>2</sub>O<sub>3</sub>-SiO<sub>2</sub> etches through the SiN antireflection coating, promotes the adhesion of the Ag contact to the silicon, reduces the melting point of Ag, and prevents Ag to diffuse into the *pn* junction causing junction shunting and space charge region recombination. However, the PbO-B<sub>2</sub>O<sub>3</sub>-SiO<sub>2</sub> layer formed between the conducting finger and the emitter is also the reason for the poor contact resistance of the screen-printed Ag contact [38]. The organic components determine the rheology of the paste. The viscosity of the paste reduces with the impact of squeegee movement to be extracted easily from the screen, it has to stay at a low-viscosity level to form a continuous finger (no string of pearls appearance), but then the viscosity has to increase again to keep a high aspect ratio and avoid that the finger flows apart [39].

The current understanding of contact formation and current transport of screen-printed contacts are given by Ballif et al. [40, 41] and Schubert et al. [38, 42, 43]. Below 600°C, the organic components burn out. Above 600°C, the contact formation takes place.

- (1) Lead borosilicate glass melts, wets, and etches the SiN surface while the Ag particles sinter to a conductive film.
- (2) A redox reaction between PbO and Si takes place forming liquid Pb. Ag and Si dissolve in liquid Pb etching inverted pyramids into the wafer surface.
- (3) During cooling, Ag and Pb separate according to the phase diagram. The Ag recrystallizes epitaxially in the inverted pyramids forming Ag crystallites at the wafer-glass interface. The Ag crystallites form isolated ohmic contacts to the emitter. Note that the sintered Ag thick film is separated from the emitter by a glass layer.
- (4) The current transport between these Ag crystallites into the sintered Ag thick film is assumed to take place at interconnections between crystallites and the sintered film, tunneling through ultra thin glass regions or multistep tunneling via metal precipitates that are formed in the glass layer during cooling.

## 2.6. Screen printing of the aluminium rear contact

The same screen printing equipment used for printing the front side is applied as well for printing the rear side. However, Al paste is used for the formation of a good ohmic rear contact and an Al back-surface field (BSF) to *p*-type silicon by Al doping of the rear surface region during firing. The doping profile and thickness of the BSF, the back surface reflectivity, the BSF homogeneity, and the wafer bow depend critically on the amount of Al paste printed onto the rear side of the wafer (between 6 and 10 mg/cm<sup>2</sup> of dried Al paste), the peak firing temperature, the type of paste and sufficient oxygen supply during firing [44]. A model for the formation of the screen-printed rear contact is given by Huster [44]. It follows a description of his model according to the numbers in Figure 4.

- (1) Al paste consists of Al powder, a glass frit to enhance sintering, and organic binders and solvents. After drying, a porous paste matrix covers the wafer surface. With the further temperature increase the organic binders burn out.
- (2) Melting of Al starts at 660°C which can be observed in a small plateau (latent heat). The aluminium oxide Al<sub>2</sub>O<sub>3</sub> surfaces of the Al particles stay in shape during the entire formation process. However, liquid Al penetrates through the Al<sub>2</sub>O<sub>3</sub> surface locally and gets in contact with the wafer surface and other Al particles. The wafer surface is not fully covered with Al at this stage.
- (3) Soon after melting, all Al paste particles reach thermal equilibrium. According to the phase diagram shown in Figure 4, more and more Si is dissolved in liquid Al with increasing temperature. The volume of the Al particles is limited by the Al<sub>2</sub>O<sub>3</sub> skin and stays therefore constant. If Si gets dissolved in the Al particles, the same volume of Al is transported out of the particles to the wafer surface.
- (4) At peak temperature, the entire wafer surface is covered with liquid Al-Si with exactly the same volume as that of the dissolved Si.
- (5) During cooling down, the process (3) occurs in reverse direction, that is, Si is rejected from the melt to recrystallize epitaxially on the wafer surface building up the Al-doped layer (Al BSF).
- (6) After reaching the eutectic temperature of 577°C, the remaining liquid phase solidifies instantly. The Al particles have the eutectic composition with 12% Si dissolved, a certain amount of Al is found on the wafer surface between the BSF and the film of Al particles.

## 2.7. Screen printing of the rear busbars

It is not possible to solder onto the screen-printed Al contact. Therefore, an Ag or Al/Ag paste is used to print busbars that can easily be soldered to tabbing ribbons for series interconnection to modules. It is important that the rear busbars or pads are kept as small as possible to reduce additional efficiency losses (no BSF underneath the Ag busbars), but that they are kept large enough to allow misalignments in the soldering process.

## 2.8. Firing

After screen printing, the front and the rear sides as described above with Ag and Al are fired simultaneously in a firing furnace (cofiring). The firing process is an inline process with the solar cells placed horizontally onto a metal conveyor belt. The furnace has several zones that can be heated up to 1000°C separately with IR heaters. The wafers can be heated from the front and the back, some furnaces have additional side heaters to adjust the lateral temperature uniformity. Firing furnaces are operated with a set air flow and exhaust. A simulated temperature profile for firing wafers is shown in Figure 4 featuring a

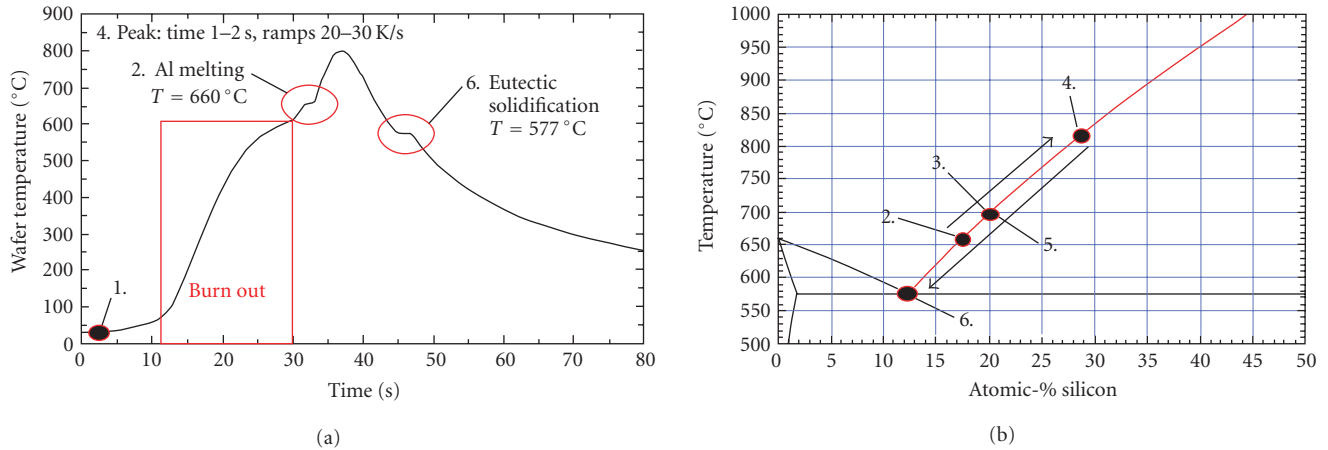


FIGURE 4: (a) Calculated temperature profile for firing Al paste through a silicon nitride layer and Al paste to form the rear contact of a silicon solar cell in a belt furnace [44]. (b) Calculated binary phase diagram of Al Si [44]. The distinctive points during the formation process are labeled in both graphs.

burn-out zone to burn organic binders and a sintering zone with a set peak temperature. In this zone, the front contact (firing through SiN, contact sintering, formation of the ohmic contact) and rear contact (BSF formation, contact sintering, formation of the ohmic contact, Al gettering) are formed and the hydrogen of the SiN<sub>x</sub>:H layer is released into the bulk of the wafer to passivate electrical defects. Profiling systems to record the temperature of a wafer traveling through the firing furnace are commercially available [45].

### 2.9. IV Measurement and sorting

At the end of the solar cell manufacturing process, the IV characteristics and the optical parameters of each individual solar cell are measured. The reason for this is (i) to determine the optical quality, (ii) to determine its current at the maximum power point and sort the cells into current classes to minimize mismatch losses in the module consisting of series-connected solar cells [46], (iii) to determine its reverse break through characteristics to avoid hot-spot heating within the module [47], and (iv) to determine solar cell parameters such as  $E_{ta}$ ,  $V_{oc}$ ,  $J_{sc}$ , and  $FF$  as a final process control.

Most IV testers consist of a halogen flash lamp that can stay constant for more than 50 milliseconds (1000 W/m<sup>2</sup>, reproducibility  $\pm 1.5\%$ , spectra class A, and uniformity of  $\pm 2\%$  after IEC60904-9). The IV characteristics are measured by a current-voltage curve tracer using a four quadrant power supply. The temperature of the solar cell is measured. A monitor cell is used to track changes in light intensity of the flash. The IV curves are measured using a four-point probe and they are corrected for changes in temperature and light intensity to 1000 W/m<sup>2</sup> and 25°C, respectively. It is important that IV testers are frequently calibrated using certified reference solar cells so that reproducibility can be controlled frequently [48].

### 3. ELECTRICAL AND OPTICAL LOSSES OF SCREEN-PRINTED SOLAR CELLS

Screen-printed fingers of industrially produced solar cells have a typical pitch of around 2 mm and are between 120 and 160  $\mu\text{m}$  wide. This, together with the two 2.0 mm wide busbars, causes a shading loss of around 8%. Research and development focus therefore on improving or replacing the current screen printing technology to achieve finer grid lines [49]. The internal back reflectance for a screen-printed Al contact is between 75% and 80% [44].

Currently, an emitter diffusion with a sheet resistance of around 40 to 60  $\Omega/\text{sq}$  and a surface doping concentration of above  $2 \times 10^{20} \text{ cm}^{-3}$  is used to fabricate screen-printed silicon solar cells. The high surface doping and low sheet resistance is necessary to achieve an acceptable contact resistance of around  $1.0 \times 10^{-3} \Omega\text{cm}^2$  as well as low junction shunting and recombination in the space charge region. However, this type of emitter has low open-circuit voltages (high surface recombination for emitters with high surface doping and Auger recombination) as well as poor short-circuit currents caused by a poor blue response (high-emitter recombination and free-carrier absorption). Good screen-printed contacts with a contact resistance of around  $1.0 \times 10^{-4} \Omega\text{cm}^2$  to “high efficiency emitters” with a sheet resistance above 100  $\Omega/\text{sq}$  and a surface doping of around  $1 \times 10^{19} \text{ cm}^{-3}$  are therefore the main task in developing high efficient industrial solar cells [38, 50, 51].

The specific line resistance of screen-printed fingers is around  $3.0 \times 10^{-6} \Omega\text{cm}$ , its average width and height is 130 and 12  $\mu\text{m}$ , respectively. The resulting line conductivity together with the contact resistance mentioned above results in average fill factors between 76% and 78%. For comparison, laboratory high efficiency solar cells using photolithography to define evaporated Ti/Pd/Ag contacts on selective emitters reach fill factors between 81% and 82% having a finger width of 20  $\mu\text{m}$ , a finger height of 8  $\mu\text{m}$ , a

specific finger resistance of  $1.7 \times 10^{-6} \Omega\text{cm}$ , and a contact resistance of  $1.0 \times 10^{-5} \Omega\text{cm}^2$ .

Fischer [52] determined for a 15% efficient multicrystalline silicon solar cell that only  $31.8 \text{ mA/cm}^2$  (its short circuit current density) of the  $35 \text{ mA/cm}^2$  generated in this solar cell are collected. These recombination losses occur with 41% in the base, 34% in the emitter, and 25% at the rear surface. In addition to these losses in short-circuit current, injected minority carriers are lost at the maximum power point (saturation current losses). Fischer [52] calculated for the 15% efficient multicrystalline silicon solar cell at the maximum power point additional losses of  $2.15 \text{ mA/cm}^2$ . 34% of these losses occur in the space charge region, 26% in the emitter, 25% in the base, 12% at the rear, and 4% via shunt resistances.

#### 4. REQUIREMENTS FOR A NEW SOLAR CELL TECHNOLOGY

Equipment, labor, land, and material costs, sales prices as well as technological aspects influence the return of investment of a company. Technology has an impact on (i) the solar cell, module, and system efficiency; (ii) the yield of the process; (iii) fixed costs; (iv) variable costs; and (v) the system lifetime.

##### 4.1. Efficiency

Improvements of the cell, module, or system efficiency reduce the cost in all process steps (wafer, cell, module, and balance of system), because most of the costs are area-related. Consequently, if the efficiency improves by a factor of  $\alpha$ , the production costs per watt decrease by a factor of  $\beta = 1/\alpha$  if everything else remains unchanged. Table 2 shows the overall cost improvements  $\beta$  associated with an efficiency improvement  $\alpha = 1.1$  in wafer, cell, or module manufacturing assuming no additional costs associated with this innovation. Rogol and Conkling [53] rate the breakdown of costs for wafer, cell processing, module manufacturing, and balance of system as  $w = 26.0\%$ ,  $c = 16.6\%$ ,  $m = 18.7\%$ , and  $s = 38.8\%$ , respectively. However, sometimes it is more interesting to know the maximum price for an improvement that is acceptable. Using (1) allows us to calculate the cost limit  $\gamma$  for wafer, cell, and module manufacturing is given in Table 2. If higher costs occur, the technology currently used is more cost-effective. Note that  $w$ ,  $c$ ,  $m$ , and  $s$  correspond to the breakdown of costs before the technology was changed,

$$\begin{aligned}\gamma_W &\leq \frac{\alpha - c - m - s}{w}, \\ \gamma_C &\leq \frac{\alpha - w - m - s}{c}, \\ \gamma_M &\leq \frac{\alpha - w - c - s}{m}.\end{aligned}\quad (1)$$

Very often, new developments to improve the solar efficiency are very expensive. Ready-made equipment does not exist.

A company has to develop its own process and equipment resulting in process sequences with more process steps, expensive equipment, and a low yield. Moreover, the screen printing technology has improved dramatically in yield and efficiency over the last years. These uncertainties are a burden for the introduction of new technologies.

##### 4.2. Yield

The yield of the overall manufacturing process from the wafer to the module is reduced by (i) wafer breakage, (ii) electrical losses such as solar cells with shunts or efficiencies below a threshold value, and (iii) solar cells that do not meet the optical requirements (color of antireflection coating, paste stains, etc.). The value of a wafer increases with each manufacturing step. Consequently, a wafer that gets lost during wafering has a smaller impact on the overall costs than a wafer that gets lost during module manufacturing. Equation (2) can be used to calculate the cost reduction  $\beta$  of the overall system costs using the yield improvement in wafering  $\alpha_W$ , cell processing  $\alpha_C$ , and module manufacturing  $\alpha_M$  as well as the cost breakdown of wafer, cell, module, and balance of system:

$$\beta = \frac{w + \alpha_W c + \alpha_W \alpha_C m + \alpha_W \alpha_C \alpha_M s}{\alpha_W \alpha_C \alpha_M}.\quad (2)$$

In a similar way as shown for efficiency improvements, it is possible to calculate the cost limit  $\gamma$  an innovation should not exceed, if a yield improvement is reached in wafer production  $\alpha_W$ , cell processing  $\alpha_C$ , and module manufacturing  $\alpha_M$  as shown in (3):

$$\begin{aligned}\gamma_W &\leq \frac{1 - c - m - s}{w} \alpha_W, \\ \gamma_C &\leq \frac{(1 - m - s)\alpha_C - w}{c}, \\ \gamma_M &\leq \frac{(1 - s)\alpha_M - w - c}{m}.\end{aligned}\quad (3)$$

If higher costs occur for an innovation in wafering  $\gamma_W$ , cell processing  $\gamma_C$ , and module manufacturing  $\gamma_M$ , the technology currently used is more cost-effective. Using (2) and (3), a yield improvement of  $\alpha = 1.1$  as well as the cost breakdown of Rogol and Conkling [53] for wafers  $w$ , cells  $c$ , modules  $m$ , and balance of system  $s$ , the cost reduction  $\beta$ , and the corresponding investment limit  $\gamma$  is shown in Table 2. It is clearly visible that the cost reduction increases with the value of the wafer within the value chain. The yield will be reduced with the introduction of thinner wafers for example. Estimating the yield reduction in wafering  $\alpha_W$ , cell processing  $\alpha_C$ , and module manufacturing  $\alpha_M$  allows you to estimate the required cost improvement in wafering  $\gamma_W$ , cell processing  $\gamma_C$ , and module manufacturing  $\gamma_M$ .

##### 4.3. Fixed costs

The costs for each process step can always be divided into fixed costs and variable costs that depend on the

TABLE 2: Calculation of the cost improvement  $\beta$  associated with a power or yield improvement  $\alpha$  in wafer, cell, or module manufacturing assuming no additional costs associated with this improvement as well as the cost breakdown of Rogol and Conkling for wafer, cell, module, and balance of system [53]. The technology cost limit  $\gamma$  gives the maximal cost increase that should be accepted for an innovation in wafer, cell, and module manufacturing. If higher costs occur, the technology currently in use is more cost-effective.

Improvement	Origin	Improvement $\alpha$	Cost improvement $\beta$	Cost limit $\gamma$
Power	Wafer	1.1	0.909	1.385
Power	Cell	1.1	0.909	1.602
Power	Module	1.1	0.909	1.535
Yield	Wafer	1.1	0.976	1.100
Yield	Cell	1.1	0.961	1.256
Yield	Module	1.1	0.944	1.328

consumption of goods (wafers, consumables, gasses, etc.). Fixed costs consist of equipment costs (cost of specific equipment and number of process steps), footprint per installed capacity for the technology, clean room requirements, and labor requirements (number of process steps and level of automation). A new technology always has to pay for the market introduction, some equipment for advanced processing is more expensive than the standard technology and new technologies require many more process steps than currently used to produce standard solar cells.

#### 4.4. Variable costs

Variable costs are all costs that depend on the consumption of raw materials and operating supplies. The consumption of these materials is related to the area of produced goods. If a new technology is able to process a thinner wafer than the current screen printing technology, this will reduce the cost of the raw materials. Furthermore, it is important for a new technology that the required consumables are unlimited. The price of Ag, for instance, has increased dramatically over the last years following a growing demand. Consequently, a new technology becomes more interesting if the consumption of Ag is replaced by cheaper materials.

#### 4.5. Lifetime of the system

A technological change should not shorten the lifetime of the final system. Extensive module reliability testing will have to be performed for new technologies. Experience with screen-printed solar cells has now been gathered over the last 30 years. Therefore, it is very safe for the photovoltaic industry to stay with this technology.

#### 4.6. Match to the current technology

It is a drawback for a new technology, if its implementation requires a change of all following manufacturing steps. For instance, the solar cell manufacturer introduces a back contact solar cell. Consequently, the module manufacturer has to change his entire fabrication method. This requires a larger investment and reduces the flexibility of the solar cell producer to sell his product to various costumers.

## 5. ADVANCED SOLAR CELL PROCESSES USED IN THE PHOTOVOLTAIC INDUSTRY

Various promising cell concepts from research and development are under investigation for commercialization. However, only a few more advanced solar cell technologies have already been introduced to industrial production. In the following, a short overview about the commercialized technologies is given first, followed by a more detailed description of the technologies.

Based on passivated emitter solar cells, the more industrial oriented technology of the laser-grooved buried contact (BC) solar cell was developed at the University of New South Wales, Australia, and licensed to a couple of companies. At BP Solar, a prominent representative of the licensees, a production was built up based on this technology and has produced up to 50 MW<sub>p</sub>/a [53].

The application of a back surface field (BSF) was known for a long time; and conventionally the screen-printed and alloyed Al-BSF is state-of-the-art. The application of boron to form the BSF has a higher efficiency potential and allows the use of thinner wafers with less bow. This technology was applied by Siemens Solar and has produced up to 70 MW<sub>p</sub>/a.

Another technological approach was the development of the heterojunction with intrinsic thin layer (HIT) solar cell by Sanyo, Japan. The peculiarity of the HIT solar cells is derived from the excellent passivation ability of the HIT structure on monocrystalline silicon. HIT cells reached already efficiencies above 20% and are fabricated by Sanyo in high volume production of about 170 MW<sub>p</sub>/a [53].

In conventional solar cells, the metal coverage on the cell front side is a compromise between shadowing and series resistance losses. A complete contact free cell front side would help effectively for an efficiency improvement and therefore back contact solar cells were developed, where all contacts are located at the solar cell rear side. Hereby, around 9% front-side metallization coverage is avoided and thus the efficiency potential is increased by about 9% relative. Moreover, the back contact solar cells allow the decoupling of the front side for optical performance, low surface recombination, and low series resistance.

First designs of interdigitated back contact (IBC) solar cells were investigated by Lammert and Schwartz [14]. The development and commercialization on monocrystalline silicon were carried out by Swanson et al. and the SunPower

Corporation. Meanwhile back contact solar cells are in production by SunPower in the range of  $60 \text{ MW}_p/\text{a}$  [53].

With regard to the trade-off between resistive and optical shadowing losses in the back contact solar cells the transport of the high currents is carried out in interconnections on the rear side. The co-planar arrangement of  $p$  and  $n$  contacts on the rear side allows also a simplified cell interconnection. Moreover, IBC solar cells can be closer spaced allowing a higher packing density within the module. The most common separation of the  $p$  and  $n$  regions on the rear side is an interdigitated structure where the  $p$  and  $n$  regions alternate.

Other concepts of back contact solar cell designs like the emitter wrap through (EWT) and the metallization wrap through (MWT) solar cells have a fraction of the collecting emitter on the cell rear side and an additional second carrier collecting junction at the cell front side leading to higher current collection. The EWT solar cell structure is especially beneficial for lower quality crystalline silicon material. EWT solar cells are produced by Advent Solar Inc. (NM, USA). MWT solar cells are also capable for the application on lower quality silicon because of their emitter and metallization gridlines on the cell front side and the emitter and base contact on the rear side, however, only a moderate reduction of the front side shadowing is reached. MWT solar cells have not been transferred into large scale production yet.

### 5.1. Buried contact solar cells

The BC solar cell concept [11] was invented at the University of New South Wales by Green et al. in 1983 and was patented in 1985 [54]. The development of BC solar cells evolved as a process simplification from high efficiency processing based on microelectronics and was motivated by the fabrication of high efficiency solar cells applying low cost technologies. Therefore the emphasis during the development of BC solar cells was on the establishment of simple and low cost processes and techniques which were suitable for large area solar cells and for mass production. In contrast to high efficiency solar cells of its time the resulting processing sequence requires no photolithography, no expensive anti reflection coatings and avoids the use of an expensive metallization scheme.

The main advantages of BC solar cells are smaller contact widths of the finger metallization compared to conventional screen printing. Smaller finger widths allow for closer finger spacing, which is important for emitters with a high sheet resistance of around  $100 \Omega/\text{sq}$ . Based on the laser grooves the metallization reaches a higher aspect ratio (ratio of finger depth to width) which results in an excellent finger conductivity. Relatively simple and reliable realization of a selective emitter structure even in an industrial environment was achieved consisting of an entire shallow emitter diffusion and a heavy diffused emitter underneath the metal contacts. This structure results in a low contact resistance and contact recombination of the finger metallization. A selective metal deposition is applied based on electro-less plating.

In 1985 BP Solar licensed the BC solar cell technology. The scope of the subsequent development work was wide

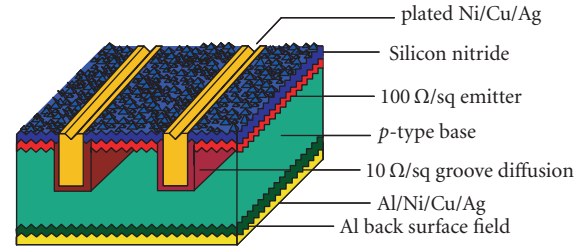


FIGURE 5: Schematic drawing of a buried contact solar cell.

TABLE 3: Inferred fabrication steps for BC solar cells of BP Solar.

- |  |
|--|
| (1) Saw damage removal, texture and cleaning of $p$ -type silicon wafer                        |
| (2) $\text{P}_2\text{O}_5$ deposition on front side  |
| (3) CVD silicon nitride deposition onto front side   |
| (4) Laser groove   |
| (5) Groove damage etch and cleaning  |
| (6) Heavy $\text{POCl}_3$ phosphorus diffusion and shallow $\text{P}_2\text{O}_5$ co-diffusion |
| (7) Al evaporation to the rear   |
| (8) Rear contact diffusion   |
| (9) Electroless plating of Ni  |
| (10) Sintering   |
| (11) Etching   |
| (12) Electroless plating of Cu and Ag  |
| (13) Laser edge isolation  |
| (14) IV measurement and sorting  |

ranging and included different methods and materials for the following key steps in cell production: Grooving of the silicon,  $pn$  junction formation, dielectric surface passivation, rear surface treatment and metallization. The result was the solar cell structure given in Figure 5.

The front grid pattern is fabricated by laser grooving cutting  $20 \mu\text{m}$  wide and  $30 \mu\text{m}$  deep into the surface of the silicon using a high speed, pulsed Nd-YAG laser [55, 56]. For the formation of the emitter a  $\text{P}_2\text{O}_5$  film is applied as the dopant source for the active silicon surface, whilst  $\text{POCl}_3$  vapor is used to dope the exposed silicon in the grooves. In this way, the surface is lightly doped for optimum current collection over the entire solar spectrum, whilst the groove regions are more heavily doped for low grid resistance characteristics and metal junction formation. The resulting sheet resistance of the  $n$ -type surface and groove region is  $100 \Omega/\text{sq}$  and  $10 \Omega/\text{sq}$ , respectively [56]. The rear surface of the cell is coated with a thin film of Al using vacuum deposition followed by a high temperature sintering process. The cometallization of the front and rear surfaces is achieved by a sequence of electro-less plating using Ni, Cu and Ag, with intermediate metal sintering. BC solar cells reach in production average efficiencies of about 17%, best solar cells with 18.3% have been demonstrated [57]. According to the descriptions in [55, 58] the following manufacturing process of BC solar cells is summarized in Table 3.

Limitations of the current BC solar cells arise from their thin Al film on the solar cell rear side as described in [58].

Therefore, latest developments are in direction of solar cells with buried contact grid on the solar cell front side and laser fired contacts on the solar cell rear side [56, 59].

### 5.2. Boron back-surface-field solar cells

Screen-printed Al paste and firing is commonly used for the formation of the BSF. A major drawback of this technology is wafer bowing, especially when the wafers become thinner. Furthermore, the passivation quality of the Al BSF is limited by the recombination rate of alloyed Al on Si. Another dopant candidate for the BSF formation on *p*-type silicon is boron. A boron BSF has a better surface passivation and avoids wafer bowing. However, the application of boron is technologically more difficult. Boron diffusion out of the gas phase needs additional processing steps to reach a BSF only on the cell rear side. Therefore a one-sided fabrication process was developed by Siemens Solar [60] using one-sided boron coating on the rear side and a subsequent boron drive-in at an elevated temperatures. An advantage of the boron BSF solar cell is that the additional process steps for the application of the boron BSF could be implemented in an unchanged remaining process sequence for conventional screen-printed solar cells. A low surface reflection was reached by the combination of a surface texture with an additional silicon nitride anti reflection coating. For the emitter formation a conventional phosphorus gas diffusion using  $\text{POCl}_3$  is used. For the metallization conventional Ag screen printing on the front and rear sides of the cells is applied. With this process an efficiency improvement of over 10% relative is achieved.

The boron BSF process was implemented into mass production and around 60  $\text{MW}_p/a$  were produced at Siemens Solar and their succeeding companies Shell Solar and SolarWorld. Table 4 and Figure 6 show the main solar cell fabrication steps and a schematic drawing of this type of solar cell, respectively.

For further improvements in efficiency a selective emitter structure was developed. With respect to retain cost effective screen printing, a locally highly doped emitter below the screen-printed contacts was developed. Applying the shallow emitter technology to boron BSF solar cells an average cell efficiency of 18.4% was reached on more than 500 cells, the best solar cell had an efficiency of 18.8% [61]. These selective emitter solar cells exhibit a high red response due to the boron back surface field and an almost constant blue response due to the shallow light receiving emitter. The red response could be even improved by the application of a light reflection layer on the solar cell rear side, for example evaporated Al, to enhance the solar cell rear side reflection.

### 5.3. Heterojunction with intrinsic thin layer solar cells

Sanyo developed the HIT solar cell combining amorphous silicon and monocrystalline silicon [13]. This approach was very successful and Sanyo achieved a total area solar cell efficiency of over 20% [62]. The high efficiency is derived from the excellent passivation ability of the HIT structure on monocrystalline silicon. The non-doped amorphous silicon

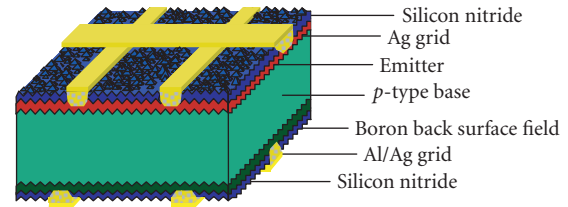


FIGURE 6: Schematic drawing of a boron BSF solar cell of SolarWorld.

TABLE 4: Fabrication steps for boron BSF solar cells by SolarWorld.

- (1) Saw damage removal, texture and cleaning of *p*-type silicon wafer
- (2) Boron coating
- (3) Boron drive-in
- (4) Boron glass removal
- (5) Phosphorus diffusion
- (6) Phosphorus glass removal
- (7) Edge isolation
- (8) Silicon nitride deposition
- (9) Screen printing front side
- (10) Screen printing rear side
- (11) Firing
- (12) IV measurement and sorting

(*i*-type a-Si:H) film is sandwiched between *p*-type a-Si:H and the *n*-type monocrystalline silicon wafer on the solar cell front side forming the heterojunction emitter. A further improvement in efficiency was reached by implementing a BSF formed from an *i*-type a-Si:H film sandwiched between *n*-type a-Si:H and the *n*-type monocrystalline silicon wafer on the solar cell rear side.

In production [62] a very thin *i*-type a-Si:H layer and a *p*-type a-Si:H layer with a total thickness of about 10 nm are deposited by plasma CVD on the front of a textured *n*-type solar grade Czochralski monocrystalline silicon wafer of about 1  $\Omega\text{cm}$  and of about 200  $\mu\text{m}$  thickness. Another very thin *i*-type a-Si:H layer and an *n*-type a-Si:H layer with a total thickness of about 20 nm are deposited at the rear side of the wafer. A transparent conductive oxide TCO is formed on each side of the wafer using sputtering. Ag electrodes are formed on the two wafer sides with a silkscreen printing method. All processes are performed at temperatures below 200°C. There is no need of photo-masking or processing cycles at temperatures as high as 1000°C that might cause thermal damage to the wafer. Besides, the symmetry of the HIT structure also allows solar electricity generation when the solar cell is illuminated from the rear side. In summary, the inferred solar cell fabrication steps as described in [62] are given in Table 5. Figure 7 shows a schematic drawing of this type of solar cell.

Sanyo developed the HIT structure and demonstrated cell efficiencies up to 21.5% [63]. After implementation of the HIT solar cell fabrication process into production the average cell efficiency is estimated to about 18% to 20% according to their module power output. Another feature of the HIT solar cells is its excellent temperature characteristics,

TABLE 5: Inferred fabrication steps for HIT solar cells produced by Sanyo, according to [62].

- (1) Saw damage removal, texture and cleaning of *n*-type silicon wafer
- (2) Deposition of *i*-type and of *p*-type a-Si:H to the front side
- (3) Deposition of *i*-type and *n*-type a-Si:H to the rear side
- (4) Deposition of TCO to the front side
- (5) Deposition of TCO to the rear side
- (6) Silver silk screen contact print to the front side
- (7) Silver silk screen contact print to the rear side
- (8) Contact sintering
- (9) Contact solder coating
- (10) IV measurement and sorting

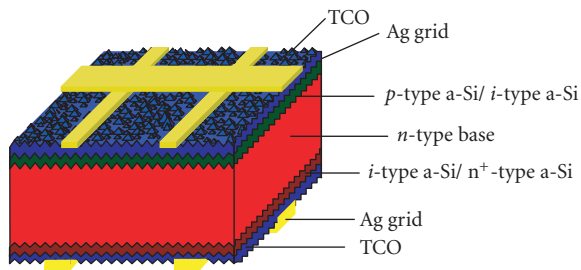


FIGURE 7: Schematic drawing of a HIT solar cell produced by Sanyo.

better than the temperature dependence of conventional *pn* junction solar cells. This superior temperature dependence results in up to 10% higher module power output at standard test conditions. An efficiency limitation of today's HIT solar cells is obviously in the moderate short circuit current density of around  $36 \text{ mA/cm}^2$ , possibly due to the transparency of the transparent conductive oxide layer on the solar cell front side.

#### 5.4. Interdigitated back contact solar cells

High efficiency back junction solar cells have a collecting junction only on the solar cell rear surface whereas the front surface is well passivated. The minority carriers, which are mainly generated at the front surface, have to diffuse a long way to the rear junction. Hence, back junction solar cells require a high ratio of bulk diffusion length to cell thickness.

First designs of interdigitated back contact (IBC) solar cells were investigated by Lammert and Schwartz [14]. For the carrier collection and transport, the doped areas and the electrode contacts are alternating (interdigitated arrangement). For the development of high-efficiency IBC solar cells, point contacts were introduced by Sinton et al. [64] to reduce the rear surface recombination. The rather complex manufacturing process in the beginning was simplified by a trench mesa design, which involves only one photolithography step and no alignment steps at all [65]. A first commercialization was carried out by the SunPower Corporation (CA, USA).

Key design features that contribute to high efficiency include localized back contacts with reduced contact recombination losses, a gridless front surface which permits

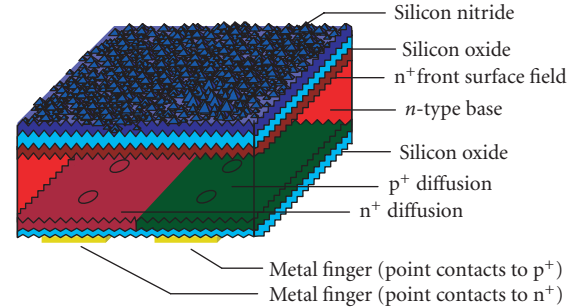


FIGURE 8: Schematic drawing of an IBC solar cell of SunPower.

optimization of light trapping and passivation, and a backside metallization approach that provides internal rear surface reflection and very low series resistance. Because the minority carriers must diffuse through the entire wafer thickness to reach the collecting junctions at the rear, the IBC solar cell design requires extraordinarily high lifetime silicon starting material. SunPower is using wafers with lifetimes greater than 1 millisecond and a thickness of  $200 \mu\text{m}$  [66]. With regard to low-cost processing of the diffusion, the wet etching and the cleaning were adapted to industrial processes. A simple texture process is used for the generation of a random texture on the front side. PECVD silicon nitride deposition is applied. To reduce fabrication cost, the pattern of the rear side for boron and phosphorus diffusion was developed with low-cost screen printing technology to replace photolithography in the fabrication of IBC solar cells [67, 68]. Silicon dioxide is formed on the entire rear side, and a pattern of holes in the oxide at the boron and phosphorus diffused areas is generated. For good light reflectance, aluminum is deposited as first metal layer on the planar silicon dioxide coated rear side and patterned according to the *p*- and *n*-doped regions. For electrical conductivity, the patterned aluminium areas are plated with Ni as a diffusion barrier and to achieve good contact resistance against Cu. The Ni plating is followed by plating of Cu for electrical conductivity and finished by a flash of Ag to protect the Cu. The solar cell fabrication is then completed by an annealing step for the contact formation. As an overview, the IBC solar cell structure is shown in Figure 8 and the inferred solar cell fabrication steps according to [65–67] are given in Table 6. SunPower demonstrated IBC solar cells with efficiencies of 21.5%. In production, the average efficiency is estimated to be over 20%.

Limitations of IBC solar cell fabrication arise from the requirement of silicon wafers with high minority carrier lifetimes, which restricts the silicon quality choice [68], but the wide tolerance on the wafer thickness and resistivity help for tolerable wafer cost [69].

#### 5.5. Emitter wrap through solar cells

The basic idea of emitter wrap through (EWT) solar cells [15] is to leave all metal contacts on the solar cell rear side, but to use a front-side emitter for additional current collection. The electrical interconnection between the front-

TABLE 6: Inferred fabrication steps for IBC solar cells of Sunpower.

- (1) Saw damage removal and cleaning of *n*-type silicon wafer
- (2) Boron diffusion
- (3) Boron glass removal
- (4) Rear-side SiN<sub>x</sub>
- (5) Front-side boron etching
- (6) Oxidation
- (7) Pattern of rear side for phosphorus diffusion
- (8) Rear-side phosphorus diffusion
- (9) Front-side oxide etching and texture
- (10) Front-side phosphorus diffusion
- (11) Diffusion glass removal
- (12) Silicon nitride deposition on front and rear sides
- (13) SiN<sub>x</sub> patterning for contact points
- (14) Aluminium sputtering
- (15) Aluminium patterning
- (16) Plating Ni, Cu, Ag
- (17) Annealing
- (18) IV measurement and sorting

side emitter and the rear-side emitter is accomplished by laser-drilled holes which have a heavy phosphorus diffusion and, if possible, are metallized for higher conductivity. The number of holes required for EWT solar cells is in the range of some tens per 1 cm<sup>2</sup>. In principal, EWT solar cells are designed similar to IBC solar cells with an additional emitter on the solar cell front side and holes for the connection of the front to the rear-side emitter. Applying sophisticated fabrication processes including photolithography, best cell efficiencies of 21.4% have been reached on a small area of 4 cm<sup>2</sup> and float-zone silicon [70]. Applying industrial process technologies, efficiencies of 16.1% were reported on 100 cm<sup>2</sup> solar cells on Czochralski silicon [71].

With regard to low-cost production, Advent Solar is going to produce EWT solar cells using multicrystalline silicon wafers and conventional industrial solar cell processing [72, 73]. Starting with about 1 Ωcm *p*-type multicrystalline wafers, EWT solar cells are fabricated by laser drilling a 2 mm × 0.75 mm hole grid pattern. The holes are about 60 μm in diameter. The wafer is then etched and cleaned. To achieve low-cost EWT solar cells, it is important to define *n*- and *p*-type regions on the rear side for the emitter and the base contact. A screen-printed glass or dielectric layer is applied by Advent Solar to the wafer base as a diffusion barrier to isolate the *p*- and *n*-type regions and to block locally the diffusion of phosphorus for the separation of *n*- and *p*-metallization regions in EWT solar cells.

The screen-printed diffusion barrier also acts as a barrier to the diffusing species, which are used to form the emitter or the base junction. The phosphorus diffusion barrier has a 0.35 μm wide open channel [72]. Al is later printed and alloyed to compensate the exposed region in the channel. After diffusion, the phosphorus glass is etched off, but the diffusion barrier is not etched off. SiN<sub>x</sub>:H is applied on both sides. Al lines are printed over the 0.35 μm channels and Ag lines are printed connecting the holes and sequentially

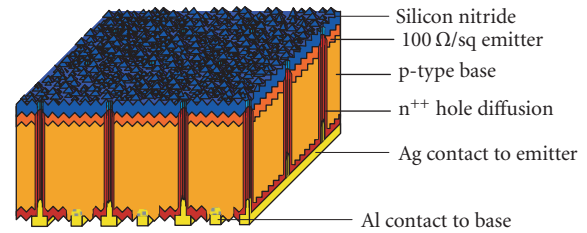


FIGURE 9: Schematic drawing of an EWT solar cell of Advent Solar.

TABLE 7: Inferred fabrication steps for EWT solar cells produced by Advent Solar according to [72].

- (1) Laser hole drilling into *p*-type silicon wafer
- (2) Saw damage removal, texture, and cleaning
- (3) Screen printing of diffusion barrier containing an open channel
- (4) Phosphorus diffusion
- (5) Phosphorus glass etching
- (6) Silicon nitride deposition to front and rear sides
- (7) Al printing to *p*-type region in channels
- (8) Ag printing to *n*-region and connecting holes
- (9) Firing
- (10) IV measurement and sorting

fired to form contacts. In this configuration, the diffusion barrier serves to isolate the *p*-metallization and provide a surface passivation on the base. A feature is also that the Al metallization is made wider than the contact width, thus allowing for improved line conductivity. The solar cell fabrication steps according to [72] are given in Table 7 and the solar cell structure is shown in Figure 9.

In production, EWT solar cells with efficiencies of 15.2%, about 600 mV open circuit voltages, 35.4 mA/cm<sup>2</sup> short circuit current densities, and 71.3% fill factors have been reached with screen-printed Ag metallization [72]. With the deposition of an additional solid metal conductor, the series resistance could be improved and best EWT solar cell efficiencies of 15.6% together with 600 mV open circuit voltages, 36.3 mA/cm<sup>2</sup> short circuit current densities, and 71.6% fill factors could be reached [73]. A number of standard optimizations, along with the attention to improve the series resistance, are expected to raise the mean EWT cell efficiency to 16% in the near future. Advent Solar offered a 170 W<sub>p</sub> module in 2006 in correspondence to the mentioned solar cell parameters.

## 6. SUMMARY

In 2006, around 86% of all wafer-based silicon solar cells are featuring screen-printed front and rear contacts as well as silicon nitride as the antireflection coating with excellent surface and bulk passivation properties. We look into this dominant solar cell technology and its fundamentals. Currently used processes and equipment for the standard screen-printed solar cell are discussed for all process steps in detail: (i) saw damage removal, texture, and cleaning, (ii) phosphorus diffusion, (iii) phosphorus glass removal and

edge isolation, (iv) silicon nitride deposition, (v) Ag screen printing of the front contact, (vi) Al/Ag screen printing of the rear busbars, (vii) Al screen printing of the rear, (viii) firing, and (ix) IV measurement and sorting. Average solar cell efficiencies of around 15% for multicrystalline and around 16.5% for monocrystalline Czochralski silicon are standard in the industry. The main optical and electrical losses of this technology are discussed. Also, the requirements for a solar cell technology under industrial environment are considered. With regard to higher cell efficiencies, advanced solar cell concepts are studied. To date, only a few of these more advanced technologies were introduced into industrial production having a market share below 15% of all wafer-based silicon solar cells in 2006.

## ACKNOWLEDGMENTS

We would like to thank C. Bellmann, B. Bitnar, H.-P. Hartmann, J. König, G. Krödel, R. Lüdemann, P. Magnucz, F. Schitthelm, E. Schneiderlöchner, D. Sontag, S. Steckemetz, and M. Wagner of Deutsche Cell, R. Schlosser of SolarWorld Industries Deutschland (München, Germany), G. Erfurt, M. Heemeier, D. Hubatsch, A. Krause, and M. Kutzer of Deutsche Solar, C. Fredrick, K. Holdermann, J. Hummel, T. Jester, B. Klebensberger, L. Mandrel, and P. Norum of SolarWorld Industries America (CA, USA) for detailed and exciting technology discussions and fruitful input. Many thanks are due to M. Prondzinski for drawing the solar cell schematics.

## REFERENCES

- [1] W. P. Hirshman, G. Hering, M. Schmela, and A. Kreuzmann, "Die neue Maßeinheit heißt Gigawatt," *Photon*, vol. 4, p. 52, 2006.
- [2] E. L. Ralph, "Recent advancements in low cost solar cell processing," in *Proceedings of the 11th IEEE Photovoltaic Specialists Conference (PVSC '75)*, pp. 315–316, Scottsdale, Ariz, USA, May 1975.
- [3] F. Duerickx and J. Szlufcik, "Defect passivation of industrial multicrystalline solar cells based on PECVD silicon nitride," *Solar Energy Materials and Solar Cells*, vol. 72, no. 1–4, pp. 231–246, 2002.
- [4] D. L. King and M. E. Buck, "Experimental optimization of an anisotropic etching process for random texturization of silicon solar cells," in *Proceedings of the 22nd IEEE Photovoltaic Specialists Conference (PVSC '91)*, vol. 1, pp. 303–308, Las Vegas, Nev, USA, October 1991.
- [5] R. Einhaus, E. Vazsony, J. Szlufcik, J. Nijs, and R. Mertens, "Isotropic texturing of multicrystalline silicon wafers with acidic texturing solutions," in *Proceedings of the 26th IEEE Photovoltaic Specialists Conference (PVSC '97)*, pp. 167–170, Anaheim, Calif, USA, September–October 1997.
- [6] F. Delahaye, M. Löhrmann, M. Bauer, et al., "Edge isolation: Innovative inline wet processing ready for industrial production," in *Proceedings of the 19th European Photovoltaic Solar Energy Conference (EU PVSEC '04)*, pp. 416–418, Paris, France, June 2004.
- [7] A. Hauser, G. Hahn, M. Spiegel, et al., "Comparison of different techniques for edge isolation," in *Proceedings of the 17th European Photovoltaic Solar Energy Conference (EU PVSEC '01)*, pp. 1739–1742, Munich, Germany, October 2001.
- [8] M. A. Green, K. Emery, D. L. King, Y. Hishikawa, and W. Warta, "Solar cell efficiency tables (version 28)," *Progress in Photovoltaics*, vol. 14, no. 5, pp. 455–461, 2006.
- [9] J. Zhao, A. Wang, and M. A. Green, "24.5% efficiency PERT silicon solar cells on SEH MCZ substrates and cell performance on other SEH CZ and FZ substrates," *Solar Energy Materials and Solar Cells*, vol. 66, no. 1–4, pp. 27–36, 2001.
- [10] O. Schultz, S. Riepe, and S. W. Glunz, "Thermal degradation and gettering of solar grade multicrystalline silicon," in *Proceedings of the 19th European Photovoltaic Solar Energy Conference (EU PVSEC '04)*, p. 604, Paris, France, June 2004.
- [11] M. A. Green, A. W. Blakers, S. R. Wenham, et al., "Improvements in silicon solar cell efficiency," in *Proceedings of the 18th IEEE Photovoltaic Specialists Conference (PVSC '85)*, pp. 39–42, Las Vegas, Nev, USA, October 1985.
- [12] K. A. Münzer, R. R. King, R. E. Schlosser, J. Schmalzbauer, S. Sterk, and H. L. Mayr, "Manufacturing of back surface field for industrial application," in *Proceedings of the 13th European Photovoltaic Solar Energy Conference (EU PVSEC '95)*, pp. 1398–1401, Nice, France, October 1995.
- [13] M. Taguchi, M. Tanaka, T. Matsuyama, et al., "Improvement of the conversion efficiency of polycrystalline silicon thin film solar cell," in *Proceedings of the 5th International Photovoltaic Science and Engineering Conference (PVSEC '90)*, pp. 689–692, Kyoto, Japan, November 1990.
- [14] M. D. Lammert and R. J. Schwartz, "The interdigitated back contact solar cell: a silicon solar cell for use in concentrated sunlight," *IEEE Transactions on Electron Devices*, vol. 24, no. 4, pp. 337–342, 1977.
- [15] R. N. Hall and T. J. Soltys, "Polka dot solar cell," in *Proceedings of the 14th IEEE Photovoltaic Specialists Conference (PVSC '80)*, pp. 550–553, San Diego, Calif, USA, January 1980.
- [16] H. Seidel, L. Csepregi, A. Heuberger, and H. Baumgärtel, "Anisotropic etching of crystalline silicon in alkaline solutions—I: orientation dependence and behavior of passivation layers," *Journal of the Electrochemical Society*, vol. 137, no. 11, pp. 3612–3626, 1990.
- [17] H. Seidel, L. Csepregi, A. Heuberger, and H. Baumgärtel, "Anisotropic etching of crystalline silicon in alkaline solutions—II: influence of dopants," *Journal of the Electrochemical Society*, vol. 137, no. 11, pp. 3626–3632, 1990.
- [18] A. Hauser, I. Melnyk, P. Fath, S. Narayanan, S. Roberts, and T. M. Bruton, "A simplified process for isotropic texturing of mc-Si," in *Proceedings of 3rd World Conference on Photovoltaic Energy Conversion (WCPEC '03)*, vol. 2, pp. 1447–1450, Osaka, Japan, May 2003.
- [19] C. J. J. Tool, G. Coletti, F. J. Granek, et al., "17% mc-Si solar cell efficiency using full in-line processing with improved texturing and screen-printed contacts on high-ohmic emitters," in *Proceedings of the 20th European Photovoltaic Solar Energy Conference (EU PVSEC '05)*, pp. 578–583, Barcelona, Spain, June 2005.
- [20] A. Hauser, I. Melnyk, E. Wefringhaus, F. Delahaye, G. Vilsmeier, and P. Fath, "Acidic texturisation of mc-Si using a high throughput in-line prototype system with no organic chemistry," in *Proceedings of the 19th European Photovoltaic Solar Energy Conference (EU PVSEC '04)*, pp. 1094–1097, Paris, France, June 2004.
- [21] C. Voyer, D. Biro, K. Wagner, J. Benick, and R. Preu, "Fabrication of textured solar cells using sprayed phosphoric

- acid as the dopant source for the in-line emitter diffusion,” in *Proceedings of the 21st European Photovoltaic Solar Energy Conference (EU PVSEC '06)*, pp. 1157–1160, Dresden, Germany, September 2006.
- [22] J. Lossen, L. Mittelstädt, S. Dauwe, K. Lauer, and C. Beneking, “Making use of silicon wafers with low lifetimes by adequate  $\text{POCl}_3$  diffusion,” in *Proceedings of the 20th European Photovoltaic Solar Energy Conference (EU PVSEC '05)*, p. 1411, Barcelona, Spain, June 2005.
- [23] A. Schneider, R. Kopecek, G. Hahn, S. Noël, and P. Fath, “Comparison of gettering effects during phosphorus diffusion for one- and double-sided emitters,” in *Proceedings of the 31st IEEE Photovoltaic Specialists Conference (PVSC '05)*, pp. 1051–1054, Lake Buena Vista, Fla, USA, January 2005.
- [24] I. Melnyk, E. Wefringhaus, F. Delahaye, G. Vilsmeier, W. Mahler, and P. Fath, “Acidic texturisation of mc-Si using a high throughput in-line prototype system with no organic chemistry,” in *Proceedings of the 19th European Photovoltaic Solar Energy Conference (EU PVSEC '04)*, p. 416, Paris, France, June 2004.
- [25] G. Emanuel, E. Schneiderlöchner, J. Stollhof, J. Gentischer, R. Preu, and R. Lüdemann, “High throughput laser isolation of crystalline silicon solar cells,” in *Proceedings of the 17th European Photovoltaic Solar Energy Conference (EU PVSEC '01)*, pp. 1578–1581, Munich, Germany, October 2001.
- [26] E. Schneiderlöchner, A. Grohe, S. W. Glunz, R. Preu, and W. Willeke, “Scanning Nd:YAG laser system for industrially applicable processing in silicon solar cell manufacturing,” in *Proceedings of the 3rd World Conference on Photovoltaic Energy Conversion (WCPEC '03)*, vol. 2, pp. 1364–1367, Osaka, Japan, May 2003.
- [27] A. G. Aberle and R. Hezel, “Progress in low-temperature surface passivation of silicon solar cells using remote-plasma silicon nitride,” *Progress in Photovoltaics*, vol. 5, no. 1, pp. 29–50, 1997.
- [28] A. G. Aberle, “Surface passivation of crystalline silicon solar cells: a review,” *Progress in Photovoltaics*, vol. 8, no. 5, pp. 473–487, 2000.
- [29] A. Cuevas, M. J. Kerr, and J. Schmidt, “Passivation of crystalline silicon using silicon nitride,” in *Proceedings of 3rd World Conference on Photovoltaic Energy Conversion (WCPEC '03)*, vol. 1, pp. 913–918, Osaka, Japan, May 2003.
- [30] H. Nagel, J. Schmidt, A. G. Aberle, and R. Hezel, “Exceptionally high bulk minority-carrier lifetimes in block-cast multicrystalline,” in *Proceedings of the 14th European Photovoltaic Solar Energy Conference (EU PVSEC '97)*, pp. 762–765, Barcelona, Spain, June–July 1997.
- [31] H. F. Sterling and R. C. G. Swann, “Chemical vapour deposition promoted by r.f. discharge,” *Solid-State Electronics*, vol. 8, no. 8, pp. 653–654, 1965.
- [32] R. Hezel and R. Schörner, “Plasma Si nitride—a promising dielectric to achieve high-quality silicon MIS/IL solar cells,” *Journal of Applied Physics*, vol. 52, no. 4, pp. 3076–3079, 1981.
- [33] K. Kimura, “Recent developments in polycrystalline silicon solar cells,” in *Proceedings of the 1st International Photovoltaic Science and Engineering Conference (PVSEC '84)*, pp. 37–42, Kobe, Japan, November 1984.
- [34] A. G. Aberle, “Overview on SiN surface passivation of crystalline silicon solar cells,” *Solar Energy Materials and Solar Cells*, vol. 65, no. 1–4, pp. 239–248, 2001.
- [35] W. Wolke, A. Jäckle, R. Preu, S. Wieder, and M. Ruske, “SiN:H anti-reflection coatings for c-Si solar cells by large scale inline sputtering,” in *Proceedings of the 19th European Photovoltaic Solar Energy Conference (EU PVSEC '04)*, p. 419, Paris, France, June 2004.
- [36] W. Wolke, J. Catoir, G. Emanuel, J. Liu, M. Ruske, and R. Preu, “Surface passivation for solar cells by large scale inline sputtering of silicon nitride,” in *Proceedings of the 20th European Photovoltaic Solar Energy Conference (EU PVSEC '05)*, pp. 733–736, Barcelona, Spain, June 2005.
- [37] P. J. Holmes and R. G. Loasby, *Handbook of Thick Film Technology*, Electrochemical Publications, Glasgow, Scotland, UK, 1976.
- [38] G. Schubert, F. Huster, and P. Fath, “Current transport mechanism in printed Ag thick film contacts to an n-type emitter of a crystalline silicon solar cell,” in *Proceedings of the 19th European Photovoltaic Solar Energy Conference (EU PVSEC '04)*, p. 813, Paris, France, June 2004.
- [39] H. Reichl, *Hybridintegration*, Dr. Alfred Hüthig, Heidelberg, Germany, 1986.
- [40] C. Ballif, D. M. Huljić, A. Hessler-Wyss, and G. Willeke, “Nature of the Ag-Si interface in screen-printed contacts: a detailed transmission electron microscopy study of cross-sectional structures,” in *Proceedings of the 29th IEEE Photovoltaic Specialists Conference (PVSC '02)*, pp. 360–363, New Orleans, La, USA, May 2002.
- [41] C. Ballif, D. M. Huljić, G. Willeke, and A. Hessler-Wyss, “Silver thick-film contacts on highly doped n-type silicon emitters: structural and electronic properties of the interface,” *Applied Physics Letters*, vol. 82, no. 12, pp. 1878–1880, 2003.
- [42] G. Schubert, B. Fischer, and P. Fath, “Formation and nature of Ag thick film front contacts on crystalline silicon solar cells,” in *Proceedings of Photovoltaics in Europe Conference (PV '02)*, pp. 343–346, Rome, Italy, October 2002.
- [43] G. Schubert, F. Huster, and P. Fath, “Current transport mechanism in printed Ag thick film contacts to an n-type emitter of a crystalline silicon solar cell,” in *Proceedings of the 14th International Photovoltaic Science and Engineering Conference (PVSEC '04)*, p. 441, Bangkok, Thailand, January 2004.
- [44] F. Huster, “Aluminum-back surface field: bow investigation and elimination,” in *Proceedings of the 20th European Photovoltaic Solar Energy Conference (EU PVSEC '05)*, p. 560, Barcelona, Spain, June 2005.
- [45] A. S. H. Van Der Heide, J. H. Bultmann, M. J. A. A. Goris, and J. Hoorstra, “Influence of grain orientation on contact resistance at higher emitter resistances, investigated for alkaline and acid saw damage removal,” in *Proceedings of the 3rd World Conference on Photovoltaic Energy Conversion (WC PVSC '03)*, pp. 1036–1039, Osaka, Japan, May 2003.
- [46] D.-H. Neuhaus, R. Mehnert, G. Erfurt, et al., “Loss analysis of solar modules by comparison of IV measurements and prediction from IV curves of individual solar cells,” in *Proceedings of the 20th European Photovoltaic Solar Energy Conference (EU PVSEC '05)*, pp. 1947–1952, Barcelona, Spain, June 2005.
- [47] D.-H. Neuhaus, J. Kirchner, R. Mehnert, et al., “Impact of shunted solar cells on the IV characteristics of solar modules,” in *Proceedings of the 21st European Photovoltaic Solar Energy Conference (EU PVSEC '06)*, p. 2556, Dresden, Germany, September 2006.
- [48] D.-H. Neuhaus, F. Dreckschmidt, and R. Lüdemann, “Suitability tests for solar cell measurement in the final quality check of an industrial production process,” in *Proceedings of the 19th European Photovoltaic Solar Energy Conference*

- (*EU PVSEC '04*), p. 817, Paris, France, June 2004.
- [49] S. W. Glunz, A. Mette, M. Alemán, P. L. Richter, A. Filipovic, and G. Willeke, "New concepts for the front side metallization of silicon solar cells," in *Proceedings of the 21st European Photovoltaic Solar Energy Conference (EU PVSEC '06)*, p. 746, Dresden, Germany, September 2006.
- [50] M. M. Hilali, A. Rohatgi, and B. To, "A review and understanding of screen-printed contacts and selective-emitter formation," in *Proceedings of the 14th Workshop on Crystalline Silicon Solar Cells and Modules*, Winter Park, Colo, USA, August 2004.
- [51] G. Schubert, J. Horzel, R. Kopecek, F. Huster, and P. Fath, "Silver thick film contact formation on lowly doped phosphorous emitters," in *Proceedings of the 20th European Photovoltaic Solar Energy Conference (EU PVSEC '05)*, p. 934, Barcelona, Spain, June 2005.
- [52] B. Fischer, "Loss analysis of crystalline silicon solar cells using photoconductance and quantum efficiency measurements," Ph.D. thesis, Cuvillier, Göttingen, Germany, 2003.
- [53] M. Rogol and J. Conkling, "Solar Power in Focus," Photon Consulting, 2007.
- [54] S. R. Wenham and M. A. Green, Buried Contact Solar Cells, Australian Patent 570309, March 1985.
- [55] N. B. Mason and D. Jordan, "A high efficiency silicon solar cell production technology," in *Proceedings of the 10th European Photovoltaic Solar Energy Conference (EU PVSEC '91)*, pp. 280–283, Lisbon, Portugal, April 1991.
- [56] N. B. Mason, O. Schultz, R. Russell, S. W. Glunz, and W. Warta, "20.1% efficient large area cell on 140 micron thin silicon wafer," in *Proceedings of the 21st European Photovoltaic Solar Energy Conference (EU PVSEC '06)*, p. 521, Dresden, Germany, September 2006.
- [57] N. B. Mason, T. M. Bruton, S. Gledhill, et al., "The selection and performance of monocrystalline silicon substrates for commercially viable 20% efficient lid-free solar cells," in *Proceedings of the 19th European Photovoltaic Solar Energy Conference (EU PVSEC '04)*, p. 620, Paris, France, June 2004.
- [58] O. N. Hartley, R. Russell, K. C. Heasman, N. B. Mason, and T. M. Bruton, "Investigation of thin aluminium films on the rear of monocrystalline silicon solar cells for back surface field formation," in *Proceedings of the 29th IEEE Photovoltaic Specialists Conference (PVSC '02)*, pp. 118–121, New Orleans, La, USA, May 2002.
- [59] O. Schultz, S. W. Glunz, W. Warta, et al., "High-efficiency solar cells with laser-grooved buried contact front and laser-fired rear for industrial production," in *Proceedings of the 21st European Photovoltaic Solar Energy Conference (EU PVSEC '06)*, p. 826, Dresden, Germany, September 2006.
- [60] K. A. Münzer, R. R. King, R. E. Schlosser, et al., "Manufacturing of back surface field for industrial application," in *Proceedings of the 13th European Photovoltaic Solar Energy Conference (EU PVSEC '95)*, p. 1398, Nice, France, October 1995.
- [61] K. A. Münzer, A. Froitzheim, R. E. Schlosser, R. Tölle, and M. G. Winstel, "Over 18% industrial screen printed silicon solar cells," in *Proceedings of the 21st European Photovoltaic Solar Energy Conference (EU PVSEC '06)*, p. 538, Dresden, Germany, September 2006.
- [62] H. Sakata, T. Nakai, T. Baba, et al., "20.7% highest efficiency large area (100.5 cm<sup>2</sup>) HIT<sup>TM</sup> cell," in *Proceedings of the 28th IEEE Photovoltaic Specialists Conference (PVSC '00)*, pp. 7–12, Anchorage, Alaska, USA, September 2000.
- [63] M. Tanaka, S. Okamoto, S. Tsuge, and S. Kiyama, "Development of HIT solar cells with more than 21% conversion efficiency and commercialization of highest performance HIT modules," in *Proceedings of 3rd World Conference on Photovoltaic Energy Conversion (WCPEC '03)*, pp. 955–958, Osaka, Japan, May 2003.
- [64] R. A. Sinton, Y. Kwark, J. Y. Gan, and R. M. Swanson, "27.5-percent silicon concentrator solar cells," *IEEE Electron Device Letters*, vol. 7, no. 10, pp. 567–569, 1986.
- [65] P. J. Verlinden, R. M. Swanson, and R. A. Crane, "7000 high-efficiency cells for a dream," *Progress in Photovoltaics*, vol. 2, no. 2, pp. 143–152, 1994.
- [66] W. P. Mulligan, D. H. Rose, M. J. Cudzinovic, et al., "Manufacture of solar cells with 21% efficiency," in *Proceedings of the 19th European Photovoltaic Solar Energy Conference (EU PVSEC '04)*, p. 387, Paris, France, June 2004.
- [67] M. J. Cudzinovic and K. R. McIntosh, "Process simplifications to the pegasus solar cell—Sunpower's high-efficiency bifacial silicon solar cell," in *Proceedings of the 29th IEEE Photovoltaic Specialists Conference (PVSC '02)*, pp. 70–73, New Orleans, La, USA, May 2002.
- [68] K. R. McIntosh, M. J. Cudzinovic, D. D. Smith, W. P. Mulligan, and R. M. Swanson, "The choice of silicon wafer for the production of low-cost rear-contact solar cells," in *Proceedings of 3rd World Conference on Photovoltaic Energy Conversion (WCPEC '03)*, vol. 1, pp. 971–974, Osaka, Japan, May 2003.
- [69] W. P. Mulligan, M. A. Carandang, W. Dawson, D. M. de Ceuster, C. N. Stone, and R. M. Swanson, "Reducing silicon consumption by leveraging cell efficiency," in *Proceedings of the 21st European Photovoltaic Solar Energy Conference (EU PVSEC '06)*, p. 1301, Dresden, Germany, September 2006.
- [70] S. W. Glunz, J. Dicker, D. Kray, et al., "High efficiency cell structures for medium-quality silicon," in *Proceedings of the 17th European Photovoltaic Solar Energy Conference (EU PVSEC '01)*, p. 1287, Munich, Germany, October 2001.
- [71] A. Kress, R. Tölle, T. Bruton, P. Fath, and E. Bucher, "10 × 10 cm<sup>2</sup> screen printed back contact cell with aselective emitter," in *Proceedings of the 28th IEEE Photovoltaic Specialists Conference (PVSC '00)*, pp. 213–216, Anchorage, Alaska, USA, September 2000.
- [72] P. Hacke, J. M. Gee, M. W. Summer, J. Salami, and C. Honsberg, "Application of a boron source diffusion barrier for the fabrication of back contact silicon solar cells," in *Proceedings of the 31st IEEE Photovoltaic Specialists Conference (PVSC '05)*, pp. 1181–1184, Orlando, Fla, USA, January 2005.
- [73] P. Hacke, J. M. Gee, M. Hilali, et al., "Current status of technologies for industrial emitter wrap-through solar cells," in *Proceedings of the 21st European Photovoltaic Solar Energy Conference (EU PVSEC '06)*, p. 761, Dresden, Germany, September 2006.

## Review Article

# High-Efficiency Crystalline Silicon Solar Cells

**S. W. Glunz**

*Fraunhofer Institute for Solar Energy Systems, Heidenhofstrasse 2, 79110 Freiburg, Germany*

Received 2 May 2007; Accepted 18 July 2007

Recommended by Armin G. Aberle

The current cost distribution of a crystalline silicon PV module is clearly dominated by material costs, especially by the costs of the silicon wafer. Therefore cell designs that allow the use of thinner wafers and the increase of energy conversion efficiency are of special interest to the PV industry. This article gives an overview of the most critical issues to achieve this aim and of the recent activities at Fraunhofer ISE and other institutes.

Copyright © 2007 S. W. Glunz. This is an open access article distributed under the Creative Commons Attribution License, which permits unrestricted use, distribution, and reproduction in any medium, provided the original work is properly cited.

## 1. INTRODUCTION

The silicon shortage in the past few years might not have been very pleasant economically for the photovoltaic industry, but it might have been beneficial from the technological point of view. If the market and the production continue to grow while the raw material is very limited and also is the highest cost share in the final product, then it is essential to increase the ratio product (i.e., output power of the fabricated cells) to raw material. In the case of silicon solar cells, this means increasing the efficiency and reducing the cell thickness with the later option being already pursued by nearly all solar cell manufacturers. Cell thicknesses in the range of 200  $\mu\text{m}$  or even less are now the industrial standard which is well beyond the old standard of 330  $\mu\text{m}$ . This development has been made possible by tremendous efforts in automation and process technology. In fact, the current photovoltaic industry has its own equipment suppliers who are very specialized while in former times, process equipment used was mostly modified microelectronic equipment, a branch which is specialized for extremely high accuracy and purity but not for 40 000 wafers per day.

The second task, that is, increasing the cell efficiency in the industrial production has also made great progress in the last few years. Cell structures like the A300 of Sunpower or the HIT cell of Sanyo are demonstrating the potential for industrial cells to achieve efficiencies greater than 20%.

This article gives an overview of the recent developments of industrially feasible high-efficiency technologies at Fraunhofer ISE and other institutes. It addresses the most important cell components which need further improvement to reach higher efficiencies.

Justus Liebig, a famous German chemist of the 19th century, has stated the Law of the Minimum: "The yield potential of a crop is like a barrel with staves of unequal length." This was the basis for the development of an efficient fertilizer technology. Similarly, we can use the Law of the Minimum to describe the efficiency potential of a solar cell (see Figure 1).

The capacity of the barrel (i.e., the efficiency potential of the cell) is limited by the length of the shortest stave (in this case, the surface recombination velocity at the rear surface  $S_{\text{back}}$ ). (Of course this is a simplified view of a complex task, since also several loss mechanisms can limit the cell potential at the same time.) Therefore, this article addresses the shortest staves in current industrial cells as surface passivation, contacts, and bulk material. Other aspects such as the front reflectance are already well optimized and need to be tackled only in a second step.

## 2. SURFACE PASSIVATION

### 2.1. Dielectric passivation versus back surface field

All cell structures which have shown efficiencies greater than 20% feature an efficient surface passivation with dielectric layers. However, the present state-of-the-art rear surface structure of industrial silicon solar cells is a screen-printed and thermally fired Al back surface field (Al-BSF) which has two major restrictions: (i) the wafer bow due to the firing process and (ii) the lower electrical and optical properties. In particular,  $S_{\text{back}}$ , the rear surface recombination velocity, is a crucial parameter, but exhibits a great range of values found

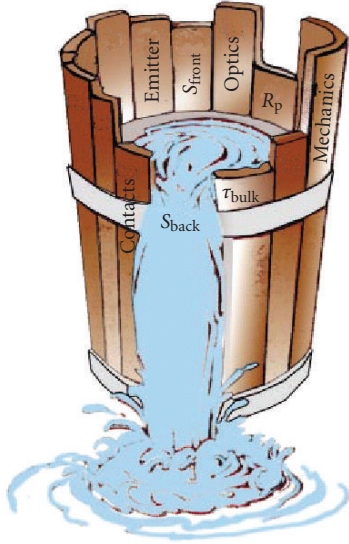


FIGURE 1: Liebig's law adapted to solar cells.

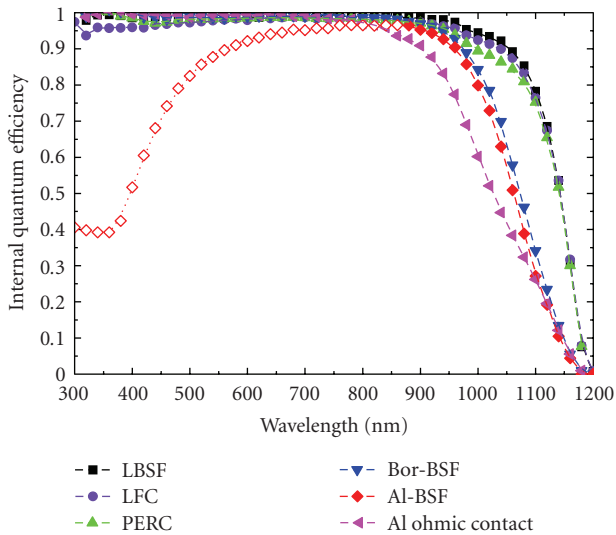


FIGURE 2: Internal quantum efficiency of different rear surface structures on  $1 \Omega \text{ cm}$   $250 \mu\text{m}$  thick FZ-Si with a high-efficiency front structure. Note: the low internal quantum efficiency for short wavelengths (open symbols) of the Al-BSF cell is due to a degradation of front surface passivation during firing. Nevertheless, the IQE starting at  $900 \text{ nm}$  is identical to the performance of industrial cells. (For abbreviations see Table 1.)

in literature. This makes it difficult to evaluate the potential of Al-BSFs versus dielectric passivation.

Thus at Fraunhofer ISE, an experimental study of different rear surface structures combined with a high-efficiency front structure which does not limit the cell performance was performed [1]. This makes it possible to determine the surface recombination velocity  $S_{\text{back}}$  and the internal reflectivity  $R_{\text{back}}$  quite accurately [2].

Figure 2 shows the measured internal quantum efficiencies of different rear structures starting from a low-quality

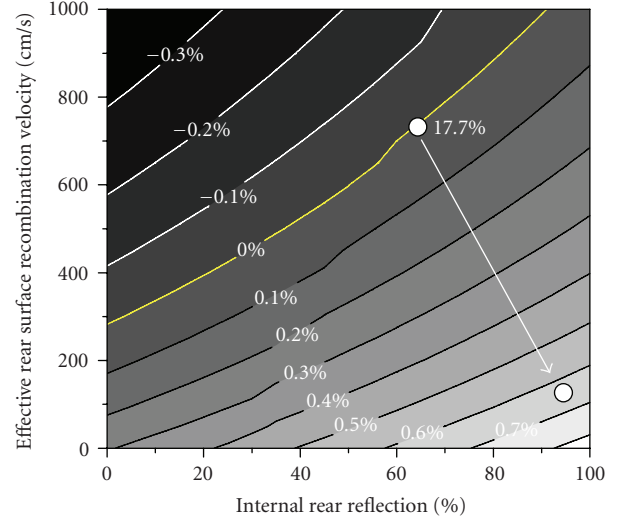


FIGURE 3: Change in efficiency gain due to variation of  $S_{\text{back}}$  and  $R_{\text{back}}$ . The 0% isoline refers to a  $220 \mu\text{m}$  thick industrial solar cell with  $60 \Omega/\text{sq}$  emitter and Al-BSF on  $1 \Omega \text{ cm}$  monocrystalline silicon with a diffusion length of  $400 \mu\text{m}$ . The second point relates to the LFC parameters.

ohmic Al contact up to a PERL[3]/LBSF[4] rear surface. The effective  $S_{\text{back}}$  and  $R_{\text{back}}$  have been extracted from the IQE and reflection measurement.

Using these parameters, it is possible to determine the influence of different rear surface structures on the performance of industrial cells (see Figure 3). The benefit of a dielectric passivation will be even higher with the introduction of a higher-quality emitter and thinner cells.

## 2.2. Passivation mechanisms of dielectric layers

There are two different mechanisms leading to good surface passivation (for a comprehensive overview about this topic, see [7]): (i) the reduction of interface states  $D_{\text{it}}$  and (ii) field effect passivation, that is, the strong reduction of one carrier type by incorporation of fixed charges  $Q_f$  in the passivation layer. Although these mechanisms or the combination of both lead to low surface recombination velocities, the resulting  $S_{\text{eff}}(\Delta n)$  curve shows different characteristics (see Figure 4). The reduction of interface states is more effectively reached for thermally grown  $\text{SiO}_2$  layers while the field effect passivation together with a moderate reduction of  $D_{\text{it}}$  is more typical for PECVD deposited layers like  $\text{SiN}_x$ . Typical values for  $\text{SiO}_2$  are  $D_{\text{it}} = 10^{10} \text{ cm}^{-2} \text{ eV}^{-1}$  and  $Q_f = 10^{10} \text{ cm}^{-2}$  while for  $\text{SiN}_x$ , values are  $D_{\text{it}} = 10^{11} \text{ cm}^{-2} \text{ eV}^{-1}$  and  $Q_f = 10^{11} \text{ cm}^{-2}$ .

## 2.3. Deposition temperature

A critical issue for the fabrication of a dielectric passivation layer is the deposition temperature. The best solar cells so far have been passivated by thermally grown oxides [8, 9]. Thermal oxides have been optimized for MOS-technology

TABLE 1: Internal reflectivities ( $R_{\text{back}}$ ) and rear surface recombination velocities ( $S_{\text{back}}$ ) as extracted from the data in Figure 2. The dielectric passivation layer for the LBSF, LFC, and PERC structure was a thermally grown 105 nm thick oxide.

Structure	$R_{\text{back}}$ [%]	$S_{\text{back}}$ [cm/s]
LBSF (local boron back surface field) [4]	94.5	60
LFC (laser-fired contacts) [5]	95.5	110
PERC (Random pyramids, passivated emitter, and rear cell) [6]	95.0	200
Bor-BSF (boron-diffused back surface field)	71	430
Screen-printed Al-BSF (alloyed Al back surface field)	65	750
Evaporated ohmic Al contact	83	$10^7$

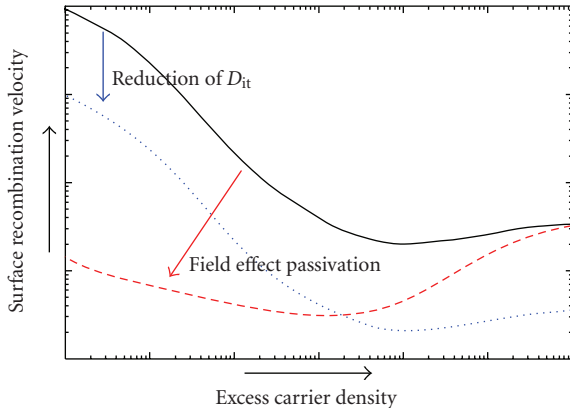


FIGURE 4: Sketch of the impact of the two passivation schemes, reduction of interface state density,  $D_{\text{it}}$  (dotted) and field effect passivation (dashed).

for decades. Therefore, extremely low interface state densities and surface recombination velocities have been achieved especially if the well-known “Alneal” treatment [10] is applied. Unfortunately, the typical temperature of thermal oxidation is around 1050°C. This temperature range imposes no problem for high-quality FZ-Si and can even increase the minority carrier lifetime in Czochralski-grown silicon [11] but it is extremely detrimental for block-cast multicrystalline silicon [12, 13]. For such material, the minority carrier lifetime can be reduced by a factor of about 10 [14]. Thus, it is essential to find passivation layers that can be deposited at lower temperatures. It is possible to grow thermal oxides in a wet ambient atmosphere at temperatures of around 850°C [15]. The wet atmosphere increases the oxidation rate drastically, which makes it possible to obtain the typical oxide thickness of 105 nm in a reasonable time. This strategy was applied to multicrystalline silicon and has led to the actual record for multicrystalline silicon of 20.3% [14]. The average efficiencies of these cells were typically higher than 18%, indicating that low-quality regions have not been degraded by this treatment. Another interesting alternative is the growth of a thin oxide layer at temperatures around 850°C in dry atmosphere. This thin oxide layer has to be combined with a second deposited layer on top and will be discussed later in this paper.

Deposited layers such as PECVD  $\text{SiN}_x$  are the second best choice. The typical deposition temperatures are in the range

of 350° to 400°C. Excellent surface recombination velocities of less than 10 cm/s have been reached [16]. An additional advantage of  $\text{SiN}_x$  is the incorporation of hydrogen in this layer which could act as a bulk passivation source for multicrystalline silicon. A very fast alternative to PECVD reactors is sputtering by which excellent surface recombination velocities below 30 cm/s have also been achieved [17].

The lowest deposition temperatures between 200°C and 250°C are needed if amorphous silicon is used as the rear passivation layer. This passivation scheme is applied successfully in the HIT structure [18] achieving efficiencies of 21%. Recently, it was shown that amorphous silicon also works well for standard cell structures with diffused emitters [19, 20] and efficiencies above 20% have been reported.

## 2.4. Preconditioning

Besides the deposition temperature, another technological issue is the preparation of the surface before the fabrication of the dielectric layer. A clean surface is substantial for oxidation processes or else surface contaminants will diffuse into the bulk. This problem is less severe for deposited passivation layers due to the lower process temperatures. However, a very shallow layer of crystal damage which could be left over after a prior etching step will decrease the passivation quality significantly. This problem is less pronounced for oxidized surfaces since a part of the upper silicon layer is taken by the oxidation process (approximately half of the final oxide layer).

Another topic is the surface geometry. In contrast to microelectronics, surfaces of industrial solar cells are generally rough due to the anisotropic damage etch or a wet-chemical texturing process.

It is important to investigate whether a rough surface structure results in lower optical and electrical performance if compared to a smooth shiny etched surface. In order to investigate this issue, we have prepared a set of solar cells with different topographies (see Figure 5) on the same material (FZ-Si) with the following identical cell structure: (front: random pyramids with 105 nm thermal oxide, 120 Ω/sq phosphorus emitter; rear: 105 nm thermal oxide, 2 μm aluminium and LFC contacts).

While the cells with the damage-etched and shiny-etched rear surface nearly show the similar performance (see Table 2), the cells with the textured rear exhibit lower efficiencies mainly due to a loss in current which can be clearly

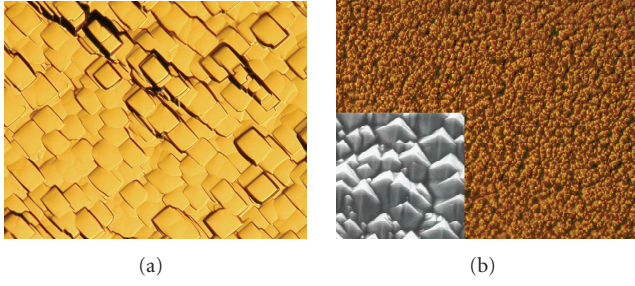


FIGURE 5: (a) Surface topography after alkaline damage etch and (b) random pyramid texturing. Both photos are taken by an optical microscope. The inset in (b) is a scanning microscope picture to show the pyramid geometry more clearly.

TABLE 2: Results of oxide-passivated cells on  $0.5 \Omega \text{ cm}$  FZ-Si with different rear surface topographies (average of 7 cells).

Rear surface topography	$V_{oc}$ [mV]	$J_{sc}$ [mA/cm <sup>2</sup> ]	FF	$\eta$ [%]
Shiny etched	677.1 +/-0.6	38.14 +/-0.15	80.4 +/-0.2	20.8 +/-0.1
Damage etched	678.9 +/-0.3	38.21 +/-0.06	80.9 +/-0.1	21.0 +/-0.04
Random pyramids	673.2 +/-2.2	37.25 0.28	80.1 +/-0.4	20.1 +/-0.2

attributed to the lower performance of the textured rear surface (see the poorer long wavelength response in Figure 6).

De Wolf et al. [21] also demonstrated a similar reduction of passivation quality with increasing surface roughness for PECVD-SiN<sub>x</sub>-layers. They also showed that this dependence on surface roughness is much less pronounced after a subsequent firing step.

## 2.5. Internal reflection

Next to the passivation quality, it is important to analyze the optical properties of a rear surface passivation layer. The “traditional” Si/SiO<sub>2</sub>/Al system has very high-internal reflectivity due to the low refractive index of SiO<sub>2</sub> ( $n = 1.46$ ) [22]. A pyramid texture on the front surface results in an oblique light path (angle  $41.4^\circ$  from perpendicular) and total reflection occurs at the rear surface. Thus, for the internal optical reflection at the rear side of the cell, ( $R_{back}$ ) values of 95% to 89% can be obtained. However, since most of the deposited layers with good passivation quality such as Si-rich SiN<sub>x</sub> have a high refractive index,  $R_{back}$  is not that high.

Figure 7 shows the reflectivity measurements of solar cells with textured front side and different rear surface passivation layers. If silicon-rich dielectric layers with high-refractive indices (SiN<sub>x</sub> = 2.9, SiC<sub>x</sub> > 3) are applied, the  $R_{back}$  values are still better than the industrial standard but much lower than the thick thermal SiO<sub>2</sub> layer. Since these layers usually show very low surface recombination velocities, it is favourable to deposit them directly onto the silicon

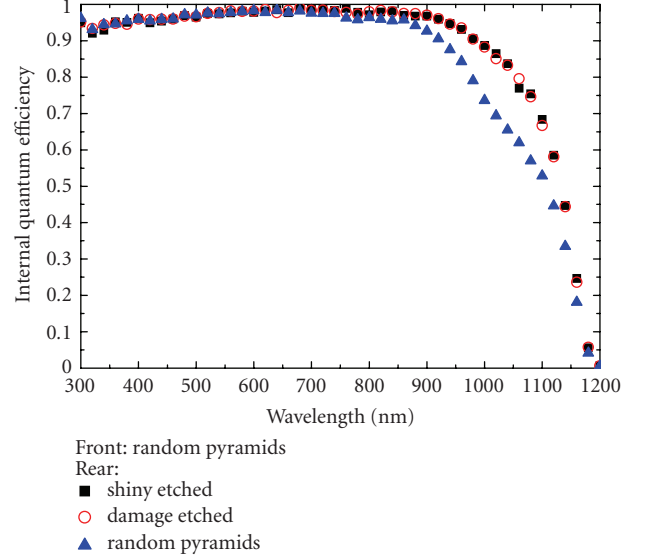


FIGURE 6: Internal quantum efficiencies of cells with oxide-passivated rear surface on  $0.5 \Omega \text{ cm}$  FZ silicon.

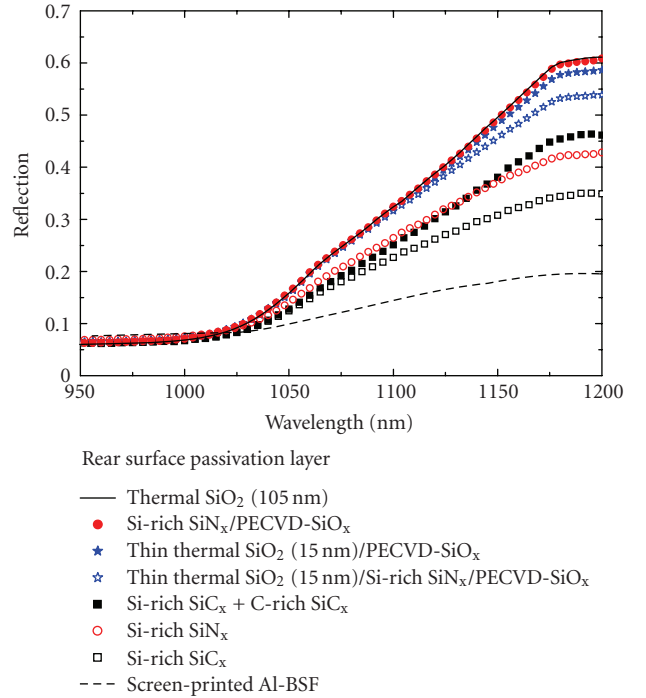


FIGURE 7: Reflectivity measurements of solar cells with front texture and different rear surface passivation layers. The upper margin is a 105 nm thermal oxide (solid line), the lower margin is screen-printed Al-BSF (dashed line).

surface. In order to improve the optical properties, a second dielectric layer with a lower refractive index [23] should be applied. In fact, a quite strong improvement is observed if a PECVD SiO<sub>2</sub> ( $n = 1.46$ ) is deposited on top of the Si-rich SiN<sub>x</sub> layer (red solid circles in Figure 7) and likewise for a C-rich SiC-layer on top of a Si-rich SiC<sub>x</sub> layer ( $n \approx 2$ ) (black

solid squares in Figure 7). Also, the optical performance of a thin thermal oxide (15 nm) can be improved by the deposition of a low-temperature PECVD SiO<sub>2</sub> (blue filled stars in Figure 7). Thus, stack systems allow the two important tasks of “passivation” and “reflection” to be achieved by different layers.

## 2.6. Application to solar cells

Although it seems possible to design a perfect layer or layer system simply by performing lifetime and optical measurements, a final decision has to be made by applying these layers to solar cells. A good example that illustrates that good surface passivation quality is only a necessary but not a sufficient condition is SiN<sub>x</sub> passivation. Although SiN<sub>x</sub> layers show the very best surface passivation quality on lifetime test wafers, even better than thermal oxidation, none has so far managed to fabricate a cell with efficiencies attainable by the ones featuring the “classical” thermal oxidation. In particular, the short-circuit current is significantly lower. This reduction was explained by Dauwe et al. [24] by the short-circuiting of the inversion layer induced by the fixed charges in the SiN<sub>x</sub> layer at the rear contact points. Since the inversion layer is a crucial part of surface passivation mechanism of SiN<sub>x</sub> layers, the apparent quality of SiN<sub>x</sub> layers on lifetime test wafers “vanishes” when applied to real cells. The best cell efficiencies reported so far using silicon nitride rear surface passivation were 21.5% [25] and 20.6% [26]. In the first case, a very sensitive plasma etch was used to open the contact holes in the SiN<sub>x</sub> layer so that the inversion layer was not shunted. In the second case a local boron BSF reduced the shunting of the inversion layer. However, if used with a “rough” process like laser-fired contacts or mechanical sawing, efficiencies higher than 20% would not be reached.

This problem can be solved in two ways: (i) by the development of SiN<sub>x</sub> layers whose passivation quality would be more dependent on the reduction of interface states than on the field effect passivation (i.e., reduction of  $D_{it}$  and  $Q_f$ ) [18] or (ii) by the application of thin thermal oxide (10–15 nm) below the SiN<sub>x</sub> layer. This oxide layer can be grown rapidly (e.g., RTO) and at relatively low temperatures (850°C). Excellent surface passivation quality has been reported [27, 28]. Additionally, the thin oxide layer will also serve as a front passivation for lighter doped emitters on the front.<sup>1</sup> When such a stack system is applied on the rear, efficiencies of 20.5% have been reported [29].

Another excellent passivation layer is amorphous silicon. For the HIT cell structure [30], it was natural choice to use amorphous silicon as the rear surface passivation since the emitter is also formed by this layer type. This type of passivation is also applied on standard silicon solar cells achieving excellent cell results [26, 31] reaching efficiencies up to 21.7% ( $V_{oc} = 677$  mV) [20].

<sup>1</sup> Since the oxide layer is very thin, it is possible to apply a second front layer with higher refractive index (i.e., SiN<sub>x</sub>), resulting in very good optical performance.

TABLE 3: Solar cell results with SiC<sub>x</sub> rear passivation.

Rear surface structure	$V_{oc}$ [mV]	$J_{sc}$ [mA/cm <sup>2</sup> ]	FF [%]	$\eta$ [%]
SiC <sub>x</sub> -layer + 2 $\mu$ m Al + LFC	665	37.5	80.3	20.2

Recently, Martín et al. [32] reported that PECVD-deposited SiC<sub>x</sub>-layers also show very good passivation quality ( $S < 30$  cm/s). At Fraunhofer ISE, SiC<sub>x</sub> layers are used as a diffusion barrier layer for recrystallization of silicon thin-film layers on low-cost substrates [33] due to their excellent thermal stability. The PECVD system used for this process step offers the possibility to perform an in situ plasma cleaning step prior to the deposition itself which would make it possible to optimize the process flow in an industrial line tremendously. In order to optimize the surface passivation quality of these SiC<sub>x</sub> layers, 1  $\Omega$  cm p-type high-lifetime FZ-Si wafers were used. The wafers were taken out of the box and plasma cleaned. Subsequently, the SiC<sub>x</sub>-layer was deposited without any additional wet-chemical process. Excellent surface recombination velocity well below 5 cm/s for  $\Delta n$  between  $1 \times 10^{14}$  cm<sup>-3</sup> and  $1 \times 10^{15}$  cm<sup>-3</sup> has been achieved [34]. After the successful development of a highly passivating SiC<sub>x</sub> layer, different layer systems based on different compositions were used for the rear passivation of solar cells with a high-efficiency front structure (oxide-passivated 120  $\Omega$ /sq emitter and evaporated contacts). Again, not only the deposition but also the surface conditioning was performed in the PECVD reactor. E-gun evaporation was used for the deposition of the 2  $\mu$ m thick Al layer and the laser-fired contacts process was applied. Although the cells have not been annealed after e-gun evaporation and LFC formation, efficiencies greater than 20% have been achieved (see Table 3).

## 2.7. Thermal stability

If a dielectric rear surface passivation has to be combined with a standard screen-printed front surface metallization, a critical factor is the stage in the process sequence where the layer will be deposited (see Figure 8). Depositing the dielectric layer on the rear surface after the firing step for the front metallization (option 1 in Figure 8) requires a strong surface conditioning, including etching of the rear emitter layer and severe cleaning since the wafer has already been subject to several “dirty” process steps at that stage. Thus, although the dielectric layer will not see any high-temperature step afterwards, it is a difficult task to obtain good surface passivation.

Alternatively, the rear dielectrical layer could be deposited after the emitter diffusion (option 2 in Figure 8) around the same time as the front surface nitride deposition taking advantage of the clean conditions of the wafer. The rear emitter layer will still need to be etched away prior to rear dielectric deposition, and the deposited layer has to be able to withstand a high-temperature step, that is, the subsequent firing step.

An even more elegant option could be the rear dielectric deposition before the emitter diffusion (option 3). At

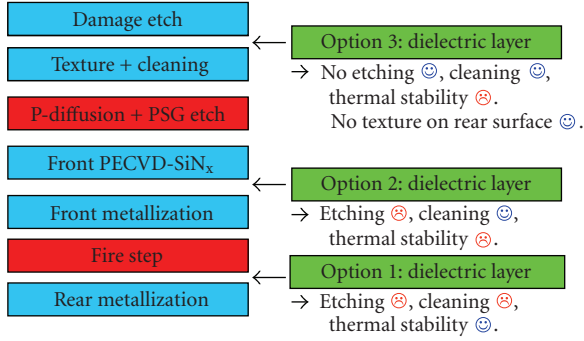


FIGURE 8: Formation of a dielectric layer within an industrial solar cell process.

that point, the wafer is definitely clean and the rear dielectric will mask the subsequent emitter diffusion from the rear, eliminating the rear etching step. The rear dielectric can also mask the surface texture on the rear side if the texturing processing is well controlled. It was shown that the passivation quality on a nontextured surface is significantly better (see Section 2.4 or [35]). Thus, this process sequence seems to be ideal but of course the passivation layer has to withstand two subsequent high-temperature steps without losing its passivation quality.

Therefore, besides good electrical and optical properties, a high thermal stability is essential for an industrially feasible passivation layer.

The classical choice for a passivation layer with good thermal stability is a silicon dioxide layer thermally grown at temperatures between 800°C and 1050°C. This layer was used for our first test to transfer the LFC technology into an industrial process sequence [36]. However, due to the high process temperature, it could be difficult to use this process in an industrial environment although it was shown that an oxidation at reduced temperatures does not degrade material quality [14] and that in diffusion of surface contaminants during the process is less critical than thought before [37].

A process closer to today’s industrial reality is the deposition of silicon nitride using PECVD. However, it was not possible to reach the same passivation quality as of thermal oxides when applied to a solar cell due to detrimental shunting of the inversion layer induced by the SiN<sub>x</sub>-layer [24]. Also, thermal stability seems to be an issue although recent works have shown that a medium passivation level can be maintained after a firing step [38].

Recently, Agostinelli et al. have shown that it is possible to reach an efficiency of 17.3% on 105 μm thin Cz-Si with their i-PERC structure which is based on a fire-stable dielectric layer [39]. Reference cells featuring an Al-BSF have shown an efficiency of only 15.1%. This improvement demonstrates impressively the superiority of dielectric rear surface passivation and the feasibility to implement it into an industrial cell process.

As mentioned above, cells passivated with PECVD-deposited amorphous silicon have reached a remarkable efficiency level, but unfortunately this layer type is only temperature stable up to 400°C [20].

TABLE 4: Carrier lifetime @  $\Delta n = 5 \times 10^{14} \text{ cm}^{-3}$  of test samples before and after a firing step at 800°C.

Layer system	Lifetime before firing	Lifetime after firing
LS-08	1126	17.8
LS-10	533	0.8
LS-66	341	250

TABLE 5: Implied open-circuit voltage before and after firing step determined from QSSPC measurement at 1 sun on a solar cell precursor. For layer system, B is the best result and the average of 7 samples after firing is given.

Layer system	max. $V_{oc}$ [mV] before firing step	max. $V_{oc}$ [mV] after firing step
A (best result)	625	639
B (best result)	635	679
B (average)	—	676 +/- 2.4

SiC<sub>x</sub> is well known to be quite stable with respect to thermal treatments. In fact, Martín et al. [32] reported that the passivation quality does not decrease after a firing step at 730°C. Thus, this material type could be extremely interesting in terms of thermal stability. In order to verify the thermal stability of SiC<sub>x</sub> layers developed at Fraunhofer ISE we conducted experiments on lifetime test samples. The lifetime of SiC<sub>x</sub>-passivated 1 Ω cm Fz-Si wafers was measured using quasi-steady-state photoconductance measurements (QSSPC) [40] before and after a firing step without any additional anneal step. The firing step was performed at a peak temperature of 800°C in a standard belt furnace. (Note: the chosen temperature of 800°C is lower than that of a standard firing step since it was shown that nonmetallized samples attain temperatures about 50°C to 80°C higher than metallized solar cells.)

The measurement results of a few representative layers in Table 4 show an interesting finding. The lifetime after deposition is not coupled with the fire stability. The layer system LS-66 which has shown good but not the best passivation quality clearly outperforms its “competitors” in terms of “fire stability.”

Based on these findings, a second experiment fabricating solar cell precursors on 0.5 Ω cm FZ-Si with an oxide-passivated 120 Ω/sq emitter and different SiC<sub>x</sub> rear passivation layers was conducted. In this case, the lifetime measured at one-sun illumination can be translated directly to the implied open-circuit voltage. Again, the structures were measured before and after an 800°C firing step.

Both layer systems shown in Table 5 are well suited for the rear surface passivation even after a firing step. In particular, layer system B is very promising since a very high open-circuit voltage of 679 mV could be obtained.

In the third experiment, solar cells have been fabricated to evaluate the potential of these layers in more detail. Again, high implied voltages of 682 mV after firing have been achieved on untextured solar cell precursors. Metal contacts

TABLE 6: Results of untextured solar cells with fired  $\text{SiC}_x$  rear passivation.

Rear surface structure	$V_{oc}$ [mV]	$J_{sc}$ [mA/cm <sup>2</sup> ]	FF [%]	$\eta$ [%]
$\text{SiC}_x$ -layer + $2\ \mu\text{m}$ Al + LFC	674	33.1	80.6	18.0

have been applied on the front and rear of these samples and the cell performance have been measured (see Table 6)

The obtained open-circuit voltage of 674 mV shows impressively the high potential of  $\text{SiC}_x$  layers for photovoltaic application.

### 3. METALLIZATION

Due to its robust process technology and high throughput, screen-printing is the most common technique for the metallization of today's industrial solar cells. However, there are several undesirable features such as poor aspect ratio of the grid lines, high line resistance, and high doping concentration of the underlying emitter required to achieve acceptable values of contact resistance. These aspects motivate the investigation of alternative metallization concepts. This effort is also justified by the tremendous growth of cell area, leading to a strong increase of resistive losses in the front-side grid.

The first industrial cell type which does not use screen-printing for the front-side metallization is the *laser-buried contact cell* [41, 42] produced by BP Solar (see Figure 9).

Here, the contacts are buried into grooves which are machined with a laser and exhibit strong phosphorus diffusion. The contact structure is a multilayer with Ni immediately contacting the silicon. The rest of the surface is covered with a lowly doped emitter which is passivated effectively by  $\text{SiN}_x$ . Due to the low shading losses and the good electrical properties of this emitter, the blue response and the overall performance of this cell structure are very high [41].

It is believed that two-layer metallization processes such as the LGBG process shown above can compete with screen-printing. In the first of the process step a narrow metallization line, the *seed layer*, is created on the silicon surface. This seed layer should have good mechanical and electrical contact to the silicon surface. In the subsequent *growth* step, this line is thickened by a plating process to increase the line conductivity. Using such a two-layer process, it is possible to optimize both steps in terms of metals and process parameters separately and to clearly improve the performance of the front surface metallization. In fact, all high-efficiency cells in our lab are processed using a multilayer process.

#### 3.1. Light-induced plating

For thickening of the seed layers (i.e., the growth step), at Fraunhofer ISE and other institutes [3], the light-induced electroplating process is used, which utilizes the photovoltaic effect of the cell and allows to contact only the fully metallized rear surface during plating (see Figure 10). Thus, the

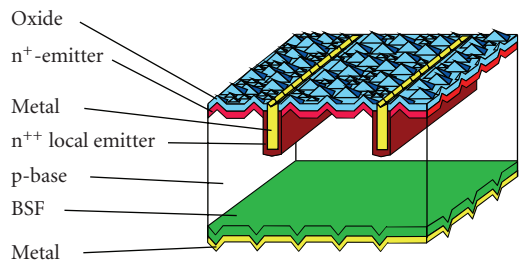


FIGURE 9: Laser grooved buried grid (LGBG) solar cell (Saturn) of BP Solar.

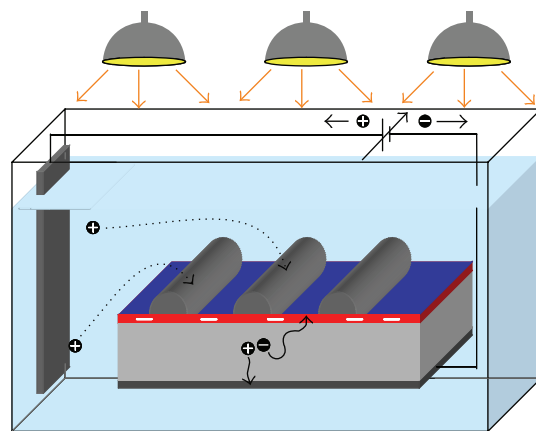


FIGURE 10: Scheme of the light-induced electroplating process (LIP). The cell is immersed in an electroplating bath with an Ag-electrode (left side) and only contacted at the fully metallized rear side. The applied potential suppresses dissolution on this side. By illuminating the cells, the front electrodes are on a more negative potential, high enough to stimulate deposition of Ag ions. This plating concept simplifies industrial transfer considerably.

complexity of this selective process is reduced considerably. Furthermore, this process has a much higher deposition rate compared to electroless plating.

The process has been used for our high-efficiency cells for more than a decade and results in highly conducting front contacts with an aspect ratio close to 1 : 2 (height : width). At Fraunhofer ISE, a small batch-type semiautomated electro-plating system was set up several years ago and is working reliably without complex maintenance. Recently, this process was used to increase the conductivity of narrow screen-printed lines. A significant efficiency increase on  $15.6 \times 15.6\ \text{cm}^2$  industrial multicrystalline cells by 0.3 to 0.5% absolute has been demonstrated [43], while saving silver paste in the screen-printing step. Thus, a short-time-scale transfer of this process into an industrial environment seems to be quite realistic.

Of course, the full potential of the light-induced plating process can only be achieved if the seed layer has better electrical and geometrical properties than screen-printed contacts. In the following sections, four different seed layer technologies, currently under development at Fraunhofer ISE, are discussed.

TABLE 7: Results of  $100 \times 100 \text{ mm}^2$  Cz-Si solar cells. The front grid structure was fabricated using pad printing, firing, and light-induced plating.

Paste	$V_{oc}$ [mV]	$J_{sc}$ [mA/cm <sup>2</sup> ]	FF [%]	$\eta$ [%]
Hot melt	624	36.1	79.7	17.9
Conventional	627	36.2	76.9	17.4

### 3.2. Pad printing

Pad printing is a very interesting alternative to screen-printing since smaller structures in the range of less than  $50 \mu\text{m}$  can be printed. Furthermore, a mature industrial high-volume technology and modified standard screen-printing pastes can be used. Thus, this technology was investigated intensively at Fraunhofer ISE [44]. Although it was possible to print very narrow contact lines, the height of the printed contacts is reduced simultaneously, resulting in decreased line conductivity.

However, in combination with a subsequent light-induced plating process, pad printing would be ideal to form the seed layer. To further increase the printing resolution and the paste transfer from pad to solar cell, we have used hot-melt pastes which have shown very promising results when applied by screen-printing as well [45]. It was necessary to modify the pad printer for the use of hot melt pastes, that is, to heat the printing pattern and the printing table. The process temperatures, printing patterns, and other process parameters have been optimized in order to achieve narrow and continuous lines and a complete transfer of the paste. We processed solar cells on textured  $100 \times 100 \text{ mm}^2$  Czochralski silicon with this process using the following principal sequence:

- (i) chemical texturing,
- (ii) emitter diffusion  $60 \Omega/\text{sq}$  + PSG etch,
- (iii) sputtering of  $\text{SiN}_x\text{:H}$  on the front side,
- (iv) screen-printing of Al on the rear,
- (v) pad printing of front grid,
- (vi) cofiring,
- (vii) edge isolation,
- (viii) light-induced plating.

The printed lines had a width of  $50 \mu\text{m}$ . Cell parameters as shown in Table 7 have been achieved. The achieved efficiency of 17.9% shows the high potential of the technology. A similar result was achieved using conventional silver screen-printing paste.

### 3.3. Laser sintering/melting of metal powder

The second seed layer technology which involves the deposition of a powder of metal particles is deposited on the surface of the cell. The metal powder is sintered or melted locally by a scanning laser to form the contact lines (see Figure 11). The rest of the powder is removed easily from the surface leaving laser-sintered contact lines [46]. Although it is possible to increase the height of the contact lines by repeating the process, we have decided to form only a small seed layer which is

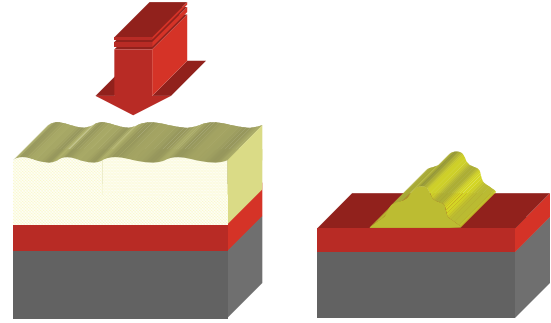


FIGURE 11: Laser microsintering of metal powder on the front surface of solar cells.

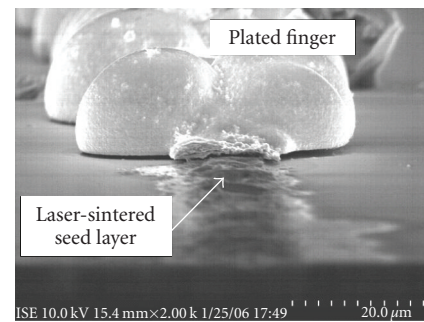


FIGURE 12: SEM image of a seed layer created by laser microsintering thickened by light-induced electroplating.

thickened subsequently by light-induced silver plating making the approach more economical.

Figure 12 shows the structure of a laser-sintered finger after the subsequent light-induced plating step. The contact formed by laser sintering is very fine and thin, while the line conductivity is generated by the plated silver on top of this seed layer.

Initial cell results on small areas ( $1 \times 1 \text{ cm}^2$ ) have shown efficiencies of 14.0%, although a heavily doped emitter ( $18 \Omega/\text{sq}$ ) was chosen for these preliminary experiments. We have achieved an open-circuit voltage of 622 mV. The pseudo FF of this cell measured using SunsVoc was determined to be 78%. Although this value is still below the optimum, it shows that it is possible to avoid severe damage in the emitter or space charge region by the laser process. Thus, it should be possible to utilize this technique for solar cell processing.

### 3.4. Chemical plating of Ni

Nickel plating is well known, used as a part of the laser-buried contact process by BP Solar to fabricate high-efficiency industrial solar cells [41]. However, in this process sequence, it is necessary to form a groove in the silicon surface which then receives a damage etch and a heavily doped phosphorus diffusion. Instead, it would be desirable to use a one-step process to form a front surface structure which initializes the local electroless Ni plating process.

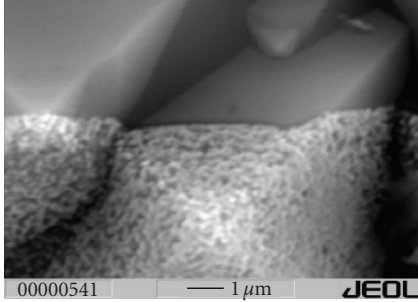


FIGURE 13: Ni plating on a textured silicon surface.

TABLE 8: Results of  $20 \times 20 \text{ mm}^2$  oxide-passivated FZ-Si solar cells. The front grid structured was fabricated using electroless Ni plating and light-induced plating.

	$V_{oc}$ [mV]	$J_{sc}$ [mA/cm <sup>2</sup> ]	FF [%]	$\eta$ [%]
Ni plating + LIP	661	38.9	73.4	18.9

This motivates the use of laser ablation process to remove lines of the front surface  $\text{SiN}_x$  layer of standard cells similar to the approach demonstrated by Dubé and Gonsiorawski [47]. SunsVoc measurements have shown that this process does not damage the underlying silicon, that is, the pn-junction [48].

The Ni plating process was optimized to work on non-grooved surfaces and medium-doped emitter profiles. It is possible to initiate a sufficient Ni plating process (see Figure 13) with the optimized process.

For the initial experiments on cell level, however, we have used cell structures with an oxide-passivated emitter and rear surface. Due to the unfavourable absorption coefficient of silicon oxide, it is not possible to ablate the oxide without damaging the silicon underneath. Thus, a photoresist was used in these experiments to mask a chemical etching step to open the grid structure in the front oxide. The efficiency of 18.9% shows the quality of the developed plating process although there is still room for improvement by reducing the series resistance. Combined with the fact that the grid opening in a  $\text{SiN}_x$  front surface layer can be achieved by damage-free laser processing [48] or ink-jet masking and subsequent etching, it is believed that Ni plating will be an interesting option for the formation of seed layers even without a heavily diffused groove.

### 3.5. Metal aerosol jetting

A very elegant way to deposit the seed layer on top of the solar cell would be metal ink jetting. However, standard pastes cannot be used due to the relatively large particle sizes (5–10  $\mu\text{m}$ ), resulting in clogging which is a severe problem for jetting. As a rule of thumb, the diameter of the nozzle should be at least six times bigger than the particle size. Thus, the resulting line width would be in the range of screen-printed fingers defeating the purpose of the development.

Therefore, in our setup, the paste is not printed directly. Instead, a metal aerosol is generated and conducted into

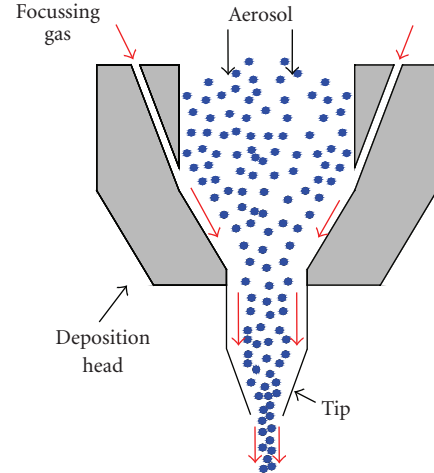


FIGURE 14: Printing head of the metal aerosol printing technique.

a specially designed printing head (see Figure 14). In this printing head, the aerosol is wrapped up in a ring-shaped gas flow to avoid the aerosol from being in contact with the tip. The ring-shaped gas flow is also responsible for focusing the aerosol achieving printed line widths to be considerably smaller than the tip diameter. It has been demonstrated, by using a nozzle with an outlet diameter of 200  $\mu\text{m}$ , that printed lines with 50  $\mu\text{m}$  width can be achieved. Additionally, the printing result is independent of the distance between nozzle and substrate which makes the technique suitable for uneven substrates. The metal aerosol jet printer was developed by Optomec Inc., NM, USA. A laboratory version of this printer was installed at Fraunhofer ISE. The set-up was modified and the process parameters for solar cell metallization were optimized [49].

A great variety of modified commercial pastes and nanoparticle inks were tested. Although the printing results (line width, etc.) of the nanoparticle inks were excellent, the electrical (contact resistance and conductivity) and mechanical (adhesion) properties were not satisfying. Thus, we have used modified standard Ag pastes and despite their relatively large particle size, we managed to get small line widths of around 50–60  $\mu\text{m}$ . This process was used to fabricate the front grid of industrial multicrystalline solar cells with the following processing sequence:

- (i) textured multicrystalline silicon,
- (ii) emitter diffusion (55  $\Omega/\text{sq}$ ) + PSG etch,
- (iii) deposition of PECVD  $\text{SiN}_x$ ,
- (iv) screen-printing of Al-BSF,
- (v) aerosol printing (modified commercial Ag Paste),
- (vi) cofiring,
- (vii) edge isolation,
- (viii) light-induced plating.

Two different finger widths were printed resulting in 160  $\mu\text{m}$  and 70  $\mu\text{m}$  wide lines after plating, respectively. Table 9 shows the results of the finished solar cells as measured at Fraunhofer ISE CalLab. The cells with a finger width of 160  $\mu\text{m}$  exhibit a high fill factor demonstrating that

TABLE 9: Results of  $50 \times 50 \text{ mm}^2$  multicrystalline solar cells with Al-BSF and  $\text{SiN}_x$  front passivation. The front grid structure was fabricated using metal aerosol jet printing, firing and light-induced plating.

Finger width	$V_{oc}$ [mV]	$J_{sc}$ [mA/cm <sup>2</sup> ]	FF [%]	$\eta$ [%]
160 $\mu\text{m}$	617	32.7	79.4	16.0
70 $\mu\text{m}$	618	34.2	77.4	16.4

TABLE 10: Results of  $125 \times 125 \text{ mm}^2$  monocrystalline solar cells with Al-BSF and  $\text{SiN}_x$  front passivation. The front grid structure was fabricated using metal aerosol jet printing, firing, and light-induced plating.

Finger width	$V_{oc}$ [mV]	$J_{sc}$ [mA/cm <sup>2</sup> ]	FF [%]	$\eta$ [%]
90 $\mu\text{m}$	620	35.8	80.2	17.8

the contact formation works excellently. However, since the shading loss is not reduced, the efficiency is similar to the screen-printing references. The cells with 70  $\mu\text{m}$  fingers show a much smaller shading loss than standard cells resulting in increased current and a significantly higher efficiency of 16.4%. The fill factor is satisfying. The overall benefit for this new and promising technique will be even higher if especially optimized pastes are used for future devices.

In a further batch, solar cells were processed on  $12.5 \text{ cm} \times 12.5 \text{ cm}$ , 3 to 6  $\Omega \text{ cm}$ , boron-doped Cz-Si wafers. These cells exhibit a textured surface with a 45  $\Omega/\text{sq}$  emitter covered by a sputtered  $\text{SiN}_x$  antireflection coating. After conventional screen-printing and drying of the back side, the front side was printed using the metal aerosol jet printer. After firing in a fast firing single wafer furnace, the front contacts were thickened by light-induced plating and edge isolated by laser scribing and breaking. The same paste as for the multicrystalline cells was used with the addition of phosphorus. The idea is to form a higher emitter doping level directly under the contacts, in order to achieve good adhesion and low contact resistivity to the emitter surface.

Remarkable efficiencies up to 17.8% have been achieved (see Table 10) compared to the best efficiency of 17.2% achieved by screen-printed reference cells, again demonstrating a significant efficiency increase for the metal aerosol jet-printed cells compared to conventional screen-printed ones.

#### 4. BULK PROPERTIES

Certainly, even the best cell structure will not result in high efficiencies if the material quality is too low. Therefore, the investigation of electrically active defects is of great importance for photovoltaic material. Especially for multicrystalline silicon, it is very important to understand thermal treatments, gettering [12, 50], and hydrogen passivation in order to increase the carrier diffusion length. These measures were extremely important to obtain the record efficiencies on small (20.3% on  $1 \text{ cm}^2$ ) [14] and large area (18.1% on  $137.7 \text{ cm}^2$ ) [51] multicrystalline substrates.

However, the material issue will become less critical as the wafers used for PV production are getting thinner. Thus,

the decisive ratio diffusion length to thickness increases by decreasing the denominator. This is especially interesting for high-efficiency cell structures since the high-quality surface structures are capable of retaining cell performance as the cell thickness decreases. For example, the world record efficiency of 20.3% on multicrystalline silicon using a fully surface passivated cell structure was achieved on 99  $\mu\text{m}$  thick material while an efficiency of “only” 19.9% was achieved for a 218  $\mu\text{m}$  thick wafer of the same material type [14]. Using high-efficiency cell structures, efficiencies greater than 20% have been achieved on extremely thin monocrystalline wafers of less than 50  $\mu\text{m}$  [52, 53].

Most of the monocrystalline silicon solar cell manufacturers use boron-doped Czochralski silicon as starting material. This material type shows a severe *degradation* of minority carrier lifetime induced by illumination or carrier injection [54, 55]. The responsible metastable defect is related clearly to the existence of boron and oxygen [11, 56]. Three options are promising for a reduction of this degradation: (i) the use of *thinner wafers* to improve the ratio diffusion length/cell thickness [57], (ii) *decreasing the boron concentration* to reduce the light-induced degradation [58, 59], or (iii) the application of the *regeneration process* as recently demonstrated by Herguth et al. [60].

But also alternative material types are of interest. In fact, cells from *gallium-doped Cz-silicon* show no degradation [61]. The only issue occurring with this material might be the large variation of doping concentration over the ingot due to the low segregation coefficient of gallium. Nevertheless, adapted cell structures show excellent results over a wide doping range [62].

A strong reduction of the oxygen concentration to values below 1 ppma results also in a perfect suppression of light-induced degradation. *Magnetic Czochralski (MCz) silicon* has shown a very high-efficiency potential [61, 63]. Another material, PV-FZ [64], with a negligible oxygen concentration was discussed to be introduced into the large-scale PV production a few years ago. This material type has shown very high and stable carrier lifetimes for p- and n-doping, but unfortunately the availability of this material type is still not clear at the moment.

Another material type of interest is certainly *n-type silicon*. *n-type Czochralski-grown material* shows no carrier-induced degradation even in the presence of a significant oxygen concentration [56, 65]. Also for multicrystalline silicon, excellent minority carrier lifetimes have been measured [66, 67] This superior material quality is mainly due to the fact that for most relevant defects, the ratio of electron to hole capture cross sections is much greater than unity. Therefore, compared to p-type silicon, the minority carrier lifetime for the same defect concentration is much greater in the case of n-type silicon since this parameter is mainly influenced by the whole capture cross section.

The only disadvantage of *n-type silicon* is the fact that it is not compatible with conventional industrial cell structures. Therefore, it is mainly used in advanced cell types. Prominent high-efficiency cell structures in industrial production which make use of this material are the amorphous silicon (a-Si)/monocrystalline silicon (c-Si) heterojunction

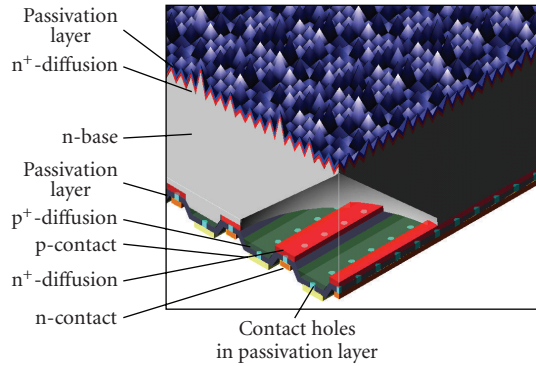


FIGURE 15: Point-contact cell of SunPower (redrawn after [68]).

with intrinsic thin layer (HIT) cell [30] and the back-contact cell A300 of SunPower [68] featuring a boron rear emitter (see next section). But also simpler cell structures using Al-diffused rear emitters have shown excellent performance [69, 70].

## 5. CELL STRUCTURES

To achieve the highest efficiencies, it is of course not enough to optimize a single aspect of a cell but different measures have to be combined in designing a cell structure to achieve high efficiencies. In what follows, a few examples of high-efficiency cell structures are described briefly.

The A-300 of SunPower [68] (see Figure 15) is a strongly simplified version of the point-contact cell originally developed for concentrator applications at Stanford University [8].

The main feature of this 20% cell in mass production is the absence of any metal contacts on the front side since both electrodes are placed on the rear surface as an interdigitated grid. Thus, nearly all carriers have to diffuse from the front surface where they are photo generated to the collecting  $pn$ -junction at the rear surface. Therefore, the bulk diffusion length has to be high (see previous section) and especially the surface recombination velocity at the front has to be very low. The task is managed by an excellently passivating  $\text{SiO}_2$  layer on a lowly doped  $n^+$ -front surface field. Although, back-contact cells are obviously extremely attractive in terms of efficiency and aesthetics, they also pose very high demands on material quality and process technology. Especially the fabrication of the rear surface structure, that is, the separation of  $p$ - and  $n$ -diffused regions or  $p$ - and  $n$ -electrodes is an issue. One interesting opportunity for this task is the use of laser technologies [71].

In contrast to the A300, the  $p^+$ -emitter on the  $n$ -substrate for the HIT cell of Sanyo [30] is not based on boron diffusion but is formed by the deposition of  $p$ -doped  $a$ -Si layer (see Figure 16). Also, the rear surface is passivated by an  $a$ -Si layer in order to obtain the full potential of the monocrystalline  $n$ -type silicon. Efficiencies above 20% can be well achieved using this cell structure.

Another cell structure utilizing excellent surface passivation is the Sliver cell (see Figure 17). Very thin ( $50\text{--}60\ \mu\text{m}$ )

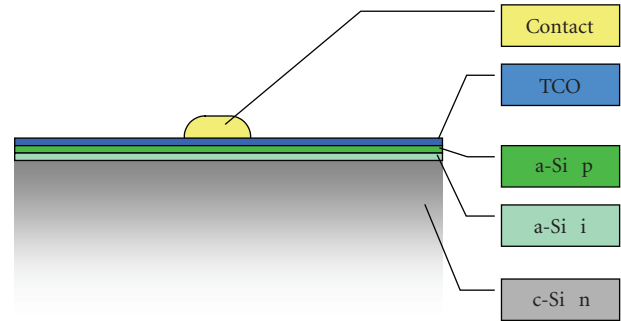


FIGURE 16: Front structure of the HIT cell.

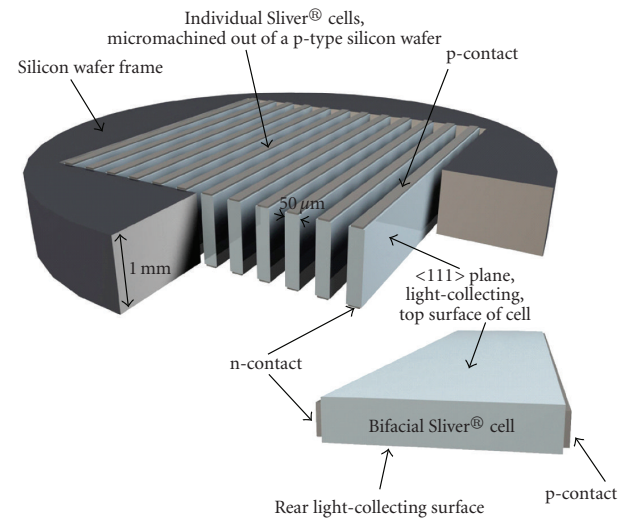


FIGURE 17: Sliver cells (taken from [73]).

strips of silicon are micro machined from a 1-2 mm thick monocrystalline wafer [72, 73]. The strips are processed including many high-efficiency features while still supported by the wafer at their edges. After processing, they are separated and mounted into a module. Due to the excellent surface passivation on these cells, it is possible to reach efficiencies above 19%.

Rear contact cells on low-quality material cannot use a back junction cell structure as in the A300. It is necessary to implement a collecting emitter on the front side of the cell to make the cell structure less sensitive to low-diffusion lengths [74]. This emitter has to be connected to the rear electrode of the cell. This can be either obtained by metallized vias connecting the front fingers with the rear bus bar in the metal-wrap-through (MWT) structure [75] (see Figure 18) or by emitter-diffused holes in the emitter-wrap-through (EWT) structure [76] (see Figure 19). For a very comprehensive review of these cell types see [77].

The big advantage of the MWT structure is that it is relatively easy to be adapted to existing industrial cell production lines. The only difference in cell design compared to the standard is the bus bar being transferred to the rear side, with the fingers remaining on the front side. Due to the high lateral conductivity of the metal grid, a relatively low number of

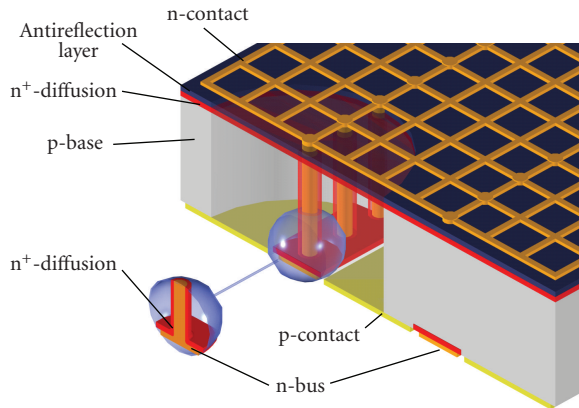


FIGURE 18: Structure of a metal-wrap-through (MWT) cell.

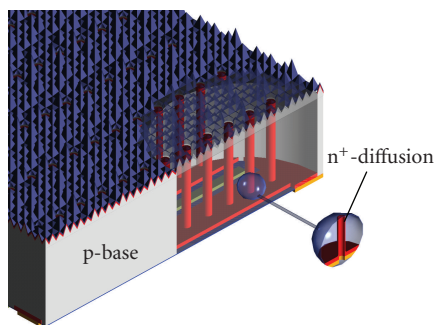


FIGURE 19: Structure of an emitter-wrap-through (EWT) cell.

vias is needed. The MWT is commercialized by Photovoltech. A similar cell structure called the PUM cell is developed by ECN [78].

In EWT cells [76, 79], the complete metal structure is located on the rear side. Due to the limited lateral conductivity of the front emitter, more vias are needed compared to the MWT structure. However, this should not be a limitation in production due to the capability of state-of-the-art laser equipment responsible for the formation of vias. The EWT cell design has been demonstrated to be capable of achieving high efficiencies of 21.4% [80], and suitable for industrial production as demonstrated by Advent Solar, Inc. Nm, USA, [81] resulting in cell efficiencies above 15%.

## 6. CONCLUSION

High-efficiency cell structures help to reduce the costs of photovoltaic energy generation in two ways: (i) by increasing the efficiency and hence the power output *per area* of used silicon or (ii) by allowing the use of thinner wafers achieving same level or even improved efficiency and hence the power output *per volume* or *per weight*. However, in order to allow for an industrial production of high-efficiency silicon solar cells, several design or technology limitations have to be addressed. This paper has discussed four important aspects associated with high-efficiency cells, that is, (i) the surface passivation, (ii) metal contacts, (iii) material quality, and (iv) cell structure.

## ACKNOWLEDGMENTS

The author would like to thank all colleagues at Fraunhofer ISE for their enthusiastic commitment. Parts of this work have been supported by the German Federal Ministry for the Environment, Nature Conservation, and Nuclear Safety (BMU).

## REFERENCES

- [1] M. Hermle, E. Schneiderlöchner, G. Grupp, and S. W. Glunz, "Comprehensive comparison of different rear side contacting methods for high-efficiency solar cells," in *Proceedings of the 20th European Photovoltaic Solar Energy Conference*, pp. 810–813, Barcelona, Spain, June 2005.
- [2] D. Kray, M. Hermle, and S. W. Glunz, "Theory and experiments on the back side reflectance of silicon wafer solar cells," to appear in *Progress in Photovoltaics: Research and Applications*.
- [3] J. Zhao, A. Wang, P. P. Altermatt, S. R. Wenham, and M. A. Green, "24% efficient PERL silicon solar cell: recent improvements in high efficiency silicon cell research," in *Proceedings of the 1st World Conference on Photovoltaic Energy Conversion (WCPEC '94)*, pp. 87–99, Waikoloa, Hawaii, USA, December 1994.
- [4] J. Knobloch, A. Aberle, W. Warta, and B. Voss, "Starting points for raising the efficiency of practical silicon solar cells," in *Proceedings of the 5th International Photovoltaic Science and Engineering Conference*, Kyoto, Japan, November 1990.
- [5] E. Schneiderlöchner, R. Preu, R. Lüdemann, and S. W. Glunz, "Laser-fired rear contacts for crystalline silicon solar cells," *Progress in Photovoltaics: Research and Applications*, vol. 10, no. 1, pp. 29–34, 2002.
- [6] A. W. Blakers, A. Wang, A. M. Milne, J. Zhao, and M. A. Green, "22.8% efficient silicon solar cell," *Applied Physics Letters*, vol. 55, no. 13, pp. 1363–1365, 1989.
- [7] A. G. Aberle, *Crystalline Silicon Solar Cells: Advanced Surface Passivation and Analysis*, The University of New South Wales, Sydney, Australia, 1999.
- [8] R. A. Sinton, Y. Kwark, J. Y. Gan, and R. M. Swanson, "27.5-percent silicon concentrator solar cells," *Electron Device Letters*, vol. 7, no. 10, pp. 567–569, 1986.
- [9] J. Zhao, A. Wang, and M. A. Green, "24% efficient PERL structure silicon solar cells," in *Proceedings of the 21st IEEE Photovoltaic Specialists Conference*, vol. 1, pp. 333–335, Kissimmee, Fla, USA, May 1990.
- [10] E. H. Nicollian and J. R. Brews, *MOS Physics and Technology*, Wiley, New York, NY, USA, 1982.
- [11] S. W. Glunz, S. Rein, W. Warta, J. Knobloch, and W. Wettling, "On the degradation of Cz-silicon solar cells," in *Proceedings of the 2nd World Conference on Photovoltaic Energy Conversion*, pp. 1343–1346, Vienna, Austria, July 1998.
- [12] D. Macdonald and A. Cuevas, "The trade-off between phosphorus gettering and thermal degradation in multicrystalline silicon," in *Proceedings of the 16th European Photovoltaic Solar Energy Conference*, pp. 1707–1710, Glasgow, UK, May 2000.
- [13] O. Schultz, S. Riepe, and S. W. Glunz, "Influence of high-temperature processes on multicrystalline silicon," *Solid State Phenomena*, vol. 95-96, pp. 235–240, 2004.
- [14] O. Schultz, S. W. Glunz, and G. P. Willeke, "Multicrystalline silicon solar cells exceeding 20% efficiency," *Progress in Photovoltaics: Research and Applications*, vol. 12, no. 7, pp. 553–558, 2004.

- [15] M. Stocks and A. Cuevas, "Surface recombination velocity of thermally oxidised multicrystalline silicon," in *Proceedings of the 2nd World Conference on Photovoltaic Energy Conversion*, pp. 1623–1626, Vienna, Austria, July 1998.
- [16] J. Schmidt, T. Lauinger, A. G. Aberle, and R. Hezel, "Record low surface recombination velocities on low-resistivity silicon solar cell substrates," in *Proceedings of the 25th IEEE Photovoltaic Specialists Conference*, pp. 413–416, Washington, DC, USA, May 1996.
- [17] W. Wolke, J. Catoir, G. Emanuel, J. Liu, M. Ruske, and R. Preu, "Surface passivation for solar cells by large scale inline sputtering of silicon nitride," in *Proceedings of the 20th European Photovoltaic Solar Energy Conference*, pp. 733–736, Barcelona, Spain, June 2005.
- [18] M. Tanaka, S. Okamoto, S. Tsuge, and S. Kiyama, "Development of HIT solar cells with more than 21% conversion efficiency and commercialization of highest performance hit modules," in *Proceedings of the 3rd World Conference on Photovoltaic Energy Conversion (WCPEC '03)*, vol. 1, pp. 955–958, Osaka, Japan, May 2003.
- [19] M. Schaper, J. Schmidt, H. Plagwitz, and R. Brendel, "20.1%-efficient crystalline silicon solar cell with amorphous silicon rear-surface passivation," *Progress in Photovoltaics: Research and Applications*, vol. 13, no. 5, pp. 381–386, 2005.
- [20] M. Hofmann, S. W. Glunz, R. Preu, and G. Willeke, "21%-efficient silicon solar cells using amorphous silicon rear side passivation," in *Proceedings of the 21st European Photovoltaic Solar Energy Conference*, pp. 609–613, Dresden, Germany, September 2006.
- [21] S. de Wolf, G. Agostinelli, G. Beaucarne, and P. Vitanov, "Influence of stoichiometry of direct plasma-enhanced chemical vapor deposited SiNx films and silicon substrate surface roughness on surface passivation," *Journal of Applied Physics*, vol. 97, no. 6, Article ID 063303, 8 pages, 2005.
- [22] M. A. Green, *Solar Cells: Operating Principles, Technology and System Applications*, The University of New South Wales, Sydney, Australia, 1998.
- [23] M. Hofmann, E. Schneiderlöchner, W. Wolke, and R. Preu, "Silicon nitride-silicon oxide stacks for solar cell rear side passivation," in *Proceedings of the 19th European Photovoltaic Solar Energy Conference*, pp. 1037–1040, Paris, France, June 2004.
- [24] S. Dauwe, L. Mittelstädt, A. Metz, and R. Hezel, "Experimental evidence of parasitic shunting in silicon nitride rear surface passivated solar cells," *Progress in Photovoltaics: Research and Applications*, vol. 10, no. 4, pp. 271–278, 2002.
- [25] S. W. Glunz, R. Preu, S. Schaefer, et al., "New simplified methods for patterning the rear contact of RP-PERC high-efficiency solar cells," in *Proceedings of the 28th IEEE Photovoltaic Specialists Conference*, pp. 168–171, Anchorage, Alaska, USA, September 2000.
- [26] S. Dauwe, L. Mittelstädt, A. Metz, J. Schmidt, and R. Hezel, "Low-temperature rear surface passivation schemes for >20% efficient silicon solar cells," in *Proceedings of the 3rd World Conference on Photovoltaic Energy Conversion*, vol. 2, pp. 1395–1398, Osaka, Japan, May 2003.
- [27] J. Schmidt, M. Kerr, and A. Cuevas, "Surface passivation of silicon solar cells using plasma-enhanced chemical-vapour-deposited SiN films and thin thermal SiO<sub>2</sub>/plasma SiN stacks," *Semiconductor Science and Technology*, vol. 16, no. 3, pp. 164–170, 2001.
- [28] J. Y. Lee, J. Dicker, S. Rein, and S. W. Glunz, "Investigation of various surface passivation layers using oxide/nitride stacks of silicon solar cells," in *Proceedings of the 3rd World Conference on Photovoltaic Energy Conversion (WCPEC '03)*, vol. 2, pp. 1069–1072, Osaka, Japan, May 2003.
- [29] O. Schultz, M. Hofmann, S. W. Glunz, and G. P. Willeke, "Silicon oxide/silicon nitride stack system for 20% efficient silicon solar cells," in *Proceedings of the 31st IEEE Photovoltaic Specialists Conference*, pp. 872–876, Orlando, Fla, USA, January 2005.
- [30] K. Kawamoto, T. Nakai, T. Baba, et al., "A high-efficiency HIT™ solar cell (21.0% 100 cm<sup>2</sup>) with excellent interface properties," in *Proceedings of the 12th International Photovoltaic Science and Engineering Conference (PVSEC '01)*, pp. 289–290, Jeju, Korea, June 2001.
- [31] P. J. Rostan, U. Rau, V. X. Nguyen, T. Kirchartz, M. B. Schubert, and J. H. Werner, "Low-temperature a-Si:H/ZnO/Al back contacts for high-efficiency silicon solar cells," *Solar Energy Materials and Solar Cells*, vol. 90, no. 9, pp. 1345–1352, 2006.
- [32] I. Martín, M. Vetter, A. Orpella, J. Puigdollers, A. Cuevas, and R. Alcubilla, "Surface passivation of p-type crystalline Si by plasma enhanced chemical vapor deposited amorphous SiC<sub>x</sub>:H films," *Applied Physics Letters*, vol. 79, no. 14, pp. 2199–2201, 2001.
- [33] S. Janz, S. Reber, F. Lutz, and C. Schetter, "SiC as an intermediate layer for CsITF solar cells on various substrates," in *Proceedings of the 20th European Photovoltaic Solar Energy Conference*, pp. 1016–1019, Barcelona, Spain, June 2005.
- [34] S. Janz, S. Riepe, M. Hofmann, S. Reber, and S. W. Glunz, "Phosphorus-doped SiC as an excellent p-type Si surface passivation layer," *Applied Physics Letters*, vol. 88, no. 13, Article ID 133516, 2 pages, 2006.
- [35] W. Warta, S. W. Glunz, J. Dicker, and J. Knobloch, "Highly efficient 115- $\mu$ m-thick solar cells on industrial Czochralski silicon," *Progress in Photovoltaics: Research and Applications*, vol. 8, no. 5, pp. 465–471, 2000.
- [36] E. Schneiderlöchner, G. Grupp, G. Emanuel, et al., "Silicon solar cells with screen printed front contact and dielectrically passivated laser-fired rear electrode," in *Proceedings of the 19th European Photovoltaic Solar Energy Conference*, pp. 447–450, Paris, France, June 2004.
- [37] D. Macdonald, A. Cuevas, K. McIntosh, L. Barbosa, and D. de Ceuster, "Impact of Cr, Fe, Ni, Ti and W surface contamination on diffused and oxidised n-type crystalline silicon wafers," in *Proceedings of the 20th European Photovoltaic Solar Energy Conference*, pp. 627–630, Barcelona, Spain, June 2005.
- [38] G. Agostinelli, P. Choulat, H. F. W. Dekkers, S. de Wolf, and G. Beaucarne, "Advanced dry processes for crystalline silicon solar cells," in *Proceedings of the 31st IEEE Photovoltaic Specialists Conference*, pp. 1149–1152, Orlando, Fla, USA, January 2005.
- [39] G. Agostinelli, P. Choulat, H. F. W. Dekkers, Y. Ma, and G. Beaucarne, "Silicon solar cells on ultra-thin substrates for large scale production," in *Proceedings of the 21st European Photovoltaic Solar Energy Conference*, Dresden, Germany, September 2006.
- [40] R. A. Sinton, A. Cuevas, and M. Stuckings, "Quasi-steady-state photoconductance, a new method for solar cell material and device characterization," in *Proceedings of the 25th IEEE Photovoltaic Specialists Conference*, pp. 457–460, Washington, DC, USA, May 1996.
- [41] T. M. Bruton, N. B. Mason, S. Roberts, et al., "Towards 20% efficient silicon solar cells manufactured at 60 MWp per annum," in *Proceedings of the 3rd World Conference on Photovoltaic Energy Conversion (WCPEC '03)*, vol. 1, pp. 899–902, Osaka, Japan, May 2003.

- [42] M. A. Green and S. R. Wenham, Australian Patent No. 5703309, 1984.
- [43] A. Mette, C. Schetter, D. Wissen, S. Lust, S. W. Glunz, and G. Willeke, "Increasing the efficiency of screen-printed silicon solar cells by light-induced silver plating," in *Proceedings of the 4th World Conference on Photovoltaic Energy Conversion*, vol. 1, pp. 1056–1059, Waikoloa, Hawaii, USA, May 2006.
- [44] D. M. Huljić, S. Thormann, R. Preu, R. Lüdemann, and G. Willeke, "Pad printed front contacts for c-Si solar cells—a technological and economical evaluation," in *Proceedings of the 29th IEEE Photovoltaic Specialists Conference (PVSC '02)*, pp. 126–129, New Orleans, La, USA, May 2002.
- [45] A. Mette, D. Erath, R. Ruiz, G. Emanuel, E. Kasper, and R. Preu, "Hot melk ink for the front side metallisation of silicon solar cells," in *Proceedings of the 20th European Photovoltaic Solar Energy Conference*, Barcelona, Spain, June 2005.
- [46] M. Alemán, A. Streek, P. Regenfuß, et al., "Laser micro-sintering as a new metallization technique for silicon solar cells," in *Proceedings of the 21st European Photovoltaic Solar Energy Conference and Exhibition*, Dresden, Germany, September 2006.
- [47] C. E. Dubé and R. C. Gonsiorawski, "Improved contact metallization for high efficiency EFG polycrystalline silicon solar cells," in *Proceedings of 21st IEEE Photovoltaic Specialists Conference*, vol. 1, pp. 624–628, Kissimmee, Fla, USA, May 1990.
- [48] A. Grohe, C. Harmel, A. Knorz, S. W. Glunz, R. Preu, and G. P. Willeke, "Selective laser ablation of anti-reflection coatings for novel metallization techniques," in *Proceedings of the IEEE 4th World Conference on Photovoltaic Energy Conversion*, vol. 2, pp. 1399–1402, Waikoloa, Hawaii, USA, May 2006.
- [49] A. Mette, P. L. Richter, M. Hörteis, and S. W. Glunz, "Metal aerosol jet printing for solar cell metallization," to appear in *Progress in Photovoltaics: Research and Applications*.
- [50] O. Schultz, S. W. Glunz, S. Riepe, and G. P. Willeke, "High-efficiency solar cells on phosphorus gettered multicrystalline silicon substrates," *Progress in Photovoltaics: Research and Applications*, vol. 14, no. 8, pp. 711–719, 2006.
- [51] M. McCann, B. Raabe, W. Jooss, R. Kopecek, and P. Fath, "18.1% efficiency for a large area, multi-crystalline silicon solar cell," in *Proceedings of the 4th World Conference on Photovoltaic Energy Conversion (WCPEC '06)*, vol. 1, pp. 894–899, Waikoloa, Hawaii, USA, May 2006.
- [52] D. Kray, H. Kampwerth, E. Schneiderlöchner, et al., "Comprehensive experimental study on the performance of very thin laser-fired high-efficiency solar cells," in *Proceedings of the 19th European Photovoltaic Solar Energy Conference*, pp. 608–611, Paris, France, June 2004.
- [53] A. Wang, J. Zhao, S. R. Wenham, and M. A. Green, "21.5% efficient thin silicon solar cell," *Progress in Photovoltaics: Research and Applications*, vol. 4, no. 1, pp. 55–58, 1996.
- [54] H. Fischer and W. Pschunder, "Investigation of photon and thermal induced changes in silicon solar cells," in *Proceedings of the 10th IEEE Photovoltaic Specialists Conference*, pp. 404–411, Palo Alto, Calif, USA, November 1973.
- [55] J. Knobloch, S. W. Glunz, V. Henninger, et al., "21% efficient solar cells processed from Czochralski grown silicon," in *Proceedings of the 13th European Photovoltaic Solar Energy Conference*, pp. 9–12, Nice, France, October 1995.
- [56] J. Schmidt, A. G. Aberle, and R. Hezel, "Investigation of carrier lifetime instabilities in Cz-grown silicon," in *Proceedings of the IEEE 26th Photovoltaic Specialists Conference (PVSC '97)*, pp. 13–18, Anaheim, Calif, USA, September–October 1997.
- [57] K. A. Münzer, K. T. Holdermann, R. E. Schlosser, and S. Sterk, "Improvements and benefits of thin crystalline silicon solar cells," in *Proceedings of the 2nd World Conference on Photovoltaic Energy Conversion*, pp. 1214–1219, Vienna, Austria, July 1998.
- [58] S. Rein, W. Warta, and S. W. Glunz, "Investigation of carrier lifetime in p-type Cz-silicon: specific limitations and realistic prediction of cell performance," in *Proceedings of the 28th IEEE Photovoltaics Specialists Conference*, pp. 57–60, Anchorage, Alaska, USA, September 2000.
- [59] S. W. Glunz, S. Rein, J. Y. Lee, and W. Warta, "Minority carrier lifetime degradation in boron-doped Czochralski silicon," *Journal of Applied Physics*, vol. 90, no. 5, pp. 2397–2404, 2001.
- [60] A. Herguth, G. Schubert, M. Kaes, and G. Hahn, "Avoiding boron-oxygen related degradation in highly boron-doped Cz silicon," in *Proceedings of the 21st European Photovoltaic Solar Energy Conference*, pp. 530–537, Dresden, Germany, September 2006.
- [61] S. W. Glunz, S. Rein, J. Knobloch, W. Wettling, and T. Abe, "Comparison of boron- and gallium-doped p-type Czochralski silicon for photovoltaic application," *Progress in Photovoltaics: Research and Applications*, vol. 7, no. 6, pp. 463–469, 1999.
- [62] S. W. Glunz, S. Rein, and J. Knobloch, "Stable Czochralski silicon solar cells using gallium-doped base material," in *Proceedings of the 16th European Photovoltaic Solar Energy Conference*, pp. 1070–1075, Glasgow, UK, May 2000.
- [63] J. Zhao, A. Wang, and M. A. Green, "24.5% efficiency PERT silicon solar cells on SEH MCZ substrates and cell performance on other SEH CZ and FZ substrates," *Solar Energy Materials and Solar Cells*, vol. 66, no. 1–4, pp. 27–36, 2001.
- [64] J. Vedde, T. Clausen, and L. Jensen, "Float-zone silicon for high volume production of solar cells," in *Proceedings of the 3rd World Conference on Photovoltaic Energy Conversion*, vol. 1, pp. 943–946, Osaka, Japan, May 2003.
- [65] T. Yoshida and Y. Kitagawara, "Bulk lifetime decreasing phenomena induced by light-illumination in high-purity p-type CZ-Si crystals," in *Proceedings of the 4th International Symposium on High Purity Silicon IV*, pp. 450–454, San Antonio, Tex, USA, October 1996.
- [66] A. Cuevas, M. J. Kerr, C. Samundsett, F. Ferrazza, and G. Colletti, "Millisecond minority carrier lifetimes in n-type multicrystalline silicon," *Applied Physics Letters*, vol. 81, no. 26, pp. 4952–4954, 2002.
- [67] S. Riepe, H. Lautenschlager, J. Isenberg, et al., "Increased wafer yield for solar cells in top and bottom regions of cast multicrystalline silicon," in *Proceedings of the 19th European Photovoltaic Solar Energy Conference*, pp. 986–989, Paris, France, June 2004.
- [68] K. R. McIntosh, M. J. Cudzinovic, D. D. Smith, W. P. Mulligan, and R. M. Swanson, "The choice of silicon wafer for the production of low-cost rear-contact solar cells," in *Proceedings of the 3rd World Conference on Photovoltaic Energy Conversion (WCPEC '03)*, vol. 1, pp. 971–974, Osaka, Japan, May 2003.
- [69] S. W. Glunz, E. Schneiderlöchner, D. Kray, et al., "Laser-fired contact solar cells on p- and n-type substrates," in *Proceedings of the 19th European Photovoltaic Solar Energy Conference*, pp. 408–411, Paris, France, June 2004.
- [70] C. Schmiga, A. Froitzheim, M. Ghosh, A. Metz, J. Schmidt, and R. Brendel, "Solar cells on n-type silicon materials with screen-printed rear aluminium-P emitter," in *Proceedings of the 20th European Photovoltaic Solar Energy Conference*, Barcelona, Spain, June 2005.

- [71] D. M. Huljic, T. Zerres, A. Mohr, et al., "Development of a 21% back-contact monocrystalline silicon solar cell for large-scale production," in *Proceedings of the 21th European Photovoltaic Solar Energy Conference*, Dresden, Germany, September 2006.
- [72] M. J. Stocks, K. J. Weber, A. W. Blakers, et al., "65-micron thin monocrystalline silicon solar cell technology allowing 12-fold reduction in silicon usage," in *Proceedings of 3rd World Conference on Photovoltaic Energy Conversion*, vol. 1, pp. 184–187, Osaka, Japan, May 2003.
- [73] A. W. Blakers, K. J. Weber, E. Everett, E. Franklin, and P. Deenapanray, "Sliver cells—a complete photovoltaic solution," in *Proceedings of the 4th World Conference on Photovoltaic Energy Conversion (WCPEC '06)*, vol. 2, pp. 2181–2184, Waikoloa, Hawaii, USA, May 2006.
- [74] D. Kray, S. Rein, D. Oßwald, et al., "High-efficiency emitter-wrap-through cells," in *Proceedings of the 17th European Photovoltaic Solar Energy Conference*, pp. 1299–1302, Munich, Germany, October 2001.
- [75] E. van Kerschavers, S. de Wolf, and J. Szlufcik, "Screen printed metallisation wrap through solar cells," in *Proceedings of the 16th European Photovoltaic Solar Energy Conference*, pp. 1517–1520, Glasgow, UK, May 2000.
- [76] J. M. Gee, K. W. Schubert, and P. A. Basore, "Emitter wrap-through solar cell," in *Proceedings of the 23rd IEEE Photovoltaic Specialists Conference*, pp. 265–270, Louisville, Ky, USA, May 1993.
- [77] E. van Kerschaver and G. Beaucarne, "Back-contact solar cells: a review," *Progress in Photovoltaics: Research and Applications*, vol. 14, no. 2, pp. 107–123, 2005.
- [78] J. H. Bultman, M. W. Brieko, A. R. Burgers, J. Hoornstra, A. C. Tip, and A. W. Weeber, "Interconnection through vias for improved efficiency and easy module manufacturing of crystalline silicon solar cells," *Solar Energy Materials and Solar Cells*, vol. 65, no. 1–4, pp. 339–345, 2001.
- [79] A. Schönecker, D. Eikelboom, P. Manshanden, et al., "ACE designs: the beauty of rear contact solar cells," in *Proceedings of the 29th IEEE Photovoltaic Specialists Conference*, pp. 106–109, New Orleans, La, USA, May 2002.
- [80] S. W. Glunz, J. Dicker, D. Kray, et al., "High-efficiency cell structures for medium-quality silicon," in *Proceedings of the 17th European Photovoltaic Solar Energy Conference*, pp. 1287–1292, Munich, Germany, October 2001.
- [81] P. Hacke, J. M. Gee, M. Hilali, et al., "Current status of technologies for industrial emitter-wrap-through solar cells," in *Proceedings of the 21st European Photovoltaic Solar Energy Conference*, pp. 761–764, Dresden, Germany, September 2006.

## Research Article

# Sliver Solar Cells: High-Efficiency, Low-Cost PV Technology

**Evan Franklin, Vernie Everett, Andrew Blakers, and Klaus Weber**

*Centre for Sustainable Energy Systems, Department of Engineering, Australian National University, Canberra, ACT 0200, Australia*

Received 5 April 2007; Accepted 30 June 2007

Recommended by Armin G. Aberle

Sliver cells are thin, single-crystal silicon solar cells fabricated using standard fabrication technology. Sliver modules, composed of several thousand individual Sliver cells, can be efficient, low-cost, bifacial, transparent, flexible, shadow tolerant, and lightweight. Compared with current PV technology, mature Sliver technology will need 10% of the pure silicon and fewer than 5% of the wafer starts per MW of factory output. This paper deals with two distinct challenges related to Sliver cell and Sliver module production: providing a mature and robust Sliver cell fabrication method which produces a high yield of highly efficient Sliver cells, and which is suitable for transfer to industry; and, handling, electrically interconnecting, and encapsulating billions of sliver cells at low cost. Sliver cells with efficiencies of 20% have been fabricated at ANU using a reliable, optimised processing sequence, while low-cost encapsulation methods have been demonstrated using a submodule technique.

Copyright © 2007 Evan Franklin et al. This is an open access article distributed under the Creative Commons Attribution License, which permits unrestricted use, distribution, and reproduction in any medium, provided the original work is properly cited.

## 1. INTRODUCTION

Sliver technology was invented [1] and developed [2–4] at the Centre for Sustainable Energy Systems at the Australian National University (ANU), supported by the Australian company Origin Energy. Sliver cells are long, narrow, thin monocrystalline silicon solar cells capable of efficiencies exceeding 20%. Sliver cells are fabricated from wafers in a dramatically different way to conventional wafer-based solar cells: rather than fabricating a single solar cell on the surface of a wafer, many hundreds of individual Sliver solar cells are fabricated within a single wafer. Cell dimensions depend upon wafer size, wafer thickness, and sliver formation or patterning method; they typically have a length of 5–12 cm, a width of 0.5–2 mm, and a thickness of 20–100  $\mu\text{m}$ . The very thin Sliver cells are symmetrical, perfectly bifacial, and quite fragile.

The technology allows for a 10- to 20-fold decrease in silicon usage, and a 20- to 40-fold reduction in the numbers of wafers processed per MW, compared to standard crystalline silicon technology. Sliver technology aims to simultaneously address three out of four issues in cost reduction of solar modules: material costs, manufacturing costs, and efficiency. Encapsulation costs for Sliver modules are similar to conventional modules. Applying Sliver technology to the processing of wafers to form Sliver cells produces a significantly larger solar cell area than can be obtained from the same amount

of silicon using conventional solar cell processing technology. Consequently, far fewer Sliver wafers need to be processed in order to obtain the same solar cell area as that produced by conventional processing, resulting in a significant reduction in processing cost per unit area of cell produced using the Sliver process. For this cost reduction to be fully realised, an efficient and robust sliver handling and module fabrication method are also required. Lastly, Sliver cells are highly efficient and therefore capable of producing more electrical power for a given cell area when compared with conventional solar cells.

Insofar as the technology is capable of realising substantial reductions in silicon consumption, Sliver technology can be compared to thin-film silicon technologies such as those under development at Fraunhofer ISE [5], ISFH [6], and UNSW [7]. However, Sliver technology also has the major advantage of yielding high-efficiency solar cells. Further reductions in material and manufacturing costs can be achieved by clever module designs, made possible by the unique size, shape, and operating characteristics of Sliver cells: a module with rear Lambertian reflector and evenly spaced-out Sliver cells can, for example, capture over 80% of incident light with only 50% of the area being covered by cells. Compared with standard wafer technology, Sliver technology allows for decreases in silicon usage by a factor of 10–20, and a reduction in the number of wafers processed per unit area by a factor of 20–40. Such a large reduction in

silicon usage and wafers processed per  $MW_p$  capacity justifies the use of moderate- to high-quality silicon, and wafer processing directed towards optimising high-efficiency cells. The result of this approach is that high cell efficiencies can be obtained at a significantly reduced  $\$/W_p$  process cost.

An important feature of Sliver technology in respect of the large reduction in silicon usage per  $MW$  is that a single 15-cm diameter host wafer can contain enough cells to populate a module with a rating of up to 100 W. This means that a longer wafer process and good process control can be afforded. However, the original Sliver cell fabrication process still contained many more processing steps than the industry standard for high-efficiency silicon solar cells. To be successful in an industrial context, a Sliver cell manufacturing process must be able to achieve both high cell efficiencies and high process yields; preferably using standard semiconductor processes and equipment in order to capitalise on existing knowledge and experience, achieving reliable results at low cost.

Recent Sliver cell research at the ANU has been directed towards delivering a greatly simplified processing sequence, capable of producing cells with better performance and at higher manufacturing yield than the originally developed process. This has resulted in a reliable and robust fabrication process that contains around half the number of separate processing steps compared to the original Sliver cell fabrication process. This process, with fewer steps, has the advantage of providing faster turnaround, and uses fewer pieces of equipment and fewer consumables. A shorter, simpler processing sequence has the inherent advantage of introducing fewer processing errors and defects, and hence leading to a significantly higher process yield. The fabrication process is described in some detail in this paper, with areas for potential improvements also indicated.

At ANU, we have recently fabricated Sliver cells with efficiencies exceeding 20% using the optimised processing sequence. Production cell efficiencies of 21% are clearly possible, given the care that can be afforded even in a production environment because of the low per unit area costs arising from the large effective cell surface area contained in each wafer.

Consideration of optimising strategies for cell fabrication and module production processes cannot be made independently or in isolation, since the most cost-effective module production methods also rely upon a cell fabrication sequence which delivers high-efficiency cells with high yield and uniform or low-variance cell performance spreads. A high yield reduces per unit cost, and a uniform yield in turn avoids the necessity of measuring and binning every cell. Details of handling and assembly technology are too complex and extensive to include in this paper; full details will be provided in a subsequent paper. However, a brief overview is included in this paper, describing one solution to the problem using a simplified modular approach.

## 2. SLIVER CELLS AND THEIR APPLICATIONS

The key to understanding the significance of Sliver technology from the cell processing perspective is to recognise

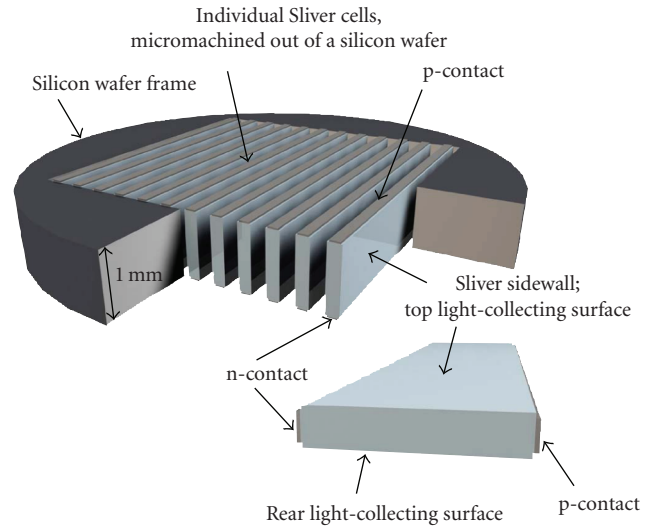


FIGURE 1: A wafer containing Sliver cells. The pn-junction is located below each of the large, light-collecting surfaces.

the fundamental difference between conventional cell processing and Sliver cell processing. In the conventional cell process, cells are formed *on the wafer surface*—essentially a 2-dimensional process. In the Sliver cell process, cells are formed *in the wafer volume*—essentially a 3-dimensional process, which produces a dramatic increase in the active surface area of solar cells per unit volume of silicon consumed and per wafer that is processed.

### 2.1. Sliver cells

Figure 1 is a depiction of a wafer with, for the sake of simplicity and ease of discussion, just a few slivers represented. The essential step in forming the slivers is to form deep narrow grooves all the way through the wafer. A variety of techniques can be used including, but not limited to, narrow focus laser, narrow blade dicing saw, anisotropic alkaline etching, or high-speed plasma etching. Several of these methods, and combinations thereof, have been used at ANU to reliably create multiple narrow ( $<50\ \mu\text{m}$ ) grooves through 1 mm thick wafers on a pitch of  $100\ \mu\text{m}$ , leaving sliver substrates approximately  $50\ \mu\text{m}$  thick and 1 mm wide, secured at their ends by the remaining wafer frame.

Individual Sliver solar cells are constructed on the narrow strips of silicon formed during the grooving process. All cell processing steps are completed while the silicon strips are still supported by the silicon substrate at the edge of the wafer. All cell processing steps are based on standard silicon solar cell processing technologies. The solar cell electrodes are also formed while the Sliver cells are retained in the wafer. The surfaces of the wafer, now corresponding to the long narrow edges of the cells, are metallised to form p-type and n-type contacts on either side of the wafer. Following extraction from the wafer, the Sliver cells are rotated about their long axis. The large face of the Sliver cell, corresponding to the sidewall formed by grooving, becomes the sun-facing surface of the cell. Since the processing treatment

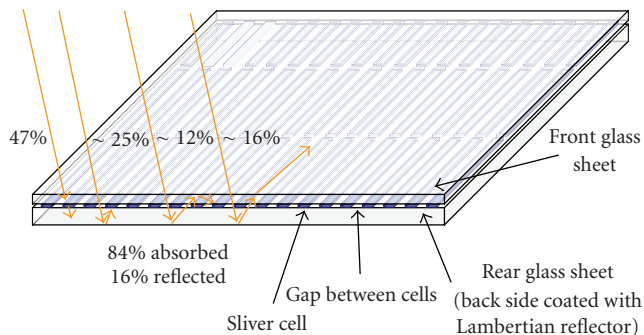


FIGURE 2: Depiction of a Sliver cell module with 50% cell coverage, showing absorption and reflection fractions for possible light paths.

of both sidewalls on a Sliver is identical, the cell is by default perfectly bifacial. Because the Sliver cell is very thin and has pn-junctions on both large faces, corresponding to the sidewalls of each groove, good surface passivation ensures that internal quantum efficiency is essentially unity across the spectrum.

In contrast to all conventional solar cells, with the exception of rear-contact solar cells, there is virtually no shading of the cell due to metallisation since the metal contacts, only 1–2  $\mu\text{m}$  thick, are on the edges of the Sliver cell rather than the sunward-facing surface. The edges of each cell occupy only a small fraction of the total surface of the cells, and doping below the metal contacts can be made to be very heavy. Excellent, low-resistivity contacts and minimal recombination are thus easily achieved. Good short-circuit currents, high open-circuit voltages, and high cell efficiencies are observed as a result.

## 2.2. Sliver cell applications

The unique shape of Sliver cells means that they can be used to produce novel module designs. One such design developed at ANU utilises a very simple Lambertian reflector and has cells occupying only a fraction (typically half) of the module surface area [8], as depicted in the diagram of Figure 2. This allows for a further reduction in silicon usage: the number of required slivers can be halved while high optical efficiency is retained via the rear surface light-trapping regime. An alternative module design has a similar arrangement of Sliver cells but a transparent rear glass sheet rather than a Lambertian reflective surface. This design produces a semitransparent module, with considerable architectural potential. Another module type utilises thin, flexible plastic sheeting to encapsulate Sliver cells, thereby creating flexible, rollable, or wearable solar modules. An example of a small flexible module is given in Figure 3. The structure and fabrication of such a submodule will be the subject of a subsequent paper.

In addition to module designs for normal terrestrial applications, Sliver cells can also be used in concentrator PV systems. Modelling has shown that, with appropriate wafers and cell fabrication conditions customised for concentrator applications, Sliver cells are very well suited for concen-

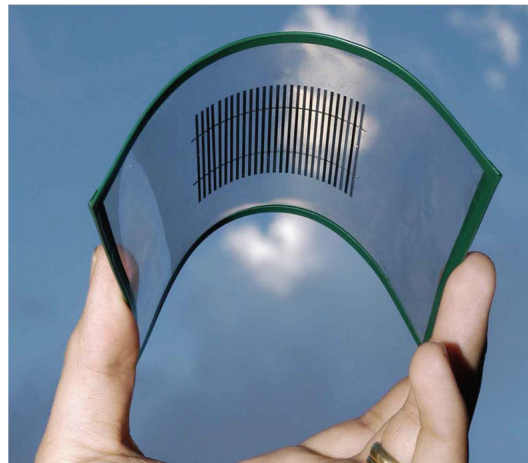


FIGURE 3: A flexible Sliver cell module.

tration ratios in the range of 5 to 50 suns [9]. This opens up the possibility of a wide variety of system applications, with the potential for considerable further reduction in cost and silicon usage compared with conventional concentrator cells and applications. The current range of concentrator PV systems, both commercially available and presently under development, generally relies on high concentration ratios (>100), high-precision optics, and expensive, very high efficiency multijunction solar cells [10–13]. A source of inexpensive, high-efficiency cells tailored for low to mid concentration ratios has the potential to unlock a whole new range of cheaply produced, low-cost, low-precision tracking and optics for concentrator systems.

An additional, very important feature of Sliver technology is that some of the oft-cited, and serious performance-compromising difficulties associated with nonuniform illumination in concentrator systems using conventional concentrator cells [14, 15] can be shown to be ameliorated by using a smart configuration of Sliver cells. A typical series-connected string of Sliver cells occupies an area comparable to that of a conventional concentrator cell yet has much lower current and much higher voltage outputs. With each string of Sliver cells connected in parallel, rather than in series as is generally required for conventional cells, the entire system output is no longer limited by the least illuminated region.

## 3. OPTIMISED SLIVER CELL FABRICATION

One of the major challenges for any newly developed product is to ensure that the manufacturing process is easily transferable from research labs to a commercial environment without introducing significant product performance or quality degradation. This can be argued to be particularly important in the case of a product such as Sliver technology. Sliver cells already differ markedly from the dominant type of commercially available solar cell. Hence, in terms of manufacturability, the Sliver cell manufacturing process needs to be robust and reliable, with maximum width process windows, and should be optimised as far as practically possible in the laboratory. Also, the reliance on nonstandard solar

TABLE 1: An optimised processing sequence overview.

Step number	Step description
1	Wafer etch and clean
2	Heavy phosphorus diffusion and in-situ oxide growth
3	Selective removal of diffusion from one wafer surface
4	Heavy boron diffusion
5	Groove mask formation
6	Initiate grooves
7	Groove formation
8	Sidewall texture
9	Sidewall emitter phosphorus diffusion
10	ARC growth/deposition
11	Remove dielectric from both wafer surfaces
12	Metallise wafer surfaces (which become the Sliver cell edges)

cell manufacturing techniques and nonstandard equipment should be minimised. Successful transfer of the Sliver technology to an industrial manufacturing environment hinges on meeting these requirements.

### 3.1. Optimised Sliver cell processing sequence

The processing sequence originally developed to produce Sliver cells was considerably longer (by a factor of about 3) than that required to produce conventional one-sun cells [16]. As discussed previously, the additional associated costs are more than compensated for by the large gains in efficiency and module area that Sliver technology establishes. However, manufacturing costs can still be appreciably reduced, with reliability correspondingly increased, by judicious design of the manufacturing process. Complex wafer processing is more expensive because it entails a larger fabrication facility, more processing equipment, higher maintenance costs, and larger consumables and waste disposal costs. Also, it is generally true that the longer the processing sequence, the lower the expected yield will be. A further disadvantage of a long process compared with a short process is that development and refinement of the process are more difficult: feedback takes longer and the level of interaction between process stages increases, with the result that the problem of lower yields commonly encountered in R&D is exacerbated.

The original Sliver cell processing sequence consisted of 59 separate processing steps, where a single processing step is defined as a set of operations that take place with the assistance of a particular piece of process equipment (such as a phosphorus diffusion), or which are similar and occur sequentially (such as a wafer-washing step consisting of an RCA1 clean, DI water rinse, RCA2 clean, DI water rinse, HF dip, DI water rinse) [16].

Recent research at ANU has focused on developing a simplified processing sequence capable of delivering higher efficiency cells, with a tight and uniform performance range, and a higher yield. The simplified processing sequence con-

tains fewer processing steps (32 steps) and utilises fewer pieces of equipment: in particular, the expensive pieces of equipment. A summary of an optimised, robust processing sequence is given in Table 1. In this instance, in the interests of saving space, only the key processing steps are shown. The steps that are omitted from the table include several wafer-washings steps (conducted at least prior to any high-temperature furnace step) and several HF deglaze and HF dip steps. Although standard texturing techniques cannot be applied to anisotropically etched sliver sidewalls, excellent texturing and light-trapping can instead be achieved via an acid etch technique through a very thin deposited silicon nitride layer [17].

### 3.2. Reduced Sliver cell loss mechanisms

During the development of the optimised processing sequence outlined above, several key Sliver cell process requirements were identified that required refinements or modifications in order to address specific problems. In particular, two significant Sliver cell performance problems were identified, and which were directly related to subtle intricacies of the cell design and cell fabrication processes. The first issue was associated with the resistance of the emitter regions; while the second issue related to heavily cross-doped compensated region of silicon at the sliver corners, located directly adjacent to the metallised contact terminals.

A significant loss mechanism for Sliver cells is associated with the resistance of the emitter region. In this respect, for the purpose of understanding the origin of the loss mechanism, a 1 mm wide Sliver cell which has been fabricated from a 1 mm thick wafer may be regarded to be equivalent to a conventional cell having a gap of 2 mm between adjacent fingers. For high-efficiency cells, the emitter should be light enough to ensure good surface passivation and high transparency for photo-generated minority carriers. However, for such a spacing between contacts, a lightly doped emitter can result in significant series resistance losses. These series resistance losses manifest as a distributed series resistance [9],

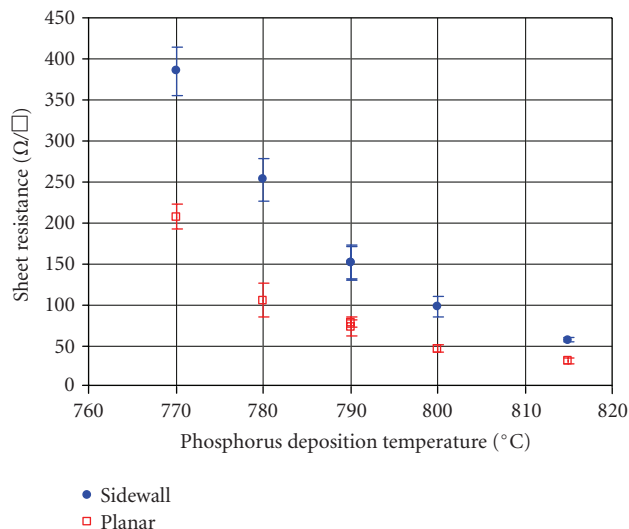


FIGURE 4: Sliver sidewall and planar sheet resistance measurements for a range of deposition temperatures.

reducing fill-factor and cell efficiency accordingly. This is a particular loss mechanism for wide Sliver cells (>1 mm), or for Sliver cells operating under concentrated illumination where the current is proportionally higher. Even at 1-sun intensity and for 1 mm wide cells, the series resistance of the emitter regions alone can account for some 3 or 4 fill-factor points, or higher for poorly controlled or very light emitter diffusions.

Owing to the unique topology of sliver-patterned wafers, sliver processing can lead to higher emitter losses than expected. Measurements have shown that the level of doping of sliver sidewalls, which are diffused while still held in the wafer frame, is considerably lower than that for normal wafer surfaces. Typically, the sheet resistance on a sliver sidewall is observed to be two to three times higher than on a planar wafer from the same diffusion parameters. An example of sliver sidewall and planar sheet resistance measurements for five consecutive phosphorus diffusions, covering a range of deposition temperatures, is given in Figure 4. The phosphorus diffusions were carried out in a tube furnace under the following conditions

- (i) A liquid dopant source ( $\text{POCl}_3$ ) was employed, having  $\text{N}_2$  bubbled through it at a rate of 133 cc/minute; oxygen reactant was added to the furnace at a rate of 45 cc/min.
- (ii) Main carrier gas flow of 250 L/h  $\text{N}_2$  was present throughout.
- (iii) Reactant gases were introduced to the furnace for 20 minutes only at a fixed and stable deposition temperature, after which they were turned off and wafers remained at the deposition temperature for further 10 minutes before being cooled down for 10 minutes to the unload temperature.
- (iv) Wafers were removed from the furnace and deglazed prior to a 30- to 90-minute 1100°C drive-in in an atmosphere of  $\text{N}_2$ .

- (v) Planar wafer sheet resistances were measured using a four-point probe.
- (vi) Sliver sidewall sheet resistances were also measured using a four-point probe, albeit with new, accurately calibrated geometry factors. It can be seen that to achieve an ideal lossless emitter, with final sheet resistance of around  $100 \Omega/\square$ , heavier doping (as low as  $40\text{--}50 \Omega/\square$ ) is required. More detailed measurements of sidewall doping profile, achieved by creating laser-isolated channels, revealed that the doping is reasonably consistent across the sliver sidewall, but marginally heavier at sliver edges (corresponding to being closer to the normal wafer surface). This is due to the fact that the final dopant density is partially limited by the ability of the diffusion reaction product to travel through the narrow gaps between slivers and deposit uniformly on sidewalls.

Improved control of the emitter diffusion on the Sliver cell sidewall is a current area of research activity and is vital for ensuring that high-efficiency cells can be reliably produced.

Another significant loss mechanism observed in Sliver cells fabricated with simplified processes is attributed to a region of heavily compensated silicon which arises due to the overlap of the phosphorus diffusion on the groove sidewalls with the Sliver cell edge boron diffusion. Without careful optimisation, this overlap region can result in a cell having reduced fill factor, characterised by a distinct high  $n$ -factor recombination component on a measured  $J_{sc}\text{--}V_{oc}$  curve. On the other hand, a low reverse breakdown voltage arises due to tunnelling in this overlap region, which provides robust tolerance of partial shading without the need for bypass diodes. Careful selection of the diffusion conditions is required to minimize the recombination problem, while at the same time retaining the beneficial effects of tunnelling, thereby offering further efficiency gains.

### 3.3. Cell performance

Cells with high open-circuit voltage and high fill factor have been consistently produced using the Sliver cell fabrication sequence outlined in the previous section. Not only have high-efficiency cells been produced but, equally importantly, the processing sequence has been shown to deliver a very high yield, and excellent consistency between Sliver cells in their measured performance. While no complete statistical analysis has been conducted, testing between 10 and 20 slivers per wafer reveals that all cells behave within a few percent of each other. The high yield and performance consistency are crucial in realising a cheap, high throughput module construction method that is suited to an industrial environment.

The highest-efficiency Sliver solar cells that have so far been fabricated at ANU were made from 1 mm thick wafers, and incorporated an LPCVD  $\text{SiN}$  ( $n \approx 2.1$ ) antireflection coating. The cells were fabricated without surface texturing, but included the application of a postprocess rear surface Lambertian reflection coating. A highly reflective, white Lambertian coating is easily applied to one sidewall surface of the Sliver cells once they have been removed from the

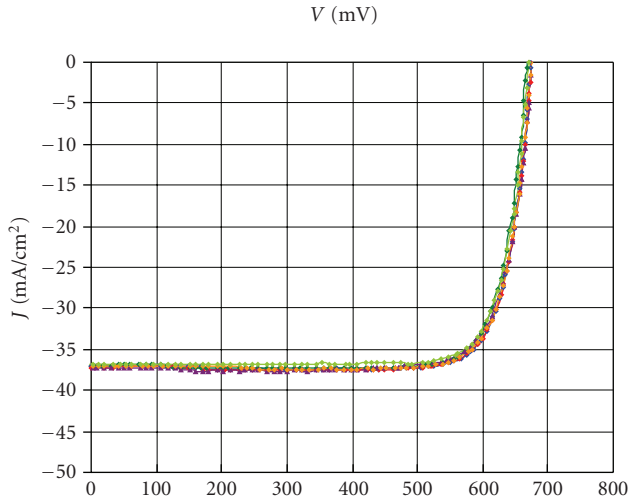


FIGURE 5: Measured IV curves for several Sliver cells fabricated using the simplified processing sequence.

TABLE 2: Measured data for six Sliver cells fabricated using the simplified processing sequence.

Median values for tested cells	$V_{oc}$ (mV)	$J_{sc}$ (mA/cm <sup>2</sup> )	FF	Eff
@ 1 sun	666	37.0	0.82	20.1%
Std Dev	3.3	0.18	0.008	0.2%

wafer. While not quite as effective, in terms of light-trapping characteristics, as excellent surface texturing, the Lambertian coating does produce a very good short-circuit current in Sliver cells. Median and standard deviation data for six cells produced using the optimised processing sequence are presented in Table 2, while the corresponding IV curves are plotted in Figure 5. Only calibrated in-house cell measurements are reported.

We have fabricated Sliver cells with efficiencies exceeding 20% using the optimised processing sequence. Production cell efficiencies of 21% are clearly possible, given the care that can be afforded even in a production environment because of the large effective cell surface area contained in each wafer.

#### 4. SLIVER MODULE CONSTRUCTION

The existence of a fast, reliable, and inexpensive construction method for producing Sliver modules is an essential ingredient in the commercial success or otherwise of a Sliver cell fabrication facility. Most industrial solar module manufacturers rely heavily upon the manual testing, binning, laying-out, tabbing, and interconnecting of cells, though some large manufacturers have now incorporated automated testing and binning into their production facilities. For Sliver cells, this is simply not an option: the sheer number and size of Sliver cells preclude the use of manual handling in any realistic commercial environment. A degree of automation is therefore required.

A solar power module constructed from such Sliver cells will contain between 5,000 and 10,000 cells per square metre of module area, compared with 70 to 80 conventional solar cells for the same module area. Furthermore, because of the physical properties of the Sliver cells, conventional cell-handling methods and PV module designs cannot be used. As an indication of the scale of the task of handling Sliver cells, a 100 MW capacity manufacturing plant would need to process in the order of 150 Sliver cells per second, 24/7, 360 days per year. It is a significant engineering challenge to devise a method for separating, testing, binning, assembling, and electrically interconnecting this very large number of solar cells in a rapid, reliable, and cost-effective manner.

Sliver cell handling and assembly could be based on a modified pick-and-place technique. In this monolithic approach, individual Sliver cells could be removed from the wafer, tested, and individually assembled in a temporary array. The assembled array could then be transferred and bonded to a substrate which defines the size of the finished module array. The electrical interconnections could then be established by printing or dispensing pads of electrically conductive material on the substrate. Depending on the process and the materials chosen, the conductive material may be placed on the substrate before or after the Sliver cell array is bonded in place.

From a manufacturing perspective, it is well known that serial monolithic assembly of large numbers of small components introduces disadvantages such as limited speed, yield compromise due to tolerance accumulation, substrate size limited to placement range capability; limited product design and layout flexibility, inability to introduce input/output buffers to any of the process stages in the entire monolithic process, a factor that compromises throughput expectation, and frequent manual intervention. This significantly increases cost and reduces yield and throughput.

A simplified modular approach to Sliver cell separation, handling, and assembly has been developed that avoids the problems of monolithic assembly.

##### 4.1. Sliver submodule concept

Rather than separating individual Sliver cells from the wafer using an expensive automated process such as described above, modular subassemblies, which can be thought of as conventional solar cell analogues, are formed. The modular subassemblies comprise arrays of parallel Sliver cells-oriented orthogonal to, and affixed on, a supporting medium and are comparable in size to a conventional solar cell. The supporting medium can be a collection of long, thin material in the form of a ribbon or a track, or the supporting medium may also be quite wide, even slightly larger than the size and shape of the Sliver cell array. The supporting medium can be transparent or opaque, and can be selected from a large range of materials depending on the subassembly application, and may be flexible or rigid. A simple method has been developed to extract the slivers from their host wafer and to subsequently lay them out on supporting beams. Sliver cells can be fixed to the supporting medium using adhesive or solder.

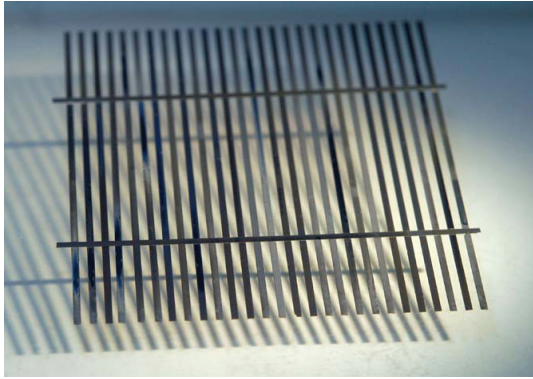


FIGURE 6: A submodule consisting of a group of Sliver cells interconnected by two thin, narrow substrate supports; it can be handled and encapsulated in the same manner as a conventional solar cell.

Problems of differential expansion introduced by the use of dissimilar materials into the structure can be controlled by using materials with similar thermal expansion coefficients, and by virtue of the small dimension of the bonded area which adheres the dissimilar material substrate supports to the individual Sliver cells. If the supporting medium is very narrow, the structure also allows the bifacial properties of Sliver cells to be utilised by placing a scattering reflector on the rear surface of the solar power module to redirect the light passing through the submodule arrays back onto the rear surface of the Sliver solar cells. A high-efficiency form of the modular subassembly structure constitutes cells abutting adjacent cells, providing 100% area cover submodules for high-efficiency solar power modules. In both these implementations, the modular subassembly produces a high voltage—up to 60 V, and a correspondingly low current—as low as 1/100th of that of a comparable conventional cell, with a total power output better than a conventional cell because of the higher efficiency of Sliver cells.

With both contiguous and spaced implementations of Sliver cell modular subassemblies, solder ideally forms the electrical interconnections as well as, in certain implementations, also providing the mechanical structural support for the subassembly. The solder can be deposited by a wide variety of methods, some of which have the potential to be very rapid because of the low thermal mass of the submodules. A solder approach would eliminate stencilling, dispensing, printing, component alignment requirements, and equipment cleaning, as well as totally eliminating the requirement for any adhesives. Crucially, the solder process provides a cheap, fast, well-understood, and reliable process that eliminates the use of nonconventional materials in Sliver cell solar power modules, which is a critical factor when considering product warranties of 25–30 years.

A submodule approach offers a means of low-cost assembly of groups of Sliver cells to form a conventional solar cell analogue. Figure 6 shows a submodule made from many Sliver cells, both physically and electrically connected using two long, thin, and narrow substrates. Submodules can then be used in place of conventional solar cells to produce a PV



FIGURE 7: A Sliver module constructed from submodules.

module of any desired size, shape, current and voltage, and power.

Successful implementation of the submodule concept requires a highly reliable Sliver cell fabrication process. Since cells are connected in series strings, via substrate supports or direct electrical interconnection for contiguous Sliver cell submodule arrangements, they must be matched closely in terms of operating current, and a single flawed cell can reduce the output of the entire modular subassembly. Therefore to achieve a high yield of manufactured submodules, the Sliver cell fabrication process must be able to reliably deliver a very high yield of working Sliver cells as described above.

#### 4.2. Sliver modules

The submodule approach avoids the placing of Sliver cells one by one into a solar power module. Modular subassemblies can be formed in sizes similar to conventional solar cells, typically  $12 \times 12 \text{ cm}^2$ . Each submodule can be incorporated as a cell analogue in a photovoltaic module, allowing the use of similar techniques for testing, binning, handling, assembly, electrical connection and encapsulation, and to those currently used for conventional solar cells. The appropriate number of submodules can be deployed to form a photovoltaic module with any desired shape, area, current and voltage characteristics, and associated output power. An example of a Sliver module based on submodules is shown in Figure 7. The highest recorded efficiency for a  $103.5 \text{ cm}^2$  Sliver cell module is 17.7%.

A very important advantage of the submodule approach is that solar power modules constructed using Sliver submodules can be manufactured using entirely conventional PV module materials—the Sliver cells, solder and conventional bus-bars, EVA and glass. The measurement of the efficiency of a large number of individual small Sliver solar cells is both inconvenient and expensive. However, the characteristics of submodules can be directly measured, thus effectively allowing dozens to hundreds of small solar cells to be measured together in a single operation and binned according to performance.

Submodules will have a large voltage and a correspondingly small current if the constituent Sliver cells are connected in series. For example, a  $12 \times 12 \text{ cm}^2$  submodule composed of sixty 1 mm wide, series-connected Sliver cells with a gap between each cell of 1 mm will have a  $V_{oc}$  and  $J_{sc}$  of about 40 V and 70 mA, respectively, after encapsulation (and including a Lambertian rear reflector for the module). This compares favourably with typical figures of 0.63 V and 5 A, respectively, for a conventional cell of the same area.

Sliver modules have advantages over conventional modules with respect to the elevated temperatures typically experienced during real operation. Since Sliver cells are high open-circuit voltage devices, they have smaller temperature coefficients. Hence at operating temperatures well above standard test conditions, Sliver module efficiency will degrade significantly less than an equivalent conventional solar module.

The submodules can be connected primarily in series to further build voltage, allowing the voltage up-conversion stage of an inverter associated with the photovoltaic system to be eliminated. Alternatively, the submodules can be primarily connected in parallel. This parallel connection ability can greatly reduce the effect on module output of nonuniformities in illumination, arising for example from shadows cast by dirt on the module surface or from neighbouring buildings.

Advantage can be taken of the flexibility of submodules fabricated using thin and flexible Sliver solar cells and substrate supports to mount the submodules conformally onto a curved supporting structure. The submodules can optionally be made semitransparent by spacing the Sliver cells apart. It is difficult to achieve such outcomes using conventional solar cells. The submodule approach lends itself readily to the fabrication of flexible modules.

## 5. CONCLUSIONS

Sliver cell and Sliver module technologies have the potential to provide low-cost solar-generated electricity. The novel Sliver cell and module design offers the potential for a 10–20 times reduction in silicon consumption for the same sized solar module, while also having the added benefit, in an industrial production environment, of requiring 20–40 times fewer wafer starts per MW than for conventional wafer-based technologies. However, successful commercial implementation of the Sliver technology hinges upon there being both a robust and high-yield Sliver cell processing sequence and a low-cost, high-throughput method for constructing modules from many thousands of wafer-bound Sliver cells. These two components go hand in hand: the fundamental Sliver properties necessitate the existence of an efficient handling method, while a cost-effective submodule assembly process demands high yield and consistency in finished sliver cells. Research at ANU has proven that it is possible to optimise the Sliver cell fabrication process so that high-efficiency cells can be produced using a simplified processing sequence that promotes high consistency and a very high yield. Simultaneously, efficient module production via the submodule method can be used, using low-cost equipment and standard

PV materials only, to reliably and rapidly produce Sliver submodule units which can then be easily handled in a similar manner to conventional solar cells.

An optimised Sliver cell processing sequence that is capable of producing 20%+ cells, when coupled with a robust, low-cost Sliver module construction method, can be expected to significantly reduce the costs of commercial PV modules. Much skilled engineering work is still required to translate the exceptional promise of Sliver technology into commercial reality. However, we believe that the essential building blocks are now in place and that the technology can, if handled appropriately, be successfully transferred to industry.

## ACKNOWLEDGMENTS

Support from Origin Energy for the initial development of sliver technology at ANU is gratefully acknowledged. Origin Energy is now undertaking commercialisation of Sliver technology in Adelaide. Sliver is a registered trademark of Origin Energy. The authors would also like to thank's all members of the Centre for Sustainable Energy Systems research laboratories for their assistance with the project.

## REFERENCES

- [1] K. Weber and A. Blakers, Semiconductor Processing PCT/AU01/01546, 2001.
- [2] K. Weber, A. Blakers, M. J. Stocks, et al., "A novel low-cost, high-efficiency micromachined silicon solar cell," *IEEE Electron Device Letters*, vol. 25, no. 1, pp. 37–39, 2004.
- [3] A. Blakers, M. J. Stocks, K. Weber, et al., "Sliver® solar cells," in *Proceedings of the 13th NREL workshop on Crystalline Si Materials and Processing*, Vail Colorado, August 2003.
- [4] K. Weber, A. Blakers, V. Everett, and E. Franklin, "Results of a cost model for sliver® cells," in *Proceedings of the 21st European Photovoltaic Solar Energy Conference*, Dresden, Germany, September 2006.
- [5] S. Reber, A. Eyer, E. Schmich, F. Haas, N. Schillinger, and S. Janz, "Progress in crystalline silicon thin-film solar cell work at Fraunhofer ISE," in *Proceedings of the 20th European Photovoltaic Solar Energy Conference*, pp. 694–697, Barcelona, Spain, June 2005.
- [6] B. Terheiden, R. Horbelt, and R. Brendel, "Thin-film solar cells and modules from the porous silicon process using 6" Si Substrates," in *Proceedings of the 21st European Photovoltaic Solar Energy Conference*, Dresden, Germany, September 2006.
- [7] A. G. Aberle, "Progress in evaporated crystalline silicon thin-film solar cells on glass," in *Proceedings of the IEEE 4th World Conference on Photovoltaic Energy Conversion*, vol. 2, pp. 1481–1484, Waikoloa, Hawaii, USA, May 2006.
- [8] K. Weber, J. MacDonald, V. Everett, P. N. K. Deenapanray, M. J. Stocks, and A. Blakers, "Modelling of sliver® modules incorporating a Lambertian rear reflector," in *Proceedings of the 19th European Photovoltaic Solar Energy Conference*, Paris, France, 2004.
- [9] E. Franklin and A. Blakers, "Sliver® cells for concentrator systems," in *Proceedings of the 19th European Photovoltaic Solar Energy Conference*, Paris, France, 2004.
- [10] R. McConnell, "Concentrator photovoltaic technologies," *Refocus*, vol. 6, no. 4, pp. 35–39, 2005.

- 
- [11] V. Diaz, J. L. Alvarez, and J. Alonso, "Mass production of cost effective systems based on high concentration," in *Proceedings of the 15th International Photovoltaic Science and Engineering Conference (PVSEC '05)*, Shanghai, China, 2005.
  - [12] J. Luther, A. Luque, et al., "Concentration photovoltaics for highest efficiencies and cost reduction," in *Proceedings of the 20th European Photovoltaic Solar Energy Conference*, Barcelona, Spain, June 2005.
  - [13] A. Slade, K. Stone, R. Gordon, and V. Garboushian, "Progress towards low-cost PV-generated electricity with the amonix high concentration photovoltaic system," in *Proceedings of the 15th International Photovoltaic Science and Engineering Conference (PVSEC '05)*, Shanghai, China, October 2005.
  - [14] I. Antón and G. Sala, "Losses caused by dispersion of optical parameters and misalignments in PV concentrators," *Progress in Photovoltaics: Research and Applications*, vol. 13, no. 4, pp. 341–352, 2005.
  - [15] J. Coventry, A. Blakers, E. Franklin, and G. Burgess, "Analysis of the radiation flux profile along a PV trough concentrator," in *Proceedings of the 20th European Photovoltaic Solar Energy Conference*, Barcelona, Spain, June 2005.
  - [16] A. Blakers, P. Deenapanray, V. Everett, E. Franklin, W. Jellett, and K. Weber, "Recent developments in sliver cell technology," in *Proceedings of the 20th European Photovoltaic Solar Energy Conference*, Barcelona, Spain, June 2005.
  - [17] K. Weber and A. Blakers, "A novel silicon texturisation method based on etching through a silicon nitride mask," *Progress in Photovoltaics: Research and Applications*, vol. 13, no. 8, pp. 691–695, 2005.

## Research Article

# Wafer Surface Charge Reversal as a Method of Simplifying Nanosphere Lithography for Reactive Ion Etch Texturing of Solar Cells

Daniel Inns, Patrick Campbell, and Kylie Catchpole

*Centre of Excellence for Advanced Silicon Photovoltaics and Photonics, University of New South Wales, Sydney NSW 2052, Australia*

Received 23 April 2007; Accepted 18 July 2007

Recommended by Armin G. Aberle

A simplified nanosphere lithography process has been developed which allows fast and low-waste maskings of Si surfaces for subsequent reactive ion etching (RIE) texturing. Initially, a positive surface charge is applied to a wafer surface by dipping in a solution of aluminum nitrate. Dipping the positive-coated wafer into a solution of negatively charged silica beads (nanospheres) results in the spheres becoming electrostatically attracted to the wafer surface. These nanospheres form an etch mask for RIE. After RIE texturing, the reflection of the surface is reduced as effectively as any other nanosphere lithography method, while this batch process used for masking is much faster, making it more industrially relevant.

Copyright © 2007 Daniel Inns et al. This is an open access article distributed under the Creative Commons Attribution License, which permits unrestricted use, distribution, and reproduction in any medium, provided the original work is properly cited.

## 1. INTRODUCTION

Multicrystalline Si wafers make up the majority of the photovoltaic market. Due to the variety of grain orientations, they cannot be textured cheaply by the anisotropic wet chemical etches used for monocrystalline silicon. One possibility for texturing is reactive ion etching (RIE). RIE can randomly texture a Si surface, with the minimum reflectance of below 5% achieved. We changed “masking” to “maskings” for the sake of clarity. Please check. [1, 2]. This maskless RIE requires the etching of several microns of Si and has the resulting long process times. The use of a mask during RIE allows greater control over the surface topography than maskless RIE and results in shallower textures with reduced etch times. The best reflection achieved to date using an RIE mask applied a photolithography process to form pyramids [3], with minimum reflectances around 5% achieved.

As an alternate to a photolithography mask, RIE masks can be formed by nanospheres. Nanospheres are highly uniform spheres (typically of silica or polystyrene) and are commercially available and very cheap. In previous work with nanosphere masks, the mask has been formed by spin-coating, resulting in a uniform monolayer of spheres across the surface. These particles are then the etch mask for subsequent RIE [4]. Without an antireflection coating, the mini-

mum reflectance is reduced around 13% by etching less than 500 nm of Si—making the process fast and high-throughput compared to other RIE textures, with or without masks.

Spinning-on of the nanosphere mask requires very careful control of the nanoparticle solution used, with many critical factors including spin speed, substrate surface treatments, and particulate concentration [5]. The typically rough wafer surface complicates spinning as some large regions are left unmasked [4]. Additionally, the throughput would be low and the masking solution wastes high for a factory application. A solution with a high nanosphere solids content is required for this spinning process and accentuates the waste problem.

Dipping a wafer into a masking solution would be attractive in a manufacturing environment, as the batch process could have very high throughput. Dipping could also coat large area wafers, 1 m<sup>2</sup> glass sheets, or other objects which are not suitable for spinning due to size, asymmetry, or weight. For some applications, it would also be an advantage to mask both sides of a wafer at once, to achieve a double-sided texture. Silicon dioxide, which comprises the surface of the standard wafer and the silica beads commonly used for the masking, has a negative surface charge when immersed in a solution with a pH above its isoelectric point of ~2.5 [6]. To electrostatically attract the negative spheres to the negative wafer

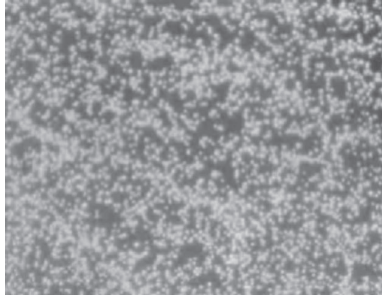


FIGURE 1: Dark field optical microscope image of the nanosphere mask applied to a wafer by reversing its surface charge. The image is  $180 \times 160 \mu\text{m}$ .

surface, the surface charge of the wafer must be reversed by the application of a positive coating.

This work shows that a simple dipping process can reverse the surface charge of a wafer, and another dip can mask the surface. Masking based on this idea can lead to high-nanosphere surface coverage, and etching through the nanosphere masks is well controlled by RIE. A variety of textures can be formed and very good reflectance reduction achieved. The geometry of the texture features can be altered by changing RIE processing parameters (primarily pressure and gas mixtures), which also controls the etch rate of the nanospheres that act as the mask.

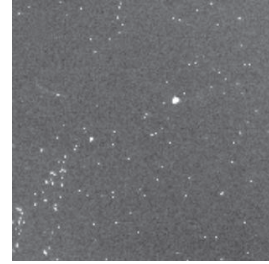
## 2. EXPERIMENTS AND DISCUSSION

Below is outlined the process used to optimize the two solutions used for dip coating wafers, first for wafer surface charge reversal, followed by electrostatic attraction of a nanosphere lithography mask. Afterwards, some RIE textured surfaces are examined by SEM and the reflectance of the best texture assessed.

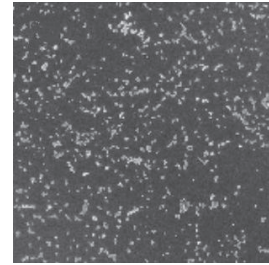
### 2.1. Reversing the surface charge of silicon wafers

Layer-by-layer coating can be used to build up a variety of types of films, by alternate deposition of positive followed by negative ions, molecules, or colloids [7]. The use of colloidal particles such as nanospheres in the layer-by-layer method was pioneered by Iler [8]. In this work, Iler's technique was used to deposit a single bilayer of hydrolyzed  $\text{Al}^+$  ions followed by negatively charged  $\text{SiO}_2$  nanospheres. The composition of the  $\text{Al}^+$  solution and the pH of the nanosphere solution were adjusted to optimize the mask coatings.

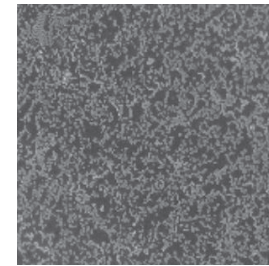
Before any surface treatments, a polished and oxide-free Cz Si wafer surface was oxidized by a 5-minute piranha clean ( $\text{H}_2\text{SO}_4 : \text{H}_2\text{O}_2$  solution, 2 : 1 mixture) and then rinsed for 10 minutes. A polished surface was chosen as its predictably high reflection is best for quantifying the benefits of the resulting texture. In order to attach a positive Al coating to the wafer, a set of  $\text{AlNO}_3$  solutions (concentration varying from 400–800  $\mu\text{M}$ ) was prepared, and small amounts of 50 mM NaOH were added to adjust the pH and concentration of the solutions. The cleaned wafer was dipped into the solution



(a)



(b)



(c)

FIGURE 2: SEM images of the nanosphere masks attached to a silicon wafer surface using 3 different pH masking solutions: (a) pH = 4, (b) pH = 3.5, (c) pH = 3.2. The images are  $80 \mu\text{m} \times 80 \mu\text{m}$ .

for 30 seconds to allow adsorption of a positive layer. Immediately afterwards, a 10 seconds dip-in-deionized water was followed by a nitrogen gas blow dry to remove excess liquid.

To test the effectiveness of the positive coating solutions, the positive coated wafers were dipped in a masking solution of negative nanospheres. The nanospheres used in this study are 400 nm diameter silica beads from Bangs Labs, product code SS02N, which comes in a colloid solution with 10% by weight nanospheres. A 3.5 pH solution of acetic acid was used, containing 2% by weight nanospheres. A 3.5 pH was chosen as it is greater than the isoelectric point of  $\text{SiO}_2$  and much less than the isoelectric point of Al and  $\text{Al}_2\text{O}_3$  (the composition of the positive coating layer), giving opposite charged surfaces.

Optical microscope imaging in dark field mode revealed that a combination of 650  $\mu\text{M}$   $\text{AlNO}_3$  with 125  $\mu\text{M}$  NaOH resulted in the most dense coating of nanospheres onto the wafer. This mixture of chemicals gives the mask solution a pH of 4.1. A picture of the surface is shown in Figure 1. It should be reiterated at this stage that an oxide was formed on the wafer by a piranha clean. Vastly, different nanosphere masks result when using a wafer which has a different surface,

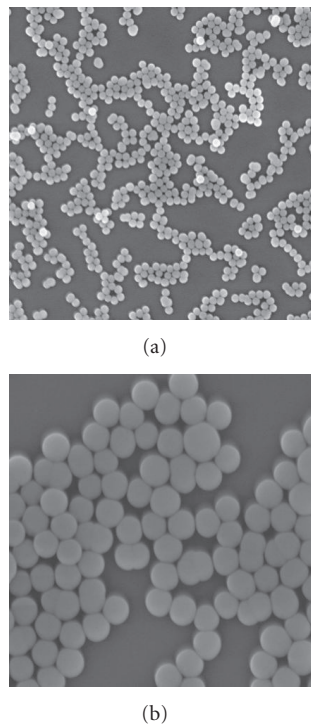


FIGURE 3: SEM images of the nanosphere coatings from the 3.2 pH masking solution. Scale can be taken from the 400 nm diameter sphere diameters.

such as a thick thermal oxide, native oxide, or no oxide at all. In addition, masking of multicrystalline wafers may require a slightly different composition due to their surface roughness. The solutions used here must be optimized for each type of surface, and each application.

### 2.2. Electrostatically attaching nanosphere masks

Varying the pH of the masking solution strongly alters the surface charge of the solids in solution and hence influences the electrostatic attraction between the positive coated wafer and the negative nanospheres. Mixtures of 50 mM acetic acid and 50 mM NaOH were used to tailor the pH of the nanosphere solutions. After pH was determined, a small volume of nanospheres was added to make the solution 2% by weight nanospheres. As expected for such a buffer solution, this amount of dilution with nanosphere solution was found to have negligible effect on the pH. The solution pH was varied upwards of 3.2 by this process, and the nanosphere masks examined by SEM. Figure 2 shows the nanosphere masks achieved.

The lowest pH gives a denser mask, covering more of the surface. SEM images of 2 different areas of the best mask can be seen in Figure 3. Around 60% of the surface is masked with large 2D nanosphere arrays, with unmasked regions usually closer than 3 sphere diameters from a nanosphere. Stronger concentrations of acetic acid were used to achieve a lower pH, but the masks were very sparse and gave poorer surface coverage than that shown in Figure 3. This may have

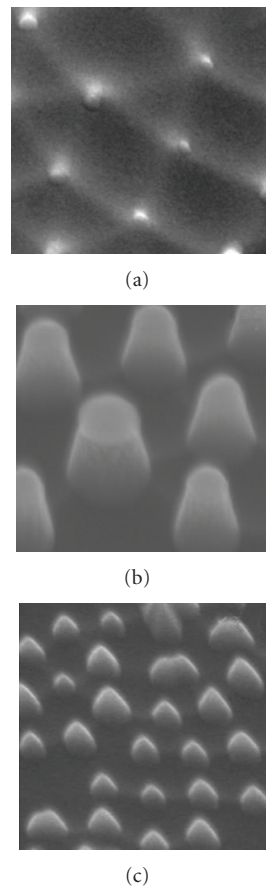


FIGURE 4: SEM images (taken on a 45° tilt) of different RIE textures made using SF<sub>6</sub> plasmas during RIE. (a) Shallow honeycomb feature. (b) Flat-topped cones, with best antireflection properties. (c) Small pointed structures.

been because the nanosphere surface charge/wafer surface charge was not well balanced, or the positive coating partially dissolved in the stronger acid. Other acids are likely to give different results, as they will have a different pH at this 50 mM concentration, and they will interact differently with the positive wafer coating. A denser or more homogeneous coating than that shown in Figure 3 may be possible using the surface charge reversal masking process. All previous work on nanosphere lithography has assumed a requirement for a continuous monolayer mask, although the merits of this have not been demonstrated. Using these simple-to-apply lithography masks and then forming an RIE texture, the reflection is shown to be as good as anything achieved using a spun on, more homogeneous monolayer mask.

### 2.3. RIE texturing results

RIE is commonly used in the microelectronic industries and the equipment appears in many labs and photovoltaics manufacturing plants where it is used for edge isolation. A handful of different textures were created by RIE using SF<sub>6</sub> gas and the best mask as shown in Figure 3. Figure 4 shows some different shaped features that were created. The surfaces were

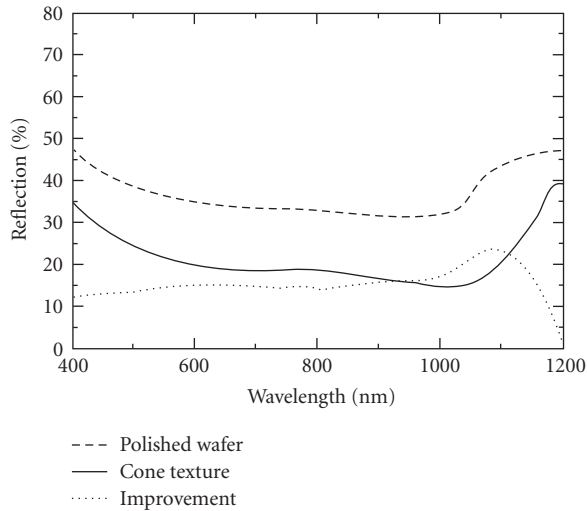


FIGURE 5: Reflectance of a polished silicon wafer, and an RIE textured wafer using the simplified nanosphere lithography mask. The difference between the two is also shown.

etched with different  $\text{SF}_6$  pressures and flow rates. The shallow honeycomb features in Figure 4(a) were made with a process pressure of 6.9 Pa in 10 minutes. The flat-topped cone-shaped texture from Figure 4(b) has the best antireflection effect, and was made using the highest process pressure of 7.5 Pa in 4 minutes. The small pointed structures in Figure 4(c) are made with 3.5 Pa and took 8 min. On the regions where there were no nanospheres, the surface is gently curved and almost flat.

After texturing, the wafers were dipped into a solution of 5% HF which removed the remains of the nanospheres and removed the oxide from the silicon surface. The hemispherical reflectance of the silicon surfaces were then measured using an integrating sphere accessory with a Varian CARY 500 spectrophotometer. As the small RIE system used in this study only etches uniformly across a 3 cm diameter area, only the central region of the wafer was measured. Figure 5 shows that the cone texture performs well across the full wavelength range, with a minimum reflectance of 14.5%.

### 3. CONCLUSION

Nanospheres are a suitable etch mask for RIE texturing. The masks are usually spun on, but this is a slow serial process and wastes a great deal of nanosphere solution. By reversing the surface charge of a polished silicon wafer, the mask has been applied by simply dipping into a dilute acidic solution of nanospheres. This process is suitable for a manufacturing environment, as the masking and drying process takes only 2 minutes, and the RIE texturing (which uses standard equipment) takes only 4 minutes.

The nanosphere masks used do not fully coat the surface in a homogeneous monolayer as seen in spun-on masks. The mask is more like a random arrangement of tendrils, stretching over the wafer surface in 2D arrays. This has proven to be no disadvantage, as the minimum front sur-

face reflectance produced with this process is as low as has been achieved by any other nanosphere lithography masking process [4]. The added advantage of the masking process developed here is the increased processing speed that should translate to factory throughput and cost savings. The application for these colloidal masks stretches beyond polished silicon wafers, as the simple dipping process could also create nanosphere coatings onto very large multicrystalline wafers or to heavy glass sheets, which would not be suitable for spinning.

### ACKNOWLEDGMENTS

Parts of this work were supported by the Australian Research Council (ARC) via its Centres of Excellence scheme. The first author acknowledges a faculty of engineering Ph.D. scholarship from UNSW. The third author has an Australian Research Council Postdoctoral Fellowship.

### REFERENCES

- [1] Y. Inomata, K. Fukui, and K. Shirasawa, "Surface texturing of large area multicrystalline silicon solar cells using reactive ion etching method," *Solar Energy Materials and Solar Cells*, vol. 48, no. 1–4, pp. 237–242, 1997.
- [2] D. S. Ruby, S. H. Zaidi, S. Narayanan, B. M. Damiani, and A. Rohatgi, "Rie-texturing of multicrystalline silicon solar cells," *Solar Energy Materials and Solar Cells*, vol. 74, no. 1–4, pp. 133–137, 2002.
- [3] S. Winderbaum, O. Reinhold, and F. Yun, "Reactive ion etching (RIE) as a method for texturing polycrystalline silicon solar cells," *Solar Energy Materials and Solar Cells*, vol. 46, no. 3, pp. 239–248, 1997.
- [4] W. A. Nositschka, C. Beneking, O. Voigt, and H. Kurz, "Texturisation of multicrystalline silicon wafers for solar cells by reactive ion etching through colloidal masks," *Solar Energy Materials and Solar Cells*, vol. 76, no. 2, pp. 155–166, 2003.
- [5] H. W. Deckman and J. H. Dunsmuir, "Natural lithography," *Applied Physics Letters*, vol. 41, no. 4, pp. 377–379, 1982.
- [6] R. Hunter, *Zeta Potential in Colloid Science: Principles and Applications*, Academic Press, London, UK, 1981.
- [7] P. T. Hammond, "Form and function in multilayer assembly: new applications at the nanoscale," *Advanced Materials*, vol. 16, no. 15, pp. 1271–1293, 2004.
- [8] R. K. Iler, "Multilayers of colloidal particles," *Journal of Colloid Interface Science*, vol. 21, no. 6, pp. 569–594, 1966.

## Research Article

# Application of CBD-Zinc Sulfide Film as an Antireflection Coating on Very Large Area Multicrystalline Silicon Solar Cell

U. Gangopadhyay,<sup>1,2</sup> K. Kim,<sup>2</sup> S. K. Dhungel,<sup>2</sup> H. Saha,<sup>1</sup> and J. Yi<sup>2</sup>

<sup>1</sup> IC Design & Fabrication Centre, Electronics & Telecommunication Engineering Department, Jadavpur University, Kolkata 700032, India

<sup>2</sup> School of Information and Communication Engineering, Sungkyunkwan University, Suwon-City 440-746, South Korea

Received 1 April 2007; Revised 18 September 2007; Accepted 20 December 2007

Recommended by Armin Aberle

The low-cost chemical bath deposition (CBD) technique is used to prepare CBD-ZnS films as antireflective (AR) coating for multicrystalline silicon solar cells. The uniformity of CBD-ZnS film on large area of textured multicrystalline silicon surface is the major challenge of CBD technique. In the present work, attempts have been made for the first time to improve the rate of deposition and uniformity of deposited film by controlling film stoichiometry and refractive index and also to minimize reflection loss by proper optimization of molar percentage of different chemical constituents and deposition conditions. Reasonable values of film deposition rate ( $12.13 \text{ \AA}/\text{min.}$ ), good film uniformity (standard deviation  $< 1$ ), and refractive index (2.35) along with a low percentage of average reflection (6-7%) on a textured mc-Si surface are achieved with proper optimization of ZnS bath. 12.24% efficiency on large area ( $125 \text{ mm} \times 125 \text{ mm}$ ) multicrystalline silicon solar cells with CBD-ZnS antireflection coating has been successfully fabricated. The viability of low-cost CBD-ZnS antireflection coating on large area multicrystalline silicon solar cell in the industrial production level is emphasized.

Copyright © 2007 U. Gangopadhyay et al. This is an open access article distributed under the Creative Commons Attribution License, which permits unrestricted use, distribution, and reproduction in any medium, provided the original work is properly cited.

## 1. INTRODUCTION

Pyramid type surface texturing is a well established process used for monocrystalline silicon solar cell. Unlike monocrystalline silicon (c-Si), multicrystalline silicon (mc-Si) can exhibit poor surface texturing due to its different grains and grain boundaries. Therefore, application of AR coating is one of the challenging issues in the area of mc-Si solar cell research. It has been demonstrated that zinc sulfide (ZnS), a wide direct band gap semiconductor with high-refractive index (2.35), can be used as single AR coating or as part of a double layer AR coating if used in conjunction with a low-refractive index material [1]. Also, ZnS thin film has been proven as one of the promising thin film materials for detector, emitter, and modulators in optoelectronics [2]. ZnS film can be used as a reflector and dielectric filter due to its high value of refractive index as well as high transmittance in visible region [3, 4]. It is used as buffer layers in CuInSe and CuGaSe<sub>2</sub>-based solar cells, respectively [5, 6]. Several techniques such as, molecular beam epitaxy [7], H<sub>2</sub> plasma chemical sputtering [8], thermal evaporation [9], MOCVD [7], and MOVPE [10] have been used to produce ZnS thin

film with adequate properties. Spray pyrolysis is an interesting technique for preparing thin films [11]. Indeed, this technique is very attractive due to its simplicity and low cost, but uniformity control over a large area is one of the major problems. Another low-cost approach for deposition of ZnS film on semiconductor or glass substrate is the chemical bath deposition (CBD) technique [12–14]. In CBD, deposition of metal chalcogenide semiconducting thin films is done by maintaining the substrate in contact with the solution of chemical bath containing the metal and chalcogen ions. The film formation on substrate takes place when ionic product exceeds solubility product. However, the precipitate formation in the bulk of solution is an inherent problem in CBD technique. This normally results in unnecessary precipitation and loss of materials during CBD-ZnS film deposition on semiconductor or glass substrate and hampers the uniformity of the deposited film. In order to avoid such problem, proper optimization of chemical constituents of bath deposition is necessary.

We have previously reported on the chemical bath deposition of ZnS thin films in the context of their application as an antireflection coating on monocrystalline silicon solar

cell [15]. For multicrystalline (mc-Si) silicon large area substrate due to different grain orientation structure, serious nonuniformity has been noticed during experiment. Bath chemical constituent percentage was changed from our previously reported values [16] in order to achieving good uniformity of deposition on the surface of m-Si wafer. This paper reports the key factors involved in proper optimization of CBD technique such as composition of chemical constituents, stoichiometry and refractive index of the deposited film, and deposition time to form uniform and reproducible viable ZnS antireflection coating in batch process by CBD on commercial mc-Si silicon solar cells.

## 2. EXPERIMENTAL

For the deposition of films, the solution conditions (molar concentrations) and mounting angle of substrates were maintained at  $60^\circ$  for better deposition [16]. During our experiment, the concentrations of different constituent chemicals were taken as zinc sulfate ( $\text{ZnSO}_4$ ) 0.08 M, ammonia solution ( $\text{NH}_4\text{OH}$ ) 0.784 M, hydrazine monohydrate ( $\text{N}_2\text{H}_4$ ,  $\text{H}_2\text{O}$ ) 0.003 M, and thiourea CS ( $\text{NH}_2$ )<sub>2</sub> 0.14 M, respectively, for achieving good uniformity of deposited ZnS film on whole area of large mc-Si substrate. Zinc sulfate was added to the required quantity of ammonia solution followed by hydrazine monohydrate in order to improve the dissolution of the  $\text{ZnSO}_4$ . Next CS ( $\text{NH}_2$ )<sub>2</sub> was added to the hot solution (temperature  $\sim 80^\circ\text{C}$ ). The temperature was maintained at  $80^\circ\text{C}$  during deposition, and silicon wafers were withdrawn from the solution after 10, 20, 30, 40, 50, 60, and 75 minutes, respectively, in order to study the variation of thickness of the ZnS film with time of deposition

The films were deposited on multicrystalline silicon substrate, which were cleaned by rinsing in running DI-water bath and subsequently drying. The optical reflectance of ZnS films was carried out using spectrophotometer. The energy dispersive X-ray (EDAX) analysis was used to determine the percentage of zinc and sulfur present in the deposited ZnS film. For large area surface study of the deposited CBD film, we have used scanning electron microscopy (SEM) study. The thicknesses of the films were measured using ellipsometry.

## 3. RESULTS AND DISCUSSION

A typical SEM micrograph of ZnS film deposited on m-Si silicon wafers by CBD technique had given in Figure 1. This film was prepared at  $80^\circ\text{C}$  at a fixed substrate tilting angle of  $60^\circ$  with a deposition period of 1 hour 20 minutes. The scanning electron microscopic (SEM) studies indicated that the coverage of deposited ZnS films on mc-Si surface was considerable uniform over an area  $156\text{ cm}^2$  (approx.). The uniformity is believed to be achieved by our slightly higher concentration of zinc sulfate and hydrazine used for our experiments on mc-Si solar cells compared to that used in our previous experiments on monocrystalline silicon solar cell [16]. In order to explain this, we need to understand that for our CBD technique, ZnS thin film is prepared by the decomposition of thiourea CS ( $\text{NH}_2$ )<sub>2</sub> in an alkaline solution containing

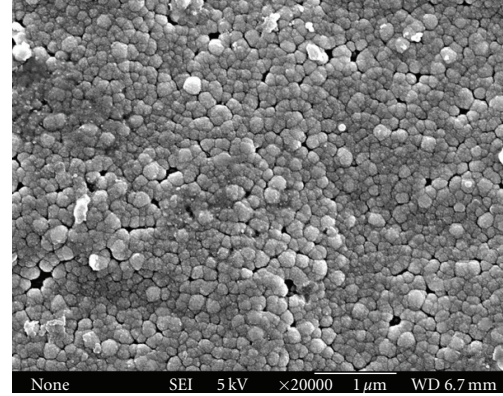
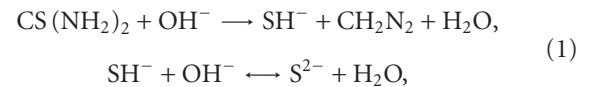


FIGURE 1: SEM micrograph of CBD-ZnS film on mc-Si substrate.

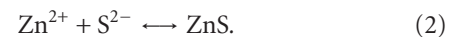
zinc salt. In our CBD experiment, we have used zinc sulfate and thiourea as source materials. Precipitation control during deposition has to be made by controlling the concentration of free  $\text{Zn}^{2+}$  ion in the CBD bath. In the solution,  $\text{ZnSO}_4$  divided into two separate ions of  $\text{Zn}^{2+}$  and  $\text{SO}_4^{2-}$ .

The decomposition of the thiourea is given by [13]



$\text{OH}^-$  ions come from hydrazine monohydrate in CBD bath by breaking at  $80^\circ\text{C}$ .

Finally, ZnS films are formed according to the relation:



Hydrazine ( $\text{N}_2\text{H}_4$ ,  $\text{H}_2\text{O}$ ) has been added to the reaction bath to promote the ZnS incorporation within the film because at elevated temperature ( $80^\circ\text{C}$ ), it dissociate and supplied necessary  $\text{OH}^-$  ion for  $\text{S}^{2-}$  ion formation which in turn formed ZnS film. However, the actual mechanism depending on the film uniformity with different grain size in mc-Si prepared by varying the concentration of Zinc sulfide and hydrazine monohydrate is not clear.

Figure 2 shows the standard deviation of the thickness of the CBD-ZnS film deposited on mc-Si samples at  $80^\circ\text{C}$  for a fixed  $60^\circ$  substrate tilt and for different deposition periods. For standard deviation calculation, we have measured the thickness of the deposited ZnS film on silicon wafers ( $125\text{ mm} \times 125\text{ mm}$ ) at nine different geometrical locations using ellipsometer. It was observed from Figure 2 that the standard deviation of film thickness falls sharply with deposition times. This is probably due to CBD bath used that requires certain amount of time to initiate heterogeneous reaction throughout the bath uniformly. The rapid fall of standard deviation after 20 minutes of deposition may be due to higher rate of film deposition throughout the whole surface of wafer leading to an increase in film uniformity. We conclude that the uniformity of the film improves (standard deviation  $< 1$ ) with deposition time. The refractive index of a 75 minutes deposition film on m-Si sample was measured to be 2.35 using ellipsometer. The film thickness

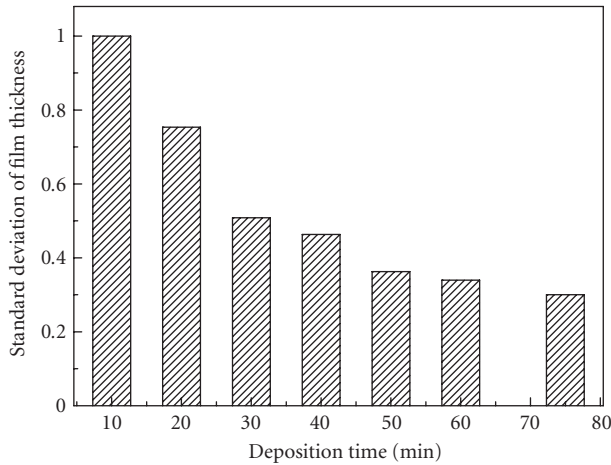


FIGURE 2: Variation of standard deviation of CBD-ZnS film on mc-Si substrate with deposition time at fixed CBD bath temperature of 80°C.

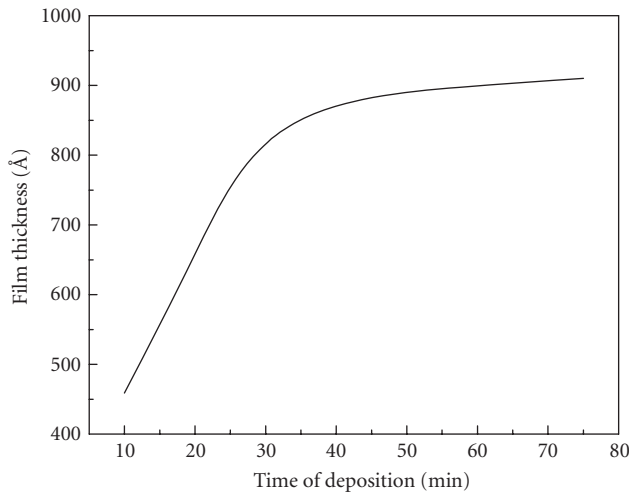


FIGURE 3: Variation of thickness of deposited CBD-ZnS film on mc-Si substrate with deposition time at fixed CBD bath temperature 80°C

verses deposition time of CBD-ZnS at fixed 60° substrate tilting deposited at 80°C is shown in Figure 3. It was observed that the film thickness increases sharply with time in the first 30 minutes of deposition and saturates afterwards. The reflectivity (%) and weighted average reflectance (%) of ZnS (900 Å) coated, PECVD silicon nitride (746 Å) coated textured mc-Si samples, and textured mc-Si sample are, respectively, shown in Figures 4 and 5. ZnS coated cells show slightly higher weighted average reflectance (7.1%) than PECVD SiN<sub>x</sub> coated cells (6.7%) in general. The presence of higher atomic percentage of oxygen is revealed from the EDAX analysis of the films (see Figure 6). This indicates that the S/Zn ratio (indicates the film stoichiometry) is around 0.71.

The illuminated I-V characteristics (LIV) of the large area (125 mm × 125 mm) solar cell with and without CBD ZnS AR coating are shown in Figure 7. From the curves,

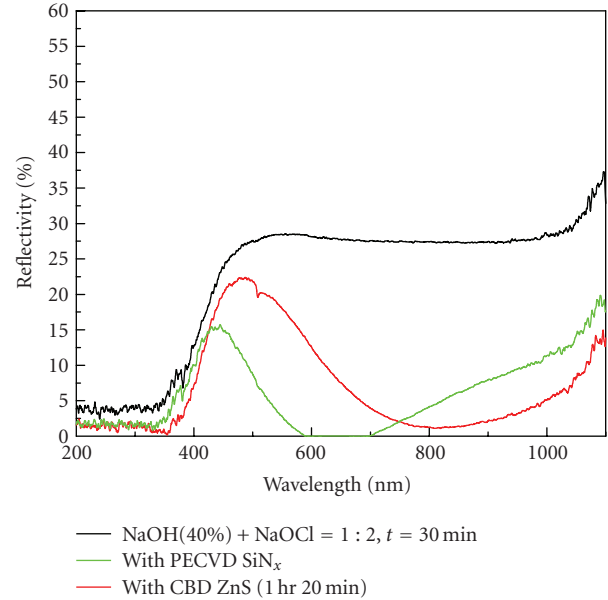


FIGURE 4: Reflectivity of NaOH–NaOCl textured mc-Si surface, CBD-ZnS coated and PECVD SiN<sub>x</sub> coated films on NaOH–NaOCl mc-Si substrate.

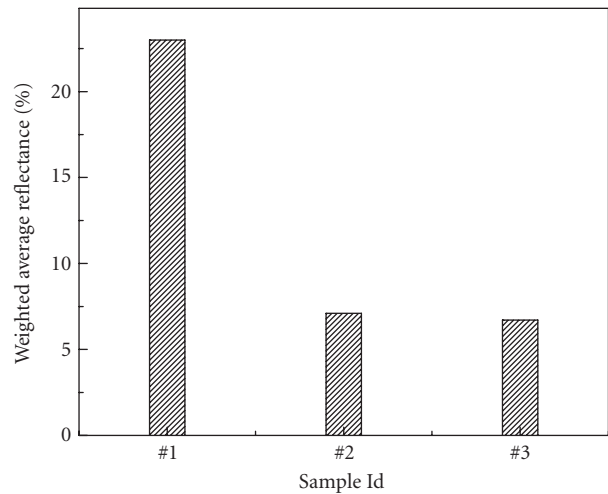


FIGURE 5: Weighted average reflectance (%) of Sample Id no. 1 (NaOH–NaOCl textured mc-Si surface), Id no. 2 (CBD-ZnS coated) and Id no. 3 (PECVD SiN<sub>x</sub> coated) films on NaOH–NaOCl textured mc-Si substrate.

it was observed that the short-circuit current of multicrystalline solar cell has increased from 3.93 A to 4.42 A after CBD-ZnS coating representing a 12.5% gain in short-circuit current and 14.9% gain in overall efficiency. It was also observed from Table 1 that except short-circuit current density and conversion efficiency, the performance parameter  $V_{oc}$  did not make significant change or degrade after CBD-ZnS coating on the finished solar cell. Spectral response curves from Figure 8 indicate substantial improvement after the application CBD-ZnS coating demonstrating the potential of CBD

TABLE 1: Performance parameters of large area (125 mm × 125 mm) multicrystalline silicon solar cell with and without CBD-ZnS AR coating,  $V_{oc}$  = open circuit voltage,  $I_{sc}$  = short circuit current,  $V_m$  = voltage at maximum Power Point,  $I_m$  = current at maximum Power Point,  $P_m$  = maximum Power output, FF = fill factor, Eff = efficiency.

Sample description	$V_{oc}$ (V)	$I_{sc}$ (A)	$V_m$ (V)	$I_m$ (A)	$P_m$ (W)	FF	Eff. (%)
Without AR coating	590.3	3.93	489.34	3.39	1.66	0.72	10.65
With ZnS AR coating	588.8	4.42	491.03	3.89	1.91	0.73	12.24

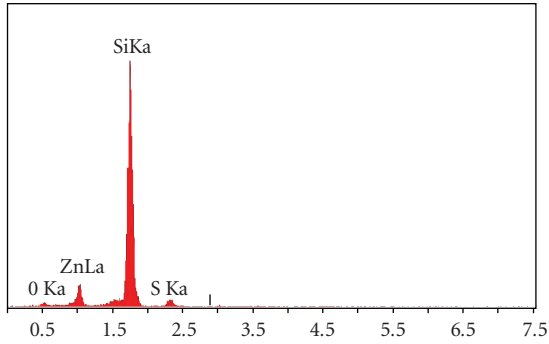


FIGURE 6: Energy Dispersive X-ray analysis curve of CBD-ZnS film on mc-Si substrate.

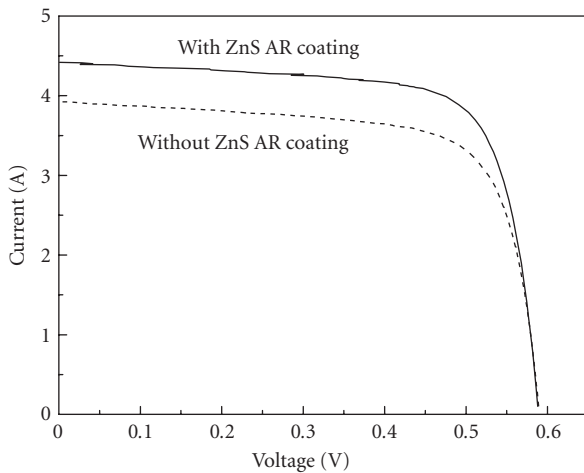


FIGURE 7: Illuminate current-voltage characteristic of large area mc-Si solar cell with and without ZnS AR coating.

ZnS as ARC on commercial multicrystalline silicon solar cells.

#### 4. CONCLUSION

Film uniformity (standard deviation < 1), good stoichiometry (0.71), high value of refractive index (2.35), and low-percentage weighted average reflection 7.1% were achieved through proper optimization of ZnS bath for depositing ZnS on mc-Si solar cell. Moreover, it has been observed that 12.5% gain in short-circuit current and 15% gain in overall efficiency have been achieved using CBD-ZnS films as AR coating on textured multicrystalline silicon solar cells. 12.24% efficiency on large area (125 mm × 125 mm) mul-

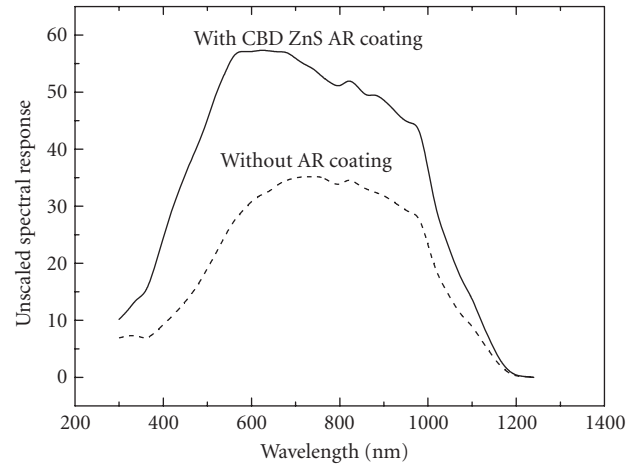


FIGURE 8: Spectral response of large area mc-Si solar cell with and without ZnS.

ticrystalline silicon solar cells is achieved by using CBD-ZnS antireflection coating on textured surface.

#### REFERENCES

- [1] G. Zhang, J. Zhao, and M. A. Green, "Effect of substrate heating on the adhesion and humidity resistance of evaporated  $\text{MgF}_2/\text{ZnS}$  antireflection coatings and on the performance of high-efficiency silicon solar cells," *Solar Energy Materials and Solar Cells*, vol. 51, no. 3-4, pp. 393-400, 1998.
- [2] B. Elidrissi, M. Addou, M. Regragui, A. Bougrine, A. Kachouane, and J. C. Bernède, "Structure, composition and optical properties of ZnS thin films prepared by spray pyrolysis," *Materials Chemistry and Physics*, vol. 68, no. 1-3, pp. 175-179, 2001.
- [3] J. A. Ruffner, M. D. Hilmel, V. Mizrahi, G. I. Stegeman, and U. J. Gibson, "Effects of low substrate temperature and ion assisted deposition on composition, optical properties, and stress of ZnS thin films," *Applied Optics*, vol. 28, no. 24, p. 5209, 1989.
- [4] A. M. Ledger, "Inhomogeneous interface laser mirror coatings," *Applied Optics*, vol. 18, no. 17, p. 2979, 1979.
- [5] R. R. Potter and J. R. Sites, "Current-voltage transients in (Cd,Zn)S/CuInSe<sub>2</sub> solar cells," *Applied Physics Letters*, vol. 43, no. 9, pp. 843-845, 1983.
- [6] K. T. R. Reddy and P. J. Reddy, "Studies of  $\text{Zn}_x\text{Cd}_{1-x}\text{S}$  films and  $\text{Zn}_x\text{Cd}_{1-x}\text{S}/\text{CuGaSe}_2$  heterojunction solar cells," *Journal of Physics D*, vol. 25, no. 9, pp. 1345-1348, 1992.
- [7] Z. Porada and E. Schabowska-Osiowska, "Surface electrical conductivity in ZnS(Cu, Cl, Mn) thin films," *Thin Solid Films*, vol. 145, no. 1, pp. 75-79, 1986.

- [8] Y. Tomomura, M. Kitagawa, A. Suzuki, and S. Nakajima, "Homoepitaxial growth of ZnS single crystal thin films by molecular beam epitaxy," *Journal of Crystal Growth*, vol. 99, no. 1-4, pp. 451-454, 1990.
- [9] M. Tonouchi, Y. Sun, T. Miyasato, H. Sakama, and M. Ohmura, "Room-temperature synthesis of ZnS:Mn films by H<sub>2</sub> plasma chemical sputtering," *Japanese Journal of Applied Physics*, vol. 2, pp. L2453-L2456, 1990.
- [10] P. J. Dean, A. D. Pitt, M. S. Skolnick, P. J. Wright, and B. Cockayne, "Optical properties of undoped organometallic grown ZnSe and ZnS," *Journal of Crystal Growth*, vol. 59, no. 1-2, pp. 301-306, 1982.
- [11] O. Briot, N. Briot, A. Abounadi, B. Gil, T. Cloitre, and R. L. Aulombard, "Reflectivity analysis of ZnS layers grown on GaAs and Si substrates by metal organic vapour-phase epitaxy," *Semiconductor Science and Technology*, vol. 9, no. 2, pp. 207-209, 1994.
- [12] H. H. Afifi, S. A. Mahmoud, and A. Ashour, "Structural study of ZnS thin films prepared by spray pyrolysis," *Thin Solid Films*, vol. 263, no. 2, pp. 248-251, 1995.
- [13] D. A. Johnston, M. H. Carletto, K. T. R. Reddy, I. Forbes, and R. W. Miles, "Chemical bath deposition of zinc sulfide based buffer layers using low toxicity materials," *Thin Solid Films*, vol. 403-404, pp. 102-106, 2002.
- [14] E. J. Ibanga, C. Le Luyer, and J. Mugnier, "Zinc oxide waveguide produced by thermal oxidation of chemical bath deposited zinc sulphide thin films," *Materials Chemistry and Physics*, vol. 80, no. 2, pp. 490-495, 2003.
- [15] J. Vidal, O. de Melo, O. Vigil, N. López, G. Contreras-Puente, and O. Zelaya-Angel, "Influence of magnetic field and type of substrate on the growth of ZnS films by chemical bath," *Thin Solid Films*, vol. 419, no. 1-2, pp. 118-123, 2002.
- [16] U. Gangopadhyay, K. Kim, D. Mangalaraj, and J. Yi, "Low cost CBD ZnS antireflection coating on large area commercial mono-crystalline silicon solar cells," *Applied Surface Science*, vol. 230, no. 1-4, pp. 364-370, 2004.

## Review Article

# Advances in Contactless Silicon Defect and Impurity Diagnostics Based on Lifetime Spectroscopy and Infrared Imaging

Jan Schmidt, Peter Pohl, Karsten Bothe, and Rolf Brendel

*Institut für Solarenergieforschung Hameln/Emmerthal (ISFH), Am Ohrberg 1, 31860 Emmerthal, Germany*

Received 19 March 2007; Accepted 12 April 2007

Recommended by Armin G. Aberle

This paper gives a review of some recent developments in the field of contactless silicon wafer characterization techniques based on lifetime spectroscopy and infrared imaging. In the first part of the contribution, we outline the status of different lifetime spectroscopy approaches suitable for the identification of impurities in silicon and discuss—in more detail—the technique of temperature- and injection-dependent lifetime spectroscopy. The second part of the paper focuses on the application of infrared cameras to analyze spatial inhomogeneities in silicon wafers. By measuring the infrared signal absorbed or emitted from light-generated free excess carriers, high-resolution recombination lifetime mappings can be generated within seconds to minutes. In addition, mappings of non-recombination-active trapping centers can be deduced from injection-dependent infrared lifetime images. The trap density has been demonstrated to be an important additional parameter in the characterization and assessment of solar-grade multicrystalline silicon wafers, as areas of increased trap density tend to deteriorate during solar cell processing.

Copyright © 2007 Jan Schmidt et al. This is an open access article distributed under the Creative Commons Attribution License, which permits unrestricted use, distribution, and reproduction in any medium, provided the original work is properly cited.

## 1. INTRODUCTION

The performance of today's commercially produced silicon solar cells is to a great extent limited by recombination via defects and impurities in the bulk. This holds in particular for solar cells produced on multicrystalline silicon (mc-Si) wafers, containing large concentrations of crystallographic defects, such as dislocations and grain boundaries, as well as recombination-active impurities, such as transition metals. Despite the fact that the concentrations of these impurities are usually extremely low (typically well below  $10^{13} \text{ cm}^{-3}$ ), their impact on cell performance can be quite detrimental already above ultra low concentrations of  $\sim 10^{11} \text{ cm}^{-3}$ . Such low impurity concentrations are not detectable by most analytical techniques. Only a few electrical techniques, such as capacitance-based deep-level transient spectroscopy (DLTS) [1] and lifetime spectroscopy (LS) [2–6], are capable of detecting and identifying electrically active impurities at concentrations below  $10^{13} \text{ cm}^{-3}$ . The main advantages of LS over DLTS are that (i) it is a contactless technique, facilitating the sample preparation, and (ii) it is most sensitive to those centers that contribute to the total recombination rate (i.e., those centers that are actually relevant to solar cells). In contrast,

standard DLTS only detects capture and emission of one type of carrier and gives, hence, in general no information on the recombination activity of the detected impurity. In the first part of this paper, we give a brief review of the different approaches to extract the characteristic defect parameters (i.e., energy level and electron-to-hole capture cross-section ratio) from LS measurements and address difficulties and limitations of the techniques.

Typically, the spatial distribution of recombination centers in mc-Si wafers is very inhomogeneous, requiring the application of spatially resolved measurement techniques. Traditionally, this is done by tedious point-by-point measurement techniques, such as the microwave-detected photoconductance decay (MW-PCD) [7, 8] technique, requiring typical measurement periods in the range of hours to obtain a high-resolution lifetime mapping. Recently, infrared-camera-based measurement techniques have been introduced [9, 10] which allow to generate high-resolution lifetime mappings within seconds to minutes. The principal idea of infrared lifetime mapping/carrier density imaging (ILM/CDI) is to make use of the free-carrier absorption or emission of sub-bandgap infrared photons. Using a suitable calibration, the spatial distribution of the light-generated

excess carrier concentration is directly obtained from the infrared absorption or emission image recorded by the camera. Provided that the photogeneration is homogeneous over the entire wafer area, a recombination lifetime mapping can be deduced directly from the excess carrier concentration image. In addition to the spatial analysis of recombination centers, the infrared camera also allows to analyze the spatial distribution of non-recombination-active minority-carrier trapping centers. This infrared trap mapping (ITM) method [11] is of particular relevance to mc-Si wafers, as the trap-density mapping predicts how a multicrystalline silicon wafer behaves during high-temperature processing. The second part of this review presents the current state of these infrared-camera-based measurement techniques, which—due to their short data acquisition times—evolve into in-line characterization tools for solar cell production lines in the near future.

## 2. LIFETIME SPECTROSCOPY

Figure 1 shows a comparison of the basic physical principles of LS and DLTS. While lifetime spectroscopy is based on measurements of recombination events via defect/impurity levels in the bandgap capturing electrons as well as holes, in standard DLTS measurements the detected defect level interacts only with the majority carriers (in Figure 1 with electrons), making it only sensitive to defect levels in the majority-carrier half of the bandgap. A major problem of DLTS measurements is that, despite the fact that energy level, majority-carrier capture cross-section, and defect concentration can be extracted from those measurements, no information on the recombination activity of the detected center is gained. This important device-relevant information is inherently obtained from lifetime spectroscopy measurements, which are particularly sensitive to such types of defects that actually result in recombination. Different variants of lifetime spectroscopy have been studied in the past of which we will give a brief overview in the following.

### 2.1. Temperature-dependent lifetime spectroscopy

Temperature-dependent lifetime spectroscopy (TDLS) measures the carrier lifetime of a sample under low-level injection conditions ( $\tau^{\text{LLI}}$ ) and determines the defect energy level  $E_t$  from the linear slope of the Arrhenius plot of  $\ln(\tau^{\text{LLI}}/T)$  versus  $1/T$  [2, 4]. However, a basic assumption of the standard TDLS analysis is that the electron and hole capture cross-sections  $\sigma_n$  and  $\sigma_p$  are independent of temperature, which is not valid in general. Moreover, the standard TDLS analysis does not allow to decide whether the defect energy level is located in the upper or in the lower half of the bandgap. The TDLS analysis has been improved by enlarging the temperature range down to temperatures well below room temperature and by fitting the complete temperature-dependent lifetime curve [6] using the Shockley-Read-Hall (SRH) equation [12, 13]. This allows an improved determination of the energy level.

### 2.2. Injection-dependent lifetime spectroscopy

Less frequently applied in the past has been the technique of injection-dependent lifetime spectroscopy (IDLS) since in most cases it results only in a relatively broad uncertainty range for  $E_t$  [3]. On the other hand, IDLS is capable of determining the  $\sigma_n/\sigma_p$  ratio with a better accuracy than TDLS. IDLS measurements on silicon wafers with varying doping concentrations is one possibility to narrow down the uncertainty range for  $E_t$  [3]. However, this approach requires many different samples with lifetimes limited by the same type of defect.

### 2.3. Temperature- and injection-dependent lifetime spectroscopy

In order to combine the advantages of TDLS and IDLS, we have recently introduced temperature- and injection-dependent lifetime spectroscopy (TIDLS) [5]. Our experimental set-up is based on an extended quasi-steady-state photoconductance (QSSPC) system [5, 14]. Importantly, TIDLS not only determines the defect energy level with improved accuracy, but also reveals the temperature dependence of the capture cross-sections and permits the distinction between shallow and deep-level centers. Despite its large potential for the identification of efficiency-limiting defects in solar-grade silicon materials, TIDLS is still not widely used by the PV community. This is mainly due to the fact that the data evaluation is relatively complex because it requires the simultaneous fitting of the SRH equation to a large number of injection-dependent lifetime curves measured at varying temperatures. The results of such fitting attempts are usually ambiguous, imposing an additional complication to the general analysis of TIDLS measurements. In an effort to facilitate the application of TIDLS, we have recently simplified the analysis of temperature- and injection-dependent lifetime measurements [15].

### 2.4. Simplified TIDLS analysis

Our simplified analysis determines the energy level  $E_t$  and the ratio of the electron-to-hole capture cross-sections  $k = \sigma_n/\sigma_p$  of the lifetime-limiting recombination center without the requirement of a simultaneous fitting of all measured  $\tau(\Delta n, T)$  curves. The simplified analysis is restricted to recombination centers which—at a characteristic temperature  $T_c$ —change their  $\tau(\Delta n)$  slope with increasing temperature from positive to negative. As the experimentally accessible temperature range of our TIDLS set-up is restricted to the temperature range 30–170°C, we are only capable of analyzing defect levels with characteristic temperatures  $T_c$  within this range. This restricts our analysis to recombination centers with a distance from one of the band edges within the range of 0.2–0.4 eV, as estimated using the SRH equation [15].

In order to demonstrate our simplified TIDLS analysis, we have applied it to an intentionally tungsten-contaminated *p*-type Czochralski-grown silicon (Cz-Si) wafer of doping concentration  $N_{\text{dop}} = 4.7 \times 10^{14} \text{ cm}^{-3}$ . Both wafer surfaces are passivated with plasma-enhanced chemical vapor

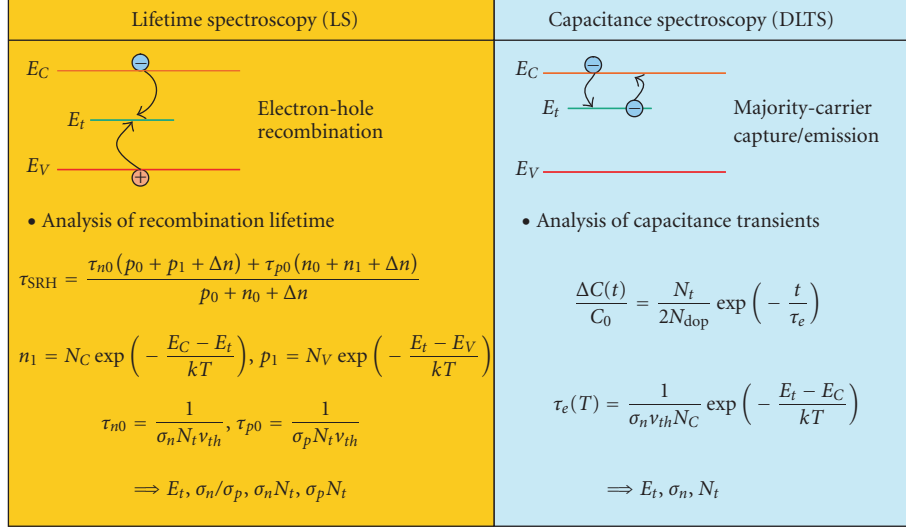


FIGURE 1: Comparison of the physical principles of lifetime spectroscopy (LS) and capacitance-based DLTS.

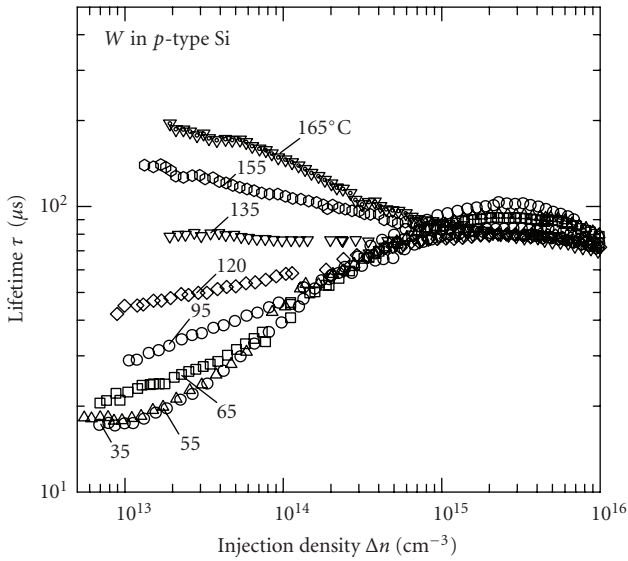


FIGURE 2: Temperature- and injection-dependent carrier lifetime measurements of a tungsten-contaminated *p*-type Cz-Si wafer of doping concentration  $N_{\text{dop}} = 4.7 \times 10^{14} \text{ cm}^{-3}$ .

deposited silicon nitride films resulting in surface recombination velocities well below 10 cm/s [16]. Due to the excellent passivation properties of our silicon nitride films, we neglect any surface recombination and identify the measured effective lifetimes with the bulk lifetimes of the wafer under test. TIDLs measurements have been performed in the temperature range between 30 and 165°C in steps of 5°C using a QSSPC set-up extended with a temperature-controlled sample stage [5, 14]. Figure 2 shows a selection of  $\tau(\Delta n)$  curves measured at different temperatures. By merely looking at the qualitative  $\tau(\Delta n, T)$  behavior, several important features of

the lifetime-limiting recombination center—in this case interstitial tungsten ( $W_i$ )—can be deduced.

First, for temperatures up to 60°C the injection-dependent lifetime curves do not change at all. This implies that for low temperatures the recombination center behaves like a deep-level center. As a consequence, we can immediately calculate the capture cross-section ratio  $k$  using the equation [15]

$$k = \left(\frac{\tau_\eta}{\tau_{n0}} - 1\right)(\eta^{-1} + 1), \quad (1)$$

which we have derived from the SRH equation. In (1),  $\eta \equiv \Delta n / N_{\text{dop}}$  is the injection level,  $\tau_{n0}$  is the low-injection lifetime, and  $\tau_\eta$  is the lifetime measured at an intermediate injection level  $\eta$ , the latter being typically chosen between 0.1 and 1.0. As can be seen from (1), the determination of  $k$  requires only two lifetime values, one measured under low-injection conditions, the second one measured at an intermediate injection level.

However, to determine the capture cross-section ratio  $k$  with improved accuracy, we have determined  $k$  at different injection levels  $\eta$  and for varying temperatures. Figure 3 shows the results for the  $k(\eta)$  curve calculated from the measured  $\tau(\Delta n)$  dependence at 35°C. As expected for a single-level defect, the analysis results in a constant  $k$ , in the present case  $k \approx 8$ . This procedure can also be regarded as a test for the applicability of the single-level defect recombination theory, which is only valid if no  $k(\eta)$  dependence is observed. The  $k$  ratio decreases slightly for injection levels above unity (not shown in Figure 3). This can be attributed to an additional shallow defect level leading to a decreasing lifetime for higher injection levels. Applying (1) to all injection-dependent lifetime curves measured in the temperature range between 30 and 60°C results in a more accurate capture cross-section ratio and a corresponding uncertainty range of  $k = 8.5 \pm 1.0$ . In the following analysis, we assume

this  $k$  value to be temperature-independent, that is, electron and hole capture cross-sections are assumed to have the same temperature dependence.

The second important feature of the measured  $\tau(\Delta n, T)$  curves shown in Figure 2 is that at injection densities below the doping concentration, the slope of the injection-dependent lifetime curves changes from positive to negative at 135°C. This characteristic temperature of  $T_c = 408$  K can be determined with an accuracy of  $\pm 5$  K without any fitting. The energy level  $E_t$  of the recombination center can now directly be calculated from the measured  $T_c$ .

However, the solution is not unambiguous because we have to consider two different cases: (i)  $E_t$  is located in the lower half of the silicon bandgap and (ii)  $E_t$  is located in the upper bandgap half. To derive the relation between  $E_t$  and  $T_c$ , we consider at first case (i). Using the analytical expression given by the SRH equation for the  $\tau(\Delta n, T)$  dependence and assuming that at  $T_c$  the slope  $\partial\tau/\partial\Delta n$  vanishes, we obtain the expression [15]

$$E_t - E_V = -k_B T_c \ln \left[ k \frac{N_{\text{dop}}}{N_V^{300\text{K}}} \left( \frac{300\text{K}}{T_c} \right)^{3/2} \right], \quad (2)$$

where  $k_B$  is Boltzmann's constant and  $N_V^{300\text{K}}$  is the effective density of states in the valence band at 300 K. Using the experimentally determined values of  $T_c = (408 \pm 5)$  K and  $k = 8.5 \pm 1.0$ , we determine an energy level of  $E_t - E_V = (0.33 \pm 0.01)$  eV.

Assuming case (ii) we obtain a slightly different equation for  $E_t$  [15]:

$$E_C - E_t = -k_B T_c \ln \left[ \frac{N_{\text{dop}}}{N_C^{300\text{K}}} \left( \frac{300\text{K}}{T_c} \right)^{3/2} \right] \quad (3)$$

with  $N_C^{300\text{K}}$  being the effective density of states in the conduction band at 300 K. Interestingly, (2) and (3) differ slightly as the energy level calculated from (2) depends on  $k$ , whereas the energy level calculated from (3) does not depend on the capture cross-section ratio. As a consequence, the energy levels may differ significantly if the capture cross-sections are strongly asymmetric, which is frequently the case. Using (3) with the measured characteristic temperature of  $T_c = (408 \pm 5)$  K, we obtain an energy level of  $E_C - E_t = (0.40 \pm 0.01)$  eV.

Due to the strong asymmetry in the capture cross-section ratio, this energy level differs considerably from the energy level determined using (2). In the next step of the analysis, it has to be decided which of the two calculated energy levels is the true one. This can simply be done by performing a standard TDLS analysis at a well-defined injection density. Figure 4 shows an Arrhenius plot of the carrier lifetimes measured at  $\Delta n = 5 \times 10^{13} \text{ cm}^{-3}$ . The lifetime data measured above  $\sim 100^\circ\text{C}$  shows a clear linear dependence in the Arrhenius plot of Figure 4, resulting in an energy level of  $\Delta E_t = (0.31 \pm 0.02)$  eV. From the standard TDLS analysis alone it cannot be decided if this energy level is located in the upper or in the lower bandgap half. However, by comparing the result of the standard TDLS analysis with our above analysis of the temperature- and injection-dependent

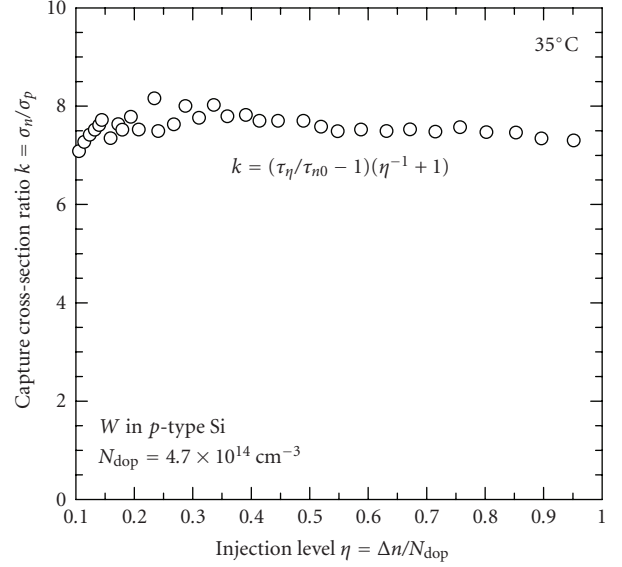


FIGURE 3: Capture cross-section ratio  $k = \sigma_n/\sigma_p$  as a function of injection level  $\eta$  at 35°C, as calculated from the corresponding  $\tau(\Delta n)$  curve in Figure 2.

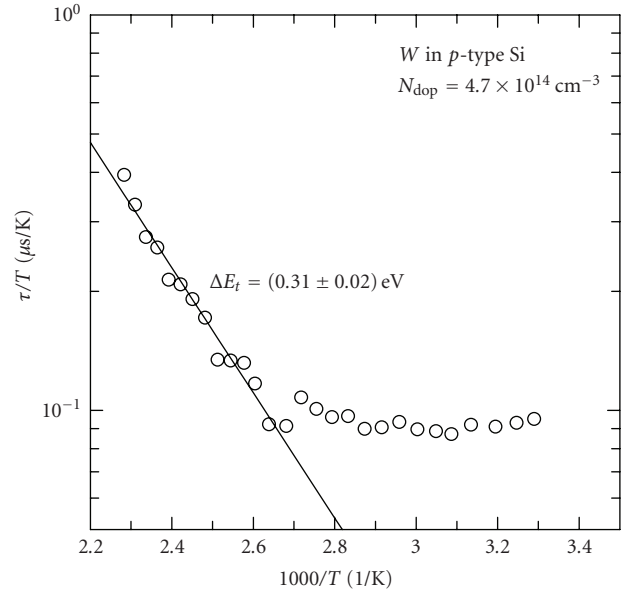


FIGURE 4: Arrhenius plot of the lifetime divided by temperature  $\tau/T$ . The lifetime data has been extracted from Figure 2 at an injection density of  $\Delta n = 5 \times 10^{13} \text{ cm}^{-3}$ . From the linear part of the curve, an energy level of  $\Delta E_t = 0.31$  eV is determined.

lifetime measurements, it can be concluded that the true energy level is located in the lower half of the silicon bandgap at  $E_t - E_V = (0.33 \pm 0.01)$  eV. This result is in excellent agreement with literature data for the energy level of interstitial tungsten in silicon [17, 18]. It is intriguing that energy level and capture cross-section ratio can both be determined with

a very high degree of accuracy without the necessity of any complex fitting routines using the simplified TIDLS evaluation method. For comparison we have also fitted all TIDLS curves simultaneously using the SRH equation. This procedure results in an energy level of  $E_t - E_V = (0.32 \pm 0.02)$  eV and a  $k$  value of  $\sim 10$ , which is also in excellent agreement with the result of our simplified TIDLS analysis.

### 3. INFRARED-CAMERA-BASED CHARACTERIZATION TECHNIQUES

Since the most common silicon wafer material used today in solar cell production is multicrystalline silicon with strongly inhomogeneous lateral distributions of defects and impurities, characterization techniques giving spatial information are indispensable. In the past, several contactless lifetime mapping techniques have been applied to characterize inhomogeneities in silicon wafers. Two prominent examples of such techniques are MW-PCD [7, 8] and modulated free-carrier absorption (MFCA) [19]. Both techniques generate the maps from point-by-point measurements, requiring typical measurement periods of hours for recording high-resolution ( $\sim 200 \mu\text{m}$ ) lifetime maps. To decrease the long measurement periods, infrared (IR)-camera lifetime mapping/carrier density imaging (ILM/CDI) has been introduced recently [9, 10]. Using an IR camera (i.e., an array of IR detectors) sensitive in the wavelength range between  $\sim 3$  and  $8 \mu\text{m}$  instead of a single detector reduces the measurement period for a high-resolution mapping from hours to minutes and sometimes even seconds. Note that IR cameras can also be used to image temperature distributions on solar cells, which has been successfully applied as “lock-in infrared thermography” to generate mappings of shunts or series resistances of solar cells [20, 21]. More recently, camera-based photoluminescence imaging has been introduced, which also allows a very fast imaging of silicon wafers and solar cells at high resolution using a conventional relatively cheap silicon CCD camera [22]. A detailed discussion of all camera-based characterization techniques currently under investigation is however beyond the scope of this review paper.

#### 3.1. Infrared lifetime mapping

Figure 5 shows a schematic of the ILM/CDI measurement principle. The technique is based on measuring the free-carrier absorption [9, 10] or, equivalently, the free-carrier emission [9, 23] of sub-bandgap photons. In order to improve the sensitivity, lock-in technique is applied. For further technical details the interested reader is referred to [24]. In this review, we focus on the basic measurement principle only. One image is recorded with above-bandgap illumination of the sample and a second one without illuminating the wafer. The difference image is proportional to the light-generated excess carrier concentration. The calibration is performed by recording the IR emission signal of several silicon wafers of known doping concentrations. The proportionality factor  $m$  between the camera signal and the free-carrier concentration times the wafer thickness is obtained

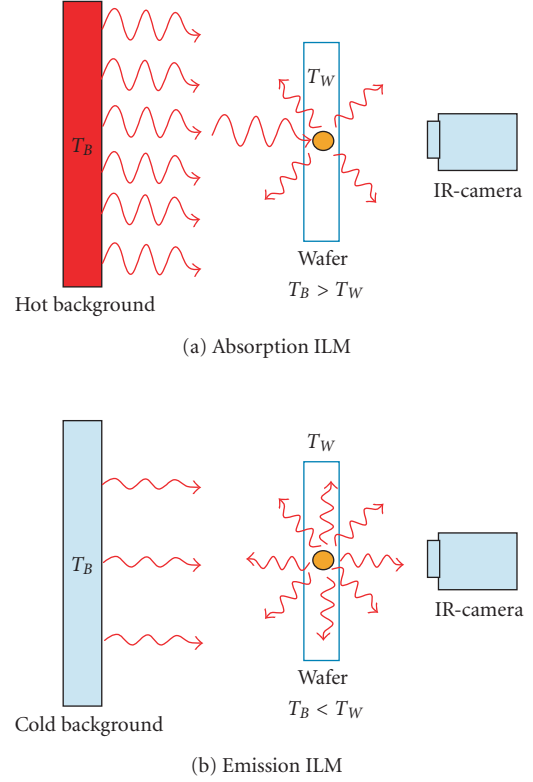


FIGURE 5: Schematic of the infrared lifetime mapping/carrier density imaging (ILM/CDI) principle: (a) absorption mode, (b) emission mode.

from a linear fit to the measured data. Using the measured photogeneration rate  $G$  of the excitation light, the lifetime mapping  $\tau(x, y)$  is calculated directly from the IR emission signal image  $S(x, y)$  using the equation [9]

$$\tau(x, y) = \frac{S(x, y)}{m(1 + \alpha_n/\alpha_p)GW} \quad (4)$$

with  $W$  being the wafer thickness and  $\alpha_{n/p}$  being the absorption coefficient of free electrons/holes at the detection wavelength. The correction factor  $(1 + \alpha_n/\alpha_p)$  accounts for the fact that under illumination, electrons as well as holes are generated, whereas in our calibration procedure only  $p$ -type silicon material is used [9, 25]. According to Kirchhoff’s law, the absorption always equals the emission. Hence, the measurement can be performed in absorption or emission mode, depending on the temperature of the material under investigation and the temperature of the background, as shown in Figure 5. The exemplary measurements on mc-Si wafers presented in Section 3.3 are carried out in emission mode.

#### 3.2. Infrared trap mapping

In multicrystalline silicon wafers as well as in Czochralski-grown monocrystalline silicon wafers, abnormally high lifetimes are frequently measured at low injection levels. This effect has been assigned to the presence of non-recombination-active minority-carrier trapping centers [26–28]. At excess

carrier concentrations comparable to or below the trap density, charge neutrality implies that the presence of minority-carrier traps causes a relative increase in the concentration of majority carriers, resulting in an increase of the steady-state photoconductance signal measured using QSSPC and the free-carrier absorption/emission signal recorded in ILM measurements. In a recent contribution, [11] we have shown that trap concentration and energy level mappings can be generated from ILM mappings recorded at different illumination intensities. This infrared trap mapping (ITM) technique is based on fitting the adapted Hornbeck-Haynes equation [11, 29] for the “apparent” lifetime

$$\tau_a = \left( 1 + \frac{N_t}{(\Delta n + N_t(\tau_t/\tau_d))} \frac{\alpha_p}{(\alpha_p + \alpha_n)} \right) \tau_r \quad (5)$$

to the measured lifetime data at each point of the infrared lifetime mapping. In (5),  $\tau_r$  is the recombination lifetime,  $N_t$  the trap density, and  $\tau_t/\tau_d$  the ratio of trapping-to-detraping time constants. The latter quantity is directly related to the energy level of the trap. For  $n$ -type material,  $\alpha_p$  in the numerator has to be replaced by  $\alpha_n$ . As our measurements are performed under low-injection conditions,  $\tau_r$  does not depend on the injection level. Moreover, the apparent excess carrier concentration  $\Delta n_a$  is calculated via the expression  $\Delta n_a = (\tau_a/\tau_r)\Delta n$  [28]. A suppression of the trapping effect can be realized by illuminating the wafer with sub-bandgap illumination in addition to the excess-carrier-generating light during the ILM measurement [30], which enables the extraction of the recombination lifetime from ILM measurements even at very low injection levels.

### 3.3. Exemplary measurements on mc-Si wafers

#### 3.3.1. As-grown state

Figure 6 shows two lifetime images  $\tau(x, y)$  of an mc-Si sample recorded at two different illumination intensities ( $3 \times 10^{-3}$  suns and 1 sun) [31]. Due to minority-carrier trapping the area-averaged apparent lifetime of  $\tau_a = 350 \mu\text{s}$  determined at  $3 \times 10^{-3}$  suns [Figure 6(a)] is much larger than the area-averaged lifetime of 110 microseconds at 1 sun [Figure 6(b)], where trapping effects are negligible and thus the actual recombination lifetime is measured. As can be seen from Figure 6, the two lifetime mappings do not correlate perfectly. Apparently, additional information on the spatial distribution of the trapping centers is provided by the lifetime image measured at an illumination intensity of  $3 \times 10^{-3}$  suns.

Fitting (5) to the lifetime images recorded at different illumination intensities results in the  $N_t$  image shown in Figures 7(a). Figure 7(b) shows a photograph of the wafer after applying a Dash etch [32] to reveal a possible correlation of the traps with dislocations. Indeed, the spatial distribution of dislocations shown in Figure 7(b) is in excellent agreement with the trap density distribution in Figure 7(a).

#### 3.3.2. Impact of phosphorus gettering

Figure 8 shows a comparison of the recombination lifetime maps recorded at an injection density of  $\Delta n = 10^{14} \text{ cm}^{-3}$  be-

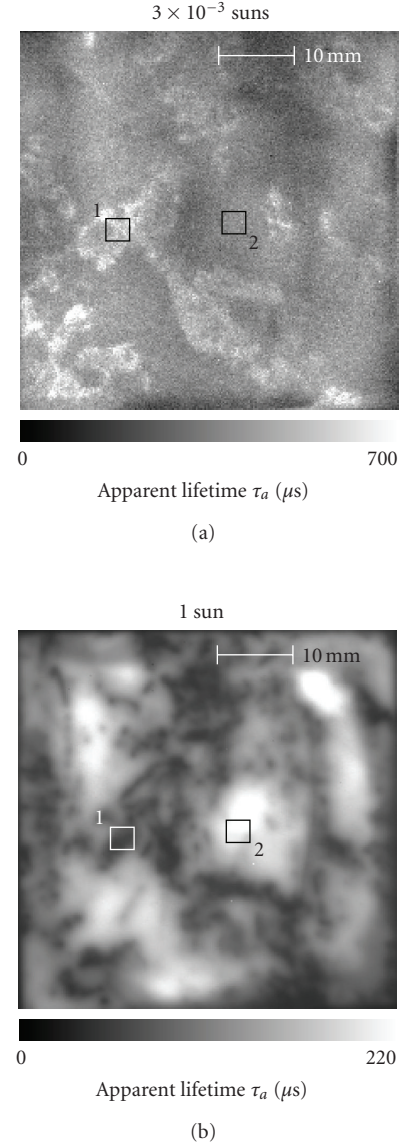


FIGURE 6: Infrared lifetime mappings of an mc-Si wafer measured at two different illumination intensities: (a)  $3 \times 10^{-3}$  suns and (b) 1 sun.

fore and after phosphorus gettering [31]. The area-averaged recombination lifetime increases from 51.9 microseconds before gettering to 65.3 microseconds after gettering. However,  $\tau_r$  increases in particular in those regions which already had the highest lifetimes before gettering. In regions of low lifetimes before gettering, the recombination lifetime shows only a small improvement or even decreases.

Figure 9 shows injection-dependent lifetime curves  $\tau_a(\Delta n_a)$  measured at two different positions on the wafer indicated in Figures 6–8. The two positions correspond to areas of highest and lowest trap densities. At position 1, we determine  $N_t = 2.1 \times 10^{13} \text{ cm}^{-3}$  and at position 2,  $N_t = 9.0 \times 10^{12} \text{ cm}^{-3}$ . The injection-dependent lifetime curves in Figure 9 show that for injection densities above  $1 \times 10^{14} \text{ cm}^{-3}$

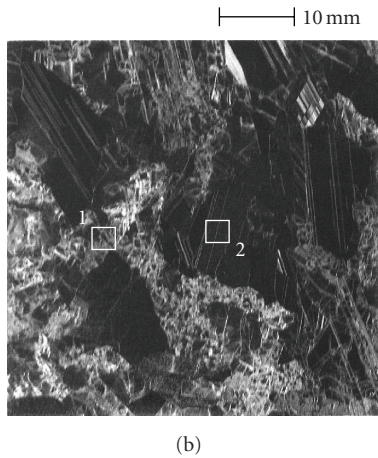
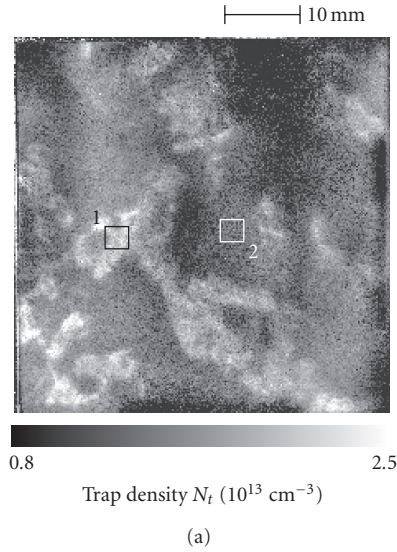


FIGURE 7: (a) Trap density image  $N_t(x, y)$  of the mc-Si wafer shown in Figure 6. (b) Photograph of the same wafer after applying a Dash etch. Brighter regions correspond to regions of increased dislocation densities.

trapping effects are negligible and, thus, the actual recombination lifetime is obtained. The curve measured at position 2 clearly reveals an increase of the recombination lifetime after gettering, whereas at position 1,  $\tau_r$  decreases after the phosphorus gettering treatment.

Our interpretation of the observed behavior is that areas exhibiting higher dislocation densities (position 1) contain significant concentrations of metallic impurities (partly in the form of metal silicide precipitates), which are captured within the stress field surrounding a dislocation. These impurities are released during the high-temperature gettering treatment and contaminate the regions surrounding the dislocations [24]. This effect leads to a severe degradation in the solar cell performance in contrast to regions with lower dislocation densities (position 2), where the phosphorus gettering treatment mainly removes recombination-active interstitial

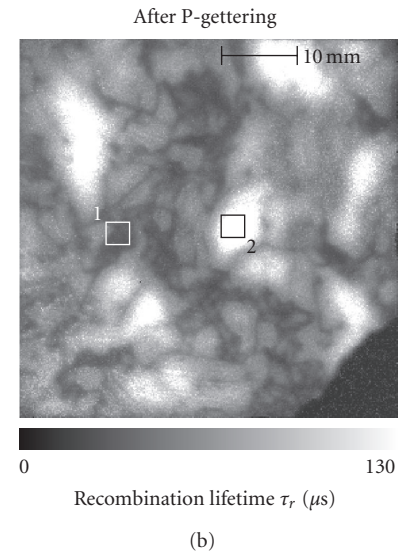
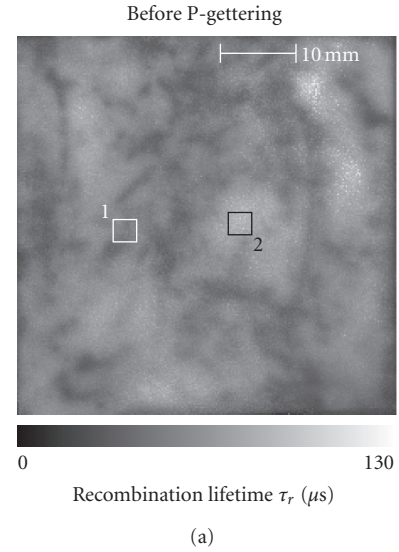


FIGURE 8: Recombination lifetime images  $\tau_r(x, y)$  determined at an injection density of  $\Delta n = 10^{14} \text{ cm}^{-3}$  as calculated using an automated fitting routine for the wafer shown in Figure 6 before (a) and after (b) phosphorus gettering.

metallic impurities. Note that more recently similar results have been published in a parallel study [33].

### 3.3.3. Trap mapping without surface passivation

As already mentioned in the previous section, the apparent lifetime image [Figure 6(a)] and the corresponding  $N_t$  image [Figure 7(a)] show a good qualitative agreement, demonstrating that a single ILM measurement already reveals if trapping at dislocations is present and which regions of the wafer are affected. In order to facilitate a possible industrial application of IR-camera-based trap imaging, we have

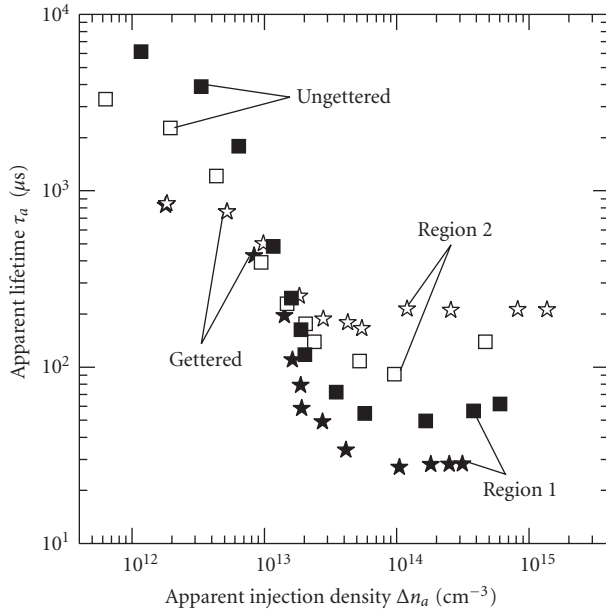


FIGURE 9: Injection-dependent lifetime curves  $\tau_a(\Delta n_a)$  at two different positions (marked in Figures 6–8) of an mc-Si wafer. The wafer was measured before (squares) and after (stars) phosphorus gettering.

performed only one single IR emission measurement on as-cut mc-Si wafers without applying any surface treatment [31]. Figure 10(a) shows the measured infrared emission picture  $S(x, y)$  of an as-cut block-cast mc-Si wafer ( $125 \times 125 \text{ mm}^2$ ) recorded at 1/100 suns. The measurement period was 20 minutes. The image reveals areas with increased dislocation densities located on the left-hand side, bottom side, and top right corner of the wafer. A comparison with the  $N_t$  image obtained using the ITM method [see Figure 10(b)] shows that the two images agree well.

Our measurements suggest that regions of increased dislocation densities correlate with increased densities of metallic impurities, mostly in the form of precipitates [31]. A high-temperature step, such as the phosphorus gettering treatment, dissolves metal precipitates and degrades the lifetime in highly dislocated areas. Hence, the application of IR camera measurements to unpassivated as-cut mc-Si wafers helps to identify poorly getterable areas. However, a further reduction of the measurement time is required to enable the application of this technique to the front-end materials characterization in solar cell production lines.

#### 4. CONCLUSIONS

Contactless characterization techniques enabling (i) a reliable identification of contaminants in silicon wafers and (ii) a fast determination of their spatial distribution are becoming increasingly important in silicon photovoltaics, since most commercially produced solar cells are still limited by defect-related recombination in the bulk. The potential of infrared-camera-based defect characterization techniques

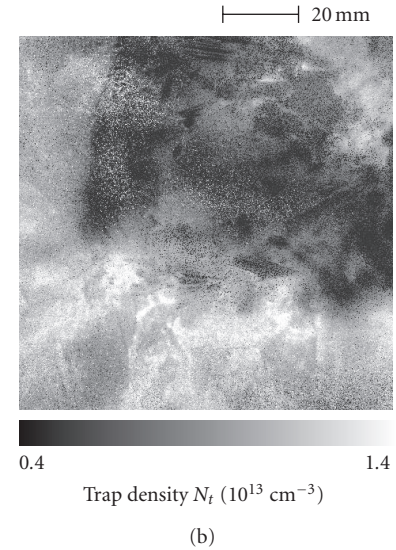
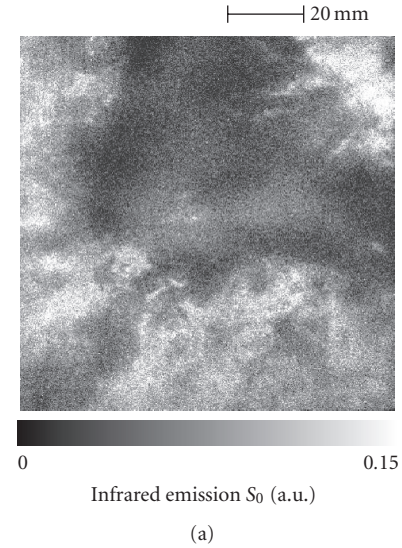


FIGURE 10: (a) Infrared emission signal  $S(x, y)$  of a block-cast mc-Si wafer without any surface passivation measured at an illumination intensity of 0.01 sun. Brighter regions correspond to areas of increased trap densities. (b) Trap density image  $N_t(x, y)$  of the same wafer after passivating both surfaces with silicon nitride.

has just started to be explored. Infrared trap mapping represents a new source of information on the defect structure of a silicon material. An important improvement to the analysis of trap parameters by quasi-steady-state photoconductance measurements is the possibility of examining spatial correlations between trapping and recombination centers as well as correlations with structural defects.

#### ACKNOWLEDGMENTS

The authors are grateful to T. Abe (ShinEtsu) for supplying tungsten-contaminated silicon wafers. Funding was provided by the German State of Lower Saxony.

## REFERENCES

- [1] D. V. Lang, "Deep-level transient spectroscopy: a new method to characterize traps in semiconductors," *Journal of Applied Physics*, vol. 45, no. 7, pp. 3023–3032, 1974.
- [2] Y. Hayamizu, T. Hamaguchi, S. Ushio, T. Abe, and F. Shimura, "Temperature dependence of minority-carrier lifetime in iron-diffused  $p$ -type silicon wafers," *Journal of Applied Physics*, vol. 69, no. 5, pp. 3077–3081, 1991.
- [3] J. Schmidt and A. Cuevas, "Electronic properties of light-induced recombination centers in boron-doped Czochralski silicon," *Journal of Applied Physics*, vol. 86, no. 6, pp. 3175–3180, 1999.
- [4] S. Rein, T. Rehrl, W. Warta, and S. W. Glunz, "Lifetime spectroscopy for defect characterization: systematic analysis of the possibilities and restrictions," *Journal of Applied Physics*, vol. 91, no. 3, pp. 2059–2070, 2002.
- [5] J. Schmidt, "Temperature- and injection-dependent lifetime spectroscopy for the characterization of defect centers in semiconductors," *Applied Physics Letters*, vol. 82, no. 13, pp. 2178–2180, 2003.
- [6] S. Rein, *Lifetime Spectroscopy*, Springer, Berlin, Germany, 2005.
- [7] M. Kunst and G. Beck, "The study of charge carrier kinetics in semiconductors by microwave conductivity measurements," *Journal of Applied Physics*, vol. 60, no. 10, pp. 3558–3566, 1986.
- [8] J. Schmidt and A. G. Aberle, "Accurate method for the determination of bulk minority-carrier lifetimes of mono- and multicrystalline silicon wafers," *Journal of Applied Physics*, vol. 81, no. 9, pp. 6186–6199, 1997.
- [9] M. Bail, J. Kentsch, R. Brendel, and M. Schulz, "Lifetime mapping of Si wafers by an infrared camera [for solar cell production]," in *Proceedings of the 28th IEEE Photovoltaic Specialists Conference*, pp. 99–103, Anchorage, Alaska, USA, September 2000.
- [10] S. Riepe, J. Isenberg, C. Ballif, S. W. Glunz, and W. Warta, "Carrier density and lifetime imaging of silicon wafers by infrared lock-in thermography," in *Proceedings of the 17th European Photovoltaic Solar Energy Conference*, pp. 1597–1599, WIP, Munich, Germany, October 2001.
- [11] P. Pohl, J. Schmidt, K. Bothe, and R. Brendel, "Mapping of trap densities and energy levels in semiconductors using a lock-in infrared camera technique," *Applied Physics Letters*, vol. 87, no. 14, Article ID 142104, 3 pages, 2005.
- [12] W. Shockley and W. T. Read Jr., "Statistics of the recombinations of holes and electrons," *Physical Review*, vol. 87, no. 5, pp. 835–842, 1952.
- [13] R. N. Hall, "Electron-hole recombination in germanium," *Physical Review*, vol. 87, no. 2, p. 387, 1952.
- [14] J. Schmidt and R. A. Sinton, "Defect characterization by temperature and injection-dependent lifetime spectroscopy," in *Proceedings of the 3rd World Conference on Photovoltaic Energy Conversion (WCPEC '03)*, pp. 947–950, Osaka, Japan, May 2003.
- [15] J. Schmidt, P. Pohl, K. Bothe, C. Schmiga, R. Krain, and R. Brendel, "Advanced defect characterisation techniques in crystalline silicon-based photovoltaics," in *Proceedings of the 21st European Photovoltaic Solar Energy Conference*, pp. 524–529, WIP, Dresden, Germany, September 2006.
- [16] T. Lauinger, J. Schmidt, A. G. Aberle, and R. Hezel, "Record low surface recombination velocities on  $1\ \Omega\ \text{cm}$   $p$ -silicon using remote plasma silicon nitride passivation," *Applied Physics Letters*, vol. 68, no. 9, pp. 1232–1234, 1996.
- [17] K. Graff, *Metal Impurities in Silicon-Device Fabrication*, Springer, Berlin, Germany, 2nd edition, 2000.
- [18] S. Diez, S. Rein, and S. W. Glunz, "Analyzing defects in silicon by temperature- and injection-dependent lifetime spectroscopy (T-IDLS)," in *Proceedings of the 20th European Photovoltaic Solar Energy Conference*, pp. 1216–1219, WIP, Barcelona, Spain, June 2005.
- [19] S. W. Glunz and W. Warta, "High-resolution lifetime mapping using modulated free-carrier absorption," *Journal of Applied Physics*, vol. 77, no. 7, pp. 3243–3247, 1995.
- [20] O. Breitenstein and M. Langenkamp, *Lock-in Thermography*, Springer, Berlin, Germany, 2003.
- [21] J. Isenberg and W. Warta, "Spatially resolved evaluation of power losses in industrial solar cells by illuminated lock-in thermography," *Progress in Photovoltaics: Research and Applications*, vol. 12, no. 5, pp. 339–353, 2004.
- [22] T. Trupke, R. A. Bardos, M. C. Schubert, and W. Warta, "Photoluminescence imaging of silicon wafers," *Applied Physics Letters*, vol. 89, no. 4, Article ID 044107, 3 pages, 2006.
- [23] P. Pohl and R. Brendel, "Temperature dependent infrared camera lifetime mapping (ILM)," in *Proceedings of the 19th European Photovoltaic Solar Energy Conference*, pp. 46–49, WIP, Paris, France, June 2004.
- [24] P. Pohl, J. Schmidt, C. Schmiga, and R. Brendel, "Defect imaging in multicrystalline silicon using a lock-in infrared camera technique," *Journal of Applied Physics*, vol. 101, no. 7, Article ID 073701, 11 pages, 2007.
- [25] D. K. Schroder, R. N. Thomas, and J. C. Swartz, "Free carrier absorption in silicon," *IEEE Transactions on Electron Devices*, vol. 25, no. 2, pp. 254–261, 1978.
- [26] R. Bube, *Photoelectronic Properties of Semiconductors*, Cambridge University Press, Cambridge, UK, 1992.
- [27] D. Macdonald and A. Cuevas, "Trapping of minority carriers in multicrystalline silicon," *Applied Physics Letters*, vol. 74, no. 12, pp. 1710–1712, 1999.
- [28] J. Schmidt, K. Bothe, and R. Hezel, "Oxygen-related minority-carrier trapping centers in  $p$ -type Czochralski silicon," *Applied Physics Letters*, vol. 80, no. 23, pp. 4395–4397, 2002.
- [29] J. A. Hornbeck and J. R. Haynes, "Trapping of minority carriers in silicon—I.  $p$ -type silicon," *Physical Review*, vol. 97, no. 2, pp. 311–321, 1955.
- [30] W. Warta, "Advanced defect and impurity diagnostics in silicon based on carrier lifetime measurements," *Physica Status Solidi (A)*, vol. 203, no. 4, pp. 732–746, 2006.
- [31] P. Pohl, J. Schmidt, K. Bothe, and R. Brendel, "Trap density imaging of silicon wafers using a lock-in infrared camera technique," in *Proceedings of the 4th IEEE World Conference on Photovoltaic Energy Conversion*, vol. 1, pp. 932–935, Waikoloa, Hawaii, USA, May 2006.
- [32] W. C. Dash, "Copper precipitation on dislocations in silicon," *Journal of Applied Physics*, vol. 27, no. 10, pp. 1193–1195, 1956.
- [33] M. Schubert, S. Riepe, and W. Warta, "Spatially resolved trapping detection and correlation with material quality in multicrystalline silicon," in *Proceedings of the 21st European Photovoltaic Solar Energy Conference*, pp. 629–633, WIP, Dresden, Germany, September 2006.

## Review Article

# Silicon Thin-Film Solar Cells

**Guy Beaucarne**

*IMEC vzw., Solar Cells Technology Group, Kapeldreef 75, 3001 Leuven, Belgium*

Received 31 May 2007; Accepted 26 August 2007

Recommended by Armin G. Aberle

We review the field of thin-film silicon solar cells with an active layer thickness of a few micrometers. These technologies can potentially lead to low cost through lower material costs than conventional modules, but do not suffer from some critical drawbacks of other thin-film technologies, such as limited supply of basic materials or toxicity of the components. Amorphous Si technology is the oldest and best established thin-film silicon technology. Amorphous silicon is deposited at low temperature with plasma-enhanced chemical vapor deposition (PECVD). In spite of the fundamental limitation of this material due to its disorder and metastability, the technology is now gaining industrial momentum thanks to the entry of equipment manufacturers with experience with large-area PECVD. Microcrystalline Si (also called nanocrystalline Si) is a material with crystallites in the nanometer range in an amorphous matrix, and which contains less defects than amorphous silicon. Its lower bandgap makes it particularly appropriate as active material for the bottom cell in tandem and triple junction devices. The combination of an amorphous silicon top cell and a microcrystalline bottom cell has yielded promising results, but much work is needed to implement it on large-area and to limit light-induced degradation. Finally thin-film polysilicon solar cells, with grain size in the micrometer range, has recently emerged as an alternative photovoltaic technology. The layers have a grain size ranging from 1  $\mu\text{m}$  to several tens of microns, and are formed at a temperature ranging from 600 to more than 1000°C. Solid Phase Crystallization has yielded the best results so far but there has recently been fast progress with seed layer approaches, particularly those using the aluminum-induced crystallization technique.

Copyright © 2007 Guy Beaucarne. This is an open access article distributed under the Creative Commons Attribution License, which permits unrestricted use, distribution, and reproduction in any medium, provided the original work is properly cited.

## 1. INTRODUCTION

Faced with the threat of global warming caused by fossil fuel consumption, humankind is looking for alternative forms of power production that lead to minimal CO<sub>2</sub> emission. Photovoltaics, the direct conversion from sunlight into electricity, promises to be a major energy technology in the future. Indeed, solar insolation is quite well distributed around the globe, and it is plentiful (although quite dilute) while photovoltaics converts solar irradiation directly into a high quality energy form with an efficiency ranging from 5 to 20%. This is much higher than most of the other energy technologies that convert (often very indirectly) solar energy into useful work.

For photovoltaic systems, to be applied on a massive scale, however, the cost of the technology has to be low, with a price per kWh, comparable to the retail price of conventional electricity. At present, the dominating photovoltaic technology is still based on the concept that led to the first practical solar cell in 1954, that is, the “bulk” or wafer-based crystalline silicon technology. Although the cost of bulk Si solar cells and modules has decreased steadily over the last decades, through better material use and improved solar cell

performance, the trend will not continue indefinitely. The process of wafering, that is, sawing slices out of a large Si ingot or brick leads to a fundamental limitation in terms of material usage. Even if wire sawing is improved drastically, it is unlikely that an Si consumption per wafer (wafer thickness + kerf loss), much less than 250  $\mu\text{m}$ , can be obtained (today, this value is typically 400  $\mu\text{m}$ ). This is a relatively large amount of a costly material prepared with a very high energy input, which is, however, not necessary for high efficiency. Indeed, the theory states that high solar cell performance can be achieved even with a very thin Si layer if optical confinement is applied [1]. As a result of the limited potential for decrease in material use, and of the expected saturation in module performance as the theoretical limit is approached, the learning curve is foreseen to slow down and the cost to eventually saturate at a given value in the order of 1 \$/Wp at module level.

Thin-film approaches aim to reach low cost by starting with a low-cost (or potentially low-cost) material system; a thin layer of semiconductor is deposited on a low-cost substrate. If high efficiency and reliability is indeed achieved, thin-film solar cell technologies could reach substantially

lower costs, 0.5 \$/Wp and even below. Although thin-film solar cells have been announced for a long time as the next best thing, they have not yet had a breakthrough. The development of these technologies has in fact been rather slow, not faster than the bulk Si technology which, however, started much earlier. Recently, because of the Si feedstock shortage, the thin-film technologies have received new momentum. Because of the limited possibility to invest in conventional Si technology due to the shortage, substantial investment capital has flown into thin-film initiatives and led to the creation of many new companies.

This article covers several thin-film technologies that use Si for the active material. Sticking to Si instead of other semiconductors presents a number of advantages. Si is nontoxic, which makes it easily accepted by the public. Moreover, Si is abundantly available in the earth crust, so that its availability (at least in its raw form) will never be an issue. Finally, Si solar cell technologies can build further upon the extensive know-how accumulated over the years in the IC industry (for crystalline Si) and the display industry (for amorphous and microcrystalline Si).

The term “thin-film crystalline Si” is in fact quite broad. It covers a wide range of technologies, from amorphous Si to monocrystalline lift-off Si solar cells. In this article, I will limit myself to the thin-film Si technologies that use only 0.1 to 5  $\mu\text{m}$  of Si. Those are amorphous Si, microcrystalline Si, and thin-film polysilicon solar cells. This article intends to give a concise overview, but excellent in-depths reviews for each of these technologies can be found in recently published books on thin-film solar cells [2, 3]. Another review paper with a similar scope to the present article but even shorter can be found in a recent issue of the MRS bulletin [4].

## 2. SINGLE JUNCTION AMORPHOUS Si SOLAR CELLS

### 2.1. Material

Amorphous Si is usually deposited using the plasma-enhanced chemical vapour deposition (PECVD) technique, and the gas silane ( $\text{SiH}_4$ ) is mostly used as precursor. As a result of decomposition, surface adsorption and surface reactions, a network of Si atoms is formed on the substrate, mostly glass or a metal foil. The deposition temperature ranges typically between 180°C and 280°C. As a result of the deposition mechanism, amorphous silicon contains a large concentration of hydrogen atoms ( $\sim 10\%$ ). Hydrogen is, in fact, crucial for the material’s electronic properties, while unhydrogenated amorphous Si is of no use for devices. Therefore, the material one usually refers to using the words “amorphous silicon” is in fact hydrogenated amorphous silicon (a-Si:H).

Amorphous Si is a material that features short-range order but lacks long-range order. As in crystalline Si, each Si atom is mostly fourfold coordinated, but the bond lengths and angles between the bonds show a wide variation. This structure has a strong impact on the electronic structure of the material. Because the structure is no longer periodic, the strict conservation of momentum does not hold. As a result, instead of the indirect bandgap of crystalline Si, it basically has a direct bandgap. The absorption coefficient in a-Si is,

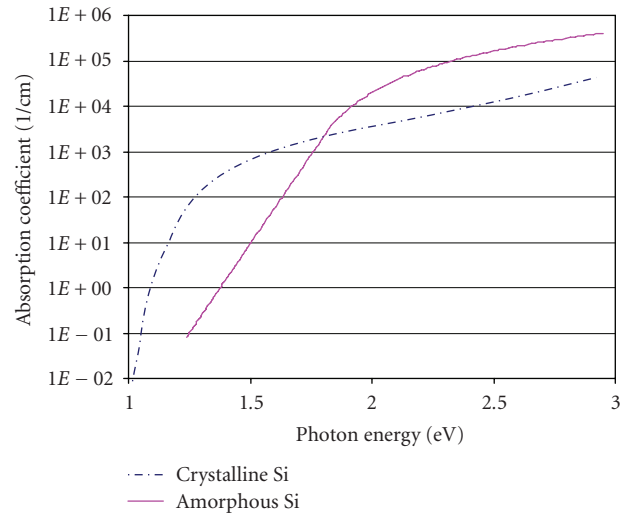


FIGURE 1: Absorption coefficient of a-Si:H versus photon energy, compared to crystalline Si.

therefore, much higher than that in crystalline Si, and, therefore, a much lower thickness is required to achieve the same absorption. However, the bandgap is also larger, 1.7 to 1.9 eV. Therefore, a large part of the infrared light cannot be absorbed in amorphous Si (Figure 1). Alloys can be deposited by adding germanium (to form a-SiGe:H) or carbon (to form a-SiC:H) precursors to the gas flow, so that the bandgap can be tuned to some extent.

In 1975, it was reported for the first time that hydrogenated amorphous Si behaved as a semiconductor, and that it was possible to vary its conductivity over many orders of magnitude by adding doping atoms [5]. Combined with the strikingly low defect concentrations that were measured (down to  $10^{15} \text{ cm}^{-3}$ ), this made the material extremely attractive for solar cells. The first amorphous Si solar cell followed soon, in 1976 [6]. Although the efficiency at the time was below 3%, it generated enormous interest and started a large research effort worldwide. Fast progress was reached in the end of the seventies and the beginning of the eighties, and, for some time, it looked like the days of crystalline Si would soon be over and that amorphous Si was going to conquer the whole PV scene. However, an important problem with amorphous Si was also identified. The new material turned out to suffer from degradation upon exposure to sunlight [7]. This phenomenon, called the Staebler-Wronski effect, causes a large increase in defect density (strong decrease in excess carrier lifetime), and is reversible upon annealing at temperatures above 150°C. From values between  $10^{15}$  and  $10^{16} \text{ cm}^{-3}$  in annealed state, defect densities increase to  $\sim 2 \times 10^{17} \text{ cm}^{-3}$  in light-soaked state. The metastable defects are believed to be dangling bonds formed by breaking weak bonds in the random network. The defect densities mentioned are valid for intrinsic amorphous Si. Doped amorphous Si, obtained by adding diborane to the gas flow for p-type material and phosphine for n-type, contains much more defect than intrinsic a-Si:H (several orders of magnitude

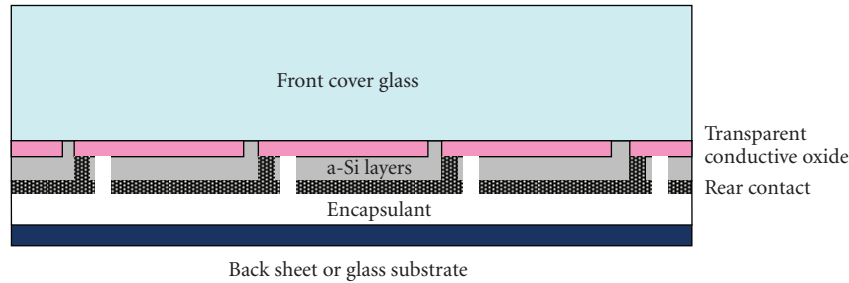


FIGURE 2: Monolithic module concept for amorphous silicon modules in superstrate configuration.

higher). Therefore, only intrinsic a-Si:H can be used as an absorber material.

Charge carrier mobility in amorphous Si is much lower than in crystalline Si. A good a-Si:H layer will show an electron mobility of around  $20 \text{ cm}^2/\text{Vs}$  at best. As a result, amorphous Si layers cannot conduct charge carriers laterally over a large distance.

The key parameters for amorphous Si are its dark conductivity, photoconductivity, and its mobility lifetime product. The conductivity of intrinsic a-Si:H in the dark is extremely low ( $< 10^{-10} \text{ S/cm}$ ) because of the low mobility, the large bandgap, and the fact that charge carriers at low concentration are trapped at defects. Under illumination, however, many of the defects get filled with photogenerated carriers and are saturated. As a result, many more charge carriers are available for charge transport, and the conductivity is many orders of magnitude higher than that in the dark. The photoresponse, defined as the ratio of the illuminated conductivity to the dark conductivity, is a good indication for the suitability of the material for devices, and should be larger than  $10^5$ . The mobility lifetime ( $\mu\tau$ ) product is the crucial parameter for the transport properties of excess charge carriers in the layer, and in device grade, amorphous Si is larger than  $10^{-7} \text{ cm}^2/\text{V}$ .

## 2.2. Solar cell and module technology

As a result of the low carrier mobility and low lifetime, collection cannot take place through diffusion. A strong drift field is an absolute requirement. This is achieved by sandwiching the intrinsic absorber layer between doped layers with opposite doping. As most of the generation takes place close to the top surface and the hole mobility is much lower than electron mobility, the device structure always features a p-doped layer on top (a side through which light enters the amorphous Si layer), while the bottom layer is n-doped. Indeed, in this way, most of the holes are generated close to the p-layer where they are majority carriers and no longer can recombine. Holes generated deeper in the layer have a higher probability of recombining and, therefore, a lower collection probability. In contrast, electrons have a high collection probability throughout the i-layer. Due to the very low lifetime in doped layers, all light absorbed in the p-layer is lost for conversion. To minimize this effect, not only the p-layer

is kept very thin ( $\sim 10 \text{ nm}$ ), but C can also be added so that the bandgap increases and the absorption decreases. The p-type layer, therefore, usually consists of a-SiC:H and is called the window layer.

The intrinsic layer thickness has to be chosen based on the  $\mu\tau$  product after light-soaking. If the layer is too thick, there will be large collection losses because holes generated deep in the layer recombine before being collected. If the layer is thin, the distance to be covered to be collected is shorter, and the electric field is stronger. Both effects have a very beneficial impact on carrier collection. However, a thin layer implies that a large fraction of the light does not get absorbed, but are lost through transmission or escape reflection. There is, therefore, an optimal thickness, which turns out to be around  $300 \text{ nm}$ . This low thickness is a clear advantage for manufacturing, as one of the most significant costs in amorphous silicon modules is the deposition cost. The drawback is that efficiencies are usually quite low and difficult to increase. It also explains why light trapping is an important topic in amorphous Si solar cell research, even though the material features high absorption coefficients.

Most types of amorphous silicon solar cells are in superstrate configuration, which means that the light enters the solar cell through the supporting substrate. This configuration requires a highly transparent substrate material and the presence of a transparent conductive oxide between the substrate and the active layer. These cells are also called “p-i-n” solar cells, referring to the sequence in which the different layers are deposited. The other option is to make a-Si:H cells in substrate configuration (“n-i-p” solar cells), which enables the use of a wider range of substrate materials.

After deposition of the different layers, the cells have to be isolated and interconnected with each other. Typically this is done using a combination of laser scribing and blanket deposition (transparent conductive oxide, the amorphous Si layers, and metal—combined or not with TCO—for the rear contact) in a monolithic module concept (Figure 2).

## 2.3. Industrial application

Over the years, many companies have been created to produce single junction a-Si:H modules. Generally, the modules are based on the monolithic concept shown in Figure 2, and have an efficiency ranging from 5 to 7%. Although many of

these companies stopped, a number of them have survived and grown over the years. Among those companies, the one with presently the largest production is Kaneka.

One of the problems encountered when producing amorphous silicon modules is the lack of reliable deposition equipment, with good uniformity, high up-time, and not requiring only moderate maintenance. This is because the deposition systems used are often specifically developed, sometime in-house, and have been produced only in small volumes. This situation has recently completely changed. Large companies that were so far involved in equipment manufacturing for LCD displays have entered the photovoltaic business. Their PECVD systems for amorphous Si deposition for displays are excellent platforms to develop equipment for amorphous silicon solar modules. Indeed, most of the issues concerning uniformity, cleaning, reliability, and so forth have already been solved, and they can concentrate on reaching the required material quality and production speed for solar cells. These companies are Unaxis (now Oerlikon Solar) and Applied Materials. They have hired experts in amorphous and microcrystalline deposition for solar cells, and are working to offer complete processes to the clients purchasing their systems. They are presently rapidly introducing their deposition systems into the photovoltaic market, or even complete production lines revolving around the deposition systems. In the last years, there have been many announcements of new large scale production lines based on such systems (e.g., Brilliant 234, Ersol thin-film, and Moser Baer), which should come on-line within two years.

Although all new players have plans to move to multi-junction solar cells at some point, they start with single junction amorphous modules, for which it is easier to reach the short-term cost targets. However, it is generally recognized that this technology can only be an intermediate step towards a technology with higher-efficiency potential.

#### 2.4. Outdoor performance of amorphous Si modules

The temperature coefficient of amorphous silicon solar cells is lower (in absolute value) than that of a crystalline Si. As a result, the modules do not lose so much in performance (relatively) when heated up. Moreover, amorphous Si modules have a good sensitivity to blue light, which is more present in diffuse illumination. Finally, the module efficiency under very low illumination is quite well maintained in contrast to standard crystalline Si modules, for which the performance collapses. As a result, the relative performance of single junction amorphous Si modules, expressed in kWh/kWp per year, which takes into account all the different conditions under which a PV module has to operate in a year, tends to be rather good for a-Si modules, better than that of conventional crystalline Si modules.

The long-term stability of amorphous Si modules is not necessarily granted. The producers have to pay special attention to the design of the modules, particularly to the type of transparent conductive oxide and to the encapsulation selected. Unfortunately, some poor quality products in the past gave amorphous Si a bad name, and there is a need to rectify this image.

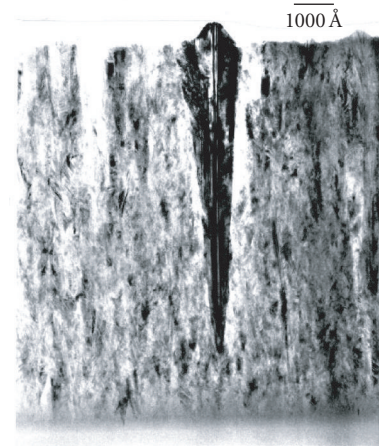


FIGURE 3: Cross-section TEM image of a microcrystalline Si layer. (Reproduced with permission from [8].)

### 3. MICROCRYSTALLINE Si SOLAR CELLS

#### 3.1. Material

Microcrystalline is a mixed phase material, containing a crystalline Si fraction and an amorphous Si fraction. The crystallites are generally only a few nanometers to a few tens of nanometers in diameters, and are present in “bunches” or “conglomerates” in the layers. These conglomerates are much larger than the crystallites themselves, up to a micron or even larger. Because the crystallites are in the nanometer range, microcrystalline Si is often referred to as “nanocrystalline Si”. The two names are nowadays used interchangeably. Like amorphous silicon, microcrystalline Si contains a lot of hydrogen (several percents), which is incorporated in situ during deposition and ensures passivation of most defects in the layers. The term “microcrystalline Si” covers, in fact, a whole range of materials, ranging from amorphous silicon with a few percents of crystalline phase to a material with only a few percents of amorphous silicon. The properties of the materials at the two extremes are quite different, and one has to pay attention not to generalize properties that are, in fact, only valid for a limited range of crystallinity. In practice, the best devices are obtained with material close to the edge between microcrystalline and amorphous Si, so most recent papers refer to this type of material, which contains a large amorphous fraction. An example of a microcrystalline layer is shown in Figure 3.

Like amorphous Si, microcrystalline Si is typically obtained by PECVD at low temperature (between 100 and 300°C). Usually, a large hydrogen flow is added, which results in microcrystalline Si instead of amorphous Si (“hydrogen dilution”). Hydrogenated microcrystalline Si was first prepared in 1968 [9], but the use of PECVD to deposit such layers was introduced in 1980 [10, 11]. The material was first used as an active layer for solar cells in 1994 by the IMT group at the University of Neuchâtel in Switzerland [12]. The deposition technique they developed was very high frequency (VHF) PECVD of microcrystalline Si. The very high

frequency (between 30 and 300 MHz) leads to a softer ion bombardment, which is more favorable to microcrystalline Si formation, and, at the same time, allows relatively high growth rates. It is, however, possible to obtain excellent results using the standard RF PECVD technique at 13.56 MHz, provided the right parameters in terms of pressure and gas flow are selected. The conditions used are the so-called “high pressure depletion” (HPD) conditions, where the relatively high pressure ( $\sim 10$  Torr) ensures that ions lose a lot of their energy before reaching the surface. It is important to ensure a high hydrogen content in the plasma in HPD regime, which is usually obtained by a high hydrogen flow, but can also be achieved with pure  $\text{SiH}_4$  by preconditioning the chamber [13]. The combination of Very High Frequency and HPD conditions has led to excellent solar cells [14], sometimes at relatively high-growth rates [15]. As the growth rate (as will be discussed later) is a crucial topic for industrial implementation, a lot of effort is put into developing deposition conditions that yield high growth rates (over 2.3 nm/min, to be compared to values below 0.5 nm/min for conventional conditions) with only slightly lower efficiency [16, 17]. Other alternatives to deposit microcrystalline silicon are hot wire deposition and microwave plasma depositions though the results obtained so far are well below the more standard techniques for microcrystalline deposition.

An important aspect for all deposition techniques is the need to control the crystallinity profile of the microcrystalline layer throughout the active layer. As the material is formed through nucleation from an initial amorphous Si layer after which the crystallites grow, the crystallinity is not constant throughout the layer if no attempt is made to control it, which may result in far from optimal layers. Therefore, research in microcrystalline Si deposition puts a lot of effort into crystallinity control during deposition through varying the deposition parameters.

The bandgap of microcrystalline Si depends on the fraction of amorphous Si in the material. Layers with a substantial crystalline fraction have a bandgap close to that of crystalline Si (1.1 eV). The apparent higher absorption for such microcrystalline layers compared to single crystalline Si has been demonstrated to be caused by light scattering at the layer surfaces [18]. The absorption below the bandgap is much higher than that for crystalline Si, and is caused by defects within the bandgap. The absorption coefficient at those long wavelengths, therefore, gives a measure for the layer quality. It can be measured in different ways, but a powerful measurement technique that is increasingly being used is the Fourier transform photocurrent spectroscopy (FTPS) [19]. In Figure 5, the absorption coefficients at 0.8 eV of different layers are plotted as a function of the measured crystallinity [20]. The lowest  $\alpha$  (corresponding to the lowest defect density) is found in the transition region.

Figure 4 also gives important insight in layer quality degradation in microcrystalline silicon. When the first microcrystalline silicon solar cells were demonstrated, tests on devices with relatively high crystallinity led to the conclusion that microcrystalline Si did not suffer from light-induced degradation. As better devices closer to the transition were made and more detailed degradation studies were carried

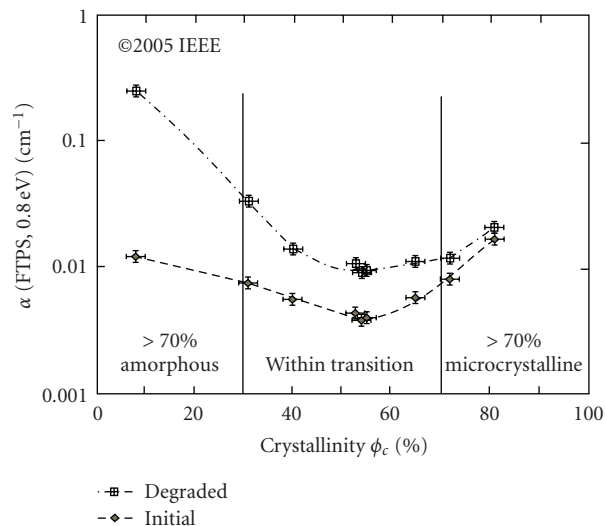


FIGURE 4: Defect-related absorption in initial and degraded state for a series of p-i-n type single-junction microcrystalline silicon solar cells with varying Raman crystallinity of the i-layer. (Reproduced with permission from [20].)

out, a more subtle picture has emerged: microcrystalline silicon suffers from a mild form of the photo-induced degradation [20, 21]. The degraded values (after 1000 hours under standard illumination) in Figure 4 show that, as expected, the degradation is worst for fully amorphous silicon, while it is negligible for almost fully crystalline layers. For microcrystalline layers in the transition region, there is a small yet significant degradation. There is, however, no degradation at all if the high energy photons are filtered out [22], as is the case in tandem solar cells.

### 3.2. Solar cell technology

The device structure of microcrystalline Si solar cells is very similar to that of amorphous Si solar cells. As with amorphous silicon, both superstrate (pin) and substrate (nip) configurations are possible. Most cells are pin cells, which requires a transparent substrate, usually soda-lime glass. To provide the top electrode, a conductive oxide is deposited, either indium tin oxide (ITO), tin oxide ( $\text{SnO}_2$ ), or zinc oxide (ZnO). ITO is highly transparent and conductive but it is not very stable in the presence of a silane plasma, and it is relatively expensive. Therefore, solutions based on  $\text{SnO}_2$  or ZnO are preferred.

The optimal thickness of the i-layer is much larger than that for amorphous Si cells, from 1 to 2  $\mu\text{m}$ . This is related with the weaker absorption by the amorphous Si and the higher  $\mu\tau$  product. In order to reach high efficiencies, the TCO is usually textured. This is either obtained as the natural morphology induced by the TCO deposition, or by subsequent etching.

It is difficult to say which group holds the record for single junction microcrystalline cells because of the issue of degradation and the fact that laboratory cells are very small, limiting the accuracy of the short-circuit values, particularly

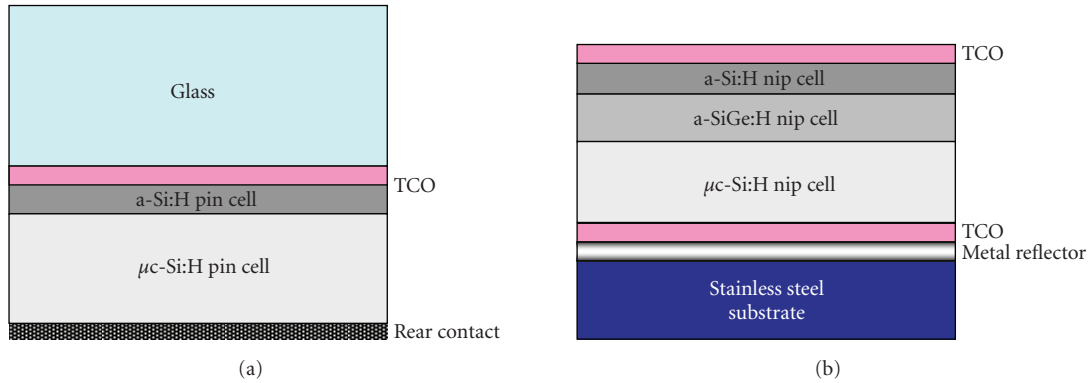


FIGURE 5: Schematic drawing of two types of tandem thin-film Si solar cells: (a) a “micromorph” or “hybrid” a-Si:H/ $\mu$ m-Si:H tandem cell, (b) a triple junction a-Si/a-SiGe:H/ $\mu$ c-Si:H solar cell.

for cells in superstrate configuration. It is, however, generally valid to say that the best solar cells have an efficiency value around 10% [14, 23, 24].

### 3.3. Issues with industrial application

The main issue for industrial application of microcrystalline silicon cells is the relatively low growth rate when a high hydrogen dilution condition is used, combined with the relatively large thickness of the layer. If the deposition time is too long, the throughput of the deposition system will be low, and the investment cost per module produced will be accordingly too high. That is why there are intense efforts to increase the deposition rate of microcrystalline Si deposition. The high pressure depletion regime combined with VHF excitation gives a good hope to reach a sufficient deposition rate while maintaining material quality, but it is a challenge to achieve sufficient uniformity on large areas in such conditions.

## 4. MULTIJUNCTION THIN-FILM Si SOLAR CELLS

Multijunction thin-film silicon solar cells consist in stacking two (tandem) or even three (triple) junction structures on top of each other, the different subcells being connected in series. This concept has the potential to increase device performance well beyond that of single junction devices, particularly when the materials are selected so as to better exploit the solar spectrum. Indeed, if a high bandgap material is used for the top cell, less thermalization losses will occur as a result of absorption of high energy photons. The longer wavelength photons, which are not absorbed in the top cell, get absorbed in the bottom cell which consists of a lower bandgap material. The fraction of unused photons from the spectrum is lower for tandem cells as the cut-off wavelength is given by the optical bandgap of the lowest bandgap material.

There are different types of multijunction thin-film Si solar cells, depending on the chosen configuration and layer type. In Figure 5, we show two structures of a particular interest.

The structure in Figure 5(a) is that of a “micromorph” solar cell, also called “hybrid” solar cell. It is a device in superstrate configuration, with an amorphous silicon top cell and a microcrystalline Si bottom cell. The substrate is a TCO covered glass substrate. This combination was first proposed by IMT [25] and is now regarded as one of the most promising concepts for thin-film solar modules.

In Figure 5(b), a triple junction solar cell in substrate configuration is depicted with an amorphous Si top cell, an amorphous SiGe middle cell, and a microcrystalline Si bottom cell. Because the p-layer always has to be on the side where light enters the cell, the subcells are all of the nip type. There is a large freedom concerning the substrate because it needs neither to be transparent nor to act as a front cover. A popular choice is a stainless steel foil, which is inexpensive and flexible, and which withstands, relatively, high temperatures. A drawback is that it is conductive and is, therefore, ill-suited for a monolithic module concept. The substrate is usually covered by a metal layer with high reflection, such as a silver layer. The United Solar Company, one of the major thin-film solar cells companies, is well known for its triple junction cells. Until recently, the middle and bottom cells were based on a-SiGe:H with two different Ge concentrations, but they have introduced new structures like the one in Figure 5(b), and even with microcrystalline Si in both the middle and bottom cells [26].

To connect the cells in series, good tunnel junctions are required, which demands a good control of the doping level of the doped layers. Another crucial aspect is current matching. One has to ensure that all subcells have about the same short-circuit current density; otherwise, the subcells will operate far from their maximum power points, leading to large losses. In the subcell optimization, one has to take light-induced degradation of the top cell into account. Indeed, the currents have to match after light-soaking, unless one only aims at a top initial efficiency. Figure 6 shows the internal quantum efficiency curves of the different subcells of a triple junction a-Si:H/a-SiGe:H/ $\mu$ c-Si:H cell.

In order to reduce losses in dual junction cells, caused by the degradation of the top cell, it has been proposed to

introduce an intermediate reflector, typically a TCO layer, and to further reduce the thickness of the top cell. Very thin amorphous Si cells show extremely limited degradation, but their current is very low due to limited absorption. By introducing an intermediate reflector, the current can be maintained at a high value, enabling high efficiencies with minimal degradation. The process complexity is increased, but promising efficiencies have been achieved with this concept [27, 28].

Efficiencies of tandem thin-film solar cells on small area devices reach impressive values of around 15% initial [26, 28] and around 13% stabilized. However, research and development is now focusing on upscaling the processes to large areas, producing minimodules and modules, and solving issues for industrial application, notably large-area TCO deposition. In Table 1, we list the best results of large-area tandem devices reported so far.

A specific issue with tandem cells is the risk of increased spectral sensitivity and its impact on the module energy yield. Indeed, losses related to current mismatch can be exacerbated by natural changes in spectrum (related to different times of the day or different seasons) because the relative absorption in the subcells may change. It has been found that, indeed, multijunction cells are more spectrally sensitive than classical modules [33]. If the module is well designed, however, it reaches its optimal energy yield for the most relevant spectra. High relative performance in kWh/kWp/year has been reported for double and even triple junction modules [34, 35].

## 5. THIN-FILM POLYCRYSTALLINE SI SOLAR CELLS

As we have seen, microcrystalline Si was introduced to improve solar cell performance and enhance stability of thin-film silicon solar cells. The development of thin-film polycrystalline silicon (polysilicon) for solar cells can be seen as the continuation of this trend towards higher crystallinity. Thin-film polysilicon is a material with grain size in the range  $1\ \mu\text{m}$  to  $1\ \text{mm}$ . In contrast to microcrystalline silicon, this material does not contain any amorphous tissue, or only a very small amount (well below 1%). One could think that the border between microcrystalline and polycrystalline silicon is not very sharp. In practice, there is a very clear distinction between the two materials because polysilicon is very far from the amorphous-to-crystalline transition, and always involves much higher temperatures than those used for microcrystalline silicon. Thin-film polysilicon solar cells have active layers that are usually thinner than  $5\ \mu\text{m}$ , often about only  $2\ \mu\text{m}$ . The technology is more recent and less mature than amorphous and microcrystalline Si, but progress in the last few years has been very fast.

### 5.1. Material

Thin-film polysilicon layers can be formed in various ways, which, however, all have in common that relatively high temperatures (between  $400$  and  $1200^\circ\text{C}$ ) are used. The films formed at moderate temperature usually undergo a short treatment at high temperature (between  $900$  and  $1000^\circ\text{C}$ )

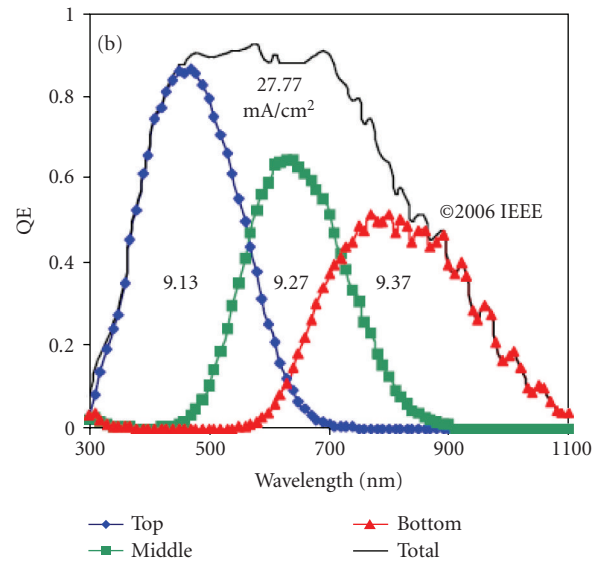


FIGURE 6: Quantum efficiency of an a-Si:H/a-SiGe:H/ $\mu\text{c}$ -Si:H triple-junction solar cell. (Reproduced with permission from [26].)

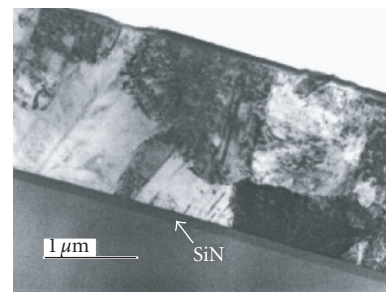


FIGURE 7: Cross-sectional transmission electron image of an SPC polysilicon film made on planar SiN-coated glass. (Figure reproduced with permission from [36].)

[36] to remove crystallographic defects, ensure full crystallinity, and enhance dopant activation. As a result, the very low-cost substrates used for microcrystalline and amorphous Si, such as soda-lime glass and polymer foils, cannot be used. Instead, borosilicate or aluminosilicate glass is used, or, if longer treatments at high temperature are needed, ceramic or glass-ceramic substrates.

The most successful film formation technique so far is solid phase crystallization (SPC) of amorphous silicon [37–39]. After deposition (by PECVD or evaporation), the a-Si films, typically  $1$  to  $3\ \mu\text{m}$  thick, are annealed at temperatures between  $550$  and  $700^\circ\text{C}$ , for a period of time ranging from a few hours to several tens of hours. The higher the temperature, the faster full crystallization will be reached, but the smaller the grains will be. If the temperature is too low, full crystallization is not reached within a reasonable time. The compromise temperature is usually  $600^\circ\text{C}$ . The doping profile is created during amorphous Si deposition, and is maintained during the crystallization process. The average

TABLE 1: Overview of the best results of tandem thin-film Si modules or minimodules.

Device structure	Company/institute	Area (cm <sup>2</sup> )	Initial efficiency (%)	Stabilized efficiency (%)	Reference
Double junction in superstrate configuration: a-Si:H/intermediate reflector/ $\mu$ c-Si:H (“Hybrid Plus”)	Kaneka	4140	13.5	?	[28]
Double junction in superstrate configuration: a-Si:H/ $\mu$ c-Si:H	IPV Jülich	64	10.8	10.1	[29]
Double junction in substrate configuration: a-Si:H/ $\mu$ c-Si:H (one single laminated cell)	United Solar	420	11.8	9.5	[30]
Double junction in superstrate configuration: a-Si:H/ $\mu$ c-Si:H	Applied Materials	676	10.1	?	[31]
Double junction in superstrate configuration: a-Si:H/ $\mu$ c-Si:H	Oerlikon Solar	64	10.0	?	[32]

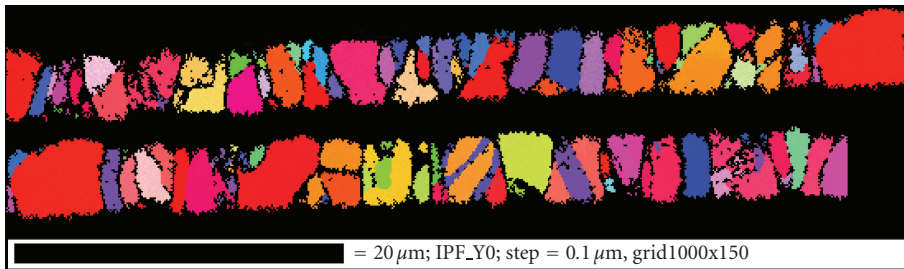


FIGURE 8: Cross-section electron backscatter diffraction image of an epitaxially thickened poly-Si AIC layer on a glass-ceramic substrate. The AIC layer is situated at the bottom but cannot be distinguished from the epitaxial layer. The scan of 100  $\mu$ m length is cut in two. The top right grain is the same as the bottom left one. (Reprinted with permission from [49].)

grain size of device grade SPC polysilicon is 1 to 2  $\mu$ m (see Figure 7). The material contains a large density of intragrain defects and many horizontal grain boundaries. Devices made in as-deposited material show extremely poor performance. However, SPC polysilicon responds particularly well to a defect anneal by rapid thermal treatment after crystallization [36].

Although SPC is a slow process, suitable throughput can be achieved in industrial conditions by using large batches. The cycle time, however, remains rather long. Polysilicon films can be formed faster by direct silicon deposition on foreign substrates [40–42], but coarse-grained continuous layers deposited in this way are never very thin.

In an effort to create thin layers with high crystallographic quality, the research focus has shifted in recent years to seed layer approaches. In a seed layer approach, a thin continuous layer with large grains is first formed. This seed layer shows good crystallographic quality but is either too thin or too highly doped, or both, to be used as an active layer in a solar cell. In the second phase, an epitaxial deposition process is applied. The main techniques to form seed layers are laser crystallization and aluminium-induced crystallization (AIC). Laser crystallization makes use of laser-light pulses to melt the silicon locally, inducing crystallization. Aluminium-

induced crystallization involves the transformation of amorphous to polycrystalline Si during thermal annealing of an a-Si/Al layer stack [43]. For the epitaxy, conventional thermal chemical vapor deposition (CVD) taking place at typically 1100°C can be used [44], but several low-temperature epitaxy techniques are also investigated, such as ion-assisted deposition (IAD) [45] and ECR-CVD [46, 47]. An example of an active layer grown by a combination of AIC and CVD on glass-ceramic is shown in Figure 8. In spite of the larger grain sizes achieved, the seed layer approach has not yet matched the SPC results (see cell results later in the text). The reason for the much more modest increase in performance than expected, based on the grain size, appears to be a very large density of electrically active intragrain defects [48]. It is, therefore, crucial to improve the intragrain quality to achieve the efficiency potential of the seed layer approach.

Thin-film polysilicon contains many defects compared to multicrystalline Si. In contrast to microcrystalline Si, in situ defect passivation by hydrogen atoms cannot take place because of the high temperatures during film formation, which causes hydrogen to diffuse out of the film. A separate, subsequent defect passivation step by hydrogenation is, therefore, carried out to obtain device quality layers [45, 50, 51]. This is typically done in a hydrogen plasma at a temperature of

TABLE 2: Best thin-film polysilicon solar cell results (unless mentioned, the cell size is 1 cm<sup>2</sup> or less). LLC stands for layer-by-layer crystallization, RTA for rapid thermal anneal, ECRCVD for electron cyclotron resonance chemical vapor deposition.

Institute/company	Substrate	Technique	V <sub>oc,max</sub> (mV)	Eff. <sub>max</sub> (%)
CSG Solar	Borosilicate glass	SPC + RTA	497 [51]	9.8 [57] (96 cm <sup>2</sup> )
Sanyo 1995 [37]	Metal	SPC	553	9.2
IMEC [58]	Ceramic	AIC + CVD	534	8.0
UNSW	Borosilicate glass	SPC + RTA	517 [59]	7.0 [55] (4.4 cm <sup>2</sup> )
IMEC [60]	High-T glass	AIC + CVD	539	5.4
IPHT [61]	Borosilicate glass	Laser + LLC	510	4.8
InESS [41]	Ceramic	CVD	500	3.3
UNSW [62]	Borosilicate glass	AIC+ IAD ("ALICIA")	480	3.0
NAIST [42]	Ceramic	CVD	410	2-3
HMI [63]	Borosilicate glass	AIC + ECRCVD or e-beam evaporation	386	1.3

400°C although studies indicate that more effective passivation can be obtained at higher temperatures [45]. In general, the effect of hydrogenation is spectacular for thin-film polycrystalline cells. It is not uncommon to observe an increase of 200 mV or more in V<sub>oc</sub> as a result of hydrogenation.

## 5.2. Solar cell and technology

Thin-film polycrystalline cells do not have a p-i-n structure, but rather than p-n structure of conventional Si solar cells. Both p-type and n-type base devices have been demonstrated with no obvious advantage for one of the two. The base doping level ranges from 10<sup>15</sup> to 10<sup>17</sup> cm<sup>-3</sup>. A highly doped region is created at the back to act as a back-surface field (BSF) to provide a high conductivity path for a majority of carriers in the base. The total layer thickness is usually in the range of 1.5 to 3 μm. At the present stage of material development, the diffusion length is very short (a few micrometers at best). Increasing the device thickness beyond the diffusion length brings no benefit. On the contrary, it results in a lower V<sub>oc</sub> (solely determined by the diffusion length) and lower current (a lot of useless absorption in the area of the base which is further away than a diffusion length from the junction).

Both substrate and superstrate configurations have been implemented, the latter giving advantages in terms of lower shadow and resistive losses but making the device processing more challenging. Both homojunction and heterojunction designs are possible. Heterojunction devices consisting of a polycrystalline Si base with a very thin (~5–10 nm) amorphous Si emitter give rise to higher V<sub>oc</sub>s than homojunctions [37, 52]. There is evidence that this is related to the reduction of dopant smearing effects due to the lower thermal budget. Indeed, during high temperature steps, dopant atoms tend to diffuse along grain boundaries and dislocations, modifying the initial profile and increasing the junction area.

An important issue to obtain high efficiency devices is light confinement because the layers are thin and the material is not an efficient light absorber. A major component of any light trapping scheme is to ensure oblique coupling of the light into the active layer. The traditional methods used for crystalline silicon, namely, etching in dedicated alkaline

or acidic solutions to texture the surface, cannot be used because they are not adapted to polysilicon materials and consume too much Si. Texturing of the glass prior to active layer formation has been successfully applied for thin-film poly cells, either by coating with an oxide film containing small beads [53] (process used at CSG Solar) or by a chemical reaction with Al [54, 55]. Another possibility is to apply a plasma texturing process after active layer formation that consumes very little silicon while causing minimal damage to the active layer. A strong increase in performance of AIC-based cells has recently been achieved with this process [56].

The best results reported for thin-film polysilicon solar cells are given in Table 2. As can be seen in the table, the best thin-film polysilicon results, so far, have been achieved by CSG Solar, with an efficiency of 9.8%, using SPC of PECVD deposited amorphous silicon. This result is remarkable in many respects, not least because it is the efficiency of a 10 × 10 cm<sup>2</sup> minimodule, and not of a small single cell. This exceeds the efficiencies of the best single junction amorphous or microcrystalline Si minimodules, and is in fact comparable to the stabilized efficiency of state-of-the-art tandem amorphous-microcrystalline minimodules (see Table 1).

Module fabrication involves the separation of the film into long and narrow segments, usually by laser scribing: cell isolation using an insulating material, formation of openings to access the base and/or the emitter, and finally the cell metallization and interconnection using a metal grid usually carried out in a single metallization step. The positive contacts of each cell are connected, over the isolation grooves, to the negative contacts of the next cell. Note that, in contrast with amorphous and microcrystalline Si, the conductivity of the doped layers in polysilicon is high enough to ensure lateral transport of the collected carriers over hundreds of micrometers. Figure 9 shows the elegant interconnection scheme used at CSG Solar. Here, the whole rear surface is covered with the isolating material (a polymer-based resin), not only the groove. The contacts are made through holes in the resin. For the negative contacts, the silicon is etched locally to access the emitter. A blanket aluminium layer is then deposited and patterned with laser into an interdigitated pattern.

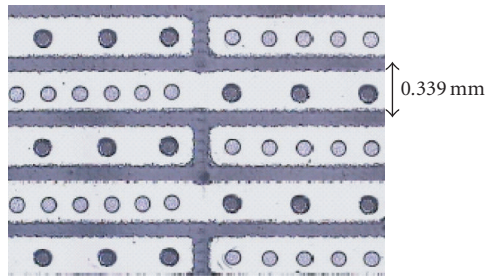


FIGURE 9: Metallization and interconnection scheme of a CSG Solar module. The positive contacts (lighter dots) are connected with the negative contacts (darker dots) of the next cell. The isolation groove runs vertically in the middle of the picture and is filled by an insulating resin. (Figure reprinted with permission from [38].)

There is very limited data on reliability and durability of thin-film polysilicon modules because the technology is so new. The expectation is that, based on the fully crystalline nature of the active layer and the absence of a degradation-prone TCO, very little degradation will occur. The scarce experimental data [64, 65] available, indeed, give very positive indications.

The first commercial thin-film polysilicon modules were delivered by CSG Solar in December 2006.

## 6. CONCLUSION

In this paper, I reviewed the field of thin-film silicon solar cells with active layer thickness of only a few microns. These solar cells are appealing because they can potentially deliver very low cost while using an abundant, non-toxic element, namely, silicon. There is a large R&D effort world-wide to reach sufficient conversion efficiency and to implement the different technologies industrially.

The oldest thin-film silicon solar cell technology is single junction hydrogenated amorphous silicon. Although this is a disordered material suffering from light-induced degradation and the thickness of the active layer is only a few hundreds of nanometers, efficiencies close above 9% have been reached on small areas. Commercial modules, however, have a stable efficiency of only 5–7%, which is not sufficient for long-term success. Nevertheless, large investments are now being made, notably by the equipment manufacturers with experience in deposition systems for the LCD display business. Everyone is well aware of the limitation of the single junction amorphous technology but is banking on the next generation of thin-film technology based on microcrystalline silicon, for which the same or similar equipment can be used.

Microcrystalline silicon, which contains nm-sized crystallites embedded in an amorphous matrix, was developed to reach higher and more stable efficiencies. This is a more complex material, and intense material research is being carried out to understand it better and improve device performance. If deposited in the right conditions, microcrystalline Si contains substantially less defects than light-soaked amorphous silicon. Efficiencies of around 10% on small areas have been reached. An important topic of research is the development

of deposition conditions which yield high growth rate while maintaining layer uniformity and electronic quality.

Multijunction thin-film solar cells, where two or three cells made of different thin-film materials are deposited on top of each other, are seen as the way forward to bring amorphous and microcrystalline technology to high module performance. Impressive efficiencies of up to 15% have been reached for devices with a-Si:H top cell and  $\mu\text{c-Si:H}$  bottom cells, but these values are before degradation and for small area devices. Stabilized efficiencies on large area devices are at present in the range of 10%, but strong R&D efforts are going on aiming at high stabilized efficiencies on large areas.

Finally, the field of thin-film polysilicon solar cells was reviewed. This material is investigated because of its high efficiency potential even for only one junction. These technologies depart quite a lot from amorphous and microcrystalline technologies because they involve relatively high temperatures and more costly substrates (although still compatible with low-cost modules). The most successful approach, so far, involves solid phase crystallization of PECVD amorphous silicon, yielding efficiencies up to 9.8% at minimodule level. A lot of research is going into developing a material with higher-crystallographic quality through a seed layer approach. In general, the field of thin-film polysilicon solar cells is not yet as mature as amorphous and microcrystalline Si technologies but there has been very rapid progress over the last few years.

## REFERENCES

- [1] T. Tiedje, E. Yablonovitch, G. D. Cody, and B. G. Brooks, "Limiting efficiency of silicon solar cells," *IEEE Transactions on Electron Devices*, vol. 31, no. 5, pp. 711–716, 1984.
- [2] J. Poortmans and V. Arkhipov, Eds., *Thin Film Solar Cells: Fabrication, Characterization and Applications*, Wiley Series in Materials for Electronic & Optoelectronic Applications, John Wiley & Sons, New York, NY, USA, 2006.
- [3] Y. Hamakawa, Ed., *Thin-Film Solar Cells: Next Generation Photovoltaics and Its Applications*, Springer Series in Photonics, Springer, Berlin, Germany, 2004.
- [4] R. E. I. Schropp, R. Carius, and G. Beaucarne, "Amorphous silicon, microcrystalline silicon, and thin-film polycrystalline silicon solar cells," *MRS Bulletin*, vol. 32, no. 3, pp. 219–224, 2007.
- [5] W. E. Spear and P. G. Le Comber, "Substitutional doping of amorphous silicon," *Solid State Communications*, vol. 17, no. 9, pp. 1193–1196, 1975.
- [6] D. E. Carlson and C. R. Wronski, "Amorphous silicon solar cell," *Applied Physics Letters*, vol. 28, no. 11, pp. 671–673, 1976.
- [7] D. L. Staebler and C. R. Wronski, "Reversible conductivity changes in discharge-produced amorphous Si," *Applied Physics Letters*, vol. 31, no. 4, pp. 292–294, 1977.
- [8] T. Kamei, M. Kondo, and A. Matsuda, "A significant reduction of impurity contents in hydrogenated microcrystalline silicon films for increased grain size and reduced defect density," *Japanese Journal of Applied Physics: Part 2*, vol. 37, no. 3 A, pp. L265–L268, 1998.
- [9] S. Veprek and V. Marecek, "The preparation of thin layers of Ge and Si by chemical hydrogen plasma transport," *Solid-State Electronics*, vol. 11, no. 7, pp. 683–684, 1968.
- [10] R. Tsu, S. R. Ovshinsky, F. H. Pollak, and M. Izu, "Electroreflectance and Raman scattering investigation of glow-discharge

- amorphous Si:F:H,” *Solid State Communications*, vol. 36, no. 9, pp. 817–822, 1980.
- [11] T. Hamasaki, H. Kurata, M. Hirose, and Y. Osaka, “Low-temperature crystallization of doped *a*-Si:H alloys,” *Applied Physics Letters*, vol. 37, no. 12, pp. 1084–1086, 1980.
- [12] J. Meier, R. Flückiger, H. Keppner, and A. Shah, “Complete microcrystalline *p-i-n* solar cell—crystalline or amorphous cell behavior?” *Applied Physics Letters*, vol. 65, no. 7, pp. 860–862, 1994.
- [13] M. N. van den Donker, B. Rech, F. Finger, W. M. M. Kessels, and M. C. M. van de Sanden, “Highly efficient microcrystalline silicon solar cells deposited from a pure SiH<sub>4</sub> flow,” *Applied Physics Letters*, vol. 87, no. 26, Article ID 263503, 3 pages, 2005.
- [14] A. Gordijn, J. K. Rath, and R. E. I. Schropp, “High-efficiency  $\mu$ c-Si solar cells made by very high-frequency plasma-enhanced chemical vapor deposition,” *Progress in Photovoltaics: Research and Applications*, vol. 14, no. 4, pp. 305–311, 2006.
- [15] Y. Mai, S. Klein, R. Carius, et al., “Microcrystalline silicon solar cells deposited at high rates,” *Journal of Applied Physics*, vol. 97, no. 11, Article ID 114913, 12 pages, 2005.
- [16] M. Kondo, T. Matsui, Y. Nasuno, et al., “Crucial processing steps for microcrystalline silicon bottom cells,” in *Proceedings of the 31st IEEE Photovoltaic Specialists Conference*, pp. 1377–1382, Lake Buena Vista, Fla, USA, January 2005.
- [17] S. Goya, Y. Nakano, T. Watanabe, N. Yamashita, and Y. Yonekura, “The effect of narrow gap length on the high-rate deposition of microcrystalline silicon,” in *Proceedings of the 19th European Photovoltaic Solar Energy Conference*, p. 1407, Paris, France, June 2004.
- [18] A. Poruba, A. Fejfar, Z. Remeš, et al., “Optical absorption and light scattering in microcrystalline silicon thin films and solar cells,” *Journal of Applied Physics*, vol. 88, no. 1, pp. 148–160, 2000.
- [19] M. Vanecek and A. Poruba, “Fourier-transform photocurrent spectroscopy of microcrystalline silicon for solar cells,” *Applied Physics Letters*, vol. 80, no. 5, pp. 719–721, 2002.
- [20] F. Meillaud, E. Vallat-Sauvain, X. Niquille, et al., “Light-induced degradation of thin film amorphous and microcrystalline silicon solar cells,” in *Proceedings of the 31st IEEE Photovoltaic Specialists Conference*, pp. 1412–1415, Lake Buena Vista, Fla, USA, January 2005.
- [21] S. Klein, F. Finger, R. Carius, and H. Stiebig, “Light-induced degradation of microcrystalline silicon thin-film solar cells prepared by hot-wired CVD,” in *Proceedings of the 19th European Photovoltaic Solar Energy Conference*, p. 1579, Paris, France, June 2004.
- [22] B. Yan, G. Yue, J. Owens, J. Yang, and S. Guha, “Light-induced metastability in hydrogenated nanocrystalline silicon solar cells,” *Applied Physics Letters*, vol. 85, no. 11, pp. 1925–1927, 2004.
- [23] Y. Mai, S. Klein, R. Carius, H. Stiebig, X. Geng, and F. Finger, “Open circuit voltage improvement of high-deposition-rate microcrystalline silicon solar cells by hot wire interface layers,” *Applied Physics Letters*, vol. 87, no. 7, Article ID 073503, 3 pages, 2005.
- [24] K. Yamamoto, A. Nakajima, M. Yoshimi, et al., “A high efficiency thin film silicon solar cell and module,” *Solar Energy*, vol. 77, no. 6, pp. 939–949, 2004.
- [25] J. Meier, S. Dubail, R. Flückiger, D. Fischer, H. Keppner, and A. Shah, “Intrinsic microcrystalline silicon ( $\mu$ c-Si:H)—a promising new thin film solar cell material,” in *Proceedings of the 1st IEEE World Conference on Photovoltaic Energy Conversion (WCPEC '94)*, vol. 1, pp. 409–412, Waikoloa, Hawaii, USA, December 1994.
- [26] B. Yan, G. Yue, J. M. Owens, J. Yang, and J. Guha, “Over 15% efficient hydrogenated amorphous silicon based triple-junction solar cells incorporating nanocrystalline silicon,” in *Proceedings of the 4th IEEE World Conference on Photovoltaic Energy Conversion*, pp. 1477–1480, Waikoloa, Hawaii, USA, May 2006.
- [27] C. Ballif, J. Bailat, D. Dominé, et al., “Fabrication of high efficiency microcrystalline and micromorph thin film solar cells on LPCVD ZnO coated glass substrates,” in *Proceedings of the 21st European Photovoltaic Solar Energy Conference*, p. 1552, Dresden, Germany, September 2006.
- [28] K. Yamamoto, A. Nakajima, M. Yoshimi, et al., “High efficiency thin film silicon hybrid cell and module,” in *Technical Digest of the 15th International Photovoltaic Science and Engineering Conference (PVSEC '05)*, vol. 1, pp. 529–530, Shanghai, China, October 2005.
- [29] B. Rech, T. Repmann, M. N. van den Donker, et al., “Challenges in microcrystalline silicon based solar cell technology,” *Thin Solid Films*, vol. 511–512, pp. 548–555, 2006.
- [30] G. Ganguly, G. Yue, B. Yan, J. Yang, and S. Guha, “Fabrication of large area amorphous silicon/nanocrystalline silicon double junction solar cells,” in *Proceedings of the 4th IEEE World Conference on Photovoltaic Energy Conversion*, pp. 1712–1715, Waikoloa, Hawaii, USA, May 2006.
- [31] T. Repmann, S. Wieder, S. Klein, et al., “Production equipment for amorphous and microcrystalline silicon solar cell manufacturing,” in *Proceedings of the 21st European Photovoltaic Solar Energy Conference*, pp. 1590–1593, Dresden, Germany, September 2006.
- [32] U. Kroll, J. Meier, S. Benagli, et al., “Overview of thin film silicon solar cell and module developments at oerlikon solar,” in *Proceedings of the 21st European Photovoltaic Solar Energy Conference*, p. 1546, Dresden, Germany, September 2006.
- [33] T. Minemoto, M. Toda, S. Nagae, et al., “Effect of spectral irradiance distribution on the outdoor performance of amorphous Si/thin-film crystalline Si stacked photovoltaic modules,” *Solar Energy Materials and Solar Cells*, vol. 91, no. 2–3, pp. 120–122, 2007.
- [34] A. V. Shah, H. Schade, M. Vanecek, et al., “Thin-film silicon solar cell technology,” *Progress in Photovoltaics: Research and Applications*, vol. 12, no. 2–3, pp. 113–142, 2004.
- [35] M. van Cleef, P. Lippens, and P. Call, “Superior energy yields of Uni – Solar<sup>®</sup> triple junction thin film silicon solar cells compared to crystalline silicon solar cells under real outdoor conditions in western Europe,” in *Proceedings of the 17th European Photovoltaic Solar Energy Conference*, Munich, Germany, October 2001.
- [36] M. L. Terry, A. Straub, D. Inns, D. Song, and A. G. Aberle, “Large open-circuit voltage improvement by rapid thermal annealing of evaporated solid-phase-crystallized thin-film silicon solar cells on glass,” *Applied Physics Letters*, vol. 86, no. 17, Article ID 172108, 3 pages, 2005.
- [37] T. Baba, M. Shima, T. Matsuyama, S. Tsuge, K. Wakisaka, and S. Tsuda, “9.2% efficiency thin-film polycrystalline silicon solar cell by a novel solid phase crystallization method,” in *Proceedings of the 13th European Photovoltaic Solar Energy Conference*, p. 1708, Nice, France, October 1995.
- [38] P. A. Basore, “Simplified processing and improved efficiency of crystalline silicon on glass modules,” in *Proceedings of the 19th European Photovoltaic Solar Energy Conference*, p. 455, Paris, France, June 2004.

- [39] D. Song, A. Straub, P. Widenborg, et al., "Polycrystalline silicon thin-film solar cells on glass by solid phase crystallization of in-situ doped evaporated a-Si," in *Proceedings of the 19th European Photovoltaic Solar Energy Conference*, p. 1193, Paris, France, June 2004.
- [40] G. Beaucarne, S. Bourdais, A. Slaoui, and J. Poortmans, "Thin-film poly crystalline Si solar cells on foreign substrates: film formation at intermediate temperatures (700–1300°C)," *Applied Physics A*, vol. 79, no. 3, pp. 469–480, 2004.
- [41] A. Focsa, I. Gordon, G. Beaucarne, O. Tuzun, A. Slaoui, and J. Poortmans, "Heterojunction a-Si/poly-Si solar cells on mullite substrates," to appear in *Thin Solid Films*.
- [42] A. Ogane, T. Yamazaki, Y. Uraoka, and T. Fuyuki, "Large grain poly-Si thin films deposited on ceramic substrate by intermittent source gas supply," in *Proceedings of the 20th European Photovoltaic Solar Energy Conference*, p. 1028, Barcelona, Spain, June 2005.
- [43] O. Nast and S. R. Wenham, "Elucidation of the layer exchange mechanism in the formation of polycrystalline silicon by aluminum-induced crystallization," *Journal of Applied Physics*, vol. 88, no. 1, pp. 124–132, 2000.
- [44] G. Beaucarne, D. V. Gestel, I. Gordon, et al., "Aluminium-induced crystallization of silicon on high temperature substrates for thin-film crystalline silicon solar cells," in *Proceedings of the 19th European Photovoltaic Solar Energy Conference*, pp. 467–470, Paris, France, June 2004.
- [45] A. Straub, D. Inns, M. L. Terry, Y. Huang, P. I. Widenborg, and A. G. Aberle, "Optimisation of low-temperature silicon epitaxy on seeded glass substrates by ion-assisted deposition," *Journal of Crystal Growth*, vol. 280, no. 3–4, pp. 385–400, 2005.
- [46] B. Rau, J. Schneider, M. Muske, et al., "Epitaxial Si growth on polycrystalline Si seed layers at low temperature," in *Proceedings of the 19th European Photovoltaic Solar Energy Conference*, pp. 1131–1134, Paris, France, June 2004.
- [47] B. Rau, J. Schneider, E. Conrad, S. Gall, and W. Fuhs, "Polycrystalline Si thin-film solar cells with absorber layers grown at temperatures below 600 °C by ECRCVD," in *Technical Digest of the 15th International Photovoltaic Science and Engineering Conference ((PVSEC '05))*, pp. 778–779, Shanghai, China, 2005.
- [48] D. van Gestel, M. J. Romero, I. Gordon, et al., "Electrical activity of intragrain defects in polycrystalline silicon layers obtained by aluminum-induced crystallization and epitaxy," *Applied Physics Letters*, vol. 90, no. 9, Article ID 092103, 3 pages, 2007.
- [49] D. van Gestel, I. Gordon, L. Carnel, et al., "Thin-film polycrystalline-silicon solar cells on high-temperature glass based on aluminum-induced crystallization of amorphous silicon," in *Materials Research Society Symposium Proceedings*, vol. 910, pp. 725–730, San Francisco, Calif, USA, April 2007.
- [50] L. Carnel, I. Gordon, K. van Nieuwenhuysen, D. van Gestel, G. Beaucarne, and J. Poortmans, "Defect passivation in chemical vapour deposited fine-grained polycrystalline silicon by plasma hydrogenation," *Thin Solid Films*, vol. 487, no. 1–2, pp. 147–151, 2005.
- [51] M. J. Keevers, A. Turner, U. Schubert, P. A. Basore, and M. A. Green, "Remarkably effective hydrogenation of crystalline silicon on glass modules," in *Proceedings of the 20th European Photovoltaic Solar Energy Conference*, p. 1305, Barcelona, Spain, June 2005.
- [52] L. Carnel, I. Gordon, D. van Gestel, et al., "Record voc-values for thin-film polysilicon solar cells on foreign substrates using a heterojunction emitter," in *Proceedings of the 4th IEEE World Conference on Photovoltaic Energy Conversion*, pp. 1449–1454, Waikoloa, Hawaii, USA, May 2006.
- [53] J. J. Ji and Z. Shi, "Texturing of glass by SiO<sub>2</sub> film," US patent no. 6,420,647, 2002.
- [54] N. Chuangsuwanich, P. I. Widenborg, P. Campbell, and A. G. Aberle, "Light trapping properties of thin silicon films on AIT-textured glass," in *Technical Digest of the 14th International Photovoltaic Science and Engineering Conference (PVSEC '04)*, p. 325, Bangkok, Thailand, January 2004.
- [55] P. I. Widenborg and A. G. Aberle, "Polycrystalline silicon thin-film solar cells on AIT-textured glass superstrates," to appear in *Advances in Optoelectronics*.
- [56] L. Carnel, I. Gordon, H. Dekkers, et al., "Improvement of the short-circuit current of thin-film polysilicon solar cells using plasma texturing," in *Proceedings of the 21st European Photovoltaic Solar Energy Conference*, pp. 830–833, Dresden, Germany, September 2006.
- [57] P. A. Basore, "CSG-2: expanding the production of a new polycrystalline silicon PV technology," in *Proceedings of the 21st European Photovoltaic Solar Energy Conference*, p. 544, Dresden, Germany, September 2006.
- [58] I. Gordon, L. Carnel, D. van Gestel, G. Beaucarne, and J. Poortmans, "8% efficient thin-film polycrystalline-silicon solar cells based on aluminum-induced crystallization and thermal CVD," *Progress in Photovoltaics: Research and Applications*, vol. 15, no. 7, pp. 575–586, 2007.
- [59] A. G. Aberle, "Recent progress in poly-Si thin-film solar cells on glass," in *Proceedings of the 21st European Photovoltaic Solar Energy Conference*, pp. 738–741, Dresden, Germany, September 2006.
- [60] I. Gordon, D. van Gestel, L. Carnel, et al., "Thin-film polycrystalline-silicon solar cells on high-temperature substrates by aluminium-induced crystallization," in *Proceedings of the 21st European Photovoltaic Solar Energy Conference*, pp. 992–995, Dresden, Germany, September 2006.
- [61] G. Andrä, A. Bochmann, F. Falk, A. Gawlik, E. Ose, and J. Plentz, "Diode laser crystallized multicrystalline silicon thin film solar cells on glass," in *Proceedings of the 21st European Photovoltaic Solar Energy Conference*, pp. 972–975, Dresden, Germany, September 2006.
- [62] A. G. Aberle, "Progress in evaporated crystalline silicon thin-film solar cells on glass," in *Proceedings of IEEE 4th World Conference on Photovoltaic Energy Conversion (WCPEC '06)*, vol. 2, pp. 1481–1484, Waikoloa, Hawaii, USA, May 2006.
- [63] S. Gall, J. Berghold, E. Conrad, et al., "Large-grained polycrystalline silicon on glass for thin-film solar cells," in *Proceedings of the 21st European Photovoltaic Solar Energy Conference*, pp. 1091–1094, Dresden, Germany, September 2006.
- [64] P. A. Basore, "Pilot production of thin-film crystalline silicon on glass modules," in *Proceedings of the 29th IEEE Photovoltaic Specialists Conference*, pp. 49–52, New Orleans, La, USA, May 2002.
- [65] P. A. Basore, "Large-area deposition for crystalline silicon on glass modules," in *Proceedings of the 3rd World Conference on Photovoltaic Energy Conversion*, vol. 1, pp. 935–938, Osaka, Japan, May 2003.

## Research Article

# Annealing Kinetic Model Using Fast and Slow Metastable Defects for Hydrogenated-Amorphous-Silicon-Based Solar Cells

Seung Yeop Myong

*Department of Physical Electronics, Tokyo Institute of Technology (TIT), 2-12-1 Ookayama, Meguro-Ku, Tokyo 152-8552, Japan*

Received 1 February 2007; Accepted 17 April 2007

Recommended by Armin G. Aberle

The two-component kinetic model employing “fast” and “slow” metastable defects for the annealing behaviors in pin-type hydrogenated-amorphous-silicon- (a-Si:H-) based solar cells is simulated using a normalized fill factor. Reported annealing data on pin-type a-Si:H-based solar cells are revisited and fitted using the model to confirm its validity. It is verified that the two-component model is suitable for fitting the various experimental phenomena. In addition, the activation energy for annealing of the solar cells depends on the definition of the recovery time. From the thermally activated and high electric field annealing behaviors, the plausible microscopic mechanism on the defect removal process is discussed.

Copyright © 2007 Seung Yeop Myong. This is an open access article distributed under the Creative Commons Attribution License, which permits unrestricted use, distribution, and reproduction in any medium, provided the original work is properly cited.

## 1. INTRODUCTION

In recent years, there has been an explosive, worldwide increase in solar module market due to the global warming and oil crisis. Because bulk crystalline silicon (c-Si) modules make up 90% of products, a severe shortage of c-Si wafers has caused an increase in the cost of the bulk c-Si solar modules. Thus, the increased cost of c-Si wafers currently threatens the photovoltaic business. Thin-film Si solar modules using hydrogenated-amorphous-silicon- (a-Si:H-) based absorbers, meanwhile, become a promising alternative to the bulk c-Si solar modules, because of their remarkably low consumption of raw Si material (<1% of consumption of bulk c-Si modules), large-scale deposition, and low-temperature production. Furthermore, thin-film Si photovoltaic technology profits from the wide experience base of the display industries [1].

However, the so-called “Staebler-Wronski effect (SWE)” in a-Si:H-based films remains as a major obstacle to the commercialization of thin-film Si solar modules. SWE is the light-induced degradation arising from the photocreation of dangling bonds (DBs) accomplished by the nonradiative recombination of photogenerated electron-hole pairs [2, 3]. Because it severely limits the conversion efficiency of a-Si:H-based films, many researchers have investigated SWE during

the past 30 years. Despite extensive investigations, there is no consensus on a microscopic mechanism that explains all the experimental phenomena. Similarly, the recovery mechanism for a-Si:H-based solar cells via thermal annealing [4, 5] or intense illumination at high temperature with a strong reverse bias [6] is still controversial. The recovery kinetics via thermal annealing is often interpreted by the stretched exponential (SE) kinetics [7, 8] wherein defect generation and annealing in a-Si:H-based materials is a dispersive process controlled by one type of metastable defect [9, 10]. However, several recent reports have provided experimental evidence that a-Si:H-based materials possess “fast” and “slow” metastable defects, and thus the total defect density cannot uniquely determine the state for the a-Si:H-based solar cells [11–14]. Yang and Chen suggested the existence of the fast and slow metastable defects in a-Si:H solar cells via two-step light soaking [11]; the cell subjected to an intense pre-soaking exhibits a thermal annealing behavior at the initial stage of 1-sun (AM 1.5, 100 mW/cm<sup>2</sup>) post-soaking, which could be linked to annealing of the fast metastable defects. Since these results are clearly contradictory to the conventional SE kinetic model, the author suggested a new model of recovery kinetics for pin-type a-Si:H-based solar cells employing the two-component (TC) metastable defect states [15]. We selected the fill factor (FF) as a measure of the state

for the a-Si:H-based solar cells due to the following reasons: (i) FF is sensitive to the quality of the intrinsic absorber (i-absorber); (ii) analytic equations relating FF to the collection length and to the defect density (or electron spin density) have been developed [16, 17]; and (iii) FF is the most degraded parameter against light-soaking in a-Si:H-based solar cells [18] and is less sensitive to the measurement temperature and illumination intensity compared to the open-circuit voltage and short-circuit current [4].

In this work, the TC model is simulated by varying its parameters. The model is also applied to experimental annealing data for the pin-type a-Si:H-based solar cells in order to verify the validity of the TC model. Finally, the microscopic mechanisms for the annealing behaviors of pin-type a-Si:H-based solar cells are discussed.

## 2. MODELING AND SIMULATION

If uniform  $E$  is assumed in i-absorber of pin-type a-Si:H-based solar cells, FF is governed by the carrier collection length ( $l_c$ ):

$$l_c = \mu\tau E = \mu\tau \frac{(V_{bi} - V_a)}{d}, \quad (1)$$

where  $\mu$  is the drift mobility,  $\tau$  is the ambipolar carrier lifetime of photogenerated carriers,  $E$  is the internal electric field in the i-absorber,  $V_{bi}$  is the built-in potential in the solar cell,  $V_a$  is the biased voltage, and  $d$  is the thickness of the i-absorber. Faughnan and Crandall [16] reported the following empirical relation:

$$FF = C_0 + A \log \frac{l_c}{d}, \quad (2)$$

with  $C_0 = 0.39$  and  $A = 0.30$  [17].

Because  $\tau$  is reciprocally proportional to the defect density in the i-absorber ( $N$ ), if  $\mu$  is assumed to be constant [17], then

$$FF \cong C_1 - A \log N = C_1 - K_1 \ln N, \quad (3)$$

where  $C_1$  and  $K_1$  ( $= 0.30 \log e = 0.13$ ) are constants.

Accordingly, normalized FF ( $FF_n$ ) can be expressed as

$$FF_n = \frac{FF(t) - FF_d}{FF_i - FF_d} = \frac{\ln(N/N_d)}{\ln(N_0/N_d)}, \quad (4)$$

where  $FF(t)$  is FF as a function of time,  $FF_d$  is degraded FF via light soaking,  $FF_i$  is initial FF before light soaking,  $N_d$  is the defect density in the degraded i-absorber, and  $N_0$  is the initial defect density in the i-absorber [8].

If it is assumed that the TC model has fast and slow metastable defect states ( $N_F$  and  $N_S$ ), then  $N = N_0 + N_F + N_S$  and  $N_d = N_0 + N_{dF} + N_{dS}$ . Furthermore, it is assumed that all the defects stem from a common pool of ground states, and there is otherwise no direct communication between the two

defect components under fixed annealing conditions. Thus, the system of rate equations for both components can be described as [11]

$$\begin{aligned} \frac{dN_F}{dt} &= G_F(N_T - N_F - N_S) - A_F N_F, \\ \frac{dN_S}{dt} &= G_S(N_T - N_F - N_S) - A_S N_S, \end{aligned} \quad (5)$$

where  $N_T$  is the total number of states which can be converted into defects,  $G_F$  and  $G_S$  are the respective constant defect generation coefficients for the fast and slow metastable defects, and  $A_F$  and  $A_S$  are the respective constant defect annealing coefficients for the fast and slow metastable defects. In the case of thermal annealing, we assume that  $G_F = G_S = 0$  and  $A_F \gg A_S$ . Then, the rate equations for  $N_F$  and  $N_S$  can be expressed as the following simple first-order approximations:

$$\begin{aligned} \frac{dN_F}{dt} &= A_F N_F = -\frac{N_F}{\tau_F}, \\ \frac{dN_S}{dt} &= A_S N_S = -\frac{N_S}{\tau_S}, \end{aligned} \quad (6)$$

where  $\tau_F$  and  $\tau_S$  are time constants for the fast and slow metastable defects. Accordingly,  $N_F$  and  $N_S$  can be given by

$$\begin{aligned} N_F &= N_{dF} \exp\left(-\frac{t}{\tau_F}\right), \\ N_S &= N_{dS} \exp\left(-\frac{t}{\tau_S}\right). \end{aligned} \quad (7)$$

After replacement of  $N$  and  $N_d$  by (7), (4) becomes the following kinetic equation:

$$FF_n = \frac{\ln\{n[1 + \alpha \exp(-t/\tau_F) + \beta \exp(-t/\tau_S)]\}}{\ln n}, \quad (8)$$

where  $n = N_0/(N_0 + N_{dF} + N_{dS}) = \exp[(FF_d - FF_i)/K_1]$  from (3),  $\alpha$  ( $= N_{dF}/N_0$ ) is the ratio of the photocreated fast metastable defect density to the initial defect density, and  $\beta$  ( $= N_{dS}/N_0 = 1/n - 1 - \alpha$ ) is the photocreated slow metastable defect density to the initial defect density. Therefore, annealing behaviors can be simulated by fitting three independent parameters,  $\alpha$ ,  $\tau_F$ , and  $\tau_S$ .

Figure 1 provides the simulated results as a function of  $t$  using (8). As shown in the figure, four different recovery rates are inspected with  $t$ : (i) initial fast rise when  $t < \tau_F$ , (ii) moderate increase when  $\tau_S < t < \tau_S$ , (iii) fast increase when  $t > \tau_S$ , and (iv) slow increase in the last tail. Figure 1(a) shows that the increase in  $\tau$  increases with an increase in  $n$ . The rate of the increase decreases with the increase in  $n$  when  $t < \tau_S$ . An increase in the fraction of the fast metastable defect [ $\alpha/(\alpha + \beta)$ ] leads to a fast recovery, as shown in Figure 1(b). It is also found that  $\tau_F$  is mainly responsible for the initial rise, whereas  $\tau_S$  affects the last tail as well as the region when  $t > \tau_S$  (see Figures 1(c) and 1(d)).

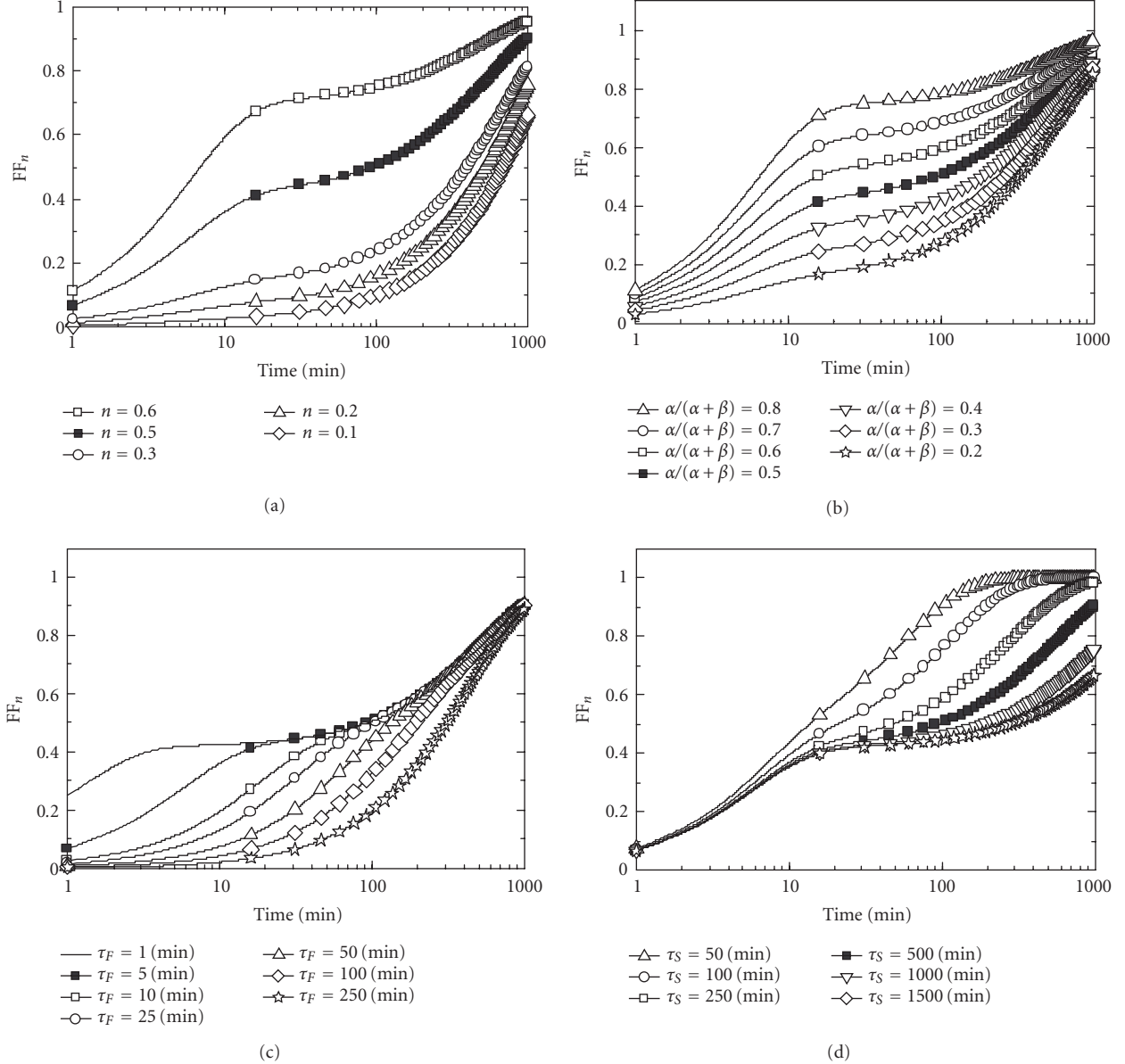


FIGURE 1: Simulation of annealing behaviors using the TC kinetic model; (a) with variable  $n$ , and fixed parameters of  $\alpha/(\alpha + \beta) = 0.5$ ,  $\tau_F = 5$  minutes, and  $\tau_S = 500$  minutes, (b) with variable  $\alpha/(\alpha + \beta)$ , and fixed parameters of  $n = 0.5$ ,  $\tau_F = 5$  minutes, and  $\tau_S = 500$  minutes, (c) with variable  $\tau_F$ , and fixed parameters of  $n = 0.5$ ,  $\alpha/(\alpha + \beta) = 0.5$ , and  $\tau_S = 500$  minutes, (d) with variable  $\tau_S$ , and fixed parameters of  $n = 0.5$ ,  $\alpha/(\alpha + \beta) = 0.5$ , and  $\tau_F = 5$  minutes. The symbols are modeled data included to distinguish each other.

### 3. RESULTS AND DISCUSSION

Figure 2 depicts the simulated results using the TC kinetic model for the experimental results with various thermal annealing temperatures ( $T_A$ ) reported in [4]. The pin-type a-Si:H solar cell was fabricated via a dc glow discharge technique with a structure of glass/transparent conducting oxide (TCO)/hydrogenated p-type amorphous silicon-carbide (p-a-SiC:H)/undiluted i-a-Si:H ( $\sim 520$  nm)/n-type a-Si:H ( $n$ -a-Si:H)/Ti/Ag.  $FF_i$  and the initial efficiency are 0.70 and 9%, respectively. In all measurements, the cell was degraded under the 1-sun illumination at 40°C for 64 hours. Thus,  $FF_d$

is always fixed at 0.55 ( $n = 0.32$ ). With an increase in  $T_A$ ,  $\tau$  declines remarkably.

Figure 3 displays information on evaluated  $\tau$  for the simulated data in Figure 2. Here,  $\tau_i$  denotes the time for  $FF$  to recover  $i\%$  of its total degradation, that is,  $FF_i - FF_d$ . As can be seen in Figure 3(a),  $\tau_i$  is thermally activated, that is,  $\tau_i = \nu_o^{-1} \exp(E_a/kT)$ , where  $\nu_o$  is the attempt frequency,  $E_a$  is the activation energy,  $k$  is Boltzmann's constant, and  $T$  is the absolute temperature. In [4], Bennett et al. demonstrated that the annealing behavior for their pin-type a-Si:H solar cells could be characterized a unique  $E_a$  of 1.2 eV. They selected  $\tau_{50}$  as a measure of  $\tau_i$ . From Figure 3(b), however, it

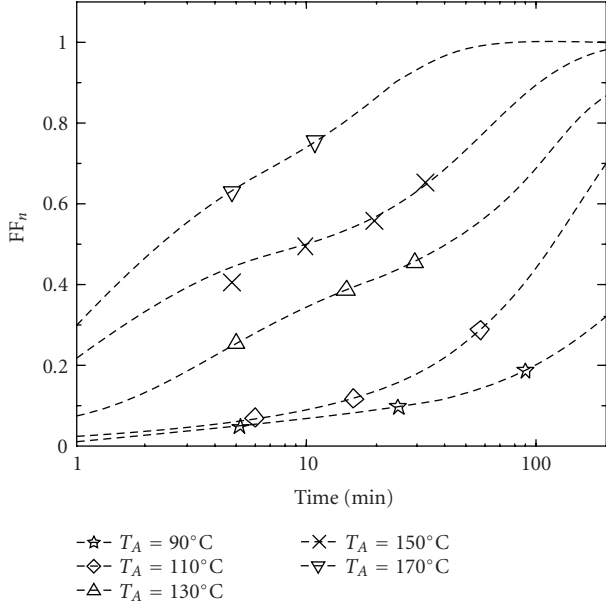


FIGURE 2: Recovery behaviors for the a-Si:H solar cell via thermal annealing as a function of  $T_A$  (from [4]). The symbols and dotted lines denote experimental data and simulated data using the TC kinetic model, respectively.

should be noted that  $E_a$  for pin-type a-Si:H-based solar cells depends on  $\tau_i$  and the TC model present a gradual decrease in  $E_a$  and  $v_o$  with an increase in  $i$ . These phenomena are mainly caused by the existence of the fast and slow metastable defects in the TC model.

Figure 4 compares the simulated results using the TC model for the experimental results reported in [6]. The pin-type solar cell was fabricated at  $\sim 200^\circ\text{C}$  via a plasma-enhanced chemical vapor deposition (PECVD) technique [5] with a structure of glass/SnO<sub>2</sub>/p-a-SiC:H/H<sub>2</sub>-diluted i-a-Si:H ( $\sim 300$  nm)/n-a-Si:H/ZnO/Al. At the open-circuit, the cell was degraded under the 50-sun illumination at  $60^\circ\text{C}$  for 30 minutes. Hence,  $n$  is always fixed at 0.43 by keeping  $FF_i$  and  $FF_d$  at 0.67 and 0.56, respectively. Then, the experimental recovery behaviors were inspected under 50-sun illumination with different  $V_a$ . It was found that FF for the pin-type H<sub>2</sub>-diluted a-Si:H solar cell recovered more rapidly under intense irradiation at  $T_A = 70^\circ\text{C}$  with an increase in reversed  $V_a$ .  $\tau_F$  and  $\tau_S$  for the TC model all gradually decrease with the increase in reversed  $V_a$ , thus indicating the high electric field induced fast recovery. The reduced  $\tau$  is mainly due to the decrease in  $\tau_S$ . It is clear that the TC model fits the experimental data well in the initial rise and last tail. Furthermore, the reported different recovery kinetics from identical  $FF_d$ , which depend on the illumination intensity [11] or temperature [4] during the light-induced degradation, prove that the photocreation of DBs, that is,  $N_d - N_0$ , is composed of different kinds of defects.

The author have developed hydrogenated protocrystalline Si (pc-Si:H) multilayer absorbers [18]. The pc-Si:H material is a highly H<sub>2</sub>-diluted a-Si:H material existing just

TABLE 1: Fitting parameters used in Figure 5.

	$n$	$\alpha/(\alpha + \beta)$	$\tau_F$ (min)	$\tau_S$ (min)
undiluted a-Si:H	0.39	0.82	3.7	214.6
pc-Si:H multilayer	0.57	0.84	3.3	59.5

below the threshold of the a-Si:H-to- $\mu\text{c}$ -Si:H transition. Using a photoassisted chemical vapor deposition (photo-CVD) technique, we prepared alternately H<sub>2</sub>-diluted i-pc-Si:H multilayers by modulating the mass flow control of the hydrogen dilution ratio (H<sub>2</sub>/SiH<sub>4</sub>), and thereby i-pc-Si:H has the repeatedly layered structure of low H<sub>2</sub>-diluted a-Si:H sublayers and highly H<sub>2</sub>-diluted sublayers. The highly H<sub>2</sub>-diluted sublayers possess isolated nanosized Si (nc-Si) grains embedded in a-Si:H matrix [19]. The i-pc-Si:H multilayers exhibit a fast light-induced metastability with a low degradation. Consequently, highly stabilized solar cells (stabilized efficiency = 9.0%) were achieved without using any back reflector [20, 21]. The pc-Si:H multilayer solar cells exhibit a very fast annealing behavior during 1-sun post-soaking, compared to a-Si:H solar cells [22], which is the clear evidence of the two-component metastable defects in the pc-Si:H multilayers. Figure 5 shows the fitted results using the TC model for the experimental recovery behaviors in an undiluted a-Si:H solar cell and a pc-Si:H multilayer solar cell in [8]. The pin-type solar cells were fabricated at  $250^\circ\text{C}$  via a photoassisted chemical vapor deposition (photo-CVD) technique with a structure of glass/SnO<sub>2</sub>/p-a-SiC:H/p- $\mu\text{c}$ -Si:H/i-absorber ( $\sim 550$  nm)/n- $\mu\text{c}$ -Si:H/Al. The initial efficiency for the undiluted a-Si:H and pc-Si:H multilayer solar cells are 10.6 and 8.9%, and  $FF_i$  values are 0.73 and 0.69, respectively. The solar cells were degraded under the 1-sun illumination at  $48^\circ\text{C}$  for 20 hours. After light soaking, the pc-Si:H multilayer cell stabilized with  $n = 0.57$ , while the undiluted a-Si:H cell is still in degrading state with  $n = 0.39$ . The fitting parameters of the cells are listed in Table 1. Thermal annealing is performed in a vacuum chamber. The pc-Si:H multilayer cell exhibits the rapider recovery than the undiluted a-Si:H cell.

From the fast metastability and annealing behaviors of pc-Si:H multilayer solar cells, the vertically regular distribution of the isolated nc-Si grains [21] and the improved medium-range-order in the a-Si:H matrix [23] are considered to localize the photocreation near the grain boundary regions [19], and thereby suppress the photocreation of slow metastable defects in the pc-Si:H multilayers. From the visible photoluminescence (PL) peak measured at room temperature, the isolated nc-Si grains tend to act as radiative recombination centers of captured carriers, which may contribute to the good stability [14].

Because the pc-Si:H multilayer has a slightly wider optical band gap (effective band gap  $> 1.7$  eV) than conventional a-Si:H layers ( $\sim 1.7$  eV), the pc-Si:H multilayer solar cell is promising as a top cell for a high-efficiency tandem cell [23]. The pc-Si:H multilayer/ $\mu\text{c}$ -Si:H ( $\sim 1.1$  eV) double-junction tandem structure opened the possibility of a significantly

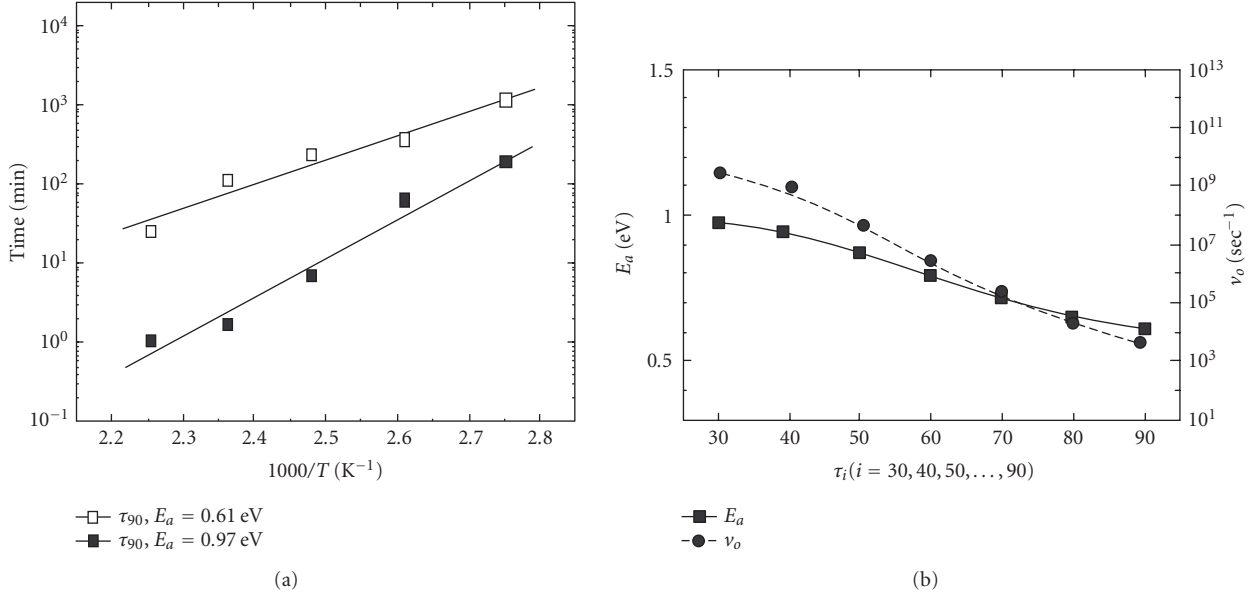


FIGURE 3: Information on evaluated  $\tau$  for the simulated data in Figure 2; (a) Arrhenius plot for  $\tau_{30}$  and  $\tau_{90}$ . The calculated values of  $E_a$  for  $\tau_{30}$  and  $\tau_{90}$  are provided. (b)  $E_a$  and  $\nu_o$  versus  $\tau_i$ .

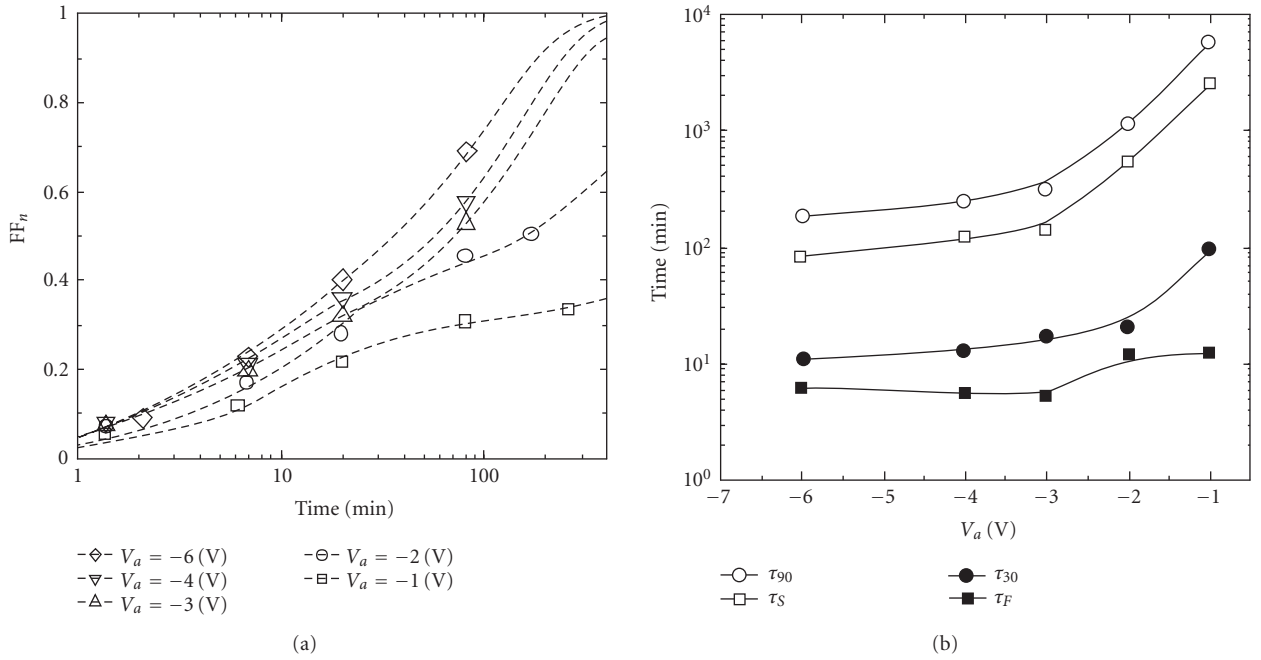


FIGURE 4: Annealing for the H<sub>2</sub>-diluted a-Si:H solar cell under intense (50-sun) illumination at  $T_A = 70^\circ\text{C}$  (from [6]); (a) recovery behaviors with different  $V_a$  and (b)  $\tau_{30}$  and  $\tau_{90}$  versus  $V_a$ . The symbols and dotted lines denote experimental data and simulated data using the TC kinetic model, respectively.

high-stabilized efficiency due to a low-degradation ratio [24].

The photocreation of DBs in an a-Si:H matrix can occur with a value of  $E_a$  [25] that is lower than  $E_a$  for light-induced long range H diffusion (0.9 eV) [26]. Hence, the breaking of strong Si-H bonds ( $\sim 3$  eV), proposed by Branz in the hy-

drogen collision model [27], cannot be easily accomplished by the nonradiative recombination of electron-hole pairs. Instead, the breaking of weak Si-Si bonds due to nonradiative recombination of electron-hole pairs is considered today as a plausible origin of SWE [28, 29]. Recently, Powell et al. [29] proposed the creation of two metastable HSiDB (complex of

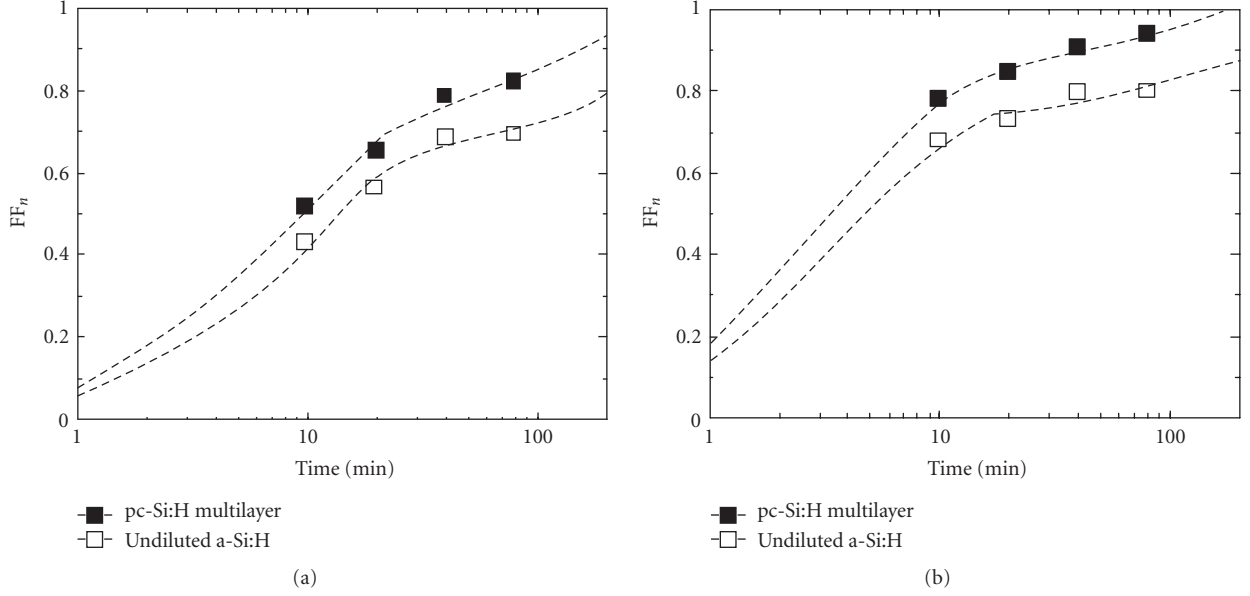


FIGURE 5: Comparison of the recovery behavior via thermal annealing between the undiluted a-Si:H and pc-Si:H multilayer solar cells (from [8]); (a)  $T_A = 108^\circ\text{C}$  and (b)  $T_A = 133^\circ\text{C}$ . The symbols and dotted lines denote experimental data and simulated data using the TC kinetic model, respectively.

a DB and an Si–H bond, where H locates in a tetrahedral-like site ( $T_d$ ), not a bond-centered site) defects; an H atom from a neighboring doubly hydrogenated weak Si–Si bond (HSiSiH) switches to a  $T_d$  site of the broken Si–Si bond and the other H from HSiSiH is also located in the energetically suitable  $T_d$  site. This model is reasonable because the spatial separation between H in the  $T_d$  site and DB is in agreement with the observed values of 4–5 Å by electron spin resonance (ESR) measurements [30]. On the other hand, it has been reported that annealing of DBs in a-Si:H films, which are photocreated at moderate temperature, has a similar value of  $E_a$  (1.1–1.2 eV) [31] to that for long range H diffusion (1.5 eV) [32]. This supports the supposition that long range H diffusion plays an important role in annealing of metastable defects. Thus, the hydrogen collision model is valid in the case of annealing and  $E_a$  can be interpreted as the energy for the thermal emission of H from a  $T_d$  site. In addition,  $\nu_o$  corresponds with the phonon frequency of Si–H bonds [29] and with the thermal emission process. However, it is difficult to define unique  $E_a$  and  $\nu_o$  for  $\tau$ , because it varies with  $\tau_i$  (see Figure 3(b)). Nevertheless,  $E$  in a solar cell is expected to lower the energy barrier for long range H diffusion [6]. From Figure 4, it can be concluded that the intense illumination at a high temperature also thermally emits mobile H by breaking Si–H bonds, and leads to high electric field induced annealing for the solar cells.

In the previous report [15], the author proposed the following mechanism for the recovery kinetics in pin-type a-Si:H-based solar cells based on the TC model: (i) mobile H is thermally emitted from a metastable HSiDB defect by breaking the Si–H bond. As reflected in Figure 2, the elevated  $T_A$  increases the thermal emission rate of mo-

bile H [32]; (ii) emission of bonded H is followed by weak Si–Si bond reconstruction. Meanwhile, mobile H migrates through the lattice [33, 34] and is subsequently captured at another weak Si–Si bond, which eventually forms an HSiDB defect. It should be noted that  $E$  in i-absorber assists the migration of mobile H to a shallower site, which is reflected in Figure 4; and (iii) thermal emission and recapturing processes of mobile H proceed until it is captured at the DB site of a metastable HSiDB defect, resulting in the annealing of two defects. Consequently, for the annealing process to reform the a-Si:H matrix, a considerable energy is required and many H atoms are involved. However, an internal field formed in solar cells can reduce the required energy for the annealing process. It should be noted that the classification between the fast and slow metastable defects is mainly determined by their activation energy and capture cross-section [14]. This classification is only relative and is dependent on the annealing conditions, that is, elevated  $T_A$  or  $V_a$  can increase  $\alpha$ .

#### 4. CONCLUSIONS

The author simulated the TC model in order to understand the effect of each parameter on the annealing kinetics in pin-type a-Si:H-based solar cells. This model displays that  $E_a$  depends on the definition of the recovery time. It is verified that the TC model fits the various experimental data. Thus, the TC model can be deemed useful for limiting the number of mechanisms responsible for annealing the photocreated defects in a-Si:H. From the thermally activated and high electric field induced nature of annealing behaviors, the plausible microscopic mechanism on the DB defect removal related to the

thermal emission of mobile H from  $T_d$  sites and long range H diffusion was discussed.

## REFERENCES

- [1] A. Shah, P. Torres, R. Tscharnner, N. Wyrsch, and H. Keppner, "Photovoltaic technology: the case for thin-film solar cells," *Science*, vol. 285, no. 5428, pp. 692–698, 1999.
- [2] D. L. Staebler and C. R. Wronski, "Reversible conductivity changes in discharge-produced amorphous Si," *Applied Physics Letters*, vol. 31, no. 4, pp. 292–294, 1977.
- [3] D. L. Staebler, R. S. Crandall, and R. Williams, "Stability of *n-i-p* amorphous silicon solar cells," *Applied Physics Letters*, vol. 39, no. 9, pp. 733–735, 1981.
- [4] M. S. Bennett, J. L. Newton, K. Rajan, and A. Rothwarf, "Kinetic studies of the annealing behavior of *a-Si:H p-i-n* solar cells," *Journal of Applied Physics*, vol. 62, no. 9, pp. 3968–3975, 1987.
- [5] D. E. Carlson and K. Rajan, "The reversal of light-induced degradation in amorphous silicon solar cells by an electric field," *Applied Physics Letters*, vol. 70, no. 16, pp. 2168–2170, 1997.
- [6] D. E. Carlson and K. Rajan, "Evidence for proton motion in the recovery of light-induced degradation in amorphous silicon solar cells," *Journal of Applied Physics*, vol. 83, no. 3, pp. 1726–1729, 1998.
- [7] A. Terakawa, H. Matsunami, S. Kiyama, and S. Tsuda, "Origin of the optical gap dependence of *a-SiGe* solar cell stability," *Journal of Applied Physics*, vol. 84, no. 8, pp. 4611–4616, 1998.
- [8] K. H. Jun, J. D. Ouwers, R. E. I. Schropp, et al., "Low degradation and fast annealing effects of amorphous silicon multilayer processed through alternate hydrogen dilution," *Journal of Applied Physics*, vol. 88, no. 8, pp. 4881–4888, 2000.
- [9] D. Redfield and R. H. Bube, "Reinterpretation of degradation kinetics of amorphous silicon," *Applied Physics Letters*, vol. 54, no. 11, pp. 1037–1039, 1989.
- [10] W. B. Jackson and J. Kakalios, "Evidence for hydrogen motion in annealing of light-induced metastable defects in hydrogenated amorphous silicon," *Physical Review B*, vol. 37, no. 2, pp. 1020–1023, 1988.
- [11] L. Yang and L. Chen, "'Fast' and 'slow' metastable defects in hydrogenated amorphous silicon," *Applied Physics Letters*, vol. 63, no. 3, pp. 400–402, 1993.
- [12] J. Pearce, X. Niu, R. Koval, et al., "Contributions of  $D^0$  and non- $D^0$  gap states to the kinetics of light induced degradation of amorphous silicon under 1 sun illumination," *Materials Research Society Symposium Proceedings*, vol. 664, no. A12.3, 2001.
- [13] J. M. Pearce, J. Deng, R. W. Collins, and C. R. Wronski, "Light-induced defect states in hydrogenated amorphous silicon centered around 1.0 and 1.2 eV from the conduction band edge," *Applied Physics Letters*, vol. 83, no. 18, pp. 3725–3727, 2003.
- [14] S. Y. Myong, S. W. Kwon, K. S. Lim, M. Kondo, and M. Konagai, "Inclusion of nanosized silicon grains in hydrogenated protocrystalline silicon multilayers and its relation to stability," *Applied Physics Letters*, vol. 88, Article ID 083118, 3 pages, 2006.
- [15] S. Y. Myong and K. S. Lim, "Modeling of annealing kinetics for hydrogenated-amorphous-silicon-based solar cells using two-component metastable defects," *Applied Physics Letters*, vol. 88, Article ID 243510, 3 pages, 2006.
- [16] B. W. Faughnan and R. S. Crandall, "Determination of carrier collection length and prediction of fill factor in amorphous silicon solar cells," *Applied Physics Letters*, vol. 44, no. 5, pp. 537–539, 1984.
- [17] Z. E. Smith, S. Wagner, and B. W. Faughann, "Carrier lifetime model for the optical degradation of amorphous silicon solar cells," *Applied Physics Letters*, vol. 46, no. 11, pp. 1078–1080, 1985.
- [18] S. Y. Myong, S. W. Kwon, K. S. Lim, and M. Konagai, "Highly stabilized protocrystalline silicon multilayer solar cell using a silicon-carbide double p-layer structure," *Solar Energy Materials and Solar Cells*, vol. 85, no. 1, pp. 133–140, 2005.
- [19] S. Y. Myong, "Recent progress in inorganic solar cells using quantum structures," *Recent Patents on Nanotechnology*, vol. 1, no. 1, pp. 67–73, 2007.
- [20] S. Y. Myong, K. S. Lim, and J. M. Pearce, "Double amorphous silicon-carbide p-layer structures producing highly stabilized pin-type protocrystalline silicon multilayer solar cells," *Applied Physics Letters*, vol. 87, Article ID 193509, 3 pages, 2005.
- [21] S. Y. Myong, S. W. Kwon, M. Kondo, M. Konagai, and K. S. Lim, "Development of a rapidly stabilized protocrystalline silicon multilayer solar cell," *Semiconductor Science and Technology*, vol. 21, no. 2, pp. L11–L15, 2006.
- [22] S. W. Kwon, J. Y. Ahn, S. Y. Myong, and K. S. Lim, "Alternately hydrogen diluted amorphous silicon multilayer solar cell with low degradation rate under 10%," in *Proceedings of the 17th European Photovoltaic Solar Energy Conference and Exhibition*, pp. 3015–3018, Munich, Germany, October 2001.
- [23] S. Y. Myong, S. W. Kwon, J. H. Kwak, K. S. Lim, J. M. Pearce, and M. Konagai, "Good stability of protocrystalline silicon multilayer solar cells against light irradiation originating from vertically regular distribution of isolated nano-sized silicon grains," in *Proceedings of the 4th IEEE World Conference on Photovoltaic Energy Conversion*, vol. 2, pp. 1584–1587, IEEE, Waikoloa, Hawaii, USA, May 2006.
- [24] J. H. Kwak, *Development of high efficiency, low degradation tandem solar cells using protocrystalline silicon (pc-Si:H) multilayer*, Ph.D. thesis, Korea Advanced Institute of Science and Technology, Taejeon, Korea, 2007.
- [25] P. Stradins and H. Fritzsche, "Photoinduced creation of metastable defects in *a-Si:H* at low-temperatures and their effect on the photoconductivity," *Philosophy Magazine B*, vol. 69, no. 1, pp. 121–139, 1994.
- [26] P. V. Santos, N. M. Johnson, and R. A. Street, "Light-enhanced hydrogen motion in *a-Si:H*," *Physical Review Letter*, vol. 67, no. 19, pp. 2686–2689, 1991.
- [27] H. M. Branz, "Hydrogen collision model: quantitative description of metastability in amorphous silicon," *Physical Review B*, vol. 59, no. 8, pp. 5498–5512, 1999.
- [28] V. Nádaždy and M. Zeman, "Origin of charged gap states in *a-Si:H* and their evolution during light soaking," *Physical Review B*, vol. 69, Article ID 165213, 6 pages, 2004.
- [29] M. J. Powell, S. C. Deane, and R. B. Wehrspohn, "Microscopic mechanisms for creation and removal of metastable dangling bonds in hydrogenated amorphous silicon," *Physical Review B*, vol. 66, no. 15, Article ID 155212, 11 pages, 2002.
- [30] J. Isoya, S. Yamasaki, H. Okushi, A. Matsuda, and K. Tanaka, "Electron-spin-echo envelope-modulation study of the distance between dangling bonds and hydrogen atoms in hydrogenated amorphous silicon," *Physical Review B*, vol. 47, no. 12, pp. 7013–7024, 1993.
- [31] M. Stutzmann, W. B. Jackson, and C. C. Tsai, "Light-induced metastable defects in hydrogenated amorphous silicon: a systematic study," *Physical Review B*, vol. 32, no. 1, pp. 23–47, 1985.

- [32] H. M. Branz, "Hydrogen diffusion and mobile hydrogen in amorphous silicon," *Physical Review B*, vol. 60, no. 11, pp. 7725–7727, 1999.
- [33] H. M. Branz, Y. Xu, S. Heck, and W. Gao, "Improved stability of hydrogenated amorphous-silicon photosensitivity by ultraviolet illumination," *Applied Physics Letters*, vol. 81, no. 18, pp. 3353–3355, 2002.
- [34] S. Y. Myong, S. S. Kim, and K. S. Lim, "In situ ultraviolet treatment in an Ar ambient upon *p*-type hydrogenated amorphous silicon-carbide windows of hydrogenated amorphous silicon based solar cells," *Applied Physics Letters*, vol. 84, no. 26, pp. 5416–5418, 2004.

## Research Article

# Polycrystalline Silicon Thin-Film Solar Cells on AIT-Textured Glass Superstrates

Per I. Widenborg and Armin G. Aberle

*Photovoltaics Centre of Excellence, The University of New South Wales (UNSW), Sydney, NSW 2052, Australia*

Received 29 April 2007; Revised 24 September 2007; Accepted 25 September 2007

Recommended by Xian An Cao

A new glass texturing method (AIT—aluminium-induced texturisation) has recently been developed by our group. In the present work, the potential of this method is explored by fabricating PLASMA poly-Si thin-film solar cells on glass superstrates that were textured with the AIT method. Using an interdigitated metallisation scheme with a full-area Al rear contact, PLASMA cells with an efficiency of up to 7% are realised. This promising result shows that the AIT glass texturing method is fully compatible with the fabrication of poly-Si thin-film solar cells on glass using solid phase crystallisation (SPC) of PECVD-deposited amorphous silicon precursor diodes. As such, there are now two distinctly different glass texturing methods—the AIT method and CSG Solar's glass bead method—that are known to be capable of producing efficient SPC poly-Si thin-film solar cells on glass.

Copyright © 2007 P. I. Widenborg and A. G. Aberle. This is an open access article distributed under the Creative Commons Attribution License, which permits unrestricted use, distribution, and reproduction in any medium, provided the original work is properly cited.

## 1. INTRODUCTION

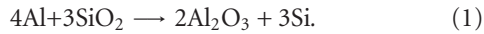
Polycrystalline silicon (poly-Si) thin-film device structures on inexpensive foreign supporting materials such as glass are becoming increasingly important, for example in thin-film solar cells and flat panel displays. In the case of solar cells, thin-films have the potential to significantly reduce the cost of manufacture of photovoltaic (PV) modules due to the fact that they only require a fraction of the silicon material as compared to traditional, silicon wafer-based modules. Furthermore, thin-film poly-Si solar cells have the advantage that it is possible to manufacture them on large-area supporting materials ( $\sim 1 \text{ m}^2$ ), streamlining the production process and further reducing processing costs. The efficiency of solar cells based on poly-Si materials (i.e., materials with a grain size larger than about  $1 \mu\text{m}$ , no amorphous tissue) is also intrinsically more stable compared to that of cells based on amorphous or microcrystalline silicon thin-films.

Due to the weak absorption of near-infrared light in crystalline silicon (c-Si), an effective light trapping scheme is essential for poly-Si thin-film solar cells (i.e., Si thickness of less than  $10 \mu\text{m}$ ). One effective way to obtain light trapping is to texture the supporting material prior to the deposition of the Si film. As a result of the texture, light is transmitted obliquely into the Si film, significantly enhancing the optical pathlength and thus increasing the optical absorption.

A texture that has steeper slopes will increase the optical absorption more strongly than a shallow texture. The optical absorption is further enhanced by depositing a high-quality reflector onto the back surface (back surface reflector—BSR). Best optical absorption is obtained if the texture and the BSR are optimised such that the total internal reflection occurs both at the front and the rear surface of the Si film, enabling multiple passes of the light through the solar cell. Apart from the light trapping benefits, the textured substrate also reduces reflection losses at the front surface of the solar cell (double-bounce effect). The most efficient poly-Si thin-film solar cells made as yet at low temperature on foreign supporting materials have energy conversion efficiencies in the range 9–10% and were fabricated by solid phase crystallization (SPC) at about  $600^\circ\text{C}$  of hydrogenated amorphous silicon (a-Si:H) precursor diodes on a textured metal substrate (9.2%) [1] or a textured glass superstrate (9.8%) [2, 3]. The a-Si:H precursor diodes were deposited by plasma-enhanced chemical vapor deposition (PECVD). Besides giving good cell efficiency, the SPC method has a number of other advantages such as simplicity of the process and low cost.

In the present work, we use the SPC method to fabricate poly-Si thin-film solar cells on glass superstrates that are textured with a new method recently developed by us [4, 5]. This method is referred to as aluminium-induced texturisation (AIT) and is based on a thermally activated chemical reaction

between the glass and a thin, sacrificial aluminium layer. All sacrificial Al films used in the present work were deposited by evaporation. The high temperature ( $\sim 600^\circ\text{C}$ ) during the subsequent thermal anneal induces a spatially nonuniform redox reaction between the Al and the glass ( $\text{SiO}_2$ ) according to



Following this anneal, the reaction products ( $\text{Al}_2\text{O}_3$ , Si) are removed by wet chemical etching. The Al layer can be deposited by evaporation or sputtering and hence the AIT method is suitable for large-area applications such as thin-film PV. All solar cells reported in this paper are made by SPC of PECVD-deposited a-Si:H precursor diodes and are referred to by us as “PLASMA” cells [6]. In addition to AIT-textured glass sheets, we also use planar glass sheets to clearly reveal the benefits of the glass texture. The cells are analysed structurally (focused ion beam microscopy, atomic force microscopy), optically (reflectance, transmission), and electrically (1-Sun current-voltage, external and internal quantum efficiency). Computer simulations are also performed to determine the cells’ light trapping properties and the diffusion length in the absorber region.

## 2. EXPERIMENTAL DETAILS

A resistively heated evaporator (Varian) was used for depositing aluminium onto clean  $15 \times 15 \text{ cm}^2$  glass sheets from Schott AG (Borofloat33, 3.3 mm thick). The thickness of the evaporated Al films was in the range of 40 to 230 nm. The evaporation rate was in the range of 3 nm/sec. The samples were then annealed at  $610^\circ\text{C}$  for 40 minutes in a nitrogen purged tube furnace, inducing a chemical reaction between the glass substrate and the aluminium layer. Removal of the aluminium layer and the reaction products was realised by immersion for 10 minutes in hot ( $130^\circ\text{C}$ ) concentrated (85%) phosphoric acid, followed by a 10-second dip in a 1:1 HF:HNO<sub>3</sub> solution. A conventional 13.56-MHz parallel-plate PECVD system (MV Systems, USA) was used for depositing a SiN layer (used as a diffusion barrier and antireflection coating with a thickness of  $\sim 70 \text{ nm}$  and a refractive index of  $\sim 2.05$ ) and a-Si:H precursor diodes onto planar and AIT textured  $15 \times 15 \text{ cm}^2$  sheets. Gas mixtures of pure silane with 0.5% phosphine in silane, 100 ppm diborane in hydrogen, and 0.5% trimethylboron in hydrogen were used for the deposition of  $n^+$ ,  $p^-$ , and  $p^+$  doped a-Si:H films, respectively. The total silane gas flow was kept fixed at 40 sccm, the total pressure was about 800 mTorr, the glass temperature about  $400^\circ\text{C}$ , and the RF power about  $25 \text{ mW/cm}^2$ . The SPC anneals (19 hours at about  $600^\circ\text{C}$ ) were performed ex situ in a conventional nitrogen-purged atmospheric pressure tube furnace. Following crystallisation, one  $5 \times 5 \text{ cm}^2$  sample was cut from the centre of each  $15 \times 15 \text{ cm}^2$  glass sheet. The samples then received an RTA process at  $900\text{--}1000^\circ\text{C}$  for up to 5 minutes, followed by a hydrogenation treatment. The hydrogenation was performed in a cold-wall vacuum system featuring an inductively coupled remote plasma source (Advanced Energy, USA), using a glass temperature

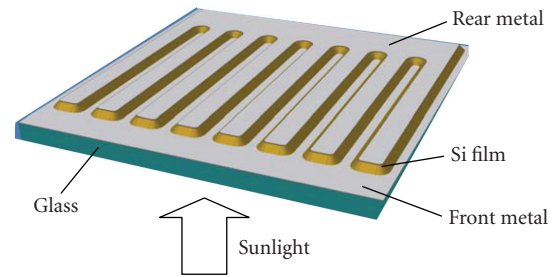


FIGURE 1: Schematic representation of the interdigitated metallisation scheme of our poly-Si thin-film solar cells on glass. The drawing illustrates a part of one cell (not to scale).

of  $610\text{--}640^\circ\text{C}$  during 15–30 minutes, a plasma power of 3200–3500 W, a hydrogen gas flow of 200 sccm, and an argon gas flow of 60 sccm [7]. The metallisation scheme used in this work consists of two interdigitated comb-like metal grids, as schematically shown in Figure 1. The rear metal grid ( $\sim 600 \text{ nm}$  thick Al) serves as the rear (i.e., air-side) electrode of the cell, the back surface reflector, and a mask for plasma etching of the grooves for the front electrode. The comb-like, front (i.e., glass-side) electrode also consists of Al and can be formed in several ways, for instance, using the self-aligned maskless photolithography (SAMPL) method [8]. The front finger spacing of the cells is 0.56 mm and the cell dimension is 1.1 cm by 4.0 cm. Each  $5 \times 5 \text{ cm}^2$  glass piece features four PLASMA solar cells of dimension 1.1 cm by 4.0 cm.

The fabricated PLASMA solar cells were investigated by optical reflectance and transmission spectroscopy (Varian Cary 5G, double-beam spectrophotometer with an integrating sphere) and the surface morphology of the cells was investigated by Focused Ion Beam microscopy (FEI xP200) and Atomic Force Microscopy (AFM). After metallisation, the solar cells were characterised by current-voltage ( $I$ - $V$ ) and external and internal quantum efficiency (EQE, IQE) measurements. The optical spectroscopy measurements as well as the EQE measurements were carried out in the superstrate configuration, using perpendicular illumination of the samples. The solar cell simulation program PC1D [9] was used to estimate the absorber region diffusion lengths and the light trapping properties of the PLASMA poly-Si thin-film solar cells.

## 3. RESULTS

### 3.1. Structural and optical properties

Figure 2 shows the surface morphology of a representative PLASMA solar cell grown on AIT-textured glass, revealing a cauliflower-like structure. In Figure 3, AFM measurements show how the roughness of the bare glass texture varies with the Al thickness used in the AIT process. As can be seen, maximum glass surface roughness is obtained for an Al thickness in the 160–200 nm range.

The impact of the AIT glass texture on the optical absorbance  $A(\lambda)$  of PLASMA cells with a silicon thickness of  $2 \mu\text{m}$  is shown in Figure 4. The bottom curve was measured on a planar cell, the middle curve on a cell textured with

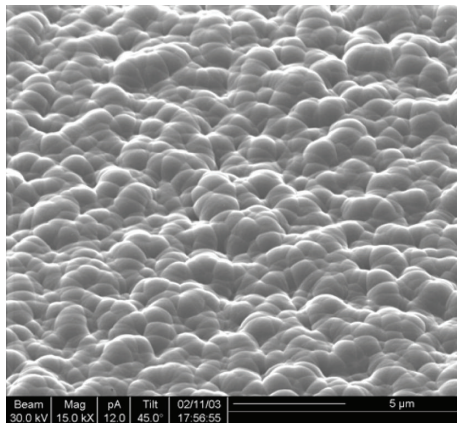


FIGURE 2: Focused ion beam (FIB) image of the rear surface of a PLASMA solar cell grown on an AIT-textured glass sheet. The length of the marker is  $5\ \mu\text{m}$ .

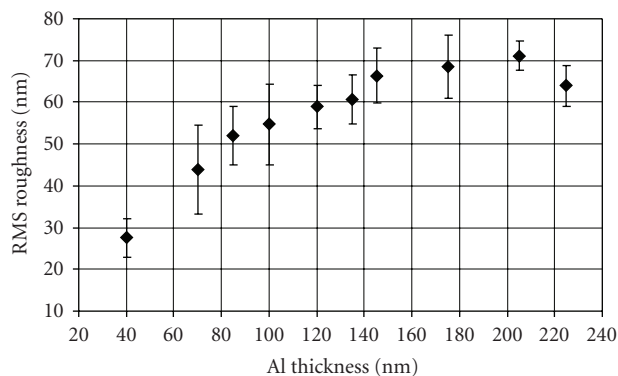


FIGURE 3: Results from AFM measurements showing how the roughness of the bare glass texture (i.e., no silicon film) varies with the Al thickness used in the AIT process.

70 nm of Al in the AIT process, and the top curve on a cell textured with 175 nm of Al in the AIT process. These absorbance results were obtained via  $A = 1 - (R + T)$ , where  $R$  and  $T$  are the measured hemispherical reflectance and transmission. These measurements were taken before the cells were metallised, and hence the back surface reflector (BSR) was air at this stage. As can be seen, compared to the planar sample, the AIT-70 nm glass almost doubles the absorbance at  $\lambda = 800\ \text{nm}$ , while the corresponding boost for the AIT-175 nm glass is even greater ( $\sim 2.5$  times). Combined with the AFM roughness results of Figure 3, these results clearly show that a rougher AIT glass surface leads to more efficient scattering and trapping of light, and hence to a larger optical absorption. For wavelengths above 800 nm, absorption in the 3 mm thick glass sheet becomes increasingly important, particularly for textured glass. As shown in [10], absorption in 3 mm thick AIT-textured glass sheets dominates over absorption in the Si thin-film for  $\lambda > 950\ \text{nm}$ , and this explains the significant absorption of the textured samples at wavelengths above the c-Si bandgap ( $\sim 1100\ \text{nm}$ ). The improved absorbance at short wavelengths ( $\lambda < 500\ \text{nm}$ ) for the top curve in Figure 4 is due to reduced front surface reflec-

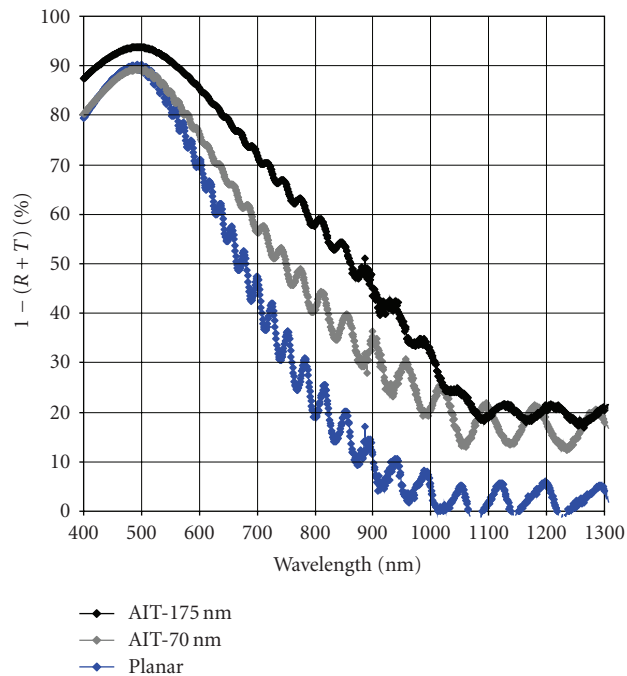


FIGURE 4: Wavelength-dependent optical absorbance  $A$  of a planar PLASMA cell (bottom curve) and two AIT-textured PLASMA cells (top curve = AIT-175 nm). Poly-Si thickness is about  $2\ \mu\text{m}$  in each case. The intended structure of the samples is glass/SiN/ $n^+p^-p^+$ .

tion caused by the rougher front surface of this Si solar cell (double-bounce effect).

The impact of the silicon film thickness on the optical absorbance  $A(\lambda)$  of planar and AIT-textured PLASMA cells is shown in Figure 5. These measurements were again taken before the cells were metallised and hence the BSR was again air. For cells on planar glass, increasing the Si thickness from 2 to  $5\ \mu\text{m}$  strongly improves the optical absorption in the 500–900 nm wavelength band (e.g., by a factor of  $\sim 1.6$  at  $\lambda = 800\ \text{nm}$ ). This is a direct consequence of the poor light trapping properties of planar cells, necessitating the use of a relatively thick planar Si film ( $>10\ \mu\text{m}$ ) to obtain good absorption of the solar spectrum. In contrast, due to good light trapping, the optical absorption of textured samples increases only slightly (e.g., by a factor of  $\sim 1.1$  at  $\lambda = 800\ \text{nm}$ ) when the Si thickness is increased from 2 to  $5\ \mu\text{m}$ . This shows that a Si thickness of  $5\ \mu\text{m}$  is more than enough for PLASMA poly-Si cells on AIT-textured glass to ensure a good absorption of the solar spectrum, provided that the back surface reflector is of high quality. It should be noted that the optical properties of the SiN antireflective coating affect the absorption curves shown in Figures 4 and 5. However, all SiN layers used in this work were nominally identical and hence the conclusions drawn from Figures 4 and 5 remain unaffected.

### 3.2. Current-voltage and quantum efficiency measurements

Upon completion of the absorption measurements, several samples were metallised and their 1-Sun  $I$ - $V$  curve measured

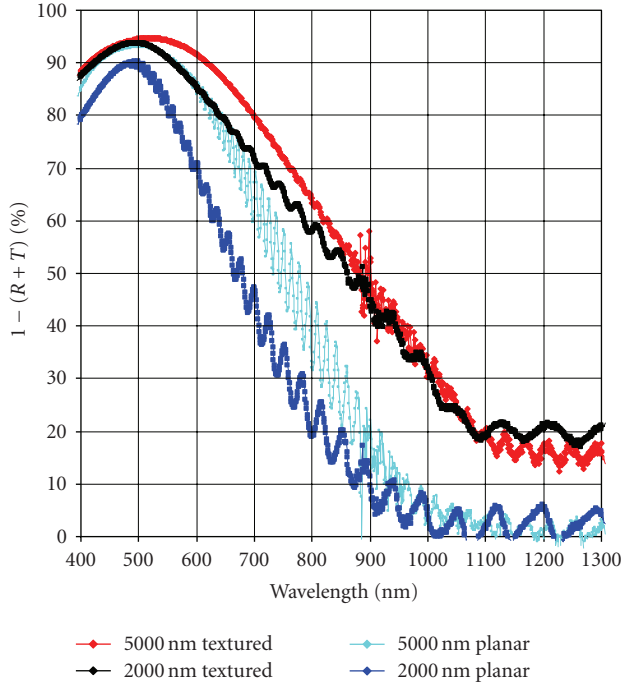


FIGURE 5: Wavelength-dependent optical absorbance  $A$  of two planar PLASMA cells (bottom curves, Si thickness 2 and  $5\ \mu\text{m}$ ) and two AIT-textured PLASMA cells (top curves, Si thickness 2 and  $5\ \mu\text{m}$ ). Both textured glass sheets were fabricated with an Al thickness of 175 nm in the AIT process. The structure of the samples is the same as in Figure 4.

on a halogen-lamp-based solar simulator. Additionally, the reflectance and the external quantum efficiency of these samples were measured. From each measured EQE curve, the 1-Sun short-circuit current ( $J_{sc,EQE}$ ) for the standard terrestrial solar spectrum (AM1.5G,  $100\ \text{mW}/\text{cm}^2$ ) was calculated. The results of the 1-Sun  $I$ - $V$  measurements are shown in Table 1, together with the corresponding  $J_{sc,EQE}$  values. Several representative EQE curves are shown in Figure 6. As can be seen from Table 1, reasonable agreement (2–9% relative difference) between the  $J_{sc}$  values obtained from the  $I$ - $V$  and EQE measurements is obtained.

Two important conclusions can be drawn from Table 1. The first is that the glass texture does not negatively affect the  $V_{oc}$  and the  $FF$  of the PLASMA cells, confirming that the AIT glass texturing method is well suited to the fabrication of these thin-film solar cells. Secondly, the  $J_{sc}$  of PLASMA cells is significantly boosted by the AIT glass texture, giving the textured cells a clear efficiency advantage (about 8–19% relative) over their planar counterparts. The highest efficiency obtained in Table 1 is 5.5%, which is a clear proof-of-concept for PLASMA solar cells on AIT-textured glass.

Taking a closer look at the short-circuit currents in Table 1, it can be seen that, for a given Si solar cell thickness, the introduction of the glass texture increases the cell's short-circuit current (EQE) by 5–17%. While this is a significant enhancement, it is well below the enhancement that might have been expected from the absorption measurements performed on the samples prior to metallisation

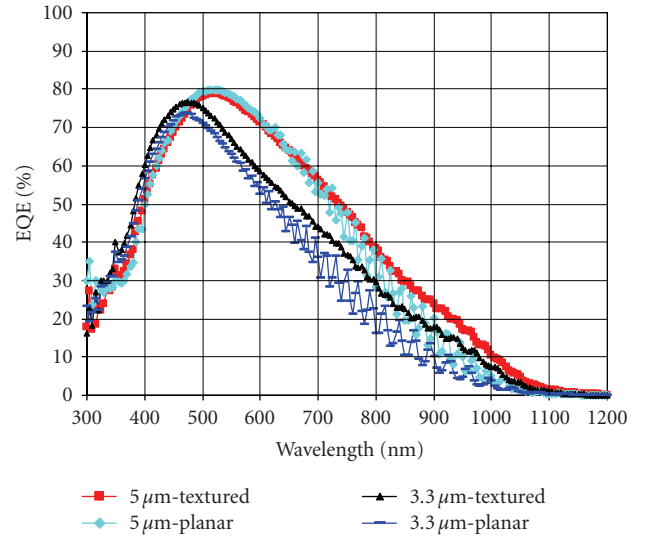


FIGURE 6: Measured EQE of two  $3.3\ \mu\text{m}$  thick PLASMA solar cells (1  $\times$  planar, 1  $\times$  textured) and two  $5.0\ \mu\text{m}$  thick PLASMA solar cells (1  $\times$  planar, 1  $\times$  textured).

(see Section 3.1). One possible reason could be a very small minority-carrier diffusion length  $L$  in the cells' absorber region (i.e.,  $L \ll W_{ab}$ , where  $W_{ab}$  is the width of the absorber layer), causing a poor  $J_{sc}$  despite good optical absorption of the solar spectrum in the Si film. To test this hypothesis, the external quantum efficiency curves of several cells were fitted with the 1-dimensional solar cell simulator PC1D [9]. Good agreement between measured and simulated EQE curves was obtained, as shown in Figure 7. The corresponding PC1D parameters are given in Table 2. To fit the short-wavelength response of these PLASMA solar cells, it was necessary to insert a lightly doped ( $1 \times 10^{16}\ \text{cm}^{-3}$ )  $n$ -type region between the highly doped  $n$ -type emitter and the lowly doped  $p$ -type part of the absorber layer, giving a  $n^+n^-p^-p^+$  solar cell structure. Sheet resistance profiling has recently shown that such a structure is typical for our present PLASMA solar cells [11]. As can be seen from Table 2, the absorber region diffusion lengths of all samples are similar to the width of the corresponding region of the absorber and hence the modest current gains due to the glass texture are *not* due to a poor diffusion length in the absorber region. Instead, modeling of the cells' EQE with PC1D reveals that the modest  $J_{sc}$  gain due to the texture is caused by a severe degradation of the internal reflection at the rear surface of the cells. Specifically, PC1D determines an internal rear reflection of about 50% at the planar Si/Al interface, whereas the corresponding value is only about 25% at the textured Si/Al interface. We believe that the poor internal reflectance of the textured samples is due to the double-bounce effect at textured rear surfaces, reducing the internal rear reflectance to  $(1/2)^2 = 0.25 = 25\%$ . These results are also in good agreement with [12] where it was found that depositing a layer of white paint (which acts as a pigmented diffuse reflector) onto the rear surface of poly-Si thin-film solar cells on glass ("ALICIA cells") strongly improves the  $J_{sc}$ , whereas deposition of an Al film degrades

TABLE 1: Results of 1-Sun  $I$ - $V$  measurements on 4 different PLASMA cells, also shown (column  $J_{sc,EQE}$ ) is the 1-Sun  $J_{sc}$  under AM1.5G illumination calculated from the measured EQE curve.

Sample	Glass surface	Si thickness (nm)	$V_{oc}$ (mV)	$J_{sc}$ (mA/cm <sup>2</sup> )	$FF$ (%)	Eff (%)	$J_{sc,EQE}$ (mA/cm <sup>2</sup> )
3.3 $\mu$ m-P	Planar	$\sim 3300$	442	13.8	68.0	4.2	14.71
3.3 $\mu$ m- <i>Tex</i>	Textured (AIT-175 nm)	$\sim 3300$	461	16.0	67.4	5.0	17.25
5.0 $\mu$ m-PI	Planar	$\sim 5000$	448	17.4	63.6	5.1	18.92
5.0 $\mu$ m- <i>Tex</i>	Textured (AIT-175 nm)	$\sim 5000$	445	19.6	63.2	5.5	19.98

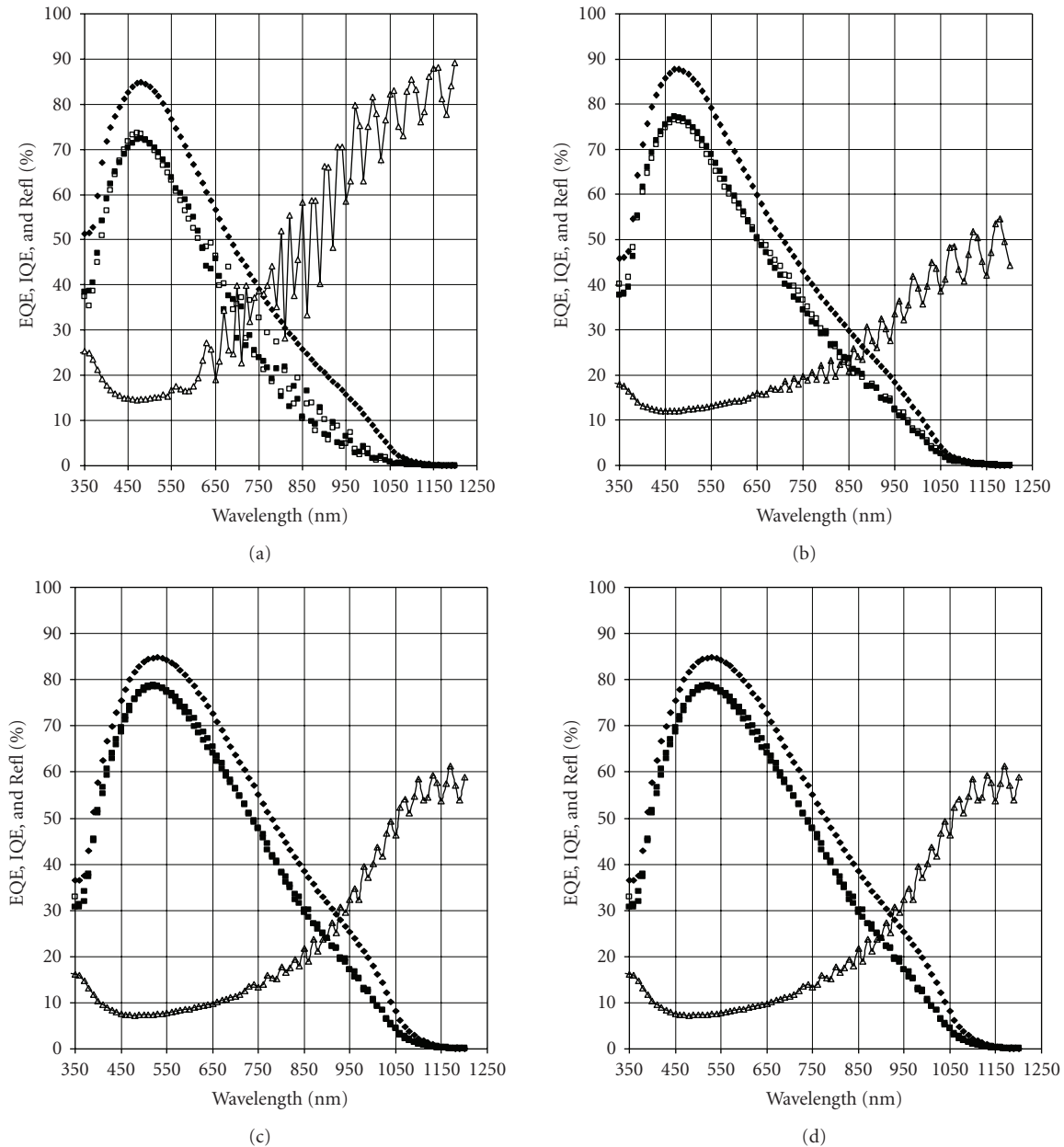


FIGURE 7: Measured EQE (open squares) and reflectance (open triangles) of PLASMA solar cells, also shown are the PC1D-simulated EQE and IQE curves (filled squares and filled diamonds). Graph (a) = sample 3.3  $\mu$ m-PI, graph (b) = sample 3.3  $\mu$ m-*Tex*, graph (c) = sample 5.0  $\mu$ m-PI, graph (d) = sample 5.0  $\mu$ m-*Tex*.

TABLE 2: PC1D simulation parameters of planar and AIT-textured PLASMA poly-Si solar cells, as obtained from fitting of the cells' measured EQE curves.

Sample	3.3 $\mu\text{m}$ -Pl	3.3 $\mu\text{m}$ -Tex	5.0 $\mu\text{m}$ -Pl	5.0 $\mu\text{m}$ -Tex
Thickness of emitter (nm)	70	80	70	100
Doping level in emitter ( $\text{cm}^{-3}$ )	$4 \times 10^{19}$	$6 \times 10^{19}$	$6 \times 10^{19}$	$6 \times 10^{19}$
Diffusion length in emitter (nm)	75	75	65	90
Thickness of $n$ -type part of absorber (nm)	750	800	1000	1000
Doping level in $n$ -type part of absorber ( $\text{cm}^{-3}$ )	$1 \times 10^{16}$	$1 \times 10^{16}$	$1 \times 10^{16}$	$1 \times 10^{16}$
Diffusion length in $n$ -type part of absorber (nm)	1300	1200	1300	1150
Thickness of $p$ -type part of absorber (nm)	2050	2200	4000	4000
Doping level in $p$ -type part of absorber ( $\text{cm}^{-3}$ )	$1 \times 10^{16}$	$1 \times 10^{16}$	$1 \times 10^{16}$	$1 \times 10^{16}$
Diffusion length in $p$ -type part of absorber (nm)	2050	2500	5000	5600
Internal reflection front surface (%)	52	94	50	94
Internal reflection rear surface (%)	48	25	52	28

the  $J_{sc}$  (whereby the degradation was found to be particularly strong for textured samples). The important result from these investigations is that evaporated Al on poly-Si films is a poor back surface reflector, and particularly so for textured samples. Work is under way in our group to replace the full-area aluminium BSR by localised Al contacts and to cover the nonmetallised rear surface regions with a good BSR such as white paint.

### 3.3. 7% efficient PLASMA cells

By further optimising the solar cell fabrication process (RTA, hydrogenation, etc.), we have been able to improve the 1-Sun  $V_{oc}$  of AIT-textured PLASMA samples to up to 491 mV and the  $FF$  to over 70%. In Figure 8, the measured 1-Sun current-voltage and power-voltage curves of the best PLASMA cell fabricated as yet by us is shown. The cell has an energy conversion efficiency (total area) of 7.0%, a  $V_{oc}$  of 491 mV, a  $FF$  of 70.5%, and a  $J_{sc}$  of 20.1 mA/cm<sup>2</sup>. Total cell area is 4.40 cm<sup>2</sup> and the silicon thickness is 4.0  $\mu\text{m}$ . The  $I$ - $V$  curve was measured using an aperture mask with an area of 4.40 cm<sup>2</sup>. From the measured EQE curve of this AIT-textured cell, a  $J_{sc,EQE}$  of 20.55 mA/cm<sup>2</sup> is obtained for the AM1.5G spectrum. It is noted that this 7% PLASMA cell has a full-area Al rear contact and hence relatively modest light trapping properties. Significant improvements of the short-circuit current (and hence the cell efficiency) are expected from the implementation of an improved back surface reflector, as discussed in the previous section.

## 4. CONCLUSIONS

A new glass texturing method (AIT—aluminium-induced texturing) has recently been developed by our group. In the present work, the potential of this method has been explored by fabricating PLASMA poly-Si thin-film solar cells on glass superstrates that were textured with the AIT method. Using an interdigitated metallisation scheme with a full-area Al rear contact, PLASMA cells with an efficiency of up to 7.0% have been realised. This promising result shows that the AIT glass texturing method is fully compatible with the fab-

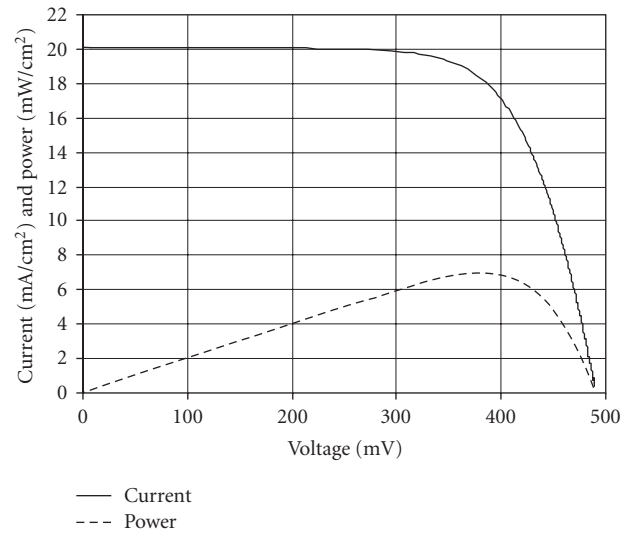


FIGURE 8: Measured current-voltage and power-voltage curves of a 7.0% efficient PLASMA solar cell made on AIT-textured glass (silicon thickness 4  $\mu\text{m}$ , total cell area 4.40 cm<sup>2</sup>, approximated AM1.5G spectrum, 100 mW/cm<sup>2</sup>, cell temperature 25°C).

rication of poly-Si thin-film solar cells on glass using solid phase crystallisation (SPC) of PECVD-deposited amorphous silicon precursor diodes. As such, there are now two distinctly different glass texturing methods—the AIT method and CSG solar's glass bead method [13]—that are known to be capable of producing efficient SPC poly-Si thin-film solar cells on glass.

While short-circuit current densities  $J_{sc}$  of up to 20 mA/cm<sup>2</sup> have been realised in the present paper, the  $J_{sc}$  potential of the AIT glass texturing method is actually significantly higher, as confirmed by optical absorption measurements taken on the samples prior to metallisation (i.e., using air as the back surface reflector). The reason why the present textured cells have relatively modest  $J_{sc}$  has been shown to be the poor internal reflectance of about 25% at the textured, full-area rear Al contact. By implementing a locally

contacting rear Al electrode and a pigmented diffuse reflector (such as white paint [12]) in the metal-free rear surface regions, the  $J_{sc}$  can be significantly boosted.

## ACKNOWLEDGMENTS

This work has been supported by the Australian Research Council (ARC) via its Centres of Excellence scheme. The authors acknowledge the contributions of present and former members of the Thin-Film Group at UNSW.

## REFERENCES

- [1] T. Matsuyama, N. Terada, T. Baba, et al., "High-quality polycrystalline silicon thin film prepared by a solid phase crystallization method," *Journal of Non-Crystalline Solids*, vol. 198–200, part 2, pp. 940–944, 1996.
- [2] M. A. Green, P. A. Basore, N. Chang, et al., "Crystalline silicon on glass (CSG) thin-film solar cell modules," *Solar Energy*, vol. 77, no. 6, pp. 857–863, 2004.
- [3] P. A. Basore, "CSG-2: expanding the production of a new polycrystalline silicon PV technology," in *Proceedings of the 21st European Photovoltaic Solar Energy Conference*, pp. 544–548, Dresden, Germany, September 2006.
- [4] N. Chuangsuwanich, P. I. Widenborg, P. Campbell, and A. G. Aberle, "Light trapping properties of thin silicon films on AIT-textured glass," in *Proceedings of the 14th International Photovoltaic Science and Engineering Conference (PVSEC'04)*, pp. 325–326, Bangkok, Thailand, January 2004.
- [5] A. G. Aberle, P. I. Widenborg, and N. Chuangsuwanich, "Glass texturing," International PCT patent application WO 2004/089841 A1, 2004.
- [6] A. G. Aberle, "Recent progress in poly-Si thin-film solar cells on glass," in *Proceedings of the 21st European Photovoltaic Solar Energy Conference*, pp. 738–741, Dresden, Germany, September 2006.
- [7] M. L. Terry, A. Straub, D. Inns, D. Song, and A. G. Aberle, "Large open-circuit voltage improvement by rapid thermal annealing of evaporated solid-phase-crystallized thin-film silicon solar cells on glass," *Applied Physics Letters*, vol. 86, no. 17, Article ID 172108, 3 pages, 2005.
- [8] T. M. Walsh, D. Song, S. Motahar, and A. G. Aberle, "Self-aligning maskless photolithography method for metallising thin-film crystalline silicon solar cells on transparent supporting materials," in *Proceedings of the 15th International Photovoltaic Science and Engineering Conference (PVSEC '05)*, p. 706, Shanghai, China, October 2005.
- [9] P. A. Basore, "Numerical modeling of textured silicon solar cells using PC-1D," *IEEE Transaction on Electron Devices*, vol. 37, no. 2, pp. 337–343, 1990.
- [10] P. Campbell, P. I. Widenborg, A. B. Sproul, and A. G. Aberle, "Surface textures for large-grained poly-silicon thin-film solar cells on glass using the AIT method," in *Proceedings of the 15th International Photovoltaic Science and Engineering Conference (PVSEC '05)*, pp. 859–860, Shanghai, China, October 2005.
- [11] P. I. Widenborg and A. G. Aberle, "Hydrogen-induced dopant neutralisation in p-type AIC poly-Si seed layers functioning as buried emitters in ALICE thin-film solar cells on glass," *Journal of Crystal Growth*, vol. 306, no. 1, pp. 177–186, 2007.
- [12] O. Berger, D. Inns, and A. G. Aberle, "Commercial white paint as back surface reflector for thin-film solar cells," *Solar Energy Materials and Solar Cells*, vol. 91, no. 13, pp. 1215–1221, 2007.
- [13] J. J. Ji and Z. Shi, "Texturing of glass by SiO<sub>2</sub> film," US patent 6,420,647, 2002.

## Research Article

# Rapid Thermal Annealing and Hydrogen Passivation of Polycrystalline Silicon Thin-Film Solar Cells on Low-Temperature Glass

Mason L. Terry, Daniel Inns, and Armin G. Aberle

*Photovoltaics Centre of Excellence, The University of New South Wales, Sydney, NSW 2052, Australia*

Received 24 April 2007; Revised 24 August 2007; Accepted 16 October 2007

Recommended by Xian An Cao

The changes in open-circuit voltage ( $V_{oc}$ ), short-circuit current density ( $J_{sc}$ ), and internal quantum efficiency (IQE) of aluminum induced crystallization, ion-assisted deposition (ALICIA) polycrystalline silicon thin-film solar cells on low-temperature glass substrates due to rapid thermal anneal (RTA) treatment and subsequent remote microwave hydrogen plasma passivation (hydrogenation) are examined.  $V_{oc}$  improvements from 130 mV to 430 mV,  $J_{sc}$  improvements from 1.2 mA/cm<sup>2</sup> to 11.3 mA/cm<sup>2</sup>, and peak IQE improvements from 16% to > 70% are achieved. A 1-second RTA plateau at 1000°C followed by hydrogenation increases the  $J_{sc}$  by a factor of 5.5. Secondary ion mass spectroscopy measurements are used to determine the concentration profiles of dopants, impurities, and hydrogen. Computer modeling based on simulations of the measured IQE data reveals that the minority carrier lifetime in the absorber region increases by 3 orders of magnitude to about 1 nanosecond (corresponding to a diffusion length of at least 1 μm) due to RTA and subsequent hydrogenation. The evaluation of the changes in the quantum efficiency and  $V_{oc}$  due to RTA and hydrogenation with computer modeling significantly improves the understanding of the limiting factors to cell performance.

Copyright © 2007 Mason L. Terry et al. This is an open access article distributed under the Creative Commons Attribution License, which permits unrestricted use, distribution, and reproduction in any medium, provided the original work is properly cited.

## 1. INTRODUCTION

Thin-film solar cells are becoming increasingly attractive due to the limitations with silicon feedstock and the drive to lower the manufacturing cost and the final module cost. During the fabrication of thin-film silicon solar cells, very little silicon is used (typical film thickness of <10 μm) and the processing steps are of relatively low cost. As such, thin-film polycrystalline silicon (pc-Si) films on low-temperature glass substrates are ideally suited to achieve the goal of less than US\$1 per Watt in a finished module.

In pc-Si thin-film solar cells, defect removal, defect passivation, and dopant activation are critical to device performance. Both point-like and extended defects are typically introduced during the fabrication of thin-film solar cells. Many of these defects generate recombination centers within the semiconductor bandgap, dramatically lowering the minority carrier lifetime. Removing and/or passivating these defects is required to obtain sufficiently high minority carrier lifetimes. This is done through thermal annealing and passivation techniques. A potential problem with thermal annealing of thin-film solar cells is extensive dopant diffusion (“smearing”),

which can eventually lead to electrical shunting of the diode structure. A second problem arises when low-temperature substrates are used, thereby limiting annealing time and/or temperature.

Rapid thermal annealing (RTA) has replaced the tube furnace in many applications to perform high-temperature (>700°C) processing steps for defect annealing, dopant activation, and/or diffusion. RTA processes are ideally suited for thin-film pc-Si solar cells on glass substrates [1–3] as precise control of the thermal profile that the device sees is achieved. Fast temperature ramp rates limit the diffusion of dopants within the device, minimize glass damage all while achieving efficient defect removal. Hydrogen passivation (hydrogenation) is crucial in passivating extended and point-like defects. In thin-film devices, this hydrogenation is typically performed using an RF or microwave-powered hydrogen plasma. The open-circuit voltage ( $V_{oc}$ ) of pc-Si thin-film solar cells on glass is typically more than doubled by the hydrogenation step [1–5].

Section 2 starts with a brief description of the investigated mesa-type solar cells and then describes the post-deposition processing systems, the different measurement

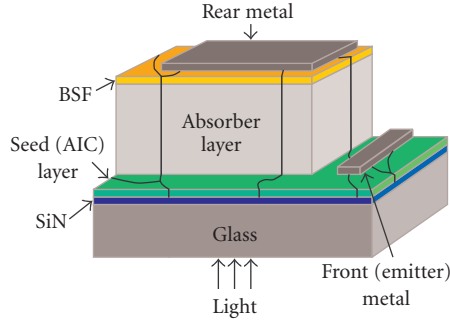


FIGURE 1: Mesa-type ALICIA cell structure as used in the present work.

techniques, and the sample fabrication processing used in this work. Section 3 first presents the experimental results obtained in this study, including Suns- $V_{oc}$ , internal and external quantum efficiency (IQE, EQE), short-circuit current densities ( $J_{sc}$ ) calculated from the measured EQE curves, and a summary of the electrical measurements. This is followed by secondary ion mass spectroscopy (SIMS) data and a discussion of the experimental results. Section 4 presents computer simulations of the investigated solar cells to determine their minority carrier lifetimes in the as-grown state, after a 1000°C RTA, and after a subsequent hydrogenation. Finally, Section 5 presents the conclusions from this study.

## 2. EXPERIMENTAL PARAMETERS

The aluminum induced crystallization, ion-assisted deposition (ALICIA) solar cell is well described in the literature [6, 7]. Figure 1 shows a Mesa-type version of this cell as used in the present paper. Planar Borofloat33 glass panes ( $5 \times 5 \text{ cm}^2$ , 3 mm thick) (Schott AG, Mainz, Germany) are used as substrates. An SiN:H layer with a thickness of  $\sim 75 \text{ nm}$  is deposited by microwave plasma-enhanced chemical vapor deposition (PECVD). The seed layer (emitter) is formed by an aluminum-induced crystallization process (AIC) [8], giving pc-Si with a typical grain size of  $\sim 20 \mu\text{m}$  and a thickness of  $\sim 200 \text{ nm}$ . The absorber (base) and back surface field (BSF) layers are then grown using ion-assisted deposition of e-beam evaporated Si and in-situ doping from effusion cells of gallium (Ga) and phosphorus (P). This gives the following structure: Glass (planar), SiN (75 nm),  $p^+$  (AIC, 200 nm,  $\sim 2 \times 10^{19} \text{ cm}^{-3}$  Al),  $p^-$  (IAD, 50 nm,  $\sim 1 \times 10^{17} \text{ cm}^{-3}$  Ga),  $n^-$  (IAD, 1000 nm,  $\sim 4 \times 10^{16} \text{ cm}^{-3}$  P),  $n^+$  (IAD, 100 nm,  $N_{\text{surface}} = \sim 1 \times 10^{19} \text{ cm}^{-3}$  P). The samples used in this study are nominally identical, with three mesa structures (two  $1 \times 15 \text{ mm}^2$  strips and one  $18 \times 14 \text{ mm}^2$  “square”) per glass substrate that all receive identical processing apart from the RTA process. During the growth of the base and BSF layers, a mask is used to cover parts of the seed layer, forming a mesa structure via shadow-mask epitaxy. This enables a simple metallization of the device with Al contacts, as shown in Figure 1.

The RTA system used in this study is tungsten-halogen lamp based, uses an  $N_2$  ambient at one atmosphere of pres-

sure, and has a graphite plate to support the glass substrates. The time at plateau and cooling rate from plateau (either controlled cooling or natural cooling with no heating from plateau down to 650°C) is varied in this investigation. To perform the hydrogenation, a pulsed remote microwave plasma source is used in a cold wall reactor. The microwave power for this study is 3.2 kW, with a 30-second pulse length for both on and off. A pulsed mode is used to avoid overheating of the microwave generator. The hydrogenation plateau is 620°C for 15 minutes, using an  $H_2:Ar$  plasma. Then the glass temperature is reduced to 325°C over 14 minutes, the plasma is turned off, and the samples removed.

The 1-Sun  $V_{oc}$  (termed “ $V_{oc}$ ” hereafter) is taken from quasisteady state  $V_{oc}$  measurements (“Suns-  $V_{oc}$  curves”) [9], and the fit parameters  $V_1$  and  $V_2$  are determined using a 2-diode model with fixed ideality factors of  $n = 1$  and  $n = 2$ , respectively, plus a shunt resistance. In fact,  $V_1$  and  $V_2$  are the 1-Sun  $V_{oc}$  of the  $n = 1$  and  $n = 2$  diodes, respectively. The crossing point  $V_x$  of the fitted  $n = 1$  and  $n = 2$  curves provides a single parameter to evaluate the relative importance of the recombination currents  $J_{01}$  and  $J_{02}$  [10]. If  $V_{oc} = V_x$ , then both recombination currents affect the 1-Sun  $V_{oc}$  equally. When  $V_x$  is greater than  $V_{oc}$  then the recombination current  $J_{02}$  becomes increasingly more important. As  $V_x$  becomes less than  $V_{oc}$  then  $J_{01}$  becomes increasingly dominant at  $V_{oc}$ . Additionally,  $V_2$  needs to be 120 mV larger than  $V_{oc}$  to negligibly ( $<10\%$ ) contribute to the total recombination rate at  $V_{oc}$ . Generally, the  $n = 2$  diode ( $J_{02}$ ) accounts for recombination in the junction space charge region and at grain boundaries, whereas the  $n = 1$  diode ( $J_{01}$ ) accounts for bulk and surface recombination. The preferable recombination current dominance of  $V_{oc}$  is  $J_{01}$  to provide the best electrical performance at the maximum power point.

External quantum efficiency (EQE) measurements are performed on an Oriel system, with a wavelength step size of 5 nm. EQE( $\lambda$ ), the measure of electron flow under short-circuit conditions into the external circuit per photon incident onto the solar cell, can be converted to IQE( $\lambda$ ) if the total hemispherical reflectance  $R(\lambda)$  and transmittance  $T(\lambda)$  are known. IQE( $\lambda$ ) is then given by

$$IQE(\lambda) = \frac{EQE(\lambda)}{1 - R(\lambda) - T(\lambda)}. \quad (1)$$

A spectrometer (Varian Cary 5G) with integrating sphere is used to measure  $R(\lambda)$  of the cell, with 1 nm steps from 300 nm to 1200 nm. Since the BSF layer in the entire probed sample region is coated with aluminum, no light will be transmitted; hence,  $T(\lambda)$  is zero in this work. Note that this expression neglects optical absorption in the Al and glass, which in turn results in a lower bound for the IQE. A point to remember is that these mesa solar cells are planar and hence, despite the Al back reflector (about half of the 600 nm light reaches the Al which itself has been shown to absorb around 30% of this light [11]), feature poor light trapping.

The EQE and reflectance measurements are performed on the large mesa cell on each glass substrate, ensuring that the entire diameter of the entering monochromatic light beam falls onto the device under test (this prerequisite is not fulfilled by the two small, stripe-like mesa cells on each glass

substrate). The measured EQE data are then used to calculate the corresponding  $J_{sc}$  of the solar cell under 1-Sun illumination. This is achieved by integration of the product of the measured EQE curve and the photon density in the standard terrestrial solar spectrum (AM1.5G, 100 mW/cm<sup>2</sup>). Note that, due to the very large series resistance of the large mesa solar cells (>100  $\Omega$ -cm<sup>2</sup>), the short-circuit current calculated from the EQE curve is larger than the short-circuit current that would be measured under actual AM1.5G illumination.

The sequence of cell fabrication and measurements used for this study was as follows: after the formation of the seed layer, the mesa structure was grown and Suns- $V_{oc}$  measurements were taken. Then the cell had Al contacts formed by evaporation using a shadow mask. After the deposition of Al on the “square-”shaped sample, a single  $V_{oc}$  measurement was performed to verify that good ohmic contact between the pc-Si and the Al was achieved (reduction in  $V_{oc} \leq 5$  mV, no short-circuiting of the diode). Then reflectance and EQE measurements were performed, followed by the IQE calculation. Then the Al was chemically removed, the cell chemically cleaned, and the RTA process performed. The measurement and contact formation sequence were then repeated. The metal contacts were then removed and the cell cleaned, followed by a hydrofluoric acid dip in preparation for the hydrogenation sequence. After the hydrogenation process, the measurement and metal contact formation were repeated.

For the  $V_{oc}$  measurements, each of the samples had between 5 and 10 measurements before the Al deposition (with typically 2 per strip and 3 to 6 per “square”). This is to ensure good statistical accuracy in the measurement and to eliminate any cell that failed during the previous processing step. Additionally, all samples within a plateau time split (900°C and 1000°C groups) were all measured at one time to minimize any drift in the measurement systems.

### 3. EXPERIMENTAL RESULTS

#### 3.1. Suns- $V_{oc}$

Figures 2 and 3 show the effect on  $V_{oc}$  and  $V_x$  before and after hydrogenation resulting from the variation in RTA plateau time at 900°C and 1000°C, respectively. RTA times at 900°C plateau temperature are as follows: no RTA, 30, 60, 135, 165, and 210 seconds. RTA plateau times at 1000°C plateau temperature are as follows: no RTA, 1, 10, 15, and 30 seconds. As might be expected, the  $V_{oc}$  increases, reaches a plateau, and then falls off, especially in the case of a 30-second, 1000°C RTA plateau where the  $V_{oc}$  is severely affected.

In Figure 2, 900°C RTA plateau,  $V_x$  is larger than  $V_{oc}$  after the RTA process, revealing that the samples are  $n = 2$  dominated. It is noted that the measured value for the 135-second plateau sample had errors in 4 of the 5 measurements after RTA—this sample appears to have been damaged during processing and has therefore been eliminated from the study. At 60 seconds, average  $V_{oc}$  values of 236 mV and 399 mV before and after hydrogenation, respectively, are measured. The trend in  $V_{oc}$  after hydrogenation indicates that, for the

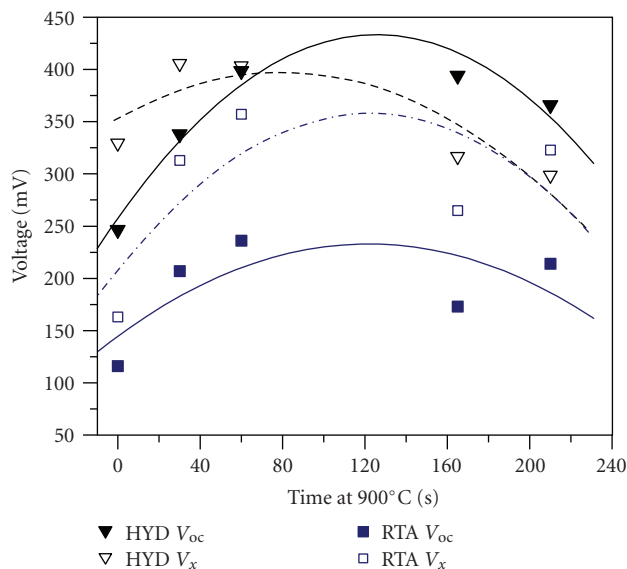


FIGURE 2: Measured  $V_{oc}$  and  $V_x$  following RTA and hydrogenation as a function of RTA plateau time at 900°C. The lines are second-order polynomial fits.

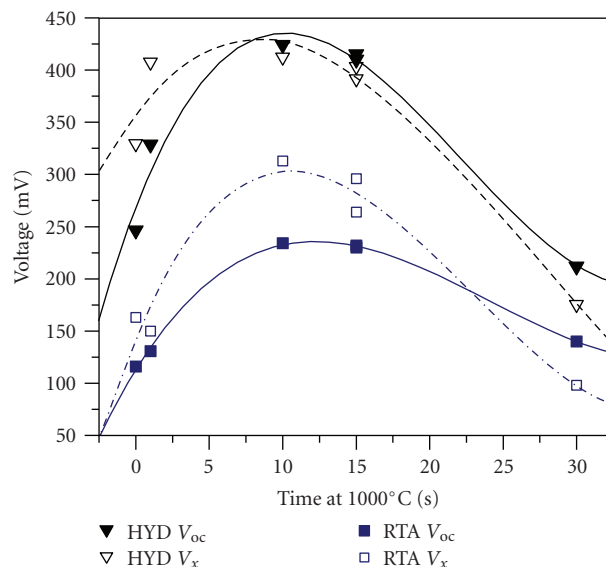


FIGURE 3: Measured  $V_{oc}$  and  $V_x$  following RTA and hydrogenation as a function of RTA plateau time at 1000°C. The lines are third-order polynomial fits.

900°C RTA, a maximum occurs between 60- and 165-second plateau time.

In Figure 3 it can be seen that for the 30-second RTA at 1000°C the device is drastically affected both before and after hydrogenation, most likely due to Al diffusion along grain boundaries (as explained later), causing shunting and drastic smearing of the junction. After the RTA treatment,  $V_x$  is greater than  $V_{oc}$  except in the case of a 30-second 1000°C RTA plateau. At around 10 seconds the  $V_{oc}$  maximizes to an average value of 235 mV and 425 mV before and after hydrogenation, respectively, and in the hydrogenated sample

is approximately equally affected by the two recombination currents.

The variation in  $V_x$  has some interesting characteristics that provide significant insight into what the limiting defects are in the cells. Before hydrogenation,  $V_{oc}$  is more  $J_{02}$  affected, as seen by  $V_x$  being greater than  $V_{oc}$  regardless of RTA temperature and time (except for the extreme case of a 1000°C, 30-second RTA). Following hydrogenation,  $V_x$  is still larger than  $V_{oc}$  for short RTA times ( $\leq 30$  seconds at 900°C and  $\leq 1$  second at 1000°C). The crossover point lies at around 70 seconds and 8 seconds for the 900°C and 1000°C RTA process, respectively. Below this crossover point the  $V_{oc}$  is mostly affected by  $J_{02}$  recombination. Above this crossover point the  $V_{oc}$  is slightly more affected by  $J_{01}$  recombination than  $J_{02}$  recombination in the case of the 1000°C RTA process, yet mostly affected by  $J_{01}$  recombination in the case of the 900°C RTA process.

### 3.2. Quantum efficiency

The effect of a 1000°C RTA process on the IQE of ALICIA cells is shown in Figure 4. Since these are planar multilayer thin-film diodes, there are interference fringes in the EQE and reflectance data. The IQE curve above about 500 nm is affected by light reflecting off of the back contact although, as noted earlier, a significant fraction of the light that reaches the Al back contact is absorbed by the Al. This reflected light effect is most apparent in the “as-grown” curve. Without an RTA the IQE peak sits at around 430 nm and then drastically drops at longer wavelengths, indicating very low effective lifetime of minority carriers in the absorber region. With an RTA the increase in total response is quite large over the entire range of relevant wavelengths (300–1100 nm), showing that the effective lifetimes in all device regions (emitter, junction depletion region, base) have been improved significantly by the RTA process. However, the peak IQE value of merely 40% after RTA shows that the IQE is still too low for efficient conversion of the solar spectrum.

Following hydrogenation for 15 minutes at 620°C, the increase in IQE from a peak of 40% to over 70% is seen (as in Figure 5), and good improvement over all other wavelengths also results. Thus, the effective lifetime in the absorber region is drastically improved by hydrogenation of the 1000°C RTA treated samples. Even with a 1-second RTA plateau time the quantum efficiency improves significantly. Looking at the peaks of the 1-, 10-, and 15-second curves, it can be seen that the longer RTA greatly improves the defect density within the junction and absorber regions, as indicated by the broadening and increased magnitude of the peak. Excessively long RTA times negatively affect the device, as confirmed by the 30-second 1000°C RTA process. Comparing the curves labeled “as-grown” and “no RTA with hydrogenation,” a dramatic increase in the peak IQE from 16% to 41% is seen. Moving to longer wavelengths from the peak response, the effect on the absorber region is large in that effective minority carrier lifetime is greatly increased. This increased effective lifetime in the absorber region is thought to be due to an efficient passivation of the bulk defects and grain boundaries. Hydrogenation alone has at least as much impact on

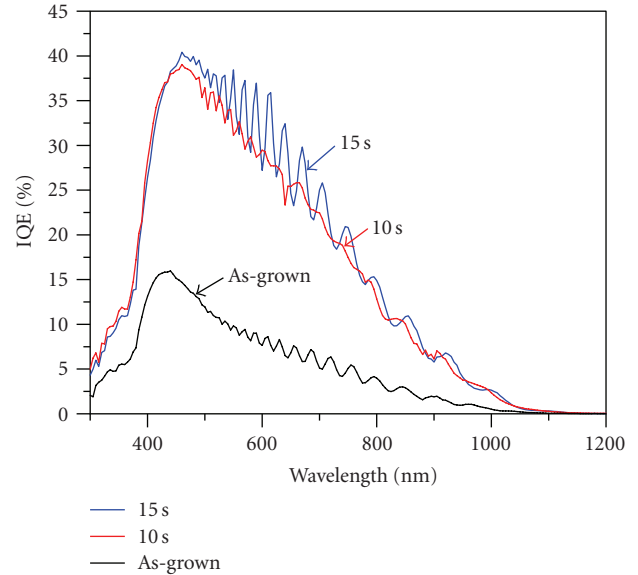


FIGURE 4: Measured IQE of ALICIA cells before and after the 1000°C RTA step. RTA plateau times are 10 and 15 seconds. The curve labeled as-grown is the best IQE measured in the course of this study on as-grown samples.

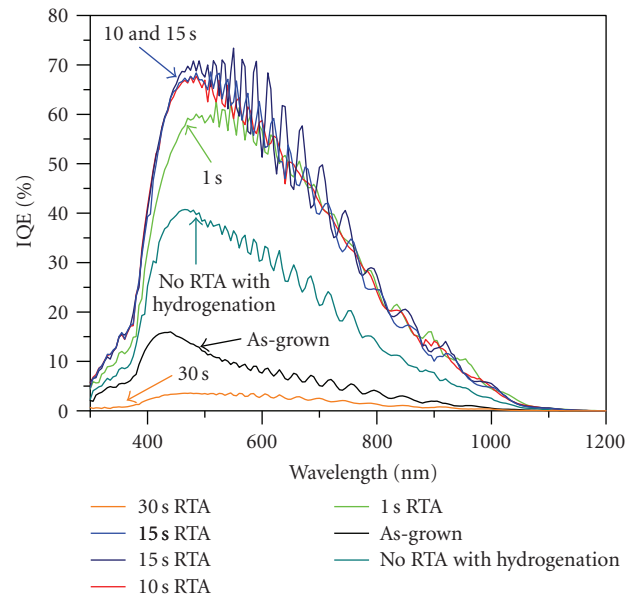


FIGURE 5: Measured IQE of hydrogenated ALICIA cells as a function of the 1000°C RTA plateau time. RTA plateau times are 1, 10, 15, and 30 seconds. Also shown, for comparison, are the IQE of the best as-grown cell and a hydrogenated cell that did not receive an RTA step.

the quantum efficiency of ALICIA solar cells as defect annealing although a combination of both gives the greatest benefit.

In Figure 6 the IQE evolution from the three processing steps for the cell that received a 15-second 1000°C RTA plateau is shown. As-grown, the IQE peaks at a rather poor value of 10% at a wavelength of 430 nm. Following the RTA, the peak IQE response is 40% at 460 nm, with good

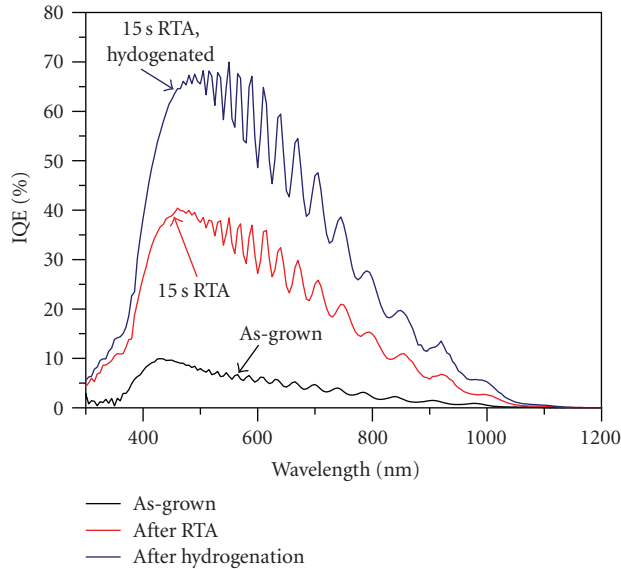


FIGURE 6: Measured improvement of the IQE of an ALICIA cell due to a 15-second 1000°C RTA process and a subsequent hydrogenation process.

improvement in all wavelengths. With a subsequent hydrogenation, the peak IQE response is 68% at 490 nm with significant improvement over all wavelengths. The RTA and subsequent hydrogenation treatment improves the peak IQE value by a factor of 6.8 compared to the as-grown device.

Figure 7 shows the IQE response of hydrogenated samples to RTA plateau time at 900°C. As the RTA plateau time is increased, the peak response moves to longer wavelengths (from around 430 nm as-grown to about 500 nm with a 210-second RTA plateau time). A 60-second RTA plateau time at 900°C shows the best peak response of about 68%. The same IQE trend seen in the 1000°C samples is also seen with a 900°C RTA although differences do exist, namely the large increase in quantum efficiency below 400 nm for two of the cells and relatively modest improvement in the absorber region for the 30-second RTA cell.

### 3.3. Short-circuit current

Using the measured EQE curves,  $J_{sc}$  values for 1-Sun illumination (AM1.5G) can be determined for each cell. Determining the  $J_{sc}$  from the IQE is due to the contacts being optimized for IQE measurements. Figure 8 shows the  $J_{sc}$  results of hydrogenated samples as a function of the 900°C RTA plateau time. Also shown in this graph are the  $V_{oc}$  results of these samples. Figure 9 shows the corresponding graph for the samples that received a 1000°C RTA process. As expected, for both RTA plateau temperatures, the  $J_{sc}$  increases initially, then reaches a maximum, and eventually falls off with increasing RTA plateau time. The IQE evolution of a single cell as it moves through the fabrication stages (see, e.g., Figure 6) has a corresponding  $J_{sc}$  evolution of 1.2, 6.1, and 10.5 mA/cm<sup>2</sup>, respectively, before the RTA process (i.e., as-grown), after the RTA process, and after subsequent hy-

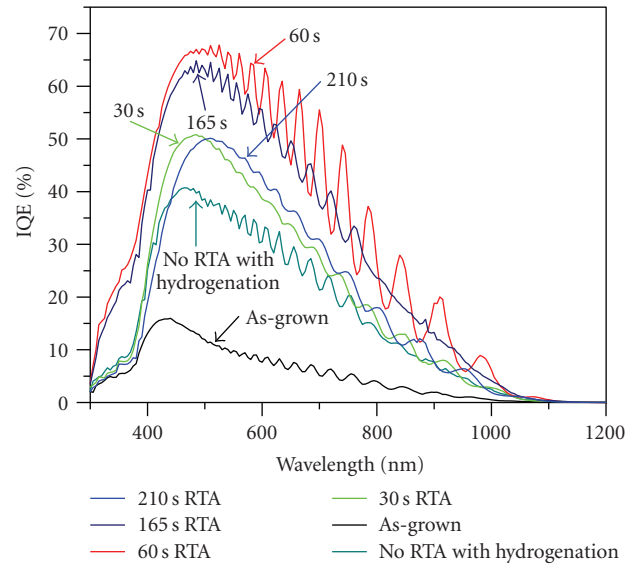


FIGURE 7: Measured IQE of hydrogenated ALICIA cells as a function of the 900°C RTA plateau time. RTA plateau times are 30, 60, 165, and 210 seconds. Also shown, for comparison, are the IQE of the best as-grown cell and a hydrogenated cell that did not receive an RTA step.

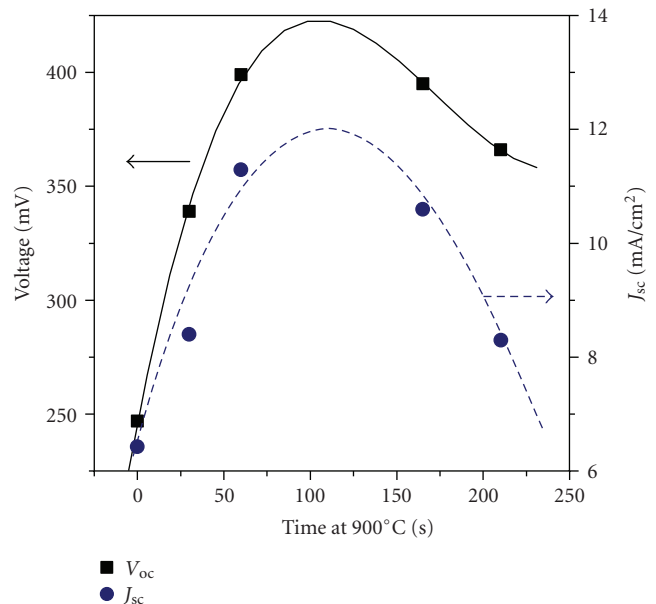


FIGURE 8:  $V_{oc}$  and  $J_{sc}$  evolution for a 900°C RTA plateau after hydrogenation. Lines are third-order polynomial fits.

drogenation. The maximum measured  $J_{sc}$  are 11.3 mA/cm<sup>2</sup> and 10.95 mA/cm<sup>2</sup> for the 900°C and 1000°C RTA process. Interestingly, the  $J_{sc}$  follows the same trend as the  $V_{oc}$  with respect to the RTA plateau time, and hence the product  $J_{sc} \times V_{oc}$  has a sharp peak at the optimal RTA plateau time. From Figures 8 and 9 it follows that the optimal RTA plateau times are about 110 and 11 seconds, respectively, for the 900°C and 1000°C RTA process. With the addition of a good light

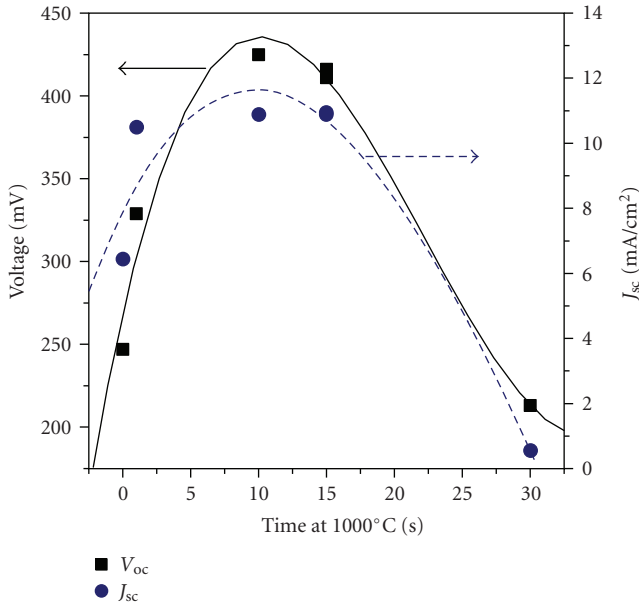


FIGURE 9:  $V_{oc}$  and  $J_{sc}$  evolution for a 1000°C RTA plateau after hydrogenation. Lines are third-order polynomial fits.

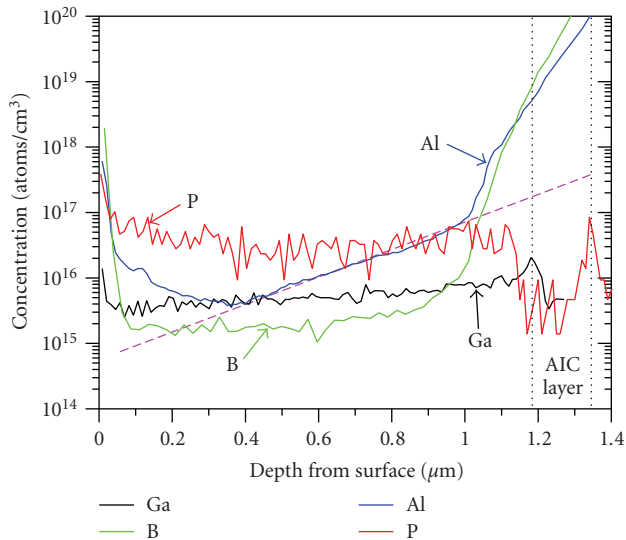


FIGURE 10: SIMS measurement of dopant atoms in the hydrogenated cell that received a 60-second RTA plateau time at 900°C. The dashed line is the estimated Al concentration due to Al diffusion along grain boundaries and in the bulk, as explained in Section 3.6.

trapping scheme such as described in [12, 13], much higher  $J_{sc}$  would result and this is presently being applied to the thin-film solar cells under development in our group.

### 3.4. Summary of electrical measurements

A summary of the measured effects of RTA plateau times at 900°C and 1000°C on peak IQE,  $J_{sc}$ , and  $V_{oc}$  is shown in Table 1. For comparison, the best as-grown cell and a hydrogenated cell that did not receive an RTA process are shown

in the first subsection. In the second subsection, the measured electrical parameters are shown for the cell of Figure 6. The impact on  $J_{sc}$  from only the 15-second 1000°C RTA is enormous, from 1.2 mA/cm<sup>2</sup> to 6.11 mA/cm<sup>2</sup>, a gain of 5, while the  $V_{oc}$  doubles to 230 mV. Similar gains in  $J_{sc}$  and  $V_{oc}$  are seen for the cell that received only a hydrogenation (i.e., no RTA), from 1.91 mA/cm<sup>2</sup> to 6.43 mA/cm<sup>2</sup> and 119 mV to 247 mV, respectively. With only a 1-second 1000°C RTA plateau time and hydrogenation, the majority of gain in  $J_{sc}$  is achieved, yet to maximize  $V_{oc}$  a much longer RTA plateau time is needed.

As seen from Table 1, the optimal RTA time for this solar cell structure is between 10 and 15 seconds at 1000°C to provide the best gain combination in  $J_{sc}$  and  $V_{oc}$ . The best  $V_{oc}$  measured within this study is 430 mV, which was obtained with a 10-second, 1000°C RTA plateau. The best  $J_{sc}$  measured within this study is 11.3 mA/cm<sup>2</sup>, obtained with a 60-second 900°C RTA plateau. Note that natural cooling (lamps are turned off for the cooling phase from 1000°C to 650°C) also results in better IQE,  $V_{oc}$ , and  $J_{sc}$ , most likely due to slightly less time at 1000°C.

### 3.5. SIMS

After the completion of the above quantum efficiency measurements, two samples (60 seconds at 900°C and 10 seconds at 1000°C) were selected, the metal contacts removed, and the samples submitted to SIMS measurements. SIMS was performed by Evans Analytical Group (Calif, USA) using Si standards to measure the requested elements with a concentration accuracy typically within  $\pm 20\%$ . The area of the measured spot was about 100  $\mu\text{m} \times 100 \mu\text{m}$  in each SIMS run. On each sample two SIMS runs were performed on adjacent areas, giving the concentration profiles of the following elements: Al, B, Ga, and P. An additional SIMS measurement was performed on the 1000°C RTA sample to obtain its C, H, N, and O concentrations. Figure 10 shows the measured density of the dopant atoms in the cell that received a 60-second RTA plateau time at 900°C, while Figure 11 shows the corresponding data for the sample that received a 10-second RTA plateau time at 1000°C.

It is noted that the Al analysis is quite complex due to two different reasons: preferential sputtering during SIMS along the grain boundaries and Al inclusions in the AIC layer. Preferential sputtering at grain boundaries, a known effect in large-grained pc-Si, is due to atoms being removed faster at grain boundaries than intragrain, resulting in a nonplanar exposed sample surface. As the sputtering proceeds, the exposed surface becomes more nonuniform. This effect is supported by the order of increase in concentration of Al, N, C, and B (see Figures 11 and 12) as the exposed surface approaches the AIC interface. Al inclusions, a parasitic by-product of the AIC process, are preferentially located at grain boundaries (see Figure 13) and interrupt the uniformity of the seed layer laterally. An SIMS measurement on an ALICIA cell in Straub et al. [7] shows the complication of the Al concentration and the  $p$ - $n$  junction profile due to what is thought to be from both effects. Both of these effects greatly

TABLE 1: Electrical characteristics of ALICIA cells as a function of the RTA plateau time. For comparison, the best as-grown cell and a hydrogenated cell that did not receive an RTA process are shown in the first subsection. Additionally, the electrical results of the cell measured in Figure 6 are shown in the second subsection. “ctrl.” means controlled cooling (lamps on) from plateau, while “natural” means the lamps are set to minimum power until the temperature has dropped to 650°C.

RTA temp. (°C)	RTA time (s)	Peak IQE (%)	$J_{sc}$ (mA/cm <sup>2</sup> )	Average $V_{oc}$ (mV)
N/A	N/A (as-grown)	16	1.91	119
N/A	N/A (no RTA, hydrogenated)	41	6.43	247
N/A	N/A (as-grown)	10	1.2	110
1000	15 (RTA only)	40	6.11	230
1000	Hydrogenated	68	10.87	411
900	30, ctrl. cool	51	8.41	339
900	60, ctrl. cool	68	11.30	399
900	165, ctrl. cool	65	10.55	395
900	210, ctrl. cool	50	8.34	366
1000	1, ctrl. cool	61	10.50	329
1000	10, ctrl. cool	67	10.90	425
1000	15, natural cool	71	10.95	416
1000	15, ctrl. cool	68	10.87	411
1000	30, ctrl. cool	3.6	0.56	213

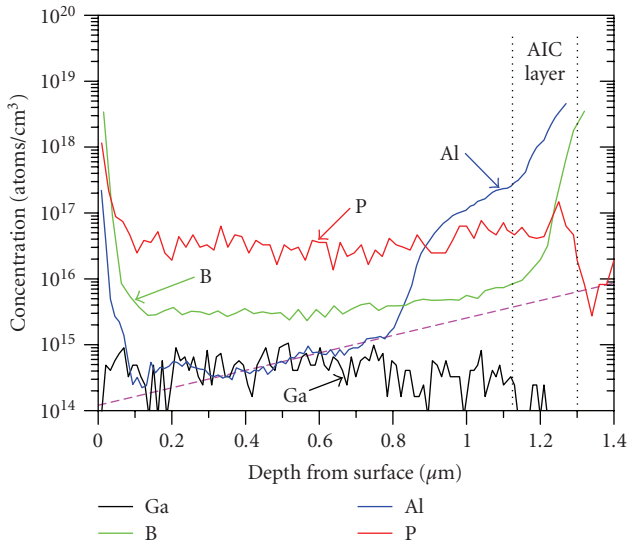


FIGURE 11: SIMS measurement of dopant atoms in the hydrogenated cell that received a 10-second RTA plateau time at 1000°C. The dashed line is the estimated Al concentration due to Al diffusion along grain boundaries and in the bulk, as explained in Section 3.6.

complicate the analysis and require care in the SIMS interpretation.

The Al profile is significantly different in the two cells. In the sample that received the 900°C RTA, the maximum Al concentration in the AIC layer is about  $9.5 \times 10^{19} \text{ cm}^{-3}$ , compared to  $6.5 \times 10^{18} \text{ cm}^{-3}$  for the 1000°C sample. The Al concentration in the AIC layer of the 900°C sample is significantly higher than that of earlier SIMS results on ALICIA cells without Al inclusions [14] which showed a peak value of about  $2 \times 10^{19} \text{ cm}^{-3}$ . In contrast, the Al concentration of the 1000°C sample is about 2 times lower. This indicates that

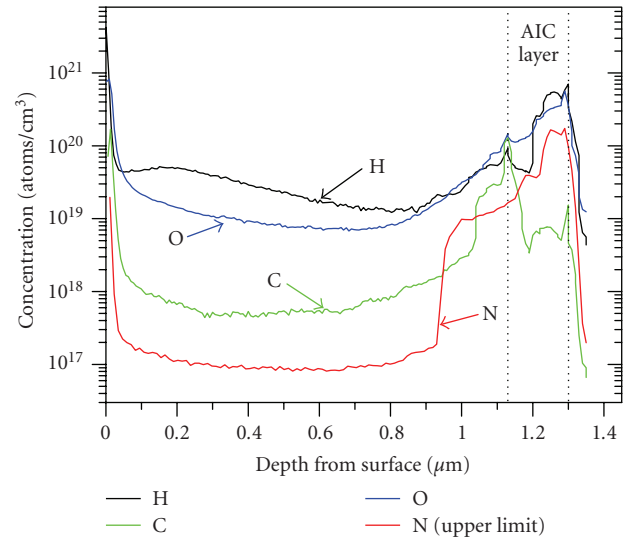


FIGURE 12: SIMS measurement of impurities and hydrogen in the hydrogenated cell that received a 10-second RTA plateau time at 1000°C.

the SIMS results from AIC seed layers must be taken with care.

The Al profiles indicated by the dashed straight lines in Figures 10 and 11 are due to diffusion of Al from the AIC layer during both growth of the absorber (Al is mobile at the temperatures used for growth) and the RTA process. This Al diffusion occurs both along grain boundaries and into the bulk of the grains. A 4-minute 900°C RTA process has previously been shown to increase the Al concentration within the absorber region of ALICIA cells by a factor of  $10^7$ . The concentration of Al in the absorber region of the cell that

received the 900°C RTA plateau is dangerously high with respect to absorber dopant density and *p-n* junction profile. In contrast, in the cell that received the 1000°C RTA plateau, the Al concentration is more than a factor of 10 lower and well below the P concentration until the junction region is reached. At a depth of 0.8  $\mu\text{m}$  in the absorber region, the concentration of Al is  $2.4 \times 10^{16} \text{ cm}^{-3}$  and  $1.5 \times 10^{15} \text{ cm}^{-3}$  for the 900°C and 1000°C RTA plateau cells, respectively.

Gallium does not incorporate well into the crystal structure during growth (due to its high mobility at the temperatures used during growth of ALICIA samples [7, 15]) and has virtually no effect on the actual doping of the samples. In the cell that received the 1000°C RTA plateau, Ga is near the detection limit of SIMS and around a factor of 10 lower than in the cell that received the 900°C RTA plateau.

The phosphorus-doped BSF layer of the SIMS samples is thinner than intended, which is due to (i) several sulfuric acid/hydrogen peroxide cleans and several HF dips between the various fabrication and measurement steps, (ii) the limited temperature ramp rate of our P effusion cell, and (iii) SIMS surface-related artefacts. Hot-probe measurements show that the surfaces of the samples are *n*-type. P concentration within the absorber region is as expected, about  $4 \times 10^{16} \text{ cm}^{-3}$ , and uniform. Figures 10 and 11 show that P smearing from the BSF layer into the absorber region of ALICIA cells is negligible for the two RTA processes examined by SIMS (60 seconds at 900°C and 10 seconds at 1000°C).

The differences in the B profiles of Figures 10 and 11 have yet to be fully explained. Again, preferential sputtering during SIMS along the grain boundaries and Al inclusions in the AIC layer complicate the analysis. The concentration of B in the absorber region is similar yet significantly different in the AIC layer and near the junction region.

The concentration of H in Figure 12 shows substantial penetration throughout the cell structure. A minimum concentration of  $2 \times 10^{19} \text{ cm}^{-3}$  is located near the *p-n* junction. In the first 200 nm of the cell, the H profile is approximately constant. A maximum of  $1.3 \times 10^{20} \text{ cm}^{-3}$  is seen within the emitter, however, this concentration must be taken with care due to the SIMS artefacts at this depth.

The concentration of O within the entire cell structure is relatively high, about one order of magnitude higher than in Cz grown Si (approx.  $1 \times 10^{18} \text{ cm}^{-3}$ ) and about two orders of magnitude higher than in a previously published ALICIA SIMS measurement [7]. This previously published result was obtained on an ALICIA cell before an RTA treatment. While this sample showed that the O contamination during our non-UHV silicon epitaxy process can be kept at low levels, it is not representative for the O content of actual ALICIA cells after RTA. The high O content of the sample of Figure 12 is believed to be due to the RTA process.

The amount of C in the absorber region is around  $5 \times 10^{17} \text{ cm}^{-3}$  as compared to the concentration of about  $1 \times 10^{16} \text{ cm}^{-3}$  in a Cz Si wafer. The C profile shows a pronounced peak of about  $1 \times 10^{20} \text{ cm}^{-3}$  at the original AIC surface. The N concentration in the absorber region is relatively low (about  $1 \times 10^{17} \text{ cm}^{-3}$ ) although does rise substantially at a depth of 0.93  $\mu\text{m}$  from the surface, just after the rise in Al

at 0.8  $\mu\text{m}$ . This sharp rise in N is believed to be due to the same reasons that cause the complications with the Al profile (i.e., enhanced sputtering rate along grain boundaries and Al inclusions).

### 3.6. Discussion

Based on the above results, conclusions can be drawn that further explain the effects that are seen from RTA and hydrogenation. One possible reason for the relatively modest improvement of the IQE around 500 nm for the 30-second 900°C RTA cell (see Figure 7) is the combination of the junction space charge region still being near the absorber/AIC interface (which is thought to have a large density of defects and impurities, especially C as shown in Figure 12) and also the need for additional grain boundary improvement through secondary grain growth (removing the assumed confined amorphous layer along grain boundaries, see [16–18]). It is possible that some amorphous Si exists in the grain boundaries after an ALICIA cell has been grown. During the RTA, this amorphous material is incorporated into the grains as the grains grow to minimize grain boundary area (reduction in overall energy [16]), shrinking, and eventually eliminating the amorphous layer. Lateral conduction is also increased by this process. Additionally, small poor-quality grains have been seen to exist between the larger-gained material in ALICIA samples. Hydrogenation further improves the cell performance by passivating dangling bonds and impurities within the cell. By passivating the dangling bonds at the grain boundaries, the width of the depletion region surrounding each grain boundary is reduced, increasing lateral conduction and reducing recombination in the entire cell.

The shift of the wavelength corresponding to the peak of the IQE curve from around 430 to around 470 nm for the 1000°C sample (see Figure 5) and the broadening of the peak response provide some idea of the smearing of the junction from emitter diffusion deeper into the absorber region as verified by SIMS. Diffusion of dopants from the AIC layer deeper into the absorber region moves the *p-n* junction away from the defected and contaminated absorber/AIC interface, also reduce recombination. As such, the initial Si crystal growth quality on the epitaxy interface must be improved along with minimizing the impurity concentration to achieve better device performance. The RTA plateau time might then be reduced to limit the diffusion of Al into the absorber region, resulting in a narrower emitter and lower Al concentration in the absorber. A thinner seed layer would help with blue response by having a much narrower dead layer (emitter).

From the Suns- $V_{oc}$  measurements and the  $J_{sc}$  values calculated from the measured EQE (see Figures 8 and 9), the optimal RTA plateau times are about 100 and 10 seconds for the 900°C and 1000°C RTA process, respectively. The solar cell efficiency is furthermore affected by the fill factor (FF) of the current-voltage curve. Given that  $n = 1$  recombination produces higher FF values than  $n = 2$  recombination, the optimum RTA time is also affected by the diode's ideality factor near the 1-Sun maximum power point. The maximum power point voltage is approximately equal to the  $V_{oc}$

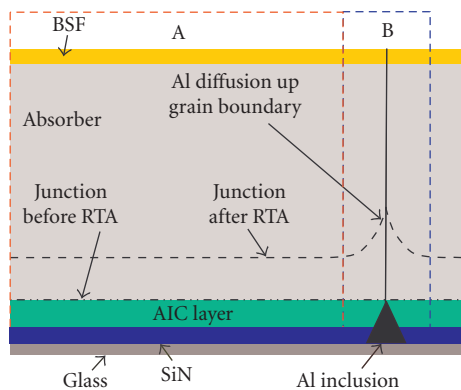


FIGURE 13: Schematic representation of  $p$ - $n$  junction location before and after RTA, including enhanced diffusion of Al along a grain boundary. The areas denoted as “A” and “B” refer to the intragrain region and grain boundary region, respectively. An Al inclusion is shown which can exist in the AIC layer at the grain boundary. Drawing not to scale.

measured at a light intensity of 0.1 Suns. In terms of  $V_x$ , the optimal FF is thus realized for the situation where the 1-Sun  $V_{oc}$  is much larger than  $V_x$ . As can be seen from Figures 2 and 3, this slightly increases the optimal RTA plateau time for both investigated RTA temperatures. With respect to solar cell efficiency, the two RTA plateau temperatures investigated are performing approximately equally, with the hotter RTA process ( $\sim 11$  seconds at  $1000^\circ\text{C}$ ) giving better  $V_{oc}$  but slightly lower  $J_{sc}$  and FF than the colder RTA process ( $\sim 110$  seconds at  $900^\circ\text{C}$ ).

Enhanced diffusion of Al along grain boundaries of ALICIA material due to the RTA process has recently been confirmed by Inns and Campbell [19] where the  $p$ - $n$  junction is shown to extend along a grain boundary using high-resolution electron-beam-induced current measurements. A schematic representation of this effect is shown in Figure 13 where there is enhanced diffusion along the grain boundary in region “B” in contrast to normal diffusion in region “A.” Al is the fastest diffuser of the typical dopants in Si [15, 20] and especially in the open structure of grain boundaries in pc-Si [16]. The depth of enhanced diffusion down grain boundaries compared to intragrain diffusion has been shown to be inversely dependent upon temperature, that is, a hotter RTA process results in a shallower diffusion depth in the grain boundary [21, 22]. The enhanced diffusion is dependent upon the grain boundary properties such as width of the grain boundary, diffusivity within the grain, and diffusivity from the grain boundary into the grain. The inverse temperature dependence reported in the literature for this effect is confirmed by our results, that is, much lower concentration of Al in the absorber region as shown by the dashed lines in Figures 10 and 11 and a sharper rise in Al at around  $0.8\ \mu\text{m}$  in depth for the  $1000^\circ\text{C}$  RTA plateau sample. The analysis is quite complicated due to preferential sputtering and Al inclusions. The determination of the diffusivity within grains and along grain boundaries for the ALICIA cell is ongoing and includes effects such as dopant and impurity segregation to grain boundaries and secondary grain growth.

The differences in the B profiles in/near the AIC layers in the two SIMS results (see Figures 10 and 11) are very likely due to the same reasons that caused the artefacts in the Al profiles and thus should be ignored. Similarly, the high boron concentration in the BSF layer is very likely a surface-related artefact of the SIMS measurements (it is well known that the results from the first  $\sim 50$  nm of probed material should not be trusted in standard SIMS). We have verified the doping polarity of the exposed surface region of our samples with hot-probe measurements, and the clear result was that the surface region is  $n$ -type. The B peak near the SiN interface is thought to come from the borosilicate glass substrate (Borfloat33).

Oxygen is well known to be a thermal donor in Si and forms at least eight different thermal donor species during annealing at  $450^\circ\text{C}$  with additionally reported donor formations for heat treatments between  $550^\circ\text{C}$  and  $800^\circ\text{C}$ . Oxygen is easily passivated by H which forms a stable bond up to above  $400^\circ\text{C}$ . In this study, the high concentration of O seems to have been well passivated resulting in substantial  $V_{oc}$  and  $J_{sc}$  gains due to hydrogenation.

It has been reported that even a thin heavily doped  $n$ -type layer greatly impedes H diffusion into  $p$ -type Si [23], however, in ALICIA material this seems not to be a problem. The most likely reason for the very effective hydrogenation of our samples is the high sample temperature ( $260^\circ\text{C}$ ) and the high plasma power (3.2 kW) used during the process. The grain boundaries could also play a role in this, as they are known to provide a pathway for enhanced diffusion of H into pc-Si films [23, 24], although this effect is dependent upon grain boundary properties. The relatively fast rise in the concentration of both H and N encountered in the emitter region supports preferential grain boundary sputtering. The SiN layer has a high concentration of both H and N which is seen well before the AIC/glass interface.

#### 4. COMPUTER MODELING

To determine the effect of the different solar cell processing steps on the minority carrier lifetimes in the devices, the one-dimensional semiconductor simulator PC1D [25] is used to fit the measured IQE and  $J_{sc}$ . For these fits, a two-region device (vertical stack) is used where region 1 is a low-lifetime region simulating the highly defective pc-Si of the AIC layer and the interface region (which together form most of the emitter of the ALICIA cell) and region 2 encompasses the remaining emitter region (formed by diffusion of Al), the base, and the BSF layer. Doping profiles are designed to approximate the results obtained from the SIMS measurements using a combination of Gaussian and erfc profiles for the emitter and  $p$ - $n$  junction, while an erfc profile is used for the BSF. The depth of the  $p$ - $n$  junction below the cells’ illuminated surface is varied until good agreement between measured and fitted peak IQE values is obtained. The material parameters of single-crystal Si were assumed. Other selected PC1D parameters include: internal reflectance front surface = 80%, rear surface = 67%; rear external reflectance = 95%; and front surface recombination  $S_n = S_p = 90000\ \text{cm/sec}$ . The main fit parameters in

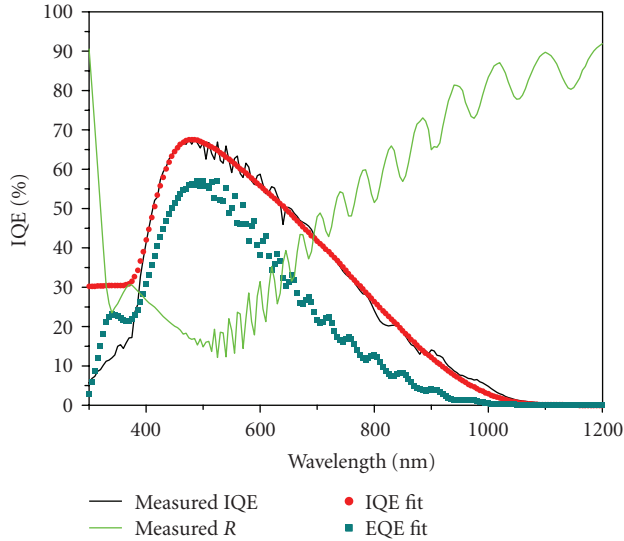


FIGURE 14: PC1D fit to the measured IQE and reflectance of an ALICIA cell.

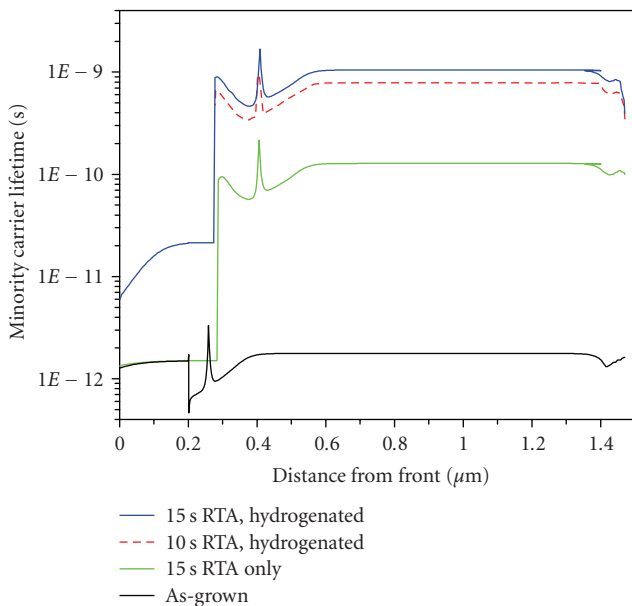


FIGURE 15: Evolution of the minority carrier lifetimes in ALICIA cells due to 1000°C RTA treatment and subsequent hydrogenation, as determined by PC1D analysis of measured IQE curves.

these PC1D simulations are the defect- (i.e., Shockley-Read-Hall recombination) related bulk lifetimes in the two regions. The mobility of free carriers in pc-Si materials is significantly lower than in high-purity single-crystal Si and is dependant on grain size and grain boundary properties [18, 26]. Due to the assumption of single-crystal silicon mobility values in the PC1D simulations, the lifetimes obtained are lower bounds to the actual lifetimes. It is noted that the crystal grains of ALICIA cells are pancake-like (i.e., the grain size is typically much larger than the film thickness) and hence the above PC1D simulations of the cells' short-circuit currents are rep-

resentative of region A in Figure 13. An IQE fit to the measured data using PC1D is shown in Figure 14.

Figure 15 shows the evolution of the minority carrier lifetimes in ALICIA cells due to a 15-second RTA treatment at 1000°C and subsequent hydrogenation, as determined by PC1D analysis of measured IQE curves. Also shown, for comparison, is the carrier lifetime of a hydrogenated sample that received a 10-second RTA at 1000°C (dashed line). As can be seen from these PC1D results, the 1000°C RTA process improves the minority carrier lifetime in the base region of the investigated cells by about 2 orders of magnitude. Subsequent hydrogenation provides a further one order of magnitude improvement of the minority carrier lifetime to a value of about 1 nanosecond, which corresponds to a lower bound for the diffusion length in the base region of about 1000 nm.

## 5. CONCLUSION

In this paper the impact of rapid thermal annealing at 900°C and 1000°C and subsequent hydrogenation at 620°C on ALICIA pc-Si thin-film solar cells on low-temperature glass has been investigated experimentally. A strong increase in  $V_{oc}$  from 120 mV to 430 mV,  $J_{sc}$  from 1.2 mA/cm<sup>2</sup> to 11.3 mA/cm<sup>2</sup>, and peak IQE from 16% to >70% in the best devices has been achieved. The effect of hydrogenation in removing defects that limit the current and voltage of the cells is enormous, resulting in a gain in  $J_{sc}$  of a factor of over 3 from hydrogenation alone. A 1-second RTA at 1000°C followed by a hydrogenation process increases the  $J_{sc}$  by more than a factor of 5. From the behavior of the cell voltages ( $V_{oc}$ ,  $V_x$ ) it follows that the RTA greatly reduces the density of grain boundary and space charge region defects, while hydrogenation is extremely effective in passivating grain boundaries, surfaces, and bulk defects of various sorts. As the RTA plateau time is increased, the evolution in defect density is seen in both  $Suns-V_{oc}$  and IQE measurements. Smearing of the junction space charge region is thought to mostly be from the diffusion of Al along-grain boundaries, limiting the RTA time at 900°C and 1000°C to  $\leq 165$  seconds and  $\leq 15$  seconds, respectively. Both  $V_{oc}$  and  $J_{sc}$  reach a maximum with the same RTA plateau time, for both RTA plateau temperatures investigated. SIMS measurements confirm that grain boundary diffusion is greatly reduced for the 1000°C RTA process compared to the 900°C process, although the time at plateau temperature is limited to 15 seconds as seen by the drastic reduction in electrical properties with a 30-second, 1000°C RTA plateau. Using PC1D simulations, minority carrier lifetime in the absorber region is shown to increase by about 3 orders of magnitude to a value of about 1 nanosecond due to RTA and subsequent hydrogenation, which corresponds to a diffusion length of at least 1  $\mu$ m in the final devices. The evaluation of the passivation of defects has led to a better understanding of the factors limiting the performance of present ALICIA cells, paving the way towards ALICIA cells with a  $V_{oc}$  greater than 500 mV and a  $J_{sc}$  above 15 mA/cm<sup>2</sup>.

## ACKNOWLEDGMENTS

This work has been supported by the Australian Research Council. M. L. Terry and D. Inns acknowledge Ph.D. scholarships from UNSW. The authors would like to thank all group members that have contributed to the present state of the ALICIA cell technology.

## REFERENCES

- [1] M. L. Terry, A. Straub, D. Inns, D. Song, and A. G. Aberle, "Large open-circuit voltage improvement by rapid thermal annealing of evaporated solid-phase-crystallized thin-film silicon solar cells on glass," *Applied Physics Letters*, vol. 86, no. 17, Article ID 172108, 1–3, 2005.
- [2] M. L. Terry, P. I. Widenborg, O. Kunz, and A. G. Aberle, "Effects of Rapid thermal annealing and hydrogen passivation on crystalline silicon thin-film solar cells on glass made by PECVD solid-phase crystallization," in *Proceedings of Technical Digest of 15th International Photovoltaic Science & Engineering Conference (PVSEC '05)*, pp. 905–906, Shanghai, China, October 2005.
- [3] M. L. Terry, D. Inns, and A. G. Aberle, "Massive improvement through rapid thermal annealing and hydrogen passivation of pc-Si thin-film solar cells on glass based on aluminum induced crystallization," in *Proceedings of the IEEE 4th World Conference on Photovoltaic Energy Conversion*, pp. 1560–1563, Waikoloa, Hawaii, USA, May 2006.
- [4] M. I. Keevers, A. Turner, U. Schubert, P. A. Basore, and M. A. Green, "Remarkably effective hydrogenation of crystalline silicon on glass modules," in *Proceedings of the 20th European Photovoltaic Solar Energy Conference (PVSEC '05)*, pp. 1305–1308, Barcelona, Spain, June 2005.
- [5] A. Slaoui, E. Pihan, I. Ka, N. Mbow, S. Roques, and J. Koebel, "Hydrogen induced passivation of fine-grained polycrystalline silicon films," in *Proceedings of the Technical Digest of 15th International Photovoltaic Science & Engineering Conference (PVSEC '05)*, pp. 951–952, Shanghai, China, October 2005.
- [6] A. G. Aberle, A. Straub, P. I. Widenborg, A. B. Sproul, Y. Huang, and P. Campbell, "Polycrystalline silicon thin-film solar cells on glass by aluminium-induced crystallisation and subsequent ion-assisted deposition (ALICIA)," *Progress in Photovoltaics: Research and Applications*, vol. 13, no. 1, pp. 37–47, 2004.
- [7] A. Straub, D. Inns, M. L. Terry, R. Gebbs, and A. G. Aberle, "The influence of defects and postdeposition treatments on the free carrier density in lightly phosphorus-doped large-grained polycrystalline silicon films," *Journal of Applied Physics*, vol. 98, no. 2, Article ID 023507, 7 pages, 2005.
- [8] P. I. Widenborg and A. G. Aberle, "Surface morphology of poly-Si films made by aluminium-induced crystallisation on glass substrates," *Journal of Crystal Growth*, vol. 242, no. 3–4, pp. 270–282, 2002.
- [9] R. A. Sinton and A. Cuevas, "A quasi-steady-state open-circuit voltage method for solar cell characterization," in *Proceedings of 16th European Photovoltaic Solar Energy Conference*, pp. 1152–1155, Glasgow, UK, 2000.
- [10] O. Kunz, D. Inns, A. B. Sproul, and A. G. Aberle, "Application of suns-voc and jsc-suns measurements to the characterization of mesotype thin-film solar cells," in *Proceedings of 21st European Photovoltaic Solar Energy Conference and Exhibition*, pp. 374–377, Dresden, Germany, September 2006.
- [11] D. Inns, T. Puzzer, and A. G. Aberle, "Localisation of the p-n junction in poly-silicon thin-film diodes on glass by high-resolution crosssectional EBIC imaging," *Thin Solid Films*, vol. 515, no. 7–8, pp. 3806–3809, 2007.
- [12] N. Chuangsuwanich, P. I. Widenborg, P. Campbell, and A. G. Aberle, "Light trapping properties of thin silicon films on AIT-textured glass," in *Proceedings of the Technical Digest 14th International Photovoltaic Science and Engineering Conference (PVSEC '04)*, pp. 325–326, Bangkok, Thailand, January 2004.
- [13] A. G. Aberle, P. I. Widenborg, and N. Chuangsuwanich, "Glass texturing," International PCT patent application PCT/AU2004/000339, 2004.
- [14] O. Nast and S. R. Wenham, "Elucidation of the layer exchange mechanism in the formation of polycrystalline silicon by aluminum-induced crystallization," *Journal of Applied Physics*, vol. 88, no. 1, Article ID 124132, 124–132, 2000.
- [15] S. K. Ghandhi, *VLSI Fabrication Principles Silicon and Gallium Arsenide*, John Wiley & Sons, New York, NY, USA, 2nd edition, 1994.
- [16] T. Kamins, *Polycrystalline Silicon for Integrated Circuits and Displays*, Kluwer Academic, Dordrecht, The Netherlands, 2nd edition, 1998.
- [17] S. Banerjee and S. T. Dunham, "Two Stream model for dopant diffusion in polysilicon incorporating effects of grain growth," in *Proceedings of the Process Physics and Modeling in Semiconductor Technology*, pp. 92–100, Pennington, NJ, USA, 1996.
- [18] P. P. Altermatt and G. Heiser, "Predicted electronic properties of polycrystalline silicon from three-dimensional device modeling combined with defect-pool model," *Journal of Applied Physics*, vol. 92, no. 5, pp. 2561–2574, 2002.
- [19] D. Inns and P. Campbell, internal communication, 2006.
- [20] O. Krause, H. Ryssel, and P. Pichler, "Determination of aluminum diffusion parameters in silicon," *Journal of Applied Physics*, vol. 91, no. 9, pp. 5645–5649, 2002.
- [21] P. H. Holloway, "Grain boundary diffusion of phosphorus in polycrystalline silicon," *Journal of Vacuum Science Technology*, vol. 21, no. 1, pp. 19–22, 1982.
- [22] H. F. Mataré, "Comments and reply," *Journal of Vacuum Science Technology B*, vol. 1, no. 1, pp. 107–108, 1983.
- [23] S. Pearton, J. Corbett, and M. Stavola, *Hydrogen in Crystalline Semiconductors*, Springer, Berlin, Germany, 1992.
- [24] N. H. Nickel, W. B. Jackson, and J. Walker, "Influence of grain boundaries on hydrogen transport in polycrystalline silicon," *Journal of Non-Crystalline Solids*, vol. 227–230, pp. 885–889, 1998.
- [25] Paul A. Basore, "Numerical modeling of textured silicon solar cells using PC-1D," *IEEE Transactions on Electron Devices*, vol. 37, no. 2, pp. 337–343, 1990.
- [26] P. P. Altermatt and G. Heiser, "Development of a three-dimensional numerical model of grain boundaries in highly doped polycrystalline silicon and applications to solar cells," *Journal of Applied Physics*, vol. 91, no. 7, pp. 4271–4274, 2002.

## Review Article

# Thin-Film Solar Cells Based on the Polycrystalline Compound Semiconductors CIS and CdTe

Michael Powalla<sup>1</sup> and Dieter Bonnet<sup>2</sup>

<sup>1</sup> *Zentrum für Sonnenenergie- und Wasserstoff-Forschung Baden-Württemberg (ZSW), Industriest 6, 70565 Stuttgart, Germany*

<sup>2</sup> *SOLARPACT, Breslauer Ring 9a, 61381 Friedrichsdorf, Germany*

Received 7 May 2007; Accepted 18 July 2007

Recommended by Armin G. Aberle

Thin-film photovoltaic modules based on Cu-In-Ga-Se-S (CIS) and CdTe are already being produced with high-quality and solar conversion efficiencies of around 10%, with values up to 14% expected in the near future. The integrated interconnection of single cells into large-area modules of  $0.6 \times 1.2 \text{ m}^2$  enables low-cost mass production, so that thin-film modules will soon be able to compete with conventional silicon-wafer-based modules. This contribution provides an overview of the basic technologies for CdTe and CIS modules, the research and development (R&D) issues, production technology and capacities, the module performance in long-term outdoor testing, and their use in installations.

Copyright © 2007 M. Powalla and D. Bonnet. This is an open access article distributed under the Creative Commons Attribution License, which permits unrestricted use, distribution, and reproduction in any medium, provided the original work is properly cited.

## 1. INTRODUCTION

A high potential for cost reduction is expected for the production of thin-film photovoltaic modules as compared to conventional silicon-wafer-based methods [1]. Regardless of the material, all thin-film techniques have advantages because of their low active material consumption and costs, the monolithic integration of cells, and independence from shortages in solar-grade silicon supplies. Thin-film module production involves fewer processing steps than silicon, and allows a higher degree of automation. Industrially produced modules attain efficiencies between 8 and 12% on the square-meter scale with individual modules exceeding  $50 \text{ W}_p$  (watts peak), and expected long-term stability over more than 20 years—all requirements to successfully gain long-term acceptance in the power market.

Thin-film PV is also especially suited to meet particular product needs, such as flexibility or utilizing an already present surface, like the product's housing or a façade, as the substrate. Furthermore, most thin-film PV producers use glass substrates and can profit from the experience and commercial equipment available from the glass-coating industry, as well as from their know-how in glass applications such as building façades. In the future, a flexible substrate will enable the production of lightweight, flexible modules by using the cost-efficient roll-to-roll method.

In this article, we will describe and compare the basic principles of CIS and CdTe solar cells and modules. We will include an overview of the potentials of these technologies and of the R&D issues under investigation. Afterwards, we will describe how the large-area mass production of CIS and CdTe solar modules is realized in real factories and present an overview of the current production activities worldwide.

## 2. BASIC PRINCIPLES

Both CdTe and CIS employ a stack of functional thin-film layers to create an efficient photovoltaic heterojunction. A window/absorber design localizes the greater part of the charge carrier generation and separation within the absorber layer, avoiding excessive recombination within the window layer or at the interface between these layers. In this construction, the window layer has a higher band gap in order to transmit the sunlight to the absorber layer and a high level of doping in order to minimize the resistive losses and provide an electrical contact. Since the crucial processes of charge carrier generation and separation take place within the absorber layer, this material largely defines the characteristics of the solar cell and traditionally lends its name to the technology—CdTe for cadmium telluride and CIS for the range of chalcopyrite compounds  $\text{Cu}(\text{In}, \text{Ga})(\text{S}, \text{Se})_2$ . Figure 1 illustrates the basic cell design for both heterojunctions.

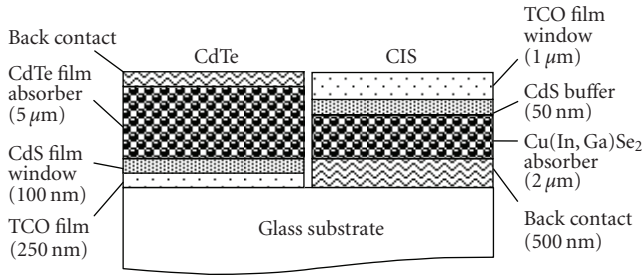


FIGURE 1: Layer sequence for polycrystalline thin-film CdTe and CIS solar cells.

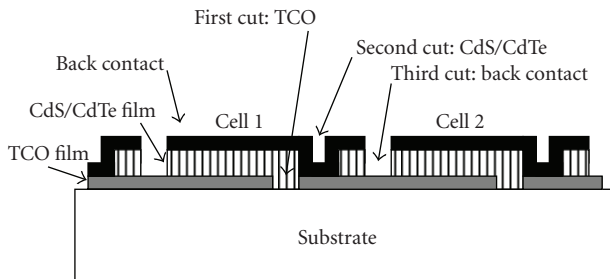


FIGURE 2: Monolithic interconnection illustrated for CdTe modules.

CdTe solar cells are processed on the front glass, so the first layer is a transparent conductive oxide (TCO) for the front contact. It is followed by the CdS window layer and the CdTe absorber layer. A back contact completes the device. The chemically very stable CdS and CdTe compounds are relatively easy to deposit stoichiometrically within a wide processing range from 400°C up to 600°C. Typically, the close-spaced sublimation method is used to deposit the semiconducting films [2]. A slight natural nonstoichiometry produces the desired p-doping of CdTe and n-doping of CdS, respectively. After deposition, the CdS-CdTe junction must be “activated” to achieve high photovoltaic efficiencies. The process involves annealing at temperatures between 400 and 500°C in the presence of Cl-containing species, generally CdCl<sub>2</sub> [3]. Efficiencies exceeding 16% have been achieved with laboratory cells [4].

The layer sequence for CIS solar cells is also illustrated in Figure 1. CIS cells are processed from back to front, so the Mo back contact does not need to be optically transparent. The CIS absorber film follows. CIS can either be deposited directly, for example, by thermal coevaporation of the elements, or indirectly by first depositing more simple precursor layers which then react in a subsequent processing step to form the compound semiconductor [5]. The CIS materials system is more complex than CdTe and has higher demands on the process control systems. However, it also offers more freedom for optimization, for example, by integrating gradients [6]. CIS solar cells typically employ an extremely thin CdS film deposited in a chemical bath followed by a sputtered intrinsic ZnO film and the transparent conductive ZnO : Al window layer, also deposited by sputtering. CIS devices have achieved the highest efficiencies of all thin-film solar cells, at values approaching 20% [7].

TABLE 1: Overview of current status of CIS and CdTe solar cells and modules.

Type	CIS	CdTe
Laboratory best (cell)	19.5% [7]	16.5% [4]
Large-area best (module)	13% [8]	11% [9]
Production average (module)	11.5% [10]	9% [11]

A major advantage of thin-film photovoltaic module processing lies in the monolithic series interconnection of cells to form modules with higher voltages. Whereas silicon wafer-based solar cells are connected by welding conductors onto both sides of the wafers, thin-film cells are flexibly defined and interconnected through simple patterning steps integrated into the processing line. The techniques are similar for both CdTe and CIS technologies. Three scribes between deposition steps accomplish the cell definition, separation, and series interconnection. The optimum cell width is defined by the amount of active area lost to scribing, the series resistance, and the desired output module voltage. The TCO properties can also be integrated into the optimization. Figure 2 illustrates the monolithic interconnection for CdTe modules. The first and third cuts separate the cells at the front and back contacts, respectively. The second cut enables the back contact of cell 1 to connect with the front contact of cell 2. The monolithic interconnection of CIS modules occurs in the same manner, just in the reverse processing sequence (the first cut separates the back contact and the third cut separates the front contact).

In the final processing steps, the contact leads are attached to the first and last cells and the modules are hermetically sealed against environmental effects by encapsulation with a lamination foil and a second glass plate. Frames and contact boxes complete the commercial modules.

An overview of the current state-of-the-art is given in Table 1. The minimum efficiencies required for profitable systems can be achieved with both systems. The large-area modules for both systems are about 6 percent points less efficient than the best laboratory cells, a good indication that module performance will continue to improve in the future. The efficiencies achieved with the CIS technology are generally 2 to 3 percent points higher than for CdTe. However, since it is the cost per watt peak which will define the commercial success of the modules, the more simple processing of CdTe can lead to lower production costs and a competitive product. Both technologies must of course compete with conventional silicon-based modules.

### 3. RESEARCH AND DEVELOPMENT TOPICS

Both the CdTe and CIS technologies have the potential to compete with traditional Si-wafer-based photovoltaic modules in the commercial market. While CdTe has a higher potential for cost reduction due to its simple processing, CIS has the potential to achieve higher efficiencies, thereby lowering the price per watt of generated power. Each material system has its specific issues requiring R&D efforts.

Two major issues for the CdTe technology are the activation step and the back contact to CdTe. The activation step leads to interdiffusion at the CdS/CdTe interface, thereby reducing the defect density and improving the morphology [12]. However, its effects are still being investigated. Research results could enable further optimization or even elimination of the activation step. The low p-type doping and relatively high energy gap of CdTe complicates the contacting. A practical solution consists of generating a highly doped back-surface layer in the semiconductor through which charge carriers can pass via the tunneling effect. The current technique involves generating a highly doped accumulation layer on the CdTe surface by chemical etching, followed by depositing a p-type narrow-band-gap chemically inert semiconductor or semimetal buffer layer and the metal contact [13].

The CIS technology would also benefit from further integration of the processing steps. One issue is the need to break vacuum for the wet-chemical CdS buffer deposition before reentering vacuum for the window deposition steps. Modifications to replace or even eliminate the buffer layer are therefore being explored [14]. Although CdS, too, can be thermally evaporated, thicker films are required for complete coverage and the process is less robust than the wet-chemical deposition. Since photons absorbed in the buffer layer do not contribute to the current generation, thicker films represent a source of loss. Absorption in the buffer layer also motivates the search for an alternative material with a higher band gap.

Significant efforts are also under way for the production of CIS solar modules on flexible substrates [15]. Changing the substrate is not trivial: it may introduce undesirable impurities in the absorber, sodium, which diffuses from the soda lime glass in the standard process and which improves the absorber film quality by increasing its charge carrier density [16], may not be present, the allowed processing temperatures may not be sufficient for high film quality, and additional films may become necessary, such as an insulating layer for the monolithic interconnection on conductive substrates.

Moreover, the long-term goal to significantly increase the CIS cell efficiency to more than 20% will only be achievable through a better fundamental understanding of CIS [17, 18]. The CIS technology has a high potential for improvement, with efficiencies of up to 25% for cells and 18% for modules believed possible. All inhomogeneities, metastabilities, doping mechanisms, and so forth, must be better understood. The wide range of compositions possible in the Cu-In-Ga-Se-S system complicates the collection and comparison of scientific data. Fundamental research is needed both on reference systems, like high-quality laboratory absorber films, and on industrially produced absorber layers. New techniques like measuring electron-beam-induced currents in the junction configuration, micro-photoluminescence, and micro-Raman spectroscopy are opening the doors for understanding the recombination mechanism [19] in real devices and for exploring the role of inhomogeneities.

Furthermore, both technologies are exploring alternative methods of material synthesis, like electrodeposition, spraying, and screen printing, because of their potential for reducing production costs and materials consumption. Several

production parameters like deposition rates and other modifications undergo continuous optimization for improved throughput and yield.

#### 4. STANDARD MODULE PROCESSING

For the industrial production of thin-film modules, high-throughput in-line coating systems are required for each processing step as well as automated mechanisms to transfer the glass panes from each step to the next one. Figure 3 illustrates a module processing line like the one used for CdTe module production. The numbers relate to Table 2 which describes the processing steps for both CIS and CdTe modules. The production begins with cleaning the substrate glass (1) in a washer. Step (2) is the sputter deposition of either the Mo back contact for CIS or the TCO front contact for CdTe. The initial film is patterned with a laser in step (3). Steps (4), (5), and (6) involve the junction deposition and formation. For CIS the absorber layer of Cu(In, Ga)Se<sub>2</sub> is first deposited, for example, by thermal coevaporation of the elements. The CdS buffer layer follows in a chemical bath deposition step after which the i-ZnO film is sputtered. Three separate deposition systems are required, one for each film. For CdTe, a single plant with different processing zones can cover the deposition by close-spaced sublimation of CdS and CdTe and the junction activation step. Step (7) is the second patterning step, usually a mechanical scribe. Step (8) is the contact deposition, the front-side TCO for CIS which consists of a doped ZnO deposited by sputtering. For CdTe modules, a chemical etch precedes contact deposition for improved current flow. A final mechanical patterning step (9) completes the separation of the individual cells. The edge insulation step involves removing all films in the boundary region around the module for perfect electric insulation from the environment after encapsulation. The contact bands between the first and last cells are applied in step (10) before the module is laminated with a clean cover glass in step (11). The modules are framed—if required—and contact bands are connected to the contact box in step (12). Step (13) is the final characterization of the module and its classification by quality.

There is currently a “boom” in the construction of thin-film solar module production plants. Eight new CIS factories recently started production, or will do so in the near future. Several of these plants are located in Germany and a few are in USA and Japan. Table 3 presents an (incomplete) list of current manufacturers of compound thin-film photovoltaic modules and their status. The number of players and their capacities are steadily increasing.

In addition to these companies, which are in mass production or very close to it, several “newcomers” are entering the field. In the CIS family, new companies located mainly in USA (e.g., Miasole, Daystar, Ascent Solar) and Germany (e.g., Odorsun, Solarion, CIS Solartechnik) are focusing on flexible cells and modules. Some companies are developing new vacuum-free deposition methods based on small particles or electrodeposition (e.g., Nanosolar, ISET, IRDEP). New commercial activities with CdTe modules have been announced by Arendi (based on the technology developed at Parma University, Italy), Primestart Solar (based on

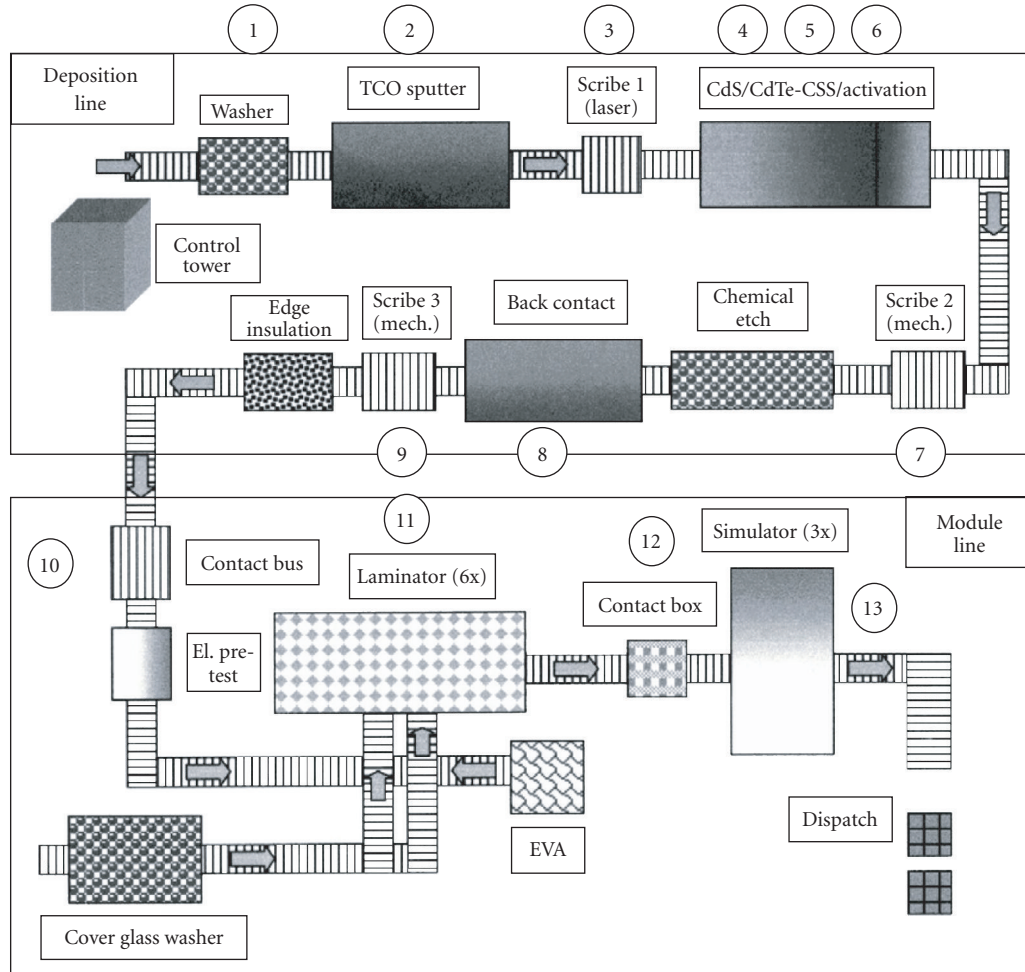


FIGURE 3: Schematic of commercial production line for CdTe thin-film solar modules.

the technology developed at NREL, USA and Applied Thin Films, Inc.), and AVA Technology (based on the know-how developed at Colorado State University, USA).

## 5. POWER GENERATORS AND OUTDOOR TESTING

Long-term outdoor testing is especially important for a new PV technology to prove itself in the existing market. The consumer expects high performance for a period of 20 years or more in order to justify the investment. Provided that the modules are properly encapsulated, neither fundamental considerations of the materials chemistry, nor accelerated and real outdoor testing indicate that long-term stability issues will be of concern for either CdTe or CIS modules. Due to the strong ionicity of the CdTe and CIS semiconductor compounds, the energy of the chemical bonds between the constituting elements is quite high, leading to an extremely high chemical and thermal stability and reducing the risk of performance degradation over time. Furthermore, the energy of any photon in the solar spectrum is lower than the binding energies so that the compounds will not degrade as a result of solar irradiation.

Extended outdoor testing of CdTe and CIS modules proves their stability. Figure 4 presents real data measured for CIS and CdTe modules, measured within a window around  $1000 \text{ W/cm}^2$  and corrected with a power factor and the temperature coefficient to reflect standard testing conditions ( $25^\circ\text{C}$  and  $1000 \text{ W/m}^2$ ). Graph (a) illustrates the performance of a CIS module in terms of efficiency, with data missing for the winter months when the irradiation did not approach  $1000 \text{ W/cm}^2$  required for significant testing or when snow covered the modules [21]. Graph (b) illustrates the corresponding performance for CdTe modules in terms of the peak power [22].

Besides testing at outdoor sites, thin-film modules have also proven themselves in large-scale installations. Architects are especially interested in the uniform black appearance of thin-film PV modules which they can use as functional design elements in building façades. As an example, Figure 5 presents an attractive integration of over 1000 CIS modules into the façade of the grain silo “Schapfenmühle” near Ulm, Germany. Several other projects have been realized with both CdTe and CIS modules and are successful ambassadors to present these technologies to the consumers.

TABLE 2: Processing steps for the production of CIS and CdTe thin-film solar modules.

Step no.	CIS	CdTe
1	Cleaning of glass substrate	Cleaning of glass superstrate
2	Deposition of back contact (Mo)	Deposition of front contact (SnO <sub>2</sub> , etc.)
3	Scribing of back contact	Scribing of front contact
4	Deposition of p-CIS film	Deposition of n-CdS film
5	Deposition of n-CdS film	Deposition of p-CdTe film
6	Deposition of i-ZnO film	“Activation”
7	Scribing of semiconductor film	Scribing of semiconductor film
8	Deposition of front contact	Deposition of back contact
9	Scribing of front contact	Scribing of back contact
10	Attachment of contact-bus structure	Attachment of contact-bus structure
11	Lamination with front glass plate	Lamination with back glass plate
12	Contact box attachment	Contact box attachment
13	Measurement, classification	Measurement, classification

TABLE 3: Some manufacturers of thin-film photovoltaic markets and their current status.

Manufacturer	Capacity in MW <sub>p</sub> /a	Substrate (m × m)	Efficiency max./mean	Market
<b>CIS</b>				
Johanna Solar, Germany	30 (2008)	0.5 × 1.2	-/9.4% [20]	no
Würth Solar, Germany	14.8 (2007)	0.6 × 1.2	< 13%/11.7%	yes
Global Solar, USA	4.2 (2006)	metal foil 1 ft wide	10%/8%	yes
Showa Shell, Japan	20 (2007)	0.6 × 1.2	14.2%/11.8%	yes
Honda Soltec Co. Ltd., Japan	27 (2007/2008)	0.8 × 1.3(0.2 × 0.2)	13%/10%	no
Sulfur Cell, Germany	5 (2007/2008)	0.65 × 1.25	8.2%/~7%	yes
AVANCIS, Germany	20 (from 2008)	0.6 × 1.2	13.1%/12.2%	no
Solibro GmbH (Q-Cells), Germany	25–30 (2009)	0.6 × 1.2	—	no
<b>CdTe</b>				
ANTEC Solar Energy AG Germany	7	0.6 × 1.2	7%/6%	yes
First Solar, USA, Germany, and Malaysia	175 (2007/2008)	0.6 × 1.2	11%/9%	yes

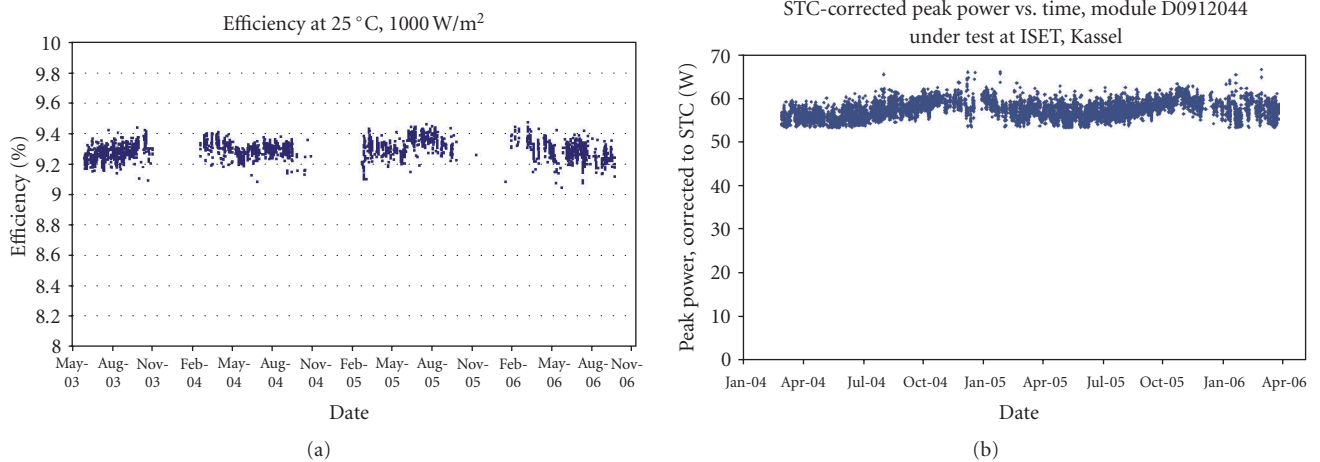


FIGURE 4: Long-term outdoor testing of thin-film modules, data adjusted to standard testing conditions of 25°C and 1000 W/m<sup>2</sup>. Graph (a) shows the efficiency of a CIS module over a period of three years and half. Graph (b) shows the peak power of a CdTe module over more than two years.



FIGURE 5: Grain silo “Schapfenmühle” on the outskirts of Ulm, Germany. Integrated into the façade are 1306 CIS modules from the Würth Solar pilot plant with a nominal installed power of 98 kW<sub>p</sub>.

## 6. CONCLUSION AND OUTLOOK

Photovoltaic modules based on the thin-film compound semiconductors CdTe and CIS are successfully being mass produced on a large scale (100 000 per annum or more) and are commercially available for PV installations. Profitable mass-production will be achieved at capacities of 1 mio. square meters of module surface area per year. Presently, the German feed-in law helps industry to achieve this goal faster. Thin-film CIS and CdTe modules of 14% efficiency can be expected within 5 to 7 years. Besides their excellent long-term performance efficiency and expected lower costs, thin-film photovoltaic modules are attractive to architects and consumers due to their very homogeneous appearance, leading to harmonious and visually pleasing installations.

## REFERENCES

- [1] J. M. Woodcock, H. Schade, H. Maurus, B. Dimmler, J. Springer, and A. Ricaud, “A study of the upscaling of thin film solar cell manufacture towards 500 MW<sub>p</sub> per annum,” in *Proceedings of the 14th European Photovoltaic Solar Energy Conference*, pp. 857–860, H. S. Stephens & Associates, Barcelona, Spain, 1997.
- [2] D. Bonnet, B. Henrichs, and H. Richter, “High-rate deposition of high-quality CdTe films for high-efficiency solar cells,” in *Proceedings of the 22nd IEEE Photovoltaic Specialists Conference*, vol. 2, pp. 1165–1168, Las Vegas, Nev, USA, October 1991.
- [3] H. M. Al-Allak, S. A. Galloway, A. W. Brinkman, K. Durose, H. Richter, and D. Bonnet, “The effect of processing conditions on the electrical and structural properties of CdS/CdTe solar cells,” in *Proceedings of 13th European Photovoltaic Solar Energy Conference*, pp. 2135–2138, Nice, France, October 1995.
- [4] X. Wu, J. C. Keane, R. G. Dhere, et al., “16.5%-efficient CdS/CdTe polycrystalline thin-film solar cell,” in *Proceedings of the 17th European Photovoltaic Solar Energy Conference*, pp. 995–1000, Munich, Germany, October 2001.
- [5] M. Powalla, “The R&D potential of CIS thin-film solar modules,” in *Proceedings of the 21st European Photovoltaic Solar Energy Conference*, p. 1789ff, Dresden, Germany, September 2006.
- [6] O. Lundberg, M. Bodegård, J. Malmström, and L. Stolt, “Influence of the Cu(In,Ga)Se<sub>2</sub> thickness and Ga grading on solar cell performance,” *Progress in Photovoltaics*, vol. 11, no. 2, pp. 77–88, 2002.
- [7] M. A. Contreras, K. Ramanathan, J. AbuShama, et al., “Diode characteristics in state-of-the-art ZnO/CdS/Cu(In<sub>1-x</sub>Ga<sub>x</sub>)Se<sub>2</sub> solar cells,” *Progress in Photovoltaics*, vol. 13, no. 3, pp. 209–216, 2005.
- [8] M. Powalla, B. Dimmler, R. Schaeffler, et al., “CIGS solar modules: progress in pilot production, new development and applications,” in *Proceedings of the 19th European Photovoltaic Solar Energy Conference*, p. 1663, Paris, France, June 2004.
- [9] H. S. Ullal, K. Zweibel, and B. Von Roedern, “Polycrystalline thin film photovoltaics: research, development, and technologies,” in *Proceedings of the 29th IEEE Photovoltaic Specialists Conference*, pp. 472–477, New Orleans, La, USA, May 2002.
- [10] CIS production average.
- [11] P. V. Meyers, “First solar polycrystalline CdTe thin film PV,” in *Proceedings of the 4th IEEE World Conference on Photovoltaic Energy Conversion*, vol. 2, pp. 2024–2027, Waikoloa, Hawaii, USA, May 2006.
- [12] J. Fritsche, T. Schulmeyer, A. Thißen, A. Klein, and W. Jaegermann, “Interface modification of CdTe thin film solar cells by CdCl<sub>2</sub>-activation,” *Thin Solid Films*, vol. 431-432, pp. 267–271, 2003.
- [13] D. Bonnet, R. Wendet, K. Durose, et al., “CADBACK: the CdTe thin film solar cell-improved back contact,” Final Report JOR3-CT98-0218, European Commission, Ghent University, Ghent, Belgium, 2002.
- [14] S. Spiering, S. Chowdhury, A. Drese, D. Hariskos, A. Eicke, and M. Powalla, “Evaporated indium sulphide as buffer layer in Cu(In,Ga)Se<sub>2</sub>-based solar cells,” in *Proceedings of the 21st European Photovoltaic Solar Energy Conference*, p. 1847, Dresden, Germany, 2006.
- [15] F. Kessler, D. Herrmann, and M. Powalla, “Approaches to flexible CIGS thin-film solar cells,” *Thin Solid Films*, vol. 480-481, pp. 491–498, 2005.
- [16] D. Braunger, D. Hariskos, G. Bilger, U. Rau, and H. W. Schock, “Influence of sodium on the growth of polycrystalline Cu(In,Ga)Se<sub>2</sub> thin films,” *Thin Solid Films*, vol. 361-362, pp. 161–166, 2000.
- [17] <http://www.nedo.go.jp/english/archives/161027/pv2030roadmap.pdf>.
- [18] <http://www.nrel.gov/docs/gen/fy03/30150.pdf>.
- [19] R. Kniese, M. Powalla, and U. Rau, “Characterization of the CdS/Cu(In,Ga)Se<sub>2</sub> interface by electron beam induced currents,” *Thin Solid Films*, vol. 515, no. 15, pp. 6163–6167, 2007.
- [20] preliminary data sheet, <http://www.johanna-solar.com/produkte/datenblatt.oem.pdf>.
- [21] ZSW Jahresbericht, 2006, <http://www.zsw-bw.de>.
- [22] M. Ross, G. Rich, L. Petacci, and J. Klammer, “Improvement in reliability and energy yield prediction of thin-film CdS/CdTe PV modules,” in *Proceedings of the 4th IEEE World Conference on Photovoltaic Energy Conversion*, vol. 2, pp. 2148–2151, Waikoloa, Hawaii, USA, May 2006.

## Research Article

# Advances in High-Efficiency III-V Multijunction Solar Cells

**Richard R. King, Daniel C. Law, Kenneth M. Edmondson, Christopher M. Fetzer, Geoffrey S. Kinsey, Hojun Yoon, Dimitri D. Krut, James H. Ermer, Raed A. Sherif, and Nasser H. Karam**

*Spectrolab, Inc., 12500 Gladstone Avenue, Sylmar, CA 91342, USA*

Received 25 May 2007; Accepted 12 September 2007

Recommended by Armin G. Aberle

The high efficiency of multijunction concentrator cells has the potential to revolutionize the cost structure of photovoltaic electricity generation. Advances in the design of metamorphic subcells to reduce carrier recombination and increase voltage, wide-band-gap tunnel junctions capable of operating at high concentration, metamorphic buffers to transition from the substrate lattice constant to that of the epitaxial subcells, concentrator cell AR coating and grid design, and integration into 3-junction cells with current-matched subcells under the terrestrial spectrum have resulted in new heights in solar cell performance. A metamorphic  $\text{Ga}_{0.44}\text{In}_{0.56}\text{P}/\text{Ga}_{0.92}\text{In}_{0.08}\text{As}/\text{Ge}$  3-junction solar cell from this research has reached a record 40.7% efficiency at 240 suns, under the standard reporting spectrum for terrestrial concentrator cells (AM1.5 direct, low-AOD,  $24.0 \text{ W}/\text{cm}^2$ ,  $25^\circ \text{C}$ ), and experimental lattice-matched 3-junction cells have now also achieved over 40% efficiency, with 40.1% measured at 135 suns. This metamorphic 3-junction device is the first solar cell to reach over 40% in efficiency, and has the highest solar conversion efficiency for any type of photovoltaic cell developed to date. Solar cells with more junctions offer the potential for still higher efficiencies to be reached. Four-junction cells limited by radiative recombination can reach over 58% in principle, and practical 4-junction cell efficiencies over 46% are possible with the right combination of band gaps, taking into account series resistance and gridline shadowing. Many of the optimum band gaps for maximum energy conversion can be accessed with metamorphic semiconductor materials. The lower current in cells with 4 or more junctions, resulting in lower  $I^2R$  resistive power loss, is a particularly significant advantage in concentrator PV systems. Prototype 4-junction terrestrial concentrator cells have been grown by metal-organic vapor-phase epitaxy, with preliminary measured efficiency of 35.7% under the AM1.5 direct terrestrial solar spectrum at 256 suns.

Copyright © 2007 Richard R. King et al. This is an open access article distributed under the Creative Commons Attribution License, which permits unrestricted use, distribution, and reproduction in any medium, provided the original work is properly cited.

## 1. INTRODUCTION

In the past decade, terrestrial concentrator multijunction III-V cells have embarked upon a remarkable ascent in solar conversion efficiency. The realization that very high conversion efficiencies can be achieved with advanced multijunction solar cells in practice, not just in theory, has prompted a resurgence of research in multijunction cells and commercial interest in concentrator III-V photovoltaics. This paper discusses recent advances in multijunction cell research that have led to experimental metamorphic (MM), or lattice-mismatched, solar cells with 40.7% efficiency under the concentrated terrestrial spectrum [1, 2]. This is the first solar cell to reach over 40% efficiency, and is the highest solar conversion efficiency yet achieved for any type of photovoltaic device. Experimental lattice-matched (LM) cells have also broken the 40% milestone, with 40.1% efficiency demonstrated for an LM 3-junction cell. Both of these cell-efficiency results have been independently verified by cell measurements at

the National Renewable Energy Laboratory (NREL). Many of the high efficiency device structures developed in the experiments leading to these record performance cells have now been incorporated in production III-V multijunction cells, increasing the average efficiency of these mass-produced solar cells as well, while other experimental device improvements will be implemented in production in the coming months and years. This paper discusses the science behind the 40.7% metamorphic and 40.1% lattice-matched cells, the opportunity to reach new levels of photovoltaic (PV) system cost-effectiveness with production III-V concentrator cells that make use of these advances, and possibilities for the next generations of terrestrial concentrator cells with efficiencies of 45%, or even 50%.

## 2. METAMORPHIC SOLAR CELLS

Perhaps the essential distinguishing feature of III-V multijunction cells is the very wide range of subcell and device

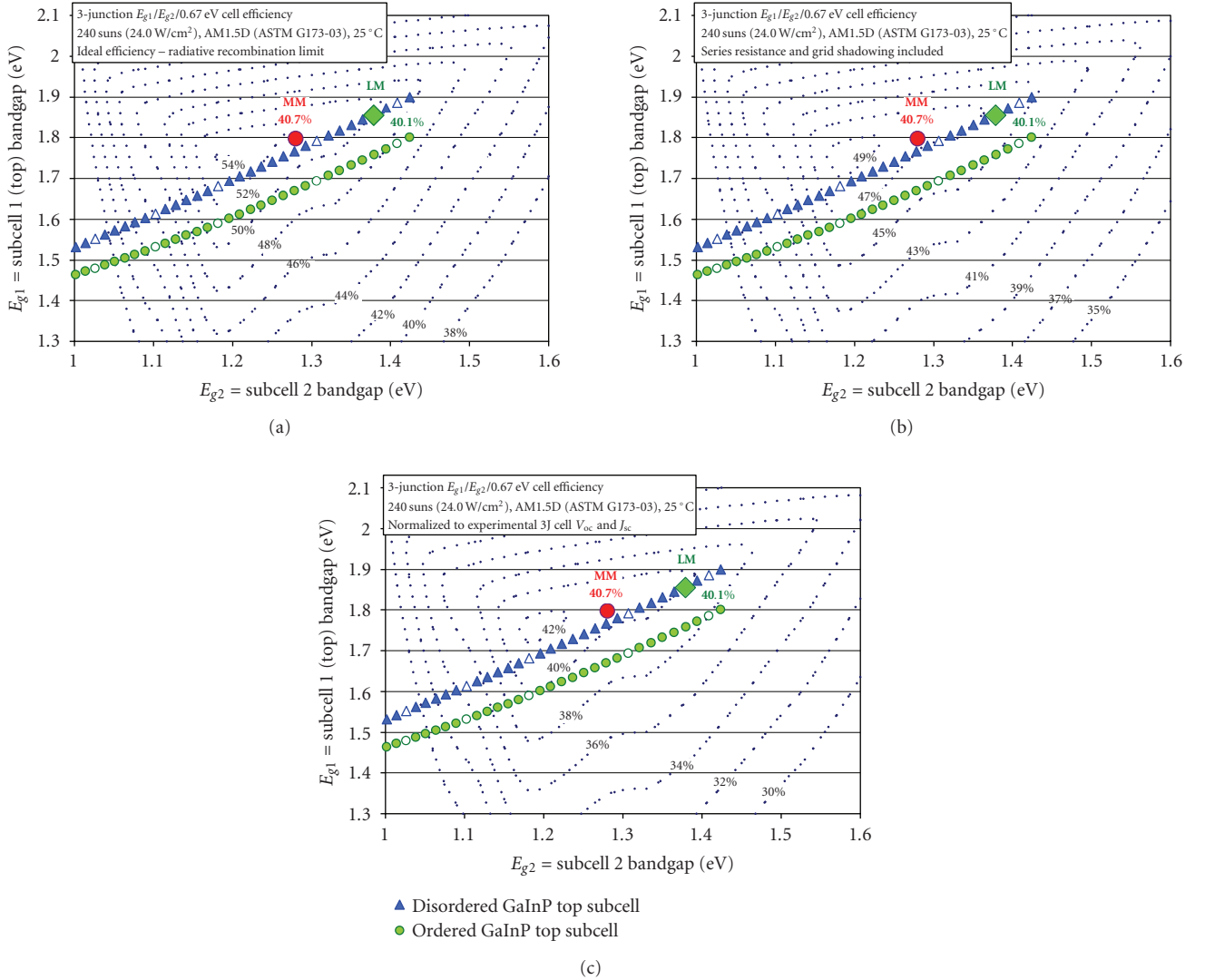


FIGURE 1: Calculated iso-efficiency contours for 3-junction terrestrial concentrator cells with variable top and middle subcell band gaps for the terrestrial solar spectrum at 240 suns: (a) theoretical efficiency based on radiative recombination [1]; (b) including the effects of grid resistance and shadowing using the metal grid design of the record 40.7%-efficient cell; and (c) additionally including empirically determined average quantum efficiency of 0.925, and 3-junction cell  $V_{oc}$  233 mV lower than the ideal voltage based on radiative recombination alone, giving an experimentally grounded prediction of practical, state-of-the-art, 3J cell efficiencies, as a function of subcell  $E_g$ . Subcell 1 and 2 band gap pairs of GaInP and GaInAs at the same lattice constant are shown for both disordered and ordered GaInP. The measured efficiencies and band gap combinations for the record 40.7% MM and 40.1% LM cells are plotted, at 240 and 135 suns, respectively, showing the theoretical advantage of the metamorphic design, now realized in practice.

structure band gaps that can be grown with high crystal quality, and correspondingly high minority-carrier recombination lifetimes. This is true for lattice-matched multijunction cells, but the flexibility in band gap selection takes on a whole new dimension when metamorphic semiconductors are used, providing freedom from the constraint that all subcells must have the same crystal lattice constant. The area of metamorphic solar cell materials has attracted interest from photovoltaic research groups around the globe [1–11].

The theoretical benefits of flexibility in subcell band gap selection are made apparent in Figure 1(a), which plots iso-efficiency contours for 3-junction terrestrial concentrator cells as a function of top (subcell 1) band gap  $E_{g1}$  and mid-

dle (subcell 2) band gap  $E_{g2}$  [1]. Figure 1(a) plots contours of ideal efficiency based on the diode characteristics of subcells limited only by the fundamental mechanism of radiative recombination, and on the shape of the terrestrial solar spectrum. The cell model is discussed in greater detail in [10]. Efficiencies up to 54% can be seen to be possible in principle at this concentration for 3-junction cells in the radiative recombination limit, increasing to over 58% for 4-junction terrestrial concentrator cells [10].

In 3-junction GaInP/GaInAs/Ge metamorphic solar cells, the GaInP and GaInAs subcells can be grown on a metamorphic buffer such that these two subcells are lattice-matched to each other, but are both lattice-mismatched to

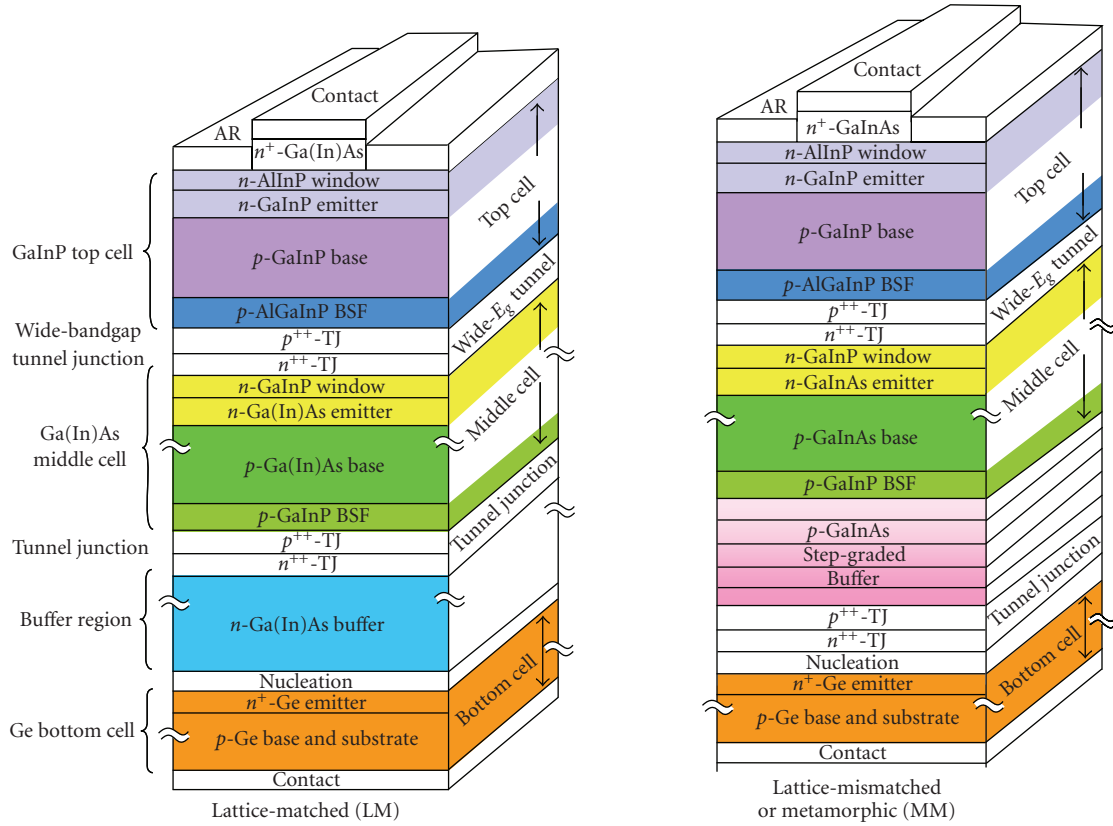


FIGURE 2: Schematic cross-sectional diagrams of lattice-matched (LM) and metamorphic (MM) GaInP/GaInAs/Ge 3-junction cell configurations, corresponding to the LM 40.1% and MM 40.7%-efficient concentrator cells.

the Ge growth substrate and subcell. The band gap combinations that are possible with GaInP and GaInAs subcells at same lattice constant, but with varying lattice mismatch to the Ge substrate, are shown in Figure 1(a). The cases with a disordered group-III sublattice in the GaInP subcell, giving higher band gap at the same GaInP composition, and with an ordered (low  $E_g$ ) group-III sublattice in the GaInP subcell, are both plotted. Metamorphic cells can be seen to bring the cell design closer to the region of  $E_{g1}$ ,  $E_{g2}$  space that has the highest theoretical efficiencies. The lower band gaps of MM subcells can use a larger part of the solar spectrum, that is wasted as excess photogenerated current in the Ge bottom cell in most lattice-matched 3-junction cells. In the past, recombination at dislocations in MM materials have often thwarted this promise of higher theoretical efficiency. However, for the recent metamorphic 40.7%-efficient and lattice-matched 40.1%-efficient cell results, plotted in Figure 1, the density and activity of dislocations have been controlled sufficiently to show the efficiency advantage of the MM design, not just theoretically but now also experimentally.

Figures 1(b) and 1(c) take this analysis a bit farther. The efficiency contours in Figure 1(b) take into account the shadowing and specific series resistance associated with the metal grid pattern used on the 40.7% record cell. The fill factor calculated for the 3-junction cell with the band gap combination of the MM 40.7% cell is 87.5% with series resistance in-

cluded, essentially identical to that measured experimentally for the 40.7% cell at 240 suns.

In Figure 1(c), additional real-life effects are included by using empirical values for the active-area external quantum efficiency (EQE), and for the decrease in 3-junction cell  $V_{oc}$  from Shockley-Read-Hall (SRH) recombination in addition to radiative recombination. The record 40.7%-efficiency 3-junction MM cell has an average active-area external quantum efficiency of 0.925, and actual  $V_{oc}$  that is 233 mV lower than the ideal  $V_{oc}$  in the radiative limit. This is equivalent to 78 mV per subcell on average, though since the GaInAs middle subcell  $V_{oc}$  is often close to the radiative limit, the difference between actual  $V_{oc}$  and ideal radiative  $V_{oc}$  is more heavily distributed in the top and bottom subcells. With the addition of these last real-life effects, the calculated contours in Figure 1(c) show a good estimate of the efficiencies that can be achieved in practical, state-of-the-art, 3-junction cells as a function of band gap. The measured efficiencies of the plotted 40.7% MM and 40.1% LM record cells correspond to the efficiency contours in Figure 1(c), but are also plotted in Figures 1(a) and 1(b) for reference. It should be noted that unlike Figure 1(a), the present, state-of-the-art, practical efficiencies of the contours in Figure 1(c) are not fundamental limits, and can be made higher by finding ways to reduce the nonfundamental EQE and  $V_{oc}$  losses that have been included in Figure 1(c).

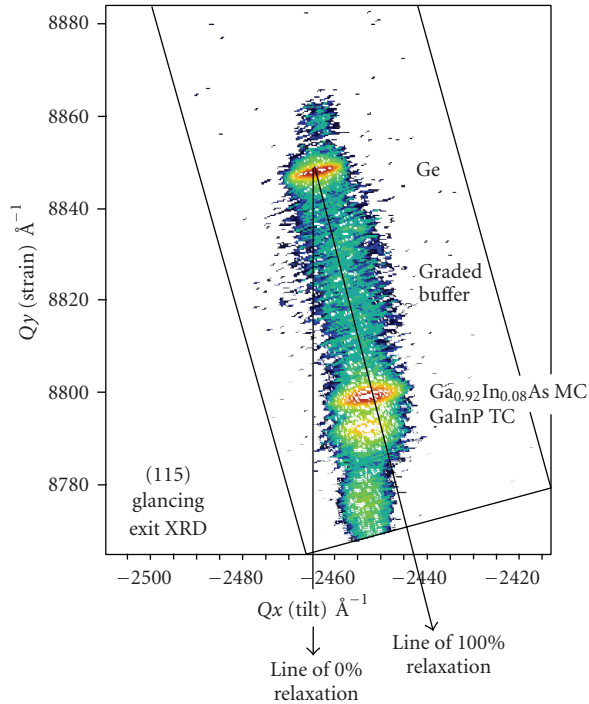


FIGURE 3: High-resolution X-ray diffraction reciprocal space map of a metamorphic 3-junction cell structure, showing a metamorphic buffer with almost no residual strain, and a GaInP top cell that is pseudomorphic with respect to the  $\text{Ga}_{0.92}\text{In}_{0.08}\text{As}$  middle cell.

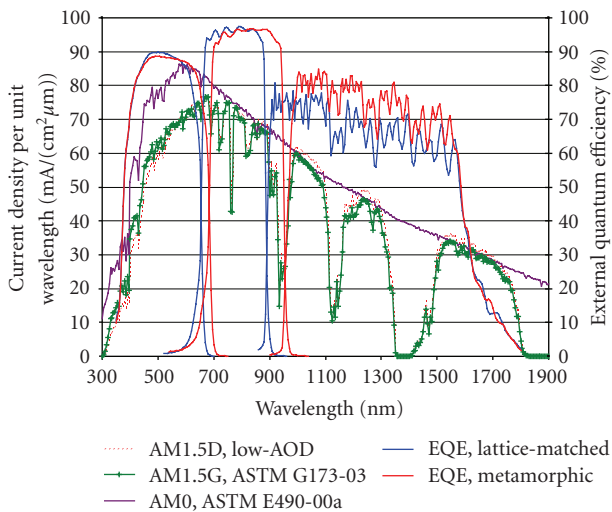


FIGURE 4: External quantum efficiency for GaInP, GaInAs, and Ge subcells of LM and MM 3-junction cells, showing extension of the lower- $E_g$  MM GaInP and GaInAs responses to longer wavelengths, allowing them to use more of the solar spectrum [1].

Schematic diagrams of LM and MM cells are shown in Figure 2, showing the step-graded metamorphic buffer used in the MM case to transition from the lattice constant of the substrate to that of the upper subcells. The lattice constants and strain in the various MM 3-junction cell layers are imaged in the high-resolution X-ray diffraction (HRXRD) re-

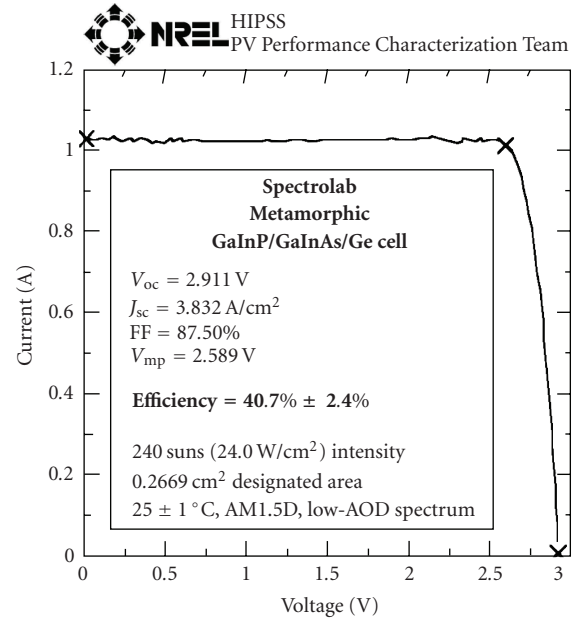


FIGURE 5: Illuminated I-V curve for the record 40.7% metamorphic 3-junction cell, independently verified at NREL. This is the first photovoltaic cell of any type to reach over 40% solar conversion efficiency.

ciprocal space map (RSM) shown in Figure 3. The buffer can be seen to be nearly 100% relaxed, with very little residual strain to drive the formation of dislocations in the active upper subcells.

The shift in the quantum efficiency of the 3 subcells in GaInP/GaInAs/Ge 3-junction cells, as a result of the higher indium composition and lower band gap of the metamorphic GaInP and GaInAs subcells, is shown in Figure 4 [1]. In this way the MM cells are able to capture some of the current density that would otherwise be wasted in the Ge subcell. The quantum efficiencies are overlaid on the AM0, and terrestrial AM1.5G and AM1.5D, low-AOD solar spectra, to show the current densities available in the response range of each subcell.

### 3. HIGH-EFFICIENCY MULTIJUNCTION CELLS

Band gap engineering of subcells in 3-junction solar cells, made possible by metamorphic semiconductor materials, has now resulted in higher measured efficiencies for metamorphic cells than in even the best lattice-matched cells. Experiments on step-graded buffers, used to transition from the substrate to the subcell lattice constant, have been used to control the classic problem of dislocations in the active cell regions due to the lattice mismatch. The band gap-voltage offset ( $E_g/q$ ) -  $V_{oc}$  is a key indicator of the quality and suppression of SRH recombination in semiconductors of variable band gap, where lower offset values are desired, since it is a measure of the separation between electron and hole quasi-Fermi levels and the conduction and valence band edges [8–10]. Metamorphic 8%-In GaInAs single-junction cells were built and tested with a band gap-voltage offset

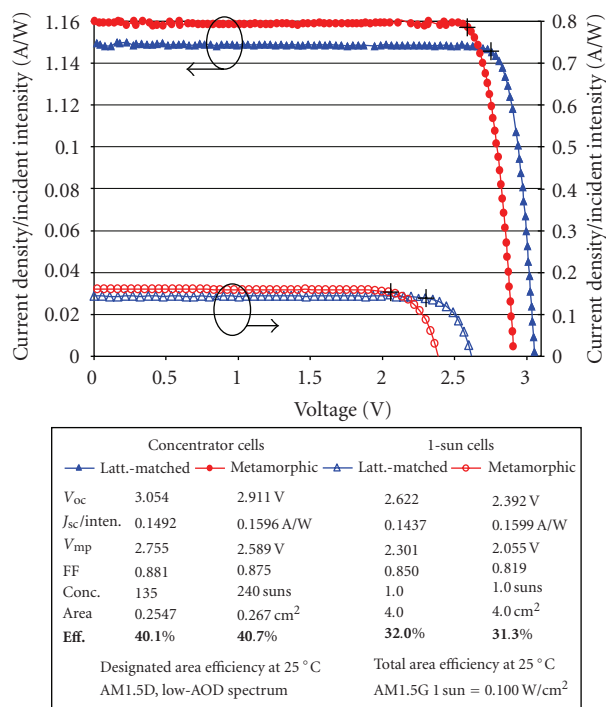


FIGURE 6: Comparison of the light I-V characteristics of the 40.1% lattice-matched and 40.7% metamorphic 3-junction concentrator cells, and earlier record one-sun cells [1]. The higher current and lower voltage of the metamorphic design is evident.

of 0.42 V at one sun, essentially the same as GaAs control cells, reflecting the long minority-carrier lifetimes that can be achieved in metamorphic materials.

An extensive experimental campaign was carried out on GaInP/GaInAs/Ge terrestrial concentrator cells, using a variety of metamorphic and lattice-matched 3-junction cell configurations, wide-band-gap tunnel junctions and other high-efficiency semiconductor device structures, current matching conditions, cell sizes, grid patterns, and fabrication processes, resulting in new understanding of the limiting mechanisms of terrestrial multijunction cells, and new heights in performance. Figure 5 plots the measured illuminated I-V curve for the record efficiency 40.7% metamorphic GaInP/GaInAs/Ge 3-junction cell at 240 suns [1], under the standard spectrum for concentrator solar cells (AM1.5D, low-AOD, 24.0 W/cm<sup>2</sup>, 25 °C). This is the first solar cell to reach over 40% efficiency, and is the highest solar conversion efficiency yet achieved for any type of photovoltaic device. A lattice-matched 3-junction cell has also achieved over 40% efficiency, with 40.1% measured at 135 suns (AM1.5D, low-AOD, 13.5 W/cm<sup>2</sup>, 25 °C). These efficiencies have been independently verified by measurements at the National Renewable Energy Laboratory (NREL). Light I-V characteristics of both the record MM and LM devices are compared in Figure 6 [1].

The highest cell efficiencies from a number of photovoltaic technologies by year since 1975 are plotted in Figure 7, showing the most recent 40.7%-efficient cell result. It is interesting to note that III-V multijunction concentrator cells not only are the highest efficiency technology, but also

have the highest rate of increase. These high III-V cell efficiencies have translated to concentrator PV module efficiencies over 30%, more than double the ~15% module efficiencies that are more typical of flat-plate silicon modules. This high efficiency is extremely leveraging for PV system economics [12], as it reduces all area-related costs of the module. Production multijunction concentrator cells with efficiency in the 40% range could cause the market growth for concentrator PV to explode, with multi-GW/year production levels.

In Figure 8, the measured efficiency,  $V_{oc}$ , and fill factor are plotted as a function of incident intensity, or concentration ratio, for the record 40.7% MM and 40.1% LM cells, as well as for an additional MM cell with good performance at high intensities. It is interesting to note that the efficiencies of both the record MM and LM cells track very closely at the same concentration, but the measurements were able to be extended to a higher concentration for the MM cell. Fill factors for both types of cell are quite high at about 88% in the 100–200 sun range. The open-circuit voltage  $V_{oc}$  increases at rates of approximately 210 mV/decade and 190 mV/decade for the MM and LM record cells, respectively, in the 100–200 suns range. Thus the MM subcells increase in voltage somewhat more rapidly with excess carrier concentration than in the LM case, as one would expect if defects in the MM materials are becoming less active at mediating recombination at higher injection levels. From the slopes of  $V_{oc}$  versus concentration (current density) we can extract values of the diode ideality factor  $n$ . Subtracting off the 59 mV/decade increase for the Ge subcell, which has diode ideality factor very close to unity, gives an average  $n$  for the upper two subcells of 1.26 in the MM case and 1.10 in the LM case in the same concentration range, with decreasing  $n$  as the incident intensity increases.

#### 4. FOUR-JUNCTION SOLAR CELLS

A 4-junction (Al)GaInP/ AlGa(In)As/ Ga(In)As/ Ge terrestrial concentrator solar cell [10] is shown in Figure 9, where the parentheses indicate optional elements in the subcell composition. This type of cell divides the photon flux available in the terrestrial solar spectrum above the band gap of the GaInAs subcell 3 into 3 pieces, rather than 2 pieces in the case of a 3-junction cell. As a result, the current density of a 4-junction cell is roughly 2/3 that of a corresponding 3-junction cell, and the  $I^2R$  resistive power loss is approximately  $(2/3)^2 = 4/9$ , or less than half that of a 3-junction cell. Figure 9 shows a lattice-matched 4-junction cell, with all the subcells at the lattice constant of the Ge substrate, but lattice-mismatched versions of the 4-junction cell are also possible, giving greater flexibility in bandgap selection.

Iso-efficiency contours for 4-junction terrestrial concentrator cells, under the AM1.5D (ASTM G173-03) solar spectrum at 500 suns (50.0 W/cm<sup>2</sup>), are plotted in Figure 10 as a function of the band gaps of subcells 2 and 3. Ideal 4-junction cell efficiency is plotted in Figure 10(a), and practical cell efficiency, consistent with the measured 3J cell efficiency, in Figure 10(b). The band gap of subcell 1 is held at 1.9 eV, corresponding to GaInP at the Ge lattice constant with a disordered group-III sublattice, and subcell 4 (the bottom



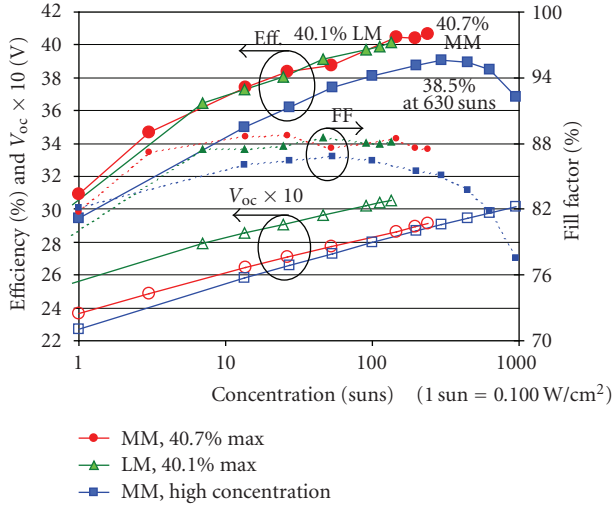


FIGURE 8: Efficiency,  $V_{oc}$ , and FF of record performance 40.7% metamorphic and 40.1% lattice-matched 3-junction cells as a function of incident intensity. An additional cell is shown which maintains an efficiency of 38.5% over 600 suns, and 36.9% over 950 suns.

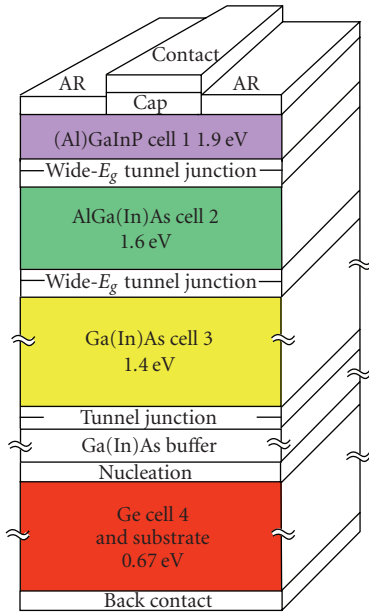
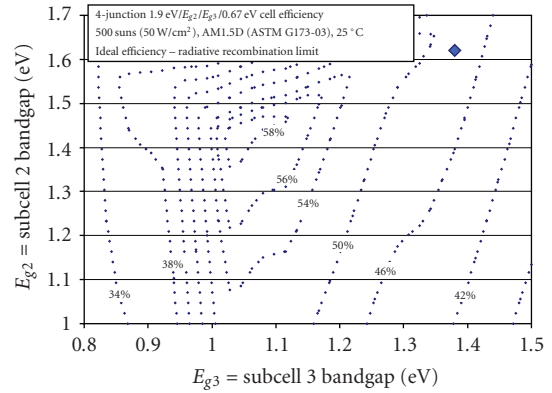


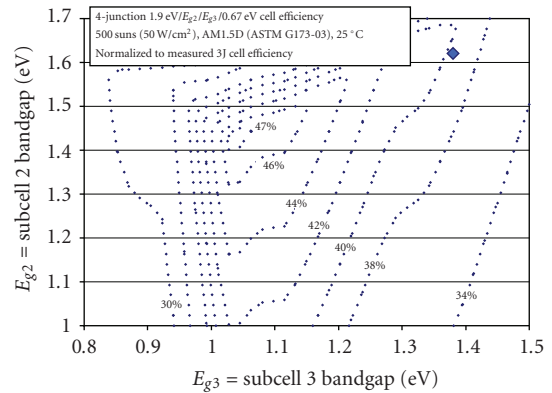
FIGURE 9: A 4-junction (Al)GaInP/ AlGa(In)As/ Ga(In)As/Ge terrestrial concentrator solar cell cross-section.

efficiencies of any type of photovoltaic device to date. These very high experimental cell efficiencies have begun to be translated to production solar cells as well.

The dependence of 3- and 4-junction terrestrial concentrator cell efficiency on the band gaps of subcells 1, 2, and 3 is calculated, and presented in contour plots of both ideal efficiency and practical cell efficiency. Ideal cell efficiencies are over 58%, and practical efficiencies of 47% are achievable for 4-junction concentrator cells [10]. The low resistive



(a)



(b)

FIGURE 10: Contour plots of (a) ideal efficiency and (b) efficiency normalized to experiment, for 4-junction solar cells, with variable subcell 3 and subcell 2 band gaps.

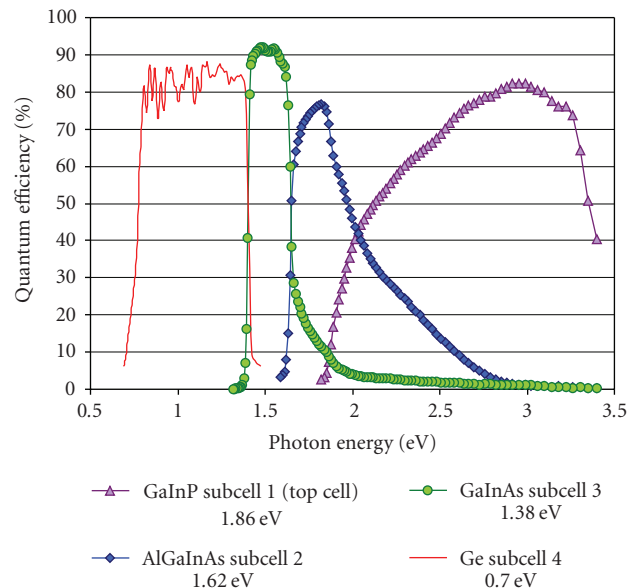


FIGURE 11: External quantum efficiency of a 4-junction (Al)GaInP/ AlGa(In)As/ Ga(In)As/ Ge terrestrial concentration cell.

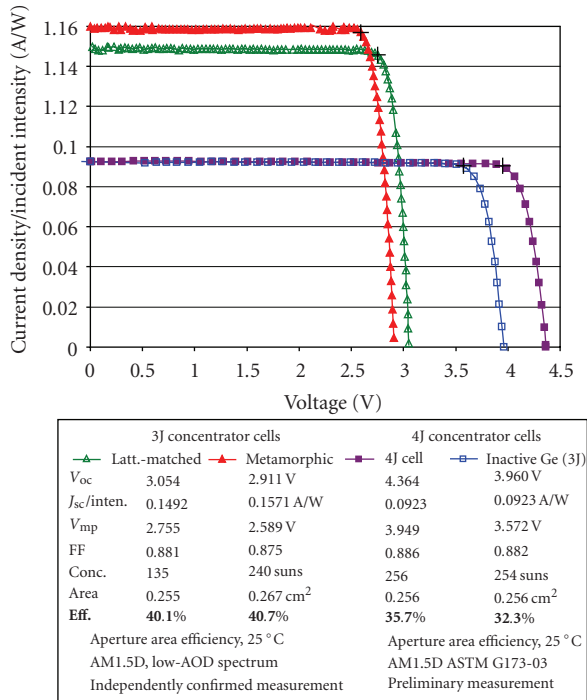


FIGURE 12: Illuminated I-V characteristics of an unoptimized 4-junction terrestrial concentrator cell with 35.7% efficiency, and  $V_{oc}$  over 4.3 volts. I-V curves for the record 40.7%-efficient metamorphic and 40.1% lattice-matched 3-junction cells are also shown.

power loss that results from the high-voltage, low-current design of cells with 4 or more junctions is a powerful advantage in concentrator applications. New 4-junction terrestrial concentrator cell architectures have been demonstrated, with 35.7% measured efficiency [10]. The recent realization of very high-efficiency III-V multijunction cells has positioned concentrator PV technology such that it may well have a game-changing effect on the economics of PV electricity generation in the near future. Terrestrial concentrator cells with 3, 4, or more junctions, coupled with advances in metamorphic materials that have resulted in record solar cell efficiency of 40.7% today, offer the promise to increase efficiency and lower the cost of terrestrial photovoltaic concentrator systems still further, to 45%, and perhaps even to 50% efficiency.

## ACKNOWLEDGMENTS

The authors would like to thank Robert McConnell, Martha Symko-Davies, Fannie Posey-Eddy, Keith Emery, James Kiehl, Tom Moriarty, Sarah Kurtz, Kent Barbour, Hector Cotal, Mark Takahashi, Andrey Masalykin, and the entire multijunction solar cell team at Spectrolab. This work was supported in part by the Department of Energy through the NREL High-Performance PV program (NAT-1-30620-01), and by Spectrolab.

## REFERENCES

- [1] R. R. King, D. C. Law, K. M. Edmondson, et al., “40% efficient metamorphic GaInP/GaInAs/Ge multijunction solar cells,” *Applied Physics Letters*, vol. 90, no. 18, Article ID 183516, 3 pages, 2007.
- [2] R. R. King, D. C. Law, K. M. Edmondson, et al., “Metamorphic concentrator solar cells with over 40% conversion efficiency,” in *Proceedings of the 4th International Conference on Solar Concentrators (ICSC-4)*, El Escorial, Spain, March 2007.
- [3] R. R. King, M. Haddad, T. Isshiki, et al., “Metamorphic GaInP/GaInAs/Ge solar cells,” in *Proceedings of the 28th IEEE Photovoltaic Specialists Conference (PVSC-28)*, pp. 982–985, Anchorage, Alaska, USA, September 2000.
- [4] F. Dimroth, U. Schubert, and A. W. Bett, “25.5% efficient Ga<sub>0.35</sub>In<sub>0.65</sub>P/Ga<sub>0.83</sub>In<sub>0.17</sub>As tandem solar cells grown on GaAs substrates,” *IEEE Electron Device Letters*, vol. 21, no. 5, pp. 209–211, 2000.
- [5] T. Takamoto, T. Agui, K. Kamimura, et al., “Multifunction solar cell technologies—high efficiency, radiation resistance, and concentrator applications,” in *Proceedings of the 3rd World Conference on Photovoltaic Energy Conversion (WCPEC-3)*, vol. 1, pp. 581–586, Osaka, Japan, May 2003.
- [6] M. W. Wanlass, S. P. Ahrenkiel, R. K. Ahrenkiel, et al., “Lattice-mismatched approaches for high-performance, III-V photovoltaic energy converters,” in *Proceedings of the 31st IEEE Photovoltaic Specialists Conference (PVSC-31)*, pp. 530–535, Lake Buena Vista, Fla, USA, January 2005.
- [7] A. W. Bett, C. Baur, F. Dimroth, and J. Schöne, “Metamorphic GaInP-GaInAs layers for photovoltaic applications,” in *Materials Research Society Symposium Proceedings*, vol. 836, p. 223, Boston, Mass, USA, November-December 2005.
- [8] R. R. King, D. C. Law, C. M. Fetzer, et al., “Pathways to 40% efficient concentrator photovoltaics,” in *Proceedings of the 20th European Photovoltaic Solar Energy Conference and Exhibition (EU PVSEC-20)*, pp. 118–123, Barcelona, Spain, June 2005.
- [9] R. R. King, D. C. Law, K. M. Edmondson, et al., “Metamorphic and lattice-matched solar cells under concentration,” in *Proceedings of IEEE of the 4th World Conference on Photovoltaic Energy Conversion (WCPEC-4)*, vol. 1, pp. 760–763, Waikoloa, Hawaii, USA, May 2006.
- [10] R. R. King, R. A. Sherif, D. C. Law, et al., “New horizons in III-V multijunction terrestrial concentrator cell research,” in *Proceedings of the 21st European Photovoltaic Solar Energy Conference and Exhibition (EU PVSEC-21)*, p. 124, Dresden, Germany, September 2006.
- [11] J. F. Geisz, S. Kurtz, M. W. Wanlass, et al., “High-efficiency GaInP/ GaAs/ InGaAs triple-junction solar cells grown inverted with a metamorphic bottom junction,” *Applied Physics Letters*, vol. 91, Article ID 023502, 3 pages, 2007.
- [12] R. A. Sherif, R. R. King, N. H. Karam, and D. R. Lillington, “The path to 1 GW of concentrator photovoltaics using multijunction solar cells,” in *Proceedings of the 31st IEEE Photovoltaic Specialists Conference (PVSC-31)*, pp. 17–22, Lake Buena Vista, Fla, USA, January 2005.

## Review Article

# Recent Advances in Dye-Sensitized Solar Cells

F. O. Lenzmann and J. M. Kroon

*Energy Research Center of the Netherlands (ECN), P.O. Box 1, Westerduinweg 3, 1755 Petten, ZG, The Netherlands*

Received 23 May 2007; Accepted 13 September 2007

Recommended by A. G. Aberle

This review describes recent advances in the research on dye-sensitized solar cells. After a brief discussion of the general operation principles and a presentation of record efficiencies, stability data and key technology drivers, current trends will be reviewed. The focus of this review is on materials development (sensitizers, nanostructured oxide films, and electrolyte), but commercialization aspects will also be briefly addressed. The review describes the most relevant characteristics and major trends in a compact way.

Copyright © 2007 F. O. Lenzmann and J. M. Kroon. This is an open access article distributed under the Creative Commons Attribution License, which permits unrestricted use, distribution, and reproduction in any medium, provided the original work is properly cited.

## 1. INTRODUCTION

Dye-sensitized solar cells (DSCs) are a prominent member of the larger group of thin film photovoltaics. All thin film technologies together currently still represent less than 10% of the annual PV module sales. They are expected to gain growing market shares in the years to come because of both an ultimately higher potential for low-cost fabrication, compared with wafer-based PV technologies, and an access to new markets, where flexible and light-weight products are desired. Next to those thin film technologies, which have already made their way to the marketplace, that is, amorphous and microcrystalline Si as well as CdTe and CI(G)S, others are still in the precommercial phase. Among the latter, dye-sensitized solar cells are the most advanced and they are currently on the verge of commercialization with—among others—a recent announcement of a manufacturing facility of significant capacity (25 MW) in the course of 2007 in Cardiff, Wales.

After a brief discussion of the general operation principles and a presentation of record efficiencies, stability data, and key technology drivers, current trends will be reviewed. The focus will be on materials development, but commercialization aspects will also be briefly addressed. This article describes the most relevant characteristics and the major trends in a compact way. Reviews including more extensive and complete descriptions of the field are referred to in the text.

## 2. OPERATION PRINCIPLES AND STRUCTURE

Dye-sensitized solar cells operate differently from other types of solar cells in many ways with some remarkable analogies to the natural process of photosynthesis. Therefore, this system has repeatedly been described in terms of artificial photosynthesis since the interest in DSCs took off with the landmark publication by O'Regan and Grätzel in the early 1990's [1]. Like the chlorophyll in plants, a monolayer of dye molecules (sensitizers) absorbs the incident light, giving rise to the generation of positive and negative charge carriers.

In more detail, the different steps of the photoconversion process can best be described in conjunction with the energy band diagram and the schematic structure of a DSC (see Figure 1).

Upon light absorption, the dye (S) is promoted into an electronically excited state ( $S^*$ ) from where it injects—within femtoseconds—an electron into the conduction band of a large bandgap semiconductor film ( $\text{TiO}_2$ ), onto which it is adsorbed (1). The electrons are transported through the  $\text{TiO}_2$  film by diffusion before reaching the anode of the cell—in general an  $\text{SnO}_2:\text{F}$  coated glass substrate—and the external circuit (2). The positive charges resulting from the injection process are transferred into a liquid electrolyte by reaction of the dye cation ( $S^+$ ) with the reduced species of a redox couple in the electrolyte solution. This leads to the regeneration of the charge neutral state of the sensitizer (3). The most typical redox couple is  $\text{I}^-/\text{I}_3^-$ . After ionic diffusion, the carrier

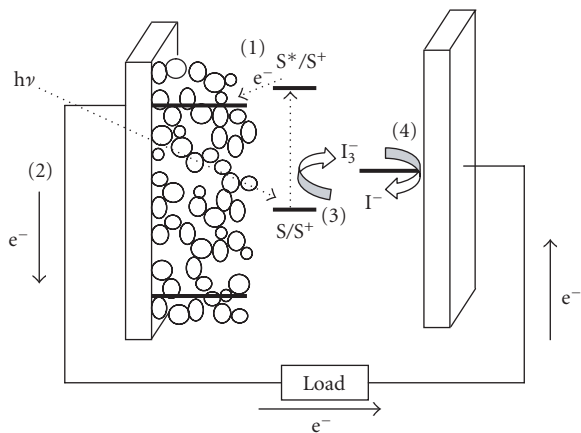


FIGURE 1: Schematic structure of a DSC, illustrating the operation principles.

of the positive charge, that is,  $I_3^-$ , reaches the cathode, where it releases its charge, thus being reduced back to  $I^-$  (4). The latter process typically requires a catalytic amount of Pt on the cathode surface. The process control is governed by kinetic competition. In optimized systems, a favorable kinetic balance [2] assures that loss mechanisms, such as the thermalization of the dye excited state and other recombination processes, are largely suppressed. Overall, the photoconversion process is regenerative; that is, there is no net change in the chemical composition of the cell.

The key to efficient light harvesting is the high surface area of the porous  $TiO_2$  film. While a single monolayer of dye molecules on a flat  $TiO_2$  film can typically absorb not more than a negligible fraction of the incoming light, the nanostructured  $TiO_2$  films provide enough surface area for more than 1000 dye monolayers. Typical maximum extinction coefficients of the dye between  $1\text{--}2 \cdot 10^4 \text{ M}^{-1} \text{ cm}^{-1}$  allow for quantitative light harvesting over a broad range of the dye absorption spectra. The open porosity of these films allows the liquid electrolyte to fill all pores of the film. The nanocomposite geometry thereby ascertains the required contact of every dye molecule to both the  $TiO_2$  as well as the electrolyte phase, and the extracted current is the sum of all active molecular charge generators (dye molecules), connected in parallel.

The operating principles and the nanocomposite nature of DSCs bring about some unique features. Unlike any other type of solar cells, charge generation takes place exclusively at the interface, where the charges are separated—the  $TiO_2$ /dye/electrolyte interface—with obvious advantages for the initial charge separation efficiency. Also, the processes of light absorption and charge transport are separated. The dye molecules only absorb the light and generate the charge carriers, while charge transport occurs in the  $TiO_2$  and the electrolyte. This implies the absence of minority carrier recombination, and hence a relatively high tolerance for impurities. More in-depth descriptions of operation principles and loss mechanisms in DSCs can be found in other recent review papers [3–6].

### 3. STATE-OF-THE-ART DEVICE PERFORMANCE AND STABILITY

The best device today with a size of more than  $1 \text{ cm}^2$  is listed with a certified efficiency of 10.4% under standard test conditions ( $1000 \text{ Wm}^{-2}$ , AM1.5, 298 K) in the solar efficiency tables [7], published regularly in *Progress in Photovoltaics: Research and Applications*. On smaller device areas, higher efficiencies have been reported, as also indicated in the solar efficiency tables in *Progress in Photovoltaics* under “notable exceptions.” Entries into the main table require a minimum size of  $1 \text{ cm}^2$ .

In Table 1, a selection of representative benchmark efficiency data from the past years is shown, including also results from devices  $< 1 \text{ cm}^2$ .

Currently, the efficiency is limited primarily by two factors:

- (1) nonoptimized  $I_{SC}$  arising from the absorption spectrum of the dyes which does not extend far enough into the near infrared range of the optical spectrum;
- (2) nonoptimized  $V_{OC}$  arising from undesirable dark currents due to interfacial electron back transfer of injected electrons to the redox electrolyte.

Research is ongoing on both of these limitations as will be discussed in Section 5.

Long-term stability is a key parameter for any type of solar cells. For a proper assessment of stability, it is generally helpful to differentiate between intrinsic and extrinsic factors [14], where intrinsic factors are related to the solar cell under the condition of a perfectly closed/sealed system, while extrinsic factors are related to degradation processes induced by potential diffusion of molecules into or out of the solar cell. Penetration of water and oxygen and escape of solvent molecules are typical examples for extrinsic factors. In the early development stage of DSC technology, the quality of device sealing was sometimes not appropriate in laboratory test cells, leading to leakage of the volatile nitrile-based solvents, typically used for the electrolytes. While this type of problems is occasionally still considered as a challenge for the technology, most research groups with longer experience, including industrial labs, seem to have overcome them by improved sealing technologies [11]. Due to the direct relevance to the manufacturing of commercial products, little is published on processing issues though [15–17].

Good results on overall system stability have been reported since several years [18], including recent publications demonstrating excellent stability characteristics under laboratory test conditions at temperatures as high as  $85^\circ \text{C}$  in the dark and  $60^\circ \text{C}$  under illumination [19–21].

These good results need to be confirmed under real outdoor conditions in order to ascertain an appropriate correlation with the published stability data obtained under laboratory test conditions.

Information, available about outdoor field testing, is too scarce to be representative, but it suggests that further work on stability may be required despite the described progress [22, 23].

TABLE 1: Record efficiencies of DSC of various device sizes.

Dye*	Surface area (cm <sup>2</sup> )	$\eta$ (%)	V <sub>OC</sub> (V)	I <sub>sc</sub> (mA/cm <sup>2</sup> )	FF (%)	Reference
N-719	<1 cm <sup>2</sup>	11.2	0.84	17.73	74	[8]
N-749	0.219	11.1	0.736	20.9	72	[9]
N-749	1.004	10.4	0.72	21.8	65	[10]
N-719	1.31	10.1	0.82	17.0	72	[11]
N-3	2.36	8.2	0.726	15.8	71	[12]
N-749	26.5 (submodule)	6.3	6.145	1.7	60	[13]

\*N-719, N-749, and N-3 are codes for molecular structures (see Section 5.1).

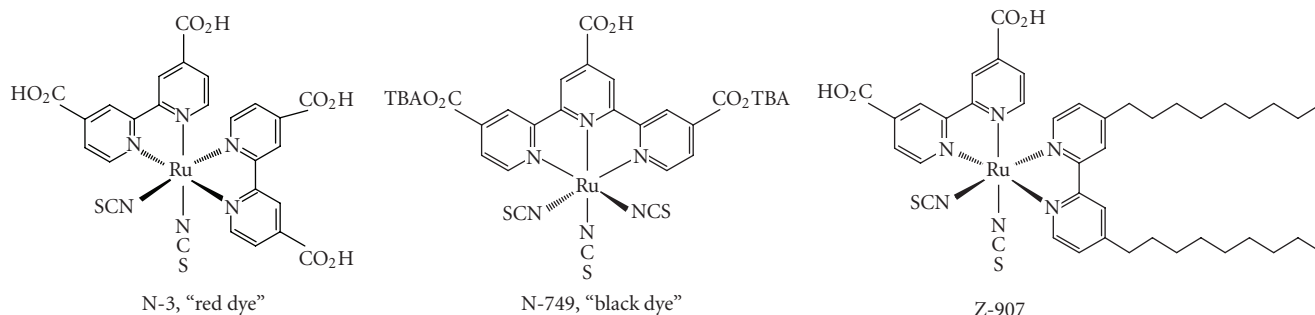


FIGURE 2: The three most frequently applied ruthenium polypyridyl complexes.

#### 4. KEY TECHNOLOGY DRIVERS

Based on low-cost and abundant materials, the expected manufacturing costs for DSCs are among the lowest of all PV technologies. Module costs of 1 €/Wp or less seem feasible [11]. Moreover, a favorable energy payback time of less than 1 year is foreseen [24] based on the relatively low-energy input for the processing of DSC modules (moderate processing temperatures below 600 °C and absence of high-vacuum steps). Furthermore, preliminary work on life cycle analysis reveals excellent sustainability characteristics [24], achieved among others because of the use of abundant, nontoxic materials in the production as well as during the processing. The electricity generation of DSCs is remarkably good in diffuse daylight and remains practically unchanged with increasing temperature. This is important in view of the constantly changing operating conditions of solar cells which may be exposed to variations in temperature, angle of incidence, or shading by clouds. A comparison between DSCs and crystalline Si modules under outdoor conditions in Japan resulted in a 10–20% higher kWh/kWp output of the DSC modules over the testing period of 6 months [23], underlining the good average performance under changing operating conditions.

The easy tunability of DSC technology in terms of colors and transparency grade as well as the possibility of processing on foils leaves a lot of rooms for product innovations in new markets. A number of products particularly for low-power applications in mobile electronics, for instance, mobile phones or laptops, are in development (see, e.g., [www.g24i.com](http://www.g24i.com)).

#### 5. STATE-OF-THE-ART MATERIALS AND CURRENT DEVELOPMENT TRENDS

There is an active materials research on practically all components of DSC devices. In this section, the most commonly applied materials are first presented, followed by a discussion of desirable improvements. The current R&D trends will be presented in a generic form with some selected illustrative examples.

##### 5.1. Dyes/sensitizers

Three dyes can be considered as the backbone of currently applied sensitizers in DSC. All of these dyes are ruthenium-based metal-organic complexes with the general formula RuL<sub>x</sub>L'<sub>y</sub>SCN<sub>z</sub>, where L and L' are polypyridyl ligands; they are readily available commercially and show excellent efficiency levels up to 11%. The molecular structures of these dyes are shown in Figure 2. Because of the complex chemical nomenclature, they are most often referred to with trivial names as indicated in Figure 2 (N-3 and N-749, which are commonly also called red and black dyes and Z-907). There is a widely used variant of the N-3 dye, which differs from it only in the degree of protonation (trivial name: N-719). The black dye shows the broadest absorption range up to 900 nm.

##### Desirable improvements

The primary goal of R&D on sensitizers is further progress in efficiency. Issues with respect to robustness, sustainability, and cost are also of relevance, though. For improvements in current output, an extension of the absorption range of DSCs

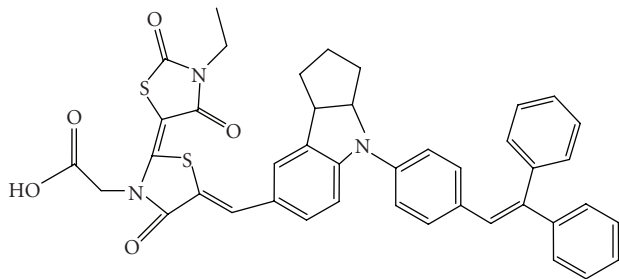


FIGURE 3: Organic sensitizer D-149.

towards longer wavelengths from currently 800–900 nm to 900–1000 nm is required.

Moreover, dyes with enhanced molar absorption coefficients are attractive for efficient light harvesting with thinner  $\text{TiO}_2$  layers. This can lead to an efficiency boost of DSC concepts, which depends so far on such thin layers (particularly solid state- but also ionic liquid-based systems) and generally to improved  $V_{OC}$  independent of the type of system.

With regard to sustainability and cost, organic dyes may be advantageous.

#### Assessment of current trends

An impressive number of new sensitizers are being developed in recent years. Many of the new dyes are derivatives of the N-3 molecule with various chemical modifications on one of its two bipyridyl moieties while leaving the rest of the molecule unchanged. This work has led to sensitizers with improved molar absorption coefficients [25], referred to in the literature as the “K-series” [26–28], as well as to the discovery that hydrophobic side chains (like in Z-907) can be beneficial for long-term stability [29]. This latter effect is assigned to the inhibition of  $\text{H}_2\text{O}$  adsorption to the  $\text{TiO}_2$  surface. Dyes in which the carboxylic acid functions are replaced by phosphonic acid functions [30, 31] may also be advantageous for long-term stability because of the stronger adsorption of these groups to the  $\text{TiO}_2$  surface.

On the other hand, efforts to further extend the spectral absorption range of the sensitizer beyond that of the “black dye,” published for the first time in 1997 [32], have not been successful yet, which is why record efficiencies have remained unaffected by this research thus far. The coadsorption of several dyes in “dye cocktails,” following this same goal, has shown to be conceptually applicable [33, 34], but it needs further elaboration. The development of tandem concepts is another promising route. A significantly enhanced absorption range and improved efficiency (15%) could be achieved by the combination of a DSC top cell with a CIGS bottom cell [35]—approaches based on DSCs exclusively are under development [36, 37].

Next to the systematic development of improved ruthenium complexes, there is also a significant number of publications on purely organic dyes with increasingly good photovoltaic performance [38–40]. This trend is driven among others by the argument of potentially lower cost. The best results thus far have been obtained with the indoline dye D-149

[41, 42], shown in Figure 3. Such dyes may become a viable alternative to ruthenium complexes in case further favorable characteristics, also on long-term stability, can be achieved.

Rather, a sideline of current research but with potential significance for new markets (decorative applications) is the development of sensitizers with different colors, such as green Zn phthalocyanine complexes [13, 43].

Another innovative research line is the replacement of molecular sensitizers by semiconductor quantum dots, for example, PbS [44]. This approach, which is still in its infancy, may profit from the very high absorption cross-sections of quantum dots as well as from the recently discovered phenomenon of impact ionization (creation of multiple excitons by excitation with a single photon when the photon energy is three times higher than the bandgap) [45]. To date, reaching competitive levels of overall conversion efficiency by sensitization with quantum dots has remained a major challenge though. A notable exception is a related approach based on a nanocomposite structure consisting only of  $\text{TiO}_2$  and  $\text{CuInS}_2$ . Here, the  $\text{CuInS}_2$  assumes the functions of sensitizer and hole conducting medium at the same time, and an overall efficiency of up to 5% has been published for this all solid-state approach [46, 47].

#### 5.2. Nanostructured oxide films

The most extensively applied and successful material by far is the high bandgap semiconductor  $\text{TiO}_2$  (bandgap: 3.2 eV). The often translucent nanocrystalline layers consist of interconnected colloidal particles in the size range of 15–30 nm with a layer thickness typically between 5 and 15  $\mu\text{m}$ . The surface area enhancement (often also referred to as roughness factor) of such layers is on the order of 100/ $\mu\text{m}^2$  and the porosity is between 50 and 70% [48]. The best photovoltaic performances have been obtained using layers with enhanced haze and by application of a  $\text{TiCl}_4$  posttreatment [49]. Enhanced haze is achieved by introduction of scattering centers (large  $\text{TiO}_2$  particles) inside [9, 48] or on top of the film with the smaller particles [42]. The colloidal  $\text{TiO}_2$  materials are prepared by a hydrothermal sol-gel method in acidic or basic aqueous media [48, 50] and the layers are generally applied by industrially relevant processes such as screen-printing. For a quantitative removal of organic additives (binders and dispersants) after printing, processing temperatures between 450 °C and 550 °C are typically required during the annealing of the films. An SEM image of a typical  $\text{TiO}_2$  film is shown here in Figure 4.

#### Desirable improvements

For liquid electrolyte-based cells, the currently applied  $\text{TiO}_2$  layers are already fairly optimized with respect to surface area, film thickness, porosity, and optical properties (haze).

On the other hand, cells in which the liquid electrolyte is replaced by solid-state hole conductors suffer from insufficient pore filling—a problem which might be relieved by other microstructures with more easily accessible pores, for example, by the use of linear pore geometries.

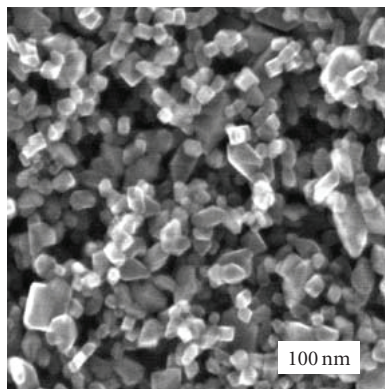


FIGURE 4: SEM micrograph of a nanocrystalline TiO<sub>2</sub> film (view from the top).

In general, the development of low-temperature processes without compromising system efficiencies is an attractive goal, particularly in order to make processing on polymer substrates possible.

Further improvements in  $V_{OC}$ —also for electrolyte-based systems—could be obtained if ways are found to hamper interfacial recombination by chemical or physical surface engineering.

#### Assessment of current trends

Efforts to replace TiO<sub>2</sub> as the material of choice for DSC have been plentiful, however, until now without convincing success [51–54]. The search for another material is motivated primarily by higher electron mobilities to reduce the electron transport resistance—this is the case of ZnO—or by higher bandgaps, as in SnO<sub>2</sub>. The latter aims at avoiding any absorption of UV photons by the oxide, which can potentially give rise to degradation processes by strongly oxidizing valence band holes. While DSC devices have been successfully prepared with a number of different oxides, including ZnO [51], SrTiO<sub>3</sub> [53], SnO<sub>2</sub> [54], and Nb<sub>2</sub>O<sub>5</sub> [52], the achieved device performances are at best half of those published for TiO<sub>2</sub>-based devices. Considering in addition the excellent chemical stability of TiO<sub>2</sub>, its large abundance, and nontoxicity, the probability of finding a more appropriate material can be considered as being quite small.

One recent trend is the application of ultrathin insulator layers like Al<sub>2</sub>O<sub>3</sub> [55] or MgO [56] on TiO<sub>2</sub>. Such coatings were found to slow down the interfacial recombination kinetics. While this approach needs further elaboration, clear benefits have typically only been observed for solid-state systems [57, 58], in which the interfacial recombination kinetics can limit the performance. For electrolyte-based systems on the other hand, no clear benefits were found as long as TiO<sub>2</sub> was used as a photoanode material [54].

A very recent development is the application of ordered TiO<sub>2</sub> microstructures [59–61]. Only some months ago, one of the major limiting factors of such materials, that is, the insufficient total surface area, has been overcome by the successful preparation of TiO<sub>2</sub> nanotubes with roughness fac-

TABLE 2: Typical current solvent-based electrolyte compositions (ACN = acetonitrile, VN = valeronitrile, MPN = 3-methoxypropionitrile, PMII = 1-propyl-3-methylimidazolium iodide, GuSCN = guanidinium thiocyanate, TBP = tert-butylpyridin, NBB = 1-butyl-1*H*-benzimidazol.).

	High $\eta$	Robust
Solvent	ACN:VN (3/1)	MPN
Iodide compound	1 M PMII	1 M PMII
Iodine	0.03 M I <sub>2</sub>	0.15 M I <sub>2</sub>
Additive 1	0.1 M GuSCN	0.1 M GuSCN
Additive 2	0.5 M TBP	0.5 M NBB
Efficiency	10.5% (<1 cm <sup>2</sup> )	9% (<1 cm <sup>2</sup> )

tors up to >1000, as required for efficient light harvesting in DSC [62]. In this work, a noncertified overall efficiency of almost 7% was published for an electrolyte-based cell. However, considering the excellent performance of the “standard” colloidal TiO<sub>2</sub> layers in electrolyte cells, this approach as well may be beneficial primarily for solid-state devices, where a facilitation of pore-filling is possible.

Low-temperature preparations of TiO<sub>2</sub> films are pursued since several years ( $T < 200$  °C) and with increasingly good results in terms of DSC performance on flexible substrates. The processing of the oxide layer at low temperature is essential in view of cost-effective production on conductive plastic foils. Methods for the fabrication of low-temperature oxide films include pressing and electrophoresis [63, 64] as well as low-temperature chemical sintering [65, 66] or electrodeposition [67]. Nevertheless, the best flexible system to date—on a titanium foil—still applies a high-temperature sintering step for the TiO<sub>2</sub> layer ( $\eta = 7.2\%$ ). [68].

### 5.3. Electrolytes/molecular hole conductors

The record conversion efficiencies up to 11%, reported in Section 3, are typically achieved with liquid electrolytes based on acetonitrile—a low-viscosity volatile solvent—and by using comparatively low iodine concentration. These high-efficiency electrolytes are not at the same time optimized for achieving the best long-term stability characteristics, for which other electrolyte formulations with less volatile solvents or ionic liquids as well as higher iodine concentrations are more appropriate. These latter electrolytes are often referred to as robust electrolytes in the literature and their application leads to a lower-efficiency output in the range of 7–9%. Next to the redox-active species and solvents, the electrolytes contain typically some additives. The function of these additives is in most cases to reduce the dark current by coordination to the TiO<sub>2</sub> surface, thus improving the  $V_{OC}$  of the solar cells. Table 2 compares the compositions of a widely used high-efficiency electrolyte and a popular robust electrolyte; both are used in conjunction with a sensitizer from the K-series (see Section 5.1) and coded K-77 in this case [21].

### Desirable improvements

The predominant technological drivers for the current work on electrolytes are aspects related to robustness, environmental sustainability, and processability for module concepts. As an example of processability, the replacement of the corrosive iodine-based electrolyte could facilitate module production on larger areas by avoiding the necessity to apply protective coatings to metallic current collector grids. Concerning system robustness and sustainability, the replacement of volatile solvents is expected to be beneficial. Full solid-state versions in which the electrolyte is completely replaced by a solid material will have clear advantages for interconnection schemes on the level of module fabrication.

Furthermore, the goal to further improve the efficiency is also an important motivation for the work on electrolytes, for instance, by the search for new additives for the suppression of interfacial recombination. This could lead to gains in  $V_{OC}$ .

### Assessment of current trends

One current research direction is the development of non-corrosive electrolytes. The most promising results so far have been obtained with the Co(II)/Co(III) redox couple with external quantum efficiency values up to 80% [69] and overall efficiencies up to 4% at full sun illumination and 8% at 1/10 sun illumination [70]. The amount of research going on in this direction is surprisingly limited considering the obvious benefits which could be achieved. This may in part be explained by the impeccable functioning of the  $I^-/I_3^-$  couple, in which a negatively charged ion carries the positive electrical charge. The resulting electrostatic repulsion between the electron in the  $TiO_2$  and the hole on the  $I_3^-$  ion may be advantageous for the slow interfacial recombination kinetics (in the millisecond time domain). A further probable factor in the context of these favorably slow kinetics is the involvement of two electrons in the recombination reaction ( $I_3^- + 2e^-_{TiO_2} \rightarrow 3I^-$ ).

Several research groups currently investigate the use of ionic liquids instead of organic solvents in liquid electrolytes. Ionic liquids are a new class of materials with a number of attractive properties for application in DSCs, such as high stability, negligible vapor pressure, nonflammability, as well as excellent environmental compatibility. On the other hand, overall power conversion efficiencies obtained with ionic liquids are so far considerably lower than those obtained with organic solvent electrolytes, typically in the range of 4–7.5% (on device areas  $< 1\text{ cm}^2$ ) [71–74]. This is due to diffusion limited current output in these systems caused by their more viscous nature. Viscosity values are higher by a factor of 10–100 than in acetonitrile-based electrolytes [42]. If these limitations can be overcome, ionic liquids may well turn out to be an attractive alternative to the liquid electrolytes based on volatile solvents. The most frequently studied class of ionic liquid materials is 1-methyl-3-alkylimidazolium iodide (see Figure 5).

An alternative approach for the replacement of volatile electrolytes is the addition of gelators to solvent-based elec-

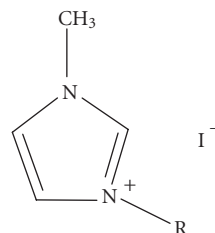


FIGURE 5: General molecular structure of a typical ionic liquid.

trolytes, leading to the formation of quasisolid gel electrolytes. A considerable number of articles have appeared on this topic in recent years. Systems with efficiencies in the range of 4–6% [75–78] have been published, with some including promising stability data [79].

A more “radical” and fundamentally different approach is the replacement of the electrolyte by a solid-state mediator. Practical preparation issues are substantially more challenging than for all liquid-based approaches though. It is not evident to fill all the nm-sized pores of the  $TiO_2$  films with another solid and to achieve a similarly quantitative and intimate interfacial contact with the dye molecules as can be achieved with a liquid. This is one of the reasons why rather thin  $TiO_2$  layers of only 2–3  $\mu\text{m}$  are typically employed in solid-state devices leading to limitations in light absorption.

Next to this, the interfacial charge recombination dynamics—for electrons in the  $TiO_2$  with holes in the mediator—are reported to be faster by a factor of about 10 compared with liquid electrolytes [80]. Special attention to interface engineering is thus required, a topic which has only been addressed in a preliminary fashion so far [28, 81, 82]. Considering these two major challenges, pore filling and recombination kinetics, the results obtained in various groups with efficiencies up to  $>4\%$  [83, 84] are promising. The best material so far investigated is the amorphous organic hole conductor spiro-OMeTAD [85] followed by crystalline Cu(I) compounds, CuSCN [86] and CuI [87]. The amorphous state seems clearly to be more appropriate for the pore-filling requirements, which is also consistent with the observation of improved device performance by the addition of a crystal inhibitor in systems based on crystalline CuI as mediator [88]. In terms of pore-filling, the development of more sophisticated deposition techniques is desirable; the methods applied so far, spin-coating and “solution-casting,” are not suited well enough. Self-assembly concepts—similar to the one successfully applied ever since for the monolayer formation of the dye molecules on the  $TiO_2$  surface—could prove to be helpful in this context.

## 6. COMMERCIALIZATION

Currently, DSC technology is on the verge of commercialization, a view which is supported by the growing number of patents in this field ( $>300$  in 2005) as well as by the recently started organization of a series of conferences dedicated specifically to the topic of industrialization of DSC (DSC-IC, [www.dyesol.com/conference](http://www.dyesol.com/conference)). A large number of

commercial companies are active in the field, presenting first module prototypes at conferences or selling DSC-specific materials and production equipment. Commercialization ambitions take place on several continents with a certain focus in Asia (Japan). Relevant names are IMRA-Aisin Seiki/Toyota, Sharp, Toshiba, Dai Nippon, Peccell Technologies (all in Japan), Dyesol (Australia), Konarka (US), G24i (UK), and Solaronix (Switzerland). G24i has announced a DSC module production of 25 MW capacity in 2007 in Cardiff, Wales (UK), with extension plans up to 200 MW by the end of 2008 (<http://www.g24i.com>). Various module types are developed by these companies, including flexible light-weight designs on plastic or metal foils as well as glass-based modules. The products envisaged by the producers cover a broad range of low- and high-power applications from charging units for mobile electronics (phones and laptops) and colorful decorative elements to electric power producing glass tiles for facade integration in buildings.

## 7. CONCLUSIONS AND OUTLOOK

DSC technology currently develops very dynamically. Progress has been made on various aspects, including efficiency, stability, and commercialization. Record efficiencies have reached more than 11% on small device areas ( $< 1 \text{ cm}^2$ ) and more than 6% on relevant submodule areas—for the most robust systems, these values are lower. Further improvements are probable; they depend critically on systematic and successful materials research. Stability data under laboratory test conditions from the last years are encouraging; field-testing is now required to confirm these results under real outdoor conditions on the module level.

These developments have fuelled an active commercial interest in the past few years.

With its attractive features, like low-cost potential, good performance under typical changes in operating conditions (temperature and illumination conditions), and application variability, the appearance of the first commercial products in the marketplace seems close.

## REFERENCES

- [1] B. C. O'Regan and M. Grätzel, "A low-cost, high-efficiency solar cell based on dye-sensitized colloidal  $\text{TiO}_2$  films," *Nature*, vol. 353, no. 6346, pp. 737–740, 1991.
- [2] S. A. Haque, E. Palomares, B. M. Cho, et al., "Charge separation versus recombination in dye-sensitized nanocrystalline solar cells: the minimization of kinetic redundancy," *Journal of the American Chemical Society*, vol. 127, no. 10, pp. 3456–3462, 2005.
- [3] J. M. Kroon, B. C. O'Regan, J. A. M. van Roosmalen, and W. C. Sinke, "Dye-sensitized solar cells. Inorganic photochemistry," in *Handbook of Photochemistry and Photobiology*, chapter 1, pp. 1–47, American Scientific, Stevenson Ranch, Calif, USA, 2003.
- [4] A. Hagfeldt and M. Grätzel, "Molecular photovoltaics," *Accounts of Chemical Research*, vol. 33, no. 5, pp. 269–277, 2000.
- [5] M. Grätzel, "The advent of mesoscopic injection solar cells," *Progress in Photovoltaics: Research and Applications*, vol. 14, no. 5, pp. 429–442, 2006.
- [6] M. Grätzel, "Perspectives for dye-sensitized nanocrystalline solar cells," *Progress in Photovoltaics: Research and Applications*, vol. 8, no. 1, pp. 171–185, 2000.
- [7] M. A. Green, K. Emery, D. L. King, Y. Hishikawa, and W. Warta, "Solar cell efficiency tables (version 28)," *Progress in Photovoltaics: Research and Applications*, vol. 14, no. 5, pp. 455–461, 2006.
- [8] M. Grätzel, "Mesoscopic solar cells for electricity and hydrogen production from sunlight," *Chemistry Letters*, vol. 34, no. 1, pp. 8–13, 2005.
- [9] Y. Chiba, A. Islam, Y. Watanabe, R. Komiya, N. Koide, and L. Han, "Dye-sensitized solar cells with conversion efficiency of 11.1%," *Japanese Journal of Applied Physics Part 2*, vol. 45, no. 25, pp. L638–L640, 2006.
- [10] Y. Chiba, A. Islam, K. Kakutani, R. Komiya, N. Koide, and L. Han, "High efficiency of dye-sensitized solar cells," in *Technical Digest of the 15th International Photovoltaic Science and Engineering Conference*, pp. 665–666, Shanghai, China, October 2005.
- [11] J. M. Kroon, N. J. Bakker, H. J. P. Smit, et al., "Nanocrystalline dye-sensitized solar cells having maximum performance," *Progress in Photovoltaics: Research and Applications*, vol. 15, no. 1, pp. 1–18, 2007.
- [12] A. Hinsch, J. M. Kroon, R. Kern, I. Uhlenndorf, R. Sastrawan, and A. Meyer, "Long-term stability and efficiency of dye-sensitized solar cells," in *Proceedings of the 17th European Photovoltaic Solar Energy Conference*, pp. 51–54, Munich, Germany, October 2001.
- [13] L. Han, A. Fukui, N. Fuke, N. Koide, and R. Yamanaka, "High efficiency of dye-sensitized solar cell and module," in *Proceedings of the 4th IEEE World Conference on Photovoltaic Energy Conversion (WCPEC '06)*, pp. 178–182, Waikoloa, Hawaii, USA, May 2006.
- [14] P. M. Sommeling, M. Späth, H. J. P. Smit, N. J. Bakker, and J. M. Kroon, "Long-term stability testing of dye-sensitized solar cells," *Journal of Photochemistry and Photobiology A*, vol. 164, no. 1–3, pp. 137–144, 2004.
- [15] M. Späth, P. M. Sommeling, J. A. M. van Roosmalen, et al., "Reproducible manufacturing of dye-sensitized solar cells on a semi-automated baseline," *Progress in Photovoltaics: Research and Applications*, vol. 11, no. 3, pp. 207–220, 2003.
- [16] R. Sastrawan, J. Beier, U. Belledin, et al., "A glass frit-sealed dye solar cell module with integrated series connections," *Solar Energy Materials and Solar Cells*, vol. 90, no. 11, pp. 1680–1691, 2006.
- [17] R. Sastrawan, J. Beier, U. Belledin, et al., "New interdigital design for large area dye solar modules using a lead-free glass frit sealing," *Progress in Photovoltaics: Research and Applications*, vol. 14, no. 8, pp. 697–709, 2006.
- [18] A. Hinsch, J. M. Kroon, R. Kern, et al., "Long-term stability of dye-sensitized solar cells," *Progress in Photovoltaics: Research and Applications*, vol. 9, no. 6, pp. 425–438, 2001.
- [19] P. Wang, C. Klein, R. Humphry-Baker, S. M. Zakeeruddin, and M. Grätzel, "Stable  $\geq 8\%$  efficient nanocrystalline dye-sensitized solar cell based on an electrolyte of low volatility," *Applied Physics Letters*, vol. 86, no. 12, Article ID 123508, 3 pages, 2005.
- [20] D. Kuang, C. Klein, S. Ito, et al., "High-efficiency and stable mesoscopic dye-sensitized solar cells based on a high molar extinction coefficient ruthenium sensitizer and nonvolatile electrolyte," *Advanced Materials*, vol. 19, no. 8, pp. 1133–1137, 2007.
- [21] D. Kuang, C. Klein, S. Ito, et al., "High molar extinction coefficient ion-coordinating ruthenium sensitizer for efficient and

- stable mesoscopic dye-sensitized solar cells," *Advanced Functional Materials*, vol. 17, no. 1, pp. 154–160, 2007.
- [22] N. Kato, K. Higuchi, Y. Takeda, et al., "Long-term stability of DSC module under outdoor working condition," in *Proceedings of Renewable Energy*, Makuhari Messe, Chiba, Japan, October 2006.
- [23] T. Toyoda, T. Sano, J. Nakajima, et al., "Outdoor performance of large scale DSC modules," *Journal of Photochemistry and Photobiology A*, vol. 164, no. 1–3, pp. 203–207, 2004.
- [24] T. Veltkamp, J. M. Kroon, P. Sommeling, and M. Wild-Scholten, "Dye sensitised solar cells for large-scale photovoltaics: determination of durability and environmental profile," in *Proceedings of Renewable Energy*, Makuhari Messe, Chiba, Japan, October 2006.
- [25] C. Klein, M. K. Nazeeruddin, P. Liska, et al., "Engineering of a novel ruthenium sensitizer and its application in dye-sensitized solar cells for conversion of sunlight into electricity," *Inorganic Chemistry*, vol. 44, no. 2, pp. 178–180, 2005.
- [26] P. Wang, C. Klein, R. Humphry-Baker, S. M. Zakeeruddin, and M. Grätzel, "A high molar extinction coefficient sensitizer for stable dye-sensitized solar cells," *Journal of the American Chemical Society*, vol. 127, no. 3, pp. 808–809, 2005.
- [27] D. Kuang, S. Ito, and B. Wenger, "High molar extinction coefficient heteroleptic ruthenium complexes for thin film dye-sensitized solar cells," *Journal of the American Chemical Society*, vol. 128, no. 12, pp. 4146–4154, 2006.
- [28] D. Kuang, C. Klein, H. J. Snaith, et al., "Ion coordinating sensitizer for high efficiency mesoscopic dye-sensitized solar cells: influence of lithium ions on the photovoltaic performance of liquid and solid-state cells," *Nano Letters*, vol. 6, no. 4, pp. 769–773, 2006.
- [29] P. Wang, S. M. Zakeeruddin, J. E. Moser, M. K. Nazeeruddin, T. Sekiguchi, and M. Grätzel, "A stable quasi-solid-state dye-sensitized solar cell with an amphiphilic ruthenium sensitizer and polymer gel electrolyte," *Nature Materials*, vol. 2, no. 6, pp. 402–407, 2003.
- [30] P. Pechy, F. P. Rotzinger, M. K. Nazeeruddin, et al., "Preparation of phosphonated polypyridyl ligands to anchor transition-metal complexes on oxide surfaces: application for the conversion of light to electricity with nanocrystalline TiO<sub>2</sub> film," *Journal of the Chemical Society, Chemical Communications*, no. 1, pp. 65–66, 1995.
- [31] P. Wang, C. Klein, J.-E. Moser, et al., "Amphiphilic ruthenium sensitizer with 4,4'-diphosphonic acid-2,2'-bipyridine as anchoring ligand for nanocrystalline dye sensitized solar cells," *Journal of Physical Chemistry B*, vol. 108, no. 45, pp. 17553–17559, 2004.
- [32] M. K. Nazeeruddin, P. Péchy, and M. Grätzel, "Efficient panchromatic sensitization of nanocrystalline TiO<sub>2</sub> films by a black dye based on a trithiocyanato-ruthenium complex," *Chemical Communications*, no. 18, pp. 1705–1706, 1997.
- [33] A. Burke, L. Schmidt-Mende, S. Ito, and M. Grätzel, "A novel blue dye for near-IR 'dye-sensitized' solar cell applications," *Chemical Communications*, no. 3, pp. 234–236, 2007.
- [34] J. Fang, L. Su, J. Wu, Y. Shu, and Z. Lu, "The photoreponse properties of nanocrystalline TiO<sub>2</sub> particulate films co-modified with dyes," *New Journal of Chemistry*, vol. 21, pp. 839–840, 1997.
- [35] P. Liska, K. R. Thampi, M. Grätzel, et al., "Nanocrystalline dye-sensitized solar cell/copper indium gallium selenide thin-film tandem showing greater than 15% conversion efficiency," *Applied Physics Letters*, vol. 88, no. 20, Article ID 203103, 3 pages, 2006.
- [36] M. Dürr, A. Bamedi, A. Yasuda, and G. Nelles, "Tandem dye-sensitized solar cell for improved power conversion efficiencies," *Applied Physics Letters*, vol. 84, no. 17, pp. 3397–3399, 2004.
- [37] W. Kubo, A. Sakamoto, T. Kitamura, Y. Wada, and S. Yanagida, "Dye-sensitized solar cells: improvement of spectral response by tandem structure," *Journal of Photochemistry and Photobiology A*, vol. 164, no. 1–3, pp. 33–39, 2004.
- [38] T. Kitamura, M. Ikeda, K. Shigaki, et al., "Phenyl-conjugated oligoene sensitizers for TiO<sub>2</sub> solar cells," *Chemistry of Materials*, vol. 16, no. 9, pp. 1806–1812, 2004.
- [39] K. Hara, Z.-S. Wang, T. Sato, et al., "Oligothiophene-containing coumarin dyes for efficient dye-sensitized solar cells," *Journal of Physical Chemistry B*, vol. 109, no. 32, pp. 15476–15482, 2005.
- [40] K. Hara, M. Kurashige, S. Ito, et al., "Novel polyene dyes for highly efficient dye-sensitized solar cells," *Chemical Communications*, no. 2, pp. 252–253, 2003.
- [41] T. Horiuchi, H. Miura, K. Sumioka, and S. Uchida, "High efficiency of dye-sensitized solar cells based on metal-free indoline dyes," *Journal of the American Chemical Society*, vol. 126, no. 39, pp. 12218–12219, 2004.
- [42] S. Ito, S. M. Zakeeruddin, R. Humphry-Baker, et al., "High-efficiency organic-dye-sensitized solar cells controlled by nanocrystalline-TiO<sub>2</sub> electrode thickness," *Advanced Materials*, vol. 18, no. 9, pp. 1202–1205, 2006.
- [43] M. Grätzel, "Electricity and hydrogen generation from sunlight by mesoscopic solar cells," in *Proceedings of the 16th International Conference on Photochemical Conversion and Storage of Solar Energy (IPS-16'06)*, Uppsala, Sweden, July 2006.
- [44] R. Plass, S. Pelet, J. Krueger, M. Grätzel, and U. Bach, "Quantum dot sensitization of organic-inorganic hybrid solar cells," *Journal of Physical Chemistry B*, vol. 106, no. 31, pp. 7578–7580, 2002.
- [45] R. D. Schaller and V. I. Klimov, "High efficiency carrier multiplication in PbSe nanocrystals: implications for solar energy conversion," *Physical Review Letters*, vol. 92, no. 18, Article ID 186601, 4 pages, 2004.
- [46] M. Nanu, J. Schoonman, and A. Goossens, "Inorganic nanocomposites of n- and p-type semiconductors: a new type of three-dimensional solar cell," *Advanced Materials*, vol. 16, no. 5, pp. 453–456, 2004.
- [47] M. Nanu, J. Schoonman, and A. Goossens, "Nanocomposite three-dimensional solar cells obtained by chemical spray deposition," *Nano Letters*, vol. 5, no. 9, pp. 1716–1719, 2005.
- [48] C. J. Barbé, F. Arendse, P. Comte, et al., "Nanocrystalline titanium oxide electrodes for photovoltaic applications," *Journal of the American Ceramic Society*, vol. 80, no. 12, pp. 3157–3171, 1997.
- [49] P. M. Sommeling, B. C. O'Regan, R. R. Haswell, et al., "Influence of a TiCl<sub>4</sub> post-treatment on nanocrystalline TiO<sub>2</sub> films in dye-sensitized solar cells," *Journal of Physical Chemistry B*, vol. 110, no. 39, pp. 19191–19197, 2006.
- [50] S. Hore, E. Palomares, H. Smit, et al., "Acid versus base peptization of mesoporous nanocrystalline TiO<sub>2</sub> films: functional studies in dye sensitized solar cells," *Journal of Materials Chemistry*, vol. 15, no. 3, pp. 412–418, 2005.
- [51] K. Keis, E. Magnusson, H. Lindström, S.-E. Lindquist, and A. Hagfeldt, "A 5% efficient photoelectrochemical solar cell based on nanostructured ZnO electrodes," *Solar Energy Materials and Solar Cells*, vol. 73, no. 1, pp. 51–58, 2002.
- [52] K. Sayama, H. Sugihara, and H. Arakawa, "Photoelectrochemical properties of a porous Nb<sub>2</sub>O<sub>5</sub> electrode sensitized by

- a ruthenium dye," *Chemistry of Materials*, vol. 10, no. 12, pp. 3825–3832, 1998.
- [53] S. Burnside, J.-E. Moser, K. Brooks, M. Grätzel, and D. Cahen, "Nanocrystalline mesoporous strontium titanate as photoelectrode material for photosensitized solar devices: increasing photovoltage through flatband potential engineering," *Journal of Physical Chemistry B*, vol. 103, no. 43, pp. 9328–9332, 1999.
- [54] K. Tennakone, P. K. M. Bandaranayake, P. V. V. Jayaweera, A. Konno, and G. R. R. A. Kumara, "Dye-sensitized composite semiconductor nanostructures," *Physica E*, vol. 14, no. 1-2, pp. 190–196, 2002.
- [55] E. Palomares, J. N. Clifford, S. A. Haque, T. Lutz, and J. R. Durrant, "Slow charge recombination in dye-sensitized solar cells (DSSC) using  $\text{Al}_2\text{O}_3$  coated nanoporous  $\text{TiO}_2$  films," *Chemical Communications*, no. 14, pp. 1464–1465, 2002.
- [56] A. Kay and M. Grätzel, "Dye-sensitized core-shell nanocrystals: improved efficiency of mesoporous tin oxide electrodes coated with a thin layer of an insulating oxide," *Chemistry of Materials*, vol. 14, no. 7, pp. 2930–2935, 2002.
- [57] K. Tennakone, J. Bandara, P. K. M. Bandaranayake, G. R. A. Kumara, and A. Konno, "Enhanced efficiency of a dye-sensitized solar cell made from  $\text{MgO}$ -coated nanocrystalline  $\text{SnO}_2$ ," *Japanese Journal of Applied Physics Part 2*, vol. 40, no. 7 B, pp. L732–L734, 2001.
- [58] B. C. O'Regan, S. Scully, A. C. Mayer, E. Palomares, and J. Durrant, "The effect of  $\text{Al}_2\text{O}_3$  barrier layers in  $\text{TiO}_2/\text{Dye}/\text{CuSCN}$  photovoltage cells explored by recombination and DOS characterization using transient photovoltage measurements," *Journal of Physical Chemistry B*, vol. 109, no. 10, pp. 4616–4623, 2005.
- [59] G. K. Mor, K. Shankar, M. Paulose, O. K. Varghese, and C. A. Grimes, "Use of highly-ordered  $\text{TiO}_2$  nanotube arrays in dye-sensitized solar cells," *Nano Letters*, vol. 6, no. 2, pp. 215–218, 2006.
- [60] M. Zukalová, A. Zukal, L. Kavan, M. K. Nazeeruddin, P. Liska, and M. Grätzel, "Organized mesoporous  $\text{TiO}_2$  films exhibiting greatly enhanced performance in dye-sensitized solar cells," *Nano Letters*, vol. 5, no. 9, pp. 1789–1792, 2005.
- [61] K. Zhu, N. R. Neale, A. Miedaner, and A. J. Frank, "Enhanced charge-collection efficiencies and light scattering in dye-sensitized solar cells using oriented  $\text{TiO}_2$  nanotubes arrays," *Nano Letters*, vol. 7, no. 1, pp. 69–74, 2007.
- [62] K. Shankar, G. K. Mor, H. E. Prakasham, et al., "Highly-ordered  $\text{TiO}_2$  nanotube arrays up to  $220\ \mu\text{m}$  in length: use in water photoelectrolysis and dye-sensitized solar cells," *Nanotechnology*, vol. 18, no. 6, Article ID 065707, 11 pages, 2007.
- [63] H. Lindström, A. Holmberg, E. Magnusson, L. Malmqvist, and A. Hagfeldt, "A new method to make dye-sensitized nanocrystalline solar cells at room temperature," *Journal of Photochemistry and Photobiology A*, vol. 145, no. 1-2, pp. 107–112, 2001.
- [64] T. Miyasaka and Y. Kijitori, "Low-temperature fabrication of dye-sensitized plastic electrodes by electrophoretic preparation of mesoporous  $\text{TiO}_2$  layers," *Journal of the Electrochemical Society*, vol. 151, no. 11, pp. A1767–A1773, 2004.
- [65] R. Gaudiana, "Dye sensitized titania photovoltaic cells on flexible substrates-concept to commercialization," *Journal of Macromolecular Science Part A*, vol. 39 A, no. 10, pp. 1259–1264, 2002.
- [66] D. Zhang, T. Yoshida, and H. Minoura, "Low-temperature fabrication of efficient porous titania photoelectrodes by hydrothermal crystallization at the solid/gas interface," *Advanced Materials*, vol. 15, no. 10, pp. 814–817, 2003.
- [67] T. Loewenstein, K. Nonomura, T. Yoshida, et al., "Efficient sensitization of mesoporous electrodeposited zinc oxide by cis-bis(isothiocyanato)bis(2,2'-bipyridyl-4,4'-dicarboxylato)-ruthenium(II)," *Journal of the Electrochemical Society*, vol. 153, no. 4, pp. A699–A704, 2006.
- [68] S. Ito, N.-L. C. Ha, G. Rothenberger, et al., "High-efficiency (7.2%) flexible dye-sensitized solar cells with Ti-metal substrate for nanocrystalline- $\text{TiO}_2$  photoanode," *Chemical Communications*, no. 38, pp. 4004–4006, 2006.
- [69] S. Cazzanti, S. Caramori, R. Argazzi, C. M. Elliott, and C. A. Bignozzi, "Efficient non-corrosive electron-transfer mediator mixtures for dye-sensitized solar cells," *Journal of the American Chemical Society*, vol. 128, no. 31, pp. 9996–9997, 2006.
- [70] H. Nusbaumer, S. M. Zakeeruddin, J.-E. Moser, and M. Grätzel, "An alternative efficient redox couple for the dye-sensitized solar cell system," *Chemistry - A European Journal*, vol. 9, no. 16, pp. 3756–3763, 2003.
- [71] P. Wang, S. M. Zakeeruddin, J.-E. Moser, R. Humphry-Baker, and M. Grätzel, "A solvent-free,  $\text{SeCN}^-/(\text{SeCN})_3^-$  based ionic liquid electrolyte for high-efficiency dye-sensitized nanocrystalline solar cells," *Journal of the American Chemical Society*, vol. 126, no. 23, pp. 7164–7165, 2004.
- [72] W. Kubo, T. Kitamura, K. Hanabusa, Y. Wada, and S. Yanagida, "Quasi-solid-state dye-sensitized solar cells using room temperature molten salts and a low molecular weight gelator," *Chemical Communications*, no. 4, pp. 374–375, 2002.
- [73] R. Kawano, H. Matsui, C. Matsuyama, et al., "High performance dye-sensitized solar cells using ionic liquids as their electrolytes," *Journal of Photochemistry and Photobiology A*, vol. 164, no. 1–3, pp. 87–92, 2004.
- [74] D. Kuang, P. Wang, S. Ito, S. M. Zakeeruddin, and M. Grätzel, "Stable mesoscopic dye-sensitized solar cells based on tetracyanoborate ionic liquid electrolyte," *Journal of the American Chemical Society*, vol. 128, no. 24, pp. 7732–7733, 2006.
- [75] W. Kubo, Y. Makimoto, T. Kitamura, Y. Wada, and S. Yanagida, "Quasi-solid-state dye-sensitized solar cell with ionic polymer electrolyte," *Chemistry Letters*, no. 9, pp. 948–949, 2002.
- [76] N. Mohmeyer, D. Kuang, P. Wang, H.-W. Schmidt, S. M. Zakeeruddin, and M. Grätzel, "An efficient organogelator for ionic liquids to prepare stable quasi-solid-state dye-sensitized solar cells," *Journal of Materials Chemistry*, vol. 16, no. 29, pp. 2978–2983, 2006.
- [77] H. Usui, H. Matsui, N. Tanabe, and S. Yanagida, "Improved dye-sensitized solar cells using ionic nanocomposite gel electrolytes," *Journal of Photochemistry and Photobiology A*, vol. 164, no. 1–3, pp. 97–101, 2004.
- [78] P. Wang, S. M. Zakeeruddin, P. Comte, I. Exnar, and M. Grätzel, "Gelation of ionic liquid-based electrolytes with silica nanoparticles for quasi-solid-state dye-sensitized solar cells," *Journal of the American Chemical Society*, vol. 125, no. 5, pp. 1166–1167, 2003.
- [79] P. Wang, S. M. Zakeeruddin, J. E. Moser, M. K. Nazeeruddin, T. Sekiguchi, and M. Grätzel, "A stable quasi-solid-state dye-sensitized solar cell with an amphiphilic ruthenium sensitizer and polymer gel electrolyte," *Nature Materials*, vol. 2, no. 6, pp. 402–407, 2003.
- [80] B. C. O'Regan and F. O. Lenzmann, "Charge transport and recombination in a nanoscale interpenetrating network of n-type and p-type semiconductors: transient photocurrent and photovoltage studies of  $\text{TiO}_2/\text{Dye}/\text{CuSCN}$  photovoltaic cells," *Journal of Physical Chemistry B*, vol. 108, no. 14, pp. 4342–4350, 2004.

- [81] J. Krüger, R. Plass, L. Cevey, M. Piccirelli, M. Grätzel, and U. Bach, "High efficiency solid-state photovoltaic device due to inhibition of interface charge recombination," *Applied Physics Letters*, vol. 79, no. 13, pp. 2085–2087, 2001.
- [82] H. J. Snaith and M. Grätzel, "Enhanced charge mobility in a molecular hole transporter via addition of redox inactive ionic dopant: implication to dye-sensitized solar cells," *Applied Physics Letters*, vol. 89, no. 26, Article ID 262114, 3 pages, 2006.
- [83] J. Krüger, R. Plass, M. Grätzel, and H.-J. Matthieu, "Improvement of the photovoltaic performance of solid-state dye-sensitized device by silver complexation of the sensitizer cis-bis(4,4'-dicarboxy-2,2'-bipyridine)-bis(isothiocyanato) ruthenium(II)," *Applied Physics Letters*, vol. 81, no. 2, pp. 367–369, 2002.
- [84] L. Schmidt-Mende and M. Grätzel, "TiO<sub>2</sub> pore-filling and its effect on the efficiency of solid-state dye-sensitized solar cells," *Thin Solid Films*, vol. 500, no. 1-2, pp. 296–301, 2006.
- [85] U. Bach, D. Lupo, P. Comte, et al., "Solid-state dye-sensitized mesoporous TiO<sub>2</sub> solar cells with high photon-to-electron conversion efficiencies," *Nature*, vol. 395, no. 6702, pp. 583–585, 1998.
- [86] B. O'Regan, F. O. Lenzmann, R. Muis, and J. Wienke, "A solid-state dye-sensitized solar cell fabricated with pressure-treated P25-TiO<sub>2</sub> and CuSCN: analysis of pore filling and IV characteristics," *Chemistry of Materials*, vol. 14, no. 12, pp. 5023–5029, 2002.
- [87] A. Konno, T. Kitagawa, H. Kida, G. R. A. Kumara, and K. Tennakone, "The effect of particle size and conductivity of CuI layer on the performance of solid-state dye-sensitized photovoltaic cells," *Current Applied Physics*, vol. 5, no. 2, pp. 149–151, 2005.
- [88] G. R. A. Kumara, S. Kaneko, M. Okuya, and K. Tennakone, "Fabrication of dye-sensitized solar cells using triethylamine hydrothiocyanate as a CuI crystal growth inhibitor," *Langmuir*, vol. 18, no. 26, pp. 10493–10495, 2002.

## Review Article

# Review of Recent Progress in Dye-Sensitized Solar Cells

Fan-Tai Kong, Song-Yuan Dai, and Kong-Jia Wang

*Division of Solar Energy Materials and Engineering, Institute of Plasma Physics, Chinese Academy of Sciences, Hefei, Anhui 230031, China*

Received 27 March 2007; Accepted 25 June 2007

Recommended by Armin G. Aberle

We introduced the structure and the principle of dye-sensitized solar cell (DSC). The latest results about the critical technology and the industrialization research on dye-sensitized solar cells were reviewed. The development of key components, including nanoporous semiconductor films, dye sensitizers, redox electrolyte, counter electrode, and conducting substrate in dye-sensitized solar cells was reviewed in detail. The developing progress and prospect of dye-sensitized solar cells from small cells in the laboratory to industrialization large-scale production were reviewed. At last, the future development of DSC was prospective for the tendency of dye-sensitized solar cells.

Copyright © 2007 Fan-Tai Kong et al. This is an open access article distributed under the Creative Commons Attribution License, which permits unrestricted use, distribution, and reproduction in any medium, provided the original work is properly cited.

## 1. INTRODUCTION

Since Professor M. Grätzel in EPFL introduced the nanoporous films into dye-derived wideband semiconductor research and made the breakthrough in the photoelectric conversion efficiency of dye-sensitized solar cells (DSCs), academic and commercial interests have been paid on DSCs for their high efficiency, their potential low-cost and simple assemble technology, especially in the past 6 years since Grätzel and his group team at EPFL were able to demonstrate the first 10% efficient cells certified by NREL in USA [1–18]. Dye-derivatized mesoporous titania film is one of the key components for high efficiency in such cells. They use bis(bipyridyl) Ru(II) complexes *cis*-di(isothiocyanato)bis(2,2'-bipyridyl-4,4'-dicarboxylate)ruthenium(II), known as the N3 dye, in conjunction with the nanocrystalline colloidal TiO<sub>2</sub> films and I<sub>3</sub><sup>-</sup>/I<sup>-</sup> solution in an organic volatile solvent mixture, to convert 10% of AM 1.5 solar radiation into electrical energy. However, the main drawback of the N3 dye is the lack of light absorption in the red region of the visible spectrum. Carboxylated terpyridyl complexes of tris-thiocyanato Ru(II), known as the black dye, display outstanding properties as a charge-transfer sensitizer and the first certified efficiency of the solar cells that based is over 10%. In recent years, great developments have been made for both the academic research and the industrial research. This paper reviewed the latest developing progress of dye-sensitized solar cells.

## 2. STRUCTURE AND OPERATING PRINCIPLE OF DYE-SENSITIZED SOLAR CELLS

Dye-sensitized solar cell is composed of nanocrystalline semiconductor oxide film electrode, dye sensitizers, electrolytes, counter electrode and transparent conducting substrate. Typically, dye-derived nanocrystalline titania films were used as photoanode, platinized counter electrode, filled with electrolyte solution of I<sub>3</sub><sup>-</sup>/I<sup>-</sup> in organic solvent, then the sandwiched solar cells are formed. The operating mechanism of the solar cells is shown in Figure 1. Under the irradiation of sunlight, the dye molecular became photo-excited and ultrafastly injected an electron into the conduction band of the semiconductor electrode, then the original state of the dye is subsequently restored by electron donation from the electrolyte, usually the solution of an organic solvent or ionic liquid solvent containing the I<sub>3</sub><sup>-</sup>/I<sup>-</sup> redox system. The regeneration of the sensitizer by iodide intercepts the recapture of the conduction band electron by the oxidized dye. The iodide is regenerated, in turn, by reduction of triiodide at the counter electrode, the circuit being completed through the external load. The voltage generated under illumination corresponds to the difference between the Fermi level of the electron in the semiconductor electrode and the redox potential of the electrolyte. Overall, electric power is generated without permanent chemical transformation. Along with these processes, electrons in the conduction band of semiconductor may be recombined with the oxidized dye sensitizers or electron acceptor species in the electrolyte solution.

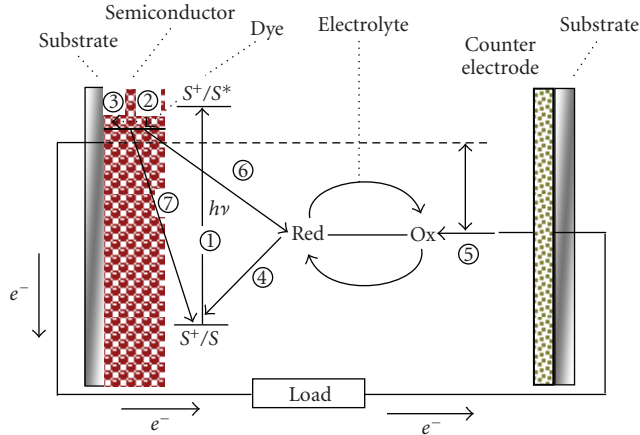


FIGURE 1: Structure and operating principle of dye-sensitized solar cells.

When it comes to solid-state dye-sensitized solar cells, the electrolyte solution is replaced by a wide band gap inorganic semiconductor of p-type polarity, such as CuI or CuSCN, or a hole-transmitting solid, for example, an amorphous organic arylamine and its derivatives. The excited dye injects electrons into the n-type oxide, and it is regenerated by hole injection in the p-type material. In recent years, organic solvent electrolyte containing  $I_3^-/I^-$  redox couple was also considered as the transport material. Then the operating principle of DSC based on liquid electrolyte is in corresponding with that of solid-state DSC.

### 3. DSC MATERIALS

#### 3.1. Nanocrystalline semiconductor film electrode

Semiconductor oxides used in dye-sensitized solar cell include  $TiO_2$ , ZnO,  $SnO_2$ ,  $Nb_2O_5$ , and so forth, which serve as the carrier for the monolayers of the sensitizer using their huge surface and the medium of electron transfer to the conducting substrate. Due to low-cost price, abundance in the market, nontoxicity, and biocompatibility, and as it is also used widely in health care products as well as in paints,  $TiO_2$  becomes the best choice in semiconductor till now. Titanium dioxide films are covered on the conducting substrate such as conducting glass, metal foil, and flexible polymer film. The two selected deposition processes, so-called doctor-blading and screen-printing, are widely used to prepare the nanocrystalline  $TiO_2$  films by spreading a viscous dispersion of colloidal  $TiO_2$  particles on a conducting glass support before sintering at high temperature. Two methods of preparation of colloidal  $TiO_2$  dispersions were typically employed [2]. Method A follows the sol-gel procedure of titanate described by Grätzel et al. with the autoclaving being performed at  $200^\circ C \sim 250^\circ C$ . After the colloid is spread on the conducting glass support and calcined, a few monolayers of  $TiO_2$  are electrodeposited onto the colloidal  $TiO_2$  film from an aqueous Ti(III) solution or treatment with titanium tetrachloride aqueous solution followed by renewed

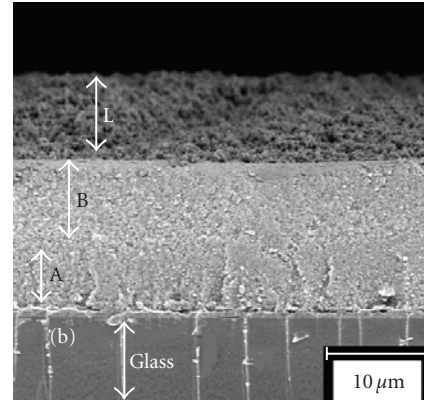


FIGURE 2: FE-SEM cross-section micrographs of  $TiO_2$  films photoelectrode; the thickness of A (compact layer), B (nanoporous layer), L (scattering layer) is  $5 \mu m$ ,  $8 \mu m$ ,  $5 \mu m$  with average particle size of 16 nm, 25 nm, 300 nm, respectively.

annealing at  $450^\circ C \sim 550^\circ C$ . This treatment was found to improve significantly the short-circuit photocurrent ( $J_{sc}$ ) as well as the open-circuit voltage ( $V_{oc}$ ) of the solar cell. The second method for preparation of nanocrystalline films (Method B) employs commercial  $TiO_2$  (P25, Degussa AG, Germany). Electron microscopy shows the mean size of primary particles to be about 25 nm. In order to break the aggregates into separate particles, the P25 powder is ground in a porcelain mortar with a small amount of water containing acetylacetone or other stabilizers such as acids, bases, or  $TiO_2$  chelating agents to prevent reaggregation of the particles. After being dispersed by the high shear forces in the viscous paste, the powder was diluted by slow addition of water under continued grinding. Finally, a detergent, Triton X-100 or ethyl cellulose, was added to facilitate the spreading of the colloid on the substrate.

In the production of large-scale dye-sensitized solar cell modules in our group, the multilayer microstructure of the semiconductor nanocrystalline  $TiO_2$  films is optimized [18].  $TiO_2$  photoelectrodes with three different layers (Figure 2), including layers of small pore-size films, larger pore-size films, and light-scattering particles on the conducting glass with the desirable thickness are being employed in large-area dye-sensitized solar cells and modules and contributed to high efficiency of DSC and DSC modules.

To make DSC a commercially competitive technology in the market for flexible solar cells, a new method that permits a film being prepared on flexible organic substrate is needed for purposes of flexibility, weight, and overall device thickness. However, the traditional methods being mentioned above are challenged while using DSC being based on organic flexible substrate. Especially, the polymer substrate is not suitable for preparing electrodes by sintering in high temperature of  $450^\circ C \sim 550^\circ C$  [1–4, 19]. Recently, some methods for preparing semiconductor films on a flexible substrate such as low-temperature annealing at the temperature below  $150^\circ C$  [20, 21] and a compressing method [22, 23] to achieve electrically connected  $TiO_2$  network have been reported. Pichot et al. [20] reported the preparation

of nanocrystalline  $\text{TiO}_2$  electrode without any organic surfactant by sintering at  $100^\circ\text{C}$  and the conversion efficiency of the solar cells is 1.2%. Hagfeldt et al. [23] demonstrated a mechanically compressed nanostructured  $\text{TiO}_2$  layer on a plastic film yielding a fill factor of 47% and a conversion efficiency of 3.0%. Miyasaka et al. [24, 25] obtained a fill factor of 61% and the high conversion efficiency up to 4.1% with an electrophoretic deposited  $\text{TiO}_2$  layer following a chemical treatment and a thermal treatment of  $150^\circ\text{C}$  for interconnecting  $\text{TiO}_2$  particles. Dürr et al. [26] reported the so-called liftoff technique, in which pre-sintered porous layers on conducting glasses substrate can be transferred to an arbitrary flexible substrate, and the original electrical properties of the transferred porous layers are maintained. They obtained a conversion efficiency of 5.8% with flexible PET (polyethylene terephthalate) substrates under AM1.5 irradiation ( $100\text{mW}\cdot\text{cm}^{-2}$ ). This method is too complicated for commercial application. Kijitori et al. [17, 27] prepared binder-free coating paste by using  $\text{TiO}_2$  sol in acidic aqueous solution as the interconnection agent, and coated the paste on ITO/polyethylene naphthalate (ITO/PEN) film by doctor-blade method followed by drying at  $150^\circ\text{C}$  to obtain  $\text{TiO}_2$  photoanode. The conversion efficiency of the plastic based DSC is large than 6%. Grätzel group [28] developed the high-efficiency (7.2%) flexible solar cells based on a Ti-metal foil substrate for photoanode and a Pt-electrodeposited counter electrode on ITO-PEN, which is the highest efficiency for flexible DSC.

Nanocrystalline semiconductor films adsorbed a large amount of dye molecules and increased the harvesting efficiency of solar energy. However, the huge surface area also increases the recombination between electrons in the conduction band of semiconductor oxides and the electron acceptor in the electrolyte. In recent years, increasing interest in DSC is addressing the use of more sophisticated device architectures in order to reduce interfacial recombination losses. Examples include the use of composite metal oxides as the semiconductor with different band gaps, for example,  $\text{Nb}_2\text{O}_5$ ,  $\text{ZnO}$ , the incorporation of spacer units between the oxidized dye and the  $\text{TiO}_2$  surface, and surface passivation by coating of semiconductor oxides with high conduction band edge or electrodeposition of insulating polymers. One particularly attractive approach involves the coating of the nanocrystalline metal oxide film with a thin overcoat of another metal oxide with a higher conduction band edge, as illustrated in Figure 3, with the aim of increasing the physical separation of injected electrons from the oxidized dye redox couple, thereby retarding the recombination reactions. When the surface of the  $\text{TiO}_2$  nanocrystalline electrode was coated with a thin layer semiconductor oxides, such as  $\text{ZnO}$ ,  $\text{Nb}_2\text{O}_5$ ,  $\text{SrO}$ ,  $\text{SrTiO}_3$ , the conversion efficiency of based DSC increased dramatically. After coating of  $\text{ZnO}$  and  $\text{Nb}_2\text{O}_5$ , the electron density of the conduction band of  $\text{TiO}_2$  increase with the reduction of charge recombination due to the core-shell barrier. As a result, the open-circuit voltage ( $V_{oc}$ ) and conversion efficiency of the solar cells that based were improved. However, the influence of the introduction of insulating layer on the conversion efficiency of based DSC was still under discussion. Lee [29], Jung [30], and Yum [31]

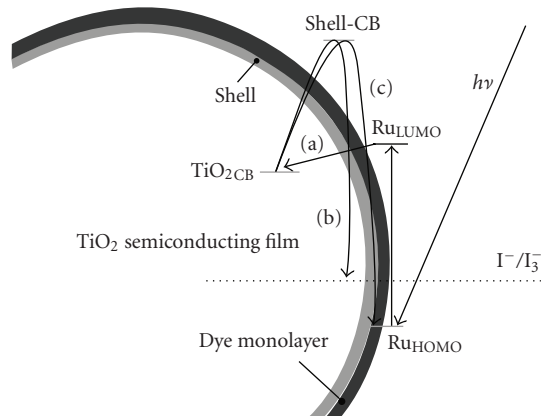


FIGURE 3: Diagrammatic sketch  $\text{TiO}_2$  coated with high-conduction-band-edge semiconductor or insulating layer. (a) Injection of electrons into the conduction band of  $\text{TiO}_2$  films. (b) Combination of electrons between electron and triiodide in the electrolyte. (c) Charge recombination between electrons of  $\text{TiO}_2$  films and oxidized dye.

adopted  $\text{CaCO}_3$ ,  $\text{MgO}$ , and metal ( $\text{Mg}$ ,  $\text{Zn}$ ,  $\text{Al}$ ,  $\text{La}$ ) hydroxide as the insulating barrier for nanometer  $\text{TiO}_2$  electrodes, respectively; and the introduction of insulating layer have increased the absorbing amount of the dye molecules and improved short-circuit current density ( $J_{sc}$ ), open-circuit voltage, fill factor ( $FF$ ), and photoelectric conversion efficiency ( $\eta$ ) of the solar cells. Durrant and so forth [32–35] found that the conversion efficiency of solar cells based  $\text{Al}_2\text{O}_3$ ,  $\text{ZrO}_2$ , or  $\text{SiO}_2$  covered  $\text{TiO}_2$  electrodes were improved obviously or just kept equal. Kay et al. [36] found the similar results for  $\text{ZnO}$ ,  $\text{TiO}_2$ ,  $\text{Al}_2\text{O}_3$ ,  $\text{MgO}$  coated  $\text{SnO}_2$  electrodes. However, when it came to the  $\text{TiO}_2$  electrode coated with  $\text{Al}_2\text{O}_3$ ,  $\text{MgO}$  and  $\text{Y}_2\text{O}_3$ , the  $V_{oc}$  and  $FF$  of the solar cells that based rise, while the short-circuit current density dropped sharply, which led to the reduction of overall photoelectric conversion efficiency of the solar cells.

The preparation of high-efficiency semiconductor electrode is of significant importance for the improvement of the efficiency and the commercial application of dye-sensitized solar cells. To prepare the semiconductor film electrode with uniform-size high-special surface area, and the porous structure whose direction is perpendicular to the conducting substrate is one of the focuses of present research [37]. In order to improve the portability of DSC and scope of application, more and more researchers were interested in the preparation methods for nanocrystalline semiconductor film electrode on flexible substrate.

### 3.2. Dye sensitizer

Dye sensitizers serve as the solar energy absorber in DSC, whose properties will have much effect on the light harvesting efficiency and the overall photoelectric conversion efficiency. The ideal sensitizer for dye-sensitized solar cells should absorb all light below a threshold wavelength of about 920 nm. In addition, it should be firmly grafted to

the semiconductor oxide surface and inject electrons to the conduction band with a quantum yield of unity. Its redox potential should be sufficiently high that it can be regenerated rapidly via electron donation from the electrolyte or a hole conductor. Finally, it should be stable enough to sustain at least  $10^8$  redox turnovers under illumination corresponding to about 20 years of exposure to natural light [38]. The best photovoltaic performance in terms of both conversion yield and long-term stability has so far been achieved with polypyridyl complexes of ruthenium and osmium. The sensitizers used in DSC were divided into two types: organic dye and inorganic dye according to the structure. Inorganic dye includes metal complex, such as polypyridyl complexes of ruthenium and osmium, metal porphyrin, phthalocyanine and inorganic quantum dots, while organic dye includes natural organic dye and synthetic organic dye.

Compared with organic dye, inorganic complexes dye has high thermal stability and chemical stability. Among these complexes, Polypyridyl ruthenium sensitizers were widely used and investigated for its high stability and outstanding redox properties and good responding for natural visible sunlight. The sensitizers anchored on the surface of semiconductor film electrode with carboxylate group or phosphonate group, which enable the electron injection into the conduction band of the semiconductor. Polypyridyl ruthenium dye may be divided into carboxylate polypyridyl ruthenium dye, phosphonate ruthenium dye, and polynuclear bipyridyl ruthenium dye. The difference between the first two types of sensitizers lies in the adsorption group. The first two types of sensitizers differ from the last type of sensitizer in the number of metal center. The carboxylate polypyridyl ruthenium dye is in level structure, which enables the electron injection into the conduction band of the semiconductor quantitatively. Among these sensitizers, N3 and its tetrabutylammonium salt N719, black dye showed the unmatched performance. The efficiency records of more than 11% for dye sensitized solar cells are based on N719 or black dye. In recent years, amphiphilic ruthenium dye represented by Z907 and high-molar-extinction-coefficient ruthenium sensitizers represented by K19 became the focuses of the research about carboxylate polypyridyl ruthenium sensitizers. Figure 4 and Table 1 showed us the molecular structure and the photovoltaic performance of based solar cells [39–50].

Carboxylate polypyridyl ruthenium sensitizers are easily to be desorbed from the surface in the aqueous solution when the pH value is lower than 5 though they have a lot of advantages. While the phosphonate polypyridyl ruthenium sensitizers used phosphonate group to be anchored to the surface of the semiconductor, which is hardly desorbed from the semiconductor surface even at high pH value, however, phosphonate group is not in conjugation with the polypyridyl plane due to their non-plane structures, which is in disadvantage to the injection of electrons. Péchy et al. [49] developed the first phosphonate polypyridyl ruthenium dye (complex 1) that have the lifetime of excited state of 15 nanoseconds and the Langmuir adsorption coefficient of  $8 \times 10^6$ , which is 80 times larger than that of the N3 dye. The incident photon-current conversion efficiency of complex 1 achieves the maximum 70% at the wavelength of 510 nm.

Grätzel et al. [48] developed the phosphonate polypyridyl ruthenium analogue of Z907 and gained the conversion efficiency of more than 8% for the solar cells that based.

Polynuclear complexes exhibiting an antenna effect have been employed in order to increase absorption coefficients. However, the antenna does not enhance the light response efficiently at longer wavelengths, where absorption coefficients and the IPCE of ruthenium charge-transfer sensitizers decrease strongly. Moreover, these bulky sensitizers require more space on the  $\text{TiO}_2$  surface and penetrate less easily in the small cavities of the nanocrystalline  $\text{TiO}_2$  than the mononuclear complexes. Hence, for polynuclear complexes, the increased absorption coefficients in solution do not necessarily lead to the enhanced light absorption on the  $\text{TiO}_2$  electrode due to the reduced surface concentration of the bulkier sensitizer molecules on the nanoporous  $\text{TiO}_2$  [51].

Organic dye is easy to be designed and various in style with molar extinction coefficient and low cost. In recent years, the development of DSC based on organic dye is very rapid and the conversion efficiency of the solar cells that based is comparable to that based on polypyridyl ruthenium dye. Generally, organic dye has the general structure of “Donor (D)- $\pi$  conjugation bridge-acceptor (A).” With the electron withdrawing and donating effects of acceptor and the donor moieties, the absorption response of the visible light are red-shifted, which improves the light harvesting and short circuit photocurrent of the solar cells. Figure 5 showed us the structure of several organic dyes and the conversion efficiency of based DSC [52–62]. Huang et al. [62] developed hemicyanine dyes BTS and IDS and get the efficiency 5.1% and 4.8% for solar cells that based. Yang et al. [59] reported the organic dye containing thienothiophene and thiophene segments and achieved high solar energy-to-electricity conversion efficiency of 6.23% for D-ST (structure shown in Figure 5) sensitized solar cells. Yanagida group [57] and Arakawa group [58] reported polyene dye or so-called phenyl-conjugated oligoene dye and gained the efficiency of 6.6% and 6.8%. Hara et al. [53–56] developed a series of coumarin derivatives and received the efficiency of 7.7%, which is comparable with that for N719. Uchida group [60] used indoline dye D149 as sensitizer and gained 8.0% conversion efficiency for solar cells without antireflection layer. Grätzel group [61] reported the 9.03% conversion efficiency for solar cells with D149 as sensitizer after optimizing nanocrystalline  $\text{TiO}_2$  films. This showed the new results for organic dye sensitized solar cells.

Sensitization with one single dye was restricted for its absorption spectrum is hardly matched with the solar emission spectrum. Cosensitization of several dyes with different spectral response instead of one single dye was used for wide-band-gap semiconductor. Zhang et al. [63, 64] used a series of squaraine dye as cosensitizer of ruthenium polypyridyl complexes and improved 13% efficiency for dye-sensitized solar cells than those sensitized with simple ruthenium polypyridyl complexes. By cosensitization of squaraine dye and polypyridyl ruthenium dye in a proper ratio, the spectral response scope was widened the photovoltaic performance of based solar cells was improved.

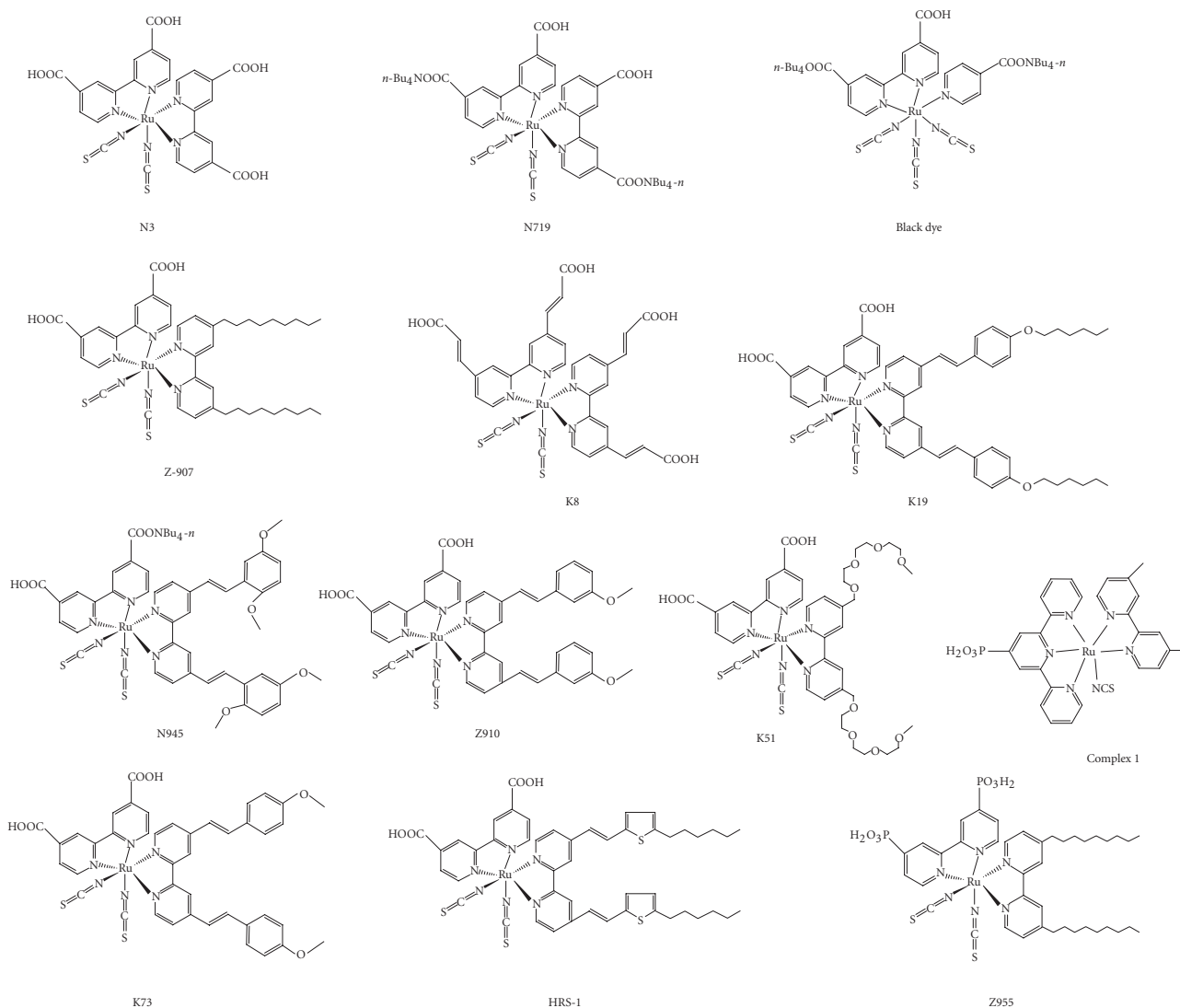


FIGURE 4: Molecular structure of several ruthenium complexes dye.

### 3.3. Electrolyte

The electrolyte is one of key components for dye-sensitized solar cells and its properties have much effect on the conversion efficiency and stability of the solar cells. The electrolyte used in DSC is divided into three types: liquid electrolyte, quasi-solid, state electrolyte, and solid electrolyte. Liquid electrolyte could be divided into organic solvent electrolyte and ionic liquid electrolyte according to the solvent used.

Organic solvent electrolytes were widely used and investigated in dye-sensitized solar cells for their low viscosity, fast ion diffusion, high efficiency, easy to be designed, and high pervasion into nanocrystalline film electrode [2–7, 65–68]. The composition of the electrolytes includes organic solvent, redox couple, and additive.

Organic solvent used in organic liquid electrolyte include nitrile such as acetonitrile, valeronitrile, 3-methox-

ypropionitrile, and esters such as ethylene carbonate (EC), propylene carbonate (PC),  $\gamma$ -butyrolactone.

The major redox couple contained  $I_3^-/I^-$  couple. Expecting that redox couple, Wang et al. [69] used  $Br^-/Br_2$  as redox couple in eosin sensitized solar cells.  $SCN^-/(SCN)_2$  couple,  $SeCN^-/(SeCN)_2$  couple were also shown in the literature [70, 71]. Sapp [72] reported the substituted bipyridyl cobalt(III/II) couple as redox couple in DSC. However, the performance of these couples can hardly match that of  $I_3^-/I^-$  couple.

Alkyl imidazolium cation and lithium cation were usually used as the counterions of  $I_3^-/I^-$  couple in DSC. Alkyl imidazolium cation may be adsorbed on the surface of semiconductor film to form the Helmholtz layer, which restricted the contact of triiodide and semiconductor films, for the recombination between triiodide and electron in the conduction band of semiconductor. As the result, the fill factor, and conversion efficiency of the solar cells were improved. On the

TABLE 1: Absorption spectra and photoelectric performance of different polybipyridyl ruthenium(II) complexes.

Dye	$Abs/nm$ ( $\epsilon/10^3 \text{ m}^2\text{mol}^{-1}$ )	IPCE <sup>(a)</sup>	$J_{sc}/\text{mA}\cdot\text{cm}^{-2}$	$V_{oc}/\text{mV}$	FF	$\eta/\%$
N3	534(1.42)	83%	18.2	720	0.73	10 [2]
N719	532(1.4)	85%	17.73	846	0.75	11.18 [8]
Black Dye	605(0.75)	80%	20.53	720	0.704	10.4 [3]
Black Dye	—	80%	20.9	736	0.722	11.1 [6, 7]
Z907	526(1.22)	72%	13.6	721	0.692	6.8 [39, 42]
Z907	526(1.22)	72%	14.6	722	0.693	7.3 [39]
K8	555(1.80)	77%	18	640	0.75	8.64 [40]
K19	543(1.82)	70%	14.61	711	0.671	7.0 [41]
N945	550(1.89)	80%	16.5	790	0.72	9.6 [43]
Z910	543(1.70)	80%	17.2	777	0.764	10.2 [44]
K73	545(1.80)	80%	17.22	748	0.694	9.0 [45]
K51	530(1.23)	70%	15.40	738	0.685	7.8 [46]
HRS-1	542(1.87)	80%	20	680	0.69	9.5 [47]
Z955	519(0.83)	80%	16.37	707	0.693	8.0 [48]

<sup>(a)</sup> Platform region. IPCE, Incident photon-current conversion efficiency.

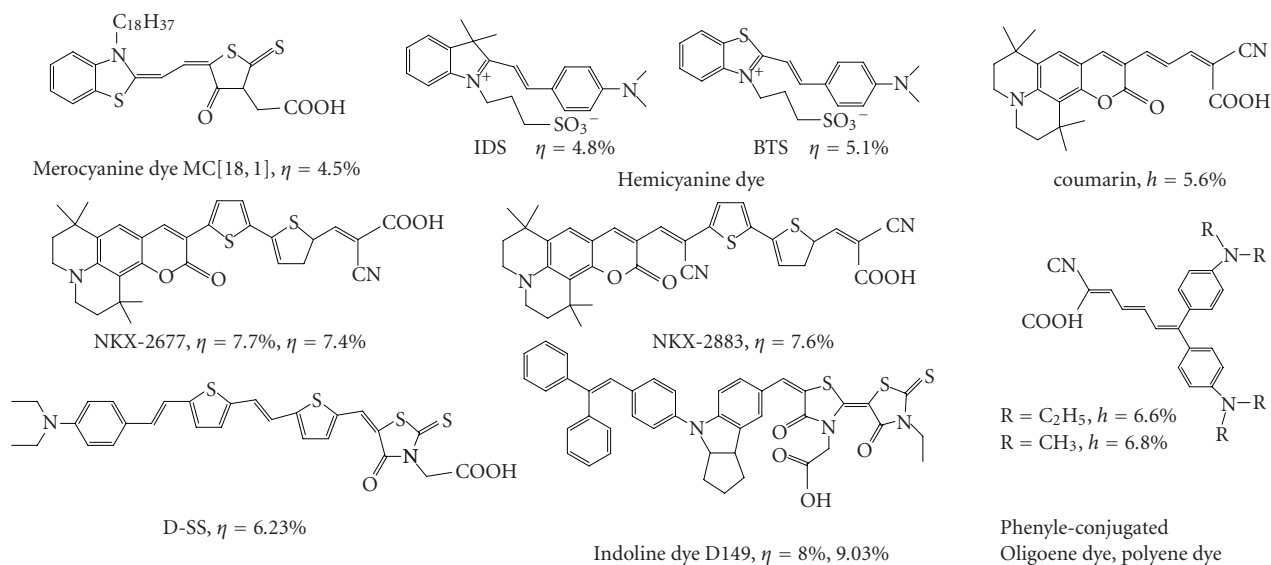


FIGURE 5: Photoelectric conversion efficiency of DSC based on several organic dyes with high extinction coefficient and their molecular structure.

other hand, the high solubility of alkyl imidazolium cation in organic solvent and the high activity of iodide increased the light harvesting efficiency and photocurrent as well as the stability of the sensitizer.

The commonly used additive used in the electrolytes for dye-sensitized solar cells contained 4-*tert*-butylpyridine (TBP) and N-methylbenzimidazole (NMBI). The addition of these additives could suppress the dark current and improve the photoelectric conversion efficiency. TBP could reduce the

recombination of electrons in the conduction band of the semiconductor and the electron acceptor in the electrolyte through the coordination between N atom and the Ti ion in incomplete coordination state on the surface of TiO<sub>2</sub> film. Then, the photovoltage fill factor and the conversion efficiency increased dramatically.

The efficiency record of DSC was obtained on the solar cells based on organic solvent electrolyte, especially the highly volatile organic solvent electrolyte due to the efficient

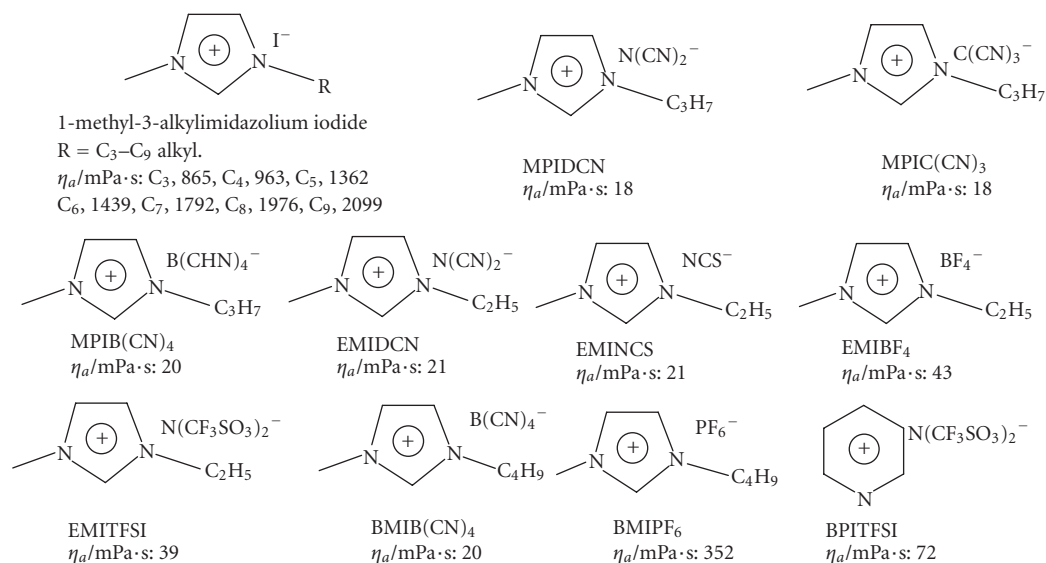


FIGURE 6: Structure and the viscosity of several ionic liquids.

infiltration of organic electrolyte in nanocrystalline films. However, the solar cells based on organic electrolyte have the disadvantages such as less long-term stability, difficulty in robust sealing and leakage of electrolyte due to the volatility of organic solvent.

Ionic liquid electrolytes were developed in recent year in view of the disadvantage of organic solvent electrolyte. Compared with normal organic solvent electrolyte, ionic liquid have a lot of advantage, such as good chemical and thermal stability, negligible vapor pressure, nonflammability, high ionic conductivity and high solubility for organic or inorganic materials, and a wide electrochemical window, which has been intensively pursued as alternative electrolytes for DSC and other electrochemical devices. In recent years, ionic liquid electrolyte was developed rapidly. Kubo et al. [73] investigated the physical and physiochemical properties of 1-alkyl-3-methylimidazolium iodides (alkyl chain: C<sub>3</sub>–C<sub>9</sub>). They found that the viscosity of the molten salts increases with increasing alkyl chain length because of van der Waals forces. The conductivity of the molten salts decreases with increasing viscosity since the diffusion of ions in a liquid depends on its viscosity. The electrolyte with 1-hexyl-3-methylimidazolium iodide gave the highest photoelectric conversion efficiency. Among these ionic liquids, alkyl imidazolium-based ionic liquids are both iodide sources and solvents of electrolytes in solar cells. The counterions in the alkyl imidazolium-based ionic liquid included I<sup>-</sup>, N(CN)<sub>2</sub><sup>-</sup>, B(CN)<sub>4</sub><sup>-</sup>, (CF<sub>3</sub>COO)<sub>2</sub>N<sup>-</sup>, BF<sub>4</sub><sup>-</sup>, PF<sub>6</sub><sup>-</sup>, NCS<sup>-</sup>, and so forth 1-Alkyl-3-methylimidazolium iodides are viscous liquids, whose viscosity is much higher than that of organic-solvent-based liquid electrolyte. Then the transport I<sub>3</sub><sup>-</sup> in the electrolyte is very slow and the mass transfer process occupies the leading position. To improve the mobility of redox couple in the electrolyte and the photovoltaic performance, various ionic liquid with low viscosity were developed. Grätzel et al. reported the solar cells based on

low-viscosity ionic liquid and MPII mixture. Figure 6 and Table 2 summarize the structure and viscosity of some ionic liquid and the photovoltaic performance of DSC based on ionic liquid electrolyte of different composition [73–83].

Besides alkyl imidazolium cation, alkyl pyridinium salt and trialkylmethylsulfonium-salt-based ionic liquid were developed for electrolytes. Paulsson et al. [74] obtained 3.7% photoelectric conversion efficiency for solar cells based on (Bu<sub>2</sub>Me)SI ionic liquid containing 1% iodine. Watanabe [81] reported 2% conversion efficiency in alkyl pyridinium-cation-based ionic liquid. Wang [75] achieved 7.5% efficiency in solvent-free EMISECN-based ionic liquid containing (SeCN)<sub>3</sub><sup>-</sup>/SeCN<sup>-</sup> electrolyte, which is comparable with I<sub>3</sub><sup>-</sup>/I<sup>-</sup> couple. However, the rareness of selenium and high costs has limited its application in DSC. Matsui [83] reported the application of ionic liquid electrolyte in large-area solar cells and gained 2.17% conversion efficiency 2.7%.

The evaporation of the liquid electrolyte often caused some practical limitations of sealing and long-term operation. Recently some attempts were made to improve the long-term stability by using a p-type semiconductor [89, 90] or hole transporting organic materials [91] to replace a liquid electrolyte. However, their conversion efficiencies are not comparable with those of the liquid solar cells. Thus, it can be seen that quasi-solid-state ionic liquid electrolytes might be a better choice to increase stability. Owing to their unique physicochemical properties such as high thermal stability, negligible vapor pressure, relatively high ionic conductivity, and good stability, Ionic liquids were widely used in dye-sensitized solar cells. In general, quasi-solid-state ionic liquid electrolyte consists of I<sub>3</sub><sup>-</sup>/I<sup>-</sup> couple such as 1-methyl-3-propylimidazolium iodine (MPII) and framework materials. In quasi-solid electrolytes, framework materials play an important role in offering a liquid channel for the I<sub>3</sub><sup>-</sup>/I<sup>-</sup> diffusion. Some polymers, [83–86, 92–97] low-molecular-weight gelator [73, 80], and silica nanoparticles [77, 87] have been

TABLE 2: Efficiency of DSC based on ionic liquid electrolyte system with different composition.

Composition of electrolyte	Dye	$\eta/\%$
I <sub>2</sub> , LiI, and NMBI in PMII and EMIDCN (13:7,v/v)	Z907	6.6 [76]
	N719	5.0 [76]
HMII, I <sub>2</sub> et al.	N719	5.0 [73]
I <sub>2</sub> and NMBI in MPII	Z907	6.0 [77]
I <sub>2</sub> , GuSCN, TBP in PMII and EMINCS (13:7,v/v)	Z907	7.0 and 6.4* [78]
I <sub>2</sub> , NMBI, and GuSCN in MPII and EMIB(CN) <sub>4</sub> (13:7,v/v)	Z907	7.0 and 6.4* [79]
I <sub>2</sub> , GuSCN, and NMBI in PMII and EMINCS (13:7,v/v)	Z955	5.5 [48]
	K19, DPA	6.3 [80]
MPII, LiI, I <sub>2</sub> TBP in EMIDCA	N3	5.5 [81]
MPII, LiI, I <sub>2</sub> , TBP in EMITFSI	N3	4.5 [81]
I <sub>2</sub> and NMBI in PMII and functional PMII derivative ionic liquids (13:7, v/v)	K19 PPA	5.4~5.9 [82]
EMII, I <sub>2</sub> , LiI, TBP in EMITFSA	N3	4.5(0.45 cm <sup>2</sup> ).
		2.7(69 cm <sup>2</sup> ) [83]
(Bu <sub>2</sub> Me)SI and 1% I <sub>2</sub> , TBP	N719	3.7 (0.1 sun)[74]
MPII, LiI, I <sub>2</sub> TBP in PTFSI	N3	2% [81]
GuSCN, K(SeCN) <sub>3</sub> , NMBI in EMISecN	Z907, PPA	7.5 [75]

\* With and without PPA as coadsorbent, PTFSI: 1-butylpyridinium bis-(trifluoromethane sulfonyl)imide.

TABLE 3: Photovoltaic performance of quasi-solid-state DSC with different gelators and ionic liquid electrolytes.

Composition	Gelator	Dye	$\eta/\%$
HMII, I <sub>2</sub> et al.	Low-molecular-weight gelator	N719	5.01 [73]
I <sub>2</sub> , MPII, NMBI	PVDF-HFP	Z907	5.3 [84]
I <sub>2</sub> and NMBI in MPII	Silica Nanoparticles	Z907	6.1 [77]
I <sub>2</sub> , GuSCN, NMBI in PMII/EMINCS (13:7,v/v)	Low-molecular-weight gelator	K-19 DPA	6.3 [80]
EMImI, I <sub>2</sub> , LiI, TBP in EMITFSA	PVDF-HFP	N3	3.8(0.45 cm <sup>2</sup> )
			2.4(69 cm <sup>2</sup> ) [83]
TMS-PMII/I <sub>2</sub> in 10:1 ratio	Self-gelation	N3	3.2 [85]
I <sub>2</sub> , LiI, TBP in MPII	Agarose	N719	2.93 [86]
I <sub>2</sub> , LiI, TBP, DMPII in EMIDCA	Agarose	N719	3.89 [86]
EMII, LiI, I <sub>2</sub> , and TBP in EMITFSI	Nanoparticles	N3	4.57~5.00 [87]

used as framework materials to solidify ionic liquid-based electrolyte in DSC. Table 3 summarizes the photovoltaic performance of DSC based on different gelators and ionic liquid electrolytes.

#### 4. SUMMARY

In the past ten years, different efficiency records were announced for dye-sensitized solar cells with different active area in the laboratories and corporations in the world. More than 11% efficiency have achieved by EPFL and Sharp Corporation in small-area DSC. The conversion efficiency record

of 8.12%, 10.1%, 10.4%, 9.9% was announced by ECN, EPFL, Sharp Corporation, Arakawa group for strip solar cells with aperture area of 1~5 cm<sup>2</sup>, which is comparable to that for small-area solar cells. Table 4 showed us the conversion efficiency record reported by the main research team of dye-sensitized solar cells or DSC modules. It can be seen that the module efficiency is still low for practical application. Since 1993, industrial researchers have led the way with teams from Germany, Australia, and Switzerland. Based on licenses to the core patents held by EPFL, these teams built strong bases for product development. A 200 m<sup>2</sup> DSC showcase in roof has been constructed by the STI Company in

TABLE 4: Photoelectric conversion efficiency of DSC in the world [5–17, 88]. EPFL: Laboratory for Photonic and Interfaces, Swiss. NREL: National Renewable Energy Laboratory, USA. ECN: Energy Research Centre of the Netherlands. STI: Sustainable Technology International, Australia. SHARP: Sharp Corporation. INAP: Institute of Photovoltaic, Germany. TUS: Tokyo University of Science. FMRC: Freiburg Materials Research Centre. IPP: Institute of Plasma Physics, Chinese Academy of Sciences. Data reported above were measured using solar simulator indoor (AM1.5, 100 mW/cm<sup>2</sup>) if there is no further statement.

	<0.5 cm <sup>2</sup>	1~5 cm <sup>2</sup>	100 cm <sup>2</sup>	300 cm <sup>2</sup>	400 cm <sup>2</sup>
EPFL	10.58% (2003) 11.04% (2004) 11.18% (2006)	10.1% (2006) (1.31 cm <sup>2</sup> )	—	—	—
NREL	9% (2000)	—	—	—	—
ECN	—	8.2% (2001)	Highest:5.9% (2003) Lowest:4.5%	—	4.7% (2003) Outdoor
STI	—	—	—	<3%	—
SHARP	10.8% (2005) (0.2227 cm <sup>-2</sup> ) 11.1% (0.219 cm <sup>2</sup> )	10.4% (2005) (1.004 cm <sup>2</sup> ) 8.0% (2006) (5 cm <sup>2</sup> )	6.3% (26.5 cm <sup>2</sup> , confirmed) 6.3%(101 cm <sup>2</sup> )	—	—
INAP	—	—	4.7% (1998) (141.4 cm <sup>2</sup> , confirmed)	—	6.8% (2000)
TUS	10.3% (2006)	9.9% (2006)	8.4% (2006) (67.5 cm <sup>2</sup> )	—	—
FMRC	—	—	—	3.5% (2006)	—
IPP	8.95% (2002)	7.4% (2003)	—	5.9%(1 sun) (2003) 7.3%(0.5 sun)	5.7% (2003) (0.95 sun, outdoor)

2003. Sharp Corporation and Arakawa group reported 6.3% (efficient area: 26.5 cm<sup>2</sup>, confirmed, 6.3% for 101 cm<sup>2</sup>) and 8.4% (100 cm<sup>2</sup>) conversion efficiency for DSC modules. Our group have prepared the DSC modules with efficiency more than 6% in the size of 15 cm × 20 cm. Many corporations in Japan have focused on DSC research and have got good results in organic dye-sensitized solar cells and flexible solar cells. Gifu University (Japan) developed colorful plastic solar cells with the efficiency of 5.6% based on organic indoline dye and electrodeposited nanocrystalline ZnO film electrode. Tojin University of Yokohama (Japan) has achieved more than 6% conversion efficiency on full flexible solar cells based on low-temperature TiO<sub>2</sub> electrode preparation technology. Peccell Technologies (Japan) have succeeded in the development of full flexible substrate DSC with the size of 12 cm × 12 cm, voltage more than 4 V, current 0.1 A and the efficiency of 4.3%~5.2%. Konarka Corporation and G24 in England are currently setting-up pilot production in their 20 MW factory facility.

Industrial research in China was under the financial support of the National Basic Research Program of China and CAS Innovation Program. After five years, 15 cm × 20 cm DSC modules were prepared and assembled to 45 cm × 80 cm DSC panel, and the efficiency of the DSC modules and panels is more than 5%. In 2004, a 500 W DSC showcase was founded and generated electricity without obvious performance degradation until now [98]. The

fundamental and industrial researches have been carried out since 1994. There are more than 30 groups engaged in the research of DSC. The research involved the dye sensitizers, nanocrystalline semiconductor film, electrolyte, counter electrode, substrate and theoretical research of interface transport, and so forth. In the near future, DSC panels that have outstanding architectural appeal are forecast to be in wide use in the commercial market. Within a few years, lower cost rigid and flexible products will become available. Later in the decade, electrophotochromic windows should be commercialized. During the next decade, the introduction of tandem water-splitting devices is possible.

## ACKNOWLEDGMENTS

This project was financially supported by National Basic Research Program of China (Grant no. 2006CB202600) and the Anhui Province Key Technologies R & D Programme (Grant no. 06012024A).

## REFERENCES

- [1] B. O'Regan and M. Grätzel, "A low-cost, high-efficiency solar cell based on dye-sensitized colloidal TiO<sub>2</sub> films," *Nature*, vol. 353, no. 6346, pp. 737–740, 1991.

- [2] M. K. Nazeeruddin, A. Kay, I. Rodicio, et al., "Conversion of light to electricity by *cis*-X<sub>2</sub>bis(2,2'-bipyridyl-4,4'-dicarboxylate)ruthenium(II) charge-transfer sensitizers (X = Cl<sup>-</sup>, Br<sup>-</sup>, I<sup>-</sup>, CN<sup>-</sup>, SCN<sup>-</sup>) on nanocrystalline TiO<sub>2</sub> electrodes," *Journal of the American Chemical Society*, vol. 115, no. 14, pp. 6382–6390, 1993.
- [3] M. K. Nazeeruddin, P. Péchy, T. Renouard, et al., "Engineering of efficient panchromatic sensitizers for nanocrystalline TiO<sub>2</sub>-based solar cells," *Journal of the American Chemical Society*, vol. 123, no. 8, pp. 1613–1624, 2001.
- [4] M. Grätzel, "Photoelectrochemical cells," *Nature*, vol. 414, no. 6861, pp. 338–344, 2001.
- [5] M. Grätzel, "Conversion of sunlight to electric power by nanocrystalline dye-sensitized solar cells," *Journal of Photochemistry and Photobiology A*, vol. 164, no. 1–3, pp. 3–14, 2004.
- [6] L. Han, Y. Chiba, A. Islam, et al., "High efficiency of dye-sensitized solar cells and module," in *The 16th International Conference of Photochemical Conversion and Solar Storage*, Uppsala, Sweden, July 2006, W4-P-11.
- [7] Y. Chiba, A. Islam, Y. Watanabe, R. Komiya, N. Koide, and L. Han, "Dye-sensitized solar cells with conversion efficiency of 11.1%," *Japanese Journal of Applied Physics*, vol. 45, no. 25, pp. L638–L640, 2006.
- [8] M. K. Nazeeruddin, F. De Angelis, S. Fantacci, et al., "Combined experimental and DFT-TDDFT computational study of photoelectrochemical cell ruthenium sensitizers," *Journal of the American Chemical Society*, vol. 127, no. 48, pp. 16835–16847, 2005.
- [9] M. Späth, J. V. Roosmalen, P. Sommeling, et al., "Dye sensitised solar cells from laboratory scale to pre-pilot stage," in *Proceedings of the 3rd World Conference on Photovoltaic Energy Conversion (WCPEC '03)*, vol. 1, pp. 196–199, Osaka, Japan, May 2003.
- [10] J. M. Kroon, N. J. Bakker, H. J. P. Smit, et al., "Nanocrystalline dye-sensitized solar cells having maximum performance," *Progress in Photovoltaics: Research and Applications*, vol. 15, no. 1, pp. 1–18, 2007.
- [11] H. Arakawa, T. Yamaguchi, A. Takeuchi, et al., "Preparation of 10 cm-by-10 cm size black dye sensitized solar cells with 8.4% efficiency," in *The 16th International Conference of Photochemical Conversion and Solar Storage*, Uppsala, Sweden, July 2006, W4-P-10.
- [12] M. A. Green, K. Emery, D. L. King, S. Igari, and W. Warta, "Solar cell efficiency tables (version 20)," *Progress in Photovoltaics: Research and Applications*, vol. 10, no. 5, pp. 355–360, 2002.
- [13] Y. Chiba, A. Islam, K. Kakutani, R. Komiya, N. Koide, and L. Han, "High efficiency dye sensitized solar cells," in *Proceedings of the 15th International Photovoltaic Science & Engineering Conference (PVSEC '05)*, pp. 665–666, Shanghai, China, October 2005.
- [14] S.-Y. Dai, J. Weng, Y. Sui, et al., "Dye-sensitized solar cells, from cell to module," *Solar Energy Society World Congress*, vol. 84, no. 1–4, pp. 125–133, 2004.
- [15] S.-Y. Dai, K.-J. Wang, J. Weng, et al., "Design of DSC panel with efficiency more than 6%," *Solar Energy Materials and Solar Cells*, vol. 85, no. 3, pp. 447–455, 2005.
- [16] T. Yoshida, T. Oekermann, L. M. Peter, et al., "Electrodeposition of nano-structured porous crystalline ZnO/Dye hybrid thin films for plastic solar cells," in *The 16th International Conference of Photochemical Conversion and Solar Storage*, Uppsala, Sweden, July 2006, W4-O-2.
- [17] T. Miyasaka, Y. Kijitori, and M. Ikegami, "Fabrication of full-plastic dye-sensitized solar cell modules based on low-temperature coating techniques," in *The 16th International Conference of Photochemical Conversion and Solar Storage*, Uppsala, Sweden, July 2006, W4-O-7.
- [18] L. Hu, S.-Y. Dai, J. Weng, et al., "Microstructure design of nanoporous TiO<sub>2</sub> photoelectrodes for dye-sensitized solar cell modules," *Journal of Physical Chemistry B*, vol. 111, no. 2, pp. 358–362, 2007.
- [19] J.-H. Yum, S.-S. Kim, D.-Y. Kim, and Y.-E. Sung, "Electrochemically deposited TiO<sub>2</sub> photo-electrodes for use in flexible dye-sensitized solar cells," *Journal of Photochemistry and Photobiology A*, vol. 173, no. 1, pp. 1–6, 2005.
- [20] F. Pichot, J. R. Pitts, and B. A. Gregg, "Low-temperature sintering of TiO<sub>2</sub> colloids: application to flexible dye-sensitized solar cells," *Langmuir*, vol. 16, no. 13, pp. 5626–5630, 2000.
- [21] C. Longo, A. F. Nogueira, M.-A. de Paoli, and H. Cachet, "Solid-state and flexible dye-sensitized TiO<sub>2</sub> solar cells: a study by electrochemical impedance spectroscopy," *Journal of Physical Chemistry B*, vol. 106, no. 23, pp. 5925–5930, 2002.
- [22] H. Lindström, A. Holmberg, E. Magnusson, S.-E. Lindquist, L. Malmqvist, and A. Hagfeldt, "A new method for manufacturing nanostructured electrodes on plastic substrates," *Nano Letters*, vol. 1, no. 2, pp. 97–100, 2001.
- [23] H. Lindström, A. Holmberg, E. Magnusson, L. Malmqvist, and A. Hagfeldt, "A new method to make dye-sensitized nanocrystalline solar cells at room temperature," *Journal of Photochemistry and Photobiology A*, vol. 145, no. 1–2, pp. 107–112, 2001.
- [24] T. Miyasaka, Y. Kijitori, T. N. Murakami, M. Kimura, and S. Uegusa, "Efficient nonsintering type dye-sensitized photocells based on electrochemically deposited TiO<sub>2</sub> layers," *Chemistry Letters*, vol. 31, no. 12, pp. 1250–1251, 2002.
- [25] T. Miyasaka and Y. Kijitori, "Low-temperature fabrication of dye-sensitized plastic electrodes by electrophoretic preparation of mesoporous TiO<sub>2</sub> layers," *Journal of the Electrochemical Society*, vol. 151, no. 11, pp. A1767–A1773, 2004.
- [26] M. Dürr, A. Schmid, M. Obermaier, S. Rosselli, A. Yasuda, and G. Nelles, "Low-temperature fabrication of dye-sensitized solar cells by transfer of composite porous layers," *Nature Materials*, vol. 4, no. 8, pp. 607–611, 2005.
- [27] T. Miyasaka and Y. Kijitori, "High efficient plastic dye-sensitized solar cell based on the low-temperature TiO<sub>2</sub> coating method," in *The 16th International Conference of Photochemical Conversion and Solar Storage*, Uppsala, Sweden, July 2006, W4-P-15.
- [28] S. Ito, N.-L. C. Ha, G. Rothenberger, et al., "High-efficiency (7.2%) flexible dye-sensitized solar cells with Ti-metal substrate for nanocrystalline-TiO<sub>2</sub> photoanode," *Chemical Communications*, no. 38, pp. 4004–4006, 2006.
- [29] S. Lee, J. Y. Kim, K. S. Hong, H. S. Jung, J.-K. Lee, and H. Shin, "Enhancement of the photoelectric performance of dye-sensitized solar cells by using a CaCO<sub>3</sub>-coated TiO<sub>2</sub> nanoparticle film as an electrode," *Solar Energy Materials and Solar Cells*, vol. 90, no. 15, pp. 2405–2412, 2006.
- [30] H. S. Jung, J.-K. Lee, M. Nastasi, et al., "Preparation of nanoporous MgO-coated TiO<sub>2</sub> nanoparticles and their application to the electrode of dye-sensitized solar cells," *Langmuir*, vol. 21, no. 23, pp. 10332–10335, 2005.
- [31] J.-H. Yum, S. Nakade, D.-Y. Kim, and S. Yanagida, "Improved performance in dye-sensitized solar cells employing TiO<sub>2</sub> photoelectrodes coated with metal hydroxides," *Journal of Physical Chemistry B*, vol. 110, no. 7, pp. 3215–3219, 2006.
- [32] D. B. Menzies, Q. Dai, Y.-B. Cheng, G. P. Simon, and L. Spiccia, "One-step microwave calcination of ZrO<sub>2</sub>-coated TiO<sub>2</sub> electrodes for use in dye-sensitized solar cells," *Comptes Rendus Chimie*, vol. 9, no. 5–6, pp. 713–716, 2006.

- [33] E. Palomares, J. N. Clifford, S. A. Haque, T. Lutz, and J. R. Durrant, "Control of charge recombination dynamics in dye sensitized solar cells by the use of conformally deposited metal oxide blocking layers," *Journal of the American Chemical Society*, vol. 125, no. 2, pp. 475–482, 2003.
- [34] G. R. R. A. Kumara, K. Tennakone, V. P. S. Perera, A. Konno, S. Kaneko, and M. Okuya, "Suppression of recombinations in a dye-sensitized photoelectrochemical cell made from a film of tin IV oxide crystallites coated with a thin layer of aluminium oxide," *Journal of Physics D*, vol. 34, no. 6, pp. 868–873, 2001.
- [35] K. Tennakone, G. R. R. A. Kumara, I. R. M. Kottegodla, and V. P. S. Perera, "An efficient dye-sensitized photoelectrochemical solar cell made from oxides of tin and zinc," *Chemical Communications*, no. 1, pp. 15–16, 1999.
- [36] A. Kay and M. Grätzel, "Dye-sensitized core-shell nanocrystals: improved efficiency of mesoporous tin oxide electrodes coated with a thin layer of an insulating oxide," *Chemistry of Materials*, vol. 14, no. 7, pp. 2930–2935, 2002.
- [37] F.-T. Kong and S.-Y. Dai, "Dye-sensitized solar cells," *Progress in Chemistry*, vol. 18, no. 11, pp. 1409–1424, 2006.
- [38] A. Hagfeldt and M. Grätzel, "Molecular photovoltaics," *Accounts of Chemical Research*, vol. 33, no. 5, pp. 269–277, 2000.
- [39] P. Wang, S. M. Zakeeruddin, R. Humphry-Baker, J. E. Moser, and M. Grätzel, "Molecular-scale interface engineering of TiO<sub>2</sub> nanocrystals: improving the efficiency and stability of dye-sensitized solar cells," *Advanced Materials*, vol. 15, no. 24, pp. 2101–2104, 2003.
- [40] C. Klein, M. K. Nazeeruddin, P. Liska, et al., "Engineering of a novel ruthenium sensitizer and its application in dye-sensitized solar cells for conversion of sunlight into electricity," *Inorganic Chemistry*, vol. 44, no. 2, pp. 178–180, 2005.
- [41] P. Wang, C. Klein, R. Humphry-Baker, S. M. Zakeeruddin, and M. Grätzel, "A high molar extinction coefficient sensitizer for stable dye-sensitized solar cells," *Journal of the American Chemical Society*, vol. 127, no. 3, pp. 808–809, 2005.
- [42] P. Wang, S. M. Zakeeruddin, J. E. Moser, M. K. Nazeeruddin, T. Sekiguchi, and M. Grätzel, "A stable quasi-solid-state dye-sensitized solar cell with an amphiphilic ruthenium sensitizer and polymer gel electrolyte," *Nature Materials*, vol. 2, no. 6, pp. 402–407, 2003.
- [43] M. K. Nazeeruddin, Q. Wang, L. Cevey, et al., "DFT-INDO/S modeling of new high molar extinction coefficient charge-transfer sensitizers for solar cell applications," *Inorganic Chemistry*, vol. 45, no. 2, pp. 787–797, 2006.
- [44] P. Wang, S. M. Zakeeruddin, J. E. Moser, et al., "Stable new sensitizer with improved light harvesting for nanocrystalline dye-sensitized solar cells," *Advanced Materials*, vol. 16, no. 20, pp. 1806–1811, 2004.
- [45] D. Kuang, S. Ito, B. Wenger, et al., "High molar extinction coefficient heteroleptic ruthenium complexes for thin film dye-sensitized solar cells," *Journal of the American Chemical Society*, vol. 128, no. 12, pp. 4146–4154, 2006.
- [46] D. Kuang, C. Klein, H. J. Snaith, et al., "Ion coordinating sensitizer for high efficiency mesoscopic dye-sensitized solar cells: influence of lithium ions on the photovoltaic performance of liquid and solid-state cells," *Nano Letters*, vol. 6, no. 4, pp. 769–773, 2006.
- [47] K.-J. Jiang, N. Masaki, J.-B. Xia, S. Noda, and S. Yanagida, "A novel ruthenium sensitizer with a hydrophobic 2-thiophen-2-yl-vinyl-conjugated bipyridyl ligand for effective dye sensitized TiO<sub>2</sub> solar cells," *Chemical Communications*, no. 23, pp. 2460–2462, 2006.
- [48] P. Wang, C. Klein, J.-E. Moser, et al., "Amphiphilic ruthenium sensitizer with 4,4'-diphosphonic acid-2,2'-bipyridine as anchoring ligand for nanocrystalline dye sensitized solar cells," *Journal of Physical Chemistry B*, vol. 108, no. 45, pp. 17553–17559, 2004.
- [49] P. Péchy, F. P. Rotzinger, M. K. Nazeeruddin, et al., "Preparation of phosphonated polypyridyl ligands to anchor transition-metal complexes on oxide surfaces: application for the conversion of light to electricity with nanocrystalline TiO<sub>2</sub> films," *Chemical Communications*, pp. 65–66, 1995.
- [50] F. Kong, S. Dai, and K. Wang, "Dye sensitizers used in dye-sensitized solar cells," *Huaxue Tongbao*, vol. 68, no. 5, pp. 338–345, 2005.
- [51] O. Kohle, S. Ruile, and M. Grätzel, "Ruthenium(II) charge-transfer sensitizers containing 4,4'-dicarboxy-2,2'-bipyridine. synthesis, properties, and bonding mode of coordinated thio- and selenocyanates," *Inorganic Chemistry*, vol. 35, no. 16, pp. 4779–4787, 1996.
- [52] K. Sayama, S. Tsukagoshi, K. Hara, et al., "Photoelectrochemical properties of J aggregates of benzothiazole merocyanine dyes on a nanostructured TiO<sub>2</sub> film," *Journal of Physical Chemistry B*, vol. 106, no. 6, pp. 1363–1371, 2002.
- [53] K. Hara, K. Sayama, Y. Ohga, A. Shinpo, S. Suga, and H. Arakawa, "A coumarin-derivative dye sensitized nanocrystalline TiO<sub>2</sub> solar cell having a high solar-energy conversion efficiency up to 5.6%," *Chemical Communications*, no. 6, pp. 569–570, 2001.
- [54] K. Hara, Z.-S. Wang, T. Sato, et al., "Oligothiophene-containing coumarin dyes for efficient dye-sensitized solar cells," *Journal of Physical Chemistry B*, vol. 109, no. 32, pp. 15476–15482, 2005.
- [55] K. Hara, M. Kurashige, Y. Dan-Oh, et al., "Design of new coumarin dyes having thiophene moieties for highly efficient organic-dye-sensitized solar cells," *New Journal of Chemistry*, vol. 27, no. 5, pp. 783–785, 2003.
- [56] Z. S. Wang, Y. Cui, K. Hara, et al., "High efficiency-light-harvesting coumarin dyes for efficient and stable dye-sensitized solar cells," in *The 16th International Conference of Photochemical Conversion and Solar Storage*, Uppsala, Sweden, July 2006, W4-P-95.
- [57] T. Kitamura, M. Ikeda, K. Shigaki, et al., "Phenyl-conjugated oligoene sensitizers for TiO<sub>2</sub> solar cells," *Chemistry of Materials*, vol. 16, no. 9, pp. 1806–1812, 2004.
- [58] K. Hara, M. Kurashige, S. Ito, et al., "Novel polyene dyes for highly efficient dye-sensitized solar cells," *Chemical Communications*, no. 2, pp. 252–253, 2003.
- [59] S.-L. Li, K.-J. Jiang, K.-F. Shao, and L.-M. Yang, "Novel organic dyes for efficient dye-sensitized solar cells," *Chemical Communications*, no. 26, pp. 2792–2794, 2006.
- [60] T. Horiuchi, H. Miura, K. Sumioka, and S. Uchida, "High efficiency of dye-sensitized solar cells based on metal-free indoline dyes," *Journal of the American Chemical Society*, vol. 126, no. 39, pp. 12218–12219, 2004.
- [61] S. Ito, S. M. Zakeeruddin, R. Humphry-Baker, et al., "High-efficiency organic-dye-sensitized solar cells controlled by nanocrystalline-TiO<sub>2</sub> electrode thickness," *Advanced Materials*, vol. 18, no. 9, pp. 1202–1205, 2006.
- [62] Z.-S. Wang, F.-Y. Li, and C.-H. Huang, "Photocurrent enhancement of hemicyanine dyes containing RSO<sub>3</sub><sup>-</sup> group through treating TiO<sub>2</sub> films with hydrochloric acid," *Journal of Physical Chemistry B*, vol. 105, no. 38, pp. 9210–9217, 2001.
- [63] W. Zhao, B. W. Zhang, Y. Cao, X. Xiao, and R. Yang, "Photoelectric conversion performance of nanocrystalline TiO<sub>2</sub> film electrodes modified with squarylium cyanine functional materials," *Journal of Functional Materials*, vol. 30, no. 3, pp. 304–306, 1999.

- [64] W. Zhao, Y. J. Hou, X. S. Wang, et al., "Study on squarylium cyanine dyes for photoelectric conversion," *Solar Energy Materials and Solar Cells*, vol. 58, no. 2, pp. 173–183, 1999.
- [65] C. Shi, S. Dai, K. Wang, X. Pan, F. Kong, and L. Hu, "The adsorption of 4-*tert*-butylpyridine on the nanocrystalline TiO<sub>2</sub> and Raman spectra of dye-sensitized solar cells in situ," *Vibrational Spectroscopy*, vol. 39, no. 1, pp. 99–105, 2005.
- [66] C.-W. Shi, S.-Y. Dai, K.-J. Wang, et al., "Application of 3-hexyl-1-methylimidazolium iodide to dye-sensitized solar cells," *Acta Chimica Sinica*, vol. 63, no. 13, pp. 1205–1209, 2005.
- [67] C. Shi, S. Dai, K. Wang, et al., "Influence of various cations on redox behavior of I<sup>-</sup> and I<sub>3</sub><sup>-</sup> and comparison between KI complex with 18-crown-6 and 1,2-dimethyl-3-propylimidazolium iodide in dye-sensitized solar cells," *Electrochimica Acta*, vol. 50, no. 13, pp. 2597–2602, 2005.
- [68] C.-W. Shi, S.-Y. Dai, K.-J. Wang, et al., "I<sub>3</sub><sup>-</sup>/I<sup>-</sup> redox behavior of alkali-metal iodide complexes with crown ether/cryptand macrocycles and their applications to dye-sensitized solar cells," *Chinese Journal of Chemistry*, vol. 23, no. 3, pp. 251–254, 2005.
- [69] Z.-S. Wang, K. Sayama, and H. Sugihara, "Efficient eosin Y dye-sensitized solar cell containing Br<sup>-</sup>/Br<sub>3</sub><sup>-</sup> electrolyte," *Journal of Physical Chemistry B*, vol. 109, no. 47, pp. 22449–22455, 2005.
- [70] B. V. Bergeron, A. Marton, G. Oskam, and G. J. Meyer, "Dye-sensitized SnO<sub>2</sub> electrodes with iodide and pseudohalide redox mediators," *Journal of Physical Chemistry B*, vol. 109, no. 2, pp. 937–943, 2005.
- [71] G. Oskam, B. V. Bergeron, G. J. Meyer, and P. C. Searson, "Pseudohalogens for dye-sensitized TiO<sub>2</sub> photoelectrochemical cells," *Journal of Physical Chemistry B*, vol. 105, no. 29, pp. 6867–6873, 2001.
- [72] S. A. Sapp, C. M. Elliott, C. Contado, S. Caramori, and C. A. Bignozzi, "Substituted polypyridine complexes of cobalt (II/III) as efficient electron-transfer mediators in dye-sensitized solar cells," *Journal of the American Chemical Society*, vol. 124, no. 37, pp. 11215–11222, 2002.
- [73] W. Kubo, T. Kitamura, K. Hanabusa, Y. Wada, and S. Yanagida, "Quasi-solid-state dye-sensitized solar cells using room temperature molten salts and a low molecular weight gelator," *Chemical Communications*, no. 4, pp. 374–375, 2002.
- [74] H. Paulsson, A. Hagfeldt, and L. Kloo, "Molten and solid trialkylsulfonium iodides and their polyiodides as electrolytes in dye-sensitized nanocrystalline solar cells," *Journal of Physical Chemistry B*, vol. 107, no. 49, pp. 13665–13670, 2003.
- [75] P. Wang, S. M. Zakeeruddin, J.-E. Moser, R. Humphry-Baker, and M. Grätzel, "A solvent-free, SeCN<sup>-</sup>/(SeCN)<sub>3</sub><sup>-</sup> based ionic liquid electrolyte for high-efficiency dye-sensitized nanocrystalline solar cells," *Journal of the American Chemical Society*, vol. 126, no. 23, pp. 7164–7165, 2004.
- [76] P. Wang, S. M. Zakeeruddin, J.-E. Moser, and M. Grätzel, "A new ionic liquid electrolyte enhances the conversion efficiency of dye-sensitized solar cells," *Journal of Physical Chemistry B*, vol. 107, no. 48, pp. 13280–13285, 2003.
- [77] P. Wang, S. M. Zakeeruddin, P. Comte, I. Exnar, and M. Grätzel, "Gelation of ionic liquid-based electrolytes with silica nanoparticles for quasi-solid-state dye-sensitized solar cells," *Journal of the American Chemical Society*, vol. 125, no. 5, pp. 1166–1167, 2003.
- [78] P. Wang, S. M. Zakeeruddin, R. Humphry-Baker, and M. Grätzel, "A binary ionic liquid electrolyte to achieve ≥ 7% power conversion efficiencies in dye-sensitized solar cells," *Chemistry of Materials*, vol. 16, no. 14, pp. 2694–2696, 2004.
- [79] D. Kuang, P. Wang, S. Ito, S. M. Zakeeruddin, and M. Grätzel, "Stable mesoscopic dye-sensitized solar cells based on tetracyanoborate ionic liquid electrolyte," *Journal of the American Chemical Society*, vol. 128, no. 24, pp. 7732–7733, 2006.
- [80] N. Mohmeyer, D. Kuang, P. Wang, H.-W. Schmidt, S. M. Zakeeruddin, and M. Grätzel, "An efficient organogelator for ionic liquids to prepare stable quasi-solid-state dye-sensitized solar cells," *Journal of Materials Chemistry*, vol. 16, no. 29, pp. 2978–2983, 2006.
- [81] R. Kawano, H. Matsui, C. Matsuyama, et al., "High performance dye-sensitized solar cells using ionic liquids as their electrolytes," *Journal of Photochemistry and Photobiology A*, vol. 164, no. 1–3, pp. 87–92, 2004.
- [82] F. Mazille, Z. Fei, and D. Kuang, "Influence of ionic liquids bearing functional groups in dye-sensitized solar cells," *Inorganic Chemistry*, vol. 45, no. 4, pp. 1585–1590, 2006.
- [83] H. Matsui, K. Okada, T. Kawashima, et al., "Application of an ionic liquid-based electrolyte to a 100 mm×100 mm sized dye-sensitized solar cell," *Journal of Photochemistry and Photobiology A*, vol. 164, no. 1–3, pp. 129–135, 2004.
- [84] P. Wang, S. M. Zakeeruddin, I. Exnar, and M. Grätzel, "High efficiency dye-sensitized nanocrystalline solar cells based on ionic liquid polymer gel electrolyte," *Chemical Communications*, vol. 8, no. 24, pp. 2972–2973, 2002.
- [85] V. Jovanovski, E. Stathatos, B. Orel, and P. Lianos, "Dye-sensitized solar cells with electrolyte based on a trimethoxysilane-derivatized ionic liquid," *Thin Solid Films*, vol. 511–512, pp. 634–637, 2006.
- [86] K. Suzuki, M. Yamaguchi, M. Kumagai, N. Tanabe, and S. Yanagida, "Dye-sensitized solar cells with ionic gel electrolytes prepared from imidazolium salts and agarose," *Comptes Rendus Chimie*, vol. 9, no. 5–6, pp. 611–616, 2006.
- [87] H. Usui, H. Matsui, N. Tanabe, and S. Yanagida, "Improved dye-sensitized solar cells using ionic nanocomposite gel electrolytes," *Journal of Photochemistry and Photobiology A*, vol. 164, no. 1–3, pp. 97–101, 2004.
- [88] R. Sastrawan, J. Beier, U. Belledin, et al., "A glass frit-sealed dye solar cell module with integrated series connections," *Solar Energy Materials and Solar Cells*, vol. 90, no. 11, pp. 1680–1691, 2006.
- [89] G. R. A. Kumara, S. Kaneko, M. Okuya, and K. Tennakone, "Fabrication of dye-sensitized solar cells using triethylamine hydrothiocyanate as a CuI crystal growth inhibitor," *Langmuir*, vol. 18, no. 26, pp. 10493–10495, 2002.
- [90] Q.-B. Meng, K. Takahashi, X.-T. Zhang, et al., "Fabrication of an efficient solid-state dye-sensitized solar cell," *Langmuir*, vol. 19, no. 9, pp. 3572–3574, 2003.
- [91] U. Bach, D. Lupo, P. Comte, et al., "Solid-state dye-sensitized mesoporous TiO<sub>2</sub> solar cells with high photon-to-electron conversion efficiencies," *Nature*, vol. 395, no. 6702, pp. 583–585, 1998.
- [92] J. Kang, W. Li, X. Wang, Y. Lin, X. Xiao, and S. Fang, "Polymer electrolytes from PEO and novel quaternary ammonium iodides for dye-sensitized solar cells," *Electrochimica Acta*, vol. 48, no. 17, pp. 2487–2491, 2003.
- [93] Y. Ren, Z. Zhang, S. Fang, M. Yang, and S. Cai, "Application of PEO based gel network polymer electrolytes in dye-sensitized photoelectrochemical cells," *Solar Energy Materials and Solar Cells*, vol. 71, no. 2, pp. 253–259, 2002.
- [94] L. Wang, S. Fang, Y. Lin, X. Zhou, and M. Li, "A 7.72% efficient dye sensitized solar cell based on novel necklace-like polymer gel electrolyte containing latent chemically cross-linked gel electrolyte precursors," *Chemical Communications*, no. 45, pp. 5687–5689, 2005.

- [95] F. Cao, G. Oskam, and P. C. Searson, "A solid state, dye sensitized photoelectrochemical cell," *Journal of Physical Chemistry*, vol. 99, no. 47, pp. 17071–17073, 1995.
- [96] J. Wu, Z. Lan, D. Wang, et al., "Gel polymer electrolyte based on poly (acrylonitrile-*co*-styrene) and a novel organic iodide salt for quasi-solid state dye-sensitized solar cell," *Electrochimica Acta*, vol. 51, no. 20, pp. 4243–4249, 2006.
- [97] L. Guo, S.-Y. Dai, K.-J. Wang, X.-Q. Fang, C.-W. Shi, and X. Pan, "Dye-sensitized nano-TiO<sub>2</sub> thin memberane solar cells based on P(VDF-HFP)-type gel electrolytes," *Chemical Journal of Chinese Universities*, vol. 26, no. 10, pp. 1934–1937, 2005.
- [98] S. Dai, J. Weng, Y. Sui, et al., "The design and outdoor application of dye-sensitized solar cells," to be available online in *Inorganica Chimica Acta*.

## Review Article

# Recent Advances in Organic Solar Cells

**Thomas Kietzke**

*Institute of Materials Research and Engineering (IMRE), 3 Research Link, Singapore 117602*

Received 24 May 2007; Accepted 16 August 2007

Recommended by A. G. Aberle

Solar cells based on organic semiconductors have attracted much attention. The thickness of the active layer of organic solar cells is typically only 100 nm thin, which is about 1000 times thinner than for crystalline silicon solar cells and still 10 times thinner than for current inorganic thin film cells. The low material consumption per area and the easy processing of organic semiconductors offer a huge potential for low cost large area solar cells. However, to compete with inorganic solar cells the efficiency of organic solar cells has to be improved by a factor of 2-3. Several organic semiconducting materials have been investigated so far, but the optimum material still has to be designed. Similar as for organic light emitting devices (OLED) small molecules are competing with polymers to become the material of choice. After a general introduction into the device structures and operational principles of organic solar cells the three different basic types (all polymer based, all small molecules based and small molecules mixed with polymers) are described in detail in this review. For each kind the current state of research is described and the best of class reported efficiencies are listed.

Copyright © 2007 Thomas Kietzke. This is an open access article distributed under the Creative Commons Attribution License, which permits unrestricted use, distribution, and reproduction in any medium, provided the original work is properly cited.

## 1. INTRODUCTION

Organic photovoltaic devices have gained a broad interest in the last few years due to their potential for large-area low-cost solar cells. From the first reports on molecular thin film devices more than 30 years ago, their power conversion efficiencies have increased considerably from 0.001% in 1975 [1] to 1% in 1986 [2] and more recently to 5.5% in 2006 [3–6]. The progresses in efficiency will possibly make them a competitive alternative to inorganic solar cells in the near future. Different concepts have been published using either small molecules [1–4, 7], conjugated polymers [7–17], combinations of small molecules and conjugated polymers [18–20], or combinations of inorganic and organic materials [21] as the active layer. “Active layer” refers here to the layer in which the majority of the incident light is absorbed and charges are generated. Small molecules and polymers differ in their molecular weights. Commonly, macromolecules with a molecular weight larger than 10 000 amu are called polymers, whereas lighter molecules are referred to as “oligomers” or “small molecules.”

Historically, small molecules were mainly deposited by vacuum deposition techniques since they showed limited solubility in common solvents. In contrast to these small molecule thin films, the preparation of thin polymer layers does not require high vacuum sublimation steps. Large

polymer thin film areas can be deposited by several methods, such as spin-coating, screen printing, spray coating, or ink jet printing, allowing for large-area, ultrathin, flexible, and low-cost devices. Currently, there is a head-to-head race going on between solution processed and sublimed organic solar cells, but the ease of processability may finally tip the balance in favour of polymers or small molecules blended with polymers. Although it should be noted that currently there are some efforts to develop soluble oligomers to allow for cost efficient solution processing techniques, the concept of efficient complete small molecules-based devices prepared from solution processing has yet to be proven.

## 2. DEVICE STRUCTURE AND OPERATION

Organic semiconductors differ from classical crystalline inorganic semiconductors (e.g., silicon) in many fundamental aspects.

First of all, the mobilities of organic semiconductors are several orders of magnitude less than those found in crystalline inorganic semiconductors [22]. Transport processes in organic semiconductors are best described by hopping transport in contrast to the band transport in most crystalline inorganic semiconductors. Even the highest reported hole mobilities ( $\mu_h$ ) for organic semiconductors reach currently only about  $15 \text{ cm}^2 \text{ V}^{-1} \text{ s}^{-1}$  for single crystals of small

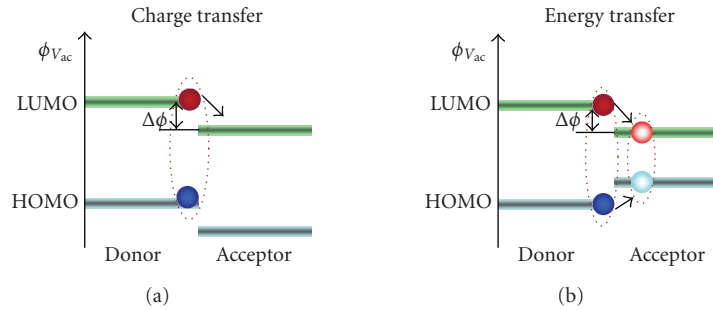


FIGURE 1: The interface between two different semiconducting polymers (D = donor, A = acceptor) can facilitate either charge transfer by splitting the exciton or energy transfer, where the whole exciton is transferred from the donor to the acceptor.

molecules [23] and  $0.6 \text{ cm}^2\text{V}^{-1}\text{s}^{-1}$  for liquid crystalline polymers [24] (silicon:  $\mu_h = 450 \text{ cm}^2\text{V}^{-1}\text{s}^{-1}$ ). Highest electron mobilities ( $\mu_e$ ) for organic materials are typically lower, hovering around  $0.1 \text{ cm}^2\text{V}^{-1}\text{s}^{-1}$  reaching higher values only in particular TFT structures using highly crystalline small molecules [25, 26] (silicon:  $\mu_e = 1400 \text{ cm}^2\text{V}^{-1}\text{s}^{-1}$ ). The mobility values for amorphous organic materials as used most commonly in organic solar cells are even several magnitudes lower. These low mobilities limit the feasible thicknesses of the organic layer in solar cells to a few hundred nanometres. Fortunately, organic semiconductors are very strong absorbers in the UV-VIS regime. Thus only *ca.* 100 nm thick organic layers are needed for effective absorption.

Second, the exciton binding energy in organic semiconductors is much higher than, for example, in silicon. Upon absorption of a photon of sufficient energy by the organic semiconductor, an electron is promoted into the lowest unoccupied molecular orbital (LUMO), leaving behind a hole in the highest occupied molecular orbital (HOMO). However, due to electrostatic interactions, this electron-hole pair forms a tightly bound state which is called singlet exciton. The exact binding energy of this exciton is still under debate but it is expected to be in a range of 200–500 meV [27, 28]. Hence, the exciton binding energy for organic semiconductors is roughly one order of magnitude larger than for inorganic semiconductors like silicon, where photoexcitations typically lead directly to free carriers at room temperature. The thermal energy at room temperature ( $\sim 25 \text{ meV}$ ) is not sufficient to efficiently generate free charge carriers in organic materials by exciton dissociation, even at typical internal electric fields ( $\sim 10^6\text{--}10^7 \text{ V/m}$ ) [29]. For example, in the widely used Poly(2-methoxy-5-(2'-ethyl-hexyloxy)-p-phenylene vinylene) (MEH-PPV) [30] experiments revealed that only 10% of the excitons dissociate into free carriers in a pure layer [31], while the remaining excitons decay via radiative or nonradiative recombination pathways. Thus, the energy efficiencies of single-layer polymer devices remain typically below 0.1% [27, 32].

The most important discovery on the route to high-efficiency organic solar cells was the finding that solar cells containing a heterojunction between hole and electron accepting organic materials exhibited performances far superior to single component devices [2, 8–10]. Using the het-

erojunction approach, photogenerated excitons (bound electron-hole pairs) in the polymer layer can be efficiently dissociated into free carriers at the interface, whereas in single component devices most excitons recombine after a short time. The charge separation occurs at the interface between donor and acceptor molecules, mediated by a large potential drop. After photo-excitation of an electron from the HOMO to the LUMO, the electron can jump from the LUMO of the donor (the material with the higher LUMO) to the LUMO of the acceptor if the potential difference  $\Delta\Phi$  between the ionisation potential of the donor and the electron affinity of the acceptor is larger than the exciton binding energy (see Figure 1). However, this process, which is called photoinduced charge transfer, can lead to free charges only if the hole remains on the donor due to its higher HOMO level. In contrast, if the HOMO of the acceptor is higher, the exciton transfers itself completely to the material of lower-band gap accompanied by energy loss.

For efficient exciton dissociation at the heterojunction, the donor and acceptor materials have to be in close proximity. The optimum length scale is in the range of the exciton diffusion length, typically a few tens of nanometres. On the other hand, the thickness of the active layer should be comparable to the penetration length of the incident light, which for organic semiconductors is typically 80–200 nm.

A heterojunction can be realised in several ways (see Figure 2). The most straightforward approach is the preparation of a bilayer by subliming or by spin-coating a second layer on top of the first, resulting in a more or less diffused bilayer structure [11, 33, 34]. If polymers are used and both materials are soluble in the same solvents, laminating techniques can be used [10, 35]. This bilayer geometry guarantees directional photoinduced charge transfer across the interface. Since both types of charge carriers travel to their respective electrodes in pure *n*-type or *p*-type layers, the chances for recombination losses are significantly reduced. However, the interfacial area and thus the exciton dissociation efficiency are limited. Higher interfacial areas and thus improved exciton dissociation efficiencies can be achieved if layers containing both the electron donor and electron acceptor in a mixture are prepared. These so-called bulk heterojunctions can be deposited either by cosublimation of small molecules or by spin-coating mixtures of polymers.

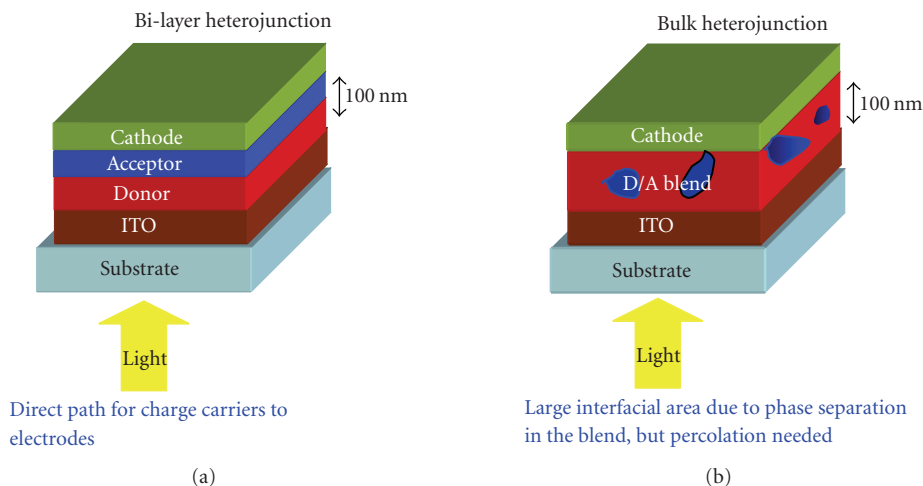


FIGURE 2: Two approaches to heterojunction solar cells.

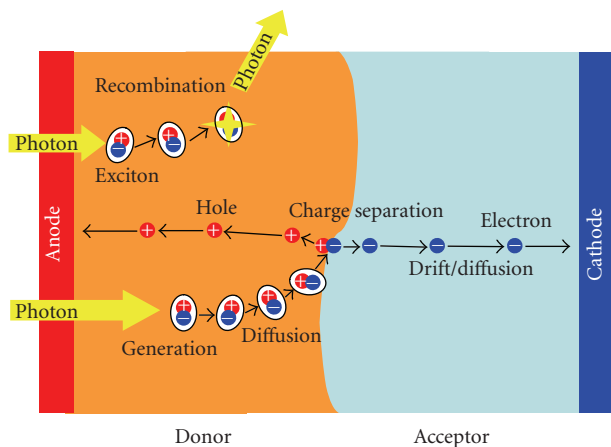


FIGURE 3: Principle of charge separation in a solar cell.

The drawback of the bulk heterojunction structure is that a percolating pathway for the hole and electron transporting phase to the electrodes is needed in order that the separated charge carriers can reach their corresponding electrodes.

If the individual layer thicknesses (in case of a bilayer structure) or the phase separated domains (in case of a blend layer) is larger than the exciton diffusion length, then most excitons will recombine (Figure 3). If, however, the excitons are generated in close proximity to an interface, they have a chance to be separated into free charge carriers which may diffuse or drift to the corresponding electrodes. The overall efficiency of this process is described by the incident photon to converted electron efficiency (IPCE). The IPCE is calculated by the number of electrons leaving the device under short circuit condition per time and area divided by the number of photons incident per time and area:

$$\text{IPCE} = \frac{\# \text{ extracted electrons}}{\# \text{ incident photons}}. \quad (1)$$

Note that the IPCE is a measure of the external quantum efficiency, meaning that losses due to reflection at the surface or transmission through the device are included in the IPCE value. Subtracting these two loss channels would lead to the internal quantum efficiency, which is, however, rarely used to compare solar cells.

Solar cells are further characterised by measuring the current-voltage  $I(V)$  curve under illumination of a light source that mimics the sun spectrum. A typical current-voltage  $I(V)$  curve of a polymer solar cell is shown in Figure 4. Since organic semiconductors show very low intrinsic carrier concentration, the metal-insulator-metal (MIM) [36] model seems to be best suited to explain this characteristic. The characteristic points used to characterise a solar cell are labelled in Figure 4. In addition, for each of these points, the energy diagram for a single-layer cell with an indium tin oxide (ITO) anode and aluminium cathode is displayed.

- The current delivered by a solar cell under zero bias is called short circuit current ( $I_{sc}$ ). In this case, exciton dissociation and charge transport is driven by the so-called built-in potential. In the MIM picture, this potential is equal to the difference in work function ( $W_f$ ) of the hole- and electron-collecting electrodes. For polymer solar cells, the transparent ITO electrode is often chosen ( $W_{f,ITO} = 4.7 \text{ eV}$ ) in combination with a low work function material ( $W_{f,Ca} = 2.87 \text{ eV}$ ,  $W_{f,Mg} = 3.66 \text{ eV}$ ,  $W_{f,Al} = 4.24 \text{ eV}$ ) [37] as counter-electrode to achieve a high internal field [38–41]. For example, the difference in work functions between ITO and Ca is approximately 2 eV.
- The voltage where the current equals zero is called open circuit voltage ( $V_{oc}$ ). In the MIM picture this situation is described by the case where the band is flat, since the applied voltage equals the difference in the work function of the electrodes. (Note that diffusion effects are neglected in this simplified picture.)
- When  $V > V_{oc}$ , the diode is biased in the forward direction. Electrons are now injected from the low work

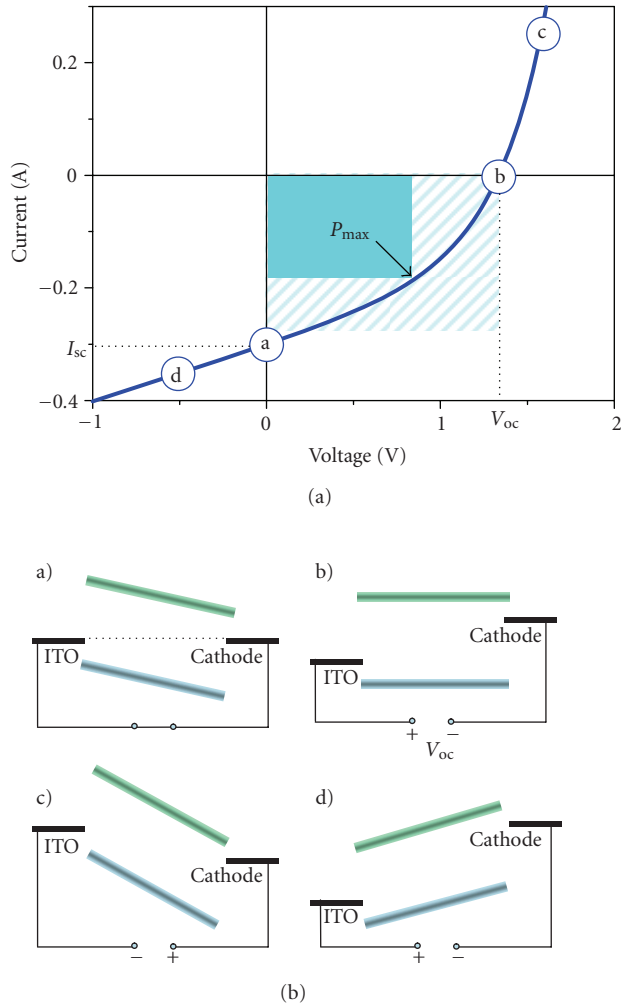


FIGURE 4: Current (voltage) characteristics of a typical organic diode shown together with the metal-insulator-metal (MIM) picture for the characteristic points. (a) Short circuit condition. (b) Open circuit condition. (c) Forward bias. (d) Reverse bias.

function electrode into the LUMO and holes from the high work function electrode into the HOMO of the organic layer, respectively.

- (d) When  $V < 0$ , the diode is driven under a reverse biased condition the solar cells works as a photodiode. The field is higher than in (a) which often leads to enhanced charge generation and/or collection efficiency.

The point where the electrical power  $P = I \times V$  reaches the maximum value represents the condition where the solar cell can deliver its maximum power to an external load. It is called the maximum power point. The ratio of this maximum electrical power  $P_{max}$  to the product of the short circuit current and the open circuit voltage is termed the fill factor (FF):

$$FF = \frac{P_{max}}{I_{sc} \times V_{oc}}. \quad (2)$$

Ideally, the fill factor should be unity, but losses due to transport and recombination result in values between 0.2–0.7 for

organic photovoltaic devices. As an example, a constant slope of the  $I(V)$  characteristic corresponds to  $FF = 0.25$ .

The photovoltaic power conversion efficiency ( $\eta$ ) is then calculated for an incident light power  $P_{light}$ :

$$\eta = \frac{I_{sc} \times V_{oc} \times FF}{P_{light}}. \quad (3)$$

### 3. SMALL MOLECULE-BASED SOLAR CELLS

The first efforts to fabricate organic photovoltaic devices using small molecules date back to 1975, however efficiencies did not reach more than 0.001% at that time. The work of Tang [2] in 1986 is commonly cited as the groundbreaking discovery that sparked the current interest in the field. Using copper phthalocyanine (CuPc) as the electron donor and a perylene derivative, 3,4,9,10-perylene tetracarboxylic bis-benzimidazole (confusingly referred to as PTCBI, PV, or PBI), as the electron acceptor in a simple bilayer structure, a power conversion efficiency of 1% was reported. The open circuit voltage reached 450 mV and the fill factor of 65% indicated excellent charge transport. For the past 20 years, CuPc has been the donor of choice in most small molecule solar cells due to its high stability, high mobility, and widespread availability. The device physics of small molecule solar cells is described in a review paper of Peumans et al. [42]. The original Tang structure was improved by cosublimation of CuPc and PTCBI leading to a blend structure followed by an annealing step [43]. Due to the improved interfacial area, a higher efficiency ( $\eta = 1.5\%$ ) was obtained. Later in 2005, a novel deposition method called vapour phase deposition (VPE) helped to increase the efficiency for this system further since a highly intermixed donor-acceptor interface could be obtained [44, 45]. The interfacial area was increased by a factor of four compared to a bilayer structure while still maintaining  $n$ -type and  $p$ -type percolating pathways, and a power conversion efficiency of 2.2% was reported [44, 45].

Although C60 (fullerene) does not show strong absorption properties in the visible region, its much larger exciton diffusion length compared to PTCBI is favorable to achieve higher efficiencies. Devices based on incorporating CuPc:C60 bulk heterojunctions reached power conversion efficiencies of up to 5% [3, 6, 46]. The highest efficiency for an organic solar cell so far was reached by Xue et al. [4] for a stacked solar cell comprising two CuPc:C60 bulk heterojunction cells separated via a layer of silver nanoclusters, which served as a charge recombination layer.

The drawback of using CuPc as an electron donor is that only relative small open circuit voltages ( $<0.6$  V) can be reached with perylenes or fullerenes as acceptors, since a large portion of photon energy is wasted when the photo-generated electron on CuPc transfers to C60 or perylene. The open circuit voltage could be increased by using boron subphthalocyanine (SubPc) instead of CuPc [47]. The HOMO level of SubPc (HOMO:  $-5.6$  eV) is shifted by approximately 400 meV compared to CuPc (HOMO:  $-5.2$  eV). As a result, the  $V_{oc}$  increased by the same amount to nearly 1 V. The SubPc:C60 device reached a power conversion efficiency of 2.1% leaving room for further improvement. If CuPc is

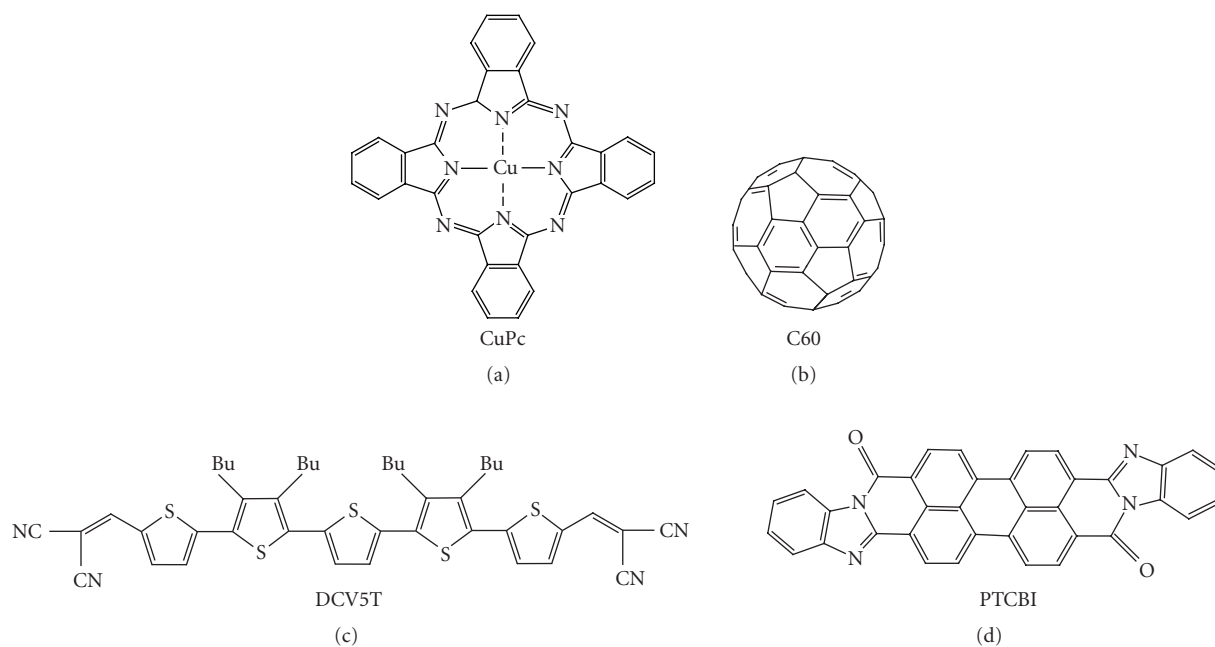


FIGURE 5: Chemical structures of most important small molecules used for organic solar cells.

substituted by tin(II) phthalocyanine (SnPc), the photoreponse increases from 800 nm to nearly 1000 nm [48]. However, the hole mobility in SnPc is very low limiting the device power conversion efficiency to around 1%.

A promising alternative to CuPc or phthalocyanines in general was presented by Schulze et al. [49] using  $\alpha,\alpha$ -bis(2,2-dicyanovinyl)-quinquithiophene (DCV5T) as electron donor in combination with C60 (see Figure 5 for the chemical structure). Since the HOMO level of DCV5T is sufficiently low ( $-5.6$  eV), open circuit voltages of 1 V could be obtained. The IPCE reached values as high as 52% leading to a high overall efficiency of 3.4%. In another approach, a glass forming thienylenevinylene triphenylamine [50] was used in combination with C60 for devices with open circuit voltages as high as 1.15 V. However, the power conversion efficiency was limited to 1.9% by its small fill factor.

An overview of small molecules solar cells can be found in Table 1.

## 4. POLYMER-BASED SOLAR CELLS

### 4.1. Introduction

For most of their history, polymers have been considered as electrical insulators. It was the discovery in 1977 by the group of Heeger, Shirakawa, and MacDiarmid that doped polyacetylene could achieve metallic conductivity which initiated intense research on conjugated polymers [53]. The work of these three pioneers was later honoured with the Nobel Prize in Chemistry in 2000 [54–56]. From this earlier work, it was not till the late 1990s that highly purified and soluble conjugated polymers became widely available. While initial research was concentrated mostly on improving the conductivity of conjugated polymers by chemical doping, serious

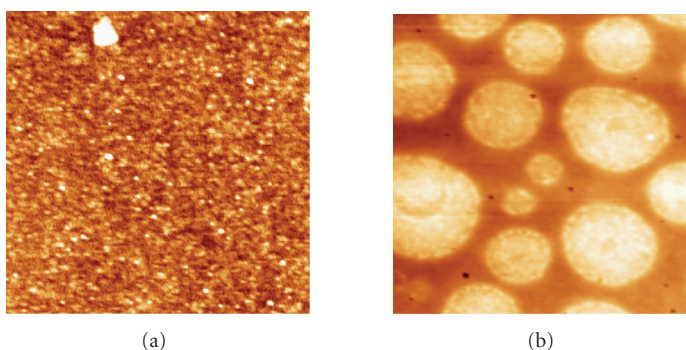
interest also grew in intrinsically semiconducting and highly soluble polymers. From then on, the application of conjugated polymers for a wide range of semiconductor devices such as light emitting diodes (LEDs) [30, 57], solar cells, and thin film transistors (TFTs) [58] was systematically investigated.

The conjugated systems of these polymers usually consist of chains and rings of carbon atoms in  $sp^1$  and  $sp^2$  hybridisation, leading to a framework of alternating double- or triple- and single-bonds. In this representation, single bonds are  $\sigma$ -bonds, and double bonds contain a  $\sigma$ -bond and a  $\pi$ -bond. However, in reality, the  $\pi$ -electrons are not constricted to the individual bonds, but rather are delocalised over the entire molecule. Thus conjugated polymers can be regarded as quasi one-dimensional semiconductors. The extent of the  $\pi$ -orbital overlap together with the bond alternation defines the band gap.

Layers containing a mixture of an electron donating and an electron accepting polymer (so-called polymer blends) can be prepared by spin-coating from a solution containing both polymers in the same solvent [8, 13, 14]. Since the entropy of mixing is generally low for polymers, solid polymer blends tend to phase-separate, leading to a distributed bulk heterojunction. A large donor-acceptor interface is formed without any additional processing steps. If donor and acceptor components are intimately mixed such that the length scale of the phase separation is in the range of the exciton diffusion length ( $<10$  nm), nearly all excitons can be separated. Moreover, when a thin layer of immiscible polymers is deposited from solution, the resulting morphology strongly depends on various parameters such as the individual solubility of the polymers in the solvent, the interaction with the substrate surface, the layer thickness, the deposition method, and the drying process [59–65]. Therefore, the adjustment

TABLE 1: Best in class solar cells: small molecule-based solar cells.

Donor	Acceptor	$\eta$	$V_{oc}$	FF	IPCE	Reference
CuPc	C60	5.7%	1.0 V	59%	NA	Xue et al. [4]
CuPc	C60	5.0%	0.6 V	60%	64%	Xue et al. [6]
MeO-TPD, ZnPc (stacked)	C60	3.8%	1.0 V	47%	NA	Drechsel et al. [51]
CuPc	C60	3.5%	0.5 V	46%	NA	Uchida et al. [46]
DCV5T	C60	3.4%	1.0 V	49%	52%	Schulze et al. [49]
CuPc	PTCBI	2.7%	0.5 V	58%	NA	Yang et al. [44, 45]
SubPc	C60	2.1%	1.0 V	57%	NA	Mutolo et al. [47]
MeO-TPD, ZnPc	C60	2.1%	0.5 V	37%	NA	Drechsel et al. [51]
TDCV-TPA	C60	1.9%	1.2 V	28%	NA	Cravino et al. [50]
Pentacene on PET	C60	1.6%	0.3 V	48%	30%	Pandey and Nunzi [52]
SnPc	C60	1.0%	0.4 V	50%	21%	Rand et al. [48]

FIGURE 6: The AFM height images (size  $2.8 \times 2.8 \mu\text{m}$ ) reveal different phase-separated morphologies for blends of PFB and F8BT (1 : 1 ratio by mass) spin-coated from (a) chloroform and (b) xylene.

of the length scale of phase separation in thin layers is often arbitrary and based on trial-and-error.

The tendency for demixing lies in the macromolecular nature of the polymers. One driving force for phase separation is the different polarity or polarisability of the polymer repeat units making the contact between identical polymers energetically favourable. However, many dissimilar molecules, such as water and ethanol, mix in any ratio. For these small molecules, the increase in entropy upon mixing overcomes the enthalpic interaction. To describe the mixing properties of a pair of polymers, the Flory and Huggins theory can be applied [66]. However, the real situation for thin blend films is much more complicated since the interactions of the two polymers with the surface and the substrate as well as the influence of the solvents and the solvent evaporation rate have to be taken into account [61, 67]. Therefore, the interplay of mixing and dewetting makes the prediction or even control of the morphology difficult.

The best studied conjugated polymer system so far is the blend of PFB [poly(9,9-dioctylfluorene-2,7-diyl-co-bis-N,N'-(4-butylphenyl)-bis-N,N'-phenyl-1,4-phenylenediamine)] [68] and F8BT [poly(9,9-dioctylfluorene-2,7-diyl-co-benzothiadiazole)] [69]. The correlation between layer composition, morphology, and photovoltaic properties for devices prepared from various organic solvents has been studied in detail for this model system [35, 64, 70–75]. F8BT has a LUMO of  $-3.2 \text{ eV}$  and an HOMO of  $-5.9 \text{ eV}$ , whereas

the LUMO and HOMO energy levels of PFB are  $-1.9 \text{ eV}$  and  $-5.1 \text{ eV}$ , respectively. Apparently, there exists a relatively large offset of  $1.3 \text{ eV}$  for the LUMO levels and of  $0.8 \text{ eV}$  for the HOMO levels, which guarantees very efficient electron dissociation at the interface. Investigations concerning its blend morphology in relation to the solar cell properties revealed that the length scale on which phase separation occurs strongly depends on the solvent used, on the interaction with the substrate, and on the deposition conditions. For example, spin-coating a 1 : 1 PFB:F8BT solution in xylene leads to phase separation at the micrometre scale whereas the length scale of the phase separation for films prepared from chloroform is less than  $100 \text{ nm}$ , as shown in the atomic force microscopy (AFM) image in Figure 6. This phenomenon was due to the more rapid evaporation of the low boiling point solvent chloroform compared to xylene which prevented large-scale reorganisation and diffusion of the polymer chains and thus leads to a finer scale of the phase separation. Heating of the substrate during spin-coating leads to a phase separation on an even smaller scale due to the more rapid evaporation, thus freezing out the onset of spinodal composition [70]. Interestingly the phase-separated morphology of the PFB:F8BT blend layer spin-coated from xylene revealed a substructure at the nanometre scale in addition to micrometre sized features.

Based on AFM and Raman microscope investigations, it was proposed that one phase is composed of almost equal

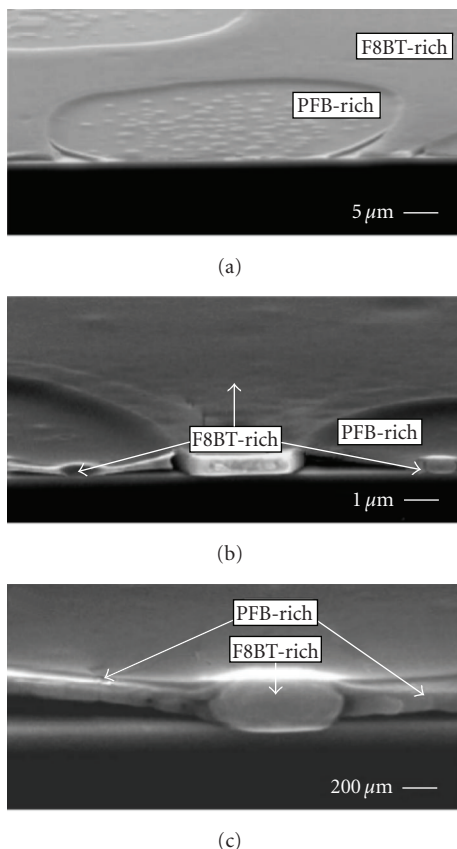


FIGURE 7: Environmental scanning electron microscopy (ESEM) images of the cross-section of an F8BT:PFB film spin-coated from a xylene solution at magnifications of (a) 4528 $\times$ , (b) 14 622 $\times$ , and (c) 58 489 $\times$  taken from [74].

proportions of PFB and F8BT whereas the second is F8BT rich and consists of 80% F8BT and only 20% PFB [74, 76]. This second phase was also found to be of larger thickness. Further analysis revealed that the blend layers can be described as PFB-rich cylinders surrounded by an F8BT-rich matrix as shown in Figure 7.

As expected, the solar cell properties depended strongly on preparation conditions. For the PFB:F8BT (1 : 1) blends the IPCE was *ca.* 2 times higher for layers spin-coated from chloroform (IPCE = 2–4.5%) solution compared to xylene solutions (IPCE = 0.5–1%) [70, 75]. This was attributed to a larger phase separation for the layers prepared from xylene. In subsequent studies, photovoltaic devices were studied with varying ratios of PFB and F8BT in layers prepared from xylene solution. It was found that the phase separation and the external quantum efficiencies were strongly dependent on the layer composition. Highest efficiencies were reported for devices containing 5 times more of the electron transporting F8BT than PFB.

In a more recent study investigating the photocurrent generation with near field photoconductivity measurements, it was found that the photocurrent is not increased at the interface of both domains. It was rather proposed that pho-

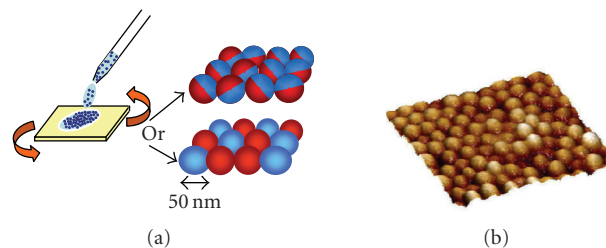


FIGURE 8: The nanoparticles allow for the preparation of nanostructured layers of conjugated polymers as shown in the AFM image on the right for particles of 50 nm diameter.

tocurrent is generated in both phases, while the phase with the smaller height seems to be more efficient [72, 77].

In conclusion, these studies clearly showed that the preparation conditions as well as the layer composition have a profound and, in part, unpredictable effect on the photovoltaic properties of the device. Moreover, since the meso-scale phase separation has been shown to depend strongly on the blend ratio, an investigation for a given length scale of phase separation but different blend ratios was not possible by using layers spin-coated from organic solvents. A method for a defined control of the phase separation formed in polymer blends would hence be highly desirable.

The most straightforward approach for a defined phase separated D-A polymer nanostructure would be to use linear block copolymers [78]. However, the drawback of this approach is that both components, A and D, with their different chemical and electronic structures have to be connected via a covalent bond, which limits the availability of possible A-D pairs. In fact, only a few examples of block copolymers containing two semiconducting polymers have been reported and solar cell efficiencies are still quite low [79–83]. Another method to obtain a nanostructured conjugated polymer layer with defined structure size in the 40–100 nm range is the nanoparticle approach as shown in Figure 8 [84–88]. Here in the first step, solid polymer nanoparticles with well-controllable size are prepared via the formation of a miniemulsion of the polymer solution in water. In addition, blend nanoparticles can be prepared by starting with a solution of both polymers. Spectroscopic investigations revealed that the latter approach indeed leads to nanospheres containing both polymers in each particle. The nanoparticles approach allows for the preparation of blend layers in two ways: either a mixture of nanoparticles of pure polymers (nanoparticle blend) or the blend nanoparticles are spin-coated on a substrate.

#### 4.2. Polymer solar cell devices

The first report on all polymer solar cells with moderate efficiencies dates back to 1995 with two independent reports from Yu and Heeger [9] and Halls et al. [89]. In both cases, MEH-PPV (Poly(2-methoxy-5-(2'-ethyl-hexyloxy)-1,4-phenylene-vinylene)) was used as the electron donor and CN-PPV (cyano-para-phenylenevinylene) as the electron acceptor. External quantum efficiencies were still low

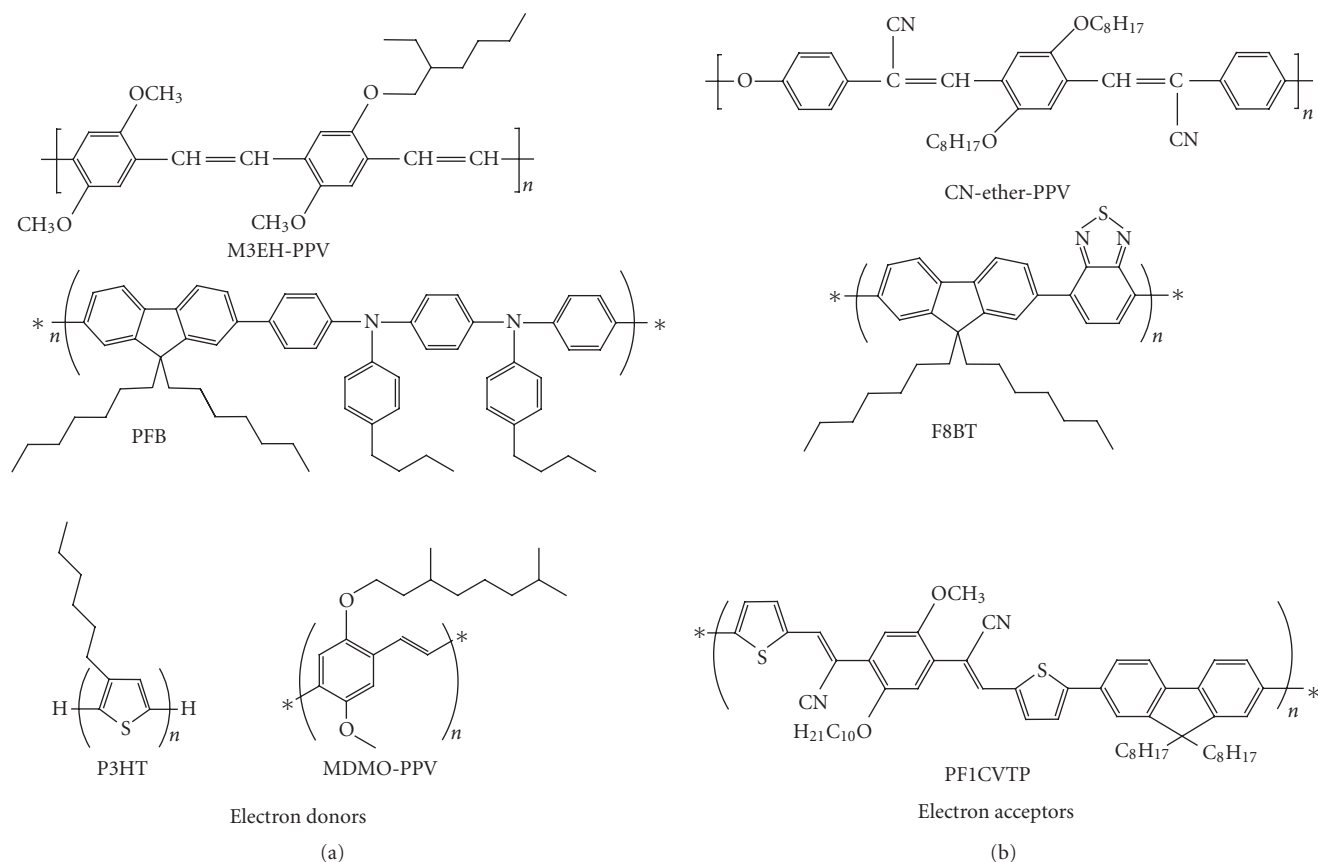


FIGURE 9: Chemical structures of conjugated polymers used in organic solar cells.

(around 5-6%), most likely due to the nanomorphology not being optimized. A big efficiency jump was obtained after the CN-PPV was modified by introduction of an ether group to increase solubility [90]. Using the copolymer M3EH-PPV (see Figure 9 for the chemical structures) as donor and CN-Ether-PPV as acceptor, Breeze et al. [91] demonstrated in 2000 external quantum efficiencies of 24% corresponding to 0.6% power conversion efficiency. Even higher efficiencies were published by the same authors in 2004 [12]. In that work, it was demonstrated for the first time that 1% power conversion efficiency could be reached in a polymer-polymer blend device. The open circuit voltage was 1 V, however the low fill factor of 25% left room for further improvement. The highest power conversion efficiency so far for solar cells composed of polymer blend was reached in 2005 by Kietzke et al. [92] using the same materials coupled with improved processing. It could be shown that annealing the layer leads to an improvement of the efficiency by a factor of two compared to the prepared layers [93]. An open circuit voltage of 1.36 V and a white light conversion efficiency of 1.7% were obtained. The fill factor reached 35% indicating improved charge transport. Photophysical studies on PPV-based blends revealed that the exciplex formation in this system might have been a major loss factor [92-94].

Recently Koetse et al. [95] reported solar cells based on MDMO-PPV as donor and a novel acceptor copolymer

PF1CVTP. A high quantum efficiency of 42% was achieved. However, the power conversion efficiency could not set a new record, since the conversion efficiency decreased at higher light intensities typical for solar illumination.

Several approaches have also been investigated for polymer bilayer structures. Alam and Jenekhe [96] reported devices based on insoluble PPV as donor and BBL as electron acceptor. BBL was deposited from methanesulfonic acid. The devices showed extremely high quantum efficiencies of up to 62%. Unfortunately, the device efficiency decreased at higher light intensities dramatically. The power conversion efficiency dropped from record breaking 5% at very low light intensities to 1.5% under standard 1 sun. Similar efficiencies could be reached for M3EH-PPV as donor and CN-Ether-PPV as acceptor.

Polymer solar cells have much room for optimization (the characteristic parameters of the best of their kind are in Tables 2 and 3). Both the fill factor and the quantum efficiency need to be doubled in order to reach 6-7% power conversion efficiency. Recent experiments indicated that the device performance is currently limited largely by the low dissociation efficiency of the photogenerated excitons into free charge carriers. Even after dissociation, the electrons tend to localise near the heterointerface in the electron accepting polymers due to their amorphous nature. To proceed to higher efficiencies more crystalline electron acceptor polymers with larger electron mobilities are needed [93].

TABLE 2: Best in class solar cells: polymer-polymer (blend) solar cells.

Donor	Acceptor	$\eta$	$V_{oc}$	FF	IPCE	Reference
M3EH-PPV	CN-Ether-PPV	1.7%	1.4 V	35%	31%	Kietzke et al. [92]
MDMO-PPV	PF1CVTP	1.5%	1.4 V	37%	42%	Koetse et al. [95]
M3EH-PPV	CN-Ether-PPV	1.0%	1.0 V	25%	24%	Breeze et al. [12]

TABLE 3: Best in class solar cells: polymer-polymer (bilayer) solar cells.

Donor	Acceptor	$\eta$	$V_{oc}$	FF	IPCE	Reference
PPV	BBL	1.5%	1.1 V	50%	62%	Alam and Jenekhe [96]
MDMO-PPV:PF1CVTP	PF1CVTP	1.4%	1.4 V	34%	52%	Koetse et al. [95]
M3EH-PPV	CN-Ether-PPV	1.3%	1.3 V	31%	29%	Kietzke et al. [97]
MEH-PPV	BBL	1.1%	0.9 V	47%	52%	Alam and Jenekhe [96]
M3EH-PPV	CN-PPV-PPE	0.6%	1.5 V	23%	23%	Kietzke et al. [97]

## 5. BLENDS OF POLYMER AND SMALL MOLECULES

After the discovery in 1991 [98] that the transfer of photoexcited electrons from conjugated polymers to fullerenes is very efficient, it took 10 years more until organic solar cells reaching 2.5% efficiency were reported [65]. Since C60 showed a strong tendency to crystallise in the polymer matrix, a new fullerene derivative called PCBM was developed. The increased solubility of PCBM resulted in the formation of smaller crystallites in the blend. It was a poly[2-methoxy-5-(3,7-dimethyloctyloxy)-1,4-phenylenevinylene] (MDMO-PPV):PCBM (weight ratio 1 : 4) device that eventually reached the 2.5% power conversion efficiency benchmark. Of crucial importance was the type of solvent used because of the different nanostructures formed for the same reasons explained in the previous paragraph for polymer-polymer blends. In the following years, PCBM-based solar cells attracted much attention with more than 200 refereed papers published on this topic. Regioregular P3HT (poly-3-hexylthiophene) soon became the material of choice as electron donor, as P3HT is able to absorb photons at longer wavelength compared to PPV derivatives. In addition a more balanced weight ratio of P3HT and PCBM (1 : 0.8) was sufficient to obtain high efficiencies. Due to the efforts of several groups worldwide [5, 13, 14, 99–103], a record power conversion efficiency of 5% could be reached in 2005 [5]. The most important finding was that slow drying of the P3HT:PCBM layer leads to increased mobilities, thus preventing the build up of space charge inside the device [104–110]. Also, the degree of regioregularity, the polydispersities, and molecular weights of P3HT seems to have an important influence on the device efficiency [111]. Highest efficiencies were recorded for P3HT with very high regioregularity due to improved molecular order which translates to higher mobilities [112]. For an excellent summary of the device physics PCBM:polymer solar cells see Blom et al. [113].

As shown in Figure 10, from 2001 to 2005 the number of published papers on PCBM-based solar cells correlate well with the published efficiencies obtained with the same year. However, it seems that the reported efficiencies stagnated in 2005. The reason is that the internal quantum efficiency for

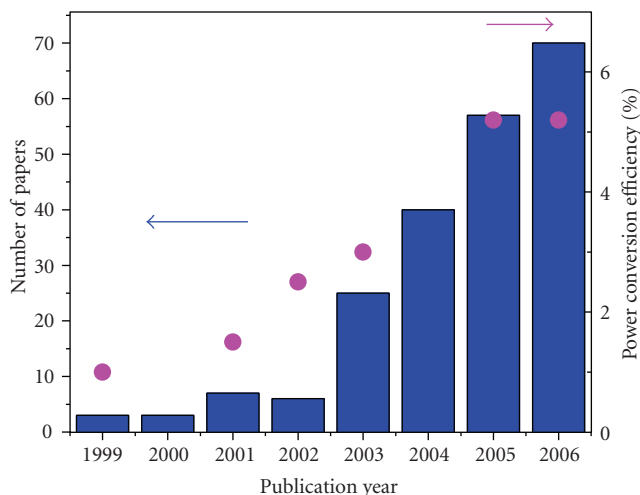


FIGURE 10: Correlation between reported solar cell efficiencies for polymer:PCBM blends and a number of papers published in this field. The information was obtained by searching ISI web of knowledge on 16.12.2006 for the terms “polymer” and “PCBM.”

the 5% efficient P3HT:PCBM devices is already nearly unity, leaving little space for further optimisation of this system.

Two main factors limit the device efficiency of the P3HT:PCBM system to 5%. First, the open circuit voltage reaches only 0.7 V, which is quite small compared to the bandgap of P3HT (1.9 eV). A large amount of energy is lost when the photoexcited electron transfers from the LUMO of P3HT (around  $-3$  eV) to the LUMO of PCBM ( $-3.8$  eV).

Recently it was pointed out that 10% efficiency may be in reach with polymer:fullerene blends if the relative energy levels could be better aligned [108, 130]. Either the PCBM LUMO level had to be raised to about 3.3 eV or both the LUMO and HOMO of the donor polymer had to be lowered sufficiently assuming that all other parameters remained unchanged.

Recently, a few P3HT-based solar cells where PCBM was replaced by an alternative electron acceptor have been reported (compare Table 5). Unlike PCBM, electron acceptors

TABLE 4: Best in class solar cells: blends of polymers and fullerene derivatives.

Donor	Acceptor	$\eta$	$V_{oc}$	FF	IPCE	Reference
P3HT	PCBM	5.0%	0.6 V	68%	NA	Ma et al. [114]
P3HT	PCBM	4.9%	0.6 V	54%	NA	Reyes-Reyes et al. [5]
P3HT	PCBM	4.4%	0.9 V	67%	63%	Li et al. [115]
MDMO-PPV	PC <sub>71</sub> BM	3.0%	0.8 V	51%	66%	Wienk et al. [17]
MDMO-PPV on PET	PCBM	3.0%	0.8 V	49%	NA	Al-Ibrahim et al. [116]

TABLE 5: Best in class solar cells: blends of polymers and nonfullerene-based oligomers.

Donor	Acceptor	$\eta$	$V_{oc}$	FF	IPCE	Reference
P3HT	V-BT	0.45%	0.7 V	37%	16%	Shin et al. [117, 118]
P3HT	PDI	0.19%	0.4 V	43%	7%	Li et al. [119]
P3HT	PDI-C8	0.18%	0.4 V	38%	19%	Shin et al. [120]
P3HT	BT1	0.07%	1.0 V	19%	NA	Camaioni et al. [121]

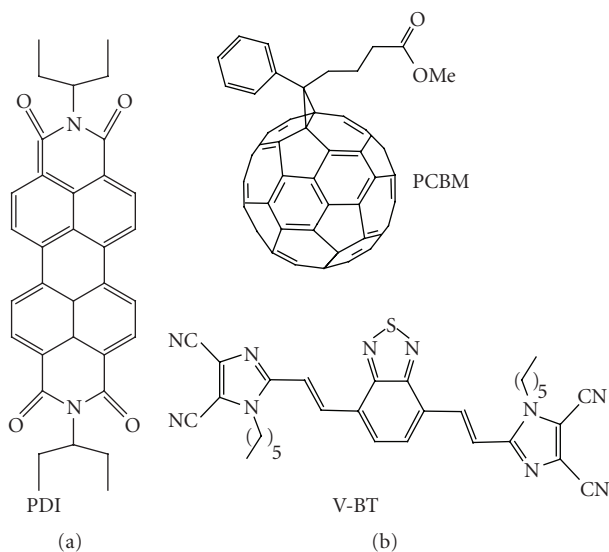


FIGURE 11: Soluble small molecules used in blends with conjugated polymers.

such as soluble perylene derivatives are advantageous as they absorb visible light strongly. However, reported efficiencies are currently a factor of 10 lower compared to P3HT:PCBM devices. The highest efficiency was achieved using a vinazene derivative (V-BT) (see Figure 11 for the chemical structure) as electron acceptor ( $\eta = 0.5\%$ ). Since not much work has been done so far on alternative acceptors, it is expected that higher efficiencies will be reported in the future.

The second factor limiting the efficiency of P3HT:PCBM cells is the absorption range of P3HT. P3HT absorbs visible light until about 650 nm, meaning that most of the red portion of the visible spectrum and all infrared photons cannot be harvested. Efforts have been undertaken to increase the absorption range by synthesizing novel low-bandgap polymers. Contrary to expectations, the low bandgap polymers synthesized with bandgaps as low as 1 eV did not result in devices with higher efficiency (see Table 6). One major problem

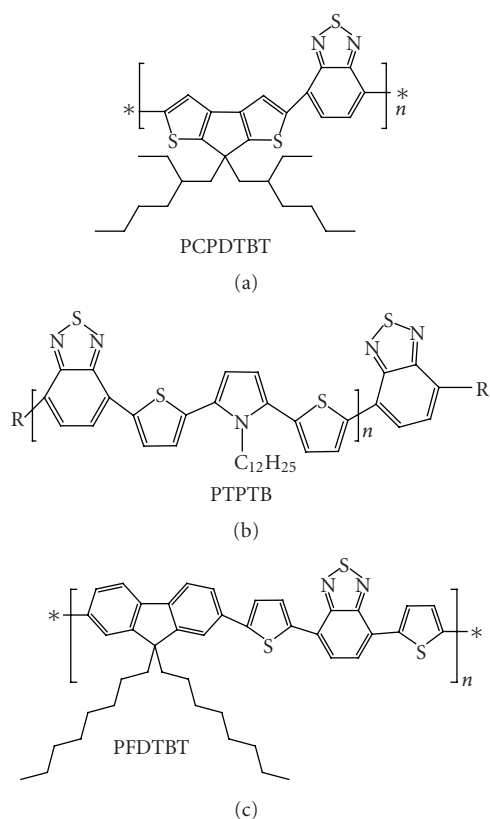


FIGURE 12: Low-bandgap polymers based on benzothiadiazole units.

with these low band-gap polymers was their low mobilities, which limited the efficiency. The mobility plays an important role especially for low-bandgap polymers, since at longer wavelength much thicker layers are needed for absorption of sunlight and the build up of a space charge has to be prevented to achieve high fill factors and short circuit voltages.

The first milestone of a 1% efficient low-bandgap solar cell was finally achieved for a polymer consisting of alternating electron-rich N-dodecyl-2,5-bis(2'-thienyl) pyrrole

TABLE 6: Best in class solar cells: blends of low-bandgap polymers and nonfullerene derivatives.

Donor	Acceptor	$\eta$	$V_{oc}$	FF	IPCE	Reference
PCPDTBT	PC <sub>71</sub> BM	3.2%	0.7 V	47%	38%	Mühlbacher et al. [122]
PCPDTBT	PCBM	2.7%	0.7 V	NA	31%	Mühlbacher et al. [122]
PFDTBT	PCBM	2.2%	1.0 V	46%	40%	Svensson et al. [123]
APFO-Green1	PCBM	2.2%	0.6 V	44%	38%	Zhang et al. [124]
PTBEHT	PCBM	1.1%	0.6 V	41%	15%	Wienk et al. [125]
PTBTB	PCBM	1.0%	0.7 V	37%	20%	Dhanabalan et al. [126], Brabec et al. [101]
APFO-Green1	BTPF70	0.3%	0.5 V	32%	8%	Wang et al. [127]
APFO-Green1	BTPF	0.7%	0.5 V	35%	28%	Wang et al. [128]
PDDTT	PCBM	0.1%	0.4 V	39%	NA	Xia et al. [129]

(TPT) and electron-deficient 2,1,3-benzothiadiazole (BT) units, called PTPTB (see Figure 12 for the chemical structure) [101, 126]. The photoresponse in combination with PCBM reached 800 nm.

The most promising low-bandgap material so far is poly[2,6-(4,4-bis-(2-ethylhexyl)-4H-cyclopenta[2,1-b;3,4-b]-dithiophene)-*alt*-4,7-(2,1,3-benzothiadiazole)] (PCPDTBT) reported by Mühlbacher et al. [122]. In combination with PCBM or PC<sub>71</sub>BM, a photoresponse extending to the infrared region exceeding 900 nm was measured. The high fill factor 47% found for this device demonstrates good charge transport capabilities leading to an overall power conversion efficiency of  $\eta = 3.2\%$ .

## 6. TANDEM SOLAR CELLS

Since it seems unlikely that a single organic material can absorb efficiently from the blue to the infrared region, tandem structures were proposed, where different subcells absorb different wavelength regions. The difficulty in designing tandem solar cells is that the current of each subcell has to be matched, since the total current in the device is limited by the lowest current generating subcell. First attempts have been made to prepare organic tandem cells. One example is the tandem cell where one subcell is made of P3HT:PCBM and the second of ZnPc:C60 [131]. The open circuit voltage was nearly doubled, but the conversion efficiency is still lower than what can be reached with a P3HT:PCBM cell alone. Shrotriya et al. [132] demonstrated LiF (1 nm)/Al(2.5 nm)/Au(12.5 nm) cathodes with a transparency between 50% and 80% in the visible region. By simply stacking an MEH-PPV:PCBM cell on a similar cell with a transparent electrode, a power conversion efficiency of 2.4% and an open circuit voltage of 1.64 V could be reached. Recently Kim et al. [133] reported tandem solar cells exceeding 6% conversion efficiency by using a TiOx interlayer to separate the two subcells.

## 7. SUMMARY

Recently, organic solar cells have broken the 5% power conversion efficiency barrier. While currently small molecules (e.g., CuPc) and polymers (e.g., P3HT) are similarly well

suiting as electron donor materials, these high efficiencies cannot currently be obtained using polymeric electron acceptors due to the low electron mobilities in these materials. Fullerenes and fullerene derivatives like PCBM are currently needed to reach 5% efficiency. However, it seems that P3HT:PCBM or CuPc:C60 devices have already been pushed fairly close to their theoretical efficiency limits, with quantum efficiencies greater than 80% already quite common. Therefore, it seems sure that new materials are needed to push the efficiencies into the 10% region, which is the generally agreed upon benchmark for economically viable photovoltaic devices. Either the open circuit voltage has to be raised by better matching of the energy levels of donor and acceptor materials or a broader spectrum of the sunlight needs to be absorbed using low-bandgap absorbers.

Developing novel crystalline electron acceptors with high electron mobilities and tunable energy levels to replace fullerene derivatives might be one promising direction for the future to achieve higher open circuit voltages, especially since not much research has been done in this direction. The tandem approach might be the key for harvesting a broader fraction of the sunlight in conjunction with novel low-bandgap materials.

## REFERENCES

- [1] C. W. Tang and A. C. Albrecht, "Photovoltaic effects of metal-chlorophyll-a-metal sandwich cells," *The Journal of Chemical Physics*, vol. 62, no. 6, pp. 2139–2149, 1975.
- [2] C. W. Tang, "Two-layer organic photovoltaic cell," *Applied Physics Letters*, vol. 48, no. 2, pp. 183–185, 1986.
- [3] J. Xue, S. Uchida, B. P. Rand, and S. R. Forrest, "4.2% efficient organic photovoltaic cells with low series resistances," *Applied Physics Letters*, vol. 84, no. 16, pp. 3013–3015, 2004.
- [4] J. Xue, S. Uchida, B. P. Rand, and S. R. Forrest, "Asymmetric tandem organic photovoltaic cells with hybrid planar-mixed molecular heterojunctions," *Applied Physics Letters*, vol. 85, no. 23, pp. 5757–5759, 2004.
- [5] M. Reyes-Reyes, K. Kim, and D. L. Carroll, "High-efficiency photovoltaic devices based on annealed poly(3-hexylthiophene) and 1-(3-methoxycarbonyl)-propyl-1-phenyl-(6,6)C<sub>61</sub> blends," *Applied Physics Letters*, vol. 87, no. 8, Article ID 083506, 3 pages, 2005.

- [6] J. Xue, B. P. Rand, S. Uchida, and S. R. Forrest, "Mixed donor-acceptor molecular heterojunctions for photovoltaic applications. II. Device performance," *Journal of Applied Physics*, vol. 98, no. 12, Article ID 124903, 9 pages, 2005.
- [7] K. Takahashi, N. Kuraya, T. Yamaguchi, T. Komura, and K. Murata, "Three-layer organic solar cell with high-power conversion efficiency of 3.5%," *Solar Energy Materials and Solar Cells*, vol. 61, no. 4, pp. 403–416, 2000.
- [8] G. Yu, J. Gao, J. C. Hummelen, F. Wudl, and A. J. Heeger, "Polymer photovoltaic cells: enhanced efficiencies via a network of internal donor-acceptor heterojunctions," *Science*, vol. 270, no. 5243, pp. 1789–1791, 1995.
- [9] G. Yu and A. J. Heeger, "Charge separation and photovoltaic conversion in polymer composites with internal donor/acceptor heterojunction," *Journal of Applied Physics*, vol. 78, no. 7, pp. 4510–4515, 1995.
- [10] M. Granström, K. Petritsch, A. C. Arias, A. Lux, M. R. Andersson, and R. H. Friend, "Laminated fabrication of polymeric photovoltaic diodes," *Nature*, vol. 395, no. 6699, pp. 257–260, 1998.
- [11] S. A. Jenekhe and S. Yi, "Efficient photovoltaic cells from semiconducting polymer heterojunctions," *Applied Physics Letters*, vol. 77, no. 17, pp. 2635–2637, 2000.
- [12] A. J. Breeze, Z. Schlesinger, S. A. Carter, H. Tillmann, and H.-H. Hörhold, "Improving power efficiencies in polymer—polymer blend photovoltaics," *Solar Energy Materials and Solar Cells*, vol. 83, no. 2-3, pp. 263–271, 2004.
- [13] C. J. Brabec, N. S. Sariciftci, and J. C. Hummelen, "Plastic solar cells," *Advanced Functional Materials*, vol. 11, no. 1, pp. 15–26, 2001.
- [14] C. J. Brabec, V. Dyakonov, J. Parisi, and N. S. Sariciftci, Eds., *Organic Photovoltaics: Concepts and Realization*, vol. 60, Springer, New York, NY, USA, 2003.
- [15] C. Winder and N. S. Sariciftci, "Low bandgap polymers for photon harvesting in bulk heterojunction solar cells," *Journal of Materials Chemistry*, vol. 14, no. 7, pp. 1077–1086, 2004.
- [16] F. Padinger, R. S. Rittberger, and N. S. Sariciftci, "Effects of postproduction treatment on plastic solar cells," *Advanced Functional Materials*, vol. 13, no. 1, pp. 85–88, 2003.
- [17] M. M. Wienk, J. M. Kroon, W. J. H. Verhees, et al., "Efficient methano[70]fullerene/MDMO-PPV bulk heterojunction photovoltaic cells," *Angewandte Chemie International Edition*, vol. 42, no. 29, pp. 3371–3375, 2003.
- [18] A. J. Breeze, A. Salomon, D. S. Ginley, H. Tillmann, H. Hörhold, and B. A. Gregg, "Improved efficiencies in polymer-perylene diimide bilayer photovoltaics," in *Organic Photovoltaics III*, vol. 4801 of *Proceedings of SPIE*, pp. 34–39, Seattle, Wash, USA, June 2002.
- [19] A. J. Breeze, A. Salomon, D. S. Ginley, B. A. Gregg, H. Tillmann, and H.-H. Hörhold, "Polymer-perylene diimide heterojunction solar cells," *Applied Physics Letters*, vol. 81, no. 16, pp. 3085–3087, 2002.
- [20] J.-I. Nakamura, C. Yokoe, K. Murata, and K. Takahashi, "Efficient organic solar cells by penetration of conjugated polymers into perylene pigments," *Journal of Applied Physics*, vol. 96, no. 11, pp. 6878–6883, 2004.
- [21] A. J. Breeze, Z. Schlesinger, S. A. Carter, and P. J. Brock, "Charge transport in TiO<sub>2</sub>/MEH-PPV polymer photovoltaics," *Physical Review B*, vol. 64, no. 12, Article ID 125205, 9 pages, 2001.
- [22] H. Sirringhaus, "Device physics of solution-processed organic field-effect transistors," *Advanced Materials*, vol. 17, no. 20, pp. 2411–2425, 2005.
- [23] V. C. Sundar, J. Zaumseil, V. Podzorov, et al., "Elastomeric transistor stamps: reversible probing of charge transport in organic crystals," *Science*, vol. 303, no. 5664, pp. 1644–1646, 2004.
- [24] I. McCulloch, M. Heeney, C. Bailey, et al., "Liquid-crystalline semiconducting polymers with high charge-carrier mobility," *Nature Materials*, vol. 5, no. 4, pp. 328–333, 2006.
- [25] T. D. Anthopoulos, B. Singh, N. Marjanovic, et al., "High performance *n*-channel organic field-effect transistors and ring oscillators based on C<sub>60</sub> fullerene films," *Applied Physics Letters*, vol. 89, no. 21, Article ID 213504, 3 pages, 2006.
- [26] D. J. Gundlach, K. P. Pernstich, G. Wilckens, M. Grüter, S. Haas, and B. Batlogg, "High mobility *n*-channel organic thin-film transistors and complementary inverters," *Journal of Applied Physics*, vol. 98, no. 6, Article ID 064502, 8 pages, 2005.
- [27] R. N. Marks, J. J. M. Halls, D. D. C. Bradley, R. H. Friend, and A. B. Holmes, "The photovoltaic response in poly(p-phenylene vinylene) thin-film devices," *Journal of Physics*, vol. 6, no. 7, pp. 1379–1394, 1994.
- [28] S. Barth and H. Bässler, "Intrinsic photoconduction in PPV-type conjugated polymers," *Physical Review Letters*, vol. 79, no. 22, pp. 4445–4448, 1997.
- [29] B. A. Gregg and M. C. Hanna, "Comparing organic to inorganic photovoltaic cells: theory, experiment, and simulation," *Journal of Applied Physics*, vol. 93, no. 6, pp. 3605–3614, 2003.
- [30] D. Braun and A. J. Heeger, "Visible light emission from semiconducting polymer diodes," *Applied Physics Letters*, vol. 58, no. 18, pp. 1982–1984, 1991.
- [31] P. B. Miranda, D. Moses, and A. J. Heeger, "Ultrafast photogeneration of charged polarons in conjugated polymers," *Physical Review B*, vol. 64, no. 8, Article ID 081201, 4 pages, 2001.
- [32] G. Yu, C. Zhang, and A. J. Heeger, "Dual-function semiconducting polymer devices: light-emitting and photodetecting diodes," *Applied Physics Letters*, vol. 64, no. 12, pp. 1540–1542, 1994.
- [33] L. C. Chen, D. Godovsky, O. Inganäs, et al., "Polymer photovoltaic devices from stratified multilayers of donor-acceptor blends," *Advanced Materials*, vol. 12, no. 18, pp. 1367–1370, 2000.
- [34] O. Inganäs, L. S. Roman, F. Zhang, D. M. Johansson, M. R. Andersson, and J. C. Hummelen, "Recent progress in thin film organic photodiodes," *Synthetic Metals*, vol. 121, no. 1–3, pp. 1525–1528, 2001.
- [35] J. A. Barker, C. M. Ramsdale, and N. C. Greenham, "Modeling the current-voltage characteristics of bilayer polymer photovoltaic devices," *Physical Review B*, vol. 67, no. 7, Article ID 075205, 9 pages, 2003.
- [36] S. M. Sze, *Physics of Semiconductor Devices*, John Wiley & Sons, New York, NY, USA, 1981.
- [37] H. B. Michaelson, "The work function of the elements and its periodicity," *Journal of Applied Physics*, vol. 48, no. 11, pp. 4729–4733, 1977.
- [38] J. M. Bharathan and Y. Yang, "Polymer/metal interfaces and the performance of polymer light-emitting diodes," *Journal of Applied Physics*, vol. 84, no. 6, pp. 3207–3211, 1998.
- [39] J. S. Kim, M. Granström, R. H. Friend, et al., "Indium-tin oxide treatments for single- and double-layer polymeric light-emitting diodes: the relation between the anode physical, chemical, and morphological properties and the device performance," *Journal of Applied Physics*, vol. 84, no. 12, pp. 6859–6870, 1998.

- [40] Y. Park, V. Choong, Y. Gao, B. R. Hsieh, and C. W. Tang, "Work function of indium tin oxide transparent conductor measured by photoelectron spectroscopy," *Applied Physics Letters*, vol. 68, no. 19, pp. 2699–2701, 1996.
- [41] Y. Park, V. Choong, E. Etdedgui, et al., "Energy level bending and alignment at the interface between Ca and a phenylene vinylene oligomer," *Applied Physics Letters*, vol. 69, no. 8, pp. 1080–1082, 1996.
- [42] P. Peumans, A. V. Yakimov, and S. R. Forrest, "Small molecular weight organic thin-film photodetectors and solar cells," *Journal of Applied Physics*, vol. 93, no. 7, pp. 3693–3723, 2003.
- [43] P. Peumans, S. Uchida, and S. R. Forrest, "Efficient bulk heterojunction photovoltaic cells using small-molecular-weight organic thin films," *Nature*, vol. 425, no. 6954, pp. 158–162, 2003.
- [44] F. Yang, M. Shtein, and S. R. Forrest, "Morphology control and material mixing by high-temperature organic vapor-phase deposition and its application to thin-film solar cells," *Journal of Applied Physics*, vol. 98, no. 1, Article ID 014906, 10 pages, 2005.
- [45] F. Yang, M. Shtein, and S. R. Forrest, "Controlled growth of a molecular bulk heterojunction photovoltaic cell," *Nature Materials*, vol. 4, no. 1, pp. 37–41, 2005.
- [46] S. Uchida, J. Xue, B. P. Rand, and S. R. Forrest, "Organic small molecule solar cells with a homogeneously mixed copper phthalocyanine: C<sub>60</sub> active layer," *Applied Physics Letters*, vol. 84, no. 21, pp. 4218–4220, 2004.
- [47] K. L. Mutolo, E. I. Mayo, B. P. Rand, S. R. Forrest, and M. E. Thompson, "Enhanced open-circuit voltage in subphthalocyanine/C<sub>60</sub> organic photovoltaic cells," *Journal of the American Chemical Society*, vol. 128, no. 25, pp. 8108–8109, 2006.
- [48] B. P. Rand, J. Xue, F. Yang, and S. R. Forrest, "Organic solar cells with sensitivity extending into the near infrared," *Applied Physics Letters*, vol. 87, no. 23, Article ID 233508, 3 pages, 2005.
- [49] K. Schulze, C. Uhrich, R. Schüppel, et al., "Efficient vacuum-deposited organic solar cells based on a new low-bandgap oligothiophene and fullerene C<sub>60</sub>," *Advanced Materials*, vol. 18, no. 21, pp. 2872–2875, 2006.
- [50] A. Cravino, P. Leriche, O. Alévêque, S. Roquet, and J. Roncali, "Light-emitting organic solar cells based on a 3D conjugated system with internal charge transfer," *Advanced Materials*, vol. 18, no. 22, pp. 3033–3037, 2006.
- [51] J. Drechsel, B. Männig, F. Kozłowski, M. Pfeiffer, K. Leo, and H. Hoppe, "Efficient organic solar cells based on a double *p-i-n* architecture using doped wide-gap transport layers," *Applied Physics Letters*, vol. 86, no. 24, Article ID 244102, 3 pages, 2005.
- [52] A. K. Pandey and J.-M. Nunzi, "Efficient flexible and thermally stable pentacene/C<sub>60</sub> small molecule based organic solar cells," *Applied Physics Letters*, vol. 89, no. 21, Article ID 213506, 3 pages, 2006.
- [53] C. K. Chiang, C. R. Fincher Jr., Y. W. Park, et al., "Electrical conductivity in doped polyacetylene," *Physical Review Letters*, vol. 30, no. 17, pp. 1098–1101, 1977.
- [54] H. Shirakawa, "Nobel lecture: the discovery of polyacetylene film—the dawning of an era of conducting polymers," *Reviews of Modern Physics*, vol. 73, no. 3, pp. 713–718, 2001.
- [55] A. G. MacDiarmid, "Nobel lecture: "Synthetic metals": a novel role for organic polymers," *Reviews of Modern Physics*, vol. 73, no. 3, pp. 701–712, 2001.
- [56] A. J. Heeger, "Nobel lecture: semiconducting and metallic polymers: the fourth generation of polymeric materials," *Reviews of Modern Physics*, vol. 73, no. 3, pp. 681–700, 2001.
- [57] J. H. Burroughes, D. D. C. Bradley, A. R. Brown, et al., "Light-emitting diodes based on conjugated polymers," *Nature*, vol. 347, no. 6293, pp. 539–541, 1990.
- [58] H. Sirringhaus, P. J. Brown, R. H. Friend, et al., "Two-dimensional charge transport in self-organized, high-mobility conjugated polymers," *Nature*, vol. 401, no. 6754, pp. 685–688, 1999.
- [59] M. Böltau, S. Walheim, J. Mlynek, G. Krausch, and U. Steiner, "Surface-induced structure formation of polymer blends on patterned substrates," *Nature*, vol. 391, no. 6670, pp. 877–879, 1998.
- [60] S. Walheim, M. Böltau, J. Mlynek, G. Krausch, and U. Steiner, "Structure formation via polymer demixing in spin-cast films," *Macromolecules*, vol. 30, no. 17, pp. 4995–5003, 1997.
- [61] R. A. L. Jones, L. J. Norton, E. J. Kramer, F. S. Bates, and P. Wiltzius, "Surface-directed spinodal decomposition," *Physical Review Letters*, vol. 66, no. 10, pp. 1326–1329, 1991.
- [62] G. Krausch, "Surface induced self assembly in thin polymer films," *Materials Science and Engineering R*, vol. 14, no. 1–2, pp. 1–94, 1995.
- [63] P. Müller-Buschbaum, J. S. Gutmann, and M. Stamm, "Influence of blend composition on phase separation and dewetting of thin polymer blend films," *Macromolecules*, vol. 33, no. 13, pp. 4886–4895, 2000.
- [64] J. J. M. Halls, A. C. Arias, J. D. MacKenzie, et al., "Photodiodes based on polyfluorene composites: influence of morphology," *Advanced Materials*, vol. 12, no. 7, pp. 498–502, 2000.
- [65] S. E. Shaheen, C. J. Brabec, N. S. Sariciftci, F. Padinger, T. Fromherz, and J. C. Hummelen, "2.5% efficient organic plastic solar cells," *Applied Physics Letters*, vol. 78, no. 6, pp. 841–843, 2001.
- [66] G. R. Strobl, *The Physics of Polymers*, Springer, Berlin, Germany, 2004.
- [67] U. Steiner, J. Klein, and L. J. Fetters, "Surface phase inversion in finite-sized binary mixtures," *Physical Review Letters*, vol. 72, no. 10, pp. 1498–1501, 1994.
- [68] M. Redecker, D. D. C. Bradley, M. Inbasekaran, W. W. Wu, and E. P. Woo, "High mobility hole transport fluorene-triarylamine copolymers," *Advanced Materials*, vol. 11, no. 3, pp. 241–246, 1999.
- [69] A. J. Campbell, D. D. C. Bradley, and H. Antoniadis, "Dispersive electron transport in an electroluminescent polyfluorene copolymer measured by the current integration time-of-flight method," *Applied Physics Letters*, vol. 79, no. 14, pp. 2133–2135, 2001.
- [70] A. C. Arias, J. D. MacKenzie, R. Stevenson, et al., "Photovoltaic performance and morphology of polyfluorene blends: a combined microscopic and photovoltaic investigation," *Macromolecules*, vol. 34, no. 17, pp. 6005–6013, 2001.
- [71] A. C. Arias, N. Corcoran, M. Banach, R. H. Friend, J. D. MacKenzie, and W. T. S. Huck, "Vertically segregated polymer-blend photovoltaic thin-film structures through surface-mediated solution processing," *Applied Physics Letters*, vol. 80, no. 10, pp. 1695–1697, 2002.
- [72] A. C. Morteani, A. S. Dhoot, J.-S. Kim, et al., "Barrier-free electron-hole capture in polymer blend heterojunction light-emitting diodes," *Advanced Materials*, vol. 15, no. 20, pp. 1708–1712, 2003.

- [73] C. M. Ramsdale, J. A. Barker, A. C. Arias, J. D. MacKenzie, R. H. Friend, and N. C. Greenham, "The origin of the open circuit voltage in polyfluorene-based photovoltaic devices," *Journal of Applied Physics*, vol. 92, no. 8, pp. 4266–4270, 2002.
- [74] C. M. Ramsdale, I. C. Bache, J. D. MacKenzie, et al., "ESEM imaging of polyfluorene blend cross-sections for organic devices," *Physica E*, vol. 14, no. 1-2, pp. 268–271, 2002.
- [75] H. J. Snaith, A. C. Arias, A. C. Morteani, C. Silva, and R. H. Friend, "Charge generation kinetics and transport mechanisms in blended polyfluorene photovoltaic devices," *Nano Letters*, vol. 2, no. 12, pp. 1353–1357, 2002.
- [76] R. Stevenson, A. C. Arias, C. Ramsdale, J. D. Mackenzie, and D. Richards, "Raman microscopy determination of phase composition in polyfluorene composites," *Applied Physics Letters*, vol. 79, no. 14, pp. 2178–2180, 2001.
- [77] C. R. McNeill, H. Frohne, J. L. Holdsworth, and P. C. Dastoor, "Near-field scanning photocurrent measurements of polyfluorene blend devices: directly correlating morphology with current generation," *Nano Letters*, vol. 4, no. 12, pp. 2503–2507, 2004.
- [78] S.-S. Sun, "Design of a block copolymer solar cell," *Solar Energy Materials and Solar Cells*, vol. 79, no. 2, pp. 257–264, 2003.
- [79] R. Güntner, U. Asawapirom, M. Forster, et al., "Conjugated polyfluorene/polyaniline block copolymers—improved synthesis and nanostructure formation," *Thin Solid Films*, vol. 417, no. 1-2, pp. 1–6, 2002.
- [80] U. Asawapirom, R. Güntner, M. Forster, and U. Scherf, "Semiconducting block copolymers—synthesis and nanostructure formation," *Thin Solid Films*, vol. 477, no. 1-2, pp. 48–52, 2005.
- [81] G. Tu, H. Li, M. Forster, R. Heiderhoff, L. J. Balk, and U. Scherf, "Conjugated triblock copolymers containing both electron-donor and electron-acceptor blocks," *Macromolecules*, vol. 39, no. 13, pp. 4327–4331, 2006.
- [82] S.-S. Sun, C. Zhang, A. Ledbetter, et al., "Photovoltaic enhancement of organic solar cells by a bridged donor-acceptor block copolymer approach," *Applied Physics Letters*, vol. 90, no. 4, Article ID 043117, 3 pages, 2007.
- [83] M. Sommer and M. Thelakkat, "Synthesis, characterization and application of donor-acceptor block copolymers in nanostructured bulk heterojunction solar cells," *The European Physical Journal-Applied Physics*, vol. 36, no. 3, pp. 245–249, 2006.
- [84] T. Kietzke, D. Neher, M. Kumke, R. Montenegro, K. Landfester, and U. Scherf, "A nanoparticle approach to control the phase separation in polyfluorene photovoltaic devices," *Macromolecules*, vol. 37, no. 13, pp. 4882–4890, 2004.
- [85] T. Kietzke, D. Neher, R. Montenegro, K. Landfester, U. Scherf, and H. H. Hoerhold, "Nanostructured solar cells based on semiconducting polymer nanospheres (SPNs) of M3EH-PPV and CN-Ether-PPV," in *Organic Photovoltaics IV*, vol. 5215 of *Proceedings of SPIE*, pp. 206–210, San Diego, Calif, USA, August 2004.
- [86] T. Kietzke, D. Neher, K. Landfester, R. Montenegro, R. Güntner, and U. Scherf, "Novel approaches to polymer blends based on polymer nanoparticles," *Nature Materials*, vol. 2, no. 6, pp. 408–412, 2003.
- [87] T. Kietzke, B. Stiller, K. Landfester, R. Montenegro, and D. Neher, "Probing the local optical properties of layers prepared from polymer nanoparticles," *Synthetic Metals*, vol. 152, no. 1–3, pp. 101–104, 2005.
- [88] T. Kietzke, D. Neher, M. Kumke, O. Ghazy, U. Ziener, and K. Landfester, "Phase separation of binary blends in polymer nanoparticles," *Small*, vol. 3, no. 6, pp. 1041–1048, 2007.
- [89] J. J. M. Halls, C. A. Walsh, N. C. Greenham, et al., "Efficient photodiodes from interpenetrating polymer networks," *Nature*, vol. 376, no. 6540, pp. 498–500, 1995.
- [90] H. Tillmann and H.-H. Hörhold, "Synthesis, optical and redox properties of novel segmented cyano-PPV derivatives," *Synthetic Metals*, vol. 101, no. 1, pp. 138–139, 1999.
- [91] A. J. Breeze, Z. Schlesinger, S. A. Carter, et al., "Nanoparticle-polymer and polymer-polymer blend composite photovoltaics," in *Organic Photovoltaics*, vol. 4108 of *Proceedings of SPIE*, pp. 57–61, San Diego, Calif, USA, August 2001.
- [92] T. Kietzke, H.-H. Hörhold, and D. Neher, "Efficient polymer solar cells based on M3EH-PPV," *Chemistry of Materials*, vol. 17, no. 26, pp. 6532–6537, 2005.
- [93] C. Yin, T. Kietzke, D. Neher, and H.-H. Hörhold, "Photovoltaic properties and exciplex emission of polyphenylenevinylene-based blend solar cells," *Applied Physics Letters*, vol. 90, no. 9, Article ID 092117, 3 pages, 2007.
- [94] T. Offermans, P. A. van Hal, S. C. J. Meskers, M. M. Koetse, and R. A. J. Janssen, "Exciplex dynamics in a blend of  $\pi$ -conjugated polymers with electron donating and accepting properties: MDMO-PPV and PCNEPV," *Physical Review B*, vol. 72, no. 4, Article ID 045213, 1–11, 2005.
- [95] M. M. Koetse, J. Sweelssen, K. T. Hoekerd, et al., "Efficient polymer: polymer bulk heterojunction solar cells," *Applied Physics Letters*, vol. 88, no. 8, Article ID 083504, 3 pages, 2006.
- [96] M. M. Alam and S. A. Jenekhe, "Efficient solar cells from layered nanostructures of donor and acceptor conjugated polymers," *Chemistry of Materials*, vol. 16, no. 23, pp. 4647–4656, 2004.
- [97] T. Kietzke, D. A. M. Egbe, H.-H. Hörhold, and D. Neher, "Comparative study of M3EH-PPV-based bilayer photovoltaic devices," *Macromolecules*, vol. 39, no. 12, pp. 4018–4022, 2006.
- [98] N. S. Sariciftci, L. Smilowitz, A. J. Heeger, and F. Wudl, "Photoinduced electron transfer from a conducting polymer to buckminsterfullerene," *Science*, vol. 258, no. 5087, pp. 1474–1476, 1992.
- [99] C. J. Brabec, "Organic photovoltaics: technology and market," *Solar Energy Materials and Solar Cells*, vol. 83, no. 2-3, pp. 273–292, 2004.
- [100] C. J. Brabec, A. Cravino, D. Meissner, et al., "Origin of the open circuit voltage of plastic solar cells," *Advanced Functional Materials*, vol. 11, no. 5, pp. 374–380, 2001.
- [101] C. J. Brabec, C. Winder, N. S. Sariciftci, et al., "A low-bandgap semiconducting polymer for photovoltaic devices and infrared emitting diodes," *Advanced Functional Materials*, vol. 12, no. 10, pp. 709–712, 2002.
- [102] D. Gebeyehu, C. J. Brabec, F. Padinger, et al., "The interplay of efficiency and morphology in photovoltaic devices based on interpenetrating networks of conjugated polymers with fullerenes," *Synthetic Metals*, vol. 118, no. 1-3, pp. 1–9, 2001.
- [103] J. K. J. van Duren, X. Yang, J. Loos, et al., "Relating the morphology of poly(*p*-vinylene)/methanofullerene blends to solar-cell performance," *Advanced Functional Materials*, vol. 14, no. 5, pp. 425–434, 2004.
- [104] V. D. Mihailetchi, L. J. A. Koster, and P. W. M. Blom, "Effect of metal electrodes on the performance of polymer: fullerene bulk heterojunction solar cells," *Applied Physics Letters*, vol. 85, no. 6, pp. 970–972, 2004.

- [105] L. J. A. Koster, V. D. Mihailetschi, R. Ramaker, and P. W. M. Blom, "Light intensity dependence of open-circuit voltage of polymer: fullerene solar cells," *Applied Physics Letters*, vol. 86, no. 12, Article ID 123509, 3 pages, 2005.
- [106] L. J. A. Koster, V. D. Mihailetschi, H. Xie, and P. W. M. Blom, "Origin of the light intensity dependence of the short-circuit current of polymer/fullerene solar cells," *Applied Physics Letters*, vol. 87, no. 20, Article ID 203502, 3 pages, 2005.
- [107] L. J. A. Koster, V. D. Mihailetschi, and P. W. M. Blom, "Bimolecular recombination in polymer/fullerene bulk heterojunction solar cells," *Applied Physics Letters*, vol. 88, no. 5, Article ID 052104, 3 pages, 2006.
- [108] L. J. A. Koster, V. D. Mihailetschi, and P. W. M. Blom, "Ultimate efficiency of polymer/fullerene bulk heterojunction solar cells," *Applied Physics Letters*, vol. 88, no. 9, Article ID 093511, 3 pages, 2006.
- [109] M. Lenes, L. J. A. Koster, V. D. Mihailetschi, and P. W. M. Blom, "Thickness dependence of the efficiency of polymer: fullerene bulk heterojunction solar cells," *Applied Physics Letters*, vol. 88, no. 24, Article ID 243502, 3 pages, 2006.
- [110] V. D. Mihailetschi, H. Xie, B. de Boer, et al., "Origin of the enhanced performance in poly(3-hexylthiophene): [6,6]-phenyl C<sub>61</sub>-butyric acid methyl ester solar cells upon slow drying of the active layer," *Applied Physics Letters*, vol. 89, no. 1, Article ID 012107, 3 pages, 2006.
- [111] R. C. Hiorns, R. de Bettignies, J. Leroy, et al., "High molecular weights, polydispersities, and annealing temperatures in the optimization of bulk-heterojunction photovoltaic cells based on poly(3-hexylthiophene) or poly(3-butylthiophene)," *Advanced Functional Materials*, vol. 16, no. 17, pp. 2263–2273, 2006.
- [112] Y. Kim, S. Cook, S. M. Tuladhar, et al., "A strong regioregularity effect in self-organizing conjugated polymer films and high-efficiency polythiophene: fullerene solar cells," *Nature Materials*, vol. 5, no. 3, pp. 197–203, 2006.
- [113] P. W. M. Blom, V. D. Mihailetschi, L. J. A. Koster, and D. E. Markov, "Device physics of polymer: fullerene bulk heterojunction solar cells," *Advanced Materials*, vol. 19, no. 12, pp. 1551–1566, 2007.
- [114] W. Ma, C. Yang, X. Gong, K. Lee, and A. J. Heeger, "Thermally stable, efficient polymer solar cells with nanoscale control of the interpenetrating network morphology," *Advanced Functional Materials*, vol. 15, no. 10, pp. 1617–1622, 2005.
- [115] G. Li, V. Shrotriya, J. Huang, et al., "High-efficiency solution processable polymer photovoltaic cells by self-organization of polymer blends," *Nature Materials*, vol. 4, no. 11, pp. 864–868, 2005.
- [116] M. Al-Ibrahim, H. K. Roth, and S. Sensfuss, "Efficient large-area polymer solar cells on flexible substrates," *Applied Physics Letters*, vol. 85, no. 9, pp. 1481–1483, 2004.
- [117] T. Kietzke, R. Y. C. Shin, D. A. M. Egbe, Z.-K. Chen, and A. Sellinger, "Effect of annealing on the characteristics of organic solar cells: polymer blends with a 2-vinyl-4,5-dicyanoimidazole derivative," *Macromolecules*, vol. 40, no. 13, pp. 4424–4428, 2007.
- [118] R. Y. C. Shin, T. Kietzke, S. Sudhakar, A. Dodabalapur, Z.-K. Chen, and A. Sellinger, "N-type conjugated materials based on 2-vinyl-4,5-dicyanoimidazoles and their use in solar cells," *Chemistry of Materials*, vol. 19, no. 8, pp. 1892–1894, 2007.
- [119] J. Li, F. Dierschke, J. Wu, A. C. Grimsdale, and K. Müllen, "Poly(2,7-carbazole) and perylene tetracarboxydiimide: a promising donor/acceptor pair for polymer solar cells," *Journal of Materials Chemistry*, vol. 16, no. 1, pp. 96–100, 2006.
- [120] W. S. Shin, H.-H. Jeong, M.-K. Kim, et al., "Effects of functional groups at perylene diimide derivatives on organic photovoltaic device application," *Journal of Materials Chemistry*, vol. 16, no. 4, pp. 384–390, 2006.
- [121] N. Camaioni, G. Ridolfi, V. Fattori, L. Favaretto, and G. Barbarella, "Branched thiophene-based oligomers as electron acceptors for organic photovoltaics," *Journal of Materials Chemistry*, vol. 15, no. 22, pp. 2220–2225, 2005.
- [122] D. Mühlbacher, M. Scharber, M. Morana, et al., "High photovoltaic performance of a low-bandgap polymer," *Advanced Materials*, vol. 18, no. 21, pp. 2884–2889, 2006.
- [123] M. Svensson, F. Zhang, S. C. Veenstra, et al., "High-performance polymer solar cells of an alternating polyfluorene copolymer and a fullerene derivative," *Advanced Materials*, vol. 15, no. 12, pp. 988–991, 2003.
- [124] F. Zhang, W. Mammo, L. M. Andersson, S. Admassie, M. R. Andersson, and O. Inganäs, "Low-bandgap alternating fluorene copolymer/methanofullerene heterojunctions in efficient near-infrared polymer solar cells," *Advanced Materials*, vol. 18, no. 16, pp. 2169–2173, 2006.
- [125] M. M. Wienk, M. G. R. Turbiez, M. P. Struijk, M. Fonrodona, and R. A. J. Janssen, "Low-band gap poly(di-2-thienylthienopyrazine): fullerene solar cells," *Applied Physics Letters*, vol. 88, no. 15, Article ID 153511, 3 pages, 2006.
- [126] A. Dhanabalan, J. K. J. van Duren, P. A. van Hal, J. L. J. van Dongen, and R. A. J. Janssen, "Synthesis and characterization of a low bandgap conjugated polymer for bulk heterojunction photovoltaic cells," *Advanced Functional Materials*, vol. 11, no. 4, pp. 255–262, 2001.
- [127] X. Wang, E. Perzon, J. L. Delgado, et al., "Infrared photocurrent spectral response from plastic solar cell with low-bandgap polyfluorene and fullerene derivative," *Applied Physics Letters*, vol. 85, no. 21, pp. 5081–5083, 2004.
- [128] X. Wang, E. Perzon, F. Oswald, et al., "Enhanced photocurrent spectral response in low-bandgap polyfluorene and C<sub>70</sub>-derivative-based solar cells," *Advanced Functional Materials*, vol. 15, no. 10, pp. 1665–1670, 2005.
- [129] Y. Xia, L. Wang, X. Deng, D. Li, X. Zhu, and Y. Cao, "Photocurrent response wavelength up to 1.1  $\mu\text{m}$  from photovoltaic cells based on narrow-band-gap conjugated polymer and fullerene derivative," *Applied Physics Letters*, vol. 89, no. 8, Article ID 081106, 3 pages, 2006.
- [130] M. C. Scharber, D. Mühlbacher, M. Koppe, et al., "Design rules for donors in bulk-heterojunction solar cells towards 10% energy-conversion efficiency," *Advanced Materials*, vol. 18, no. 6, pp. 789–794, 2006.
- [131] G. Dennler, H.-J. Prall, R. Koeppel, M. Egginger, R. Autengruber, and N. S. Sariciftci, "Enhanced spectral coverage in tandem organic solar cells," *Applied Physics Letters*, vol. 89, no. 7, Article ID 073502, 3 pages, 2006.
- [132] V. Shrotriya, E. H.-E. Wu, G. Li, Y. Yao, and Y. Yang, "Efficient light harvesting in multiple-device stacked structure for polymer solar cells," *Applied Physics Letters*, vol. 88, no. 6, Article ID 064104, 3 pages, 2006.
- [133] J. Y. Kim, K. Lee, N. E. Coates, et al., "Efficient tandem polymer solar cells fabricated by all-solution processing," *Science*, vol. 317, no. 5835, pp. 222–225, 2007.

## Research Article

# Silicon Quantum Dots in a Dielectric Matrix for All-Silicon Tandem Solar Cells

Eun-Chel Cho,<sup>1</sup> Martin A. Green,<sup>1</sup> Gavin Conibeer,<sup>1</sup> Dengyuan Song,<sup>1</sup> Young-Hyun Cho,<sup>1</sup> Giuseppe Scardera,<sup>1</sup> Shujuan Huang,<sup>1</sup> Sangwook Park,<sup>1</sup> X. J. Hao,<sup>1</sup> Yidan Huang,<sup>1</sup> and Lap Van Dao<sup>2</sup>

<sup>1</sup>ARC Photovoltaics Centre of Excellence, University of New South Wales, Sydney 2052, NSW, Australia

<sup>2</sup>ARC Centre of Excellence for Coherent X-Ray Science, Swinburne University of Technology, Hawthorn 3122, VIC, Australia

Received 1 April 2007; Accepted 26 June 2007

Recommended by Armin G. Aberle

We report work progress on the growth of Si quantum dots in different matrices for future photovoltaic applications. The work reported here seeks to engineer a wide-bandgap silicon-based thin-film material by using quantum confinement in silicon quantum dots and to utilize this in complete thin-film silicon-based tandem cell, without the constraints of lattice matching, but which nonetheless gives an enhanced efficiency through the increased spectral collection efficiency. Coherent-sized quantum dots, dispersed in a matrix of silicon carbide, nitride, or oxide, were fabricated by precipitation of Si-rich material deposited by reactive sputtering or PECVD. Bandgap opening of Si QDs in nitride is more blue-shifted than that of Si QD in oxide, while clear evidence of quantum confinement in Si quantum dots in carbide was hard to obtain, probably due to many surface and defect states. The PL decay shows that the lifetimes vary from 10 to 70 microseconds for diameter of 3.4 nm dot with increasing detection wavelength.

Copyright © 2007 Eun-Chel Cho et al. This is an open access article distributed under the Creative Commons Attribution License, which permits unrestricted use, distribution, and reproduction in any medium, provided the original work is properly cited.

## 1. INTRODUCTION

Wafer-based first-generation photovoltaic technologies are presently booming, a situation likely to continue for the next decade. However, second-generation thin-film approaches also appear attractive because of their potential reduction in material costs. Third-generation approaches aim to reduce the manufacturing cost of thin-film second-generation technologies by increasing the efficiency through using multiple energy thresholds, whilst still using abundant and non-toxic materials. The effects of increasing efficiency and lowering the cost of thin-film processes can significantly leverage costs per peak watt (Wp) of generating capacity, perhaps to less than US \$ 0.20/Wp [1].

Figure 1 shows main loss mechanisms in a standard p-n junction solar cell. The most important loss mechanisms in single p-n junction solar cells are the nonabsorption of below-bandgap photons (① in Figure 1) and thermalization of electron-hole pairs generated by absorption of short-wavelength photons, through electron (hole) relaxation to the conduction (valence) band edge (② in Figure 1). Other losses are junction loss (③ in Figure 1) and contact loss (④ in Figure 1), which can be arbitrarily small in an ideal device. Recombination loss (⑤ in Figure 1) can be reduced to purely radiative recombination again in an ideal device.

There have been proposed three families of approaches for tackling these first two major loss mechanisms [2]: (a) increasing the number of energy levels; (b) capturing hot carriers before thermalisation; and (c) multiple electron-hole pair generation per high energy photon or generation of one higher energy-carrier pair with more than one low energy photon. An implementation of strategy (a), the tandem cells, is the only technology thus far to have been realized with efficiencies exceeding the Shockley-Queisser limit.

The concept of the tandem solar cell is the use of several solar cells of different bandgaps stacked on top of each other, each absorbing photons of different energies, such that the uppermost cell has the highest bandgap and lets the photon less than its bandgap pass through to lower bandgap cells underneath. Most commonly, these cells are contacted in series. The highest efficiency examples are monolithically grown single-crystal lattice-matched devices based on a GaInP/GaAs/Ge triple-junction structure [3]. Another example in less exotically grown materials is micromorph a-Si/ $\mu$ c-Si tandem cells [4]. Use of silicon also conveys the very significant advantage of use of an abundant nontoxic material.

A further example which shares these advantages is the use of a silicon quantum dot nanostructure in a matrix of

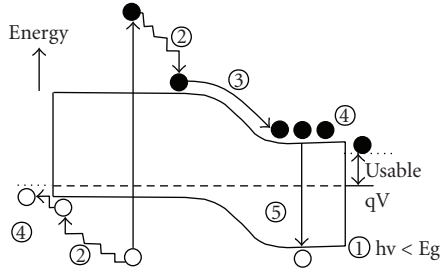


FIGURE 1: Loss mechanism in a standard p-n junction solar cell: (1) nonabsorption of below-bandgap photons, (2) lattice thermalisation loss, (3) junction loss, (4) contact voltage loss, and (5) recombination loss.

silicon oxide, nitride, or carbide to engineer the bandgap of a solar cell material for an “all-Si” tandem cell, whilst also giving a wide range of design flexibility [5, 6]. In the current paper, we report material properties of silicon nanostructures for all-silicon tandem solar cells and recent progress on silicon nanostructures for all-silicon tandem cell fabrication.

## 2. ALL-SILICON QUANTUM DOT TANDEM SOLAR CELL

Silicon is unique in that it has an almost ideal bandgap not only for a standard single p-n junction cell (just a little on the low side of optimal) but also for the lower cell in a two-cell or even a three-cell tandem stack (a little on the high side). The efficiency limit for a single silicon cell is 29%, when only radiative and Auger recombination is considered, but this increases to 42.5% and 47.5% for two-cell and three-cell stacks, respectively [1]. The optimal bandgap of the top cell to maximize conversion efficiency is  $1.7 \sim 1.8$  eV for a two-cell tandem with an Si bottom cell [7]. The optimal upper and middle bandgaps for a three-cell tandem are 1.5 eV and 2.0 eV, respectively. Figure 2 shows the schematic diagram of a silicon-based or “all-silicon” tandem solar cell. The top cell is connected to the bottom cell by an interband tunnel junction, most likely using a defect dominated high interband recombination junction. The material in the interconnection region could also be comprised of quantum dot material, but most likely employing smaller dots than the absorbing regions.

The quantum confinement, achieved by restricting at least one dimension of silicon less to the Bohr radius of the bulk crystalline silicon (around 5 nm), causes its effective bandgap to increase. Our early experiments involved carefully thinning the thin silicon layer (50 nm thick) in commercially available silicon-on-insulator (SOI) wafers, resulting in an  $\text{SiO}_2/\text{Si}/\text{SiO}_2$  quantum well [8]. For possibly the first time, clear evidence for a quantum-confined bandgap in an  $\text{SiO}_2/\text{Si}/\text{SiO}_2$  quantum well increase was demonstrated by photoluminescence measurements on such devices, with a lowest energy level (the effective bandgap) of up to 1.7 eV measured for layers about 1 nm thick. The blue shift of the PL and its rapidly increasing intensity with decreasing Si thickness are indicative of quantum confinement effects. Enhanced PL intensity is directly related to the absorption

from the principle of detailed balance [9], which provides an added bonus for solar applications.

The strongest quantum confinement effect is obtained if the silicon is constrained in all three dimensions, as in quantum dots, such that the same increase in effective bandgap can be achieved with a much less stringent size constraint. If these dots are spaced close enough and there is a significant overlap of the wavefunction, carriers can tunnel between them to produce a true quantum dot superlattice. Such a superlattice can then be used as the higher bandgap material in a tandem cell.

Each of the n-type and p-type regions will typically include 20–50 bilayers formed by alternating the growth of a quantum dot (QD) and a dielectric barrier layer. The n-type and p-type regions are typically each in the range of 75–200 nm thick.

The material requirements for the dielectric layers are ease of thin-film growth and use of abundant nontoxic materials, hence it is most likely to be an oxide, nitride, or carbide of silicon. It is also necessary that carriers from the quantum dot layers have a high probability of tunneling through the dielectric layers. This is achieved by creating each dielectric layer with a thickness in the range of 1.5 to 2.5 nm for the case of oxide.

The semiconductor material of the quantum dots is preferably silicon or another group IV element such as tin or germanium, or a group IV alloy such as silicon germanium. For a nanostructure to have a high conductivity requires formation of a true superlattice with overlap of the wave function for adjacent quantum dots; which in turn requires either close spacing between QDs or a low barrier height. The wavefunction of an electron confined to a spherical dot penetrates into the surrounding material, decaying approximately as  $\exp(-r/L_d)/r$ , where  $r$  is the distance from the centre of the dot. The decay length  $L_d$  is determined by the barrier height of the material in which the dot is embedded, which in the present case is either a silicon carbide, nitride, or oxide matrix [10]. In the simplest case, the decay length ( $L_d$ ) is given by (1):

$$L_d = \frac{1}{\sqrt{2m^*(V_o - E_n)}} = \frac{0.1952 \text{ nm}}{\sqrt{m^* \cdot \Delta E/m_o}}. \quad (1)$$

The latter expression holds when  $\Delta E$ , the difference between the conduction band edge of the matrix and the confined energy level, is in eV.  $m^*$  and  $m_0$  are the effective mass and electron mass in the matrix material, respectively.  $V_0$  is the corresponding band offset and  $E_n$  is the confined energy level in a quantum dot. Without considering the confined energy of QDs, energy difference  $\Delta E$  [5] are 3.2 eV, 1.9 eV, and 0.5 eV for the conduction edge of bulk Si and  $\text{SiO}_2$ ,  $\text{Si}_3\text{N}_4$ , and SiC, respectively. Electrons effective masses of  $\text{SiO}_2$ ,  $\text{Si}_3\text{N}_4$ , and 3C-SiC are 0.86 [11], 0.05–0.13 [12], and  $0.24 \pm 0.1$  [13], respectively. Following this line of argument, the results suggest that dots in an  $\text{SiO}_2$  matrix would have to be separated by no more than 1–2 nm of matrix for a reasonable overlap of the wavefunction and hence of conductivity, while they could be separated by more than 4 nm of SiC. The same type of calculation allows the effect of fluctuations in spacing and size

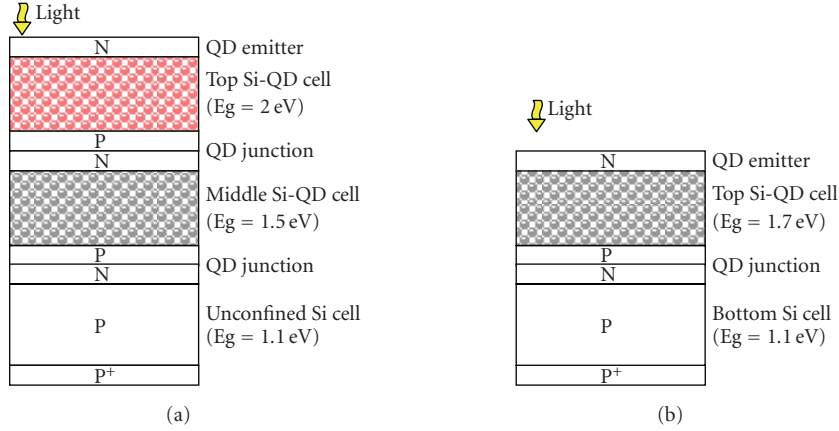


FIGURE 2: Schematic of (a) three-cell and (b) two-cell tandem solar cell with an Si bottom cell.

of the dots to be investigated. It is found that the calculated Bloch mobilities do not depend strongly on variations in the dot size but do depend strongly on dot spacing uniformity within the QD material [14].

Another requirement for a tandem cell element is the presence of some form of junction for carrier separation. This can either be a grown or a diffused p-n junction or a p-i-n junction with the superlattice as i-region. The latter requires careful control of the work functions (and therefore doping) of the p- and n-regions, but also means that it is not essential for the superlattice itself to be doped.

### 3. SILICON QUANTUM DOT SUPERLATTICE

#### 3.1. Fabrication of silicon quantum dots

##### 3.1.1. Phase precipitation from Si-rich layer

The effect of quantum confinement obtained by limiting at least one spatial dimension of material has been understood since at least the 1960s and superlattices have been known since 1970. Superlattices were manufacturable with the epitaxial growth techniques available to III-V compound semiconductor technology at that time [15]. Amorphous silicon superlattices of a-Si : H and a-Si<sub>1-x</sub>N<sub>x</sub> : H were first reported [16]. Lu et al. reported quantum confinement and light emission of superlattices of silicon and SiO<sub>2</sub> fabricated by molecular beam epitaxy (MBE) [17].

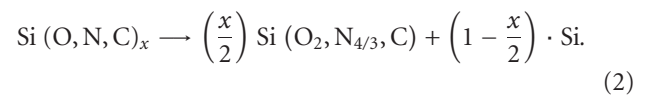
Several techniques have been reported for fabricating silicon quantum dots from one of two directions—“bottom up” and “top down.” The “bottom up” approach builds up QDs from individual atoms or molecules. This is the basis of most “cluster science” as well as crystal materials synthesis, usually via chemical or vacuum deposition techniques. The methods include gas evaporation [18], high temperature aerosol reaction [19], phase separation of silicon-rich oxide (SRO) by a sputtering [20] and reactive evaporation [21], chemical vapor deposition (CVD) [22], Si implantation into the SiO<sub>2</sub> substrate [23], laser ablation [24], and solution synthesis [25].

The “top down” approach generates silicon nanostructures by breaking up bulk materials. This is the basis for

techniques such as mechanical milling [26], particle selection formed by electrochemical etching of the silicon substrate (i.e., porous silicon) [27], and precision oxidation of SOI substrates [8]. Approaches explored for producing two-dimensional superlattices in a low cost have not previously proved to be particularly encouraging [8, 28]. We have demonstrated a bandgap, as measured by PL, of up to 1.7 eV, using both an Si/SiO<sub>2</sub> quantum well [8] and an Si/SiO<sub>2</sub> superlattice [28] for layers about 1 nm thick. The reproducibility of such a thin silicon layer is questionable. The quantum dot superlattice is a promising material because of the additional degree of confinement which gives greater design flexibility than the two-dimensional quantum well structures. The first confined energy level in a 1 nm wide quantum well will be approximately the same as in a 2 nm diameter quantum dot [5].

Si ion implantation into an oxide layer can be used to produce Si QDs at an irregular position with a relatively large size distribution. Solution synthesis, mechanical milling, and particle selection from porous silicon can be used to fabricate a volume of Si QDs, but it is difficult to control the size uniformity of distributed QDs or an additional process to select the particle with the same size.

Si QD fabrication by various vacuum deposition techniques is preferable because of the greater potential of integration into conventional devices. Gas phase in situ Si QD growth in an Si<sub>3</sub>N<sub>4</sub> matrix film [29] and nanocrystalline precipitations from silicon-rich layers [21] are two examples of fabrication of Si QD systems by means of vacuum deposition techniques. In situ, Si QD growth is an interesting method because a high temperature annealing process is not required. For Si precipitation from an Si-rich layer, high temperature annealing of excess Si in an inert atmosphere is necessary to form Si nanocrystals with a few nm diameters, for example, Si QD precipitation in oxide [21, 28, 30], nitride [31], and carbide [32, 33] (Figure 3(a)). Equation (2) describes this Si precipitation mechanism:



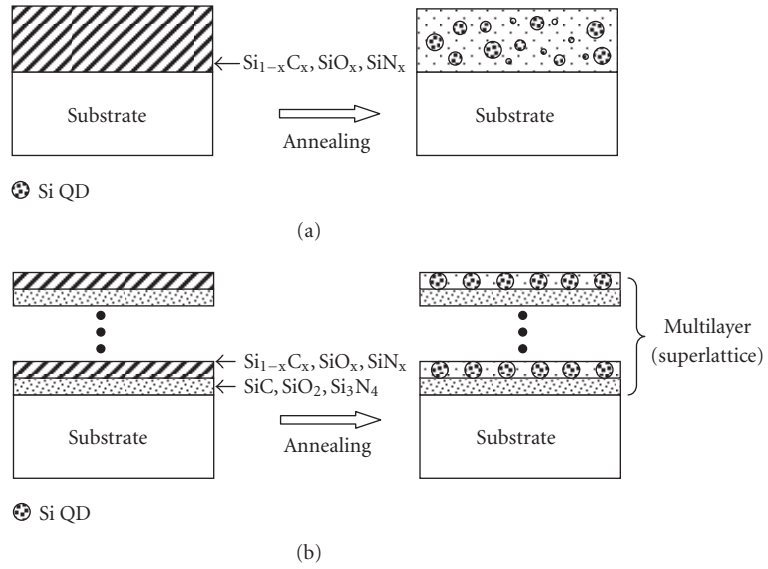


FIGURE 3: Si QDs from phase separation of (a) a single silicon-rich precursor layer and (b) a multilayer structure.

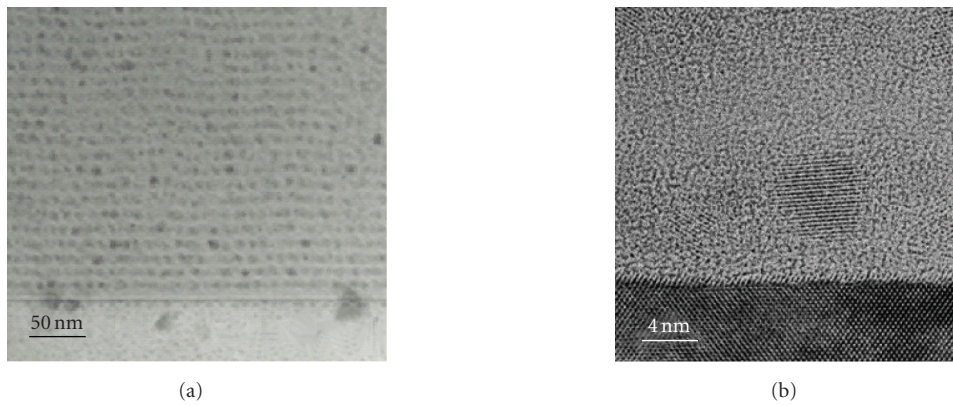


FIGURE 4: Transmission electron microscopy (TEM) images of Si QDs in  $\text{SiO}_2$  matrix with (a) low magnification and (b) HRTEM lattice image of Si quantum dots.

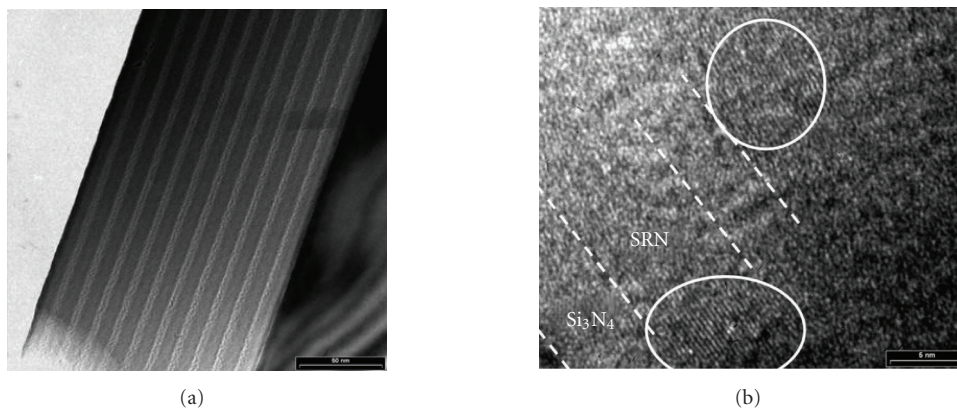


FIGURE 5: Si QDs dispersed in an  $\text{Si}_3\text{N}_4$  matrix fabricated by gas phase in situ deposition: (a) low-magnification TEM and (b) high-resolution TEM.

More accurate size control and a narrow size distribution were achieved by growth of an Si QD multilayer structure, which is fabricated by alternating layers of stoichiometric insulating materials and silicon-rich layers [21, 28] shown in Figure 3(b). Depending on the annealing conditions, silicon precipitates from the silicon-rich layers as approximately spherical QDs of a diameter close to the original layer thickness. Hence controls of the diameter and of one spatial coordinate of the dots are possible. Si QDs in oxide [6, 28] and nitride [31] are actively studied materials, but Si QDs in carbide has only recently been attempted [32, 33]. TEM images in Figure 4 show Si QDs interspersed in the oxide matrix.

### 3.1.2. Si quantum dots in a nitride matrix

The bandgap of  $\text{Si}_3\text{N}_4$  is significantly lower than that of  $\text{SiO}_2$ . Hence Si QDs in the nitride offer a lower barrier height and much increased carrier tunneling probability between quantum dots. (SiC offers a lower barrier still.) For this reason, we have explored transferring the technology of Si QDs in  $\text{SiO}_2$  to the growth of Si nanocrystals in silicon nitride by both sputtering and PECVD [31]. For sputtering, growth parameters are very similar to the oxide. In addition, two separate PECVD systems, remote plasma and parallel capacitor plasma, have been used for the growth of Si nanocrystals by depositing alternate Si-rich and stoichiometric nitride layers. Annealing is carried out again at  $1100^\circ\text{C}$  but with a preannealing at  $500^\circ\text{C}$  to drive off hydrogen incorporated from the PECVD process. Again, HRTEM images showing even clearer nanocrystals have been obtained. To the best of our knowledge, this is the first Si QDs in multilayered structure in nitride matrix [31].

We have now also extended the layered Si QDs in nitride technology to gas phase in situ deposition. Figure 5 shows in situ Si QD dispersed in a nitride matrix. A stoichiometric  $\text{Si}_3\text{N}_4$  layer and an in situ Si QD layer are alternately deposited on an Si substrate. This technique allows QDs to form during deposition without a postdeposition annealing. We are actively studying this technique because it is a low temperature process and may be potentially beneficial to doping of Si QDs owing to high equilibrium temperature of the plasma and free of high temperature postannealing described in Figure 3.

### 3.1.3. Si QDs in silicon carbide

SiC nanocrystals of a few nm diameters in an  $\text{SiO}_2$  matrix were produced by silicon and carbon implantation into thermal oxide [34]. However, to our knowledge, little has been reported on the experimental properties of Si QDs embedded in an SiC matrix [32, 33].

A Si-rich amorphous silicon carbide precursor layer can be achieved by control of the sputtering parameters of Si and carbon containing targets (e.g., pure carbon, silicon carbide, boron carbide, etc.). One way to fabricate Si-rich silicon carbide is cosputtering from silicon and carbon containing targets. Alternatively, small chips of carbon attached to a silicon target can produce an Si-rich silicon carbide precursor layer. A high temperature anneal ( $800\text{--}1200^\circ\text{C}$  in an inert gas or

in vacuum) of a silicon-rich carbide precursor layer precipitates Si and/or SiC nanocrystals, depending on its chemical composition as shown in (2).

Raman, TEM, and XRD spectra for a silicon-rich  $\text{Si}_{0.75}\text{C}_{0.25}$  precursor layer grown on a quartz substrate with subsequent annealing are shown in Figure 6. There is clear evidence for the formation of nanocrystalline Si at an anneal temperature greater than  $1000^\circ\text{C}$ . This is shown in the Raman peak at  $\sim 508\text{ cm}^{-1}$  [35]. TEM lattice fringe spacing, consistent with  $\{111\}$  Si planes and XRD, peaks at  $2\theta = 28.4^\circ$  with peak broadening indicating nanocrystal of 3–7 nm (estimated using the Scherrer equation). (It should be noted that the nanocrystal size determined by TEM is, in our experience, always slightly smaller than that determined by XRD.)

Other Si and C concentrations were also investigated [33]. As the concentration of C in  $\text{Si}_{1-x}\text{C}_x$  is increased to the nearly stoichiometric  $\text{Si}_{0.495}\text{C}_{0.505}$ , Raman evidence (not shown here), for the stretching vibration modes of Si–C and C–C bonds, can be easily identified. Intensities of both TO and LO bands of Raman spectra are increased with increasing annealing temperature, indicating the formation of crystalline SiC during annealing. In addition, there is a dramatic decrease in the intensity of Si–Si vibration modes, indicating the formation of far fewer Si nanocrystals.

HRTEM data (not shown here) shows crystallites with lattice fringes corresponding to  $\beta\text{-SiC}$   $\{111\}$  planes, with a mean size in the range of 3–10 nm. However, in contrast to the spherical Si nanocrystals in the oxide and nitride matrices (see Figures 4 and 5), SiC nanocrystals are irregular with some nanocrystals joined together to form an extended crystal. The difference of nanocrystal shapes from silicon-rich SiC and near-stoichiometric SiC is due to the differing mechanisms for nanocrystal formation. For the Si-rich carbide precursor, nanocrystals precipitate to nucleating sites, due to an excess of Si in the matrix, with surface energy minimization favoring the formation of spheres. For the near-stoichiometric composition, SiC nanocrystals formation does not depend on precipitation and hence random shapes occur, dependent more on local concentration variations.

Hence the best data so far for Si nanocrystals in an SiC matrix are obtained for an  $\text{Si}_{0.75}\text{C}_{0.25}$  precursor composition. Optical bandgap of  $\text{Si}_{0.75}\text{C}_{0.25}$  thin film is in the ranges of  $\sim 1.4$  (as-deposited) to  $\sim 2.0\text{ eV}$  (annealed at  $1100^\circ\text{C}$ ). In order to control the size of Si nanocrystals multilayer structures, based on this concentration, have been fabricated and further measurement is underway.

As before, a multilayer approach was used to fabricate Si QDs in carbide of uniform size. A multilayer with stoichiometric SiC and silicon-rich  $\text{Si}_{1-x}\text{C}_x$  precursor layer was fabricated, as shown in Figure 7(a), and annealed at a high temperature to selectively precipitate Si nanocrystals in a carbide matrix. However, the lattice fringes in HRTEM image correspond to  $\beta\text{-SiC}$   $\{111\}$  crystalline planes (Figure 7(b)). One possible reason for SiC QDs, instead of Si QDs, is that the C/Si ratio in layered structure has an increase, compared to the original design.

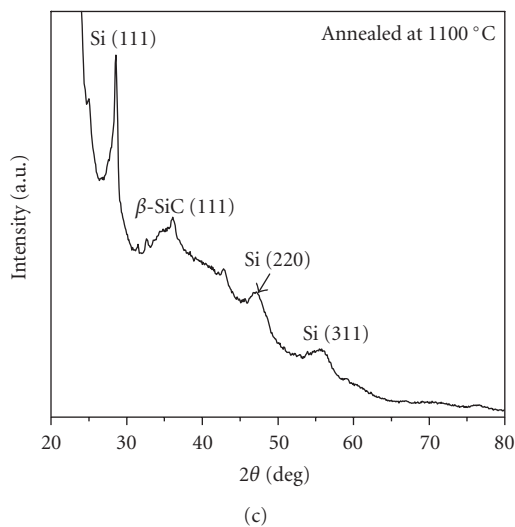
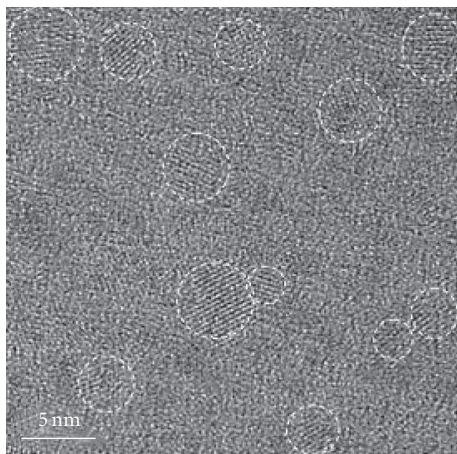
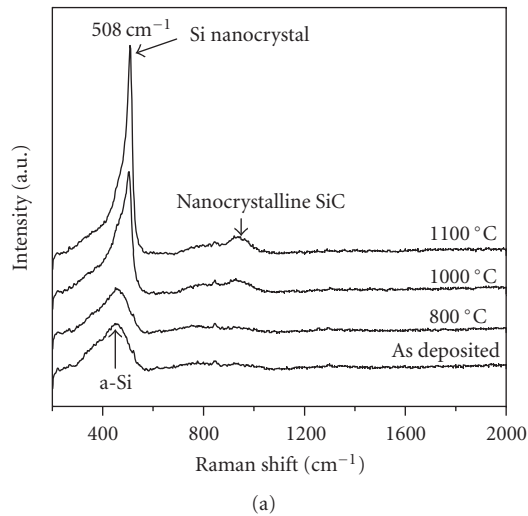


FIGURE 6: Silicon-rich SiC precursor layer: (a) Raman spectra with different annealing temperature, (b) cross-sectional HRTEM image, and (c) X-ray diffraction pattern.

### 3.2. Bandgap engineering of silicon nanostructure

In indirect bandgap semiconductors, the optical transitions are allowed only if photons are absorbed or emitted to conserve the crystal momentum. The spatial confinement of electrons and holes inside a QD relaxes this  $k$ -conservation requirement and creates a quasidirect bandgap [36]. Our measurements of photoluminescence (PL) from Si QDs in silicon oxide confirmed that we get the 1.7 eV bandgap from 2 nm quantum dots [5, 6, 28]. They also show that there is a large increase in PL intensity as the QD size decreases, which is consistent with the increase in radiative efficiency with the onset of pseudodirect bandgap behavior.

The photoluminescence peaks from Si QDs in nitride are more blue-shifted than that of Si QD in oxide. Figure 8 shows the PL peak energies from Si QD dispersed in oxide [37–39] and nitride [40, 41]. PL peak energies of Si QDs in oxide are less than 2.0 eV, while Si QDs in nitride have peak energies less than 3.0 eV. Puzder et al. [42] have explained that the main reason for the PL peak energy reduction in oxide matrix is the distortion of the local  $sp^3$  network by double-bonded oxygen. However, Yang et al. [43] claimed that the reason for the stronger blue shift in nitride is better passivation of Si QDs by nitrogen atoms, eliminating the strain at the Si/Si<sub>3</sub>N<sub>4</sub> interface nearly completely. Our PL results from the Si precipitation are in quite good agreement with the results from other authors [37–43].

Clear evidence of confinement in Si quantum dots in carbide was hard to obtain, probably due to many surface and defect states which dominate the photoluminescence process [34]. An observation of clear quantum confinement in the Si QDs, dispersed in SiC matrix, is also very challenging since usually metastable alloy films relax by diffusion and/or misfit dislocation formation to reduce chemical modulation and strain. It is likely that the mechanism of precipitation of excess Si atoms to nucleating sites in Si-rich SiC is a less active process than in nitride or oxide. This would be because the difference in Si–Si and Si–C lattice spacing is less than in the nitride and oxide. Also because SiC is an isoelectronic covalently bonded material as is Si; there is a much smaller tendency for segregation of Si than in oxide or nitride matrices.

### 3.3. Mobility-lifetime product

Photo-generated carriers in an Si quantum dot superlattice need to be collected at the metal contacts and hence require a reasonable mobility. A knowledge of mobility variation for the Si QDs in different matrices, with different barrier thickness and different doping densities in the Si QDs, is important to achieving a working device. Simulations of large bandgap cells using PC1D suggest mobility-lifetime products above  $10^{-9} \text{ cm}^2/\text{V}$  which are required for good current collection for an indicative top tandem cell design thickness of 100–200 nm (Figure 2). Such a narrow absorber layer is thought reasonable given the improved optical absorption properties of the QD material.

The carrier lifetime of a thin-film material can be characterized by PL decay. Photoluminescence in QD structures involves electron-hole recombination between discrete energy

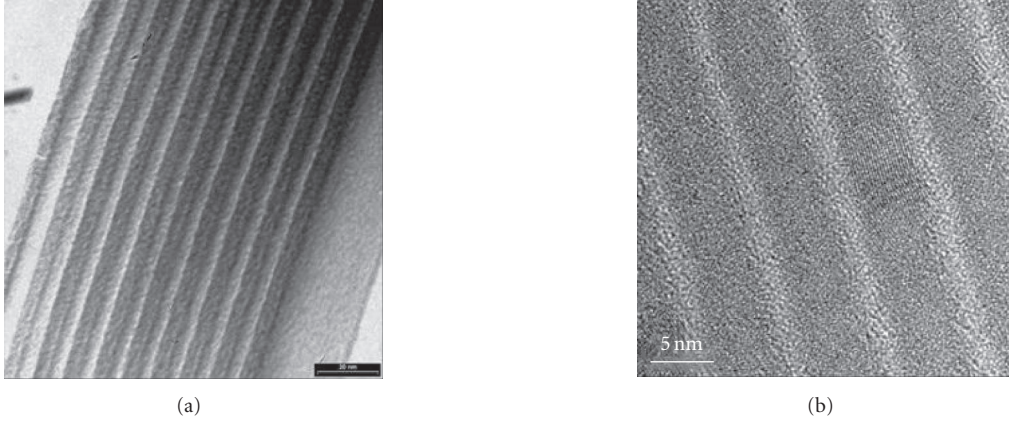


FIGURE 7: TEM images of SiC/Silicon-rich SiC multilayer (a) deposited and (b) annealed at 1100°C for 20 minutes.

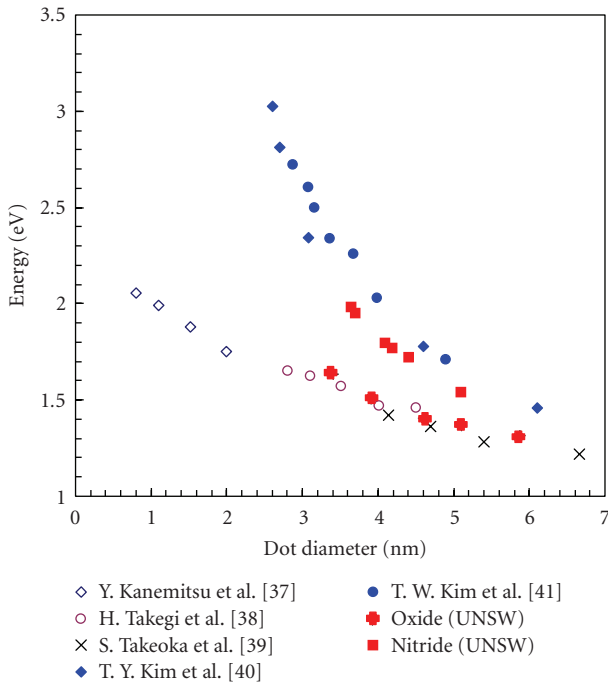


FIGURE 8: Energy gaps of three-dimensionally confined Si nanocrystals in SiO<sub>2</sub> and SiN<sub>x</sub> (300°K).

states in the conduction band and the valence band. A PL signal around 750 nm with a very broadband ( $\sim 350$  meV) is observed for the QD diameter of 3.4 nm (Figure 9). Despite the broadness of the peaks, there is evidence in Figure 9 that as the excitation intensity is increased the PL intensity of the low energy part of the spectrum (800 and 850 nm in Figure 9) increases more slowly than that of the high energy part. According to state-filling effect theory, lower energy levels with a low density of states (triplet states) will become saturated as intensity increases, but higher energy levels with a larger DOS (singlet states) will still be available for excitation as high excitation intensities increase [44]. These triplet

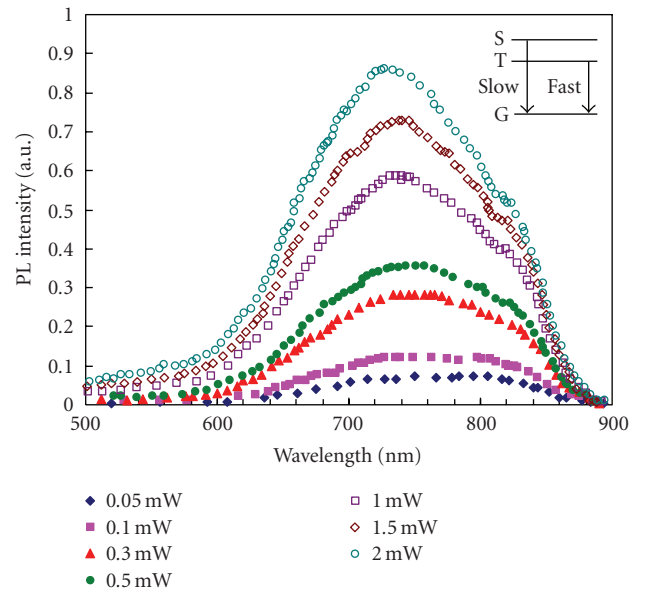


FIGURE 9: Time-integrated spectrum of Si quantum dot sample measured at different excitation intensities for 3.4 nm dot size.

TABLE 1: Decay time for different detection wavelengths with  $\beta = 0.6$  for dot diameter of 3.4 nm and  $\beta = 0.54$  for dot diameter of 4.2 nm.

Detection $\lambda$ (nm)	600	650	700	750	800	850
3.4 nm dots ( $\mu$ s)	4	7	12	20	35	60
4.2 nm dots ( $\mu$ s)	2	4	10	18	20	55

and singlet states seem to occur in Si QDs in oxide matrix at about 820 and 740 nm, respectively, as in Figure 9.

Because the PL spectrum of the Si QDs is very broad and the recombination of carriers in different energy levels cannot be clearly resolved, information about the PL lifetime for different levels (with a spectral window of 2 nm in 50 nm) is spread across the spectrum (600–850 nm). Temporal evolution of the PL can be expressed as a stretched exponential function. This approach is frequently used to describe

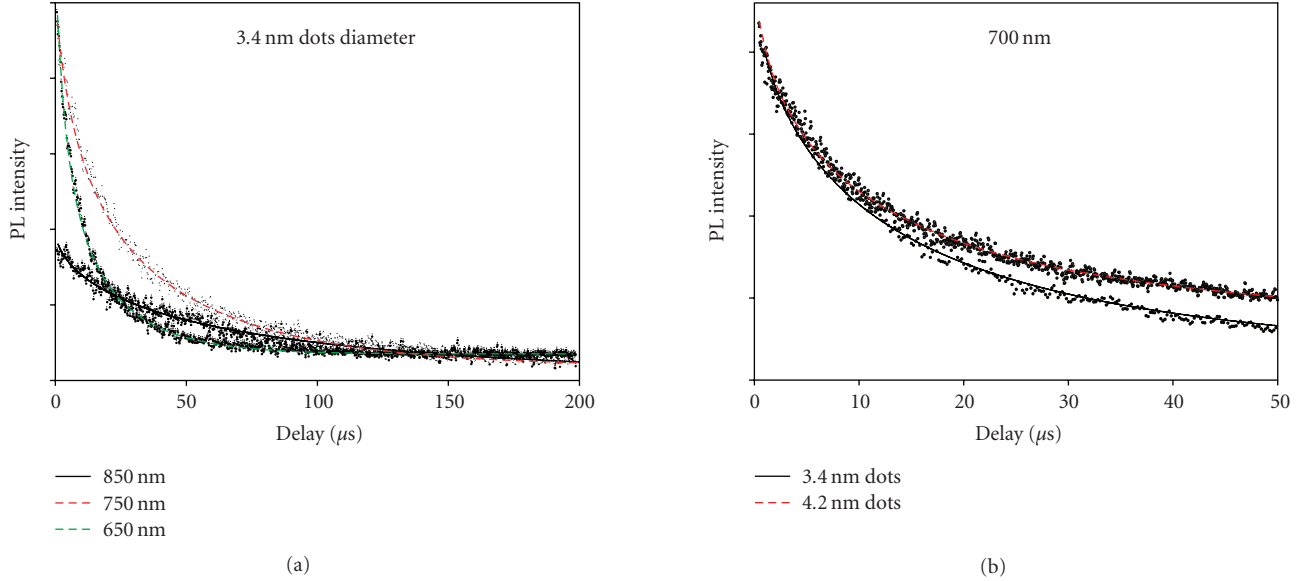


FIGURE 10: Time-evolution of the PL intensities (a) at detection wavelengths of 650 nm, 750 nm, and 850 nm for 3.4 nm Si QDs fitted with a stretched exponential function and (b) at a detection wavelength of 700 nm for 3.4 nm and 4.2 nm Si QDs.

dispersive processes in disordered systems, for example, porous silicon, having a distribution of relaxation times, and is given by

$$I(t) = I_0 \cdot \exp \left[ - (t/\tau)^\beta \right], \quad (3)$$

where  $\tau$  is the PL lifetime and  $0 \leq \beta \leq 1$  is the dispersion exponent. The PL decay shows that the lifetimes vary from 2 to 60 microseconds for diameter of 3.4 nm dot with increasing detection wavelength [44]. Figure 10 shows time-evolution of the PL intensities (a) at detection wavelengths of 650 nm, 750 nm, and 850 nm for 3.4 nm Si QDs fitted with a stretched exponential function and (b) at a detection wavelength of 700 nm for 3.4 nm and 4.2 nm Si QDs, demonstrating that the stretched exponential makes a good fit to the data at both the long and short time scales. Table 1 summarizes the PL decay times from the different detection wavelengths. The dispersion factor is  $\beta = 0.6$  for sample 3.4 nm dot and  $\beta = 0.54$  for 4.2 nm dot.  $\beta$  does not reflect microscopic properties which depend on the size of the QD but rather a macroscopic property of the system associated with the character of the medium [45]; thus the two samples exhibit a difference in the structure of the SRO layer and QDs surface states. The stretched function is related to a distribution of relaxation times or a time-dependent relaxation rate which reflects the interlevel relaxation processes in the QD. In all samples, the lifetime of a high energy level is short. The time decay in nitride matrix is under investigation.

### 3.4. Doping and work function control

The impurities, like phosphorous and boron in the bulk crystalline silicon, increase the conductivity of bulk Si by several orders of magnitude. There are several questions about the impurity doping in a low-dimensional structure [46]. Important questions arise as to whether the dopants will con-

tinue to play a role similar to that in bulk semiconductors, or alternative methods of work function control will be required. It is not clear at present whether or not the doping of Si QDs provides the generation of free charge carriers [47]. Also when silicon-rich precursor layers experience phase separation process described in (2), doping impurities may be thermodynamically unfavorable to incorporate into QDs since very small QDs are often regarded as structurally perfect. As a result, in worst case, impurity may not exist inside QDs after high temperature postannealing process.

To study the doping in Si QDs, we choose atoms with a high solid solubility in silicon at the annealing temperature. From this aspect, phosphorus and boron would be the best material for n-type and p-type doping materials, respectively. In our experiments, the phosphorus doping in the Si QD superlattices was achieved using  $\text{P}_2\text{O}_5$  co-sputtering during the deposition of silicon-rich oxide (Si and  $\text{SiO}_2$  co-sputtering), which forms Si QDs upon high temperature postannealing. The P concentration in the silicon-rich oxide was controlled by the deposition rate of three targets and is initially chosen to be very high in order to increase the chances of detection. Phosphorus 2p X-ray photoelectron spectroscopy (XPS) spectra show that P–O bonds (peak around 135 eV) and P–Si bonds and/or free phosphorus (peak around 129 eV) are observed from highly P-doped silicon-rich oxide (Figure 11).  $\text{SiO}_{1.41}$  with 0.67 at % phosphorus shows both Si–P and O–P bonding, while silicon-rich  $\text{SiO}_{0.94}$  with 0.27 at % phosphorus shows only Si–P bonding. Control of the P concentration in this way was high, in the ranges of 0.26 at %  $\sim$  3.02 at %. The XPS results indicate that the phosphorus in silicon-rich oxide may exist in Si–P bonds inside Si QDs. However, it is necessary to carry out more analytical experiments for both n-type and p-type Si QDs in different matrices.

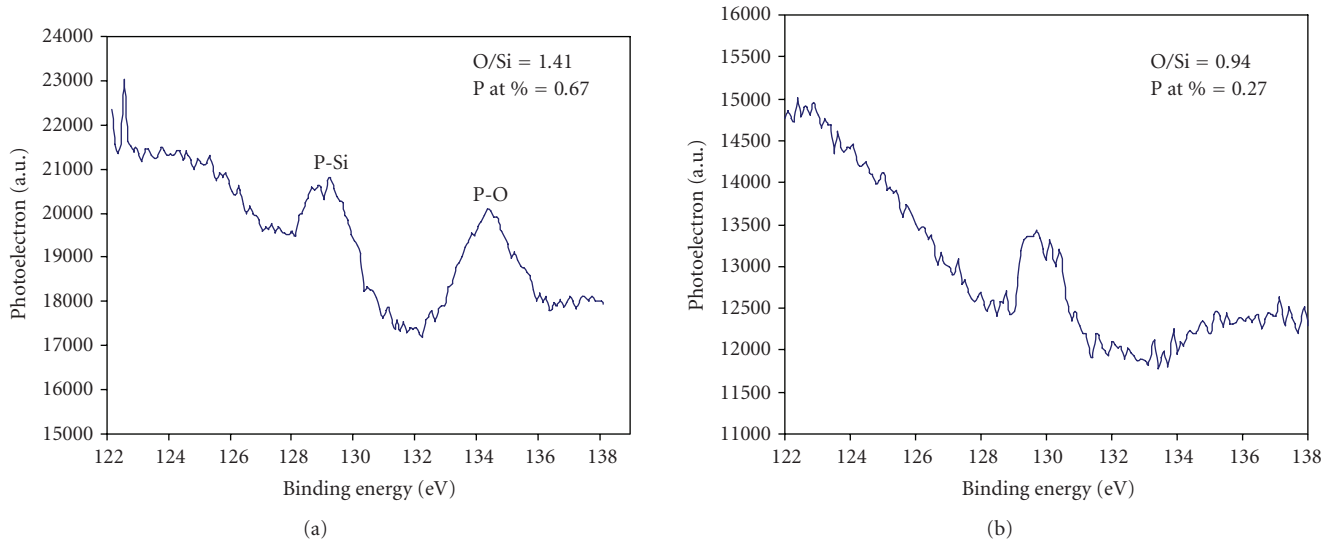


FIGURE 11: XPS spectra of P–Si and P–O bonding from (a)  $\text{SiO}_{1.41}$  with phosphorus concentration of 0.67 at % and (b)  $\text{SiO}_{0.94}$  with phosphorus concentration of 0.27 at %.

#### 4. CONCLUSIONS

Third generation photovoltaic devices aim to tackle the losses associated with the nonabsorption of below bandgap photons and the thermalisation of above bandgap photons to the band edge. To tackle these losses, we are using silicon-based nanostructures as a high bandgap material for the concept of tandem solar cell.

Silicon has a bandgap just slightly larger than the ideal value for the lower cell in a two-cell or even a three-cell tandem stack. An upper material bandgap of 1.7 ~ 1.8 eV for a two-cell tandem solar cell with an Si bottom cell will maximize conversion efficiency. The optimum bandgaps for a three-cell tandem are 1.5 eV and 2.0 eV for middle and uppermost cells, respectively. The current work discusses the engineering of materials with appropriate bandgaps, using Si QDs dispersed either in silicon oxide, silicon nitride, or silicon carbide.

The formation of Si QDs in oxide and nitride matrices has been demonstrated, with good dot size control and evidence of nanocrystallinity from HRTEM and XRD. Quantum confinement has been demonstrated, using PL for the matrices of oxide and nitride, with PL energy increasing as dot size decreases by the correct relative amounts predicted by confined quantum confinement theory. A transfer of the technology to Si QDs in a silicon carbide matrix has been successfully demonstrated in single layer and multilayer structures, but demonstration of clear quantum confinement in the Si QDs is challenging due to a dominant surface state.

PL decay measurements of Si QDs dispersed in oxide show a slow decay (several tens of microseconds) in the lower part of PL spectrum and fast decay (few microseconds) in the higher part of the PL spectrum. This may be due to singlet-triplet splitting in Si QDs dispersed in oxide. There is some initial evidence for n-type doping in Si QDs, which may enable us to make a fully working device.

#### ACKNOWLEDGMENTS

This work was supported by the Stanford University Global Climate and Energy Project (GCEP) as well as by the Australian Research Council (ARC) via its Centres of Excellence scheme.

#### REFERENCES

- [1] M. A. Green, *Third Generation Photovoltaics: Advanced Solar Energy Conversion*, Springer, Berlin, Germany, 2003.
- [2] J. Nelson, *The Physics of Solar Cells*, Imperial College Press, London, UK, 2003.
- [3] W. E. McMahon, S. Kurtz, K. Emery, and M. S. Young, "Criteria for the design of GaInP/GaAs/Ge triple-junction cells to optimize their performance outdoors," in *Proceedings of the 29th IEEE Photovoltaic Specialists Conference*, pp. 931–934, New Orleans, La, USA, May 2002.
- [4] A. V. Shah, J. Bailat, E. Vallat-Sauvain, et al., "Microcrystalline and "micromorph" solar cells and modules: status and potential," in *Proceedings of the 31st IEEE Photovoltaic Specialists Conference*, pp. 1353–1358, Lake Buena Vista, Fla, USA, January 2005.
- [5] M. A. Green, E.-C. Cho, Y. Cho, et al., "All-silicon tandem cells based on "artificial" semiconductor synthesised using silicon quantum dots in a dielectric matrix," in *Proceedings of the 20th European Photovoltaic Solar Energy Conference and Exhibition*, p. 3, Barcelona, Spain, June 2005.
- [6] G. Conibeer, M. A. Green, R. Corkish, et al., "Silicon nanostructures for third generation photovoltaic solar cells," *Thin Solid Films*, vol. 511-512, pp. 654–662, 2006.
- [7] F. Meillaud, A. Shah, C. Droz, E. Vallat-Sauvain, and C. Mizza, "Efficiency limits for single-junction and tandem solar cells," *Solar Energy Materials and Solar Cells*, vol. 90, no. 18-19, pp. 2952–2959, 2006.
- [8] E.-C. Cho, M. A. Green, J. Xia, R. Corkish, P. Reece, and M. Gal, "Clear quantum-confined luminescence from crystalline silicon/SiO<sub>2</sub> single quantum wells," *Applied Physics Letters*, vol. 84, no. 13, pp. 2286–2288, 2004.

- [9] W. van Roosbroeck and W. Shockley, "Photon-radiative recombination of electrons and holes in germanium," *Physical Review*, vol. 94, no. 6, pp. 1558–1560, 1954.
- [10] M. A. Green, G. Conibeer, D. König, et al., "Progress with all-silicon tandem cells based on silicon quantum dots in a dielectric matrix," in *Proceedings of the 21th European Photovoltaic Solar Energy Conference*, Dresden, Germany, June 2006.
- [11] S. Zafar, K. A. Conrad, Q. Liu, et al., "Thickness and effective electron mass measurements for thin silicon dioxide films using tunneling current oscillations," *Applied Physics Letters*, vol. 67, no. 7, pp. 1031–1033, 1995.
- [12] P. C. Arnett and D. J. DiMaria, "Contact currents in silicon nitride," *Journal of Applied Physics*, vol. 47, no. 5, pp. 2092–2097, 1976.
- [13] C. Persson and U. Lindelfelt, "Detailed band structure for 3C-, 2H-, 4H-, 6H-SiC, and Si around the fundamental band gap," *Physical Review B*, vol. 54, no. 15, pp. 10257–10260, 1996.
- [14] C.-W. Jiang and M. A. Green, "Silicon quantum dot superlattices: modeling of energy bands, densities of states, and mobilities for silicon tandem solar cell applications," *Journal of Applied Physics*, vol. 99, no. 11, Article ID 114902, 7 pages, 2006.
- [15] L. L. Chang, L. Esaki, W. E. Howard, and R. Ludeke, "The growth of a GaAs-GaAlAs superlattice," *Journal of Vacuum Science and Technology*, vol. 10, no. 1, pp. 11–16, 1973.
- [16] B. Abeles and T. Tiedje, "Amorphous semiconductor superlattices," *Physical Review Letters*, vol. 51, no. 21, pp. 2003–2006, 1983.
- [17] Z. H. Lu, D. J. Lockwood, and J.-M. Baribeau, "Quantum confinement and light emission in SiO<sub>2</sub>/Si superlattices," *Nature*, vol. 378, no. 6553, pp. 258–260, 1995.
- [18] H. Morisaki, H. Hashimoto, F. W. Ping, H. Nozawa, and H. Ono, "Strong blue light emission from an oxygen-containing Si fine structure," *Journal of Applied Physics*, vol. 74, no. 4, pp. 2977–2979, 1993.
- [19] K. A. Littau, P. J. Szajowski, A. J. Muller, A. R. Kortan, and L. E. Brus, "A luminescent silicon nanocrystal colloid via a high-temperature aerosol reaction," *Journal of Physical Chemistry*, vol. 97, no. 6, pp. 1224–1230, 1993.
- [20] Y. Maeda, N. Tsukamoto, Y. Yazawa, Y. Kanemitsu, and Y. Masumoto, "Visible photoluminescence of Ge microcrystals embedded in SiO<sub>2</sub> glassy matrices," *Applied Physics Letters*, vol. 59, no. 24, pp. 3168–3170, 1991.
- [21] M. Zacharias, J. Heitmann, R. Scholz, U. Kahler, M. Schmidt, and J. Bläsing, "Size-controlled highly luminescent silicon nanocrystals: a SiO/SiO<sub>2</sub> superlattice approach," *Applied Physics Letters*, vol. 80, no. 4, pp. 661–663, 2002.
- [22] L. Tsybeskov, K. D. Hirschman, S. P. Duttagupta, et al., "Fabrication of nanocrystalline silicon superlattices by controlled thermal recrystallization," *Physica Status Solidi A*, vol. 165, no. 1, pp. 69–77, 1998.
- [23] T. Shimizu-Iwayama, S. Nakao, and K. Saitoh, "Visible photoluminescence in Si<sup>+</sup>-implanted thermal oxide films on crystalline Si," *Applied Physics Letters*, vol. 65, no. 14, pp. 1814–1816, 1994.
- [24] L. Patrone, D. Nelson, V. Safarov, M. Sentis, and W. Marine, "Size dependent photoluminescence from Si nanoclusters produced by laser ablation," *Journal of Luminescence*, vol. 80, no. 1–4, pp. 217–221, 1998.
- [25] R. A. Bley and S. M. Kauzlarich, "A low-temperature solution phase route for the synthesis of silicon nanoclusters," *Journal of the American Chemical Society*, vol. 118, no. 49, pp. 12461–12462, 1996.
- [26] C. Lam, Y. F. Zhang, Y. H. Tang, C. S. Lee, I. Bello, and S. T. Lee, "Large-scale synthesis of ultrafine Si nanoparticles by ball milling," *Journal of Crystal Growth*, vol. 220, no. 4, pp. 466–470, 2000.
- [27] O. Akcikir, J. Therrien, G. Belomoin, et al., "Detection of luminescent single ultrasmall silicon nanoparticles using fluctuation correlation spectroscopy," *Applied Physics Letters*, vol. 76, no. 14, pp. 1857–1859, 2000.
- [28] E.-C. Cho, Y.-H. Cho, T. Trupke, R. Corkish, G. Conibeer, and M. A. Green, "Silicon nanostructures for all-silicon tandem solar cells," in *Proceedings of the 19th European Photovoltaic Solar Energy Conference and Exhibition*, p. 235, Paris, France, June 2004.
- [29] N.-M. Park, T.-S. Kim, and S.-J. Park, "Band gap engineering of amorphous silicon quantum dots for light-emitting diodes," *Applied Physics Letters*, vol. 78, no. 17, pp. 2575–2577, 2001.
- [30] S. Lombardo and S. U. Campisano, "Electrical and optical properties of semi-insulating polycrystalline silicon thin films: the role of microstructure and doping," *Materials Science and Engineering*, vol. 17, no. 8, pp. 281–336, 1996.
- [31] Y. Cho, E.-C. Cho, Y. Huang, T. Trupke, G. Conibeer, and M. A. Green, "Silicon quantum dots in SiN<sub>x</sub> matrix for third generation photovoltaics," in *Proceedings of the 20th European Photovoltaic Solar Energy Conference and Exhibition*, p. 47, Barcelona, Spain, June 2005.
- [32] Y. Kurokawa, S. Miyajima, A. Yamada, and M. Konagai, "Preparation of nanocrystalline silicon in amorphous silicon carbide matrix," *Japanese Journal of Applied Physics*, vol. 45, no. 40, pp. L1064–L1066, 2006.
- [33] D. Song, E.-C. Cho, Y.-H. Cho, et al., "Evolution of Si (and SiC) nanocrystal precipitation in SiC matrix," (In press) *Thin Solid Films*.
- [34] J. Y. Fan, X. L. Wu, and P. K. Chu, "Low-dimensional SiC nanostructures: fabrication, luminescence, and electrical properties," *Progress in Materials Science*, vol. 51, no. 8, pp. 983–1031, 2006.
- [35] J. Zi, H. Büscher, C. Falter, W. Ludwig, K. Zhang, and X. Xie, "Raman shifts in Si nanocrystals," *Applied Physics Letters*, vol. 69, no. 2, pp. 200–202, 1996.
- [36] D. Kovalev, H. Heckler, M. Ben-Chorin, G. Polisski, M. Schwartzkopff, and F. Koch, "Breakdown of the *k*-conservation rule in Si nanocrystals," *Physical Review Letters*, vol. 81, no. 13, pp. 2803–2806, 1998.
- [37] Y. Kanemitsu, "Light-emitting silicon materials," *Journal of Luminescence*, vol. 70, no. 1–6, pp. 333–342, 1996.
- [38] H. Takagi, H. Ogawa, Y. Yamazaki, A. Ishizaki, and T. Nakagiri, "Quantum size effects on photoluminescence in ultrafine Si particles," *Applied Physics Letters*, vol. 56, no. 24, pp. 2379–2380, 1990.
- [39] S. Takeoka, M. Fujii, and S. Hayashi, "Size-dependent photoluminescence from surface-oxidized Si nanocrystals in a weak confinement regime," *Physical Review B*, vol. 62, no. 24, pp. 16820–16825, 2000.
- [40] T.-Y. Kim, N.-M. Park, K.-H. Kim, et al., "Quantum confinement effect of silicon nanocrystals in situ grown in silicon nitride films," *Applied Physics Letters*, vol. 85, no. 22, pp. 5355–5357, 2004.
- [41] T.-W. Kim, C.-H. Cho, B.-H. Kim, and S.-J. Park, "Quantum confinement effect in crystalline silicon quantum dots in silicon nitride grown using SiH<sub>4</sub> and NH<sub>3</sub>," *Applied Physics Letters*, vol. 88, no. 12, Article ID 123102, 3 pages, 2006.
- [42] A. Puzder, A. J. Williamson, J. C. Grossman, and G. Galli, "Surface control of optical properties in silicon nanoclusters," *Journal of Chemical Physics*, vol. 117, no. 14, pp. 6721–6729, 2002.
- [43] M.-S. Yang, K.-S. Cho, J.-H. Jhe, et al., "Effect of nitride passivation on the visible photoluminescence from

- Si-nanocrystals,” *Applied Physics Letters*, vol. 85, no. 16, pp. 3408–3410, 2004.
- [44] L. Van Dao, X. Wen, M. T. T. Do, et al., “Time-resolved and time-integrated photoluminescence analysis of state filling and quantum confinement of silicon quantum dots,” *Journal of Applied Physics*, vol. 97, no. 1, Article ID 013501, 5 pages, 2005.
- [45] M. Dovrat, Y. Goshen, J. Jedrzejewski, I. Balberg, and A. Sa’ar, “Radiative versus nonradiative decay processes in silicon nanocrystals probed by time-resolved photoluminescence spectroscopy,” *Physical Review B*, vol. 69, no. 15, Article ID 155311, 8 pages, 2004.
- [46] S. Ossicini, F. Iori, E. Degoli, et al., “Understanding doping in silicon nanostructures,” *IEEE Journal on Selected Topics in Quantum Electronics*, vol. 12, no. 6, pp. 1585–1590, 2006.
- [47] G. Polisski, D. Kovalev, G. Dollinger, T. Sulima, and F. Koch, “Boron in mesoporous Si—where have all the carriers gone?” *Physica B*, vol. 273–274, pp. 951–954, 1999.